Lecture Notes in Electrical Engineering 526

Banmali S. Rawat
Aditya Trivedi
Sanjeev Manhas
Vikram Karwal *Editors*

Advances in Signal Processing and Communication

Select Proceedings of ICSC 2018

Springer

Lecture Notes in Electrical Engineering

Volume 526

Lecture Notes in Electrical Engineering (LNEE) is a book series which reports the latest research and developments in Electrical Engineering, namely:

- Communication, Networks, and Information Theory
- Computer Engineering
- Signal, Image, Speech and Information Processing
- Circuits and Systems
- Bioengineering
- Engineering

The audience for the books in LNEE consists of advanced level students, researchers, and industry professionals working at the forefront of their fields. Much like Springer's other Lecture Notes series, LNEE will be distributed through Springer's print and electronic publishing channels.

More information about this series at http://www.springer.com/series/7818

Banmali S. Rawat · Aditya Trivedi
Sanjeev Manhas · Vikram Karwal
Editors

Advances in Signal Processing and Communication

Select Proceedings of ICSC 2018

Springer

Editors
Banmali S. Rawat
University of Nevada, Reno
Reno, NV, USA

Aditya Trivedi
Atal Bihari Vajpayee Indian Institute of Information Technology and Management, Gwalior
Gwalior, Madhya Pradesh, India

Sanjeev Manhas
Indian Institute of Technology Roorkee
Roorkee, Uttarakhand, India

Vikram Karwal
Jaypee Institute of Information Technology
Noida, Uttar Pradesh, India

ISSN 1876-1100 ISSN 1876-1119 (electronic)
Lecture Notes in Electrical Engineering
ISBN 978-981-13-2552-6 ISBN 978-981-13-2553-3 (eBook)
https://doi.org/10.1007/978-981-13-2553-3

Library of Congress Control Number: 2018954032

This Springer imprint is published by the registered company Springer Nature Singapore Pte Ltd.
The registered company address is: 152 Beach Road, #21-01/04 Gateway East, Singapore 189721, Singapore

Committee

Chief Patron

Sh. Jaiprakash Gaur Ji
Sh. Manoj Gaur Ji

Patron

Prof. S. C. Saxena

General Chair

Prof. Hari Om Gupta
Prof. R. C. Jain

Advisory Committee

Prof. Banmali S. Rawat, University of Nevada, Reno
Prof. Vinod Kumar, IIT Roorkee
Prof. George Jandieri, University of Georgia
Prof. Thomas Otto, Deputy Director of Fraunhofer ENAS and Head of the Department
Prof. Pistora Jaromir, VŠB-Technical University of Ostrava, Czech Republic
Prof. Babau R. Vishvakarma, BHU, Varanasi
Prof. J. W. Tao, Département Electronique et traitement du signal, Ecole Nationale Supérieure d'Electrotechnique, d'Electronique, d'Informatique, d'Hydraulique et des Télécommunications
Prof. N. Gupta, BIT, Mesra, Ranchi
Prof. D. Singh, IIT Roorkee
Prof. R. Bahl, IIT Delhi
Prof. Arun Kumar, IIT Delhi
Prof. Ekram Khan, AMU, Aligarh
Prof. K. N. Venkatesh, IIT Kanpur
Prof. M. M. Suffiyan Beg, AMU, Aligarh

Prof. Omar Farooq, AMU, Aligarh
Prof. Sudhanshu Maheshwari, AMU, Aligarh

Keynote Speaker

Prof. Banmali S. Rawat, University of Nevada, Reno, USA
Prof. Thomas Otto, Deputy Director of Fraunhofer ENAS and Head of the Department
Dr. Reinhard Streiter, Professor, Fraunhofer Institute for Electronic Nano Systems (ENAS)
Dr. Ing. Michal Lesňák, Department of Physics, VŠB-Technical University of Ostrava, Czech Republic
Prof. Rajeev Saxena, Director, Jaypee University, Anoopshahr
Mr. TaranjitKukal, Senior Architect, Cadence Design Systems
Prof. Satyabrata Jit, BHU
Prof. Ashok De, DTU

Organizing Secretary

Prof. Shweta Srivastava

Editors

Prof. Banmali S. Rawat, University of Nevada, Reno, Reno, USA
Prof. Aditya Trivedi, ABV-IIITM, Gwalior, India
Dr. Sanjeev Manhas, IIT Roorkee, Roorkee, India
Dr. Vikram Karwal, Jaypee Institute of Information Technology, Noida, India

Technical Program Committee

Prof. B. K. Mohanty, JUET, Guna
Prof. Brahmjit Singh, NIT Kurukshetra
Prof. C. M. Markan, Dayalbagh Educational Institute, Agra
Prof. D. K. P. Singh, AIMT, Greater Noida
Prof. J. K. Rai, Amity University, Noida
Prof. J. S. Roy, KIIT, Bhubaneswar
Prof. Krishna Gopal, JIIT, Noida
Prof. M. M. Sufyan Beg, Zakir Husain College of Engineering and Technology, AMU
Prof. Mahesh Chandra, BIT, Mesra
Prof. Manoj Kumar Singh, Institute of Science, BHU, Varanasi
Prof. Mridula Gupta, University of Delhi, Delhi
Prof. P. K. Sahu, NIT Rourkela, Odisha
Prof. S. K. Ghorai, BIT, Mesra
Prof. Sunil Bhooshan, JUIT, Waknaghat
Prof. V. R. Gupta, BIT, Mesra
Dr. A. K. Gautam, GBPEC, Uttarakhand
Dr. A. K. Mohapatra, IGDTUW, Delhi
Dr. Abhinav Gupta, JIIT, Noida

Dr. Adesh Kumar, UPES, Dehradun
Dr. Adhish Prasoon, Samsung Research, Noida
Dr. Ajay Singh Raghuvanshi, NIT Raipur
Dr. Alok Joshi, JIIT, Noida
Dr. Amit Singhal, JIIT, Noida
Dr. Angshul Majumdar, IIIT Delhi
Dr. Anil Kumar Shukla, Amity University, Noida
Dr. Anil Kumar, IIIT Jabalpur
Dr. Anubha Gupta, IIIT Delhi
Dr. Anuj Kumar, CBRI, Roorkee
Dr. Anurag Singh Baghel, GBU, Greater Noida
Dr. Archana Pandey, JIIT, Noida
Dr. Arjun Kumar, Bennett University, Greater Noida
Dr. Arun Khosla, NIT Jalandhar
Dr. Arun Kumar, NUS, Singapore
Dr. Arvind Kumar Pandey, Meerut Institute of Engineering and Technology, Meerut
Dr. Ashish Bagwari, NIT Kurukshetra
Dr. Ashish Goel, JIIT, Noida
Dr. Ashish Gupta, JIIT, Noida
Dr. Astik Biswas, Stellenbosch University, South Africa
Dr. B. Acharya, NIT Raipur
Dr. B. N. Tiwari, Intel Corporation, USA
Dr. Bajrang Bansal, JIIT, Noida
Dr. Baljit Kaur, NIT Delhi
Dr. Bhagwan Das, Tun Hussein Onn University, Malaysia
Dr. Bhartendu Chaturvedi, JIIT, Noida
Dr. Bhaskar Gupta, Thapar University, Patiala
Dr. Brajesh Kumar Kaushik, IIT Roorkee
Dr. Deepak Joshi, IIIT Delhi
Dr. Deepali Sharma, GTBIT, Delhi
Dr. Devesh Singh, AKGEC, Ghaziabad
Dr. Dharmendra Kumar Jhariya, JIIT, Noida
Dr. Dharmendra Kumar, MMMUT, Gorakhpur
Dr. Dinesh Vishwakarma, DTU, Delhi
Dr. Garima Kapur, JIIT, Noida
Dr. Gopi Ram Hardel, VIT University, Vellore
Dr. Govind Moormu, IIT-ISM, Dhanbad
Dr. Hari Shankar Singh, Thapar University, Patiala
Dr. Hemdutt Joshi, Thapar University, Patiala
Dr. Hemender Pal Singh, Amity University, Noida
Dr. J. S. Saini, DCR University, Sonipat
Dr. Jasmine Saini, JIIT, Noida
Dr. Jitendra Kumar, IIT-ISM, Dhanbad
Dr. Jitendra Mohan, JIIT, Noida
Dr. K. K. Pattanaik, IIITM, Gwalior

Dr. K. L. Pushkar, MAIT, Delhi
Dr. K. Soami Dayal, Dayalbagh Educational Institute, Agra
Dr. Kapil Dev Tyagi, JIIT, Noida
Dr. Kuldeep Baderia, JIIT, Noida
Dr. Kuldeep Singh, Scientist, BEL
Dr. Kushmanda Saurav, IIT Kanpur
Dr. Lotika Singh, Dayalbagh Educational Institute, Agra
Dr. M. K. Meshram, BHU, Varanasi
Dr. Madhu Jain, JIIT, Noida
Dr. Mamta Khosla, NIT Jalandhar
Dr. Manish Goswami, IIIT Allahabad
Dr. Manish Km. Singh, NIT Hamirpur
Dr. Manoj Duhan, DCR University, Sonipat
Dr. Meenakshi Sood, JUIT, Waknaghat
Dr. Megha Agarwal, JIIT, Noida
Dr. Megha Dadel, BIT, Mesra
Dr. Mohammed Israel, Al Jouf University, Kingdom of Saudi Arabia
Dr. Mohd Sharique, AMU, Aligarh
Dr. Mona Aggarwal, NCU, Gurugram
Dr. Nafis U. Khan, JUIT, Waknaghat
Dr. Neeta Pandey, DTU, Delhi
Dr. Nidhi Goel, IGDTUW, Delhi
Dr. Nikhil Rajput, DU, Delhi
Dr. Nikhil Sharma, LNMIIT, Jaipur
Dr. Nitin Rakesh, Amity University, Noida
Dr. Pankaj Yadav, JIIT, Noida
Dr. Parul Puri, JIIT, Noida
Dr. Pawan Verma, MNNIT, Allahabad
Dr. Pradeep Kumar Chauhan, University of KwaZulu-Natal, Durban, South Africa
Dr. Pradeep Kumar, JUIT, Waknaghat
Dr. Pramod K. Tiwari, IIT Patna
Dr. Pramod Kumar Singhal, MITS, Gwalior
Dr. Prerana Gupta Poddar, BMS College, Bangalore
Dr. Pushpendra Singh, Bennett University, Greater Noida
Dr. R. K. Chauhan, MMMUT, Gorakhpur
Dr. Radha Raman Pandey, IIT-ISM, Dhanbad
Dr. Raghvendra Chaudhary, IIT Kanpur
Dr. Raghvendra Kumar Chaudhary, IIT-ISM, Dhanbad
Dr. Rahul Kaushik, JIIT, Noida
Dr. Rajeeb Jena, NTU, Singapore
Dr. Rajesh Kumar Dubey, JIIT, Noida
Dr. Rajeshwari Pandey, DTU, Delhi.
Dr. Ravi Kumar Gangwar, IIT-ISM, Dhanbad
Dr. Ravinder Dahiya, Glasgow University, UK
Dr. Richa Gupta, JIIT, Noida

Dr. Richa Srivastava, AKGEC, Ghaziabad
Dr. Richa Yadav, IGDTUW, Delhi
Dr. Rishi Srivastava, Graphic Era Hill University, Dehradun
Dr. S. K. Mohapatra, KIIT, Bhubaneswar
Dr. S. Kumar, BIT, Mesra
Dr. S. Kumar, Troy University, USA
Dr. S. Sampath, JSSATE, Noida
Dr. Sachin Kumar, SRM University, Chennai
Dr. Sachin Singh, NIT Delhi
Dr. Sajai Vir Singh, JIIT, Noida
Dr. Samar Ansari, AMU, Aligarh
Dr. Sandeep Kumar, NIT Silchar
Dr. Sanjay Kumar Soni, GBPEC, Uttarakhand
Dr. Santanu Dwari, IIT-ISM, Dhanbad
Dr. Sanya Anees, IIIT Guwahati
Dr. Sarang Thombere, FGI, NLS, Finland
Dr. Satish K Singh, IIIT Allahabad
Dr. Satish Kumar Singh, JIIT, Noida
Dr. Shailendra Tripathi, MNIT Jaipur
Dr. Shamim Akhter, JIIT, Noida
Dr. Shrivishal Tripathi, IIT Jodhpur
Dr. Sudheer Sharma, LNMIIT, Jaipur
Dr. Sunildatt Sharma, JUIT, Waknaghat
Dr. Surbhi Sharma, Thapar University, Patiala
Dr. Sushrut Das, IIT-ISM, Dhanbad
Dr. Tapan Gandhi, IIT Delhi
Dr. Tarek Djerafi, University of Montreal, Canada
Dr. Tirupathiraju Kanumuri, NIT Delhi
Dr. Varun Bajaj, IIIT Jabalpur
Dr. Vibhor Kant, LNMIIT, Jaipur
Dr. Vijay Khare, JIIT, Noida
Dr. Vikram Karwal, JIIT, Noida
Dr. Vikrant Bhateja, SRMGPC, Lucknow
Dr. Vinay Kumar, Thapar University, Patiala
Dr. Vineet Khandelwal, JIIT, Noida
Dr. Vipin balyan, CPUT, Capetown, South Africa
Dr. Vipin Vats, Philadelphia
Dr. Viranjay Srivastava, University of KwaZulu-Natal, Durban, South Africa
Dr. Vishal Jain, Bharati Vidyapeeth, Delhi
Dr. Vivek Dwivedi, JIIT, Noida
Dr. Wriddhi Bhowmik, HIT, Haldia

Messages

MANOJ GAUR
Executive Chairman

JAIPRAKASH
ASSOCIATES LIMITED

15 March, 2018

Message

It gives me immense pleasure to know that the **Department of Electronics and Communication Engineering, Jaypee Institute of Information Technology, Noida** is organizing an **"International Conference on Advances in Signal Processing and Communication (ICSC 2018)" from 21st - 23rd March, 2018**.

I am confident that the outcome of this conference will be very informative to all researchers, academicians and scientists working in various fields of Signal Processing, Communication, VLSI Technology and Embedded Systems. I am certain that this conference will provide a broad range of information about recent developments and emerging future growth in these areas.

I would like to express my thanks to all authors for their outstanding contributions in emerging technology. Likewise, I would also express my appreciation to the organizing committee and wish them a grand success in the organization of this conference.

Manoj Gaur

JAYPEE GROUP

Corp. & Regd. Office: Sector-128, Noida - 201 304, Uttar Pradesh (India)
Ph. : +91 (120) 4963100 Direct : +91 (120) 4972140 / 4972141
Fax : +91 (120) 4972777, 4972160 E-mail : manoj.gaur@jalindia.co.in
Delhi Office : JA House, 63, Basant Lok, Vasant Vihar, New Delhi-110 057 (India)
CIN : L14106UP1995PLC019017 Website: www.jalindia.com

Jaypee Institute of Information Technology
(Declared Deemed to be University u/s 3 of the UGC Act)

March 14 , 2018

Prof. (Dr.) S. C. Saxena
Vice-Chancellor

Message

I am very much delighted to know that the **Department of Electronics and Communication Engineering, Jaypee Institute of Information Technology, Noida** is organizing an **"International Conference on Advances in Signal Processing and Communication (ICSC 2018)" from 21st - 23rd March 2018.**

I am certain that this conference will provide opportunities for students, researchers and scientists to share their research, get new ideas, valuable feedback and suggestions for their research studies. I am sure that the conference will prove a highly rewarding experience for the participants.

I convey my best wishes to the organizers and participants and wish a grand success to the conference.

I am looking forward to seeing you in ICSC 2018, JIIT Noida.

With best wishes,

(S.C Saxena)

Preface

Welcome to 2018 International Conference on Signal Processing and Communication

On behalf of Jaypee Institute of Information Technology (JIIT), Noida, it gives us immense pleasure to welcome you all to the 2018 International Conference on Signal Processing and Communication (ICSC 2018). This event is being organized by the Department of Electronics and Communication Engineering, JIIT, with technical co-sponsorship of Springer.

Signal processing and communication play a significant role in the growth of this technology-dominant era. Over the years, this field of study has been developed to give great advancement in the areas of microchips, digital systems, and computer hardware. The applications of signal processing are vast and interdisciplinary, ranging from engineering to economics, astronomy to biology, sports to smart grids, and much more. Sports like cricket and tennis use the Hawk-Eye system which uses the real-time signal processing for decision review. In this connected world, we talk about the Internet of things (IoT), where inter-networked smart devices embedded with electronics, software, sensors, and actuators are capable of collecting and exchanging data.

There is always a need to meet the ever-increasing demand for providing a forum to scientists and researchers to discuss and put forward their ideas and research findings with the co-researchers from all over the world. ICSC 2018 will provide an opportunity to highlight recent developments and to identify emerging and future areas of growth in these exciting fields. It will further give impetus to the researchers toward bringing out newer and efficient techniques.

ICSC 2018 will certainly be an excellent platform for close interaction, discussion, and presentation. The conference would definitely benefit the participants and the authors whose quality papers have been accepted for the presentation in this conference, in the fields of signal processing, communication, VLSI technology, and embedded systems. With the participation of several experts and their diverse areas of research, it is expected that the conference will help in meeting the future

challenges of the industry, academia, and research. The conference will be addressed by keynote speakers of eminence including

1. Prof. Banmali S. Rawat, University of Nevada, Reno, USA
2. Prof. Thomas Otto, Deputy Director of Fraunhofer ENAS and Head of the Department
3. Dr. Reinhard Streiter, Professor, Fraunhofer Institute for Electronic Nano Systems (ENAS)
4. Dr. Ing. Michal Lesňák, Department of Physics, VŠB-Technical University of Ostrava, Czech Republic
5. Prof. Rajeev Saxena, Director, Jaypee University, Anoopshahr
6. Mr. Taranjit Kukal, Senior Architect, Cadence Design Systems
7. Prof. Satyabrata Jit, BHU
8. Prof. Ashok De, DTU

We look forward to your active participation and discussion on current research areas in signal processing, communication, VLSI technology, and embedded systems.

Organizing Committee
ICSC 2018

Contents

Part I Communication

Photonic Crystal Fiber (PCF) Raman Amplifier 3
Abdelghafor Elgamri and Banmali S. Rawat

Recent Trends in IoT and Its Requisition with IoT Built Engineering: A Review 15
Arun Kumar, Ayodeji Olalekan Salau, Swati Gupta and Krishan Paliwal

Mathematical Analysis of Commonly Used Feeding Techniques in Rectangular Microstrip Patch Antenna 27
Ekta Thakur, Dinesh Kumar, Naveen Jaglan, Samir Dev Gupta and Shweta Srivastava

A Miniaturized Elliptically Shaped Split Ring Resonator Antenna with Dual-Band Characteristics 37
Ashish Gupta and Raghvenda Kumar Singh

A Compact Fish Spear-Shaped UWB BPF with Dual Notch Bands Using SSIR Resonator 45
Dharmendra Kumar Jhariya and Akhilesh Mohan

News Analysis Using Word Cloud 55
Chandrapaul, Rounak Soni, Shubham Sharma, Hemraj Fagna and Sangeeta Mittal

Low-Complexity Side Information-Free Novel PTS Technique for PAPR Reduction in OFDM Systems 65
Samriti Kalia and Alok Joshi

GA with SVM to Optimize the Dynamic Channel Assignment for Enhancing SIR in Cellular Networks 73
Sharada N. Ohatkar and Dattatraya S. Bormane

Deployment of a Wireless Sensor Network in the Presence of Obstacle and Its Performance Evaluation 85
Pratit Nayak, Ekta Nashine and Sanjeet Kumar

Analysis of Empty Substrate-Integrated Waveguide H Plane Horn Antenna for K Band Applications 95
Abhay Kumar, Nitin Muchhal, Arnab Chakraborty and Shweta Srivastava

PAPR Reduction Comparison in FFT-Based OFDM Versus DWT-Based OFDM 107
Alok Joshi, Apoorv Manas, Samarth Garg and Rahul Wason

Slot Integrated Folded Substrate Integrated Waveguide Bandpass Filter for K Band Applications 117
Nitin Muchhal, Tanvi Agrawal, Abhay Kumar, Arnab Chakraborty and Shweta Srivastava

Mutation-Based Bee Colony Optimization Algorithm for Near-ML Detection in GSM-MIMO 125
Arijit Datta, Manish Mandloi and Vimal Bhatia

Novel Substrate-Integrated Waveguide Incorporated with Band-Pass Filter 137
Tanvi Agrawal, Nitin Muchhal and Shweta Srivastava

PAPR Reduction Analysis of OFDM Systems Using GA-, PSO-, and ABC-Based PTS Techniques 145
Alok Joshi, Aashi Garg, Esha Garg and Nayna Garg

An Active Polarization-Insensitive Ultrathin Metamaterial Absorber with Frequency Controllability 157
Prakash, Mayank Agarwal and Manoj Kumar Meshram

The Internet of Things: A Vision for Smart World 165
Brahmjit Singh

Part II Signal Processing

Special Pedestrian and Head Pose Detection for Autonomous Vehicles 175
Sachin Shetty, S. M. Meena, Uday Kulkarni and Harish Basavaraj Hebballi

Sorted Outlier Detection Approach Based on Silhouette Coefficient 187
Pooja Lodhi, Omji Mishra and Dharmveer Singh Rajpoot

The Terrain's Discrimination Criterion for the Lengthened Objects Identification 199
Artem K. Sorokin and Vladimir G. Vazhenin

Effective Way to Simulate the Radar's Signal Multi-path Propagation 211
Alexander S. Bokov, Artem K. Sorokin and Vladimir G. Vazhenin

Distributed Arithmetic Based Hybrid Architecture for Multiple Transforms 221
Meghna Nair, I. Mamatha and Shikha Tripathi

Real-Time Video Surveillance for Safety Line and Pedestrian Breach Detection in a Dynamic Environment 233
Arjun Prakash, Santosh Verma and Shivam Vijay

Human Activity Recognition in Video Benchmarks: A Survey 247
Tej Singh and Dinesh Kumar Vishwakarma

SITO Type Voltage-Mode Biquad Filter Based on Single VDTA 261
Chandra Shankar, Sajai Vir Singh, Ravindra Singh Tomar and Vinay A. Tikkiwal

Despeckling of Medical Ultrasound Images Using Fast Bilateral Filter and NeighShrinkSure Filter in Wavelet Domain 271
Amit Garg and Vineet Khandelwal

Density-Based Approach for Outlier Detection and Removal 281
Sakshi Saxena and Dharmveer Singh Rajpoot

An Improved Design Technique of Digital Finite Impulse Response Filter for Notch Filtering 293
Anil Kumar, Kuldeep Baderia, G. K. Singh, S. Lee and H.-N. Lee

Leakage Reduction in Full Adder Circuit Using Source Biasing at 45 nm Technology 307
Candy Goyal, Jagpal Singh Ubhi and Balwinder Raj

Dual-Mode Quadrature Oscillator Based on Single FDCCII with All Grounded Passive Components 317
Bhartendu Chaturvedi, Jitendra Mohan and Atul Kumar

Hybrid Color Image Watermarking Algorithm Based on DSWT-DCT-SVD and Arnold Transform 327
Palak Garg, Lakshita Dodeja, Priyanka and Mayank Dave

A Brief Study and Analysis to Investigate the Effect of Various Dielectric Materials on Substrate-Integrated Waveguide 337
Fatima Haider and Megha Dade

Multi-objective Cuckoo Search Algorithm-Based 2-DOF FOPD Controller for Robotic Manipulator 345
Himanshu Chhabra, Vijay Mohan, Asha Rani and Vijander Singh

Study of Noise Interfering with Dolphin Clicks 353
Kapil Dev Tyagi, Rajendar Bahl, Arun Kumar, Shivam Saxena and Sandeep Kumar

Optical Flow Estimation in Synthetic Image Sequences Using Farneback Algorithm 363
Shivangi Anthwal and Dinesh Ganotra

Development of Self-stabilizing Platform Using MPU-6050 as IMU 373
Vinayak Tripathi, Aditya Bansal and Richa Gupta

Real-Time Mental Workload Detector for Estimating Human Performance Under Workload 383
Rajesh Singla, Anand Agrawal, Vikas Kumar and Om Prakash Verma

De-seasoning-Based Time Series Data Forecasting Method Using Recurrent Neural Network (RNN) and Tensor Flow 393
Prashant Kaushik, Pankaj Yadav and Shamim Akhter

R-Peaks Detection Using Shannon Energy for HRV Analysis 401
Om Navin, Gautam Kumar, Nirmal Kumar, Kuldeep Baderia, Ranjeet Kumar and Anil Kumar

Index Seek Versus Table Scan Performance and Implementation of RDBMS 411
Akshit Manro, Kriti, Snehil Sinha, Bhartendu Chaturvedi and Jitendra Mohan

Industrial Simulation of PID and Modified-MPID Controllers for Coupled-Tank System 421
Rajesh Singla, Anand Agrawal, Vikas Kumar, Nikhil Pachauri and Om Prakash Verma

A VDCC-Based Grounded Passive Element Simulator/Scaling Configuration with Electronic Control 429
Pranjal Gupta, Mayank Srivastava, Aishwarya Verma, Arshi Ali, Ayushi Singh and Devyanshi Agarwal

Current Tunable Voltage-Mode Universal Biquad Filter Using CCTAs 443
Sajai Vir Singh and Ravindra Singh Tomar

Maximum Power Point Tracking Techniques for Photovoltaic System: A Review 455
Shikha Gupta, Omveer Singh and M. A. Ansari

Effect of Tonal Features on Various Dialectal Variations of Punjabi Language 467
Ashima Arora, Virender Kadyan and Amitoj Singh

Part III VLSI and Embedded Systems

Optical Functions of Methanol and Ethanol in Wide Spectral Range 479
Michal Lesňák, Kamil Postava, František Staněk and Jaromír Pištora

A Novel Method to Detect Program Malfunctioning on Embedded Devices Using Run-Time Trace 491
Garima Singhal and Sahadev Roy

Performance Analysis of Comparator for IoT Applications 501
Mansi Jhamb, Tejaswini Dhall and Tamish Verma

Adiabatic Logic Based Full Adder Design with Leakage Reduction Mechanisms 511
Dinesh Kumar and Manoj Kumar

IP Protection of Sequential Circuits Using Added States Watermark with Property Implantation 521
Ankur Bhardwaj and Shamim Akhter

Design of Low Power and High-Speed CMOS Phase Frequency Detector for a PLL 529
Nitin Kumar and Manoj Kumar

Comparative Analysis of Standard 9T SRAM with the Proposed Low-Power 9T SRAM 541
Balraj Singh, Mukesh Kumar and Jagpal Singh Ubhi

Fabrication and Characterization of Photojunction Field-Effect Transistor 553
Yogesh Kumar, Hemant Kumar, Gopal Rawat, Chandan Kumar, Varun Goel, Bhola N. Pal and Satyabrata Jit

Sarcasm Detection of Amazon Alexa Sample Set 559
Avinash Chandra Pandey, Saksham Raj Seth and Mahima Varshney

Reducing Efficiency Droop for Si-Doped Barrier Model of GaN/InGaN Multi-quantum Well Light-Emitting Diode by Designing Electron Blocking Layer 565
Pramila Mahala, Amit K. Goyal, Sumitra Singh and Suchandan Pal

Mole Fraction Dependency Electrical Performances of Extremely Thin SiGe on Insulator Junctionless Channel Transistor (SG-OI JLCT) 573
B. Vandana, Prashant Parashar, B. S. Patro, K. P. Pradhan, S. K. Mohapatra and J. K. Das

Analysis of Graphene/SiO_2/p-Si Schottky Diode by Current–Voltage and Impedance Measurements 583
Pramila Mahala, Ankita Dixit and Navneet Gupta

Simulation Study of Uncoupled Electrical Equivalent Model of Piezoelectric Energy Harvesting Device Interfaced with Different Electrical Circuits 591
Shradha Saxena, Rakesh Kumar Dwivedi and Vijay Khare

Variability Study Using α-Power-Based MOSFET Model for Ultradeep Submicron Digital Circuit Design 601
Shruti Kalra and A. B. Bhattacharyya

Field-Plated AlInN/AlN/GaN MOSHEMT with Improved RF Power Performance 611
Satya Narayan Mishra, Kanjalochan Jena, Rupam Goswami and Anand Agrawal

Analysis of RSNM and WSNM of 6T SRAM Cell Using Ultra Thin Body FD-SOI MOSFET 619
Vimal Kumar Mishra, Narendra Yadava, Kaushal Nigam, Bajrang Bansal and R. K. Chauhan

About the Editors

Prof. Banmali S. Rawat received his Ph.D. in electronics and communication engineering from Sri Venkateswara University, Tirupati, in 1976. He joined DRDO, India, as Senior Scientist in 1975. In 1981, he joined the Department of Electrical Engineering, University of North Dakota, and was Professor until 1988 before moving to the University of Nevada, Reno, as Professor and Head of the Department of Electrical Engineering and Computer Science. He has been a consultant to many top organizations and is also a visiting professor in various technical institutions. He is Fellow of IETE, CIE, The Electromagnetics Academy established at MIT, JSPS, Optical Society of India, Sigma Xi North, Optical Society of America, SPIE, and Eta Kappa Nu (IEEE-HKN), as well as Life Senior Member of IEEE. His areas of interest include the analysis, design, and fabrication of microstrip components, optical fiber communication, free space optical communication, microwave and millimeter wave systems, and wavelength division multiplexing.

Prof. Aditya Trivedi holds a Ph.D. in the area of wireless communication engineering from IIT Roorkee. Currently, he is Professor in the Department of Information and Communication Technology (ICT), ABV Indian Institute of Information Technology and Management, Gwalior. He has over 20 years of teaching experience. Before joining ABV-IIITM in 2006, he was Associate Professor in the Department of Electronics and Computer Science, MITS, Gwalior. He has published over 60 papers in various national and international journals and conference proceedings. He is Fellow of the Institution of Electronics and Telecommunication Engineers (IETE). In 2007, he was honored with the K. S. Krishnan Memorial Award for the best system-oriented paper by IETE. His areas of interest include digital communication, CDMA systems, signal processing, and networking.

Dr. Sanjeev Manhas completed his master's in Solid State Technology at IIT Madras and his Ph.D. in electronics and electrical engineering at De Montfort University, Leicester. He joined Tech Semiconductor, Singapore, as Member Technical Staff in 2003, and the Institute of Microelectronics, Singapore, as Senior

Research Engineer in 2007. Currently, he is Associate Professor at IIT Roorkee, India. His areas of interest include nanoscale MOSFET modeling and reliability, cantilever-based MEMs and application sensors, VLSI technology, DRAM leakage mechanisms, and organic thin-film transistors.

Dr. Vikram Karwal received his M.S. and Ph.D. in electrical and computer engineering from the University of North Carolina, Charlotte. He is Associate Professor in the Department of Electronics and Communication Engineering at the Jaypee Institute of Information Technology, Noida. He is Senior Member of IEEE, Life Member of the Institute of Electronics and Telecommunication Engineers (IETE), and Life Member of the Indian Society for Technical Education (ISTE). He is also Member of Eta Kappa Nu (IEEE-HKN). His current research interests are in estimation theory and distributed networks.

Part I
Communication

Photonic Crystal Fiber (PCF) Raman Amplifier

Abdelghafor Elgamri and Banmali S. Rawat

Abstract An accurate design for a Photonic Crystal fiber (PCF) Raman amplifier has been developed. In this PCF, the geometric parameters, Raman gain coefficient, effective mode area, the Germania concentration in the doped area, and dispersion and confinement loss characteristics have been investigated at 1.55 μm. The flexibility of the geometrical parameters and doping concentrations that allowed to optimize these parameters to increase the amplifier efficiency have been studied. For $\bigwedge = 3.2$ μm, $d_1 = 1.44$ μm, $d_2 = 1.47$ μm, Raman gain coefficient of 9.25 $W^{-1}km^{-1}$ and almost zero dispersion are achieved for 7.5 km low loss hexagonal Photonic Crystal Fiber with an effective area of 20 μm^2.

Keywords Photonic Crystal Fiber (PCF) · Raman amplifier · Effective area Confinement loss · FDTD · Nonlinear optics

1 Introduction

After the arrival of optical fiber technology in the early 1970s, the use and demand of optical fibers have grown at a rapid rate. The increasing demand for bandwidth with high capacity for handling vast amount of information due to Internet, multimedia, voice data, and video has made fiber optics with its comparatively infinite bandwidth the only solution. Recently, there has been growing interest in fiber Raman amplifiers due to their capability to upgrade the wavelength-division multiplexing bandwidth and arbitrary gain bandwidth product which is determined by the pump wavelength only and the low noise figure. In the last few years, photonic crystal fibers have been widely modeled, studied, and fabricated due to their special properties such as endless

A. Elgamri · B. S. Rawat (✉)
Department of Electrical and Biomedical Engineering, University of Nevada, Reno, NV 89557, USA
e-mail: rawat@unr.edu

A. Elgamri
e-mail: abdu.elgamri@gmail.com

B. S. Rawat et al. (eds.), *Advances in Signal Processing and Communication* ,
Lecture Notes in Electrical Engineering 526,
https://doi.org/10.1007/978-981-13-2553-3_1

single-mode, high-nonlinearity, very high numerical aperture, strong birefringence multicore designs, and unusual chromatic dispersion properties. The objective of this paper is to develop and simulate a zero dispersion and low confinement loss photonic crystal fiber Raman amplifier.

2 Photonic Crystal Fiber Structure Used for Analysis

The PCF structure analyzed in this paper is Hexagonal Photonic Crystal Fiber (HPCF), i.e., the air holes around the core are arranged in hexagonal shape. Thus, the hole diameter (d) and the pitch Λ offer better flexibility to demonstrate the propagation mechanism in PCF and to analyze the design parameters. The azimuth view of the basic two-dimensional hexagonal lattice photonic crystal is shown in Fig. 1. As it was shown that the central area with no holes has higher refractive index, similar to the core in the conventional fibers.

OptiFDTD is used in this analysis to run 2D-FDTD numerical simulation for the PCF structure in Fig. 1. The excitation of the field pattern in the first step results in the steady-state oscillations in the periodic cells. Figure 2 is used to do FDTD simulation and analysis for a pure silica fiber with hexagonal air hole shape along the fiber axis.

As shown in Fig. 2, the confinement of the light wave in the core is possible for the modes that satisfy Maxwell's equations. The input field used is Sine-Modulated Gaussian Pulse that has 2.262 (μm) full width at $1/e^2$ and amplitude of 1 (V/m). The corresponding propagating mode has power of 0.634 (V/m) and confinement loss of 0.289 (V/m). These losses are due to the leaky nature of the modes and the PCF non-perfect structure. However, by controlling the geometrical structure parameters (hole and pitch diameters) and the operating wavelength, these losses can be minimized and the modes are guided inside the core.

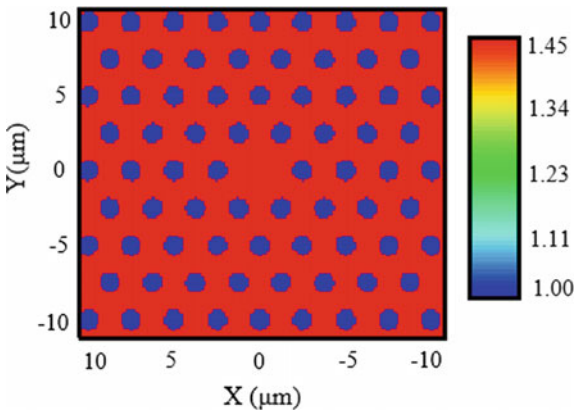

Fig. 1 Structure of photonic crystal fiber with air fraction ratio (d/Λ) = 0.45

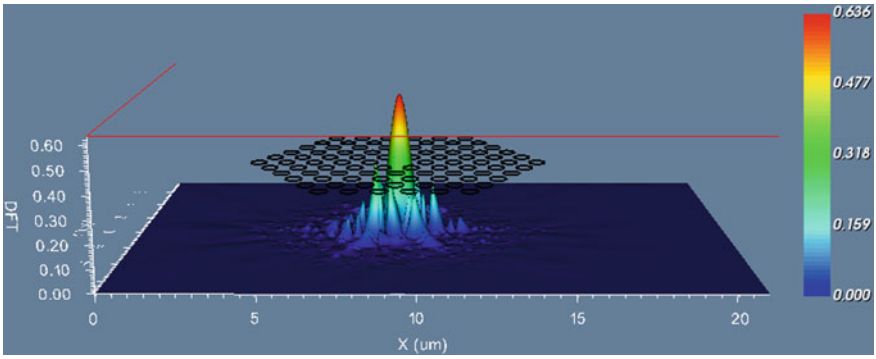

Fig. 2 Propagation of modes through Hexagonal PCF at $\lambda = 1.5$ μm

3 PCF Raman Amplification Model

In this section, parameters such as the ratio of the hole to pitch diameter, the pitch, GeO2 concentration, and the effective doped core area are chosen to obtain maximum Raman amplification. Raman amplification properties for Hexagonal PCF are investigated by manipulating the geometrical parameters (d, Λ). As a consequence, the cladding effective index is changed. Thus, the propagating field distribution, effective area, and Raman gain coefficient are modified. The PCF is considered a silica bulk fiber with Λ between 0.4 and 4.8 μm and d/Λ=0.45, 0.6, 0.75, 0.9 [1]. The profile of Raman effective area and Raman gain coefficients as a function of the pitch is presented in Fig. 3. (a)and (b), respectively. Here, the Raman gain coefficient is inversely proportional to the effective area. Thus, for fixed (d/Λ) PCF and the optimum value of Λ (≈ 1.5 μm in this case), the effective cross section area is minimized to maximize the Raman gain coefficient. This situation is obtained by applying a very narrow high field in a small core radius PCF with large difference between the core and the cladding refractive indices.

In addition, the smallest effective area occurs in PCF with $d/\Lambda = 0.9$ and results in the largest Raman amplification coefficient. However, in spite of high Raman coefficient, high Raman amplification is not achieved due to high attenuation losses and high nonlinearity in the fiber [2]. The effect of adding Germania dopants on PCF core is shown in Fig. 4. GeO_2 concentration has been increased from 0 to 20% for PCFs with fixed air fraction ratio, $d/\Lambda = 0.45$, 0.60, 0.75, and 0.90 with $\Lambda = 3.5$ μm. The effect of increasing the doping level (GeO_2) on the effective mode index is given in Table 1 [2]. Raman gain coefficient is calculated for each PCF structure.

However, in this case, Raman gain coefficient γ_R is not inversely proportional to A_{eff} like silica bulk PCF shown in Fig. 3. This is because it depends on the amount of the field that lies in the Germania-doped region. Hence, maximum value of γ_R does not necessarily occur at minimum A_{eff}. It is important to mention that the PCF core

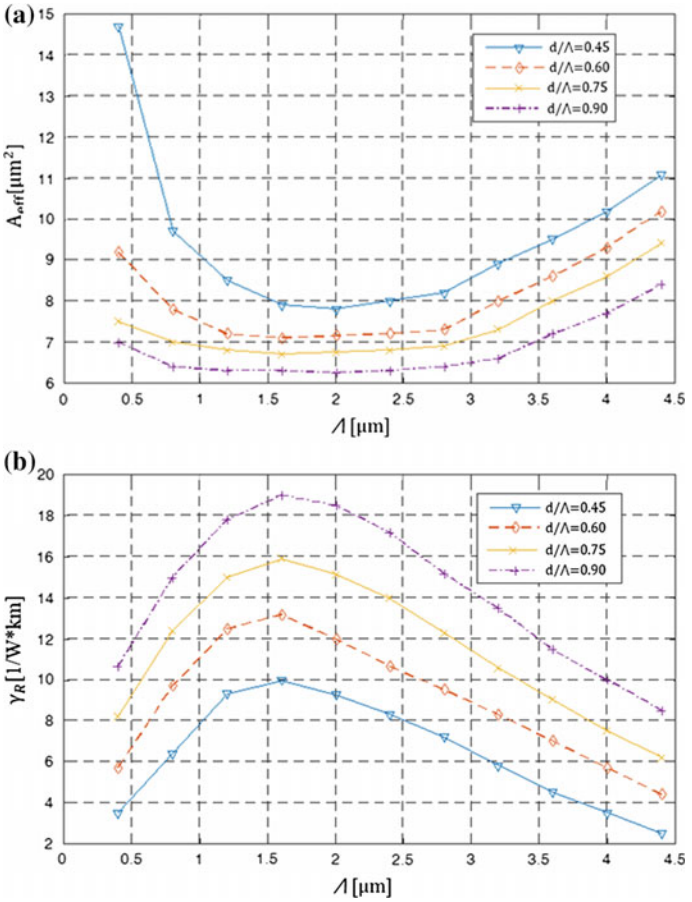

Fig. 3 **a** Raman effective area for different PCFs structures as function of the pitch $\bigwedge$. **b** Raman gain coefficient for different PCFs structures as function of the pitch $\bigwedge$

Table 1 Effective refractive index for different doping levels [2]

Refractive index *(n)*	Effective refractive index *Re* (n_{eff})	Effective refractive index *Im* (n_{eff})
1.46 (pure silica)	1.44037166	0.000000102
1.48	1.46048416	0.000000123
1.49	1.47054253	0.000000132
1.60	1.58124464	0.000000197

radius R_c is calculated using $R_c = \bigwedge - d/2$ to obtain the minimum A_{eff}. This is according to the optimal combination between the core dimension and core-cladding refractive index difference. Doped PFCs have shown great improvement in γ_R so that

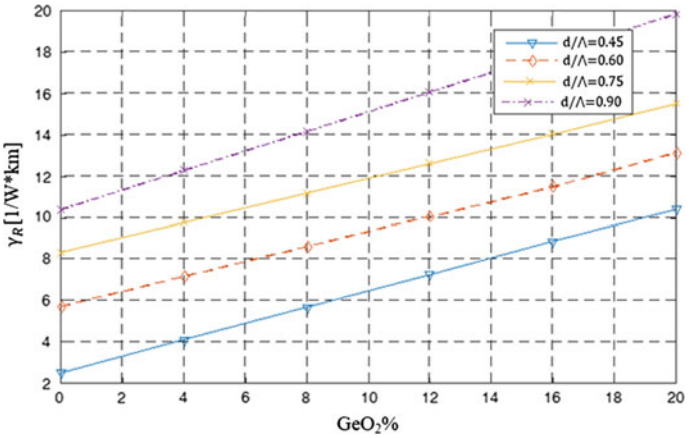

Fig. 4 Raman gain coefficient as function of Germania concentration with $\Lambda = 3.5\ \mu m$

Table 2 Comparison between Raman gain coefficients for different fibers

Fiber type	$\gamma_R[W^{-1}km^{-1}]$
Single-Mode Fiber (SMF)	0.50
Nonzero Dispersion-Shifted Fiber (NZ-DSF)	0.75
Dispersion-Shifted Fiber (DSF)	0.75
Dispersion-Compensation Fiber (DCF)	3
Raman Amplifier Fiber (RA)	5

value as high as 20 $[W^{-1}km^{-1}]$ is calculated for 20% GeO_2 concentration. Table 2 compares peak γ_R obtained here with other commercially available fibers to show the large enhancement achieved using doped PCFs [3].

4 PCF Attenuation and Dispersion Analysis

Attenuation and dispersion in PCF are caused by almost the same mechanisms found in conventional fibers such as, confinement loss, bending losses, local imperfections, polarization loss, and Rayleigh scattering. However, the effects of these mechanisms on the overall loss, the level of each of them, and their dependence on wavelength are different from conventional fibers. The minimum level of attenuation of ≈ 0.15 dB/km achieved in conventional fibers is limited by material absorption and fundamental scattering in bulk silica glass. In PCFs, most of the light propagates in

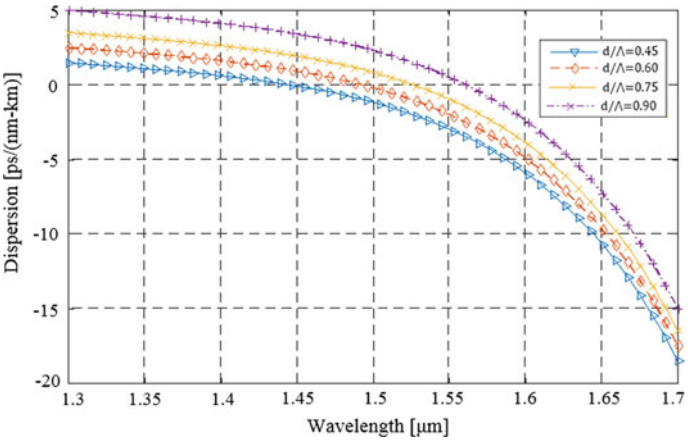

Fig. 5 Chromatic dispersion curve as function of wavelength

the air, and in Hollow Core Photonic Crystal Fibers (HC-PCF), 99% of the light propagates in air. Thus, decreasing the bulk attenuation below 0.002 dB/km is achievable. The effective mode refractive index (n_{eff}) at a given wavelength is calculated using FDTD method to solve Maxwell's equations for any guided mode and is given by

$$n_{eff} = \frac{\beta}{k_0}, k_0 = \frac{2\pi}{\lambda} \tag{1}$$

where β is the propagation constant and the k_0 is free space wave number. The n_{eff} is described by both real and imaginary parts. Hence, chromatic dispersion D (λ) and confinement loss (L_c) are obtained from

$$D(\lambda) = -\frac{\lambda}{c}\frac{d^2 Re[n_{eff}]}{d\lambda^2} \tag{2}$$

$$L_c = 8.868 \times k_0 \times Im[n_{eff}] \tag{3}$$

In Fig. 5, the chromatic dispersion for four different PCFs structures is compared. As shown, the change obtained in the dispersion is small, and it increases by increasing the air fraction ratio. For $d/\Lambda = 0.9$ at $\lambda = 1.55\,\mu m$, the positive dispersion is obtained as 2.345 ps/(nm–km). Thus, in order to reduce the dispersion, the hole diameter needs to be reduced. On the other hand, as shown in Fig. 6, the confinement loss decreases as the hole diameter increases. At 1.55 μm wavelength, the confinement loss is 0.352 dB/km for $d/\Lambda = 0.45$ and 0.189 dB/km for $d/\Lambda = 0.45$.

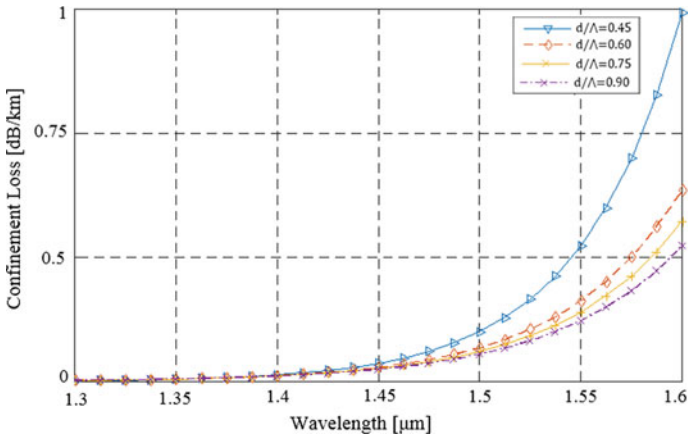

Fig. 6 Confinement loss curve as function of wavelength

5 PCF Scattering Loss Analysis

In addition to dispersion and confinement losses, PCFs are limited by scattering losses which depend on the wavelength, effective index, and surface roughness.

5.1 Surface Roughness

Surface roughness occurs due to Surface Capillary Waves (SCWs) existing during PCF fabrication. As glass solidifies, the SCWs freeze, creating a surface roughness given by the Spectral Density δ(κ) as [4]:

$$\delta(\kappa) = \frac{k_B T_g}{4\pi\gamma\kappa} \coth\left(\frac{\kappa W}{2}\right) \tag{4}$$

where κ is the spatial frequencies between κ and κ + dκ, γ is the surface tension, T_g is the glass transition temperature, and W is the hole perimeter.

5.2 Dependence on Effective Index

The surface roughness causes some of the light energy to scatter from the fundamental mode with refractive index n_0 to other scattered mode with refractive index n.

The overlapping between the fundamental mode and the surface mode F is approximated by

$$F = \left(\frac{\varepsilon_0}{\mu_0}\right) \frac{\oint_{\text{hole perimeter}} |\boldsymbol{E}|^2 dl}{\oint_{\text{cross section}} \boldsymbol{E} \times \boldsymbol{H}^* dA} \tag{5}$$

where E and H are the electric and magnetic field distributions of the fundamental mode, respectively. The fraction of power α_n (n) scattered from those modes is obtained as

$$\alpha_n(n) \propto \frac{F}{|n - n_0|} \tag{6}$$

This equation represents the intensity of the scattered modes by effective index and thus, the direction of scattering.

5.3 Dependence on Wavelength

From the two previous sections, the attenuation is proportional to the intensity of roughness component between n and $n + \delta_n$ given by

$$u^2 = \frac{4k_B T}{4\pi\gamma(n - n_0)} \coth\left(\frac{(n - n_0)kW}{2}\right)\delta_n \tag{7}$$

where k_B is Boltzmann constant and T is the temperature. The attenuation to these modes is proportional to u^2 Attenuation unit is inverse length, and hence it is inversely proportional to the cube of the minimum attenuation wavelength (λ_c). So that the net attenuation α is given by

$$\alpha(\lambda_c) \propto \frac{1}{\lambda_c^3} \tag{8}$$

For the PCF amplifier design, the experimental values of attenuation reported by *Katsusuke Tajima and Jian Zhoue* in [5] are used as the attenuation reference for the PCF amplifier.

6 PCF Raman Amplifier Design

The design is based on *Saeed Olyaee's* modeled successfully using Finite-Difference Time Domain (FDTD) method. In addition, PCF dispersion and confinement losses are analyzed for a chosen wavelength, a low confinement loss, almost zero dispersion, and small effective area PCF was designed using FDTD. The PCF design is based

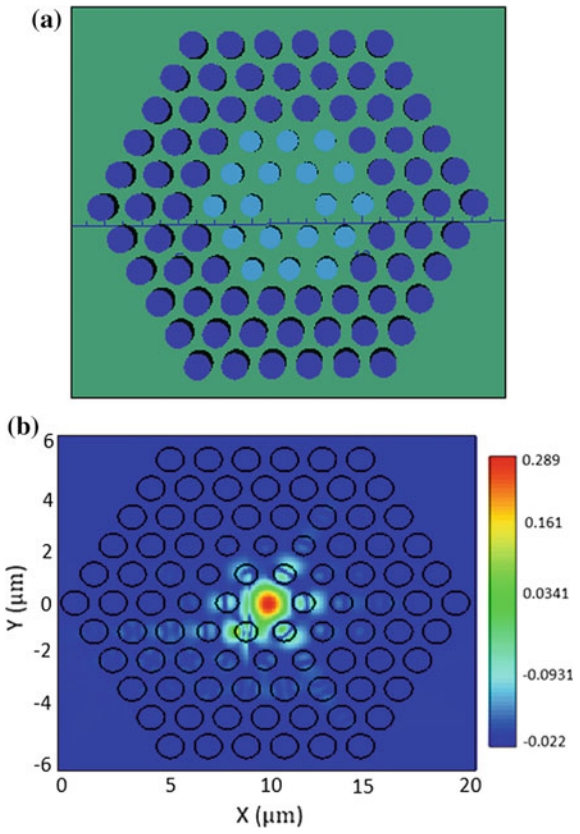

Fig. 7 **a** PCF structure with $\Lambda = 3.46$, $d_1 = 0.95$ and $d_2 = 0.95$. **b** PCF mode field distribution

on the simple equal air hole structure shown in Fig. 1. Reducing the air fraction ratio decreases the dispersion but at the same time, it increases the confinement loss. Therefore, the structure has a small d/Λ rate and the low confinement loss is achieved by changing the outer air holes diameter. The design is shown in Fig. 7(a) and (b). The structure parameters are described in Table 3.

As seen, the ultra-loss fiber used as a medium has attenuation of 0.37 dB/km at 1.55 μm. Although it was not specifically designed for nonlinear applications but by manipulating the geometrical characteristics of the PCF amplifier (Λ, d_1, d_2, d/Λ, R_c) and the doping concentration levels (GeO_2), it was able to achieve Raman gain coefficient of 9.25 $\left[\mathrm{W}^{-1}\mathrm{km}^{-1}\right]$.

Table 3 Proposed PCF Parameters

Parameter	Sample	Value	Unit
Wavelength	λ	1.55	μm
Effective area	A_{eff}	20	μm^2
Raman gain coefficient	γ_R	9.25	$W^{-1}km^{-1}$
Attenuation losses	$\alpha(\lambda)$	0.37	dB/km
Doping level	GeO_2	*20%*	–
Inner hole diameter	d_1	1.44	μm
Outer hole diameter	d_2	1. *74*	μm
Pitch	$\bigwedge$	3.2	μm
Air fraction ratio	$d/\bigwedge$	0.45	–
Core radius	R_c	*2.48*	μm
Dispersion	$D(\lambda)$	2.5×10^{-4}	Ps/(nm.km)
Confinement loss	L_c	15.34×10^{-4}	dB/km

7 Conclusion

A 2-D Hexagonal Photonic Crystal Fiber (PCF) and wave propagation have been modeled successfully using Finite-Difference Time Domain (FDTD) method. In addition, PCF dispersion and confinement losses are analyzed for a chosen wavelength, a low confinement loss, almost zero dispersion, and small effective area PCF were designed using small inner holes rings and big outer holes rings. This design has been developed for proposed PCF Raman amplifier because of the small effective area and the compatibility with low loss fiber optics. The properties of the proposed PCF Raman amplifier for different air hole fraction ratios have been thoroughly investigated. Moreover, the effect of the geometrical parameters and Germania dopant concentration levels on the PCF cross section have been investigated for the gain and noise performance. It was found that PCF suffers from high background loss for small effective areas. Thus, a trade-off between loss and PCF effective area has to be made to obtain high Raman gains. The gain and attenuation of the designed PCF-RA can be significantly improved using Vapor-Phase Axial Deposition (VAD) fabrication technique to prepare extremely pure optical glass fiber with very low attenuation and optimal optical properties. Moreover, eliminating the presence of OH contamination improves the gain and reduces the attenuation to a larger exert in small area PCF.

References

1. Biswas, S., Rafi, R.S., AbdullahAlAmin, M., Alam, S.: Analysis of the effect of air hole diameter and lattice pitch in optical properties for hexagonal photonic crystal fiber. Opt. Photonics J. **2015(** 5), 227–233 (2015)
2. Mahbub Hossain, M., Maniruzzaman, M.: Analysis of dispersion and confinement loss in photonic crystal fiber. In: International Conference on Electrical Engineering and Information and Communication Technology (ICEEICT) (2014)
3. Cucinotta, A., Selleri, S., Vincetti, L., Zoboli, M.: Holey fiber analysis through the finite-element method. IEEE Photon. Technol. Lett. **14**, 1530–1532 (2002)
4. Jäckle, J., Kawasaki, K.: Intrinsic roughness of glass surfaces. J. Phys.: Condens. Matter **7**, 4351–4358 (1995)
5. Tajima, K., Zhou, J., Nakajima, K., Sato, K.: Ultralow loss and long length photonic crystal fiber. J. Wavelength Technol. **22**(1) (2004)

Recent Trends in IoT and Its Requisition with IoT Built Engineering: A Review

Arun Kumar, Ayodeji Olalekan Salau, Swati Gupta and Krishan Paliwal

Abstract One of the trendy expressions in recent times in information technology is the Internet of Things (IoT). IoT is the connection and systems administration of physical devices, vehicles (additionally alluded to as "savvy gadgets" and "associated gadgets"), structures, and different things connected to hardware, sensors, actuators, programming, and system network, which empower these gadgets (devices) to gather and exchange information. Recent trends in IoT have changed the present reality of device Interconnectivity on a network into insightful virtual connections of machines over the Internet. In the light of this, recent research tends to introduce new innovations in the area of IoT through a thorough review of academic research papers, corporate white papers, and proficient exchanges of knowledge with specialists and evaluation of research results with online databases. Nonetheless, in this paper, we present a review of recent works in IoT and also, propose a framework for IoT and its requisition for IoT built Engineering.

Keywords IoT · Internet · WSN · RFID · Raspberry Pi

A. Kumar · S. Gupta · K. Paliwal (✉)
Department of Electronics and Communication,
Kurukshetra University, Kurukshetra, India
e-mail: director@piet.co.in

A. Kumar
e-mail: ranaarun1@gmail.com

S. Gupta
e-mail: swatigupta13@gmail.com

A. O. Salau
Department of Electronic and Electrical Engineering,
Obafemi Awolowo University, Ile-Ife, Nigeria
e-mail: ayodejisalau98@gmail.com

B. S. Rawat et al. (eds.), *Advances in Signal Processing and Communication* ,
Lecture Notes in Electrical Engineering 526,
https://doi.org/10.1007/978-981-13-2553-3_2

1 Introduction

The Internet of Things (IoT) is a vital field, which in recent times has brought about a number of innovations in industries, network technologies, cyber-physical systems, informatics, and in the field of intelligent transportation systems (ITS). These innovations are encapsulated in a wide range of organized items, frameworks, electronics, and sensors, which exploit headways in processing power, hardware scaling down, and arranged device interconnections to offer new abilities that are not yet fully harnessed in the field of IoT. These innovations are advantageous to individuals with inabilities and also to the elderly. This is achieved by empowering enhanced levels of freedom and personal satisfaction at a low cost. IoT frameworks like connected vehicles, wise activity frameworks, and sensors implanted in streets for intelligent traffic control and management, and further extensions, draw us nearer to "brilliant urban communities", which help to limit blockage and enhance vitality utilization [1]. Various organizations and research associations have offered a number of insightful projections about the potential effects of IoT on the Internet and economy amid the following 5–10 years. Companies like Cisco, for instance, expects more than 24 billion Internet-associated devices by 2019; Morgan Stanley, in any case, predicts the use of 75 billion arranged gadgets by 2020 on the IoT [2]. With the constant progression in innovations in IoT and its potential development, IoT is rapidly expanding as a pervasive worldwide registering system where everybody and everything will be associated with the Internet [3, 4]. IoT is constantly advancing and is fast becoming a hot research subject where innovations are boundless. Creative abilities are unlimited which puts it among one of the hottest and most divisive topics in information technology. The number of gadgets (devices) connected to the web is expanding each day and having each of them connected by wire or remotely will readily make available a wellspring of data (big data). The idea of empowering connections between clever machines is a front line innovation; however, advances in IoT are still emerging [5]. IoT, as you can figure by its name, is a means of focalizing information got from various types of things to any virtual stage on existing Internet framework [6]. Typically, IoT is expected to offer advanced connectivity of devices, systems, and services that goes beyond machine-to-machine (M2 M) communication and covers a variety of applications, domains, and protocols as shown in Fig. 1. The interconnection of these embedded devices (including smart objects) is expected to introduce automation in nearly all fields. This will also enable advanced applications like smart grids and other areas such as smart cities to function efficiently.

Prior to IoT, there was a straightforward manual method for taking care of machine/device interconnectivity. However, with the headway in recent technology, better approaches need better acquaintance for controlling machines to preserve time, cost, and energy, i.e., in the health sector, in agriculture, health, and for mechanization. With the touch of a button, we can get an extensive measure of data because of proficiency in communication of machines, especially via the web. Everyone needs a competitive, yet secure approach to control and manage their machines.

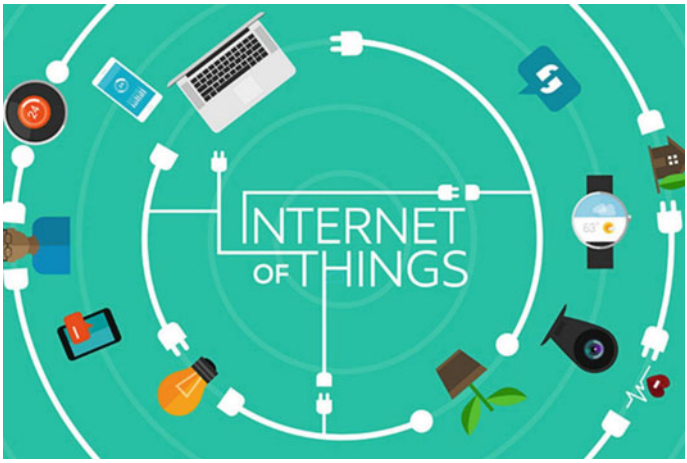

Fig. 1 IoT offers advanced connectivity of devices, systems, and services

In this paper, we present a review of recent trends in IoT and also, we propose a framework for IoT and discuss the various applications of IoT such as in industry and manufacturing processes.

2 Related Works

In each organization, there are various means of information dissemination for important message notification to their clients and staff [7]. IoT can be used to better enhance such task. In 2005, the International Telecommunication Union (ITU) revealed a pervasive systems administration period in which everyone on the system were interconnected and everything from tires to clothing types were a piece of this gigantic system, with the sole aim of information sharing, dissemination, and control [8]. In [9], a roadmap for future research interest in the area of IoT, various technological trends in IoT and its numerous applications were presented. Similarly, the authors in [10] presented an approach for the future architecture of the IoT. They included a review of recent developments and also presented a technical design for possible implementation of the future IoT.

The authors in [11], discussed the future challenges in IoT and furthermore presented a state-of-the-art review of recent applications of IoT technology and the different perspectives in academics and the industrial community. Some of the challenges highlighted were how to improve the degree of smartness of interconnected devices by enabling their adaptation and autonomous behavior, meanwhile guaranteeing security and privacy of the users and their data. A factor in designing an IoT is the task of integrating the wireless sensor networks (WSNs) with the Internet. Typically, this is quite a challenging task [12], three ways have been pointed out for

integrating WSNs with the Internet for the effective communication of devices over the network. Also, a possible implementation in an emergency response application is presented.

IoT aims at device communication via the Internet, information sharing, and dissemination to perform errands through machine learning. However, extraordinary individuals and associations have their own diverse dreams for the IoT [13]. In reality, IoT alludes to wisely associated gadgets and frameworks to assemble information from connected sensors, actuators, and other physical items. IoT is required to spread quickly in the coming years. In [14], a cloud-centric approach for the worldwide implementation of IoT is presented. This cloud approach employs the use of Aneka, which is an interactive platform for private and public clouds. Their research finding pointed out the need for expanding the possibility of convergence of WSN, the Internet, and distributed computing directed at developing technological research communities. In [15], the authors presented a framework of IoT for Singapore transportation network. The proposed framework utilizes IoT for the commuter to comprehend and assess distinctive transport alternatives in a productive way. In [16], a three-layered system development of IoT specialized technique for high-voltage transmission line which includes WSNs, optical ground wire (OPGW), and general packet radio service (GPRS) was presented. The work in [17] highlighted different architectural models for the IoT and identified their related functionalities. Furthermore, in [18], a survey of the existing IoT Architecture was presented.

3 Applications

Most applications used today are already smart but still are unable to communicate with each other. Solving this challenge will enable a wide range of applications to operate effectively in an IoT application as depicted in Fig. 2. Areas where IoT can be applied include brilliant homes, wearables which are discussed in Sects. 3.1 and 3.2 respectively. In addition to these, innovations in the savvy city, mechanical web, associated auto, associated health and keen inventory network are now common.

3.1 Brilliant Home

Brilliant home devices like Internet refrigerators, structured wiring, and others have unmistakably emerged as the most featured application of IoT presently, positioning itself as the most astounding IoT application which is highly sought after. At present, more than 60,000 individuals search for the expression “Keen Home” every month. This is not a shock, as the IoT analytics organization database for Smart Home is made up of 256 new businesses, organizations, and companies [19]. A greater number of the organizations are vast in keen home technology than some other applications in the field of IoT. This is noticed from the aggregate sum of financing for Smart Home,

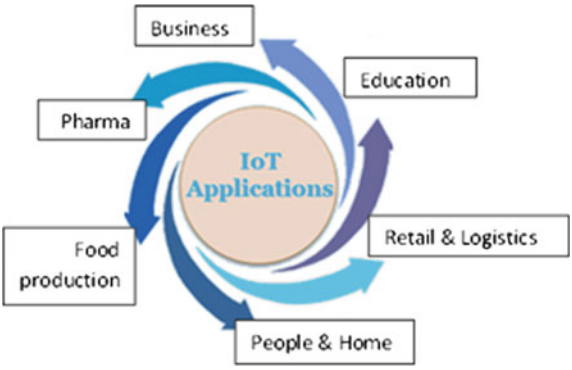

Fig. 2 IoT applications

which is now greater than $2.5bn [20]. This rundown includes startup names, i.e., Alert Me or Nest and not excluding various multinational organizations like Philips, Belkin, or Haier.

3.2 Wearables

Wearables like smart watches, fitness trackers, tech togs, or fashion electronics remain an intriguing issue. As customers anticipate the arrival of Apple's new savvy in April 2015, there are a number of other wearable advancements to look out for: like the Look See arm jewelry, the Myo signal control or the Sony Smart B Trainer. Noticeably, among the new IoT companies, wearable creator Jawbone are most likely the ones with the highest subsidized rates till date.

4 Technologies

The improvement of a universal framework where digital objects can be remarkably recognized and can have the capacity to think and cooperate with different devices to gather information on the premise of which mechanized moves are made, requires a blend of new and successful innovations which is conceivable through a mixture of various advancements which can make the devices to be distinguished and communicate more efficiently. In this segment, we discuss the significant advances that are contributing to the vast improvement of IoT.

4.1 Radio-Frequency Identification (RFID)

RFID is an important innovation which is used in device identification. Its cost and small size make it integrate easily with any device [21]. It is a handset microchip that is like a cement sticker which could be both dynamic and inactive, contingent depending on its use. Dynamic labels have a battery appended to them because they are constantly dynamic and they consistently produce information signals while passive labels simply get initiated when activated. Dynamic labels are more expensive than the passive labels and have an extensive variety of valuable applications.

4.2 Wireless Sensor Network (WSN)

A WSN is a bidirectional remotely associated system of sensors in a multi-bounce form, which works from a few hubs scattered in a sensor field each associated with one or more sensors which gather the devices' particular information, for example, temperature, speed, etc., and after that pass them to the control center [22].

4.3 Cloud Computing

With a huge number of gadgets anticipated to be connected to the Internet by 2020, the cloud is by all accounts the most significant innovation that can break down and cause loss of stored information. It is a smart processing innovation, which houses a number of servers information on one cloud stage to permit sharing of assets between each other which can be retrieved whenever and wherever [23].

4.4 Nanotechnologies

This is a part of the technology that acknowledges little and enhanced adaptation of the things that are interconnected that are about a billionth of a meter in size. It can diminish the utilization of a framework by empowering the improvement of gadgets in nanometers which can be utilized as a sensor and an actuator simply like an ordinary gadget. Such a nanogadget is produced using nanoparts and the subsequent system characterizes another systems administration called the Internet of Nano-Things [24].

4.5 Optical Technologies

Fast advancements in the field of optical technology such as Li-Fi and Cisco's Bi-Directional (BiDi) innovations are a noteworthy leap forward for the improvement of Li-Fi, IoT, and visible light communication (VLC) innovative research. These give an extraordinary availability and higher transmission capacity for items interconnected through IoT technology. Likewise, BiDi innovations are likely to use up 40G of Ethernet for major information from diverse gadgets.

5 Proposed IoT Framework

In computer science, client–server may be a product building design model comprising of two parts, customer frameworks and also server systems, both connected through a workstation system alternately on the same machine. A client–server requisition will be a conveyed framework made dependent of claiming both client and furthermore server product as shown in Fig. 3. Customer (client) server provision furnishes a fine path to drive the workload. The customer continuously initiates a connection with the server, at the same time the server procedure constantly sits tight to solicit for the customer. The point when both the customer requisition and server procedure run on the same computer is called a 'single seat setup'.

Internet of things (IoT) interconnects installed frameworks. It requires two evolving technologies: remote connectivity with more keen sensors joined with other devices clinched alongside a microcontroller. These new "things" are constantly associated with the web, undoubtedly and inexpensively introducing a second mechanical upset.

The proposed framework is divided into three parts namely: the client, the server, and an Internet connection. A control supply is given, sensors begin sensing the relating parameters and connections are made as shown in Fig. 4. The information gathered by the sensors will eventually be stored and transmitted to the op amplifier which is interfaced with the Raspberry Pi framework through the analog-to-digital converter (ADC) as shown in Fig. 5.

Fig. 3 Server/Client model

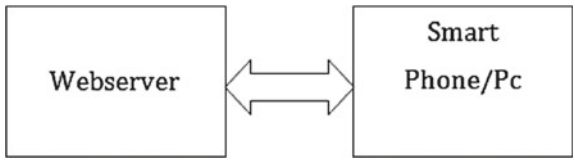

Fig. 4 Block diagram of server operation

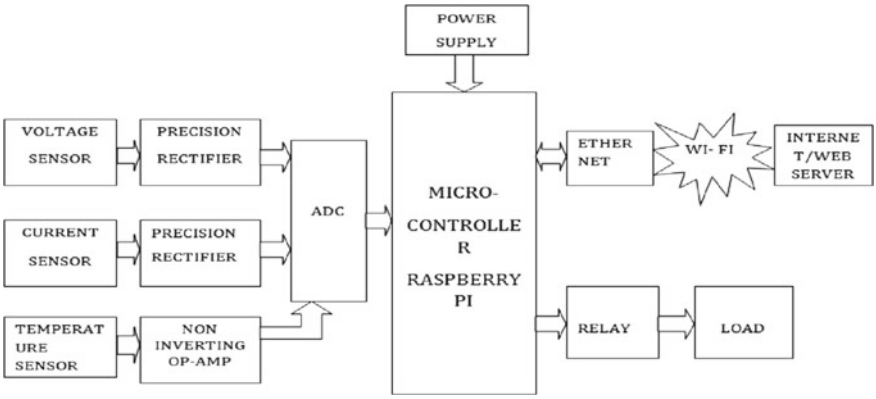

Fig. 5 Block diagram of the proposed framework showing client and server subsections

At the same time, the sensed qualities are uploaded onto the webpage. The authorized individuals can log in by utilizing a username and password.

5.1 Client Operation

5.1.1 Raspberry Pi

A Raspberry Pi contains an ARMv6 CPU, 256 or 512 MB RAM, although many models have been developed after this. For example, the ARM11 processor (Raspberry Pi) utilizes low power and is a 32-bit processor for RISC construction modeling. Furthermore, it is mounted on a PCB alongside reset out and clock out.

5.1.2 Relay

The relay in Fig. 5, performs the function of a switch. Most of the connected sensors are interfaced with the relay through the Raspberry Pi. This is, in turn, used to drive a load. Such loads (appliances) could include bulb, DC engine, and so forth.

5.1.3 Temperature Sensor

The temperature sensor is used to sense the temperature of chemical operations in industrial sites. It can also be used to monitor the temperature of machines, so they do not exceed their work limit. When the temperature surpasses specific temperature limit, then a warming notification will be triggered.

5.1.4 Precision Rectifier

The precision rectifier is an ideal diode or in another term, a super diode which performs the function of rectification. The precision rectifier is used to rectify fluctuations in current and voltage obtained from the sensors.

5.1.5 Web Server

The web server is a computer system used to process requests via the Hypertext Transfer Protocol (HTTP). The web server is used to host websites and to deliver content or services to end users over the Internet, i.e., contents are stored here. It is connected to the Raspberry Pi via wireless fidelity (Wi-Fi) to control necessary operations.

5.1.6 Voltage and Current Sensor

The voltage and current sensor are used to measure the voltage and current, respectively. The current sensor detects and monitors the change in current. When current flows through a wire or circuit, a voltage drop occurs as exemplified in Ohm's law. The sensor converts this current to an easily measured output voltage, which is directly proportional to the current that was measured.

6 Conclusion

IoT introduces a progressive, completely interconnected "shrewd" world, with connections among objects and individuals ending up more firmly interwoven. In this paper, we have presented the review of the key state-of-the-art developments in IoT and have also presented a low-cost framework for IoT for industries whose workers are far from their point of duty and who need to control different units of their operations. This framework will help to improve on the existing challenges in the architectural designs of existing IoT frameworks.

References

1. Pablo, V.: Internet of things: an overview. In: Information Week, pp. 1–50 (2015)
2. Cloud and Mobile Network Traffic Forecast-Visual Networking Index (VNI), Cisco (2015). http://cisco.com/c/en/us/solutions/serviceprovider/visual-networking-index-vni/index.html
3. Danova, T.: Morgan Stanley: 75 Billion Devices Will Be Connected to the Internet of Things by 2020. Business Insider (2013)
4. Khan, R., Khan, S. U., Zaheer, R., Khan, S.: Future internet: the internet of things architecture, possible applications and key challenges. In: Proceedings of Frontiers of Information Technology (FIT), pp. 257–260 (2012)
5. Shen, G., Liu, B.: The visions, technologies, applications and security issues of internet of things. In: International Conference of E-Business and E-Government (ICEE), pp. 1–4 (2011)
6. Zeng, L.: A security framework for internet of things based on 4G communication. In: International Conference of Computer Science and Network Technology (ICCSNT), pp. 1715–1718 (2012)
7. Salau, A.O., Ejidokun, A.O., Adewara, O., Ajala, O.S., Aliyu, E., Yesufu, T.K.: A GSM-based SMS power notification system for network operation centers. Int. J. Sci. Eng. Res. (IJSER). **8**(7), 830–837 (2017)
8. Dhillon, H.S., Huang, H., Viswanathan, H.: Wide-area Wireless communication challenges for internet of things. IEEE Commun. Mag. **55**(2), 168–174 (2017)
9. Vermesan, O., Friess, P., Gulliemin, P., Jubert, I. S., Mazura, M., Harrison, M., Eisenhauer, M., Doody, P.: Internet of things strategic research roadmap. In: Internet of Things-Global Technological and Societal Trends, pp. 9–52 (2011)
10. Uckelmann, D., Harrison, M., Michahelles, F.: An Architectural Approach towards the Future Internet of Things, Architecting the Internet of Things, pp. 1–24. Springer, Berlin (2011)
11. Bandyopadhyay, D., Sen, J.: Internet of things: applications and challenges in technology and standardization. Wirel. Personal Commun. Springer. **58**(1), 49–69 (2011)
12. Yang, S.H.: Internet of things. In: Wireless Sensor Networks. Signals and Communication Technology, Springer, London, pp. 247–261 (2014)
13. Takeshi, Y., Kobayashi, S., Koshizuka, N., Sakamura, K.: An internet of things (IoT) architecture for embedded appliances. In: IEEE Region 10 Humanitarian Technology Conference, Sendai, Japan, pp. 314–319 (2013)
14. Gubbi, J., Buyya, R., Marusic, S., Palaniswami, M.: Internet of things (IoT): a vision, architectural elements, and future directions. Future Gener. Comput. Syst. **29**(7), 1645–1660 (2013)
15. Menon, A., Sinha, R.: Implementation of internet of things in bus transport system of Singapore. In: Asian Journal of Engineering Research, pp. 5–15 (2013)
16. Rao, B.P., Saluia, P., Sharma, N., Mittal, A., Sharma, S.V.: Cloud computing for internet of things and sensing based applications. In: Sixth International Conference on Sensing Technology (ICST), IEEE, pp. 374–380 (2012)
17. Lee, G.M., Crespi, N., Choi, J.K., Boussard, M.: Internet of Things. Telecommunication Services Evolution, pp. 257–282. Springer, Berlin (2013)
18. Atzori, L., Iera, A., Morabito, G.: The internet of things: a survey. Comput. Netw. Sci. Direct **54**(15), 2787–2805 (2010)
19. Yoganathan, S.: Introduction to Internet of Things. Sachin Tech, Technology and Games (2017). http://www.sachintech.com/2017/07/iot-technology.html
20. Alaswad, T.A.M.: An Investigation into the Security Challenges and Implications Surrounding Smart Home Technologies. Unpublished B.Sc. Thesis, Cardiff Metropolitan University, pp. 39 (2017)
21. Lee, I., Lee, K.: The internet of things (IoT): applications, investments, and challenges for enterprises. Bus. Horiz. **58**(4), 431–440 (2015)

22. Akyildiz, I.F., Su, W., Sankarasubramaniam, Y., Cayirci, E.: Wireless sensor networks: a survey. Comput. Netw. **38**, 393–422 (2015)
23. Ma, H.D.: Internet of things: objectives and scientific challenge. In: Journal of Computer Science and Technology, pp. 919–924 (2011)
24. Akyildiz, I., Jornet, J.: The internet of nano things. IEEE Wirel. Commun. **17**(6), 58–63 (2010)

Mathematical Analysis of Commonly Used Feeding Techniques in Rectangular Microstrip Patch Antenna

Ekta Thakur, Dinesh Kumar, Naveen Jaglan, Samir Dev Gupta and Shweta Srivastava

Abstract In the presented work, different feeding techniques are employed to design microstrip patch antenna for wireless applications. These feeding techniques are as follows: microstrip inset feed, quarter wavelength feed, and coaxial probe feed. Parameters valuated for comparing these feeding techniques are: return loss, directivity, gain, and radiation efficiency. In the presented work, it is observed that by using coaxial probe feed, the values achieved for maximum directivity and gain are 5.43 dBi and 5.33 dB, respectively.

Keywords Microstrip patch antenna · Feeding techniques · Directivity · Gain Bandwidth

1 Introduction

The Microstrip Patch Antenna (MPA) antennas are popularly engaged for improving the performance of wireless application. This is due to their conformal structure, small

E. Thakur · D. Kumar · N. Jaglan
Department of Electronics and Communication Engineering,
Jaypee University of Information Technology, Solan, Himachal Pradesh, India
e-mail: ektathakurbu92@gmail.com

D. Kumar
e-mail: dineshparee@gmail.com

N. Jaglan
e-mail: naveen.jaglan@juit.ac.in

S. D. Gupta · S. Srivastava (✉)
ECE Department,
Jaypee Institute of Information Technology, Sector 128, Jaypee Wish Town Village, Sultanpur, Noida 201304, Uttar Pradesh, India
e-mail: shweta.srivastava@jiit.ac.in

S. D. Gupta
e-mail: samirdev.gupta@jiit.ac.in

B. S. Rawat et al. (eds.), *Advances in Signal Processing and Communication* ,
Lecture Notes in Electrical Engineering 526,
https://doi.org/10.1007/978-981-13-2553-3_3

size, moderate efficiency, lightweight, and ease of integration with active devices. The MPA consists of metallic ground plane, dielectric substrate, and radiating patch. The ground plane and patch are made up of conducting material like gold and aluminum whereas substrate is made up of dielectric material like RT/duroid, FR4, etc. There are multiple approaches to feed the microstrip antennas which are generally divided into two varieties namely, the contacting and the non-contacting approach [1]. In the former, the microstrip line is used to feed patch however, in the latter, the coupling is exploited to transfer the power among the patch and the microstrip line. In this microstrip feed line method, the radiating patch is connected to a straight feed using conducting copper strip line. The width of the microstrip line is less as compared to width of the patch. There are various substrates that are used to design and fabricate the antenna with dielectric constant ranging between $2.2 \leq \varepsilon_r \leq 12$ [1]. The coaxial feed or probe feed is mostly used to feed the MPA. Due to the easy implementation of the coaxial feed, it is one of the popular feeding techniques used. The internal and external conductors are separated by dielectric in the coaxial feed. The internal conductor of the coaxial feed is attached to the patch, while the external conductor is attached to the ground plane [2]. The MPA can also be designed using inset feed, which is the simplest method due to easy impedance matching.

Among the various non-contacting feeding techniques, proximity coupling [3] and aperture coupling are studied by the researchers [4]. In the former technique, the strip line is amid two dielectric substrates and the patch is on the top of upper substrate. In the latter technique, the ground plane is in between the patch and feed line. Among the four feeds discussed, the proximity coupling consumes the largest bandwidth despite its difficulty.

2 Antenna Design

For the better antenna performance, the thick dielectric substrate is used because it provides larger bandwidth and better radiation however, the thick dielectric substrate results in the large antenna dimension [4]. Moreover, the thick dielectric substrate has low dielectric constant value. The three antennas are simulated using high-frequency structure simulator (HFSS) software.

2.1 Coaxial Feed MPA Design

The MPA is designed at the frequency of 2.4 GHz, where the FR4 substrate is used with dielectric constant 4.7 and loss tangent 0.002. The parameters of the patch are calculated by using the given formulas.

The patch length is calculated by

$$L = L_{eff} - 2\Delta L \tag{1}$$

$$L_{eff} = \frac{c}{f\sqrt{\in_{eff}}} \tag{2}$$

where L, L_{eff} represents the length of the patch, effective length. The width and the effective dielectric constant of the patch is obtained by

$$W = \frac{c}{2f\sqrt{\in_r + 1}} \tag{3}$$

$$\in_{eff} = \frac{\in_r + 1}{2} + \frac{\in_r - 1}{2}\left(1 + 12\frac{h}{W}\right)^{-1/2} \tag{4}$$

where f, c, W, ε_r, h and ε_{eff} represents the resonant frequency, speed of light, width of the patch, dielectric constant, height of substrate, and effective dielectric constant, respectively. The effective length of the patch is $\mathrm{L} = \frac{\lambda}{2}$ for TM_{010} mode with no fringing [5].

$$\Delta L = 0.412h\frac{\left(\in_{eff} + 0.3\right)\left(\frac{W}{h} + 0.264\right)}{\left(\in_{eff} - 0.258\right)\left(\frac{W}{h} + 0.8\right)} \tag{5}$$

Characteristic impedance is given by [6]

$$Z_C = \begin{pmatrix} \frac{60}{\sqrt{\in_{eff}}}\ln\left(\frac{8h}{w_0} + \frac{w_0}{4h}\right) & \frac{w_0}{h} \le 1 \\ \frac{120\pi}{\sqrt{\in_{eff}}\left[\frac{w_0}{h} + 1.393 + 0.667\left(\frac{w_0}{h} + 1.444\right)\right]} & \frac{w_0}{h} \ge 1 \end{pmatrix} \tag{6}$$

where w_0 is the width of the microstrip line. The calculated effective dielectric $\left(\varepsilon_{eff}\right)$ is equal to 4.04.

Therefore, the length due to fringing effect (ΔL) is equal to 1.116 mm. Further, the calculated dimensions like width and length of patch of coaxial feed MPA are presented in Table 1. The calculated effective dielectric $\left(\varepsilon_{eff}\right)$ is equal to 4.04. The length and width of ground plane is the same as the substrate dimensions.

Table 1 Dimensions of coaxial feed MPA Design

Parameters	Values (mm)
Width of patch (W_{P1})	30
Length of patch ($\mathrm{L_{P1}}$)	39.5
Width of substrate ($\mathrm{W_{S1}}$)	90
Length of substrate ($\mathrm{L_{S1}}$)	100
Feeding point (Y_O)	4.3
Radius of internal conductor	0.7
Radius of external conductor	1.7

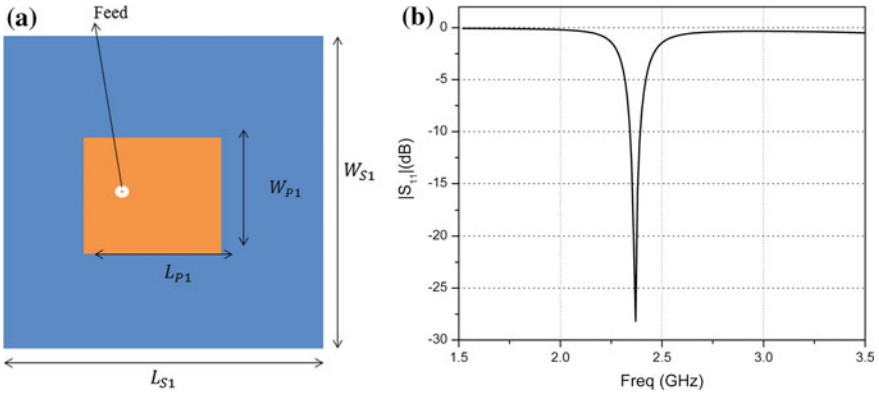

Fig. 1 **a** Antenna designed using coaxial probe feed. **b** Return loss of coaxial feed MPA

2.2 Results of Coaxial Probe Feed MPA

Return loss of the coaxial probe feed MPA at 2.4 GHz is −26 dB as shown in Fig. 1b. If the dip is below −10 dB, this means that 1/10th of incident power is reflected back at the interferences of the transmissions lines and the antenna [6]. Bandwidth achieved for 50 MHz is calculated by the formula given in Eq. (8). The return loss and bandwidth are given as [7]

$$RL = -20\log(\Gamma) \tag{7}$$

$$BW = \frac{(f_h - f_l)}{f_c} \times 100 \tag{8}$$

where the RL, Γ, BW, f_l, f_h, and f_c signify the return loss, reflection coefficient, bandwidth, lower frequency, upper frequency, and center frequency, respectively. The ideal matching between the transmitter and antenna is achieved when the reflection coefficient and RL is zero and 0 dB, respectively. This signifies that there is zero power reflected back however, when the reflection coefficient and RL is one and infinity, respectively, indicates the total reflection of incident power. The field pattern of the MPA with coaxial feed is obtained as Fig. 3a.

2.3 Inset Feed MPA Design

The impedance of feedline should match to the patch to obtain good antenna efficiency which can be achieved using inset feed. The input impedance can be altered by using an inset feed. The input resistance for the inset feed is calculated as [8]

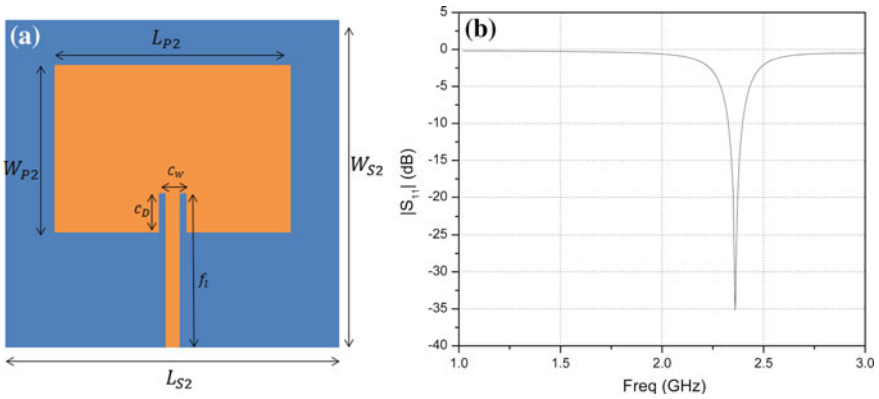

Fig. 2 **a** Antenna designed using inset feed. **b** Return loss of inset feed MPA

$$R_{in}(C_D) = \frac{1}{2(G_1 + G_{12})} \cos^2\left(\frac{\pi}{L} C_D\right) \tag{9}$$

$$G_1 = \begin{pmatrix} \frac{1}{90}\left(\frac{W}{\lambda}\right)^2 & W \ll \lambda \\ \frac{1}{120}\left(\frac{W}{\lambda}\right) & W \gg \lambda \end{pmatrix} \tag{10}$$

$$G_{12} = \frac{1}{120\pi^2} \int_0^{\pi} \left[\frac{\sin^2\left(\frac{k_0 W}{2}\right)^2}{\cos\theta}\right] J_0(k_0 \sin\theta) \sin^3\theta d\theta \tag{11}$$

where $R_{in}\ (C_D)$ is the input impedance at point C_D.

2.4 Results of Inset Feed MPA

Figure 2b illustrates the return loss of the inset feed. The calculated dimensions of inset MPA are shown in Table 2. The electric field plane and magnetic field plane pattern of a rectangular microstrip antenna with inset feed at 2.4 GHz center frequency shown in Fig. 3b [9] (Fig. 4).

2.5 Quarter Wavelength Feed MPA Design

The characteristic impedance of quarter wavelength transmission line [10–15]

$$Z_{in} = \frac{Z_0^2}{Z_A} \tag{12}$$

Table 2 Dimensions of inset feed MPA Design

Parameters	Values (mm)
Width of patch (W_{P2})	29.44
Length of patch (L_{P2})	38.04
Width of substrate (W_{S2})	49.75
Length of substrate (L_{S2})	50
Slot width (C_W)	2.4
Slot Depth (C_D)	5
Feed Length (f_l)	20
Feed width (f_w)	1.6

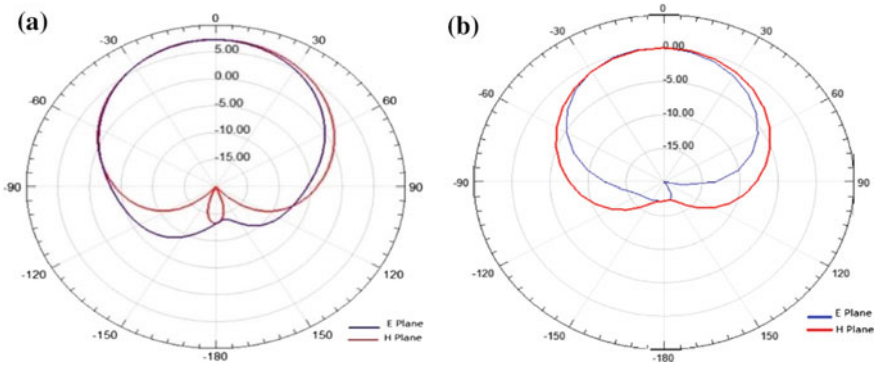

Fig. 3 **a** E plane and H plane of coaxial feed MPA. **b** E plane and H plane of inset feed MPA

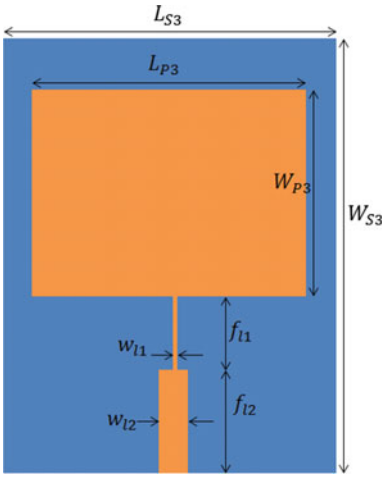

Fig. 4 Antenna designed using quarter wavelength feed

Table 3 Dimensions of quarter wavelength MPA

Parameters	Values (mm)
Width of patch (W_{P3})	29.26
Length of patch (L_{P3})	36.26
Width of substrate (W_{S3})	45
Length of substrate (L_{S2})	60.94
Feed length (f_{l1})	5
Feed length (f_{l2})	15
Feed width (w_{l1})	0.62
Feed width (w_{l2})	3.05

$$Z_0 = \sqrt{Z_A Z_{in}} \tag{13}$$

where Z_0 is characteristic impedance, Z_{in} is input impedance, and Z_A is load impedance. The calculated dimensions of quarter wavelength feed microstrip patch antenna is shown in Table 3.

2.6 Results of Quarter MPA Feed

The return loss of the quarter wavelength feed antenna at 2.4 GHz is −27 dB shown in Fig. 5b. The bandwidth achieved 80 MHz that is calculated by using Eq. (8). The radiation pattern of a rectangular microstrip antenna with quarter wavelength feed at 2.4 GHz center frequency shown in Fig. 5a.

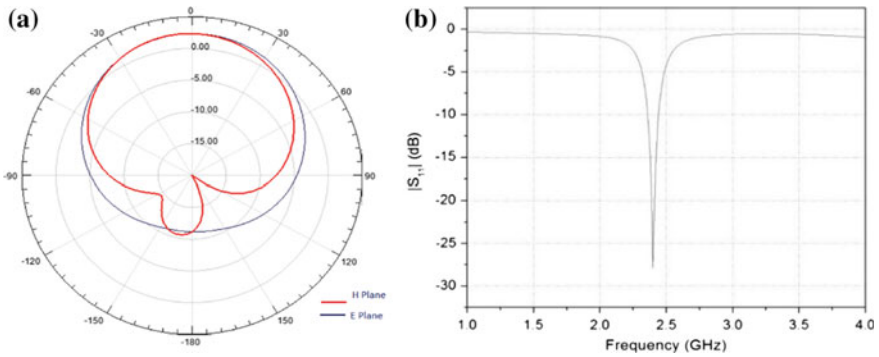

Fig. 5 **a** Radiation pattern of quarter wavelength feed MPA. **b** Return loss of quarter wavelength feed MPA

Table 4 Comparison of various feeding techniques of MPA

Parameters	Coaxial feed	Inset feed	Quarter wavelength feed
Return loss (dB)	−26	−35	−27
Frequency (GHz)	2.4	2.4	2.4
Max U(W/sr)	0.0036528	0.070014	0.13607
Bandwidth(MHz)	50	10	80
Peak Gain(dB)	5.3308	1.2	1.7167
Radiated Power (W)	0.0084524	0.047574	0.54238
Peak Directivity(dBi)	5.4309	1.8494	3.152
Accepted power(W)	0.008611	0.86261	0.99607
Incident Power (W)	0.010122	0.0094294	1
Radiation Efficiency	0.98157	0.5515	0.5452
Front to Back Ratio	113.48	56.188	25.795

3 Comparison

The simulated result of all feeding techniques is shown in Table 4. Those feeding methods are microstrip inset feed, quarter wavelength, and co-axial probe feed. Table 4 also gives the variation in different parameters like directivity, gain, etc.

4 Conclusion

It is observed that all considered feeding techniques of the microstrip patch antenna provide different results. Selection of feed is a significant decision because it varies almost all the parameters of the antenna (Fig. 4).

The variations in bandwidth, directivity, gain, and efficiency of MPA under different feeding techniques are considered. It can be seen that coaxial feed achieves better gain and directivity of 5.43 dBi and 5.33 dB, respectively. These values are better as compared to other feeding methods.

References

1. Balanis, C.A.: Antenna Theory: Analysis and Design, 3rd edn. Wiley, New Jersey (2005)
2. Garg, R., Bhartie, P., Bahl, I., Ittipiboon, A.: Microstrip Antenna Design Handbook, pp. 253–316. Artech House Inc., Norwood (2001)
3. Chen, H.D.: Compact circularly polarised microstrip antenna with slotted ground plane. Electron. Lett. **13**(2), 616–617 (2002)

4. Caloz, C., Itoh, T.: Transmission line approach of left-handed (LH) materials and microstrip implementation of an artificial LH transmission line. IEEE Trans. Antennas Propag. **52**(4), 1159–1166 (2004)
5. Heidari, A.A., Heyrani, M., Nakhkash, M.: A dual-band circularly polarized stub loaded microstrip patch antenna for GPS applications. Prog. Electromagn. Res. **92**, 195–208 (2009)
6. Jaglan, N., Kanaujia, B. K., Gupta, S. D., Srivastava, S.: Triple band notched Uwb antenna design using electromagnetic band gap structures. Prog. Electromagn. Res.C. **66**, 21–37 (2017)
7. Jaglan, N., Gupta, S. D., Kanaujia, B. K., Srivastava, S., and Thakur, E.: Triple band notched Dg-Cebg structure based Uwb MIMO/diversity antenna. Prog. Electromagn. Res.C. **80,** 21–37 (2018)
8. Mobashsher, A.T., Abbosh, A.: Utilizing symmetry of planar ultra-wideband antennas for size reduction and enhanced performance. IEEE Antennas Prop. Mag. **57**(2), 153–166 (2015)
9. Massie, G., Caillet, M., Clemet, M., Antar, M.M.: A new wideband circularly polarized hybrid dielectric resonator antenna. IEEE Antennas Wirel. Propag. Lett. **9**, 347–350 (2010)
10. Wang, Z., Fang, S., Fu, S., Lu, S.: Dual-band probe-fed stacked patch antenna for GNSS applications. IEEE Antennas Wirel. Propag. Lett. **9**, 100–103 (2009)
11. Jaglan, N., Kanaujia, B., Gupta, S., Srivastava, S.: Dual band notched Ebg structure based Uwb Mimo/diversity antenna with reduced wide band electromagnetic coupling. Freq. J. RF-Eng. Telecommun. **71**, 1–11 (2017)
12. Ali, W.A., Moniem, R.: Frequency reconfigurable triple band notched ultra wideband antenna with compact size. Prog. Electromagn. Res. C **73**, 37–46 (2017)
13. Zhang, Q., Fukuoka, Y., Itoh, T.: Analysis of a suspended patch antenna excited by an electromagnetically coupled microstrip feed. IEEE Trans. Antennas Propag. **33**(8), 895–899 (1985)
14. Sánchez, L., Roy, J.L., Iglesias, E.: Proximity coupled microstrip patch antenna with reduced harmonic radiation. IEEE Trans. Antennas Propag. **5**, 2392–2396 (2009)
15. Chen, W.S.: Single feed dual frequency rectangular microstrip antenna with square slot. Electron. Lett. **4**, 231–232 (1998)

A Miniaturized Elliptically Shaped Split Ring Resonator Antenna with Dual-Band Characteristics

Ashish Gupta and Raghvenda Kumar Singh

Abstract In this paper, an electrically small dual-band antenna has been proposed by the applications of an elliptically shaped SRR (split ring resonator). This antenna has a physical size of 28 mm × 22 mm × 1.6 mm and electrical size of 0.259 λ_0 × 0.203 λ_0 × 0.014 λ_0, where λ_0 is the free space wavelength with respect to f_0 = 2.78 GHz. bandwidths, respectively. The first band is due to the coupling between inner and outer SRR while the second band is due to the coupling between feed and partial ground plane. In addition, this antenna is showing a dipolar-type pattern in *xz*-plane while omnidirectional pattern in *yz*-plane with great cross-polarization level. Due to the satisfactory radiation characteristics, the proposed antenna is a suitable candidate for surveillance radar and WLAN/Wi-Fi applications.

Keywords Split ring resonator (SRR) · Wireless local area network (WLAN) Miniaturization · Elliptical SRR · Partial ground plane · Dual-band

1 Introduction

In the recent years, the miniaturized antenna has become very popular due to high market demands [1–3]. There is a steep increment in manufacturing the compact wireless devices which are handy for the user's convenience. Therefore, miniaturized antennas are very essential so that they can be accommodated well in wireless/wired devices such as Bluetooth, Wi-Fi routers, mobile phones, laptops, radars, etc. Planar antennas are quite suitable to be integrated due to the complex arrangements of several components [4, 5]. Metamaterial antennas bring a revolution in design-

A. Gupta (✉) · R. Kumar Singh
Jaypee Institute of Information Technology, Noida 201301, Uttar Pradesh, India
e-mail: ashish.gupta@jiit.ac.in

R. Kumar Singh
e-mail: raghvenda.singh@jiit.ac.in

B. S. Rawat et al. (eds.), *Advances in Signal Processing and Communication* ,
Lecture Notes in Electrical Engineering 526,
https://doi.org/10.1007/978-981-13-2553-3_4

ing of miniaturized antennas due to its outstanding characteristics such as negative refractive index, anti-parallel group and phase velocity, and zeroth-order propagation [6–8]. Usually, metamaterials can be realized using a split ring resonator (SRR) [9], complementary split ring resonator (CSRR) [10], and thin wire structures. Antennas with modified SRR are investigated recently but they are suffering from relatively large electrical size.

In this paper, a miniaturized antenna using elliptical SRR has been proposed for dual-band operations. It has been observed that elliptical shape offers more miniaturization due to the uneven coupling (major and minor radius) between elements. In order to extinguish the effect of reflections from the ground plane, a partial ground plane has been used. As a result of this proposed antenna can be operated in two bands, i.e., 2.7−2.81 GHz and 5.22−6.75 GHz. It has an electrical size of 0.259 λ_0 $\times$ 0.203 λ_0 $\times$ 0.014 λ_0, where λ_0 is the free space wavelength to the $f_0 = 2.78$ GHz. the antenna has also an excellent pattern in both the planes with cross-polarization level is as below as −40 dB.

2 Antenna Geometry

The proposed antenna is implemented on an FR4 Glass Epoxy substrate ($\varepsilon_r = 4.4$, $tan\delta = 0.02$) with a 1.6 mm thickness. On the top plane of the antenna, an elliptically shaped SRR is designed in order to have additional resonance. This SRR is excited via 50Ω microstrip feedline. On the bottom plane, the partial ground plane is used in order to reduce the reflections. Figure 1 shows the perspective, top, and bottom view of the designed antenna with optimized dimensions. The ratio of the minor to the major axis of the ellipse is chosen as 0.65. All simulations have been carried out using High-Frequency Structure Simulator (HFSS 13.0) software.

3 Antenna Design and Analysis

The proposed antenna is designed such that an additional resonance can be obtained at a smaller frequency than that of conventional resonance. To do this, an elliptical shape is chosen and an SRR is designed. The dimensions of the SRR are carefully optimized and it is observed that the effect of these dimensions is the prominent effect on resonant frequencies. Previous studies show that SRR is helpful to achieve an additional resonance which can be configured by varying dimensions of the SRR [11]. It has been observed that miniaturization is achieved due to the uneven coupling between two rings in case of elliptically shaped SRR, instead of circular SRR. The partial ground plane has been used in order to reduce reflections from the ground and has been used widely in the recent years [9]. In order to see the contribution

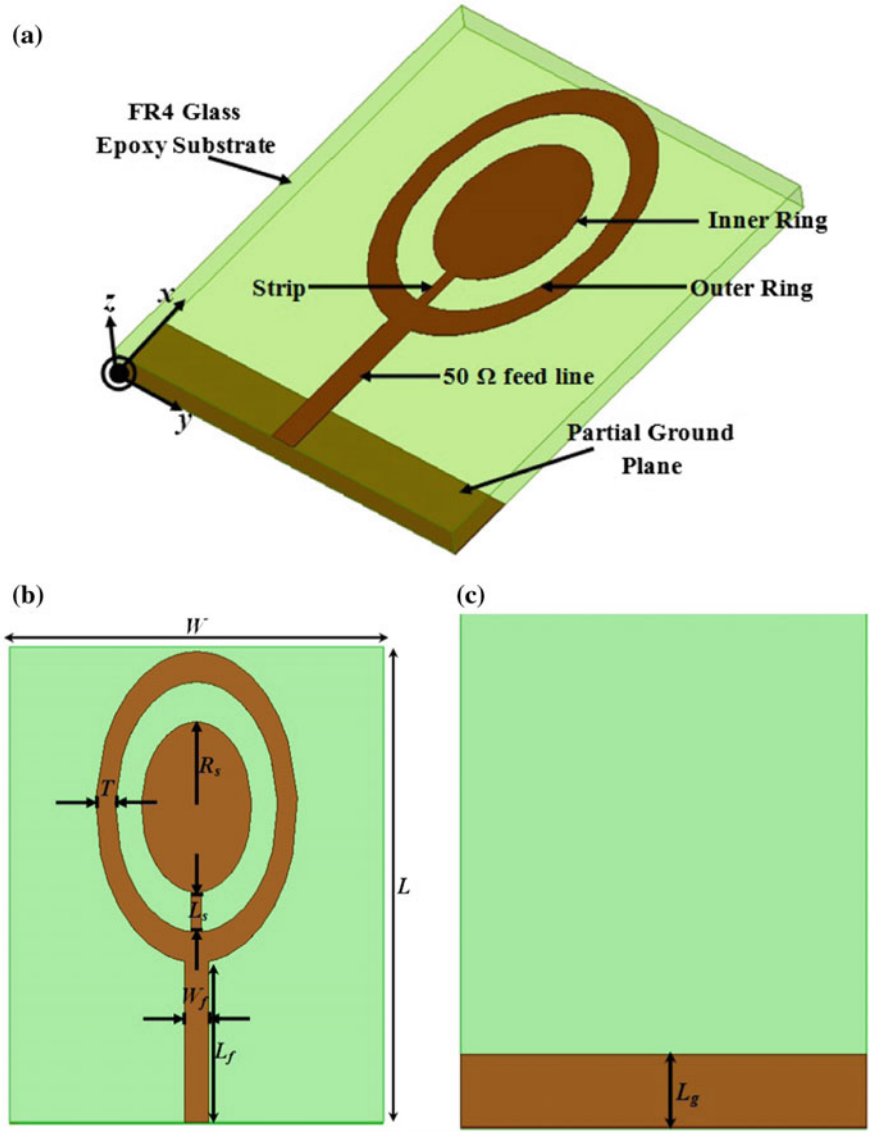

Fig. 1 Geometry of the proposed antenna, **a** perspective view, **b** top view, **c** bottom view. $L = 28$, $W = 22$, $L_f = 9.5$, $W_f = 1.4$, $L_s = 2.4$, $T = 1.8$, $R_s = 5$, $L_g = 4$ (All dimensions are in mm)

of different elements, current distributions in the two modes have been shown in Fig. 2. Figure 2a shows the current distribution at first mode (at 2.78 GHz). It can be observed that current is concentrated on elliptical rings and stripline. Therefore, it can be said that this resonance is due to the coupling between inner and outer SRR.

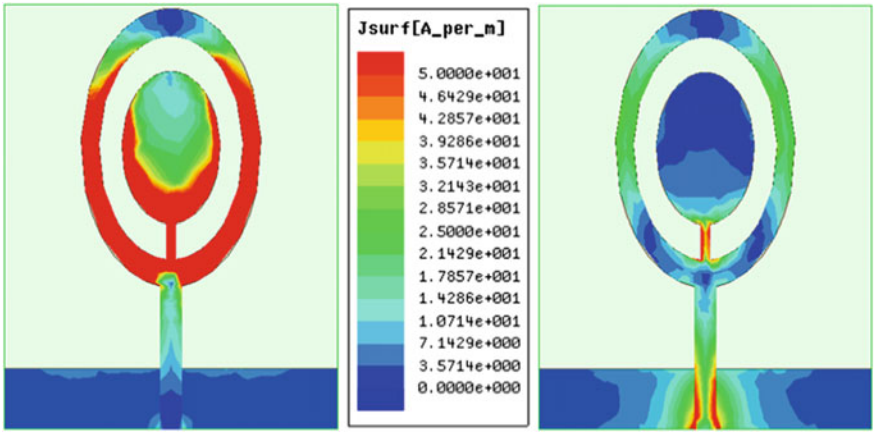

(a) at 2.78 GHz, (b) at 6.02 GHz

Fig. 2 Current distributions of the proposed antenna

On the other hand, Fig. 2b shows the higher resonance is due to the coupling between feed and ground plane.

Parametric studies also have been carried out for monitoring the behavior of resonance due to different elements. Figure 3 shows the input reflection coefficients of the proposed antenna by the varying length of the ground plane (L_g). It can be expected that this parameter should vary the higher one resonance rather than the lower one and Fig. 3 verifies this statement. Figure 4 shows the variation of input reflection coefficients by varying radius of the ellipse (R_s).. It can be observed that this parameter has a big importance in the designing of this antenna and should be carefully chosen. It can be observed that both resonant frequencies are getting decreased by increasing the radius of the ellipse (R_s) as it is an inversely proportional relationship between size and resonant frequency. Furthermore, the length of the strip (L_s) has been optimized in Fig. 5, which shows some effect on first resonant frequency as well. This performance is usual as this dimension deals with the coupling between inner and outer rings.

4 Results and Discussion

The proposed antenna is implemented on an FR4 Glass Epoxy substrate ($\varepsilon_r = 4.4$, $tan\delta = 0.02$) with a 1.6 mm thickness. Figure 6 shows the simulated input reflection coefficient of the proposed antenna with optimized dimensions as in Fig. 1. It is showing two bands at 2.71–2.81 GHz and 5.22–6.75 GHz with a fractional bandwidth of 3.59% and 25.41%, respectively.

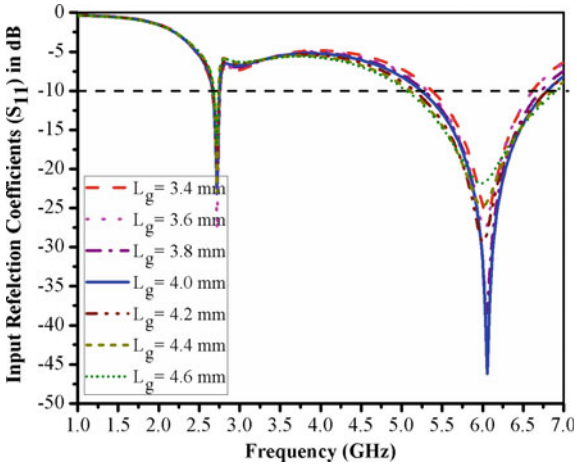

Fig. 3 Input reflection coefficients of the proposed antenna by varying L_g

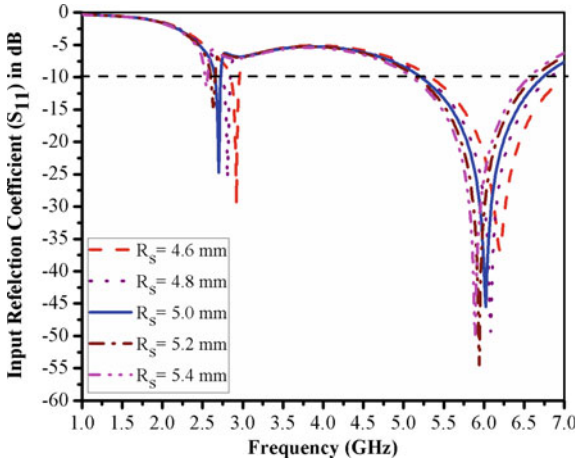

Fig. 4 Input reflection coefficients of the proposed antenna by varying R_s

Figure 7 shows the simulated radiation patterns of the proposed antenna. It can be observed that it exhibits dipolar-type radiation pattern at *xz*-plane while omnidirectional pattern in *yz*-plane. It also shows less cross-polarization is as below as −40 dB in both planes which makes it suitable to be used in modern wireless communication. Peak gain and radiation efficiency profile for both the bands are shown in Fig. 8. Figure 8a shows the less peak gain as compared to the peak gain in a higher band. Because conductor and dielectric losses are dominant in this frequency band, which defines the radiation efficiency. This radiation efficiency is closely related to the antenna gain as antenna gain is radiation efficiency times directivity. The radiation

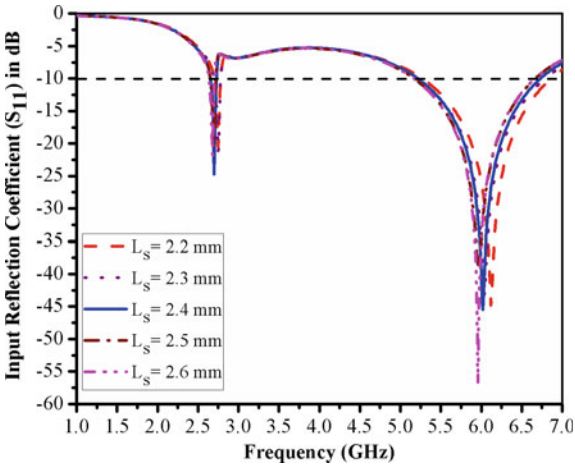

Fig. 5 Input reflection coefficients of the proposed antenna by varying L_s

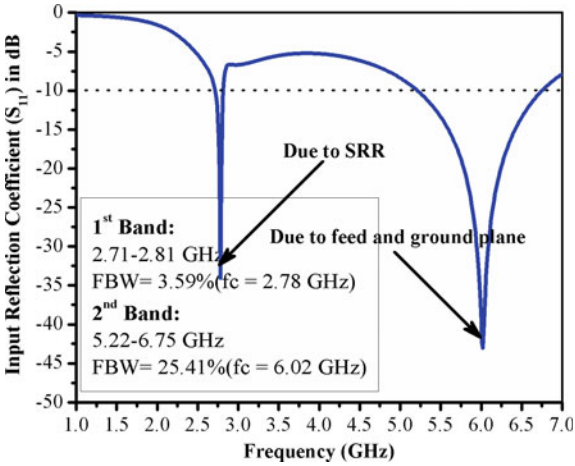

Fig. 6 Simulated input reflection coefficients of the proposed antenna with optimal dimensions

efficiency ranges from 34.10 to 83.33% in the first band while 96.04−99.38% in the second band. In addition to the first band, antenna suffers from the high-level miniaturization, therefore, electric and magnetic fields are not able to radiate properly [12]. Therefore, the proposed antenna is suffering from low gain at lower frequencies.

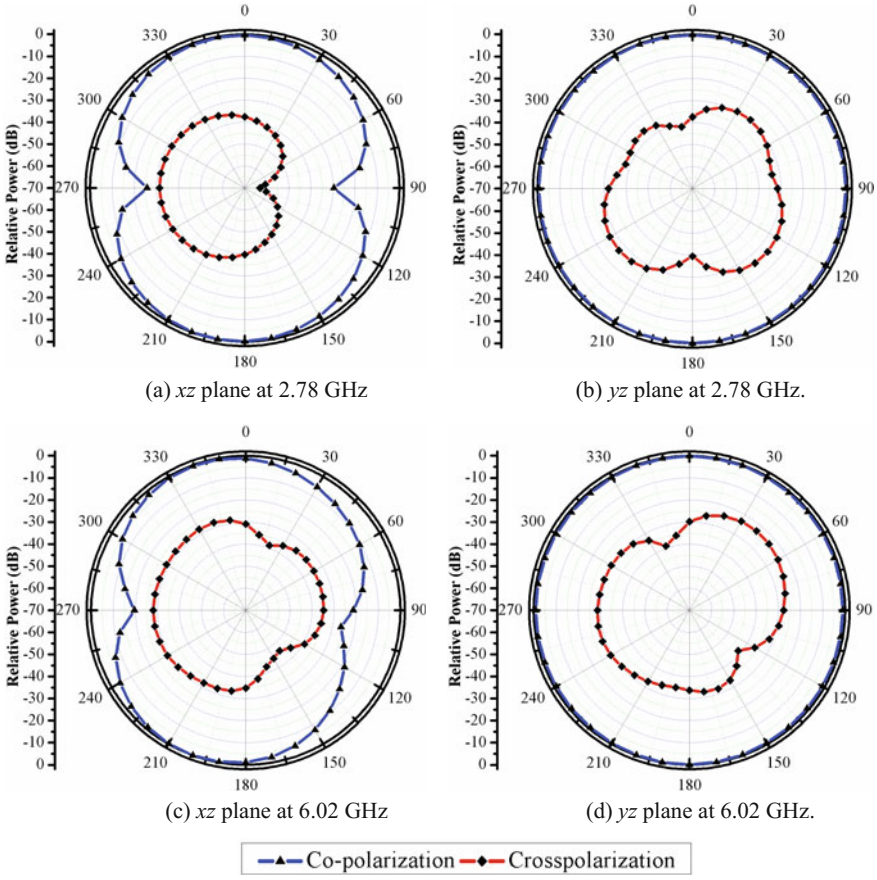

(a) *xz* plane at 2.78 GHz (b) *yz* plane at 2.78 GHz.

(c) *xz* plane at 6.02 GHz (d) *yz* plane at 6.02 GHz.

Fig. 7 Simulated radiation patterns of the proposed antenna

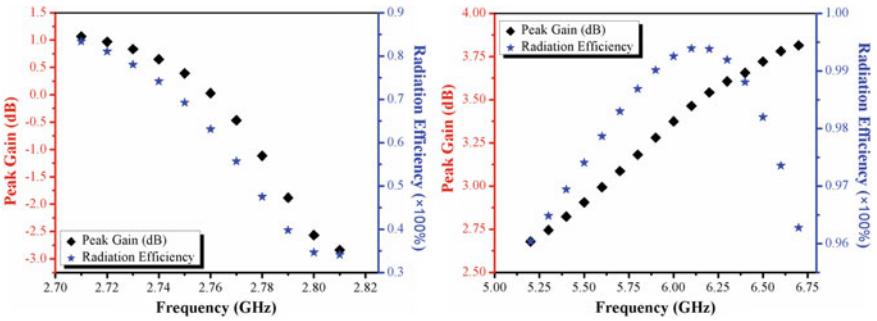

(a) at first band, (b) at second band

Fig. 8 Peak gain and radiation efficiency profile of the proposed antenna

5 Conclusion

An elliptically shaped SRR antenna with dual-band characteristics has been designed and proposed in this paper. It has been observed that by incorporating split ring resonator onto the top plane of the antenna an extra mode can be originated, which is useful in order to decrease the electrical size of the antenna. The antenna has an electrical size of $0.259\ \lambda_0 \times 0.203\ \lambda_0 \times 0.014\ \lambda_0$ by optimizing all the involved dimensions into the antenna. The partial ground plane has been used to minimize the reflections from the ground plane. For the futuristic aspects, this approach might be helpful to achieve the miniaturization in the antennas. Excellent radiation characteristics make this antenna useful for modern wireless communication such as WLAN/Wi-Fi, and surveillance radar applications.

References

1. Lee, B., Harackiewicz, F.J.: Miniature microstrip antenna with a partially filled high-permittivity substrate. IEEE Trans. Antennas Propag. **50**, 1160–1162 (2002)
2. Wang, C.-J., Hsu, D.-F.: A frequency reduction scheme for spiral slot antenna. IEEE Antennas Wirel. Propag. Lett. **1**, 161–164 (2002)
3. Wang, C.-J., Lee, J.-J., Huang, R.-B.: Experimental studies of a miniaturized CPW-fed slot antenna with the dual-frequency operation. IEEE Antennas Wirel. Propag. Lett. **2**, 151–154 (2003)
4. Cui, Y., Gao, X.N., Fu, H.Z., Chu, Q.X., Li, R.L.: Broadband dual- polarized dual-dipole planar antennas. IEEE Antennas Propag. Mag. **59**, 77–87 (2017)
5. Hotte, D., Siragusa, R., Duroc, Y., Tedjini, S.: Design of a planar passive MMID tag antenna. IET Microwaves Antennas Propag. **11**, 1770–1775 (2017)
6. Lai, A., Leong, K.M.K.H., Itoh, T.: Infinite wavelength resonant antennas with monopole radiation pattern based on periodic structures. IEEE Trans. Antennas Propag. **55**, 868–875 (2007)
7. Gupta, A., Chaudhary, R.K.: A compact pentagonal ring CPW-fed zeroth order resonating antenna with gain enhancement. Freq. J. RF-Eng. Telecommun. **71**, 261–266 (2017)
8. Sanada, A., Caloz, C., Itoh, T.: Novel zeroth order resonance in composite right/left-handed transmission line resonators. In: Asia-Pacific Microwave Conference 2003, Seoul, Korea (2003)
9. Sharma, S.K., Gupta, A., Chaudhary, R.K.: UWB ring-shaped metamaterial antenna with modified phi-shaped SRR. In: IEEE International Symposium on Antennas and Propagation and USNC/URSI National Radio Science Meeting 2015, Vancouver, Canada (2015)
10. Gupta, A., Sharma, S.K., Chaudhary, R.K.: A compact dual-mode metamaterial-inspired antenna using rectangular type CSRR. Prog. Electromagn. Res. C **57**, 35–42 (2015)
11. Caloz, C., Itoh, T.: Electromagnetic Metamaterials: Transmission Line Theory and Microwave Applications. Wiley, IEEE Press, New York (2005)
12. Mehdipour, A., Denidni, T.A., Sebak, A.-R.: Multi-band miniaturized antenna loaded by ZOR and CSRR metamaterial structures with monopolar radiation pattern. IEEE Trans. Antennas Propag. **62**, 555–562 (2014)

A Compact Fish Spear-Shaped UWB BPF with Dual Notch Bands Using SSIR Resonator

Dharmendra Kumar Jhariya and Akhilesh Mohan

Abstract A compact and novel ultra-wideband (UWB) bandpass filter with dual notch band characteristics is presented in this paper. The ultra-wideband characteristics of the presented bandpass filter are obtained from a fish spear-shaped multimode resonator (MMR). The dual notch bands are realized by introducing shorted-stepped impedance resonator (SSIR) near the fish spear-shaped MMR. By varying the dimensions of the SSIR resonator, the frequencies of the notch bands can be tuned. To validate the present design approach, the proposed filter is fabricated and measured. The measured results match well with simulated ones. The measured passband of the proposed filter is from 3.67 to 11.34 GHz, with two notches at 5.31 and 8 GHz. The design BPF has passband insertion loss of 1.5 dB and return loss better than 12 dB in the passband. The proposed filter with has a compact size of 24.6 mm × 9.25 mm.

Keywords Bandpass filter · Dual notch bands · Microstrip filter
Multimode resonator (MMR) · Ultra-wideband band (UWB)

1 Introduction

For short distance and high data rate communication, 3.1–10.6 GHz frequency band is exploited for the commercial applications after the Federal Communications Commission (FCC) allowed its unlicensed use in 2002 [1]. Since then, a lot of researches have been performed by the researchers in both the academia and industry for the development of ultra-wideband (UWB) technology. Filters are one of the essential

D. Kumar Jhariya (✉)
Department of Electronics and Communication Engineering, Jaypee Institute of Information Technology, Sector 62, Gautam Buddh Nagar, 201309, Noida, Uttar Pradesh, India
e-mail: dharmendra.jhariya@jiit.ac.in

A. Mohan
Department of Electronics and Electrical Communication Engineering, Indian Institute of Technology Kharagpur, Kharagpur 721302, India
e-mail: am@ece.iitkgp.ernet.in

B. S. Rawat et al. (eds.), *Advances in Signal Processing and Communication* ,
Lecture Notes in Electrical Engineering 526,
https://doi.org/10.1007/978-981-13-2553-3_5

components in the UWB communication systems. Several types of wideband filters are reported in the literature [2–6]. In [2], ring resonator based wideband bandpass filter is designed. In [3], a UWB bandpass filter is implemented by cascading a high-pass and low-pass filters. Numerous UWB bandpass filters based on multimode resonator is designed [4–6]. Most of these UWB bandpass filters have very good passband performance, but their out-of-band rejection is poor. Different methods are employed in order to improve the out-of-band performances of these UWB bandpass filters [7–10]. Moreover, the undesired interferences such as WLAN (5.15–5.825 GHz), X-band satellite communication signal (7.7–8.4 GHz) which lie in the UWB spectrum needs to be rejected for good system performance. A number of techniques/methods are presented to overcome the undesired interferences [11–13]. In these methods, they either reject only one interfering signal at a time [12] or they use the complex multilayer technology to reject more than one frequency bands [13, 14].

In this paper, a compact UWB bandpass filter with two notch bands is designed, fabricated and measured. The ultra-wideband bandpass characteristics are realized with the help of a novel fish spear-shaped multimode resonator (MMR). The shorted-stepped impedance resonator (SSIR) is used to obtain the dual notch band properties. By tuning the dimensions of SSIR resonator, the interfering notch bands at WLAN (5.18–5.52 GHz) and X-band (7.40–8.28 GHz) are rejected.

2 UWB Filter Design and Analysis

Figure 1 shows the proposed UWB BPF filter with dual-band notch characteristics. The proposed filter is designed using substrate RT/duroid 5880 having dielectric constant 2.2, loss tangent of 0.0009 and thickness of 0.787 mm. The analysis and design of UWB BPF filter and dual-band SSIR resonator are presented in the following sections.

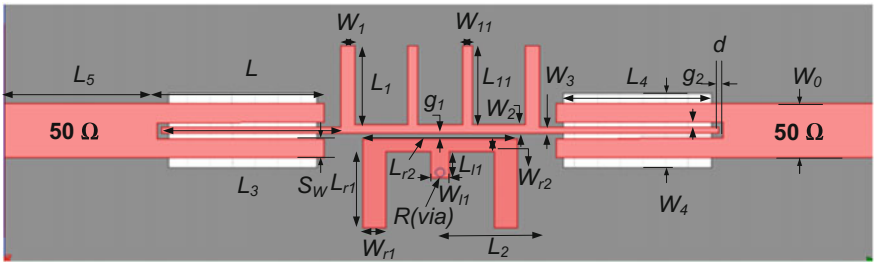

Fig. 1 Schematic of the proposed UWB BPF

2.1 UWB Bandpass Filter

Figure 2 shows the fish spear-shaped multimode resonator (MMR) based UWB bandpass filter. The fish spear-shaped MMR consists of two open stubs at each side of the symmetrical plane A-A'. At the backside of MMR, two rectangular apertures are created in order to increase the input/output couplings. The fish spear-shaped MMR is symmetrical in nature, so odd–even-mode analysis can be performed to evaluate its resonant frequencies.

Figure 3 shows the equivalent circuit of the fish spear-shaped MMR for odd- and even-mode excitations. The resonant frequencies can be extracted by using $Y_{in,odd} = 0$ and $Y_{in,even} = 0$ [15] as follows:

$$Y_3^2 \tan\theta_3 \tan\theta_5 + Y_1 Y_3 \tan\theta_1 \tan\theta_5 + Y_2 Y_3 \tan\theta_2 \tan\theta_5 - Y_2 Y_4 \tan\theta_2 \tan\theta_3 \tan\theta_4 - Y_5 \tan\theta_3 - Y_3 Y_4 \tan\theta_4 \tan\theta_5 - Y_3 Y_5 - Y_1 Y_4 \tan\theta_1 \tan\theta_3 \tan\theta_4 - Y_1 Y_5 \tan\theta_1 \tan\theta_3 = 0 \quad (1)$$

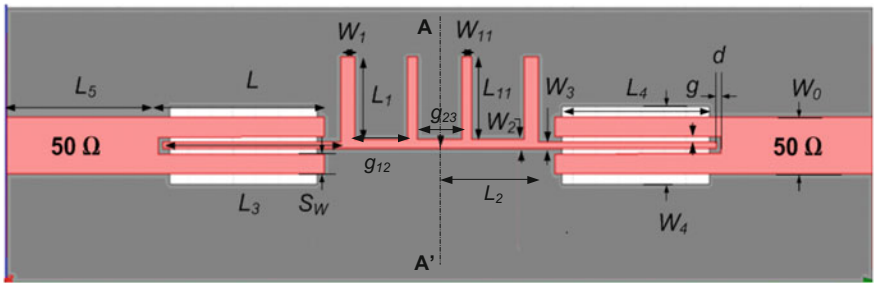

Fig. 2 Schematic of the basic UWB bandpass filter using fish-spear-shaped MMR resonator

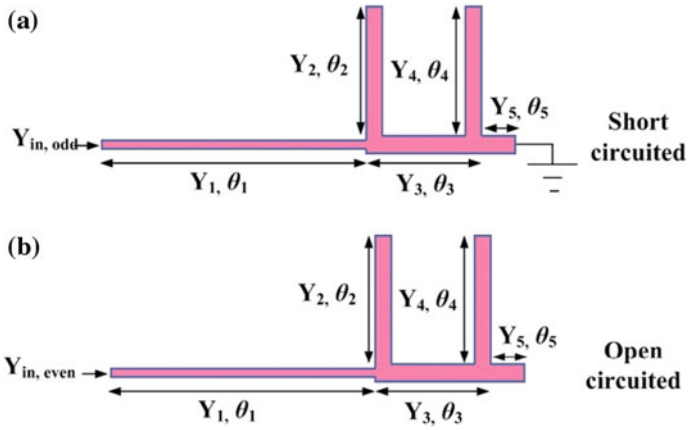

Fig. 3 Equivalent circuit of fish spear-shaped MMR **a** for odd-mode excitation and **b** even-mode excitation

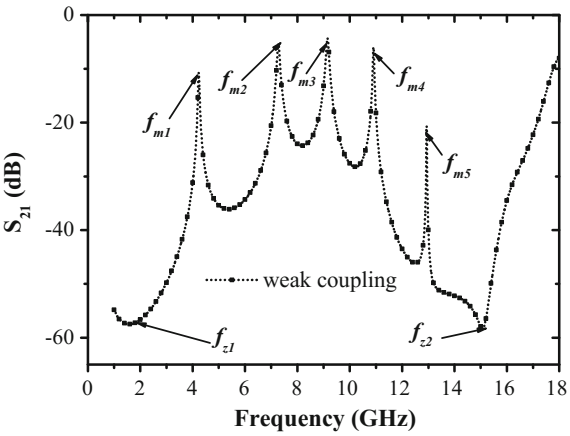

Fig. 4 Simulated S_{21} of the fish spear-shaped MMR under weak coupling with L = 0.3 mm

(for odd-mode excitation)

$$Y_3^2 \tan\theta_3 + Y_1 Y_3 \tan\theta_1 + Y_2 Y_3 \tan\theta_2 - Y_2 Y_4 \tan\theta_2 \tan\theta_3 \tan\theta_4 - Y_2 Y_5 \tan\theta_2 \tan\theta_3 \tan\theta_5 - Y_3 Y_4 \tan\theta_4 - Y_1 Y_4 \tan\theta_1 \tan\theta_3 \tan\theta_4 - Y_1 Y_5 \tan\theta_1 \tan\theta_3 \tan\theta_5 = 0 \quad (2)$$

(for even mode excitation)

Figure 4 shows the simulated S_{21} of the fish spear-shaped MMR with weak coupling. It is clear from the figure that the five resonant modes are generated that lies in the passband of the UWB spectrum. The five resonances are at fm_1 = 4.23 GHz, fm_2 = 7.25 GHz, fm_3 = 9.13, GHz, fm_4 = 10.9 GHz and fm_5 = 12.94 GHz are generated along with two transmission zeros at 1.39 and 14.96 GHz.

Figure 5 shows the simulated S-parameters of the fish spear-shaped MMR-based UWB filter. The passband of the filter is from 3.5 GHz to 11.6 GHz, with a return loss better than 15 dB. The designed UWB bandpass filter is having good out-of-band performance.

2.2 SISR Resonator

In order to reject the interfering signals that lie in the UWB spectrum, filters with multiple band notch characteristics are required.

This is accomplished by the introduction of shorted-stepped impedance resonator (SSIR) near to the multimode resonator (MMR) presented in the above section. The dual-mode SSIR is shown in Fig. 6. It consists of a high–low impedance short line and a stub which is grounded through via hole. This SSIR resonator has inherent

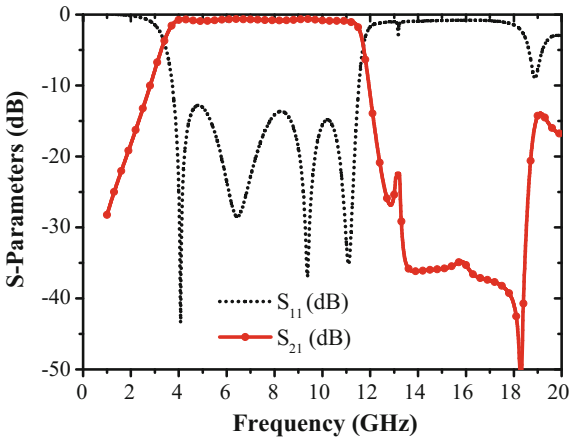

Fig. 5 Simulated S-parameters of UWB bandpass filter using fish-spear-shaped MMR

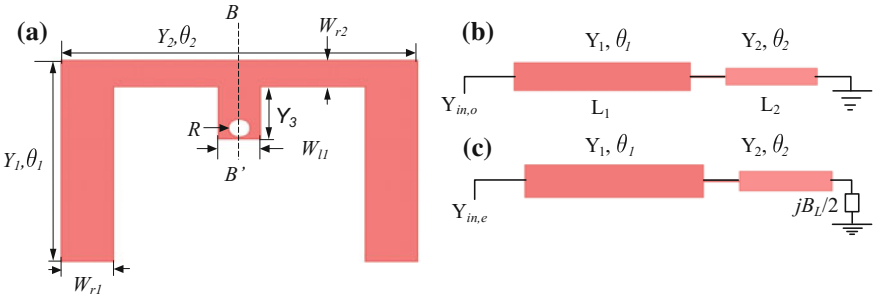

Fig. 6 **a** Geometry of SSIR Resonator. **b** Equivalent circuit for odd-mode excitation. **c** Equivalent circuit for even-mode excitation

dual mode characteristics, which give rise to two resonant frequencies, which are presented by its odd–even-mode analysis.

Even- and odd-mode analysis method is applied to analyze the SSIR resonator since the structure is symmetrical to the B–B′ plane. For odd-mode and even-mode excitations, the equivalent circuits are shown in Fig. 6a and b, respectively. The input admittance for odd-mode and even-mode equivalent circuits, $Y_{in,odd}$ and $Y_{in,even}$ can be expressed as

$$Y_{in,odd} = jY_1\left[\frac{Y_1\tan\theta_1 - Y_2\cot\theta_2}{Y_1 + Y_2\tan\theta_1\cot\theta_2}\right] \tag{3}$$

$$Y_{in,even} = jY_1\left[\frac{Y_2\left(\frac{B_L}{2} + Y_2\tan\theta_2\right) + Y_1\tan\theta_1\left(Y_2 - \frac{B_L}{2}\tan\theta_2\right)}{Y_1 - \left(\frac{B_L}{2} + Y_2\tan\theta_2\right) - Y_2\tan\theta_1\left(\frac{B_L}{2} + Y_2\tan\theta_2\right)}\right] \tag{4}$$

where $B_L = -Y_3\cot\theta_3$.

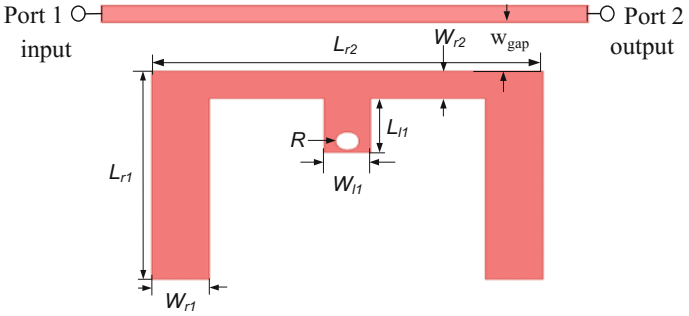

Fig. 7 Geometry of shorted-stepped impedance resonator (SSIR) along with transmission line

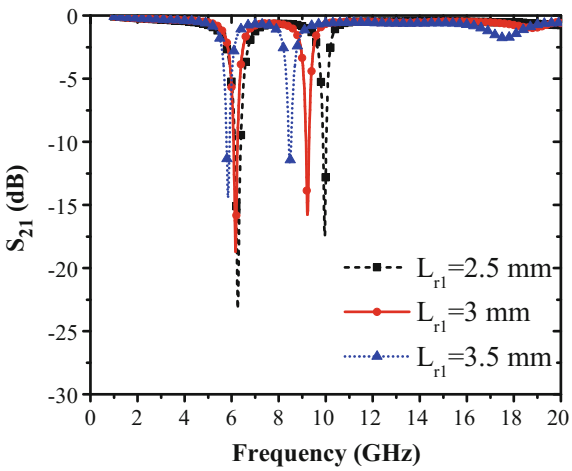

Fig. 8 Simulated S_{21} of the geometry using SSIR resonator shown in Fig. 7 for different lengths L_{r1}

From the resonance condition, i.e.,$Y_{in,odd} = 0,\ Y_{in,even} = 0$, the following equations are obtained:

$$K_1 = \tan\theta_1 \tan\theta_2 = Y_2/Y_1 \tag{5}$$

$$K_2 = 2(K_1 \tan\theta_2 + \tan\theta_1)/\tan\theta_3(\tan\theta_1 \tan\theta_2 - K_1) = Y_3/Y_2 \tag{6}$$

By properly choosing the values of θ_1, θ_2, *and* θ_3 for a given value of Y_1, Y_2, *and* Y_3, the desired resonant frequencies of the SSIR resonator are obtained. When this SSIR resonator is placed near the transmission line as shown in Fig. 7, it will generate two notch bands at its resonant frequencies.

It is observed from Fig. 8 that both the notch band frequencies increase as the value of L_{r1} increases. However, in Fig. 9 when L_{l1} is varied, only the first resonant frequency of shorted-stepped impedance resonator (SSIR) changes. Hence, by choosing the proper values of L_{r1} and L_{l1}, the desired dual-band notch characteristics at 5.3 and 8 GHz can be easily obtained.

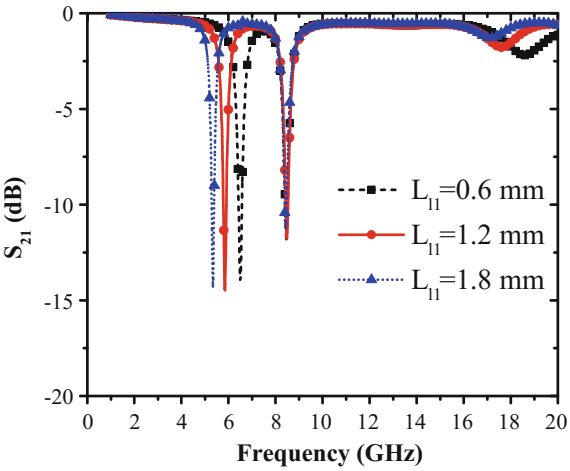

Fig. 9 Simulated S_{21} of the geometry using SSIR resonator shown in Fig. 7 for different lengths L_{l1}

The optimized dimensions of SSIR resonator are as follows (all are in mm): $W_0 = 2.43$, $L_{r1} = 4$, $W_{r1} = 1$, $L_{r2} = 6.75$, $W_{r2} = 0.6$, $L_{l1} = 1.2$, $W_{l1} = 0.8$, $W_{gap} = 0.2$.

2.3 *Proposed Fish Spear-Shaped UWB BPF with SSIR Resonator*

In order to design the dual-band notch UWB bandpass filter, the SSIR resonator is placed near the fish spear-shaped MMR as shown in Fig. 1. The simulated S-parameters of the proposed UWB bandpass filter are shown in Figs. 11 and 12. This filter has the passband from 3.3 GHz to 11.8 GHz with the notches at 5.21 and 8.1 GHz. The bandwidths of notches for 5.21 and 8.1 GHz are 2.4% and 3.6%, respectively. The proposed filter has good out-of-band performance. The attenuation is 20 dB from 12.5 GHz to 19 GHz. The optimal design parameters of the proposed filter shown in Fig. 1 are as follows (all the dimensions are in mm): $L = 7.3$, $S_W = 0.875$, $L_1 = 3.6$, $W_1 = 0.6$, $L_2 = 4.35$, $W_2 = 0.4$, $L_3 = 7.85$, $W_3 = 0.3$, $L_4 = 6.5$, $W_4 = 3.4$, $L_5 = 6.7$, $g_{12} = 2.35$, $g_{23} = 2$, $h = 0.787$, $W_0 = 2.43$, $L_{r1} = 4$, $W_{r1} = 1$, $L_{r2} = 6.75$, $W_{r2} = 0.6$, $L_{l1} = 1.2$, $W_{l1} = 0.8$, $g_1 = 0.2$, $d = 0.2$, $g_2 = 0.2$.

3 Results and Discussion

The proposed UWB bandpass filter is designed and fabricated and its S-parameter responses are measured using Agilent E5071C VNA. The top and bottom views of

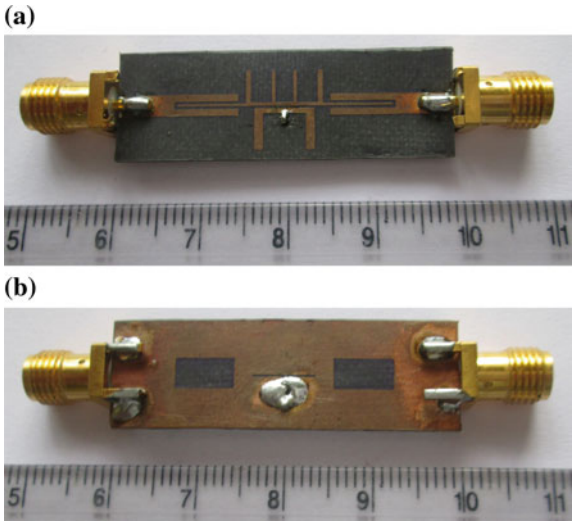

Fig. 10 Photograph of the fabricated UWB filter. **a** Top view. **b** Bottom view

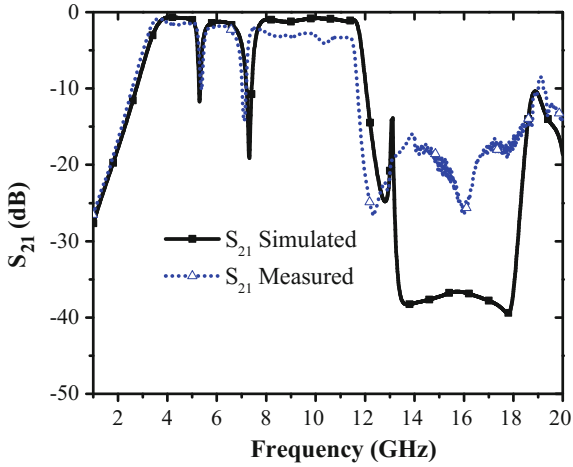

Fig. 11 Simulated and measured frequency responses (S_{21}-insertion loss) of the fabricated UWB BPF with the dual-notched band

the fabricated UWB filter are shown in Fig. 10. The size of the proposed filter is 24.6 mm × 9.25 mm.

The simulated and measured S-parameters of the proposed filter are shown in Figs. 11 and 12. However, there are some mismatches between them which can be attributed toward the fabrication tolerances, SMA connectors, etc., can be seen from the figure that the proposed filter has two notch bands which lie within the FCC specified UWB range. The measured passband of the filter is from 3.67 GHz to 11.34 GHz, except for two notch bands (5.17–5.47 GHz, 6.89–7.82 GHz). The simulated and measured group delay of the proposed filter is shown in Fig. 13. It has nearly flat group delay performance in the passband.

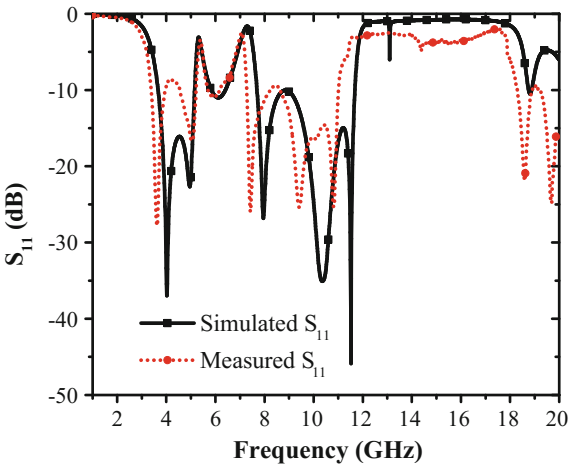

Fig. 12 Simulated and measured frequency responses (S_{11}-return loss) of the fabricated UWB BPF with the dual-notched band

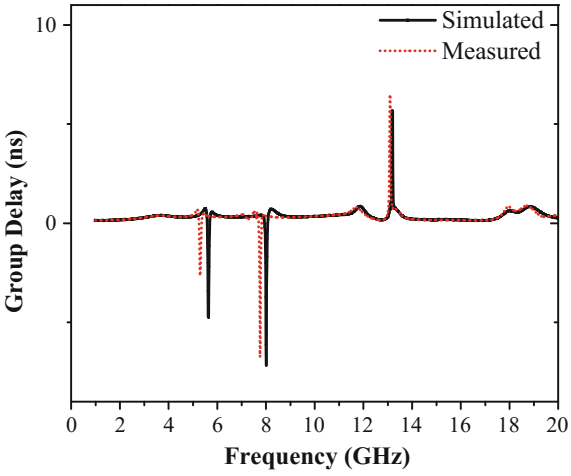

Fig. 13 Simulated and measured group delay of the UWB filter

4 Conclusion

A dual-band-notched ultra-wideband bandpass filter is designed in this paper. The ultrawide-band characteristics are achieved by the use of fish spear-shaped MMR. The interfering WLAN and X-band signals are rejected by introducing shorted-stepped impedance resonator (SSIR) near fish spear-shaped MMR. The measured results are in good agreement with the simulated ones. The measured passband bandwidth of the filter is from 3.67 GHz to 11.34 GHz with dual notches at 5.31 and 8 GHz. The proposed filter is having good out-of-band performance with dual-band reject characteristics.

References

1. FCC, Revision of Part 15 of the Commission's Rules Regarding. Ultra-Wideband Transmission Systems, Washington, DC, Technical Report, ET-Docket, pp. 98–153 (2002)
2. Sun, S., Zhu, L.: Wideband microstrip ring resonator bandpass filters under multiple resonances. IEEE Trans. Microw. TheoryTech. **55**, 2176–2181 (2007)
3. Lee, K.-C., Su, H.-T., Wong, W.-S.: Realization of a wideband bandpass filter using cascaded low-pass to high-pass filter. In: ICMMT Proceedings (2008)
4. Hsieh, L.-H., Chang, K.: Compact, low insertion-loss, sharp-rejection, and wide-band microstrip bandpass filters. IEEE Trans. Microw. Theory Tech. **12**, 1241–1246 (2003)
5. Hsu, C.L., Hsu, F.C., Kuo, J.T.: Microstrip Bandpass Filters for Ultra-Wideband (UWB) Wireless Communications, 679–682 (2005)
6. Zhu, L., Sun, S., Menzel, W.: Ultra-wideband (UWB) bandpass filters using multiple-mode resonator. IEEE Microw. Wirel. Compon. Lett. **15**, 796–798 (2005)
7. Han, L., Wu, K., Chen, X.-P.: Compact ultra-wideband bandpass filter using stub-loaded resonator. Electron. Lett. **45**(10) (2009)
8. Gao, J., Zhu, Lei, Menzel, W., Bögelsack, F.: Short-circuited CPW multiple-mode resonator for ultra-wideband (UWB) bandpass filter. IEEE Microw. Compon. Lett. **16**, 104–106 (2006)
9. Wong, S.W., Zhu, L.: EBG-embedded multiple-mode resonator for UWB bandpass filter with improved upper-stopband performance. IEEE Microw. Wirel. Compon. Lett. **17**, 421–423 (2007)
10. Wang, Z.-Li., Zhang, G.-M., C.-X., Long, G.-N.: .An ultra-wideband bandpass filter with good out- of-band performance. Microw. Opt. Tech. Lett. **50**, 1735–1737 (2008)
11. Chen, P., Wei, F., Shi, X., Huan, Q.: A compact ultra-wideband bandpass filter with defected ground structure. Microw. Opt. Tech. Lett. **51**, 979–981 (2009)
12. Guan, X., Chen, P., Fu, W., Liu, H., Li, G.: A novel ultra-wideband bandpass filter with notched band using slotline and microstrip resonators. Microw. Opt. Tech. Lett. **53**, 2949–2951 (2011)
13. Xu, J., Miao, C.G., Cui, Y.-L., Zhang, J.-D., Ji, Y.-X., Wu, W.: Compact and sharp rejection microstrip UWB BPF with dual narrow notched bands. J. Electro. Waves Appl. **25**, 2464–2473 (2011)
14. Hao, Z.-C., Hong, J.-S., Alotaibi, S.K., Parry, J.P., Hand, D.P.: Ultra-wideband bandpass filter with multiple notch-bands on multilayer liquid crystal polymer substrate. IET Microw. Antennas Pro. **3**, 749–756 (2009)
15. Pozar David, M.: Microwave Engineering, *3*rd Edn, Wiley (2004)

News Analysis Using Word Cloud

Chandrapaul, Rounak Soni, Shubham Sharma, Hemraj Fagna and Sangeeta Mittal

Abstract In internet era, one can get news from huge number of sources. However, many news sources are biased in giving more coverage to specific content, persons or party. Eventually, the reader's thoughts are also influenced by the news source's biases. In this paper, a method has been proposed to instantly visualize the news topics discussed by various sources on internet. Word clouds make it very easier to decide the biases of a news source. Various algorithms, namely, Porter stemmer, Snowball, Lancaster, Rake, tf-idf, text-rank, and tag cloud algorithm have been tested to effectively extract the key words covered by a news source. Extraction time and count of correctly identified terms have been used as metrics to compare the algorithms. It is concluded that tf-idf is better than rake and text rank algorithm due to its right balance between speed and accuracy.

Keywords News analysis · RAKE · TF-IDF · Word cloud

Chandrapaul · R. Soni · S. Sharma (✉) · H. Fagna · S. Mittal
Jaypee Institute of Information Technology, Noida, India
e-mail: shubham1611997@gmail.com

Chandrapaul
e-mail: raghuvanshicp@gmail.com

R. Soni
e-mail: rounak.soni2009@gmail.com

H. Fagna
e-mail: hemrajfagna@gmail.com

S. Mittal
e-mail: sangeeta.mittal@jiit.ac.in

B. S. Rawat et al. (eds.), *Advances in Signal Processing and Communication* ,
Lecture Notes in Electrical Engineering 526,
https://doi.org/10.1007/978-981-13-2553-3_6

1 Introduction

Extraction of the most important information from unstructured text documents is an important field of research interest. The results of this extraction can be used in many different areas including document keyword assignment and document classification [1]. Traditionally the information from documents has been extracted with statistical methods using inputs from the entire corpus to determine the most important words. The problem with this approach is that most of the semantic context is lost. Instead extracting phrases of words from each individual document it is possible to retain most of the semantic context. The purpose of this work is to use individual document key phrase extraction to find most stressed upon phrases of that document. The phrases should also be discriminating towards other documents. The extracted key words have been placed in a word cloud to give visual summary of the document.

A word cloud is a visual summary of a document highlighting most important words and their frequency in a document [1]. The size of a word in the cloud highlights its frequency of occurrence in the document. The visual appeal instantly gives an idea about context of the document. Tag cloud is a related term that is being popularly used in various sites of different domains like social media etc. Word clouds are immensely useful in analyzing multiple documents in one go.

Sometime two or more words co-occur in a text to reinforce relation between them atleast on that category. We study the problem of computing semantics preserving word clouds in which semantically related words are close to each other. However, keeping the semantically related words together may negatively impact results on other parameters.

Word clouds have been used for many applications. Authors in [2] have used word clouds for dissemination of local community information by extracting keywords from microblogs and effectively display popular news topics in vicinity. User reviews have become important reference for decision making in day to day chores of shopping, entertainment places and eating out. However, making use of large number of reviews is a time-consuming process and thus people tend to use just few of them. Authors in [3] have conducted experiments to show improved understanding of users in understanding the given reviews as compared to line by line reading. Word clouds have also been used in summarization of subjective open ended answers to help the teachers in evaluation [4]. Another interesting application has been proposed as *"Pediacloud"* a smartphone app that represents location based information in word clouds [5]. In this paper, word clouds have been used to analyze how a particular person has been covered by major news sites. Sometimes two or more words co-occur in a text to reinforce relation between them atleast on that category. We study the problem of computing semantics preserving word clouds in which semantically related words are close to each other. However, keeping the semantically related words together negatively impacts results on other parameters [6, 7].

```
Pseudocode 1: News Analysis using Wordcloud
For each news URL
     Remove Stop Words
     Apply Stemming and store resultant terms in URL
   specific vectors
For each vector
    For each term
      Calculate TF/IDF weights and prepare list of top
    weighted terms
      Apply Textrank algorithm and enumerate top ranked
    words in separate list
    Apply RAKE algorithm, find list of top phrases
For each of the three lists

      Compare with manually created keyword list of each
    URL and list intersecting words in final_word list

For each final_word list
      For each word in the final_word
    Select random unique colors for each word
    Assign font size to each word according to its weight
      Display the word cloud on canvas
end.
```

Fig. 1 Pseudocode for news analysis using wordcloud

Top five search results from Google search engine have been considered as sources for information on person being looked for. Data from these URLs were then extracted using "urllib" library. The extracted data was pre-processed by removing stop words, lemmatizing the text by applying various stemming algorithms and constructing word clouds.

The work has been divided into following subsections. Section 2 discusses the steps of preprocessing and their results. Placement of shortlisted important words in a word cloud has been discussed in Sect. 3. Results in terms of various word cloud extraction time has been shown and discussed in Sect. 4. The paper has been concluded in Sect. 5.

2 Document Preprocessing

Detailed algorithm for word processing has been given as pseudocode in Fig. 1. Word cloud is obtained through three major steps explained in the subsections below.

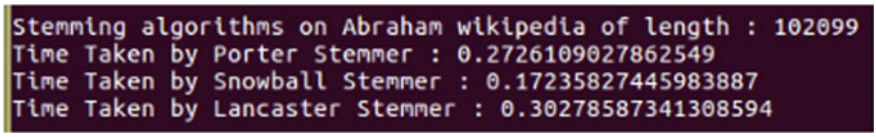

Fig. 2 Comparison of execution time of porter, snowball and lancaster stemmers

2.1 Preprocessing of Each News URL

Each news URL has to be preprocessed to generate potential terms that can provide semantics and context to the article. First step in this is to remove stop words. Stop words are the set of words used to make the English text syntactically correct but do not add anything to the meaning of the document [8, 9]. These are connectors like articles, preposition, pronouns, for example, {a, the, of, with, for etc.…}. The connectors occur frequently in a text and thus can have high frequency based weights. Therefore, to get actual analysis of important words these have to be removed from the documents.

Next step is Stemming, where the purpose is to identify groups of words that are syntactic variants of one another and represent them by a one common word stem per group. For example, "development", "developed" and "developing" will be all treated as "develop". Porter stemming algorithm has been used here as in intial study on a set of URLs, it was found to be giving stemming results in lesser time as compared to other approaches for this problem. Figure 2 shows comparison of time taken by porter stemmer, snowball and Lancaster algorithms for stemming a document having more than 1 lakh words.

Porter Stemmer gave the results in shortest time, therefore it was chosen for processing of other documents.

2.2 Keywords Extraction

Extracting most important keywords out of all the words present in a document or set of documents is not a straight forward task [10–12]. As explained in Algorithm 1, three approaches have been applied to extract important keywords from any text. The first approach is based on TF-IDF, where TF the term frequency is count of occurrence of a particular stem in a particular document and IDF, the Inverse Document Frequency is logarithmic count of ratio of number of documents considered for keyword extraction to the number of times the term is occurring in them. Equations (1) and (2) mathematically define these terms.

$$\begin{aligned} \mathrm{TF(t)} = &\ (\text{Number of times term 't' appears in a document}) \\ &/(\text{Total number of terms in the document}), \end{aligned} \tag{1}$$

Table 1 Comparison of keyword extraction from different news sources by various ranking algorithms

News serial no.	Keywords in heading	Common keywords in Tf-idf	Common keywords in rake	Common keywords in text-rank
1	7	5	0	3
2	7	4	1	3
3	10	5	2	3
4	13	10	5	5
5	4	4	2	2

$$\text{IDF(t)} = \log_e(\text{Total number of documents}/\text{Number of documents with term t in it}), \tag{2}$$

For each term the normalized weight is calculated as per Eq. (3). Importance of the word in document is decided by this weight where more weight means more importance.

$$\text{Norm\_wt(t)} = \text{tf(t)} * \text{idf(t))} \tag{3}$$

Another approach is Rapid Automatic Keyword Extraction (RAKE) method that extracts key phrases in the document. For example, names like "Virat Kohli" have to be considered a single phrase instead of two different words. Weights are assigned by finding all the key phrases and their relevance in the document. Phrases are identified by calculating degree and frequency of each phrase where degree can be seen as how frequently the word co-occurs with other words to make a phrase and frequency is how many times it occurs in the document. The total score of a word in RAKE can be calculated as per Eq. 4 and these weights are used to identify key words and keyphrases of a document.

$$\text{Wordscore(w)} = \text{degree(w)}/\text{frequency(w)} \tag{4}$$

Third and last approach used here for finding keywords is the textrank approach. Each stem word is considered as graph vertex and edges represent relation of each word with other words. Using page ranking method, scores are assigned to each vertex in multiple iterations. 'N' words with highest score are picked from the list as keywords.

Table 1 shows, comparison of keyword extraction by different algorithms in five news search terms namely Narendra Modi, Mahatma Gandhi, Abraham Lincoln, Demonetization and Ram Rahim. From results of Table 1, it can be concluded that Tf-Idf produces most common keywords and hence is most effective. Therefore, from current set of approaches, this is best for keyword creation.

```
Pseudocode 2: Assign_Term_Size_on_Cloud

Input: List of top words from Keyword extraction
Algorithms along with their weights

Output: Font size of each term
for each word/phrase in the list
       if max_size== min_size
           size_words = min_size + (max_size -
         min_size)/2
       else
           size_words = min_size + (max_size -
         min_size)*(count*1/(max_count- min_count))**0.8
end for
```

Fig. 3 Algorithm for font size calculation of terms to be placed in word cloud

3 Word Cloud Creation

Word cloud creation of top keywords and key phrases obtained in previous steps has been done using PyGame library as it provides inbuilt functions for convolution, deciding mask, drawing rectangle as canvas, surface transform and specifying font size and color. These functions are required for placing words in the cloud. All top ranked word obtained from each keyword extraction algorithm have been assigned random colors and size calculated from minimum and maximum size allowed on canvas, weight of that word and minimum and maximum weight of all words. This size calculation is also depicted in pseudocode Fig. 3.

A sprite, which is a two dimensional image part of larger graphical scene, has been created for each word. A rectangle has been created around every placed term. Each term is assigned an initial position (0, 0) with total area covered by its sprite being calculated according to its length. The obtained sprite is t then convolved with image. If the sprite overlaps with some other tag, then the layout is checked. If horizontal overlapping is found then layout is changed to vertical. If it overlaps again, then Archimedean spiral or rectangular spiral positioning is applied. An example of a word cloud created from top 5 links on searching “Mahatma Gandhi” has been shown in Fig. 4a, b and searching “Modi” in Fig. 4c, d. Figures 4a and 5a are outputs of Rake key extraction while Figs. 4b and 5b are outputs of tf-idf and Text rank algorithm.

4 Results

We tested our algorithms on two small and three large documents of size less than 12000 words and greater than 1 lakh words respectively and got results shown in

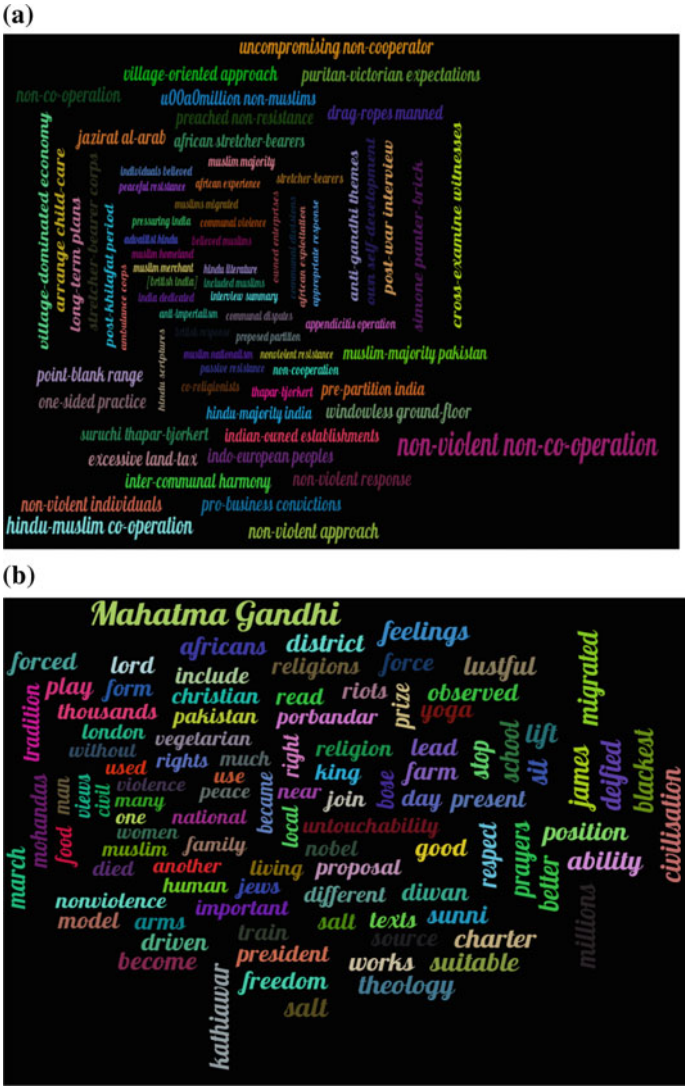

Fig. 4 Word clouds generated using URLs related to **a** Mahatma Gandhi using Rake. **b** Mahatma Gandhi using Tf-Idf

Table 2. Extraction times of three topics that fetched data of more than 1 lakh words took about ten times more time than smaller sized datasets on current news topics.

It can also be seen from Figs. 6, 7 and Table 2 that RAKE algorithm extracts the keywords at a much higher speed than the other two algorithms. In fact it is about 2000 times faster than Text Rank and 40 times faster than Tf-Idf approach. However,

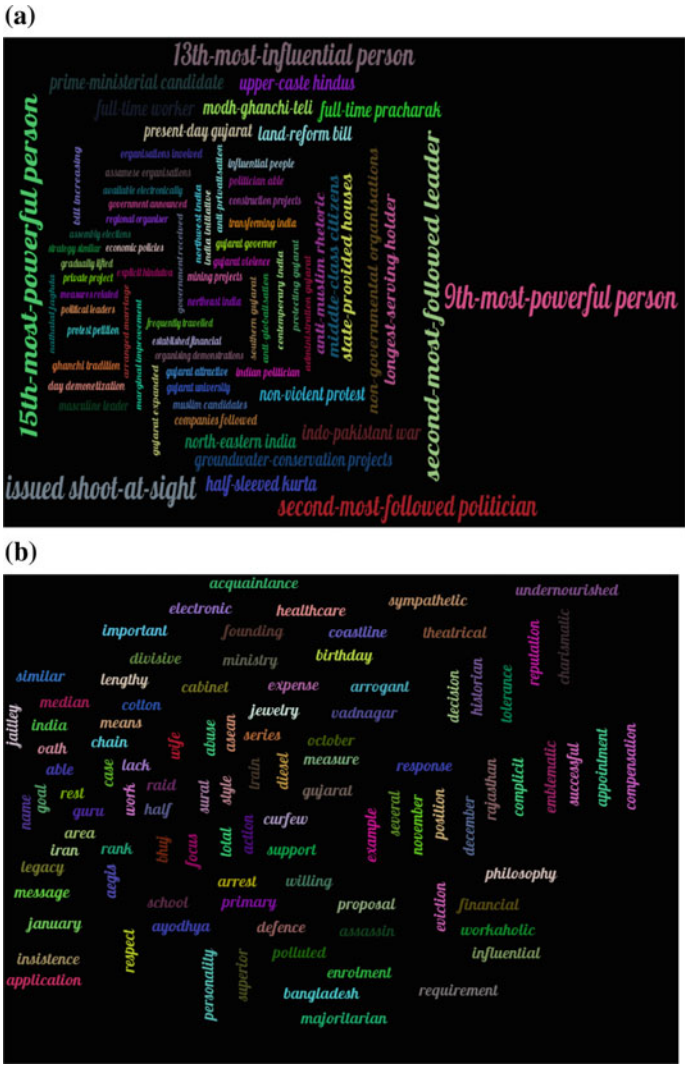

Fig. 5 Word clouds generated using URLs related to **a** Modi using Rake. **b** Modi using Textrank

as shown in Table 1 in Sect. 2, the keywords extraction accuracy is not good for this algorithm. Hence, it cannot be used for word cloud creation, despite its speed.

Table 2 Comparison of keyword extraction from different news sources by various ranking algorithms

Search term	Count of words	Text rank extraction time	Text rank word cloud creation time	Tf-Idf extraction time	Tf-Idf word cloud creation time	Rake extraction time	Rake word cloud creation time
Narendra Modi	117788	915.87	1.70	22.45	7.64	0.21	3.31
Mahatama Gandhi	112776	895.10	2.28	22.3	6.99	0.39	2.31
Abraham Lincoln	102099	734.63	1.60	16.17	8.49	0.33	4.68
Demonetization	12163	17.50	7.50	0.20	6.10	0.01	1.1
Ram Rahim	8855	7.33	1.80	0.3	10.00	0.001	0.6
Barack Obama	83487	703.31	1.35	11.76	6.78	0.27	4.78
Donald Trump	90442	925.14	1.85	38.03	16.14	0.66	5.46
Vladimir Putin	76755	699.04	1.72	26.78	19.00	0.58	5.57
MS Dhoni	36795	113.20	1.24	5.08	12.80	0.31	11.28
Virat Kohli	58870	289.66	1.27	13.27	17.97	0.37	5.51

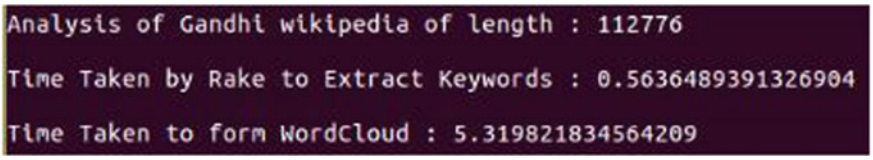

Fig. 6 Extraction time taken by RAKE algorithm on Mahatma Gandhi dataset

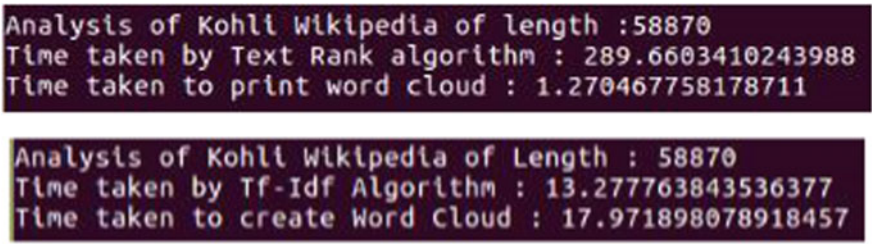

Fig. 7 Extraction time taken by text rank and Tf-Idf algorithms on Kohli dataset

5 Conclusion

In this work, the problem of visualizing coverage of specific news topics by different sites has been addressed. Various steps include preprocessing the news URL to extract information, relevant tokens and then key phrases from them. The top weighted keywords and phrases according to three different algorithms have been visualized in word clouds. Word Cloud based visualization has been shown for some topics of interest. RAKE is fastest among keyword extraction algorithms but

generally news articles are small documents and on small documents RAKE generates insufficient number of keywords, so we conclude that TF-IDF can be used for news analysis as it gives a good combination of both speed and accuracy.

References

1. Heimerl, F., Lohmann, S., Lange, S., Ertl, T.: Word cloud explorer: text analytics based on word clouds. In: 2014 47th Hawaii International Conference on System Sciences (HICSS), pp. 1833–1842. IEEE (2014)
2. Han, K., Shih, P.C., Carroll, J.M.: Local news chatter: augmenting community news by aggregating hyperlocal microblog content in a tag cloud. Int. J. Hum.-Comput. Interact. **30**(12), 1003–1014 (2014)
3. Wang, J., Zhao, J., Guo, S., North, C., Ramakrishnan, N.: ReCloud: semantics-based word cloud visualization of user reviews. In: Proceedings of Graphics Interface 2014, pp. 151–158. Canadian Information Processing Society (2014)
4. Jayashankar, S., Sridaran, R.: Superlative model using word cloud for short answers evaluation in eLearning. Educ. Inf. Technol. **22**(5), 2383–2402 (2017)
5. Tessem, B., Bjørnestad, S., Chen, W., Nyre, L.: Word cloud visualization of locative information. J. Locat. Based Serv. **9**(4), 254–272 (2015)
6. Barth, L., Kobourov, S.G., Pupyrev, S.: Experimental comparison of semantic word clouds. In: International Symposium on Experimental Algorithms, pp. 247–258. Springer, Cham (2014)
7. Chi, M.T., Lin, S.S., Chen, S.Y., Lin, C.H., Lee, T.Y.: Morphable word clouds for time-varying text data visualization. IEEE Trans. Visual Comput. Graph. **21**(12), 1415–1426 (2015)
8. Straková, J., Straka, M., Hajič, J.: Open-source tools for morphology, lemmatization, POS tagging and named entity recognition. In: Proceedings of 52nd Annual Meeting of the Association for Computational Linguistics: System Demonstrations, pp. 13–18 (2014)
9. Balakrishnan, V., Lloyd-Yemoh, E.: Stemming and lemmatization: a comparison of retrieval performances. Lect. Notes Softw. Eng. **2**(3), 262 (2014)
10. Onan, A., Korukoğlu, S., Bulut, H.: Ensemble of keyword extraction methods and classifiers in text classification. Expert Syst. Appl. **57**, 232–247 (2016)
11. Thomas, J.R., Bharti, S.K., Babu, K.S.: Automatic keyword extraction for text summarization in e-newspapers. In: Proceedings of the International Conference on Informatics and Analytics, p. 86. ACM (2016)
12. Zhang, L.J., Li, Y.L., Zeng, Q.T., Lei, J.L., Yang, P.: Keyword extraction algorithm based on improved text rank. J. Beijing Inst. Graph. Commun. **24**(4), 51–55 (2016)

Low-Complexity Side Information-Free Novel PTS Technique for PAPR Reduction in OFDM Systems

Samriti Kalia and Alok Joshi

Abstract This paper proposes a new PTS scheme with reduced complexity and without side information to solve the high peak-to-average power ratio (PAPR) problem in orthogonal frequency-division multiplexing (OFDM) systems. The proposed technique which is known as level shift partial transmit sequence (LS-PTS) is based on shifting the signal level of data vectors of any of the subblocks, which further causes change in phase of these data vectors. This technique eliminates the exhaustive search required for finding optimum phase factors as in conventional partial transmit sequence (C-PTS). Simulation results show an excellent improvement in PAPR reduction by level shift PTS as compared to C-PTS.

Keywords Orthogonal frequency-division multiplexing (OFDM)
Partial transmit sequence (PTS) · Peak-to-average power ratio (PAPR)
Level shift partial transmit sequence (LS-PTS) · Side information (SI)

1 Introduction

OFDM being a digital multi-carrier modulation technique has fulfilled the demand for high data rate, high spectral efficiency, and high mobility [1]. Another important advantage of OFDM is its ability to alleviate the effects of frequency-selective fading [2]. Numerous advantages of OFDM makes its use imperative in multiple wireless applications. But one major issue with OFDM systems is high PAPR which occurs due to the coherent addition of subcarriers when they are in the same phase. The actual problem arises when high PAPR OFDM signal is passed through the high power amplifier. It leads to in-band and out-of-band distortions [3]. Increasing the

S. Kalia (✉) · A. Joshi
ECE Department, Jaypee Institute of Information Technology University,
Noida 201301, India
e-mail: mesamriti@yahoo.co.in

A. Joshi
e-mail: alok.joshi@jiit.ac.in

B. S. Rawat et al. (eds.), *Advances in Signal Processing and Communication* ,
Lecture Notes in Electrical Engineering 526,
https://doi.org/10.1007/978-981-13-2553-3_7

linear range of high power amplifier makes it expensive and reduces its efficiency. Hence, reducing the peak power of the OFDM signal is the optimum solution. Many techniques [4] have been developed till date such as clipping, selective mapping (SLM), active constellation extension (ACE), coding techniques, and many more to lower the PAPR of OFDM signals but the best and promising technique among all is PTS as it is a distortionless technique and involves easy implementation [5]. But this technique has also a few drawbacks. It demands extensive search to find out the ideal phase factors out of $B = W^{L-1}$ total combinations, where L denotes the total subblocks and W is the total phase factors used which may be $\{\pm 1\}$, $\{\pm 1, \pm j\}$, and so on. The other important issue with C-PTS is to convey this information to the transmitter for perfect recovery of data, which requires $\log_2 W^{L-1}$ bits [6] for transmitting side information. This drops spectral efficiency. In the recent years, various PTS techniques have been developed. Some techniques reduce computational complexity [7–9] and some techniques eliminate the need for transmitting side information for the receiver [10].

The technique developed in [11] is based on segregating the phase factors into various subsets and then uses basis vectors of all phase vectors and the correlation among phase factors in each subset to reduce complexity. This technique only reduces complexity and does not improve PAPR reduction performance. Reference [12] developed a technique based on a cost function which is generated by adding the power of time domain samples at a particular instant of time n in each subblock. The samples which are greater than or equal to a predefined threshold are used for peak power calculation while transmitting lowest PAPR OFDM signal. Although complexity is reduced PAPR performance is almost similar to C-PTS. Reference [13] is based on the selection of dominant time domain samples of OFDM signal and crest factor of alternative OFDM signal vectors is utilized to transmit a low PAPR OFDM signal. The PAPR reduction performance for this technique is also similar to C-PTS. Reference [14] proposes a PTS technique without side information in which the candidates are generated by cyclically shifting every subblock time domain sequence. The receiver utilizes the natural diversity of a phase constellation for different candidates to detect the originally transmitted signal. But no improvement in bit error rate is achieved. It is almost similar to C-PTS. Reference [15] suggested another PTS technique without side information which is based on constellation extension. Although it eliminates the need for sending side information to the receiver PAPR reduction performance is not improved. It is the same as C-PTS technique.

2 Preliminaries

2.1 OFDM Systems and PAPR

In OFDM systems, the discrete-time OFDM signal sequence is obtained by independently modulating N number of orthogonal subcarriers by input data symbols $X(g) = [X(0), X(1), \ldots\ldots X(N-1)]$ and is given by

$$x(n) = \frac{1}{\sqrt{N}} \sum_{g=0}^{N-1} X(g) e^{\frac{j2\pi gn}{N}} \qquad 0 \le n \le N-1 \tag{1}$$

where n is discrete time index. The orthogonality of subcarriers is sustained by selecting $\Delta f = \frac{1}{T}$ where T is time duration of one OFDM symbol. The PAPR of discrete time OFDM signal $x(n)$ is written as

$$PAPR = 10 \log 10 \frac{\underset{0 \le n \le N-1}{Max} |x(n)|^2}{E\left[|x(n)|^2\right]} \tag{2}$$

3 Level Shift Partial Transmit Sequence (LS-PTS)

The proposed technique LS-PTS reduces complexity at the transmitter as well as receiver and also eliminates the requirement of sending side information to the receiver. This technique provides a small complex level shift to the time domain samples of OFDM subblocks. The complex level shift can be provided in any of the subblocks. This results in a change of phase and amplitude of the data sequences of that subblock. Each data sequence undergoes a different phase change when the same level shift is provided to all data sequences. Hence, phase optimization is done without searching for optimum phase factor as in C-PTS. The algorithm for LS-PTS is explained below:

(1) Input data stream X_m is separated into L disjoint subblocks.
(2) The mth time domain sample $x_m^{(l)}$ is obtained by calculating IFFT of each subblock $X_m^{(l)}$.
(3)

$$x_m^{(l)} = IFFT\left[X_m^{(l)}\right] = \left[x_0^{(l)}, x_1^{(l)}, \ldots\ldots x_{(N-1)}^{(l)}\right] \quad 1 \le l \le L \tag{3}$$

(4) Add a small complex level shift "ξ" to the data samples of the first subblock. Other subblocks are kept unchanged.
(5)

$$x^{(l)'} = complex\ level\ shift(x_m^{(l)}, \xi) \quad (In\ general) \tag{4}$$

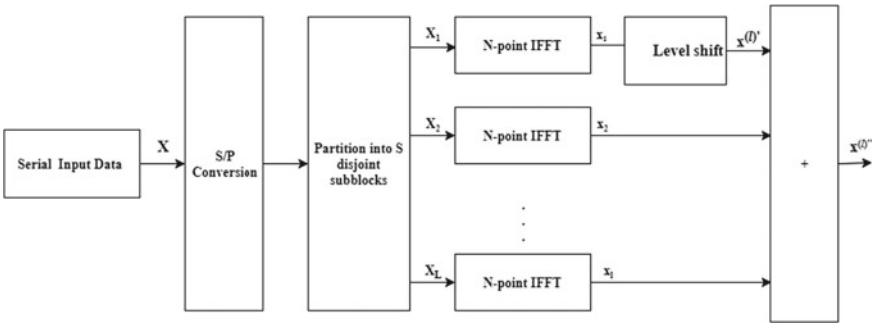

Fig. 1 Schematic diagram of LS-PTS technique

(6) The equation for subblock with complex level shift ξ is given by

$$\left[x_0^{(l)}, x_1^{(l)}, \ldots..x_{(N-1)}^{(l)}\right] + \xi_{cmplx} = x^{(l)'} \tag{5}$$

where $x^{(l)'}$ is the time domain sequence of the level-shifted subblock.

(7) Finally, the level-shifted data sequences of the first subblock are summated with the unchanged time domain samples of other subblocks and a low PAPR OFDM signal $x^{(l)''}$ is obtained as mentioned below

$$x^{(1)'} + \sum_{l=2}^{L} x_m^l = x^{(l)''} \tag{6}$$

Thus, the main advantage of LS-PTS is that profound search required to identify the optimum phase factor from a large number of phase factor combinations is removed as phase optimization is simply done by adding a known value of complex level shift to all-time domain sequences of a subblock. Hence, computational complexity is highly reduced since multiplication with phase factors is avoided. It is a SI-free transmission technique as the known value of level shift provided at the transmitter can be easily removed at the receiver. This level shift information can be easily stored in a look-up table at the receiver. Another important advantage of LS-PTS technique is outstanding PAPR reduction performance as compared to recently developed PTS techniques which are shown and proved in simulation results. The functional diagram of LS-PTS technique is shown in Fig. 1.

Table 1 CCRRS of LS-PTS technique over PTS [14] technique for $B=4$, $p=6$

LS-PTS L = 4			LS-PTS L = 6	
No. of subcarriers N				
	128	256	128	256
C-PTS	31.68%	28.98%	27.01%	24.57%
PTS [14]	62.46%	59.42%	55.10%	51.92%

3.1 Computational Complexity Reduction Performance of LS-PTS

This section gives the differentiation of the computational complexity of the LS-PTS with the C-PTS and PTS scheme proposed in [14].

The complexity equation of the C-PTS technique is given as

$$\begin{aligned} n_{mul} &= (L+1)N/2\log_2(N) + (p+2)N \\ n_{add} &= (L+1)N\log_2 N + B(L-1)N + 2pN \end{aligned} \tag{7}$$

The complexity equation for cyclic shifting PTS scheme mentioned in [14] is given as

$$\begin{aligned} n_{mul} &= (L+1)N/2\log_2 N + (p+2)WN \\ n_{add} &= (L+1)N\log_2 N + B(L-1)N + 2pWN \end{aligned} \tag{8}$$

The complexity equation of the proposed LS-PTS scheme is given by

$$\begin{aligned} n_{mul} &= (L+1)N/2\log_2(N) \\ n_{add} &= (L+1)N\log_2 N + (L+1)N \end{aligned} \tag{9}$$

The computational complexity reduction performance by LS-PTS over other PTS schemes is given by computational complexity reduction ratio (CCRR), which is mentioned in (10). CCRRs of LS-PTS technique over technique proposed in [14] for various FFT sizes and different subblocks is given in Table 1

$$CCRR = \left(1 - \frac{Complexity\ of\ LS-PTS\ Technique}{Complexity\ of\ other\ PTS\ Technique}\right) \times 100[\%] \tag{10}$$

In the above table, the comparison of CCRRs of LS-PTS technique over C-PTS and PTS [14] is done for subblocks $L=4$ and 6, a number of phase factor combinations $B=4$ and size of constellation $p=6$ for subcarriers $N=128$ and 256. LS-PTS shows good complexity reduction performance over C-PTS and PTS [14]. For instance, LS-PTS reduces complexity by 31.68% and 28.98% for $N=128$, $L=4$ and $N=256$, $L=4$, respectively, as compared to C-PTS. Similarly, complexity reduction range is from 51.92% to 62.46% in contrast to PTS [14] for various values of L and N. Thus, LS-PTS technique is highly effective in reducing computational complexity.

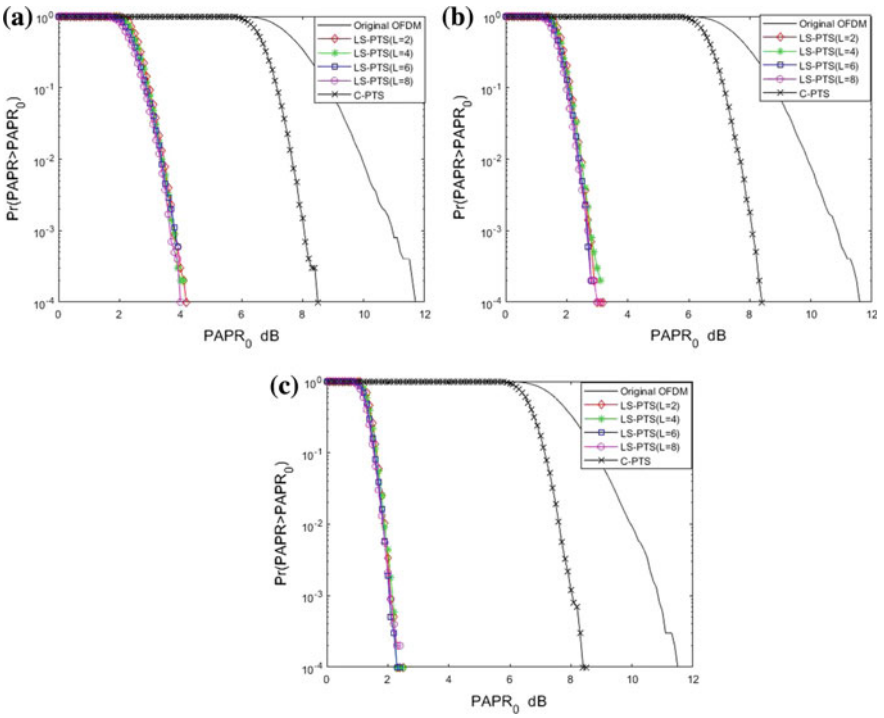

Fig. 2 PAPR reduction performance comparison of the proposed LS-PTS scheme with C- PTS scheme and original OFDM for different subblocks and FFT size N = 256 when the level shift is added in one subblock. **a** $\xi_{cmplx} = 0.2$ **b** $\xi_{cmplx} = 0.3$ **c** $\xi_{cmplx} = 0.4$

3.2 Simulation Results

Various simulations are performed which shows an outstanding reduction in PAPR. The simulations are obtained for 10^4 randomly generated OFDM symbols with FFT size $N = 256$ for 64 QAM modulation. The CCDF versus PAPR graphs are plotted for a complex level shift in one subblock. The CCDFs of the proposed LS-PTS technique with subblock $L = 2, 4, 6, 8$ and level shift $\xi_{cmplx} = 0.2, 0.3, 0.4$ for first subblock with FFT size, $N = 256$ are shown in Fig. 2a–c, respectively. The simulation graphs show that as the value of level shift increases PAPR reduces. But there is a limitation on the increase of the maximum value of level shift. A higher value of level shift leads to an increase in transmission power. The maximum level shift that can be added is dependent on the maximum allowable value of transmission power in OFDM systems according to power transmission standards. Hence proposed LS-PTS scheme reduces PAPR by 7 dB as compared to the original OFDM and 4.6 dB as compared to C-PTS when $\xi_{cmplx} = 0.2$ in one subblock. PAPR reduces further by 8.4 dB as compared to original OFDM and by 5.4 dB as compared to C-PTS when

$\xi_{cmplx} = 0.3$. The PAPR reduces substantially by 9.2 dB in comparison to original OFDM and 6.2 dB in contrast to C-PTS when $\xi_{cmplx} = 0.4$ is added.

4 Conclusion

This work proposed a novel PTS scheme, which reduces PAPR to a large extent with reduced complexity and without side information. The scheme is based on adding a complex level shift to the time domain samples of one subblock which changes both the phase and amplitude of these data samples. Simulation results show the effectiveness of the LS-PTS scheme in reducing PAPR which is 9.2 dB in contrast to original OFDM and 6.2 dB as compared to C-PTS.

References

1. Ghassemi, A., Aaron Gulliver, T.: PAPR reduction of OFDM using PTS and error-correcting code subblockings. IEEE Trans. Wirel. Commun. **9**(3), 980–989 (2010)
2. Ku, S.-J., Wang, C.-L., Chen, C.-H.: A reduced-complexity PTS-based PAPR reduction scheme for OFDM systems. IEEE Trans. Wirel. Commun. **9**(8), 2455–2460 (2010)
3. Chen, H., Chung, K.-C.: A low complexity PTS technique using minimal trellis in OFDM systems. IEEE Trans. Veh. Technol. **99** (2017)
4. Taspinar, N., Kalinli, A., Yildirim, M.: Partial transmit sequences for PAPR reduction using parallel tabu search algorithm in OFDM systems. IEEE Commun. Lett. **15**(9), 974–976 (2011)
5. Rahmatallah, Y., Mohan, S.: Peak-to average power ratio reduction in OFDM systems: a survey and taxonomy. IEEE Commun. Surv. Tutor. **15**(4), 1567–1592 (2013)
6. Wang, L., Liu, J.: PAPR reduction of OFDM signals by PTS with grouping and recursive phase weighting methods. IEEE Trans. Broadcast. **57**(2), 299–306 (2011)
7. Cho, Y.-J., No, J.-S., Shin, D.-J.: A new low-complexity PTS scheme based on successive local search using sequences. IEEE Commun. Lett. **16**(9), 1470–1473 (2012)
8. Jiang, T., Xiang, W., Richardson, P.C., Guo, J., Zhu, G.: PAPR reduction of OFDM signals using partial transmit sequences with low computational complexity. IEEE Trans. Broadcast. **53**(3), 719–724 (2007)
9. Jiang, T., Xiang, W., Richardson, P.C., Guo, J., Zhu, G.: PAPR reduction of OFDM signals using partial transmit sequences with low computational complexity. IEEE Trans. Broadcast. **53**(3), 719–724 (2007)
10. Joo, H.-S., Kim, K.-H., No, J.-S., Shin, D.-J.: New PTS schemes for PAPR reduction of OFDM signals without side information. IEEE Trans. Broadcast. **63**(3), 562–570 (2017)
11. Hou, J., Ge, J., Li, J.: Peak-to-average power ratio reduction of OFDM signals using PTS scheme with low computational complexity. IEEE Trans. Broadcast. **57**(1), 143–148 (2011)
12. Sheng-Ju, K., Wang, C.-L., Chen, C.-H.: A reduced-complexity PTS-based PAPR reduction scheme for OFDM systems. IEEE Trans. Wirel. Commun. **9**(8), 2455–2460 (2010)
13. Cho, Y.-J., Kim, K.-H., Woo, J.-Y., Lee, K.-S., No, J.-S., Shin, D.-J.: Low-complexity PTS schemes using dominant time- domain samples in OFDM systems. IEEE Trans. Broadcast. **63**(2), 440–445 (2017)
14. Yang, L., Soo, K.K., Li, S.Q., Siu, Y.M.: PAPR reduction using low complexity PTS to construct of OFDM signals without side information. IEEE Trans. Broadcast. **57**(2), 284–290 (2011)
15. Zhou, Y., Jiang, T.: A novel multi-points square mapping combined with PTS to reduce PAPR of OFDM signals without side information. IEEE Trans. Broadcast. **55**(4), 831–835 (2009)

GA with SVM to Optimize the Dynamic Channel Assignment for Enhancing SIR in Cellular Networks

Sharada N. Ohatkar and Dattatraya S. Bormane

Abstract There is a reduction in the signal-to-noise ratio of cellular networks due to interference caused by assigning the channels to the cell. As the demand for connectivity is on rise with limited spectrum availability, the interference may increase, so channels are required to be assigned optimally. This work presents applying Genetic algorithm (GA) along with Support Vector Machine (SVM) to assigning the channels dynamically for reducing co-channel and co-site interference with constraints. In this paper, we propose to adopt the GA to solve the minimum interference channel assignment problem (MICAP) and the nonlinear dataset are best classified using SVM. The fitness function is designed using SVM and the optimization is done with GA with a focus on MICAP. The performance of the GA-SVM is enhanced SIR, reduces interference, and requires less computation time than the work reported by GA.

Keywords Genetic algorithm · Support vector machine · MICAP · SIR

1 Introduction

As the demand for connectivity is rising with limited bandwidth, the SIR is reduced as a result of interference during assigning the channels to cells. The channels need to be assigned to cell optimally in order to reduce interference. The main objective of channel assignment techniques is to stabilize the fluctuations in the probability of call blockage over the entire coverage area of a cellular network over a period of time [1, 2]. The requisite number of channels is to be assigned to cells with efficient

S. N. Ohatkar (✉)
SPPU, MKSSS, Cummins College of Engineering, Pune, India
e-mail: sharada.ohatkar@cumminscollege.in

D. S. Bormane
SPPU, AISSMS College of Engineering, Pune, India
e-mail: bdattatraya@gmail.com

B. S. Rawat et al. (eds.), *Advances in Signal Processing and Communication* ,
Lecture Notes in Electrical Engineering 526,
https://doi.org/10.1007/978-981-13-2553-3_8

spectrum utilization resulting in fewer call drops and minimum interference is called "Channel assignment problem" (CAP).

The channel assignment types—in Fixed Channel assignment (FCA), each cell assigns its own frequency channel to mobile subscribers within its cell. In a dynamic channel assignment (DCA), the centralized pool contains the available channels. Channels are assigned dynamically as new demand arrives in the system. In Hybrid Channel assignment (HCA), each cell has a fixed/static channel set and a dynamic channel set.

The interferences in a cellular network: co-channel (CC), adjacent channel (AC), and co-site channel (CS). CC results when the same channel is assigned simultaneously to a couple of cells, which are within the reuse distance. When adjacent channels are assigned to a pair of cells simultaneously its results in AC and CS results when the channels which are assigned has separation less than some minimum spectral distance. FCA has least CCC and ACC while CBP is highest in the cellular system. It shows good performance under uniform heavy traffic loads. DCA is adaptable to traffic load changes, has a better utilization of available channel resources, improved load balancing, and has better performance in low traffic conditions. For massive traffic, DCA leads to interferences resulting in call drop which degrades the QoS [1, 2].

The CAP variants are min. Span (MSCAP), min. Blocking (MBCAP), and min. Interference (MICAP) [3]. In MSCAP, the span between channels to be assigned is minimized with no objectionable interference. In MBCAP, call blocking probability is minimized with no unacceptable interference. In MICAP, the total sum of weighted interference is minimized with a limited number of channels. The main objective is to minimize interference.

The Heuristic method gives near-optimum solutions at a sensible computational cost of algorithmically complex/time-consuming problems like CAP. These methods assure that the spectrum assigned for use will be optimally utilized. The key techniques presently in use are expert systems, fuzzy systems, neural networks, genetic algorithm, and swarm intelligence. Intelligent systems have wide application in various fields. Depending on the problem that is to be solved, a suitable solution technique can be adopted. Expert systems are used in diagnosis, fuzzy systems in control applications, and mobile robot navigation, neural networks in predictions, load forecasting, classification of soil, and hot extraction of steel. The GA is having application in tuning fuzzy controller performance, composite laminates, and optimization problems [4–6]. The superior solution generated by GA relies on the fitness function. SVM classifier produces better compartmentalization; the fitness function of GA is designed through SVM.

In this work, MICAP is considered with DCA by applying GA (heuristic method) and SVM (classifier). The working of GA and SVM is explained in the first section. The combination of GA and SVM for DCA is detailed in the second section. The simulation results are plotted for benchmark problems and compared with the reported work in the following sections.

2 Genetic Algorithm (GA) and Support Vector Machine (SVM)

2.1 GA

First, GA is a stochastic search technique based on natural evolutionary activity. In GA, the initial population is randomly generated it evolves into better solutions for the generations to come. The important steps in GA are selection, crossover, and mutation [4]. The fittest candidates (parents) are selected. The best selected candidates create the future generation (children) using the crossover operator. The mutation operator randomly picks candidates and alters its value in the chromosome and produce solution [5–7]. The probability of crossover operation is kept higher than the mutation probability.

Steps of GA:

1. Randomly generate an initial population.
2. Evaluate fittest among total candidates.
3. Repeating the steps until an adequate solution is obtained
    a. Select the parents from the population, according to fitness
    b. Create children from choosing parents with crossover function
    c. Mutation function is done on candidates with less fit value
    d. Create a future generation
    e. Measure the fitness for every candidate in the fresh population
    f. If the chromosomes are fit, then the allocation is done.
    g. If the chromosomes are not fit to be carried for allocation then go to step a.
4. Termination condition: terminate the process of GA when 50 generations are reached.

2.2 SVM

SVM binary classification method discovers a hyperplane, which detaches the data absolutely into two classes. There is linear and nonlinear SVM. To separate linearly the two classes, the hyperplane must have maximal margin. Initially, a hyperplane is formed as H: $y = wx - b$. The collateral hyperplanes are taken at equivalent distances of H: $y = wx - b = +1$ and $y = wx - b = -1$, provided none of the data points are along the hyperplane edge and the spacing between them is maximized [8]. The data points which cross the hyperplane boundaries are support vectors as alone these locations take part in detaching hyperplane. In the nonlinear SVM, the data points are changed to some other high dimensional space such that they change to linearly separable. A dual problem is developed in the classification of SVM, by solving it obtains the optimized parameters required for classification [8, 9].

2.3 Combining GA with SVM

This work proposes GA-SVM to assign channels dynamically leading to higher SIR. With GA the channel assignment to the cells is obtained as per the demand. The effectiveness of GA can be enhanced by designing the fitness function with SVM. An optimized solution is obtained with this combination in terms of call blocking, interference in terms of co-channel and co-site edges and SIR.

As per the demand, the channels assigned to cell are separate into sets—static, i.e., fixed and dynamic. The reuse factor is taken as 3. The demands are satisfied initially through static set till fully utilized. If the demand still persists, then the dynamic set is utilized to assign channels to the further demands. The DCA is worked out by applying GA along with SVM.

GA starts by selecting the initial population, then crossover and mutation operations are performed on the dynamic set to bring forth the pair-frequency and base station vector and are stored as changeable "fitness".

SVM classifies these two base stations and frequency vectors and they are stocked as variable "f1". The set "fitness" and "f1" are checked for comparability at the fitness evaluation step.

3 Dynamic Assignments with GA-SVM

The superiority of solution generated by GA relies on the fitness function, which is designed with SVM. SVM is a supervised machine learning that is required to be trained initially, then the data points can be classified. In this work, to solve MICAP the classification of existing frequencies is done into two classes, then there suitability is checked regarding its assignment to the base station as per the demand through SVM. This helps in better optimization than performing with the only GA. This leads to reduction in interference which results in better SIR.

To start with Fig. 1, GA comprises of random set of the population to which crossover and mutation are performed to produce solutions. For better crossover and mutation, the probability rate is taken as 0.8 and 0.01, respectively, after rigorous experimentation. The GA generates pairing (chromosomes) of base stations and frequency as per the demand which will be verified for its fitness. In the fitness evaluation these chromosomes are contributing to SVM, if the set "fitness" and "f1" are equivalent resulting in minimum interference, then the channels are finally assigned, else a better set is produced in further generations. The stopping criterion is taken up as 50 generations, which results in better solutions with higher SIR.

The reason for SVM training is to generate the support vectors for finding the hyperplane line which defines margin for classification [8]. The SVM is trained by mapping elements of two vectors of equal size—traindata (row) represents base station and class (column) represents frequency. The Lagrangian multiplier value "α" is found by solving the Langrangian dual problem. The "α" are the data points in

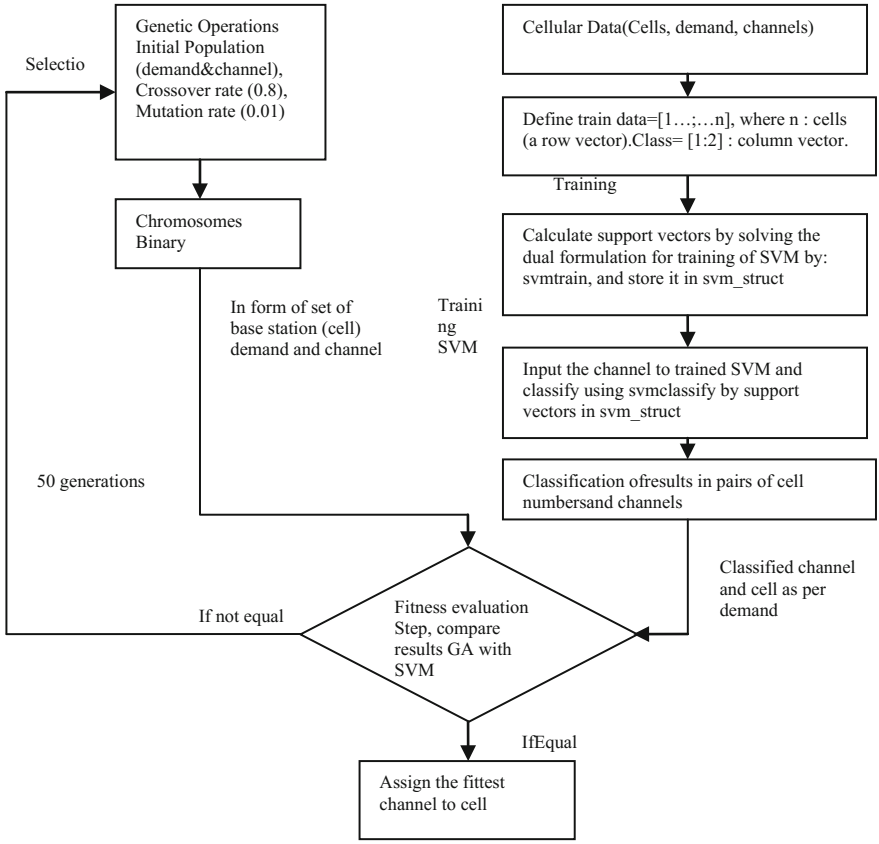

Fig. 1 GA with SVM flow

traindata with same indices, which are called as support vectors and they define the distinctive line for classifying the two classes. The base station after classification produces sufficient frequencies as per the demand and store it in an array indicating base station number. The SVM is able to find out best classification, but not the assignment of frequencies in the network.

For assigning the frequencies to the appropriate base station, we require a heuristic technique algorithm, one of this is GA. The frequency assignment generated by GA is weighed against the classified position of base station number and frequency found with SVM at the fitness evaluation step. If the comparison between the sets is equal for every iteration, then that set is considered for assignment. If they do n'ot match, then the solution obtained with GA is iterated until it equals the classification in SVM. The stopping criterion is 50 generations for assignment. A channel assignment matrix is generated.

Table 1 Benchmark details

Problem	Number of cells	Number of channels	Demand vector D (per cell)
Kunz 1	10	30	10,11,9,5,9,4,4,7,4,8
Kunz 2	15	44	10,11,9,5,9,4,4,7,4,8,8,9,10,7,7
Kunz 3	20	60	10,11,9,5,9,4,5,7,4,8,8,9,10,7,7,6,4,5,5,7
Kunz 4	25	73	10,11,9,5,9,4,5,7,4,8,8,9,10,7,7,6,4,5,5,7,6,4,5,7,5

4 Benchmark Applied

The proposed method GA-SVM is simulated on Kunz 1, 2, 3 and 4 benchmarks. Kunz [10] proposed these benchmarks to find satisfactory solutions for the CAP, with CC and CS, constraints, he applied neural network in which the solution required a large number of iterations. The detail about the benchmark is tabulated in Table 1.

5 Simulation Results

The results focus on MICAP. The GA with SVM aims to assign channels in a best possible way to create a channel assignment (CA) plan for the benchmark instances. The interferences CC and CS are attained in the form of edges and are matched up to [11, 12]. In [11], GA is the chromosomes that are represented with binary string. In [12], the GA fitness function is designed with graph theory. SIR in dBm is plotted for the CA generated. The attenuation of the signal is forecast by the Hata propagation model. The time required is calculated.

Figure 2 shows the obtained CA for Kunz 4 benchmark with proposed GA-SVM. The blue dots indicate a channel assigned to a particular cell.

As per the CA, the CC and CS are represented as "edges" indicating interference. The plot in Fig. 3 depicts, a round in the cell is the demand, which needs to be fulfilled by an appropriate channel to reduce the interference. A solid line between two cells indicates a similar channel assigned with the reuse distance of 3 is the CC. If channel assigned in a cell has spanned less than 4, a dotted line emerges indicating CS.

In [2], the method to calculate the S/I ratio in the network is given as SIR = the desired signal power level at the receiver/the sum of the cc power level and received power. The Received power = (Transmitted Power – Attenuation).The amount of signal attenuated can be foreseen with a propagation model. It characterizes mathematically the signal propagated as a function of distance, frequency, and others; The Hata propagation model which is suitable for the urban region is applied to evaluate the losses in the path. Figure 3, shows the comparison of obtaining SIR (dB) of GA-SVM with other reported results, as per the assignment of channels to the cells. The plot shows better results with proposed GA-SVM. In order to compare SIR in

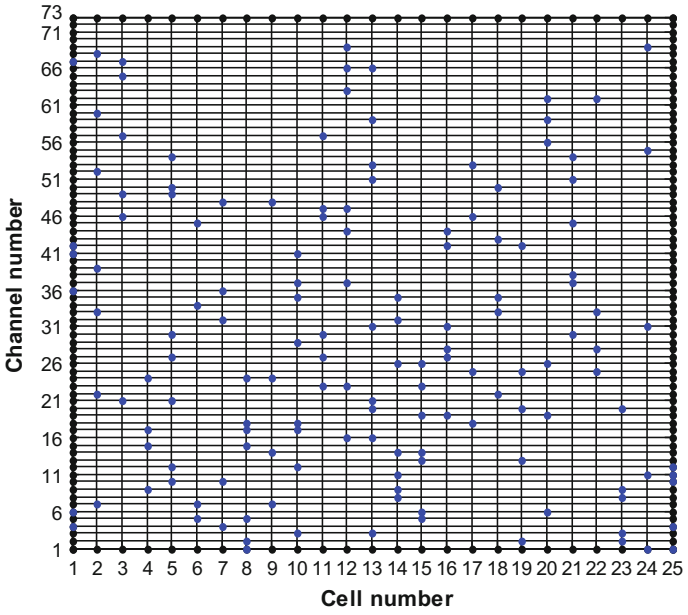

Fig. 2 Assigned channel to cell (CA)

dB, the fourth demand in each cell is considered. Table 2 shows the comparison with different methods where GA-SVM develops fewer edges.

The number of generations required to attain the best solution is given in Table 2. Also, the time required to run the simulation to attain better solution is calculated. It is simulated in MATLAB, with OS Windows 7, on a core I3 processor, 3.5 GHz speed, and 2 GB RAM.

In [2], the method to calculate the S/I ratio in the network is given as

SIR = the desired signal power level at the receiver/the sum of the cc power level and received power. The received power = (transmitted power - attenuation). The amount of signal attenuated can be foreseen with a propagation model. It characterizes mathematically the signal propagated as a function of distance, frequency, and others, The Hata propagation model which is suitable for the urban region is applied to evaluate the losses in the path. Figures 4, 5, 6, 7, shows the comparison of obtaining SIR (dB) of GA-SVM with other reported results, as per the assignment of channels to the cells. The plot shows better results with proposed GA-SVM. In order to compare SIR in dB, the fourth demand in each cell is considered.

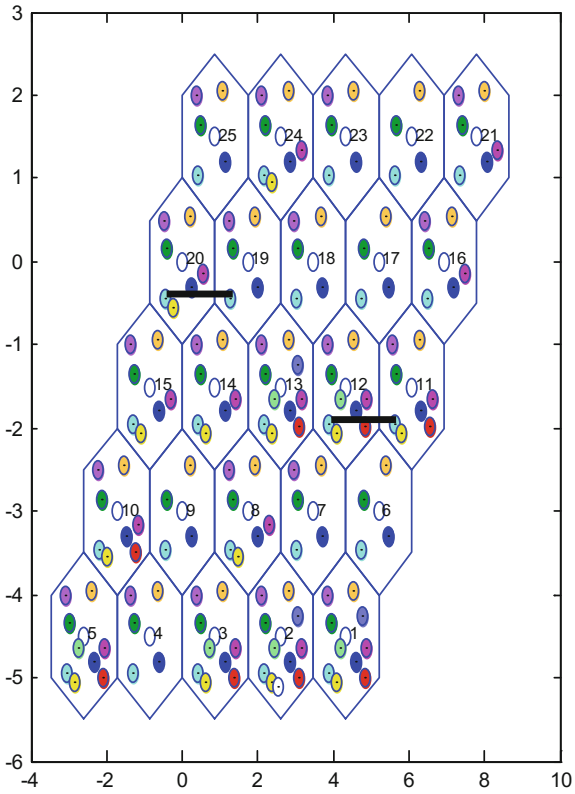

Fig. 3 Edges in Kunz 4 with GA-SVM

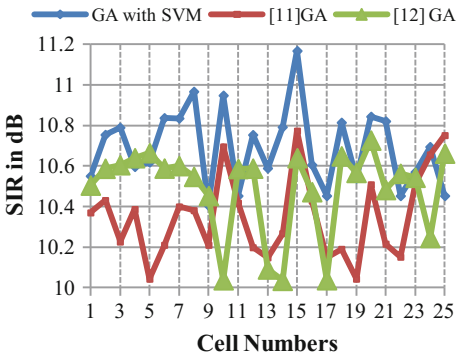

Fig. 4 Kunz 4 SIR

Table 2 CC and CS edges in Kunz benchmarks

Benchmark		Proposed GA-SVM	[12] GA	[11] GA
Kunz 4	CC edges	2	6	15
	CS edges	0	2	16
	Time (Sec.)	0.5460	0.8021	–
	Generation	50	229	2450
Kunz 3	CC edges	1	3	58
	CS edges	0	6	21
	Time (Sec.)	0.4602	0.5582	–
	Generation	50	284	50000–100000
Kunz 2	CC edges	1	0	32
	CS edges	0	1	27
	Time (Sec.)	0.4461	0.3251	–
	Generation	50	217	–
Kunz 1	CC edges	1	0	32
	CS edges	0	15	21
	Time (Sec.)	0.4648	0.2931	–
	Generation	50	300	–

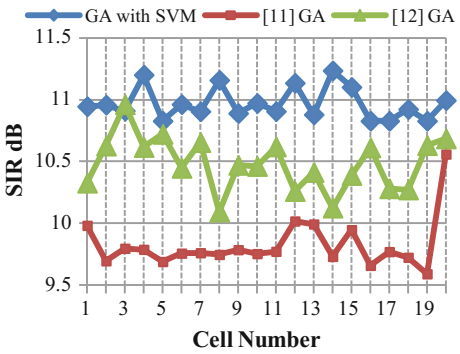

Fig. 5 Kunz 3 SIR

Fig. 6 Kunz 2 SIR

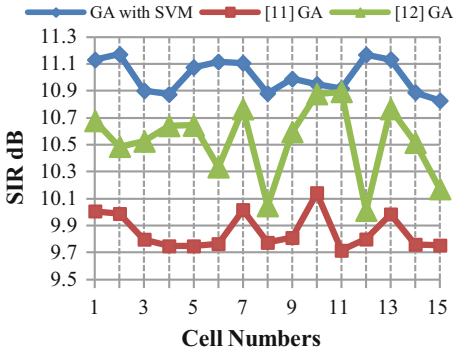

Fig. 7 Kunz 1 SIR

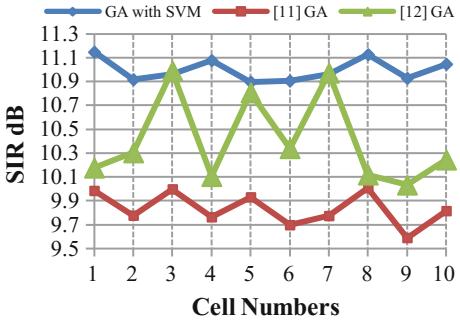

6 Conclusion

GA for optimization and SVM to classify are put together to minimize interference with the wireless network. The effectiveness of the proposed algorithm is tested on Kunz benchmark. The results are simulated to find an interference level based on the channels assigned considering zero call blocking. The proposed GA-SVM shows a reduction in interference, time for computation, and the iterations as compared to work reported on GA. The SIR is found to be between 10 and 11 dB. This work can be extended to the cognitive cellular network. The swarm intelligence heuristic techniques like ACO, ABC can be experimented for real-time application.

References

1. Singal, L.: Wireless communications, 5th edn. McGraw Hill Education, New Delhi (2014)
2. Theodore, R.: Wireless Communications - Principles and Practice. 2nd edn. Pearson education (2009)
3. http://fap.zib.de. Accessed Dec (2015)
4. Padhy, N.P..: Artificial Intelligence and Intelligence Systems. Oxford University Press, Oxford (2013)

5. Deepak, K.: A First Course in Artificial Intelligence. McGraw Hill Education (2013)
6. Saxena, P.C., Mishra, M.P.: Survey of channel allocation algorithms research for cellular systems. Int. J. Net. Comm. **2/5**, 75–104 (2012)
7. Ohatkar, S.N., Bormane, D.S.: Channel allocation technique with genetic algorithm for interference reduction in cellular network. In: Annual IEEE India Conference (INDICON) Mumbai, pp. 1–6 (2013)
8. Platt, J.C: Sequential Minimal Optimization- A fast algorithm for training Support Vectors Machines. Technical Report MSR-TR-98-14, pp. 1–6 (1998)
9. Ying, R., Jiang, T., Xing, Z.: Classification of transmission environment in UWB communication using a support vector machine. In: 2012 IEEE Globecom Workshops, Anaheim, CA 1389–1393 (2012)
10. Kunz, D.: Channel assignment for cellular radio using Neural Networks. In: IEEE Trans.Veh.Tech, pp. 188–193 (1991)
11. Wang, L., Sa, Li., Sokwei, L.: Genetic algorithms for optimal channel assignments in mobile communications. NNW.12/6 599–619 (2006)
12. Ohatkar, S., Bormane, D.: Hybrid channel allocation in cellular network based on genetic algorithm and particle swarm optimisation methods. IET Commun. **10/13**, 1571–1578 (2016)

Deployment of a Wireless Sensor Network in the Presence of Obstacle and Its Performance Evaluation

Pratit Nayak, Ekta Nashine and Sanjeet Kumar

Abstract Energy consumption of a wireless sensor network plays an important role in determining the lifetime of a network. Lifetime of any network is the total number of rounds it completes before the failure of a certain number of nodes. In harsh and inaccessible environments, the aerial deployment is done instead of manual deployment of nodes. In this process, some of the nodes are not properly deployed while some get wasted. Here, the fifty percent nodes die out time is taken as the lifetime of the network. The wastage of nodes considerably affect lifetime of the network. The main focus of the paper is on network deployment algorithms in presence of obstacles. Further, the effect of probabilities of selection of a node as cluster head, size of the obstacles and position of obstacles on the lifetime has been considered for evaluation.

Keywords Wireless sensor networks · Energy consumption
Deployment of a WSN · Lifetime evaluation

1 Introduction

Sensor networks are deployed for the monitoring of various industrial, scientific, medical and personal activities such as animal tracking, vehicle tracking, precision agriculture, security and surveillance, environmental monitoring, smart buildings, health care and so on [1]. In general, they consist of huge number of sensor nodes deployed randomly or based on certain pattern depending on an application [2]. Each individual node possesses a fixed amount of energy associated with it which gradu-

P. Nayak (✉) · E. Nashine · S. Kumar
Birla Institute of Technology, Mesra, Ranchi, Jharkhand, India
e-mail: p.nayak.911@gmail.com

E. Nashine
e-mail: ektanashine@gmail.com

S. Kumar
e-mail: sanjeet@bitmesra.ac.in

B. S. Rawat et al. (eds.), *Advances in Signal Processing and Communication* ,
Lecture Notes in Electrical Engineering 526,
https://doi.org/10.1007/978-981-13-2553-3_9

ally decreases in sensing, data aggregation, processing and transmission. Once the energy of a node is depleted below a threshold level, it can no longer contribute to the operation of the sensor network. Further, if a significant number of nodes die out, the life of the network is over. Often there is a tradeoff between lifetime and optimization of coverage area [3]. Apart from this, there are other several challenges that a Wireless Sensor Network faces, such as unreliability and unavailability of nodes, the presence of obstacles and irregular nature of network, etc. Various technological advancements have been made for example, controlling the locations of mobile nodes so as to maximize the probability of detecting randomly occurring events in real time scenarios such as mission space or any military or civilian mission [4].

In certain applications like monitoring of Volcanoes, Battlefields, Rough terrains, Wildlife etc., the deployment is done aerially [2]. In such scenarios certain number of nodes may fail or get wasted [5] due to the presence of obstacles in the communication path. Although there has been a vast amount of research work in the area of wireless sensor networks, as per our knowledge there are a few which consider the deployment in the presence of obstacles. An obstacle model for simulation of wireless sensor network by characterising different sizes of obstacles has been proposed in [6]. An obstacle mobility model for mobile ad hoc networks is also proposed in [7].

Our work takes into consideration the presence of obstacles in the deployment as well as calculation of the lifetime of wireless sensor network depending on various parameters like the probabilities of selection of clusterhead, sizes and positions of the obstacles.

In a wireless sensor network, the nodes gather information from the surrounding area and transmit the processed data in the form of packets. Each packet consists of a fixed number of bits. A cluster based approach [8] is chosen for efficient utilization of energy and to extend the lifetime of the network. The sensor nodes group themselves into clusters and a sensor node from each cluster is chosen as the cluster head. All the sensor nodes in a cluster transmit information to the cluster head which then transmits it to the base station or a sink. This saves energy as compared to individual transmission of packets from nodes to the base station [8, 9].

One of the most established work is Low Energy Adaptive Clustering Hierarchy (LEACH) protocol [9] which uses a probabilistic model to select the cluster head. The cluster head is selected every round. Based on this protocol, we have stressed upon the following cases:

i. The effect of probability of cluster head selection in the presence of obstacles. Increasing the probability of a sensor node being selected as cluster head directly affects the number of total clusters in our network [8].
ii. Presence of obstacles in the network may lead to the wastage of the nodes [11]. If deployment is aerial then the nodes that fall on the area of obstacle do not collect any data [2]. The wastage of nodes causes a change in the total amount of information gathered and hence, the energy consumption is different from obstacle-less scenario.
iii. In case of manual deployment there is a prior knowledge of the areas where the obstacle is present. Therefore, if the number of nodes and the area of deployment

is kept fixed there is an increase in the sensor node density as the size of obstacle increases. The effect of the change in position of obstacles (size being the same) may/may not alter the lifetime.

In this paper, Sect. 2 discusses our proposed model for node deployment and the algorithm, Sect. 3 deals with the effect of various parameters on the lifetime and are shown in 3 sub sections. The results obtained are summarized in Sect. 4.

2 Proposed Model for Node Deployment

In our work, we have assumed a large number of sensor nodes deployed in fixed area which contain obstacles. The deployment is in unattended area and in a random fashion. All the nodes are capable of sensing data and transmitting it.

It is based on the LEACH protocol [9]. The model is probabilistic and the cluster head is selected every round according to a fixed probability [8, 9]. The following assumptions have been made:

1. After random deployment the position of all the sensor nodes and the base station is kept fixed.
2. All the sensor nodes are homogeneous in nature, i.e. they have same initial energies and similar sensing radius.
3. The sensor nodes which lie on the area of obstacle are assumed to be wasted, i.e. they are not capable of gathering or transmitting any information [4].
4. The Obstacles that are dealt with are rectangular in shape.

Normally, in traditional LEACH protocol [9], nodes organize themselves into clusters where few of them having highest energies (advanced nodes) are selected as the cluster heads of the respective clusters with a certain probability. The probability actually helps in deciding the total number of clusterheads existing in a particular round. Due to the presence of the obstacle, no node can make cluster with any other node across an obstacle in the path.

Initially, clusterhead is selected randomly. The energy of clusterhead depletes faster than a normal node. Now, in the next cycle when advanced nodes are again selected, the chance of any previous clusterhead being selected again decreases. In our case, if a sensor node X requires some amount of energy to transmit data to sensor node Y, then Y requires same amount of energy to transmit the same amount of data from Y to X.

Main advantage of this kind of protocol is that the individual nodes don't need any control signal from base station and also the knowledge of the global network layout. Instead, they function just by communicating with their cluster head which then communicates with the centralized base station.

Energy Calculation

The energy required for the circuitry for transmission of bit E_{tx} is same as that required for by the circuitry for reception $E_{rx.}$ Also some of the energy is required

Table 1 Energy abbreviations and values in joules

Initial Energy Eo	0.5 Joules
Transmission energy ETX	50×10^{-9} Joules
Transmission energy ERX	50×10^{-9} Joules
Transmit Amplifier Energy Efs	10×10^{-12} Joules
Amplification Energy Eamp	0.0013×10^{-12} Joules
Data Aggregation Energy EDA	5×10^{-9} Joules

for data aggregation. It is denoted by EDA. Also energy is required for amplification while transmission E_{amp} to maintain a certain signal level [9].

The initial energy parameters were considered as follows (Table 1).

There are various amplifiers on different levels needed for transmission, received energy amplification etc. The Energy calculation is done on the basis of comparision of the distance between two nodes (transmitter and receiver) with a predetermined variable 'do'.

$do = (Efs/Eamp)^{1/2}$
Energy of a node per round is given by:
If (Distance > do)
Energy of the node = Present Energy- ((ETX + EDA) x (4000) + Eamp × 4000 x $(distance)^4$)
If(Distance <=do)
Energy of the node = Present Energy – ((ETX + EDA) x (4000) + Efs × 4000 x $(distance)^2$)

This calculation is kept fixed in all the rounds for which the proposed model is run.In our case we Consider that the network stops functioning (assuming non linear network) when 50% of the total nodes stop functioning (Half nodes dead) [4]. Many factors like the probability of the selection of the cluster heads, Size of the obstacles, Position of obstacles affect the Lifetime of our network. So a random deployment database was fixed and the above said parameters of the network were varied to observe the pattern of change in the lifetime of our network [4].

2.1 Algorithm Used for Deployment and Lifetime Evaluation

Step-1*: 'n' Nodes are deployed randomly.*
Step-2*: Initial energy is associated with all the nodes.*
Step-3*: The number of obstacles are input by the user.*
Step-4*: The position of obstacles are generated randomly.*
Step-5*: Nodes lying on the obstacle are considered to be wasted.*
Step-6: *For Rounds: 1 to rmax(maximum number of rounds)*

Step-a*: Cluster heads are selected on the basis of a fixed probability and energy(considered from 2nd round).*
Step-b*: Clusters are formed depending on the shortest distance from a cluster head given that no obstacle lies between the sensor node and cluster head.*
Step-c*: Energy Calculation (as mentioned above) is done on the basis of packets of data to be transferred and distance.*
Step-d*: if Energy of node==0, Increment Dead counter (Node dead)*
Step-e: *Go to Step-a.*
Step-7*: End.*

3 Effects of Various Parameters on the Lifetime of a Wireless Sensor Network

3.1 Effect of Probability of Cluster Head Selection on the Lifetime in the Presence of Obstacle

We assume the following deployment model shown in Fig. 1 for studying the effect of probability on the lifetime of the network with the parameters:

Total area: 100 units × 100 units
Total number of nodes: 100;
Size of obstacles: 20 units × 20 units.

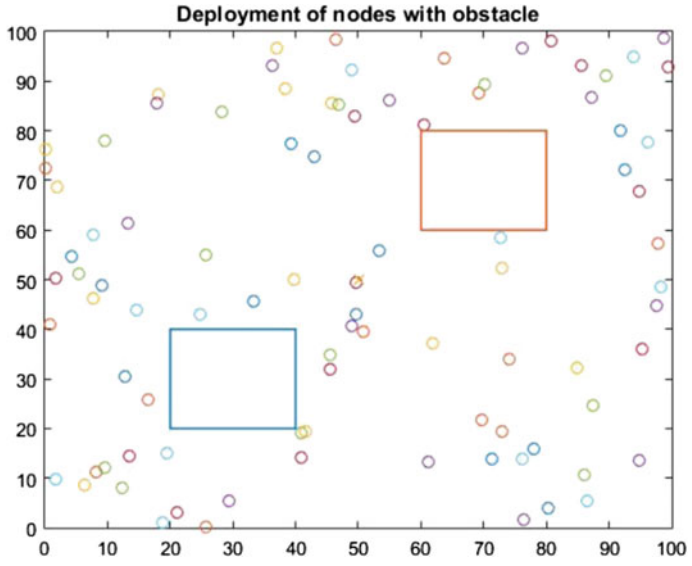

Fig. 1 Node deployment

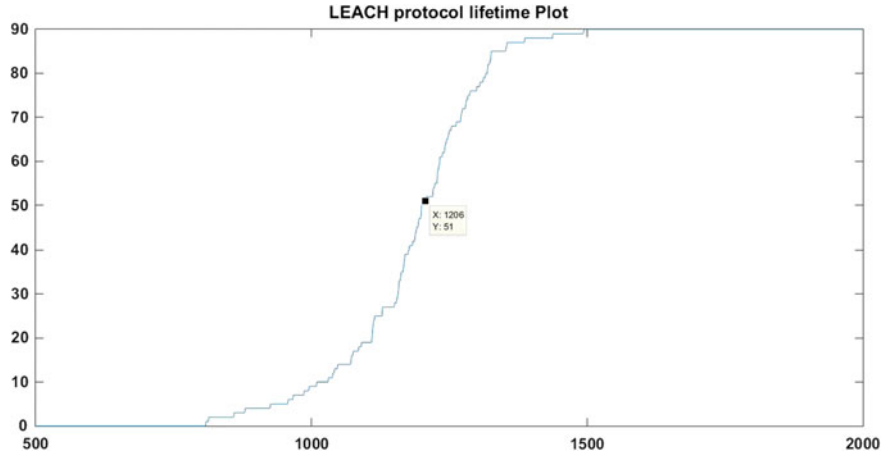

Fig. 2 Rounds versus dead nodes

Table 2 Effect of probability of cluster head selection on the lifetime of the network

Probabilty	0.05	0.1	0.2	0.3	0.5	0.7
Lifetime (in rounds)	1178	1200	1261	1302	1388	627

The nodes which were deployed on the obstacles were considered as wasted nodes.

The model was simulated for 4000 rounds on the algorithm given above [9].

The probability of clusterhead selection in tradition LEACH is 0.1, for this the lifetime of the network was observed to be 1200 as shown in Fig. 2. The lifetime of the network as calculated [4] for various probabilities at $p = 0.05$, $p = 0.1$, $p = 0.2$, $p = 0.3$, $p = 0.5$, $p = 0.9$ and the lifetimes are tabulated as follows: (Table 2).

Here we observe, increase in the probability of selection of a cluster head increases the lifetime as shown in the plot (Fig. 3). The cluster head needs to transmit a large amount of data to base station located at distant place, so its energy gets depleted at a much faster rate as compared to other nodes. However, increase in the probability of a node being selected as a cluster head increases the total number of clusters in the network. This decreases the amount of data that each cluster head will transmit (due to the presence of fewer nodes in its cluster) decreasing the energy dissipated by cluster heads while at the same time increasing the number of cluster heads.

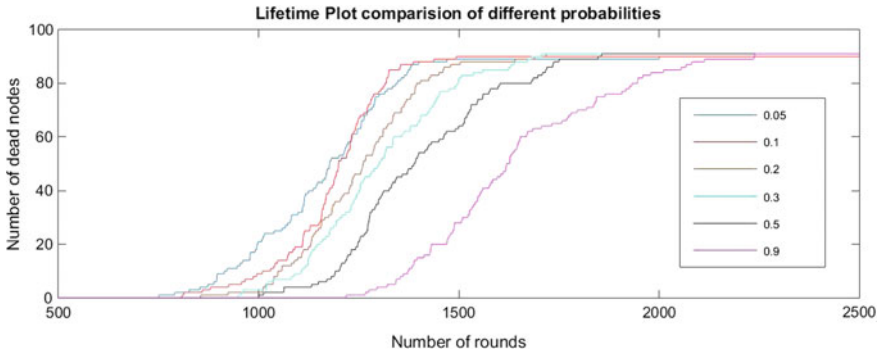

Fig. 3 Comparision of lifetime plots for different cluster head selection probabilities. Here each coloured lines represents a particular probability as shown in the legend

3.2 Effect of Size of Obstacle on the Lifetime in the Presence of Obstacle

For deployment we consider two obstacles of small size and gradually the size is increased. The number of rounds vs dead nodes plot is shown in Fig. 4 (Table 3).

The major drawback of obstacles is that the area occupied by them cannot be sensed and it wastes our nodes.We observe that increase in the size of obstacle causes a marginal increase in the lifetime of the network till a certain limit. Increase in the size of the obstacle causes more number of nodes being wasted so the overall number of nodes become less. Thus, the number of packets which are transmitted become less. Thus, Lesser energy per round will be spent in the case of larger obstacles as compared to that of smaller obstacles. However, The number of nodes gettingwasted during deployment increases from A to E as size of obstacle increase. This is clearly indicated in the graph of Fig. 4.

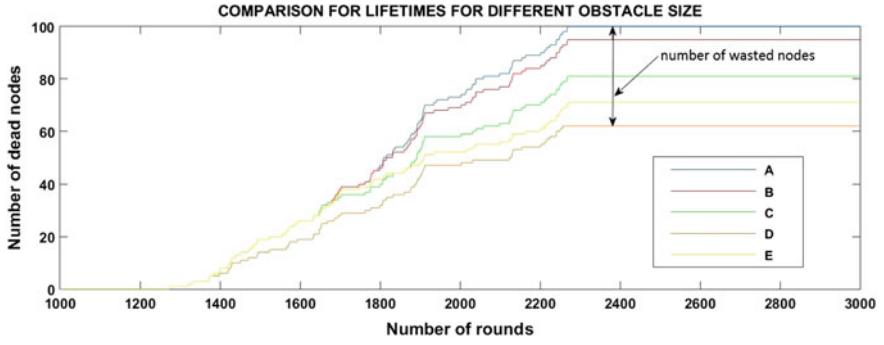

Fig. 4 The Number of rounds versus number of dead nodes. when size of obstacle is varied. Different colour lines show different obstacle sizes represented by A, B, C, D, E

Table 3 The lifetime (Half node dead), First node dead, Last node dead

Index	Size of obstacle	First node dead (rounds)	Half node dead (rounds)	Last node dead (rounds)
A	10 units × 10 units	1276	1813	2269
B	20 units × 20 units	1275	1831	2270
C	30 units × 30 units	1275	1892	2269
D	40 units × 40 units	1276	2124	2257
E	20 units × 70 units	1275	1911	2269

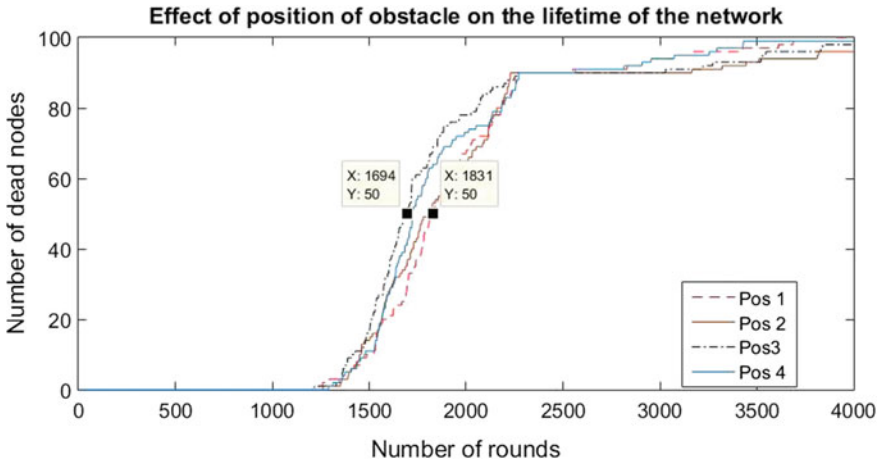

Fig. 5 Number of rounds versus number of dead nodes for different obstacle positions. Here different types of lines represent the dead nodes versus no. of rounds for various positions of the obstacles

3.3 Effect of Position of Obstacle on the Lifetime of the Network

In this case we assume an obstacle of size 20 units × 70 units occupying different positions in the same area. Also the overall node density is kept constant. It is observed that there is only a marginal change in the lifetime of the network for different cases. The graphs for each case taken is compared in the Fig. 5. Pos 1, 2, 3, 4 represent 4 random positions of the obstacle D (20 units × 70 units).

4 Conclusion

An improvement of 35.5% in the lifetime of the wireless sensor network is thus observed on increasing the probability of cluster head selection to 0.9. The larger the number of clusters the lesser the rate of energy dissipation per cluster. In case of variable obstacle size larger obstacles result in lower number of useful nodes. Since the total data collected,processed and transmitted in this case is less than that of obstacle less region, the total energy depleted per round decreases thus improving the lifetime of the network. But the improvement is very marginal and up to some extent. When the position of obstacle is changed keeping the size of obstacle and number of nodes constant slight deviations occur about the average lifetime (1762.5 rounds).

References

1. Jino Ramson, S.R., Jackuline Moni, D.: Applications of wireless sensor networks – a survey. In: International Conference on Innovations in Electrical, Electronics, Instrumentation and Media Technology (ICEEIMT) (2017)
2. Wang, Y.-C., Hu, C.-C., Tseng, Y.-C.: Efficient deployment algorithms for ensuring coverage and connectivity of wireless sensor networks internet, In: 2005. Proceedings of the first International Conference on 10–15 July 2005
3. Liu, C., Cao, G.: Spatial-temporal coverage optimization in wireless sensor networks. IEEE Trans. Mob. Comput. **10**(4), 465–478 (2011)
4. Vajdi, A., Zhang, G., Wang, Y., Wanglf, T.: Management model for large-scale event-driven wireless sensor networks. IEEE Sens. J. **16**(20) (2016)
5. Zhong, M., Cassandras, C.G.: Distributed coverage control and data collection with mobile sensor networks. IEEE Trans. Autom. Control **56**(10), 2445–2455 (2011)
6. Chatzigiannakis, I., Mylonas, G., Nikoletseas, S.: Modeling and evaluation of the effect of obstacles on the performance of wireless sensor networks. In: 39th Annual Simulation Symposium (ANSS'06) (2006)
7. Jardosh, A., Belding-Royer, E., Almeroth, K., Suri, S.: Towards realistic mobility models for mobile ad hoc networks. In: 9th ACM/IEEE Annual International Conference on Mobile Computing (MOBICOM 2003) (San Diego, CA), pp. 217–229 (2003)
8. Tripathi, R.K., Singh, Y.N., Verma, N.K.: Clustering algorithm for non-uniformly distributed nodes in wireless sensor network, 14 Feb 2013
9. Heinzelman, W., Chandrakasan, A., Balakrishnan, H.: Energy-efficient communication protocols for wireless microsensor networks. In: Proceedings of the 33rd Hawaaian International Conference on Systems Science (HICSS) (2000)

Analysis of Empty Substrate-Integrated Waveguide H Plane Horn Antenna for K Band Applications

Abhay Kumar, Nitin Muchhal, Arnab Chakraborty and Shweta Srivastava

Abstract This paper presents the analysis of Empty Substrate-Integrated Waveguide (ESIW) H plane horn antenna for K band application. The paper also compares the ESIW with Substrate-Integrated Waveguide (SIW) technology on various parameters for making the horn antenna. For K band applications, the SIW horn antenna provides various advantages over normal microstrip horn antenna. SIW technology is easy to fabricate and test and it provides all advantage of the conventional waveguide horn antenna. The SIW horn antenna is planer in design and can be easily interfaced with planer active and passive circuits. To improve the performance of SIW, the air-filled substrate cut is made to form ESIW, which is presented in this paper. The cut in substrate allows less dependency of an ESIW horn antenna over dielectric losses. The ESIW horn antenna does not require any extra element to improve the impedance matching at the end of the aperture; hence it shows an advantage over normal SIW horn antenna. The ESIW horn antenna can be used to make low profile short-range radar working in the K band.

Keywords Substrate-integrated waveguide (SIW)
Empty substrate-integrated waveguide (ESIW) · Horn antenna · Parametric study
K band · Radar · Automotive · HFSS

A. Kumar (✉) · N. Muchhal · A. Chakraborty · S. Srivastava
ECE Department, Jaypee Institute of Information Technology, Sector 128, Jaypee Wish Town Village, Sultanpur, Noida 201304, Uttar Pradesh, India
e-mail: abhay.kumar@jiit.ac.in

N. Muchhal
e-mail: nmuchhal@gmail.com

A. Chakraborty
e-mail: arnab.chk@hotmail.com

S. Srivastava
e-mail: shweta.srivastava@jiit.ac.in

B. S. Rawat et al. (eds.), *Advances in Signal Processing and Communication* ,
Lecture Notes in Electrical Engineering 526,
https://doi.org/10.1007/978-981-13-2553-3_10

1 Introduction

Empty Substrate-Integrated Waveguide is the advance version of Substrate-Integrated Waveguide. In ESIW, the portion of the substrate is removed, which minimized the substrate losses and hence improvement in gain for the desired frequency can be seen over normal SIW antenna [1, 2]. The increase in frequency, decrease the size of the antenna. Various technologies can be used to implement a high-frequency application antenna. At high frequency, the microstrip antenna shows spurious radiations, this results in a decrease of efficiency. The thin substrate increases the impedance mismatch of the antenna substrate and the air which further reduces the antenna gain [3–5]. To improve the result SIW technology can be used. SIW is comparable to conventional waveguide. In SIW, parallel lines of the alternative metallic vias are sandwiched between the two metal sheets. Due to via, only TE mode is possible [6]. The SIW can be used to implement several planar antennas for various applications [7, 8]. As waveguide is a high pass filter, the cutoff frequency of SIW is kept near about 19.4 GHz, so that the K band antenna design can be easily accomplished. The horn antenna is designed to resonate between 22 and 28 GHz. The automotive radar finds their applications in this frequency region; hence SIW and ESIW technology is best suited for such applications. The simulation for SIW, H plane SIW horn antenna, and H plane ESIW horn antenna is done on HFSS software. The paper is divided into three sections. The first section discusses the SIW, SIW horn antenna, and ESIW horn antenna design. The second portion shows the parametric analysis of the ESIW horn antenna. The third and the last portion talks about the comparison of SIW and ESIW horn antenna.

2 Design of SIW and Empty SIW H Plane Horn Antenna

For designing Empty SIW H plane horn antenna, it is required to design the SIW. The waveguide is a high-pass filter so the cutoff frequency is to be set for proper frequency resonance. Once SIW is designed, we can use it as a feeding element to the H plane horn antenna. This section discusses SIW, SIW horn antenna, and ESIW horn antenna design.

2.1 Substrate-Integrated Waveguide Design for Cutoff Frequency of 19.4 GHz

The design of the SIW horn antenna starts with the design of SIW. As per the requirement of the application, the feeding SIW to a horn antenna should have a cutoff frequency lesser than the desired frequency. For K band application the horn antenna should resonate between 18 and 27 GHz. We have designed our SIW to

have a cutoff frequency of 19.4 GHz. The 19.4 GHz cutoff can be calculated from Eq. (1). The substrate used is RT/duroid 5870 with $\varepsilon_r = 2.33$. The value of $'a'$ can be calculated by approximating the cutoff frequency. Here, $'a'$ is the dimension of the larger side of air-filled conventional waveguide. If the waveguide is dielectric filled the dimension reduces to $'a'_d$.

$$f_c = \frac{c}{2a} \tag{1}$$

The dimension $'a'_d$ can be calculated using Eq. (2). Here, $'\varepsilon'_r$ is the permittivity of dielectric filled in the waveguide.

$$a_d = \frac{a}{\sqrt{\varepsilon_r}} \tag{2}$$

The dimension of SIW, i.e., a_{SIW} can be calculated by using Eq. (3) [9, 10]. Here $'p'$ is the pitch of via and $'d'$ is the diameter of via in SIW.

$$a_{SIW} = a_d + \frac{d^2}{0.95p} \tag{3}$$

The diameter $d = 1$ mm and pitch $p = 1.5$ mm, these values are selected to minimize the leakage across the via. The value of $a_{SIW} \approx 5.35$ mm. The guided wavelength use in Eq. (4) can be calculated using Eq. (5) [11].

Here,

$$d < \lambda_g/5 \quad and \quad p < 2d \tag{4}$$

And,

$$\lambda_g = \frac{2\pi}{\sqrt{\frac{\varepsilon_r(2\pi f)^2}{c^2} + \left(\frac{\pi}{a}\right)^2}} \tag{5}$$

The height (h) of the substrate is taken as 1.6 mm. The gain of antenna improves with the increase in the height of the substrate. In smaller height the bandwidth is less.

Figure 1 shows the design of SIW with various parameters. Figure 1a clearly shows the SIW design and current distribution. The proper selection of pitch and diameter of via does not allow the leakage of field. The cutoff frequency for TE_{10} mode is set at 19.4 GHz.

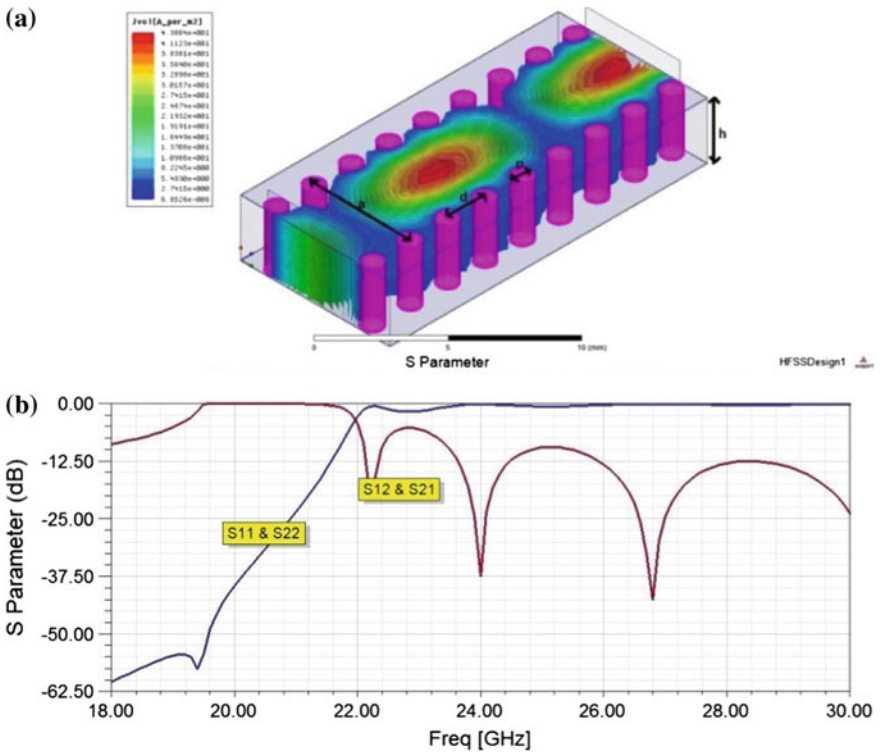

Fig. 1 **a** SIW with current distribution. **b** S Parameter

2.2 *H Plane Substrate-Integrated Waveguide Horn Antenna for K Band Application*

The SIW H plane horn antenna can be implemented by taking the right design of SIW feed. The substrate is similar to SIW with the same height. The flaring angle decides the gain as well as the frequency of operation. The gain increases with increase in substrate height and reduced flaring angle up to a certain limit. The feed length (L6) from the start of SIW also plays a significant role in the antenna resonance frequency. The various horn antenna parameters can be calculated by the formula given in Eq. (6)–(9).

Figure 2 clearly shows the various parameters of the horn antenna operating in the K band. The parameter taken is specific for particular frequency resonance. Figure 2 also shows the current distribution across the antenna flared portion.

Table 1 gives the various parameters of H plane SIW horn antenna. Few parameters are directly taken from the SIW parameter, the rest can be calculated using the formula given in Eq. (6)–(9). The various parameters of the horn antenna are selected to provide a minimum phase error [12].

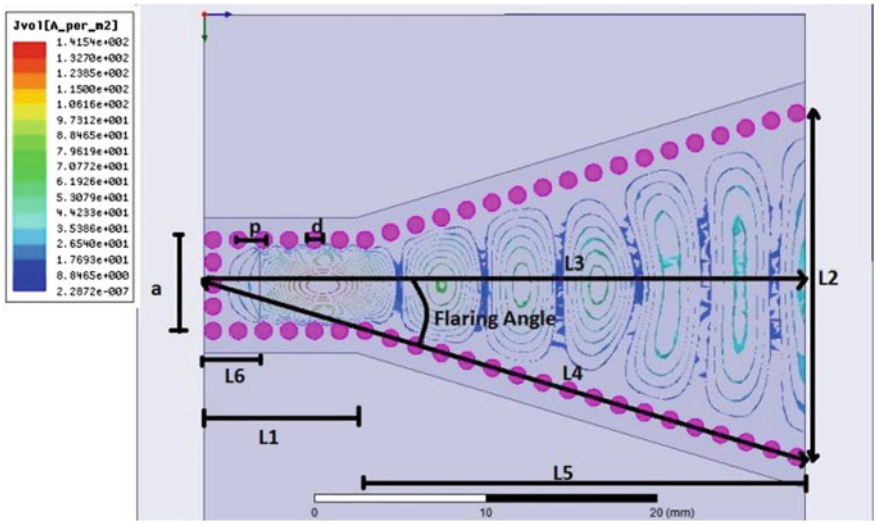

Fig. 2 The SIW H Plane Horn antenna with various parameters and current distributions

Table 1 SIW H plane horn antenna dimension

Parameter	a	p	d
Value (mm)	5.35 mm	1.5 mm	1 mm
Parameter	L1	L2	L3
Value (mm)	9 mm	20.31 mm	35.5 mm
Parameter	L4	L6	Flaring angle
Value (mm)	37 mm	3.3 mm	16.37°

$$L4^2 = L3^2 + \left(\frac{L2}{2}\right)^2 \tag{6}$$

$$Flaring\ Angle = arctan\left(\frac{L2}{2L3}\right)^2 \tag{7}$$

$$L5 = (L2 - a)\sqrt{\left(\frac{L4}{L2}\right) - \frac{1}{4}} \tag{8}$$

$$L2 = \sqrt{3\lambda L3} \tag{9}$$

Figure 3 explains the behavior of H plane SIW horn antenna. The S11 parameter shown in Fig. 3a describes the working of the horn antenna in the K band. The pattern is directional on a plane where phi = 0° and theta = 90°, i.e., H-plane of the horn antenna, as shown in Fig. 3d if the antenna is drawn on theta = 90° plane.

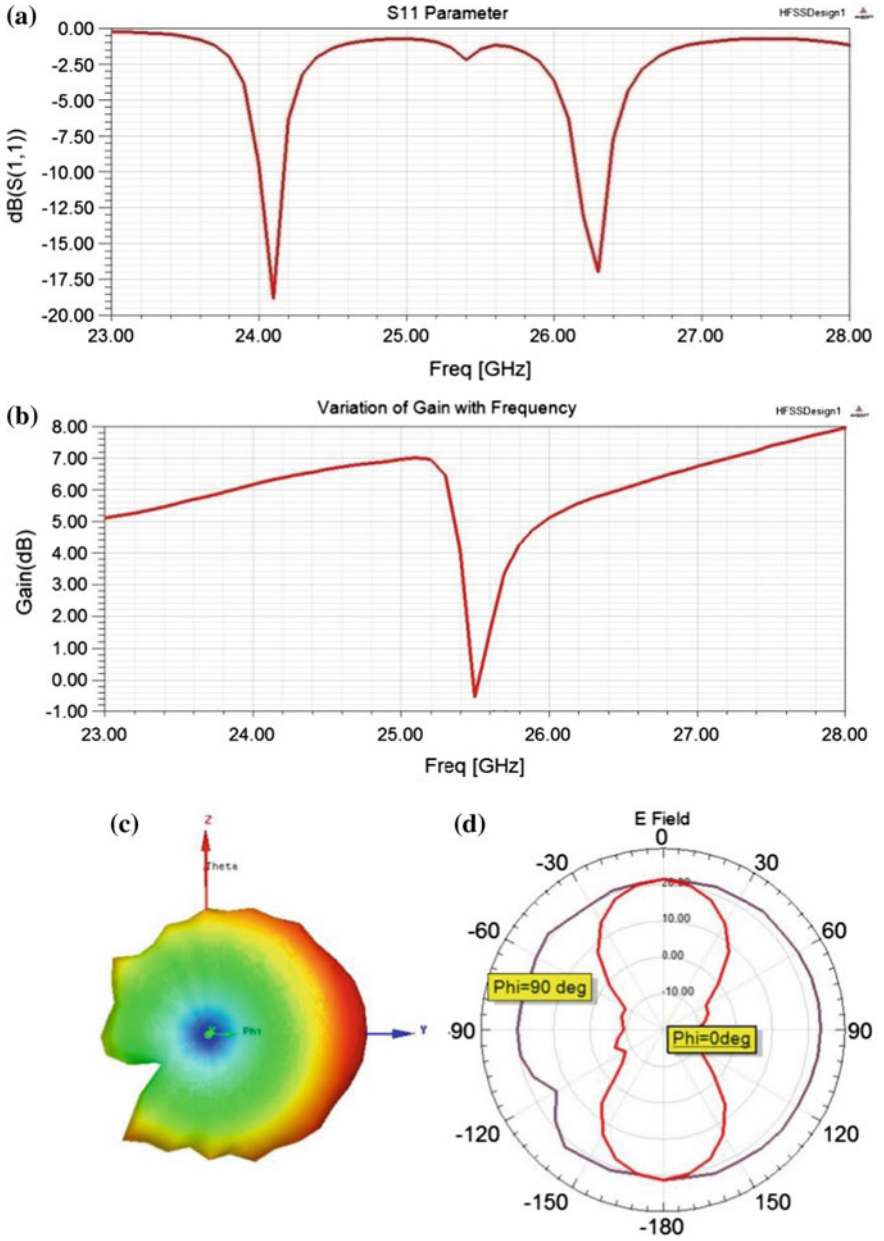

Fig. 3 SIW H Plane Horn Antenna. **a** S11 parameter. **b** Gain versus Frequency. **c** 3D E-field. **d** E-field at phi = 0^o and 90^o

2.3 H Plane Empty Substrate-Integrated Waveguide Horn Antenna for K Band Application

The reason to empty the substrate is to increase the gain efficiency by reducing the substrate loss. The air-filled empty substrate helps to easily match to the free space impedance, hence the requirement of transition at the end of the aperture is nil.

The ESIW horn antenna has four new parameters. Another parameter is similar to SIW horn antenna mention in Fig. 2. The new parameter L7–L10 decides the left frequency shift on S11 parameter with respect to the SIW horn antenna. The size of the cut in the substrate also decides the amount of gain improvement on the resonant frequency, i.e., at 23.5 and 26.4 GHz. The design of both SIW and ESIW horn antenna are kept similar to see the improvement and the importance of each structure.

Figure 4 and Table 2 show various parameters of an ESIW horn antenna. From the S11 parameter given in Fig. 6a, it is clear that the horn antenna resonates at two frequencies 23.5 and 26.4 GHz. The maximum gain that the horn antenna can achieve is 6.45 dB as plotted in Fig. 6b. Figure 5 is a radiation pattern plot of an ESIW horn antenna.

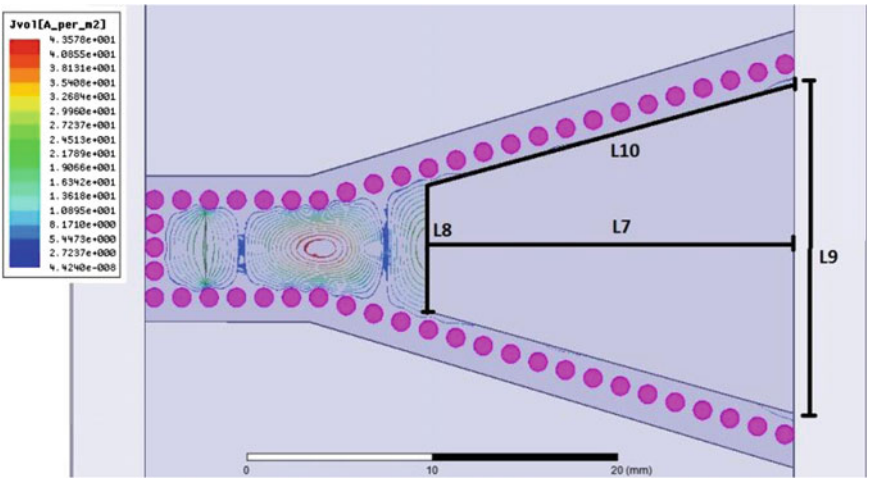

Fig. 4 ESIW H plane horn antenna and current distribution

Table 2 ESIW antenna dimension

Parameter	L7	L8	L9	L10
Value (mm)	20 mm	6.87 mm	18 mm	20.76 mm

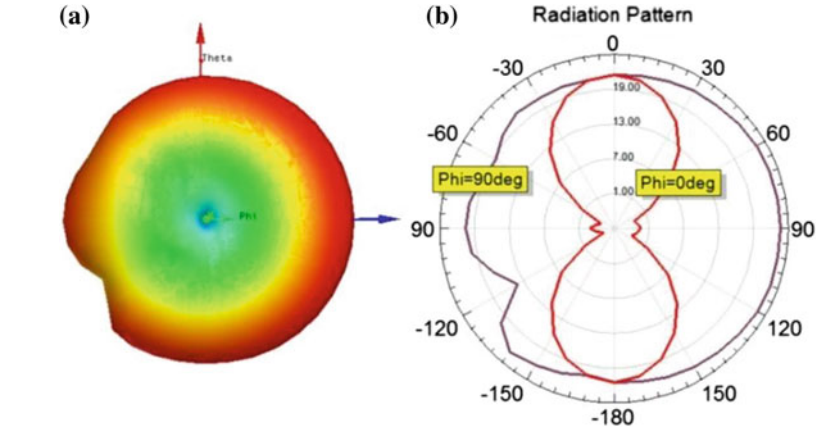

Fig. 5 **a** 3D E field at 23.5 GHz. **b** E Field at 23.5 GHz

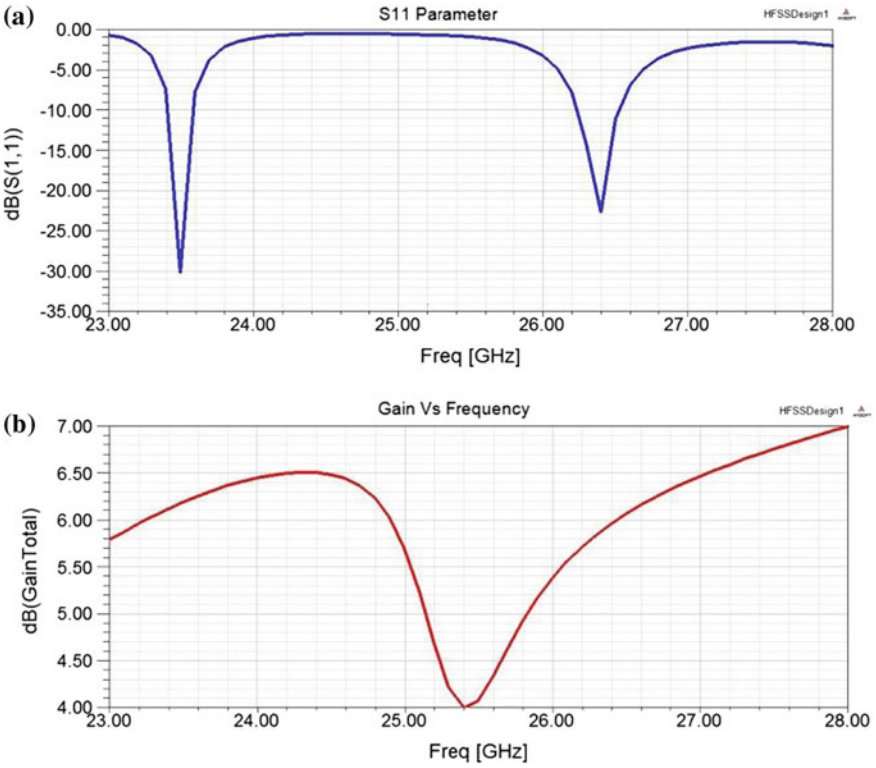

Fig. 6 **a** S11 parameter (minimum at 23. 5 GHz and 26.4 GHz). **b** Gain versus Frequency at Phi = 90 and Theta = 90

3 Parametric Study of ESIW H Plane Horn Antenna

The parametric study of Empty SIW H plane horn antenna depends upon the flaring angle, feed length 'L6', substrate cut length 'L7' from the aperture and dimension of feed length 'a'.

Figure 7 shows the S11 parameter shifts toward the right-hand side while 'a' decreases. The best result is seen when a = 5.35 mm. Figure 8 explains how the feed length L6 affects the S11 parameter. With the increase in L6 from 2.9 mm to 3.5 mm the S11 parameter shifts toward right. One thing can also be seen that the S11 parameter near 26 GHz, i.e., the second band shifts right while increasing the L6.

Hence, in conclusion, as we keep on increasing the L6 the gap between the two bands remains almost same, To get the best result out of it L6 is kept similar to SIW horn antenna, i.e., L6 = 3.3 mm.

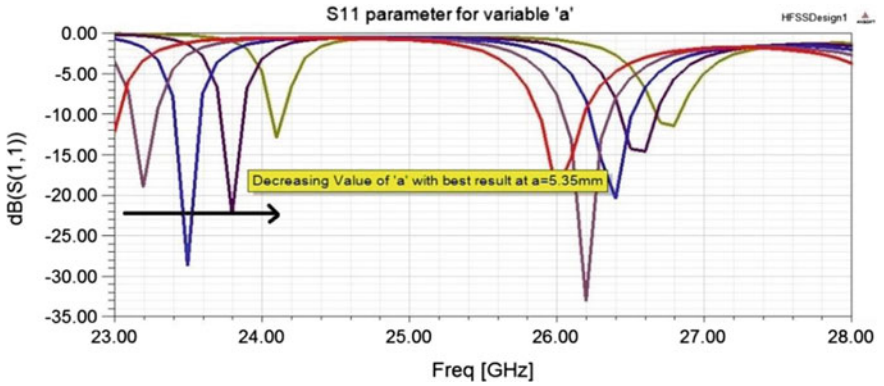

Fig. 7 Change of feed dimension 'a' with L6 = 3.3 mm and flaring angle = 16.35°

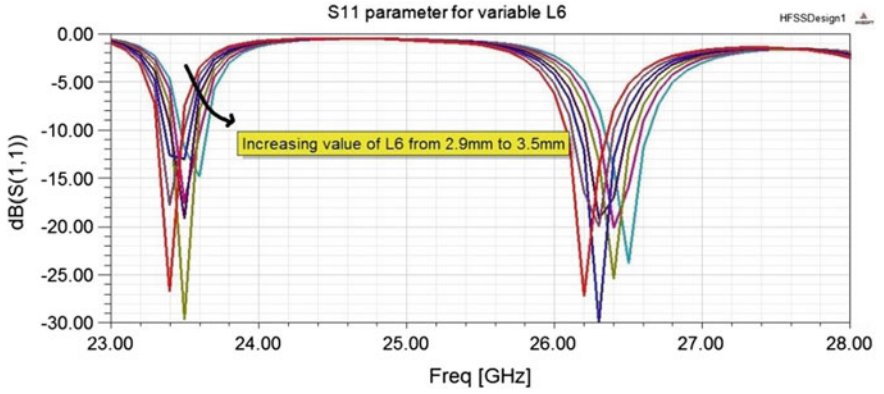

Fig. 8 Variable feed length 'L6' and a = 5.35 mm and flaring angle = 16.35°

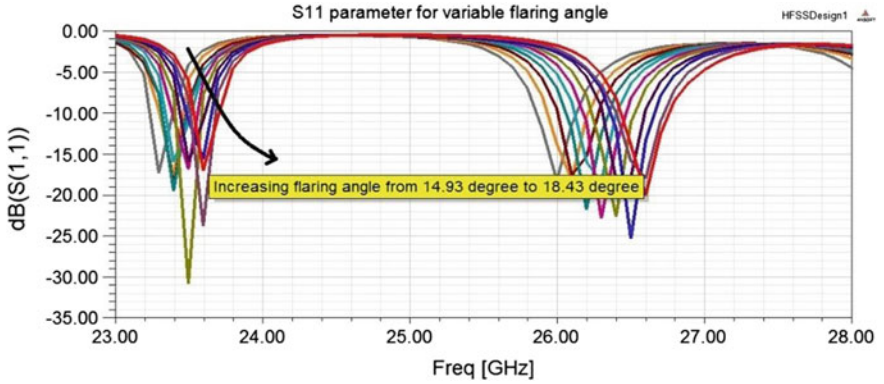

Fig. 9 Effect of flaring angle with a = 5.35 mm, L6 = 3.3 mm

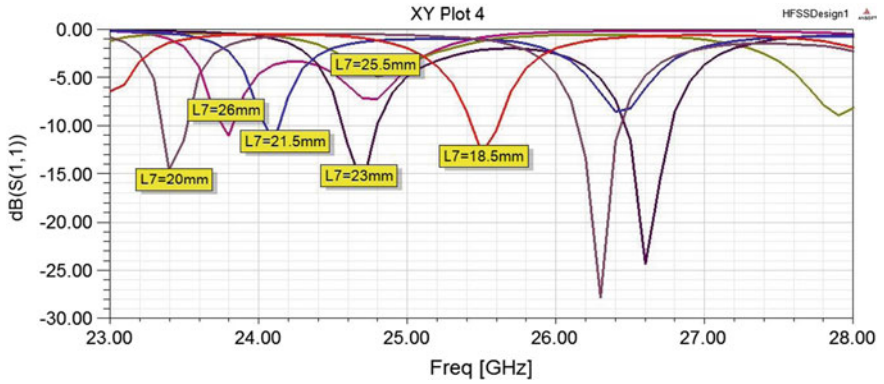

Fig. 10 S11 parameter for change in L7

Figure 9 explains the resultant change in the S11 parameter while decreasing the flaring angle. It can be seen from the Fig. 9 that the S11 parameter shifts left while decreasing the flaring angle. The best result can be seen at flaring angle = 16.35°. The flaring angle changes from 14.93° to 18.43°.The last change in the design that affects the resonant frequency drastically is the change of L7, i.e., the increase and decrease of the substrate cut. Figure 10 explains the nonlinear trends in S11 parameter with the increase in the dimension L7.

4 Results

To compare the SIW and ESIW horn antenna, we have plotted S11 parameter and gain versus Frequency curve.

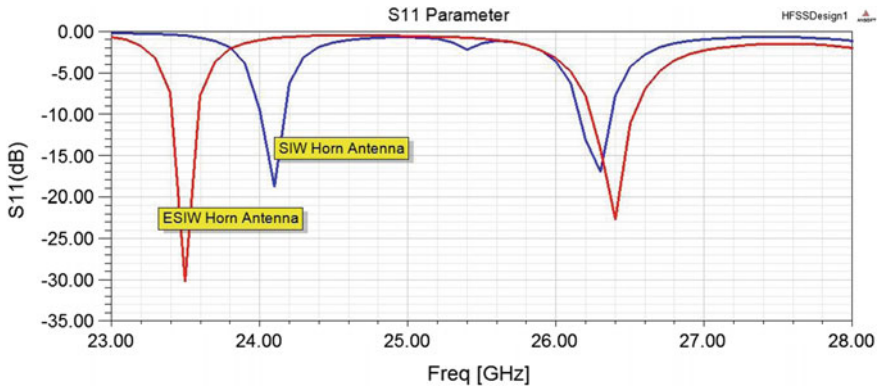

Fig. 11 S11 parameter comparison SIW and ESIW Horn antenna

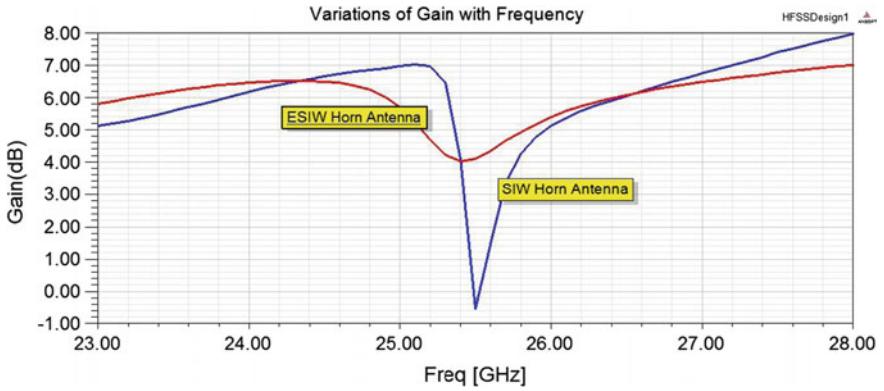

Fig. 12 Gain versus frequency comparison of SIW and ESIW horn antenna

The Fig. 11 explains the effect of removing the substrate from SIW horn antenna. The removal of the substrate shifts the S11 parameter to the left-hand side. This means for the same cutoff frequency the size of the antenna is increased. The impedance matching in case of SIW horn antenna is less when compared to ESIW horn antenna.

Figure 12 shows the gain versus frequency plot. It is clearly visible that for the resonance frequency 23.5 GHz the gain of ESIW is 0.8 dB greater than the SIW horn antenna and at 26.4 GHz the gain of both antennas is similar.

5 Conclusion and Future Scope

The ESIW horn antenna is a better method for high gain front end antenna design in an automotive radar application. The ESIW provides better results equivalent to the conventional waveguide horn antenna. The ESIW is easy to fabricate and light in weight hence can be easily installed in the vehicle. Further work can be done with the different design of substrate cut and its analysis.

References

1. Angel Belengue, H.: Novel empty substrate integrated waveguide for high-performance microwave integrated circuits. IEEE Trans. Microw. Theory Tech. **62**(4), 832–839 (2014)
2. Jorge Mateo, A.: Highly efficient and well-matched empty substrate integrated waveguide H-plane horn antenna. IEEE Antennas Wirel. Propag. Lett. **15**, 1510–1513 (2016)
3. Esquius-Morote, M., Fuchs, B.: A printed transition for matching improvement of SIW horn antennas. IEEE Trans. Antennas Propag. **61**(4), 923–1930 (2013)
4. Liu, J., Jackson, D.: Substrate integrated waveguide (SIW) leaky-wave antenna with transverse slots. IEEE Trans. Antennas Propag. **60**(1), 20–29 (2012)
5. Che, W., Fu, B.: A compact substrate integrated waveguide H-plane horn antenna with dielectric arc lens. Int. J. RF Microw. Comput.-Aided Eng. **17**(5), 473–479 (2007)
6. Tarek Djerafi, A.: Substrate integrated waveguide antennas. In: Handbook of Antenna Technologies. Springer, Singapore (2015)
7. Li, Z., Wu, K.: A new approach to integrated horn antenna. In: Proceedings of ANTEM, Ottawa, pp. 535–538 (2004)
8. Li, Z., Chen, X.-P.: A surface mountable pyramidal horn antenna and transition to substrate integrated waveguide. In: Proceedings of ISSSE, pp. 607–610 (2007)
9. Deslandes, D., Wu, K.: Accurate modeling, wave mechanisms, and design considerations of a substrate integrated waveguide. IEEE Trans. Microw. Theory Tech. **54**(6), 2516–2526 (2006)
10. Feng Xu, K.: Guided-wave and leakage characteristics of substrate integrated waveguide. IEEE Trans. Microw. Theory Tech. **53**(1), 66–73 (2005)
11. Rayas-Sanchez, J.E., Gutierrez-Ayala, V.: A general EM-based design procedure for single-layer substrate integrated waveguide interconnects with microstrip transitions, In IEEE MTT-S International Microwave Symposium Digest, pp. 983–986 (2008)
12. Pozar, D.M.: Microwave Engineering. Wiley, Hoboken (2009)

PAPR Reduction Comparison in FFT-Based OFDM Versus DWT-Based OFDM

Alok Joshi, Apoorv Manas, Samarth Garg and Rahul Wason

Abstract In this paper, we have compared the performance of DWT OFDM and FFT OFDM. The DWT OFDM can act as a possible substitute for the Fast Fourier Transform (FFT) as there is no requirement of Cyclic Prefix due to the overlapping properties of DWT. This satisfies the orthogonality principle with the ideal reconstruction of the signal. Discrete Wavelet Transform (DWT), which is the basis of DWT OFDM, has many beneficial characteristics over FFT OFDM. Simply by replacing the FFT block with DWT in OFDM system, an improvement in performance has been detected which creates a new DWT-based OFDM system. Our simulation result shows that DWT OFDM system is superior to FFT OFDM in terms of PAPR by up to 2.3 dB with an affordable decrease in overall complexity of the system.

Keywords Orthogonal frequency division (OFDM) · DWT OFDM
Wavelet transform · PAPR · Cyclic prefix · Low complexity

1 Introduction

Multi-carrier Orthogonal Frequency-Division Multiplexing (OFDM) scheme uses parallel processing techniques, allowing simultaneous data transmission over a very closely spaced orthogonal subcarrier signal with an overlapping spectrum. With the addition of guard interval and cyclic prefix, it provided better orthogonality in

A. Joshi · A. Manas · S. Garg (✉) · R. Wason
Jaypee Institute of Information Technology University, Noida 201301, India
e-mail: smarth9625@gmail.com

A. Joshi
e-mail: alok.joshi@jiit.ac.in

A. Manas
e-mail: apoorvmanas96@gmail.com

R. Wason
e-mail: rahulwason007@gmail.com

B. S. Rawat et al. (eds.), *Advances in Signal Processing and Communication* ,
Lecture Notes in Electrical Engineering 526,
https://doi.org/10.1007/978-981-13-2553-3_11

transmission channels affected by multipath propagation. An OFDM Transmitter System uses Inverse Fast Fourier Transform (IFFT), whereas an OFDM Receiver System uses Fast Fourier Transform (FFT). Some advantages of an OFDM System include an improved Bandwidth efficiency, narrowband interference, higher spectral efficiency and resistance to frequency selective fading with low computation [1]. But have major issues like low resistance to Inter Carrier Interference (ICI) and Inter Symbol Interference (ISI), wastage of bandwidth as cyclic prefix insertion is needed, higher side lobes with increased time and frequency synchronization issues and high Peak to Average Power Ratio (PAPR) of the system [2].

The Wavelet Transform based OFDM is a new technique which is implemented here by using DWT. Here, we do not require adding of cyclic prefix as the DWT has good robustness against ICI and ISI due to the finite length of its subcarriers. DWT has lower side lobes, when we transmit these side lobes it results in increasing the spectral and reduction of implementation complexity of the OFDM system. DWT OFDM is then compared with FFT OFDM for further reductions in PAPR.

The rest of the paper is organized as follows: Sect. 2 summarizes the conventional FFT OFDM System. Section 3 gives the DWT OFDM System. Section 4 evaluates the obtained performance to verify the robustness and feasibility of the presented analysis and finally, the conclusion is presented in Sect. 5.

2 Fast Fourier Transform OFDM (FFT OFDM)

The Orthogonal Frequency-Division Multiplexing (OFDM) is a technique used to alleviate frequency selective channels, where channel bandwidths (W) is divided into M lower rate data stream, which are transmitted simultaneously by many subcarriers. The bandwidth of each subcarrier, i.e., W/M is smaller than the coherence bandwidth B_c. The channel is considered as a flat fading channel as W/M is much smaller than the B_c. The subcarriers in the OFDM system are overlapping due to its principle of orthogonality. Orthogonality for OFDM signal is expressed as

$$\frac{1}{\mathrm{T}}\int_{0}^{\mathrm{T}} \mathrm{e}^{\mathrm{j}2\pi \mathrm{f_a t}} \times \mathrm{e}^{-\mathrm{j}2\pi \mathrm{f_b t}} \mathrm{dt} = \begin{cases} 0 \ \forall \, \mathrm{a} \neq \mathrm{b} \\ 1 \ \forall \, \mathrm{a} = \mathrm{b} \end{cases}, \tag{1}$$

Taking discrete samples whose sampling instances are at time $t = mT_s = \frac{mT}{M}$, $m = 0, 1, 2, 3 \ldots, M-1$. The time domain representation is given as

$$\frac{1}{M}\sum_{a=0}^{M-1} e^{\frac{j2\pi a}{T} mT_s} \times e^{\frac{-j2\pi b}{T} mT_s} = \frac{1}{M}\sum_{a=0}^{M-1} e^{\frac{j2\pi (a-b)}{M} m} = \begin{cases} 0 \ \forall \, a \neq b \\ 1 \ \forall \, a = b \end{cases}, \tag{2}$$

Effective utilization of the frequency spectrum through overlapping subcarriers without interference with being orthogonal to each other making them totally different from one another acts as an advantage in OFDM communication systems.

2.1 OFDM Transmitter

FFT based OFDM transmitter is shown in Fig. 1, $U[n]$ is a stream of binary digits. Initially, this stream is serial which is changed into M parallel streams by demultiplexing. Each of these streams is converted to a symbol stream, after which IFFT performed on these set of symbols which results in complex time-domain samples of the signal. These are then converted using digital-to-analog converters (DACs) to analog domain at the carrier frequency fc. The transmission signal $u(t)$ is obtained by summation of the analogs.

The OFDM symbol duration is Tu seconds. The time domain representation with the inverse Fourier transformed and with time interval as $T_u = MT$ the spectrum is denoted as

$$T_u = \frac{2\pi}{\Delta\omega} \Leftrightarrow \Delta\omega = \frac{2\pi}{T_u} = 2\pi\Delta f, \tag{3}$$

Using the above equation, the Fourier series spectrum for sth OFDM symbol is given as

$$U_s(\omega) = \sum_{a=0}^{M-1} U_s[a]\delta_c(\omega - a\Delta\omega), \tag{4}$$

Its time domain representation is

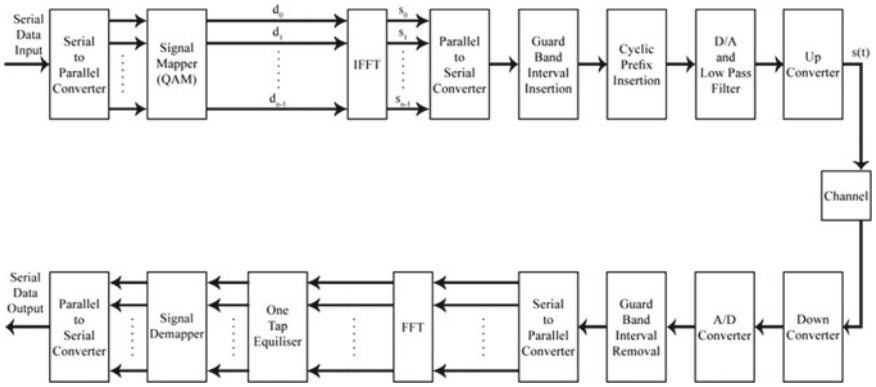

Fig. 1 Block diagram of FFT OFDM

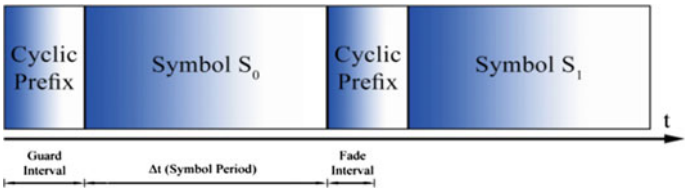

Fig. 2 Cyclic prefix for FFT-based OFDM

$$u(t) = \frac{1}{\sqrt{T_u}} \sum_{a=0}^{M-1} U_a e^{j2\pi f_a t}, \quad 0 \le t \le T_u, \tag{5}$$

2.2 Guard Interval and Cyclic Prefix

OFDM system uses low symbol rate modulation; therefore, the ISI in multipath propagation is lower as compared to single path propagation. We can take advantage of this feature and can transmit many low symbol rate streams in parallel rather than transmitting one high symbol rate stream in serial. Guard interval is added as shown in Fig. 2, between each OFDM symbol, as OFDM symbols are long and cause ISI, adding guard interval reduces the effect of ISI. OFDM reduces time synchronization sensitivity hence the pulse shaping filter is not needed.

However, the addition of guard band makes problem in the orthogonality of the carriers and introduces another problem ICI. The cyclic prefix is a methodology to resolve ICI. The cyclic prefix consists of the latter part of an OFDM symbol which is added to the signal along with guard interval and is then transmitted by the system. This ensures continuity in the signal as well as orthogonality between carriers. In each multipath propagation, when an OFDM receiver performs FFT demodulation, a cyclic prefix is required so that it can be integrated over an integer number of sinusoid cycles.

2.3 Peak-to-Average Power Ratio (PAPR)

A number of independent subcarriers which make up an OFDM signal are modulated and when added up with same phases, result in large peak values as these symbols across the subcarriers are added up. These high instantaneous power peaks are very high compared to the mean swing, the amplifier moves to a nonlinear region. The property of orthogonality is lost and the synchronization problem occurs when the system performs non-linear amplification and would result into extreme inter carrier interference. Hence high PAPR leads to Inter Symbol Interference (ISI), due to amplifier saturation [3, 4]. The PAPR for OFDM transmitter signal $u(t)$ is given by

the ratio of the maximum instantaneous power (maximum$\left[|u(t)|^2\right]$) and the average power ($E\{|u(t)|^2\}$). By definition,

$$PAPR = \frac{P_{peak}}{P_{avg}} = \frac{\text{maximum}\left[|u(t)|^2\right]}{E\left\{|u(t)|^2\right\}}, \quad for\ 0 \le t \le MT \tag{6}$$

Here, T is symbol period. The probability that the PAPR of a certain data block exceeds a given threshold is measured by the Complementary Cumulative Distribution Function (CCDF) is given as

$$Probability(PAPR > z) = 1 - (1 - e^{-z^2})^M, \tag{7}$$

3 Wavelet Transform

Wavelet means a "small wave", and is defined as a group of small waveforms that are nonzero for a given limited time period, i.e., oscillatory shapes. Wavelet analysis is an extension of Fourier analysis, but representation of brief, unpredictable and nonstationary signals is much more difficult in Fourier analysis [5]. The Continuous Wavelet Transform of a signal $u(t)$ is given as the sum of all signal time multiplied by scaled and shifted by versions of the wavelet $\varphi(t)$. This is expressed as

$$\gamma(e, f) = \frac{1}{\sqrt{e}} \int_{-\infty}^{\infty} u(t)\varphi^*\left(\frac{t-f}{e}\right)dt, \tag{8}$$

where γ is the result obtained from the operation and is a collection of many wavelet coefficients, which are functions of scale and translation. Signal reconstruction can be obtained from inverse transform given by

$$u(t) = \frac{1}{C_\psi} \int_{-\infty}^{\infty}\int_{-\infty}^{\infty} \gamma(e, f)\varphi^*\left(\frac{t-f}{e}\right)de\frac{df}{|e|^2}, \tag{9}$$

where $C_\psi = \int_{-\infty}^{\infty} \frac{|\psi(\omega)|^2}{|\omega|}$ and $\psi(\omega)$ is the Fourier transform of $\varphi(t)$.

The discrete wavelet transform examines the input signal at different time samples and frequencies and according to that signal is decomposed into an estimated signal which contains two coefficients which are known as "coarse" and "detailed" coefficients. The type of wavelet function and scaling factor decides the nature of high pass and low pass filters associated. The signal is decomposed in the time domain by feeding the input signal successively into high-pass and low-pass filters of different frequency bands. The input signal u[n] is passed through two filters at the beginning. One of the filters is a half-band high pass filter w[n] which blocks all frequencies

that are lower than half of the maximum frequency. The other filter is a half-band low-pass filter v[n] which blocks all the frequencies that are more than half of the maximum frequency. The later filter which is low pass halves the resolution and do not change the scale. Then the sub-sampling of the input signal is done by two. This decomposition of the input signal can be mathematically expressed as

$$y_{highpass}[k] = \sum_n u[k]w[2k-n] \text{ and } y_{lowpass}[k] = \sum_n u[k]v[2k-n], \qquad (10)$$

where, $y_{highpass}[k]$ and $y_{lowpass}[k]$ represent the high pass and low pass filter's output, respectively.

3.1 Discrete Wavelet-Based OFDM System (DWT OFDM)

DWT based OFDM system is shown in Fig. 3, in Discrete Wavelet-based OFDM (DWT OFDM), "Wavelet Carriers", obtained by discrete wavelet transform which are orthogonal in nature, replaces the "time domain windowed complex exponentials", obtained by Inverse Fast Fourier transform, at different positions on the time axis (h) as well as scales (g).

The "Wavelet's Mother", denoted by $\psi(t)$, is a unique function which is translated and dilated which generates the following function

$$\psi_{g,h}(t) = 2^{-g/2}\psi\left(2^{-g}t - h\right), \qquad (11)$$

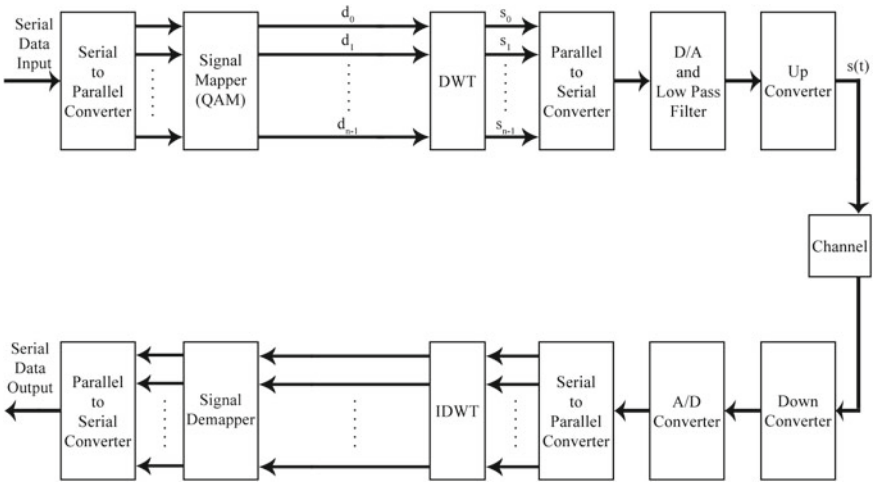

Fig. 3 DWT based OFDM block diagram

Time location (h) and scale index (g) [6] ensure the principle of orthogonality for these carriers as they exhibit better frequency behavior of signal which is localized in time domain i.e. "time frequency localization". The principle of "Orthogonality" is attained by producing the wavelet family members, according to Eq. (11)

$$\psi_{g,h}(t), \psi_{m,n}(t) = \begin{cases} 1, \; if \; \boldsymbol{g} = m \; and \; h = n \\ 0, \; otherwise \end{cases}, \tag{12}$$

If infinite number of scales $\boldsymbol{g} \in Z$ are taken then these functions contain the orthonormal basis of $L^2(R)$. A scaling function $\varphi(t)$ is used to obtain a finite number of scales. DWT OFDM symbol $r(t)$ gives us the weighted sum of wavelet and these scale carriers, as expressed in the equation below which represents the Inverse Wavelet Transform (IDWT) [7].

$$r(t) = \sum_{g \leq G} \sum_{h} w_{g,h}(t) \psi_{g,h}(t) + \sum_{h} a_{G,h} \varphi_{G,g}(t), \tag{13}$$

where wavelet coefficients $w_{g,h}$ and approximation coefficients $a_{J,h}$ are examined by the IDWT modulator. The scale with the poorest time resolution and best frequency localization for these carriers are represented by G [8]. As DWT OFDM scheme does not need CP; therefore, they enhance the spectral efficiency and bandwidth efficiency by up to 20% since there is no use of an overhead.

3.2 Computational Complexity

The DWT algorithm does an up-sampling by a factor of 2 with wavelet coefficients $w_{g,h}$ and approximation coefficients $a_{G,h}$, respectively, by a low passband filter v and high passband filter w. Considering the length of filters h and $\boldsymbol{g}$ as K, the numbers of multiplications are $2\frac{M}{2} log_2 M$ and the numbers of additions are $M log_2 M$, the W-OFDM system has a complexity of $O(M log_2 M)$ [9]. Knowing the complexity of FFT OFDM as $O(M log_2 M)$, the number of multiplications are $\frac{M}{2} log_2 M$ and number of additions as $(M log_2 M)$. The complexity decreases in W-OFDM further due to the removal of Cyclic Prefix.

4 Simulation Results

The PAPR values and simulation parameters are given in Tables 1 and 2 respectively. The PAPR is observed to be reduced by a significant value. The DWT implemented was of Daubechies family (db1) which helped in further decreasing the PAPR value

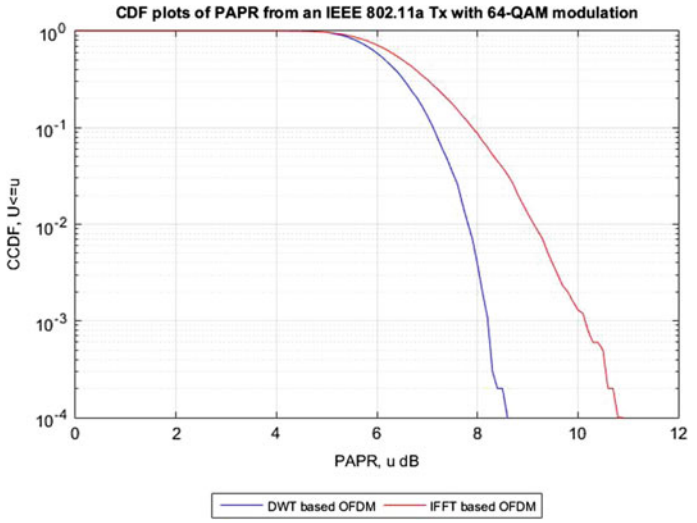

Fig. 4 Simulation result plot of CCDF versus PAPR

Table 1 PAPR values at different CCDFs

CCDF	10^{-4} (dB)	10^{-3} (dB)	10^{-2} (dB)	10^{-1} (dB)
PAPR of FFT OFDM	10.9	10.15	9.125	7.9
PAPR of DWT OFDM	8.6	8.21	7.815	7.1

Table 2 Considered parameters while simulation

S. no	Parameters	FFT based OFDM	DWT based OFDM
1.	Number of bits per symbol	52	52
2.	Number of bits	10,000	10,000
3.	FFT/DWT size	64	–
4.	Modulation type	QAM	QAM
5.	Number of subcarriers	1200	1200
6.	Cyclic prefix use	Yes	No

compared to the IFFT block. The plot of CCDF versus PAPR for DWT as well as IFFT can be seen in Fig. 4. For example at CCDF 10^{-4} the FFT OFDM system has PAPR 10.9 dB and DWT OFDM has a PAPR of 8.5 db.

5 Conclusion

The DWT-based OFDM is provided as a substitute to the FFT-based OFDM for PAPR reduction, without the use of Cyclic Prefix and Guard Interval which cuts back the PAPR by 2.3 dB over the conventional FFT OFDM at a CCDF 10^{-4}. Theoretical analysis and simulation outcome show the proposed scheme outperforms the FFT OFDM scheme in the PAPR discount performance with an affordable computational complexity decrease because of removal of Guard Band & Cyclic Prefix insertion block and hence increases the rate of OFDM block and shows a superior performance of DWT over the FFT OFDM in terms of spectral efficiency and bandwidth usage without decreasing the bandwidth efficiency.

References

1. Han, S.H., Lee, J.H.: An overview of peak-to-average power ratio reduction techniques for multicarrier transmission. IEEE Wirel. Commun. **12**(2), 56–65 (2005)
2. Han, S.H., Lee, J.H.: PAPR reduction of OFDM signals using a reduced complexity PTS technique. IEEE Signal Process. Lett. **11**(11), 887–890 (2004)
3. Jiang, T., Wu, Y.: An overview: peak to average power ratio reductions techniques for OFDM signals. IEEE Trans. Broadcast. **54**(2), 257–268 (2008)
4. Sharma, P.K., Basu, A.: Performance analysis of peak to average power ratio reduction for wireless communication use OFDM. In: International conference on advances in recent technologies for wireless communication using OFDM signals, pp. 89–95 (2010)
5. Saad, W., El-Fishawy, N., El-Rabaie, S,, Shokair, M.: An Efficient Technique for OFDM System Using Discrete Wavelet Transform. Springer, Heidelberg, pp. 533–541 (2010)
6. Dilmaghani, R., Ghavami, M.: Comparison between wavelet-based and fourier-based multicarrier UWB systems. IET Commun. **2**(2), 353–358 (2008)
7. Lee, J., Ryu, H.G.: Performance comparison between wavelet-based OFDM system and iFFT-based OFDM system. In: 2017 International Conference on Information and Communication Technology Convergence (ICTC), Jeju, pp. 957–960 (2017)
8. Abdullah, K., Mahmoud, S., Hussain, Z.M.: Performance analysis of an optimal circular 16-QAM for wavelet based OFDM systems. Int. J. Commun. Netw. Syst. Sci. **2**(9), 836–844 (2009)
9. Burrus, C.S., Gopinath, R.A., Guo, H.: Introduction to wavelets and wavelet transforms, pp. 1–55. Prentice Hall, Upper Saddle River (1998)

Slot Integrated Folded Substrate Integrated Waveguide Bandpass Filter for K Band Applications

Nitin Muchhal, Tanvi Agrawal, Abhay Kumar, Arnab Chakraborty and Shweta Srivastava

Abstract This paper proposes the study and analysis of various slot loaded folded substrate integrated waveguide band pass filter for K-band applications. Three prototypes of filer are simulated and analyzed with different resonant slot lengths for enhancing the impedance bandwidth. By incorporating a slotted structure of I shape geometry at middle of central septum, the filter achieves the maximum bandwidth of 4.33 GHz (20.8–25.13 GHz) with FBW of 18.89%. Further it achieves compact size by virtue of its folded nature which reduces its width by half.

Keywords Folded SIW · I slot · Wide bandwidth · Compact size

1 Introduction

In recent times, the communication systems are expanding rapidly to higher frequency ranges and there has been tremendous growth, demand, and immense prospects in microwave region (bands) especially X, Ku, and K bands. K band's microwave domain is used for radar and satellite applications [1] whereas the part in

N. Muchhal (✉) · A. Kumar · A. Chakraborty · S. Srivastava
ECE Department, Jaypee Institute of Information Technology, Sector 128, Jaypee Wish Town Village, Sultanpur, Noida 201304,
Uttar Pradesh, India
e-mail: nmuchhal@gmail.com

A. Kumar
e-mail: abhay.2t@gmail.com

A. Chakraborty
e-mail: arnab.chk@hotmail.com

S. Srivastava
e-mail: shweta.srivastava@jiit.ac.in

T. Agrawal
ECE Department, KIET Group of Institutions, Ghaziabad, India
e-mail: tanviagrawal88@gmail.com

B. S. Rawat et al. (eds.), *Advances in Signal Processing and Communication* ,
Lecture Notes in Electrical Engineering 526,
https://doi.org/10.1007/978-981-13-2553-3_12

the infrared domain is used for astronomical observations. The conventional rectangular waveguide (RWG) have benefits of possessing high Q and low loss. However, they are tedious to design, integrate with planar circuits, and expensive in mass production. Also, higher frequencies prevent the application of planar technology due to high transmission losses. The prospective solution for overcoming this problem at higher frequency is substrate-integrated waveguide (SIW) technology [2]. SIW technology is becoming the future technology for planar transmission line as it takes the benefit of easy integration and compact size in comparison to the traditional microstrip structures [3].

The present paper proposes the design of wideband and compact BPF using Folded SIW technology for K band. There are various methods which are being used to increase the bandwidth of substrate integrated waveguide bandpass filter. Jin et al. [4] designed a wideband bandpass filter for the RFID system by coupling the CSRR ring with SIW structure. Chen et al. [5] proposed a novel multiple-mode resonator (MMR) to achieve a wide passband of operation. He designed MMR by etching U-shape slots on the upper layer of SIW cavity with. Fahraji et al. [6] proposed a wideband bandpass filter for millimeter-wave by cutting slots in a rectangular shape on the upper metallic plane of SIW cavity and achieved wide bandpass response. Recently Liu et al. [7] proposed a bandpass filter by integrating modified dumbbell-defected ground structure (DGS) cells with substrate integrated waveguide (SIW) and achieved a wide band of operation.

2 Design of Folded Substrate-Integrated Waveguide (FSIW)

SIW has several benefits such as lightweight, less leakage losses, better invulnerability to electromagnetic interference, etc. However, compared with stripline or microstrip components, SIW has the disadvantage of larger width for same circuits. To overcome this problem, the concept of Folded Substrate Integrated Waveguides (SIFW) was introduced by [8]. To miniaturize the SIW components, various techniques have been reviewed by [9]. The design equations [10] for a substrate integrated waveguide (SIW) are:

The equivalent width of dielectric-filled rectangular waveguide

$$W_{EQ} = \frac{c}{2f_c\sqrt{\varepsilon_r}} \tag{1}$$

Width of SIW

$$W_{SIW} = W_{EQ} + \frac{D^2}{0.95P} \tag{2}$$

In addition to selecting P and D, following inequalities should be satisfied

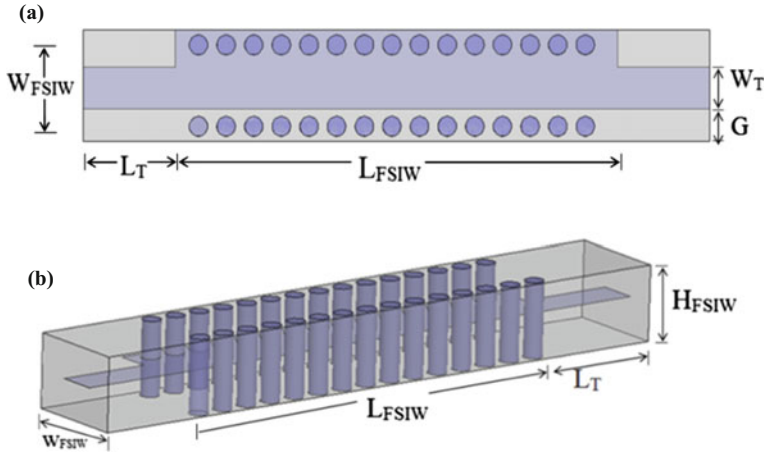

Fig. 1 **a** Top view of FSIW. **b** Side view of FSIW

$$P < 4D \text{ and } P < \frac{\lambda_0}{2}\sqrt{\varepsilon_r} \tag{3}$$

For the design of a SIW for K band with cut off frequency $f_c = 18$ GHz, dielectric constant $\varepsilon_r = 2.55$ and height of SIW, H = 1.6 mm, the design parameters are found as P = 1.2 mm, D = 0.80 mm and $W_{SIW} = 7.20$ mm. Figure 1a, b shows the top and side view of a (C type) folded SIW with the transition. Here, W_{FSIW} is the width of folded SIW which reduces to half of conventional SIW, L_{FSIW} is length of FSIW and G is the gap between the middle conductive septum and the right sidewall. Therefore, design parameters of folded SIW (FSIW) are $W_{FSIW} = 3.60$ mm, $H_{FSIW} = 3.2$ mm, G = 1.1 mm, $L_{FSIW} = 19$ mm, length of rectangular transition $L_T = 4$ mm, width of transition $W_T = 1.4$ mm.

Figure 2 compares the return loss and insertion loss curves of SIW and FSIW. From the figure, it is evident that FSIW has the similar high-pass performance as SIW with the same cut-off frequency.

3 Filter Design with Various Slot Shapes

Since FSIW has the same high-pass performance as SIW and the band-pass function can be realized by introducing narrow slots on the central metal septum of the FSIW. In this paper, three filters with different slot shapes and sizes are analyzed for bandwidth and return loss. The proposed filters are simulated using EM simulator HFSS by taking dielectric substrate (Arlon Cuclad 250GT) having dielectric constant 2.55, loss tangent 0.0018 and height 3.2 mm. The dimension of the slot is taken in terms of λ_0, where λ_0 is the free space wavelength in mm. Figure 3 shows the geometry

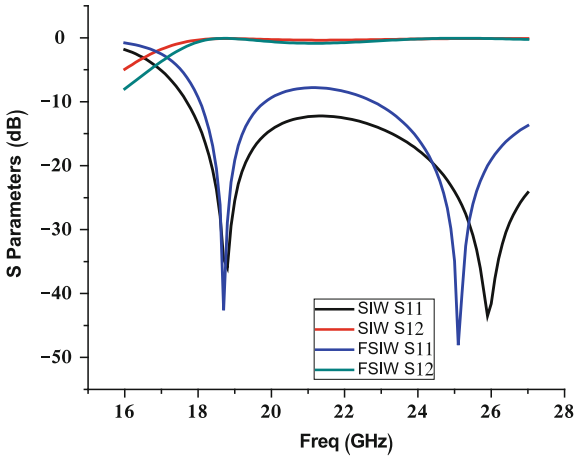

Fig. 2 Comparison of S parameters of SIW and FSIW

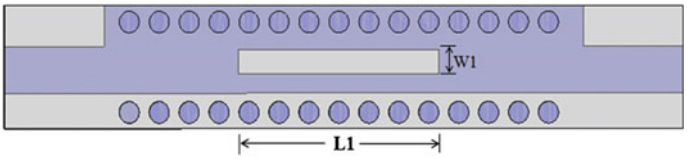

Fig. 3 Folded SIW with rectangular slot on the central septum

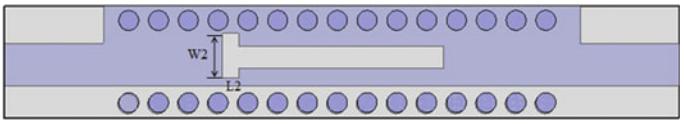

Fig. 4 Folded SIW with T shaped slot on the central septum

of the first prototype with basic rectangular slot embedded in the central septum of FSIW. It consists of a rectangular slot of length L1 = 8 mm (0.5 λ_0) and width W1 = 1 mm (0.0625λ_0). The dimensions are concluded after a parametric analysis of the slot size for optimum performance. For the second design, a vertical slot is added to the left side of the horizontal slot which forms a T slot as depicted in Fig. 4. The optimum dimensions of the vertical slot are found as: Length L2 = 0.40 mm (0.025 λ_0) and width W2 = 1.6 mm (0.1 λ_0). In the third and final design, one more identical vertical slot of the same dimension is introduced at the right end of the horizontal slot to form an I shape structure as shown in Fig. 5. This design with a wide middle slot has high bandwidth. This shape provides a suitable number of degree of freedom. Further, it achieves the desired electromagnetic effect and optimizing the frequency response of the microwave component [11].

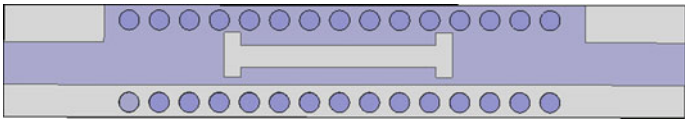

Fig. 5 Folded SIW with I shaped slot on the central septum

4 Results and Discussion

The three prototypes of folded SIW filter with different slot shapes are simulated and analyzed using HFSS [12]. Figure 6a, b shows the S parameter response and current distribution of basic rectangular slot FSIW bandpass filter. From Fig. 6a, it is clear that there is a single passband due to the presence of single slot. The passband has an absolute bandwidth of 1.18 GHz (21.12–22.30 GHz). The maximum value of return loss is found to be −27.7 dB at 21.58 GHz. Also, the fractional bandwidth (FBW) can be computed using the formula:

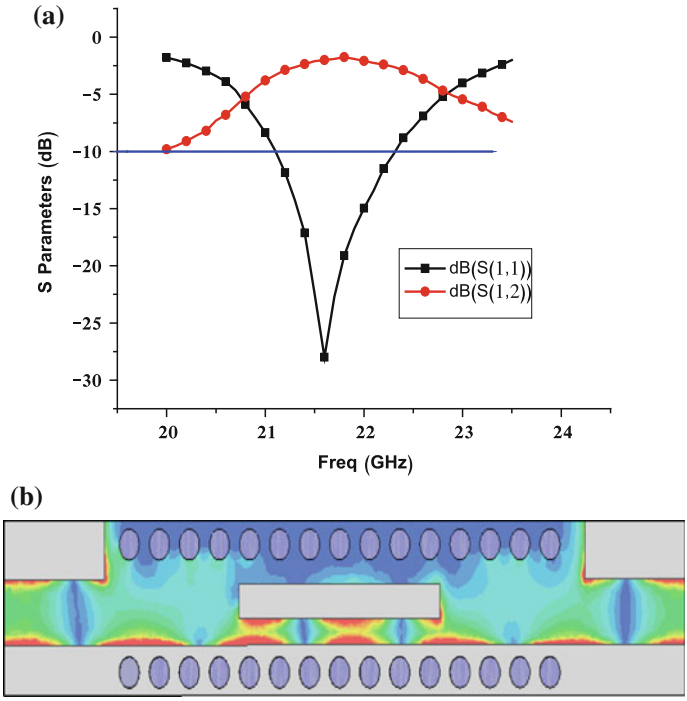

Fig. 6 **a** S-parameter response of rectangular slot FSIW. **b** Current distribution of rectangular slot FSIW

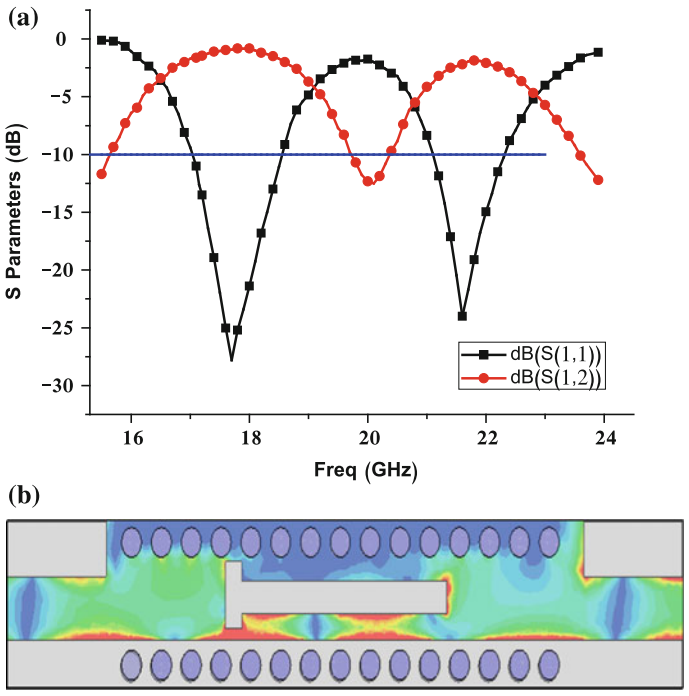

Fig. 7 **a** S-Parameter Response of T slot FSIW. **b** Current distribution of T slot FSIW

$$\%\text{FBW} = \left[\frac{f_2 - f_1}{f_r}\right] \times 100 \tag{4}$$

where f_1 and f_2 are lower and upper cut-off frequencies of the passband and f_r is the center frequency between f_1 and f_2. The % FBW using above formula is calculated to be 5.44%.

For designing T slot, one vertical rectangular slot with length, L2 = and width, W2 = is added to the left end of the basic rectangle. Since it consists of a grouping of two different slots (one horizontal and one vertical at left end) as shown in Fig. 4, it has two passbands. Figure 7a, b shows the S parameter response and current distribution of T slot FSIW bandpass filter. As can be seen, an additional resonance is created due to one vertical slot introduced at the left end of the horizontal slot. The first pass band has a bandwidth of 1.34 GHz (17.12–18.46 GHz) with FBW of 7.56% caused by the vertical slot. The first band has a maximum return loss of −28.6 dB at 17.6 GHz. The second passband has a bandwidth of 1.12 GHz (21.18–22.30 GHz) with FBW of 5.14% caused by horizontal slot. The second passband has a maximum return loss of −23.84 dB at 21.65 GHz. So, the overall absolute bandwidth with the T slot becomes 2.56 GHz and %FBW is 12.70%. There is an enhancement in bandwidth by 133% as compared to the previous case.

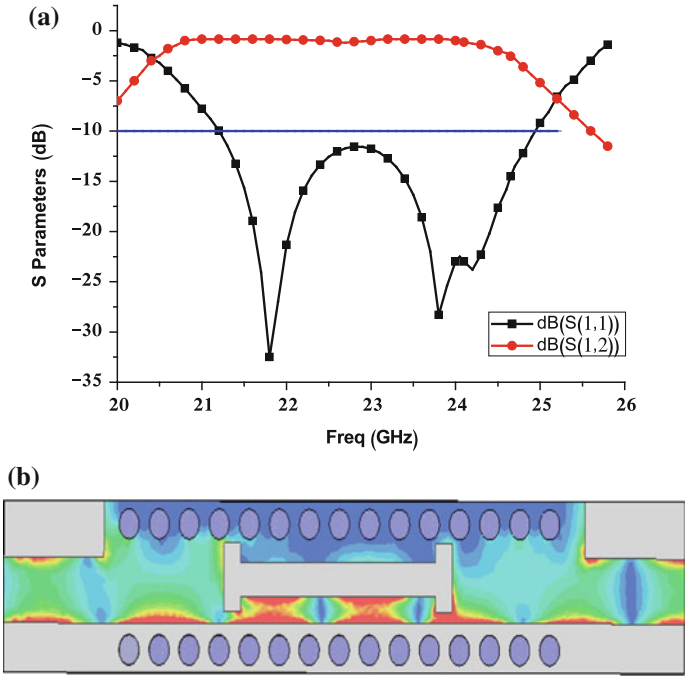

Fig. 8 **a** S-Parameter Response of I slot FSIW. **b** Current distribution of I slot FSIW

For making an I slot, three slots (one horizontal and two vertical slots at two ends) are joined together as shown in Fig. 5. Figure 8a, b shows the S parameter response and current distribution of I slot FSIW bandpass filter. In this filter, there is one additional resonance created in vicinity of second passband due to the presence of rightly placed vertical slot. These two bands overlap with each other and also combine with the first band to get a wider response [13]. As it is evident, it has bandwidth of 4.33 GHz (20.8–25.13 GHz) with FBW of 18.89%. Due to three slots, it has three resonances with return losses of values −32.5 dB, −28.48 dB and −21.83 dB at resonant frequencies of 21.85, 23.88, and 24.20 GHz respectively. There is an overall improvement in impedance bandwidth by 48.6% as compared to T slot FSIW and 247% as compared to basic rectangular slot (Table 1).

5 Conclusion

From the detailed simulation study and analysis of three prototypes of folded SIW, it is found that the impedance bandwidth of Folded SIW can be enhanced from 5.44 to 18.89% by loading I shaped slot on middle conductive septum. As the number of slots is added to the structure, its impedance bandwidth enhances due to additional

Table 1 Result summary

Slot shape	No. of bands	Overall FBW (%)	Return loss
Rectangular slot	1	5.44	−27.7 dB at 21.58 GHz
T slot	2	12.70	−28.6 dB at 17.6 GHz −23.84 dB at 21.65 GHz
I slot	1	18.89	−32.5 dB at 21.85 GHz −28.48 dB at 23.88 GHz −21.83 dB at 24.2 GHz

resonance created by the resonating slots. The single band of rectangle slot FSIW is converted into dual bands by loading T-slot and the dual bands are converted again into the single band by embedding I slot with the highest impedance bandwidth. The proposed filters are simple in their geometry and small in size.

References

1. Pachiyaannan, M., Prasanna Venkatesan, G.K.D.: Dual-band UWB antenna for radar applications: design and analysis. In: 8th International Conference on Computational Intelligence and Communication Networks (CICN) Tehri (India) (2016)
2. Wu, K., Deslandes, D., Cassivi, Y.: The substrate integrated circuits - a new concept for high-frequency electronics and optoelectronics. In: 6th International Conference on Telecommunications in Modern Satellite, Cable and Broadcasting Service, 2003 TELSIKS (2003)
3. Bozzi, M., Georgiadis, A., Wu, K.: Review of substrate-integrated waveguide circuits and antennas. IET Microw. Antennas Propag. **5**(8), 909–920 (2011)
4. Jin, J., Yu, D.: Substrate integrated waveguide band-pass filter with coupled complementary split ring resonators. In: 2014 XXXIth URSI General Assembly and Scientific symposium (URSI GASS), Beijing, China (2014)
5. Sen Chen, R., Wong, S.-W., Zhu, L.: Wideband bandpass filter using U-slotted Substrate Integrated Waveguide (SIW) Cavities. IEEE Microw. Wireless Compon. Lett. **25**(1), 2015
6. Hosseini-Fahraji, A., Mohammadpour-Aghdam, K., Faraji-Dana, R.: Design of wideband millimeter-wave bandpass filter using substrate integrated waveguide. In: IEEE Iranian Conference on Electrical Engineering (ICEE), Shiraz, Iran (2016)
7. Liu, C., An, X.: A SIW-DGS wideband bandpass filter with a sharp roll-off at upper stopband. Microw. Opt. Technol. Lett. **59**(4), 789–792 (2017)
8. Izquierdo, B.S., Young, P.R.: Substrate integrated folded waveguides (SIFW) and filters. IEEE Microw. Wireless Compon. Lett. **15**(12), 829–831 (2005)
9. Muchhal, N., Srivastava, S.: Review of recent trends on miniaturization of substrate integrated waveguide (SIW) components. In: 3rd IEEE International Conference on Computational Intelligence and Communication Technology (CICT), ABES Ghaziabad, India (2017)
10. Kordiboroujeni, Z., Bornemann, J.: Designing the width of substrate integrated waveguide structures. IEEE Microw. Wireless Compon. Lett. **23**(10), 518–522 (2003)
11. Garg, R., Bahl, I., Bozzi, M.: Microstrip Lines and Slotlines. 3rd Edn., Artech House
12. HFSS user manual
13. Sameena, N.M., Konda, R.B., Mulgi, S.N.: A novel slot for enhancing the impedance bandwidth and gain of rectangular microstrip antenna. Prog. Electromagn. Res. C **11**, 11–19 (2009)

Mutation-Based Bee Colony Optimization Algorithm for Near-ML Detection in GSM-MIMO

Arijit Datta, Manish Mandloi and Vimal Bhatia

Abstract Generalized spatial modulation multiple-input multiple-output (GSM-MIMO) is a promising technique to fulfil the ever-growing need for high data rates and high spectral efficiency for 5G and beyond systems. Maximum likelihood (ML) detection achieves optimal performance for GSM-MIMO systems. However, ML detection performs an exhaustive search and hence, ML have intractable exponential computational complexity. Hence, low complexity detection algorithms are needed to be explored for reliable detection in GSM-MIMO systems. In this paper, a novel and robust GSM-MIMO detection algorithm are proposed based on artificial bee colony optimization with mutation operator. Simulation results validate that the proposed algorithm outperforms minimum mean square error detection and achieves near-ML bit error rate performance for GSM-MIMO systems, under both perfect and imperfect channel state information at the receiver.

Keywords Artificial bee colony · Mutation · Generalized spatial modulation MIMO detection · Maximum likelihood

1 Introduction

Multiple-input multiple-output (MIMO) systems are the key technology for 5G and beyond systems due to their advantages of high spectral efficiency, high throughput, and enhanced link reliability as compared to Single-input single-output (SISO) systems [1]. These advantages of MIMO are achieved by employing multiple numbers

A. Datta · V. Bhatia (✉)
Indian Institute of Technology Indore, Indore, Madhya Pradesh, India
e-mail: vbhatia@iiti.ac.in

A. Datta
e-mail: phd1601102003@iiti.ac.in

M. Mandloi
NMIMS, Shirpur Campus, Shirpur, Maharastra, India
e-mail: manish.mandloi@nmims.edu

B. S. Rawat et al. (eds.), *Advances in Signal Processing and Communication* ,
Lecture Notes in Electrical Engineering 526,
https://doi.org/10.1007/978-981-13-2553-3_13

of antennas at the transmitter and receiver. Hence, multiple radio frequency (RF) chains are needed to be maintained at both the transmitter and receiver. RF chains are generally expensive as compared to antennas [2]. As a consequence, MIMO systems face issues of high maintenance cost, hardware complexity, and inter-antenna synchronization.

One of the cost-effective solutions to resolve the above issues associated with conventional MIMO is to use Spatial Modulation (SM) [2]. SM-MIMO is a multiple antenna approach, which employs the index of the active transmit antenna to transmit additional information bits. Hence, SM-MIMO is more robust to Inter-Channel Interference (ICI) than conventional MIMO systems [2]. However, SM-MIMO utilizes only one active transmit antenna in each time slot. As a consequence, the throughput of SM-MIMO is limited by the base-two logarithm of the number of transmit antenna and hence, it yields low spectral efficiency as compared to conventional MIMO systems when the numbers of transmit antennas scale up in the system.

To tackle the issue of low spectral efficiency of SM-MIMO, Generalized Spatial Modulation MIMO (GSM-MIMO) is introduced [3]. GSM-MIMO improves the spectral efficiency of SM-MIMO by employing more than one active transmit antenna at each time slot. However, one of the challenging research problems in GSM-MIMO is the optimal detection of transmitted symbols. Maximum Likelihood (ML) detection achieves near-optimal solution, however, ML is a nonlinear detection technique which contains exponential computational complexity and hence, ML detection for GSM-MIMO systems is practically unacceptable. Linear decorrelator-based detection for GSM-MIMO systems is proposed in [4]. However, the performance of the algorithm [4] is far inferior as compared to ML detection. Hence, the design of low complexity near-optimal detection algorithms for GSM-MIMO attracts keen research interest among communication and signal processing community.

Since nature-inspired algorithms involve fewer complex computations, they yield promising solutions for low complexity detection in MIMO systems [5–7]. However, the major challenge to apply these nature-inspired algorithms in communication and signal processing is to develop a proper update mechanism so that the nature-inspired algorithms do not get stuck at local minimum. Among the wide range of bio-inspired algorithms, ant colony optimization (ACO) and particle swarm optimization (PSO) gained prominence in MIMO symbol detection. ACO-based MIMO detection proposed in [6] is sensitive to the initial solution and algorithms proposed in [7] shows premature convergence to the local optimal solution. PSO-based MIMO detection algorithm proposed in [5] converges prematurely and provides a suboptimal solution. Hence, nature-inspired algorithms are needed to be explored to design a low complexity near-ML performance robust algorithm for GSM-MIMO systems.

Hence, with an eye to the advantages of nature-inspired algorithms, this paper proposes a novel and robust detection algorithm for uplink GSM-MIMO systems. Since Artificial Bee Colony optimization (ABC) [8] is found to be superior to other swarm-based algorithms [9] due to its simplicity, ease of implementation and good exploration capability, we propose an uplink GSM-MIMO detection algorithm inspired by ABC Optimization. To the best of authors' knowledge, this paper is the first work

to successfully exploit the ABC algorithm for symbol detection in GSM- MIMO systems. Main contributions of this paper are twofold, (a) a mutation operation is introduced to improve the performance of ABC algorithm for GSM- MIMO systems and (b) a novel and robust low complexity detection algorithm is proposed for GSM-MIMO systems. The proposed algorithm achieves near-ML bit error rate (BER) performance. Moreover, simulation results validate the robustness of the proposed detection algorithm for GSM-MIMO systems under different Channel State Information (CSI) at the receiver.

The rest of the paper is organized as follows. Section 2 discusses the underlying idea of ABC optimization. Section 3 represents the system model of GSM-MIMO systems. The proposed GSM-MIMO detection algorithm is discussed in Sect. 4. Simulation results are depicted and compared in Sect. 5. Section 6 concludes the paper.

2 Artificial Bee Colony Optimization

ABC [8] optimization is a nature-inspired swarm-based meta-heuristic optimization exploiting the social behaviour of honey bees. ABC consists of three groups of honey bees, namely (a) employee bees, (b) scouts, and (c) onlookers. Employee bees are responsible for searching and gathering food items. Scouts are those employee bees whose searched food's information are abandoned and search new food sources in the region of abandoned food sources. Onlooker bees remain in the hive and check the quality of the food items depending on waggle dances of employee bees and loyalty decision criteria.

2.1 Assumptions

There are several assumptions for successful implementation of the ABC algorithm in optimization problems. The decisive assumptions are listed below.

- The number of employee bees in the colony is equal to the number of food sources in the population.
- The quality of a food source is determined by its nectar amount. Higher the nectar amount, higher is the quality of food.

2.2 Working Principle

This subsection describes the steps involved in ABC optimization.

Foraging Initially, employee bees come out of the hive and randomly search for nectar-enriched food sources. If a food source is found, employee bees update their positions using the following perturbation:

$$\hat{\mathbf{x}}_i^{(k+1)} = \mathbf{x}_i^{(k)} + \gamma\left(\mathbf{x}_i^{(k)} - \mathbf{x}_j^{(k)}\right), i \neq j \tag{1}$$

where $\mathrm{x}_i^{(k)}$ denotes the position of the ith bee/food source at kth iteration and $\gamma \in [0, 1]$. Next, employee bees come back to the hive to inform onlooker bees about the food using a dancing ritual called waggle dance.

Waggle Dance and Loyalty Decision The waggle dance is a special figure-of-eight dance performed by employee bees in a special area of the hive to share the food source information with the onlooking bees. A new food location is chosen by the onlooker bees based on the nectar amount of the food, i.e., the value of the objective function $\zeta(.)$ to be minimized. Onlooker bees use a selection rule called loyalty decision to choose the present best solution based on a probability metric given by

$$p_i^{(k+1)} = \frac{\zeta\left(\mathbf{x}_i^{(k+1)}\right)}{\sum_{j=1}^{N} \zeta\left(\mathbf{x}_j^{(k+1)}\right)} \tag{2}$$

where N is the population size. The probability metric (2) decides where employee bee should be loyal to the food location (1).

Recruiting Process In this step, the onlooker bees engage employee bees into searching of new food sources to improve the present solution $\hat{\mathrm{x}}_i^{(k+1)}$. After N_{itr} numbers of trails, worst solutions are abandoned and the employee bees engaged in searching those worst solutions are declared as scouts.

3 System Model for GSM-MIMO

We consider an uplink GSM-MIMO systems with N_r receive antennas and N_t transmit antennas ($N_r \geq N_t$). The source information bits are transmitted through only $N_{RF} \leq N_t$ number of active transmit antennas after being modulated through M-QAM constellation set A, where N_{RF} is the number of RF chains. A $N_{RF} \times N_t$ switch connects the RF chains with the transmit antennas. Hence, only N_{RF} antennas remain active and $N_t - N_{RF}$ antennas are silent at each time slot. The received symbol vector y can be represented as [4]

$$\mathbf{y} = \mathbf{H}\mathbf{x} + \mathbf{n} \tag{3}$$

where $\mathbf{y} \in \mathbb{C}^{N_r \times 1}$, $\mathbf{x} \in \mathbb{C}^{N_t \times 1}$ are the uncoded transmitted symbol vector, $\mathbf{H} \in \mathbb{C}^{N_r \times N_t}$ is complex normal channel matrix and $\mathbf{n} \in \mathbb{C}^{N_r \times 1}$ is the additive white Gaussian

noise vector. The entries of $\mathbf{H}$ are independent and identically distributed (i.i.d) and $\sim \mathcal{CN}(0, 1)$. The entries of $\mathbf{n}$ are also i.i.d and $\sim \mathcal{CN}(0, \sigma^2)$. Since, only N_{RF} antennas are active at each time slot, $\|\mathbf{x}\| = N_{RF}$. The system model (3) can be formulated as

$$\mathbf{y} = \sum_{i \in \mathbf{T}} \mathbf{h}_i x_i + \mathbf{n} = \tilde{\mathbf{H}}\mathbf{x} + \mathbf{n} \tag{4}$$

Hence, ML detection problem for GSM-MIMO is given as

$$\left(\hat{\mathbf{T}}, \hat{\mathbf{x}}\right) = \underset{\mathbf{T} \in \mathcal{T}}{\arg\min} \underset{\mathbf{x} \in \mathcal{S}}{\min} \left\| \mathbf{y} - \tilde{\mathbf{H}}\mathbf{x} \right\|_F^2 \tag{5}$$

where $\mathcal{T} = \{\mathbf{T}_1, \mathbf{T}_2, \ldots, \mathbf{T}_N\}$, $\mathbf{T}_i$ is the set of active antenna indexes in ith Transmit Antenna Combination (TAC) and $\mathrm{S} = \mathcal{A}^{N_{RF} \times 1}$. $\|.\|_F$ denotes Frobenius norm. Without loss of generality, using QR decomposition of $\mathbf{H} = \mathbf{QR}$, ML detection problem (5) can be formulated as

$$\left(\hat{\mathbf{T}}, \hat{\mathbf{x}}\right) = \underset{\mathbf{T} \in \mathcal{T}}{\arg\min} \underset{\mathbf{x} \in \mathbb{S}}{\min} \left\| \tilde{\mathbf{y}} - \tilde{\mathbf{R}}\mathbf{x} \right\|_F^2 \tag{6}$$

where $\mathbf{Q}$ is an orthogonal matrix and $\mathbf{R}$ is an upper triangular matrix.

4 Proposed Algorithm for GSM-MIMO

This section presents the steps involved in the proposed GSM-MIMO detection algorithm based on the social behaviour of honey bees. Numerous algorithms [8] are proposed in the literature to mimic the intelligent social behaviour of honey bees. However, all the above honey bee-inspired algorithm are problem specific and have severe drawbacks while applying to optimization scenarios for communication and signal processing. In this paper, we propose a novel GSM-MIMO detection algorithm with a cue from ABC optimization [8] by removing the drawbacks of conventional ABC and making it suitable for GSM-MIMO systems with a genetic mutation operation. Crucial steps of the proposed GSM-MIMO detection algorithm are discussed below.

4.1 Mutation-Based Foraging

Mutation [10] is a genetic operation which maintains genetic diversity and makes candidate solution more immune to be trapped at a local minima. On the other hand, crossover [10] is a selection operation which assures convergence. The position

update Eq. (1) of ABC can be considered as a crossover operation with crossover probability of γ. Hence, the conventional ABC algorithm does not consider any mutation operation, which reduces the exploration and diversity of the ABC algorithm. As a result, the ABC algorithm suffers from premature convergence to local optima for GSM-MIMO systems. However, it is well studied in the literature that a mutation operation is superior to crossover to avoid rapid convergence to any sub-optimal solution [11]. Moreover, we are interested to consider a real-valued 4-QAM constellation set, hence, a mutation operation will eventually increase the convergence speed over crossover operation for coordinate-wise minimization of the cost function (6) and we assume that each coordinate of the food location has values either -1 or $+1$. Hence, to utilize the ABC algorithm for MIMO detection with 4-QAM constellation, we replace the Eq. (1) with a mutation-based foraging, where onlooker bees are forced to mutate using the following update rule.

$$x_i^{(k+1)} = \begin{cases} -x_i^{(k)}, \text{ if } \zeta_i^{(k)} > r \\ x_i^{(k)}, \text{ otherwise} \end{cases} \tag{7}$$

where $x_i^{(k)}$ refers to the position of the ith honey bee and k denotes the iteration number. $k \leq N_{itr}$. $r \in [0, 1]$ is a uniformly generated random number and ζ is the probability computed by the onlookers during loyalty decision phase.

4.2 Loyalty Decision

In the proposed detection algorithm, we define the loyalty decision rule as follows.

$$\zeta_i^{(k)} = \frac{\psi\left(x_i^{(k)}\right)}{\sum_{j \in \mathcal{S}} \psi\left(x_j^{(k)}\right)} \tag{8}$$

where $\psi\left(x_i^{(k)}\right)$ is the function to be minimized and defined as

$$\psi\left(x_i^{(k)}\right) = \left| \hat{y}_i - \sum_{j=i+1}^{2N_t} r_{ij} x_j^{(k)} - r_{ii} x_i^{(k)} \right|^2 \tag{9}$$

where r_{ij} is the element in ith row and jth column of matrix $\tilde{\mathbf{R}}$ and $\mathcal{S} \in \{-1, 1\}$ denotes the symbol to be detected. The proposed GSM-MIMO detection algorithm is outlined in Algorithm 1.

4.3 Termination Condition

To reduce the computational load on the proposed GSM-MIMO detection algorithm, we choose a threshold $\mathcal{V}_{th} = 2\sigma^2 N_R$ [12] to terminate the algorithm using the following termination rule

Algorithm 1: Proposed detection algorithm

Input: $\tilde{\mathbf{y}}, \tilde{\mathbf{R}}, N_t, N_{RF}, \mathcal{T}, \mathcal{V}_{th}$
Output: $\hat{\mathbf{x}}, \hat{\mathbf{T}}$
Preprocessing: $\eta_i = (\|\tilde{\mathbf{R}}_i\|^2)^{-1}\tilde{\mathbf{R}}_i^T$, $i = 1, 2, ..., 2N_t$
Compute ordering metric:
$\omega_i = \sum_{j\in\mathbf{T}_i} \eta_j^2$, $i \in \{1, 2, ..., N_{TAC}\}$
$k = 1$
while $k \leqslant N_{TAC}$ **do**
  for $l = 1 : N_{bees}$ **do**
    for $i = 1 : 2N_{RF}$ **do**
      Compute nectar amount:
      $\psi\left(x_i^{(k)}\right) = |\hat{y}_i - \sum_{j=i+1}^{2N_t} r_{ij}x_j^{(k)} - r_{ii}\hat{x}_p^{(k)}|^2, \hat{x}_p^{(k)} \in \mathcal{S}$
      Compute loyalty probability:
      $\zeta_i^{(k)} = \frac{\psi\left(x_i^{(k)}\right)}{\sum_{j,x_j^{(k)}\in\mathcal{S}} \psi\left(x_j^{(k)}\right)}$
      Perform mutation:
      $x_i^{(k+1)} = \begin{cases} -x_i^{(k)}, & \text{if } \zeta_i^{(k)} > r \\ x_i^{(k)}, & \text{otherwise} \end{cases}$
    end
    Update best food location $\mathbf{x}_{Best}$
  end
  Check termination condition
  $\mathbf{V} = \tilde{\mathbf{y}} - \tilde{\mathbf{R}}\mathbf{x}_{Best}$
  $d_{th} = tr(\mathbf{V}\mathbf{V}^T)$
  if $d_{th} \leq \mathcal{V}_{th}$ **then**
    $\hat{\mathbf{T}} = \mathbf{T}_k$
    $\hat{\mathbf{x}} = \mathbf{x}_{Best}$;
    Declare $\hat{\mathbf{x}}$ and $\hat{\mathbf{T}}$ as final outputs.
  else
    $k = k + 1$;
  end
end
if $k \geq 1$ **then**
  Select $\hat{\mathbf{T}}$ and $\hat{\mathbf{x}}$ corresponding to minimum d_{th} ;
end
Final output: $\hat{\mathbf{x}}, \hat{\mathbf{T}}$

$$\hat{\mathbf{x}} = \mathbf{x}_{Best}, d_{th} \leq \mathcal{V}_{th} \tag{10}$$

where $\mathbf{x}_{Best}$ is the best food location chosen so far by the onlooker bees. $\mathbf{V} = \tilde{\mathbf{y}} - \tilde{\mathbf{R}}\mathbf{x}_{Best}$ and $d_{th} = tr\left(\mathbf{V}\mathbf{V}^T\right)$. $tr()$ denotes trace operation.

5 Simulation Results and Analysis

This section depicts and discusses the simulation results for BER performance of the proposed detection algorithm for uplink 4×4 and 8×8 GSM-MIMO systems with 4-QAM modulation under both perfect and imperfect CSI at the receiver. We consider 10^3 number of errors for averaging the simulated BER performance in MATLAB. The TAC information is assumed to be modulated with Generalized Space Shift Keying (GSSK) and $V_{th} = 2\sigma^2 N_R$.

Figure 1a compares BER performance of the proposed detection algorithm with MMSE and ML for 4×4 GSM-MIMO systems. As depicted in Fig. 1a, an SNR gain of approximately 5.6 dB is achieved in the proposed GSM-MIMO detection algorithm as compared to MMSE for a targeted BER of 5×10^{-2} for NRF = 3. Moreover, the proposed algorithm achieves near-ML BER performance for 4×4 GSM-MIMO systems with $N_{RF} = 3$.

In Fig. 1b, BER performance of the proposed algorithm is illustrated for 8×8 GSM-MIMO systems with NRF = 7. It is observed that the proposed detection outperforms MMSE with an SNR gain of 5.8 dB for a targeted BER of 6×10^{-2} and achieves near-ML BER performance.

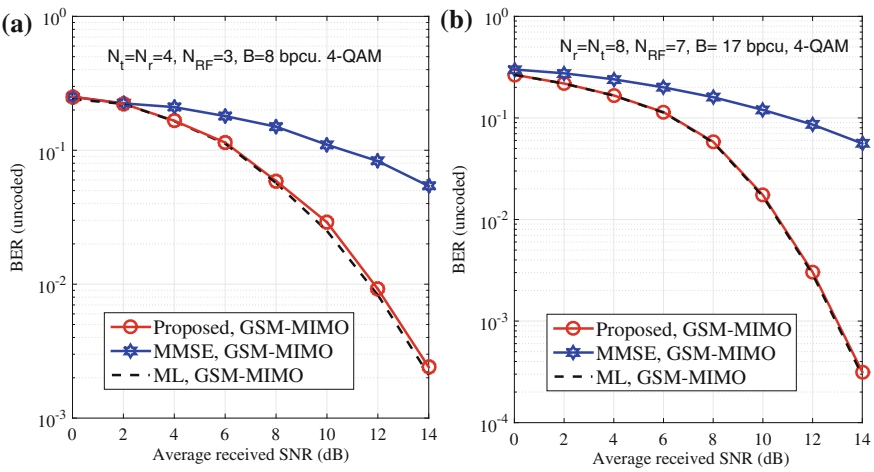

Fig. 1 BER performance comparison for 4×4 and 8×8 GSM-MIMO systems

Figure 2a depicts that the performance of the proposed algorithm improves with with the increase in number of antennas and moves towards SISO-AWGN. Moreover, Fig. 2b shows the effect of decreasing number of RF chains in the proposed detection algorithm. It is found that BER performance of the proposed algorithm improves from 3×10^{-4} to 1.7×10^{-4}, when the number of RF chains is reduced from $N_{RF} = 7$ to

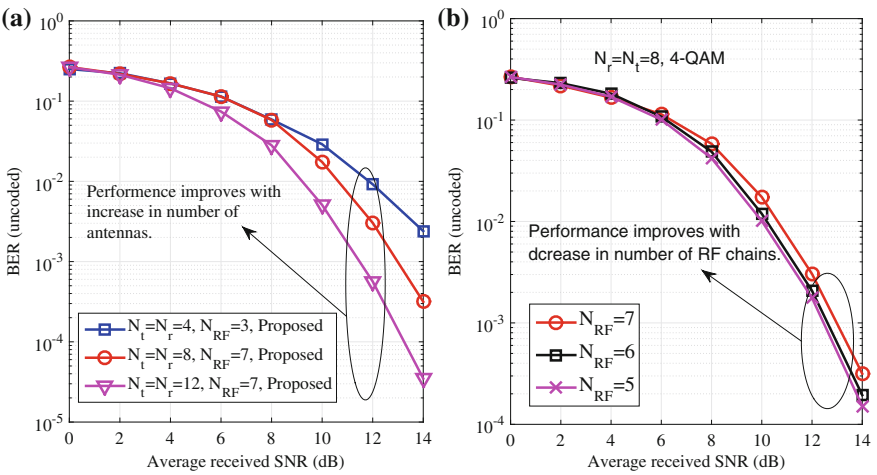

Fig. 2 BER comparison of the proposed detection algorithm with different number of antennas and RF chains for 8×8 GSM-MIMO systems

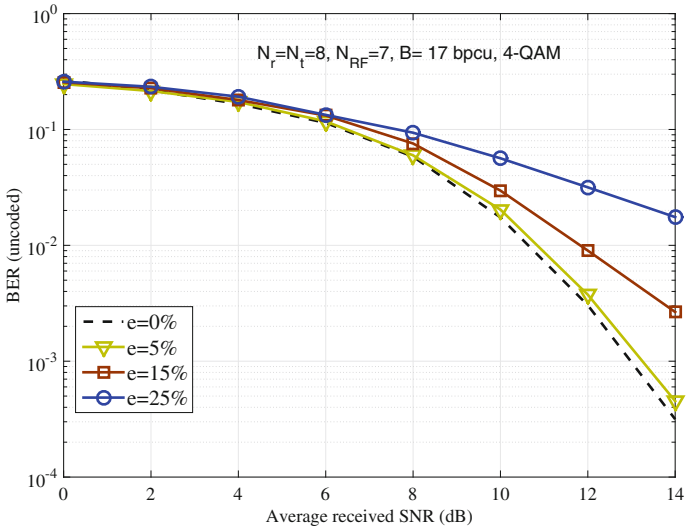

Fig. 3 BER performance of the proposed detection algorithm for 8×8 GSM-MIMO system under imperfect CSI at the receiver

$N_{RF} = 5$. This BER improvement is due to the fact that Inter-Channel Interference (ICI) decreases when the number of RF chains reduces and as a consequence, BER performance improves.

Figure 3 considers the effect of imperfect CSI at the receiver on the proposed detection algorithm. As shown in Fig. 3, the proposed algorithm is capable to yield near-ML BER performance even under CSI mismatch of $e = 5\%$. This corroborates robustness of the proposed detection algorithm.

6 Conclusion

In this paper, we propose a novel and robust detection algorithm for GSM-MIMO systems. The algorithm is inspired by mutation-based artificial bee colony optimization introduced in this paper. Simulation results reveal that the proposed GSM-MIMO detection algorithm achieves near-ML BER performance with less number of bees ($N_{ants} = 100$). Moreover, the performance of the proposed detection algorithm improves with an increase in the number of antennas. It concludes that the proposed algorithm is capable to achieve SISO-AWGN performance when the number of antennas is sufficiently large. This proves the suitability of the proposed detection algorithm for low complexity symbol detection in GSM-MIMO systems. Additionally, to validate the robustness, the proposed algorithm is simulated under different imperfect CSI mismatch conditions at the receiver. It is observed that the proposed algorithm achieves near-ML performance even under considerable CSI error scenarios. Hence, the proposed detection algorithm is a significant candidate for reliable symbol detection in GSM-MIMO systems.

Acknowledgements This publication is an outcome of the R&D work undertaken project under the Visvesvaraya PhD Scheme of Ministry of Electronics & Information Technology, Government of India, being implemented by Digital India Corporation.

References

1. Datta, A., Bhatia, V.: Social spider optimizer based large MIMO detector. In: 2017 IEEE International Conference on Advanced Networks and Telecommunications Systems (ANTS) (2017)
2. Mesleh, R.Y., Haas, H., Sinanovic, S., Ahn, C.W., Yun, S.: Spatial modulation. IEEE Trans. Veh. Technol. **57**(4), 2228–2241 (2008)
3. Di Renzo, M., Haas, H., Ghrayeb, A., Sugiura, S., Hanzo, L.: Spatial modulation for generalized MIMO: challenges, opportunities, and implementation. Proc. IEEE **102**(1), 56–103 (2014)
4. Wang, J., Jia, S., Song, J.: Generalized spatial modulation system with multiple active transmit antennas and low complexity detection scheme. IEEE Trans. Wireless Commun. **11**(4), 1605–1615 (2012)
5. Khan, A.A., Naeem, M., Shah, S.I.: A particle swarm algorithm for symbols detection in wideband spatial multiplexing systems. In: Proceedings of the 9th Annual Conference on Genetic and Evolutionary Computation, pp. 63–69. ACM (2007)

6. Khurshid, K., Irteza, S., Khan, A.A.: Application of ant colony optimization based algorithm in MIMO detection. In: 2010 IEEE Congress on Evolutionary Computation (CEC), pp. 1–7. IEEE (2010)
7. Mandloi, M., Bhatia, V.: Congestion control based ant colony optimization algorithm for large MIMO detection. Expert Syst. Appl. **42**(7), 3662–3669 (2015)
8. Karaboga, D., Akay, B.: A survey: algorithms simulating bee swarm intelligence. Artif. Intell. Rev. **31**(1–4), 61–85 (2009)
9. Yang, X.S., Karamanoglu, M.: Swarm intelligence and bio-inspired computation: an overview. In: Swarm Intelligence and Bio-Inspired Computation, pp. 3–23. Elsevier (2013)
10. Goldberg, D.E.: Genetic Algorithms. Pearson Education India (2006)
11. Hinterding, R., Gielewski, H., Peachey, T.C.: The nature of mutation in genetic algorithms. In: ICGA. pp. 65–72 (1995)
12. Wu, X., Thompson, J.: Accelerated sphere decoding for multiple-input multiple output systems using an adaptive statistical threshold. IET Signal Proc. **3**(6), 433–444 (2009)

Novel Substrate-Integrated Waveguide Incorporated with Band-Pass Filter

Tanvi Agrawal, Nitin Muchhal and Shweta Srivastava

Abstract A novel substrate-integrated waveguide antenna incorporated with filter is presented in this paper. The band-pass filter is designed using substrate-integrated waveguide technology. The filter has a range from 11 to 11.5 GHz. A slot has been etched on the upper layer of SIW to work filter as an antenna. The designed antenna has a wide bandwidth with resonant frequency of 11.4 GHz. The gain at this frequency is 6.67 dBi. All the results are simulated in ANSYS HFSS software.

Keywords Substrate-integrated waveguide · Band-pass filter · Slot
X-band applications

1 Introduction

The fundamental concept of Substrate-Integrated Waveguide (SIW) is to synthesize nonplanar structures in a planar form which it is completely compatible with other planar structures. This can be achieved by creating artificial channels [1–4]. Substrate-integrated waveguide is used as converting nonplanar structure to planar structure. It is a technology which is dielectric-filled waveguide with metallic vias on the sidewalls of the waveguide. These artificial wave-guiding channels are embedded in planar substrate with arrays of periodic metalized vias or slots. The vias or slots act as electrical walls for waveguides. Various Band-Pass Filters (BPFs) were implemented with different technologies of transmission line such as waveguide [5],

T. Agrawal (✉) · N. Muchhal · S. Srivastava
Jaypee Institute of Information Technology, Sector 128, Jaypee Wish Town Village, Sultanpur, Noida 201304, Uttar Pradesh, India
e-mail: tanviagrawal88@gmail.com

N. Muchhal
e-mail: nmuchhal@gmail.com

S. Srivastava
e-mail: shweta.srivastava@jiit.ac.in

B. S. Rawat et al. (eds.), *Advances in Signal Processing and Communication* ,
Lecture Notes in Electrical Engineering 526,
https://doi.org/10.1007/978-981-13-2553-3_14

SIW [6], and microstrip [7]. A BPF is defined as that passes range of frequencies within a band while rejecting all other set of frequencies that is outside band.

A number of works have been published using SIW with different types of transitions at input and output. In [8], Microstrip-to-SIW transitions have been presented which is based on a simple taper. The taper here is used for converting the quasi-TEM mode in microstrip line to TE10 mode in SIW. Wong et al. [9] designed a wide band-pass filter by making three resonators on top metallic plane of single SIW cavity. This was achieved by engraving slots on the top metal plane and reported insertion loss was 1.923 dB at 140 GHz with a fractional bandwidth of 13.0%. In [10], tunable SIW band-pass filter is designed using liquid crystals. This antenna is working in wireless frequency range with the frequency of 2 GHz.

In this paper, a band-pass filter is designed using substrate-integrated technology. A filter has passband range of 11–11.5 GHz. A slot has been etched out on an upper edge of the SIW. The slot will radiate through it and it will be working as an antenna. The antenna has a resonant frequency of 11.4 GHz with a gain of 6.67 dBi.

The antenna is designed on Roger RT/duroid substrate with $\in_r = 12$.The basic parameters of antenna, i.e., Gain, Radiation pattern, Current distribution and S parameter are simulated in ANSYS HFSS software [11].

2 SIW Filter Design

Proposed substrate-integrated waveguide filter is shown in Fig. 1. Substrate-Integrated Waveguide (SIW) aims to work for a cutoff frequency of 10 GHz with the design specifications of substrate-integrated waveguide such as width of the SIW a = 15 mm, center-to-center distance between the metallic vias p = 2 mm and diameter of the metallic vias d = 1.5 mm. These values are calculated using the design equations of SIW given below.

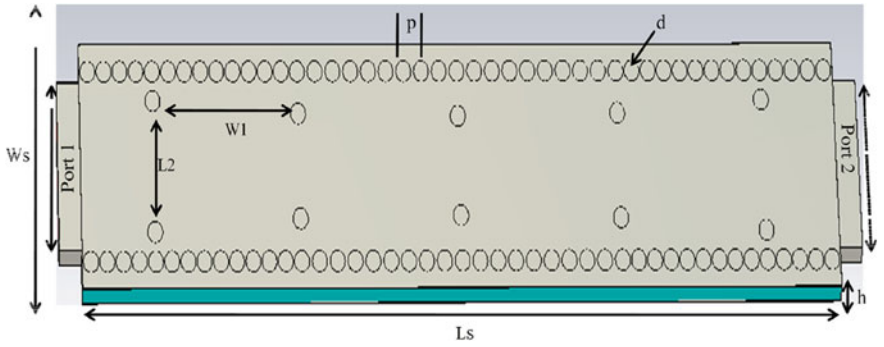

Fig. 1 Proposed geometry of SIW band-pass filter with design parameters Ls = 90 mm, W = 50 mm, $\in_r = 12$ h = 3.2 mm, a = 15 mm, p = 2 mm, d = 1.5 mm, W1 = 3 mm, and L2 = 10 mm

2.1 Design Equations of Substrate-Integrated Waveguide

SIW consists of two parallel conducting arrays of via holes represented by "d". *TE*10 mode is the dominant mode for wave propagation in SIW as of the conventional rectangular waveguide [12–16]. "a" is the parameter between the two arrays which determines the propagation constant of the fundamental mode. Similarly, parameters "d" is the diameter of vias d and p are set so as to minimize the leakage through the vias.

(A) The metalized via hole diameter is

$$d < \frac{h_g}{5}$$

(B) The spacing between the via holes is

$$P \leq 2d$$

(C) The physical width of SIW is

$$w_{eff} = a - 1.08\frac{d^2}{p} + 0.1\frac{d^2}{a},$$

where weff is the width of the waveguide. The SIW is designed on Roger RT/Duroid with thickness "h" = 3.2 mm. Band-Pass Filter (BPF) presented here was designed with the following parameters: center frequency f0, 11.3 GHz; fractional bandwidth FBW, 4.5%, and passband return loss RL, 60 dB. The BPF model has been designed using technique given in [18]. As given in [18], [20]; L is the inductance, C is the capacitance, and J is the inverter values of the circuit. Design parameters of SIW filter are $W_s = 50$ mm, $L_s = 90$ mm, a = 15 mm, p = 2 mm, d = 1.5 mm, W1 = 3 mm, and L2 = 10 mm.

2.2 Results of SIW Filter

The substrate-integrated waveguide cavity for BPF was modeled to resonate the filter at TE_{101} mode with a resonance frequency, f_0 of 11.3 GHz using (1). The filter was designed on a Rogers RT/Duroid substrate with $\epsilon_r = 12$, h = 3.2 mm and $\mu r = 1$. Figure 2 shows the simulated S parameters of SIW filter. The waveport has been assigned on both the ends of the filter (port 1 and port 2) as shown in Fig. 1. The filter has a passband of frequencies with a range of 11–11.5 GHz, with a return loss of maximum −60 dB, and with a negligible insertion loss.

The simulated current distribution for the filter is shown in Fig. 3. The current distribution for the filter is calculated for two frequencies, i.e., at 11 and 11.4 GHz.

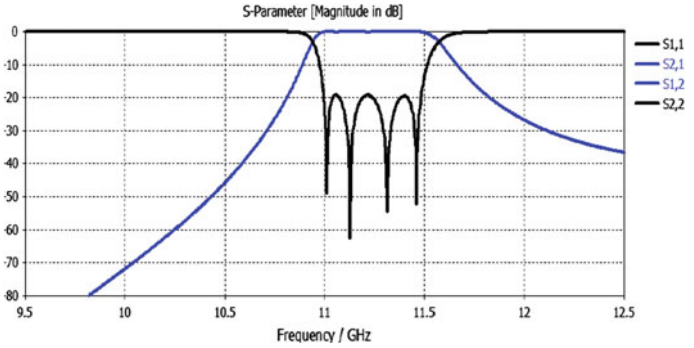

Fig. 2 S parameter response of SIW filter showing passband range of 11–11.5 GHz

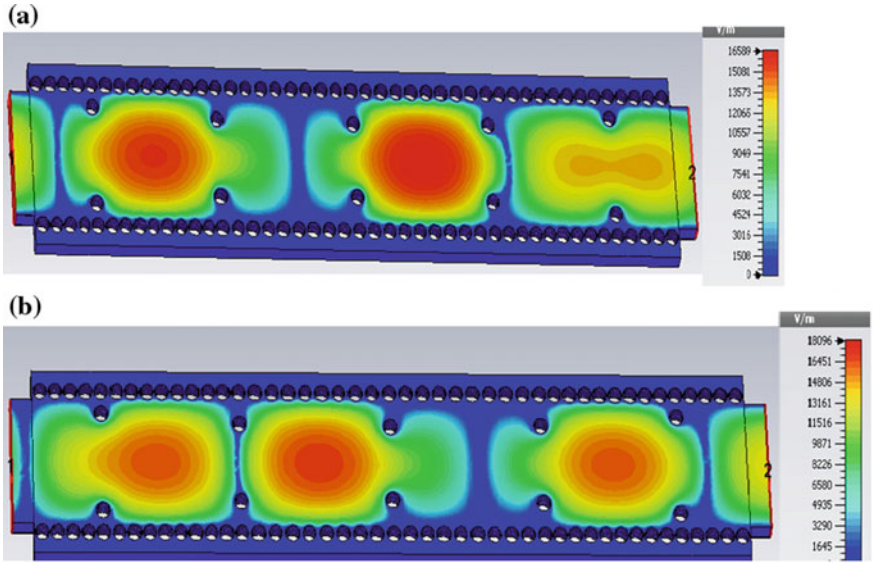

Fig. 3 Current distribution for SIW filter **a** 11 GHz, **b** 11.4 GHz

From the figure, it is clearly showing that the current is properly flowing at these respective frequencies.

3 SIW Antenna Design Using Slots

To work this filter as an antenna, a slot has been etched on the upper surface of the SIW filter. A slot of length Lp = 12 mm and Wp = 1.2 mm. The slot as a space of s = 2.5 mm. This antenna is novel as they are behaving as both the filter and the antenna

within the same band of frequencies. By etching slot at the upper surface of the SIW, the field is radiated in the broadside direction.

3.1 Results of SIW Antenna

Figure 5 shows the simulated return loss of SIW antenna. The antenna has a resonant frequency of 11.4 GHz with a return loss of −15 dB. It has a wide band of 200 MHz Hence, the antenna is showing wide bandwidth. The current distribution (Fig. 6) is calculated using ANSYS HFSS software. The E-field distribution in the figure clearly shows that the field is radiated at the slots and hence, the filter is now working as an antenna. Waveport is applied (port 1) as shown in Fig. 4.

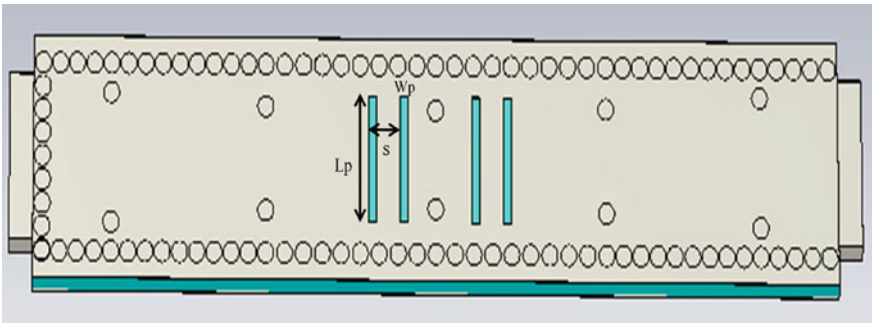

Fig. 4 Proposed SIW antenna with design parameter: Lp = 12 mm, Wp = 1.2 mm, s = 2.5 mm

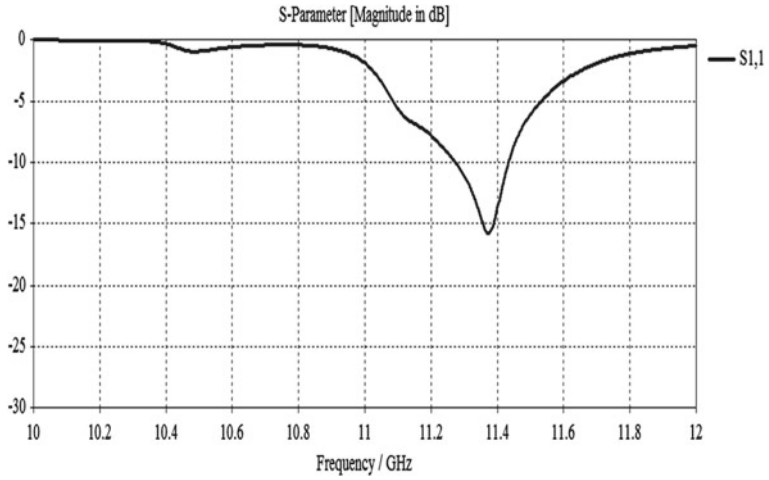

Fig. 5 Return loss response of SIW antenna with a resonant frequency of 11.4 GHz

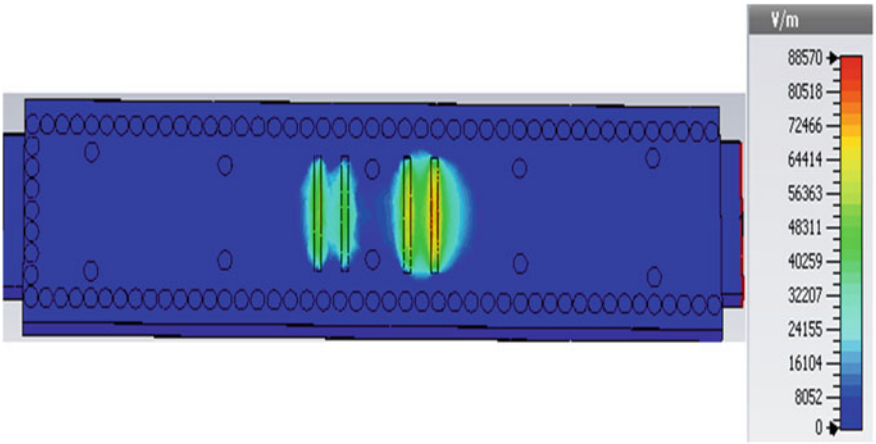

Fig. 6 Current distribution for SIW antenna at 11.4 GHz

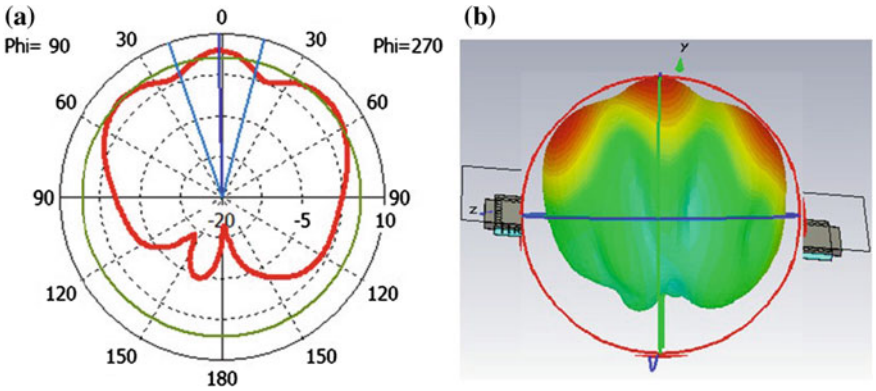

Fig. 7 2D and 3D radiation pattern for SIW antenna with slot at 11.4 GHz

3.2 Radiation Pattern

The radiation pattern for the SIW antenna is shown in Fig. 7. The slot etched at the upper surface of the SIW makes filter to radiate in the broadside direction. Hence, the antenna is working as a broadside radiator with a gain of 6.67 dBi. The 3D radiation pattern of the antenna is calculated using ANSYS HFSS software.

4 Conclusion

A substrate-integrated waveguide antenna incorporated with band-pass filter is designed in this paper. A band-pass filter has passband range of 11–11.5 GHz. To work this filter as an antenna, a slot has been etched on the upper surface of the SIW filter. The antenna has a resonant frequency of 11.4 GHz with a gain of 6.67 dBi. This antenna has a both of the advantage of using same SIW to work as filter and an antenna with a same range of frequencies. SIW technology is used to design the filter as well as antenna.

References

1. Kumari, S., Srivastava, S.: Waveguide and substrate integrated waveguide for Ku Band. In: International Conference on RecentAdvances in Information Technology, pp. 1–8 (2012)
2. Agrawal, T., Srivastava, S.: Two Element MIMO antenna using Substrate Integrated Waveguide (SIW). In: IEEE International Conference of Signal Processing and Communication, JIIT Noida (2016)
3. Kordiboroujeni, Z., Bornemann, J.: Designing the width of substrate integrated waveguide structures. In: IEEE Microwave and wireless components letters, pp. 518–522 (2003)
4. Mukherjee, S., Biswas, A.: Design of SIW cavity backed slot antenna for wideband applications. In: IEEE Asia Pacific Microwave conference (2016)
5. Chen, C.F., Chang, S.F., Tseng, B.H.: Design of compact microstrip sept-band bandpass filter with flexible passband allocation. In: IEEE Microwave and Wireless Components Letters, pp. 346–348 (2016)
6. Mohottige, N., Glubokov, O., Jankovic, U., Budimir, D.: Ultra compact inline E- plane waveguide bandpass filter using cross coupling. In: IEEE Transactions on Microwave Theory and Techniques, pp. 2561–2571 (2016)
7. Rhbanou, A., Sabbane, M., Bri, S.: Design of K-band substrate integrated waveguide bandpass filter with high rejection. In: Journal of Microwave, Optoelectronics and Electromagnetic Applications, pp. 155–169 (2015)
8. Ding, Y., Wu, K.: Substrate integrated waveguide-to-microstrip transition in multilayer substrate. In: IEEE Transactions on Microwave Theory and Techniques, pp. 2839–2844 (2007)
9. Wong, S.W., Wang, K., Chen, Z.N., Chu, Q.X.: Design of millimeter-wave bandpass filter using electric coupling of Substrate Integrated Waveguide (SIW). In: IEEE Microwave and Wireless Components Letters, pp. 26–29 (2014)
10. Missaouia, S., Missaouia, S., Kaddour, M.: Tunable SIW bandpass filter-combined microstrip antenna using liquid crystals. In: Elsevier- International Journal of Hydrogen Energy, pp. 8804–8812 (2017)
11. User Manual Ansys Inc. High Frequency Structural Simulator (HFSS) Software, version -13
12. Deslandes, D., Wu, K.: Single-substrate integration technique of planar circuits and waveguide filters. IEEE Transactions on Microwave Theory and Techniques, pp. 593–596 (2003)
13. Bozzi, M., Georgiadis, A., Wu, K.: Review of substrate-integrated waveguide circuits and antennas. In: IET Microwave Antennas Propagation, pp. 909–920 (2011)
14. Yan, L., Hong, W., Hua, G., Chen, J., Wu, K., Cui, T.J.: Simulation and experiment on SIW slot array antenna. In: IEEE Microwave and Wireless Components Letters, pp. 446–448 (2004)
15. Doucha, S., Abri, M., Badaoui, H.A.: Leaky wave antenna design based on SIW technology for millimeter wave applications. In: WSEAS Transactions on Communications, pp. 108–112 (2015)

16. Deslandes, D., Wu, K.: Accurate modeling, wave mechanisms, and design considerations of a substrate integrated waveguide. In: IEEE Transactions on Microwave Theory and Techniques, pp. 2516–2526 (2006)
17. Yan, L., Hong, W., Hua, G., Chen, J., Wu, K., Cui, T.J.: Simulation and experiment on SIW slot array antenna. In: IEEE Microwave and Wireless Components Letters, pp. 446–448 (2004)

PAPR Reduction Analysis of OFDM Systems Using GA-, PSO-, and ABC-Based PTS Techniques

Alok Joshi, Aashi Garg, Esha Garg and Nayna Garg

Abstract The major drawback of OFDM systems is the high peak-to-average power ratio of the transmitted signal. The paper describes the PAPR reduction and some of the important PTS-based optimization techniques for the reduction of various factors of complexity comprising computational, time, and space complexity, thus making the system more optimized. The algorithms include Genetic Algorithm (GA), Particle Swarm Optimization (PSO), Artificial Bee Colony (ABC), and Biogeography-Based Optimization (BBO). A comparison between these optimization techniques is done. Also, PTS method and the difficulty of PAPR in OFDM systems are briefly described.

Keywords Orthogonal frequency-division multiplexing (OFDM)
Partial transmit sequence (PTS) · Peak-to-average power ratio (PAPR)
Genetic algorithm (GA) · Particle swarm optimization (PSO)
Artificial bee colony (ABC) · Biogeography-based optimization (BBO)

1 Introduction

Orthogonal frequency-division multiplexing (OFDM) is a multi-carrier modulation system which decreases interference and noise efficiently. It has many advantages over single-carrier modulation technique such as rapid data transmission, great spectral efficiency, inclination towards flat fading, and less impact of inter-symbol interference. High Peak-to-Average Power Ratio (PAPR) at the transmitter's output is

A. Joshi · A. Garg (✉) · E. Garg · N. Garg
Jaypee Institute of Information Technology University, Noida 201301, India
e-mail: aashigarg.in@gmail.com

A. Joshi
e-mail: alok.joshi@jiit.ac.in

E. Garg
e-mail: esghagarg1996@gmail.com

N. Garg
e-mail: nayna.gargdec15@gmail.com

B. S. Rawat et al. (eds.), *Advances in Signal Processing and Communication* ,
Lecture Notes in Electrical Engineering 526,
https://doi.org/10.1007/978-981-13-2553-3_15

the chief drawback of OFDM. Passing a high PAPR signal over a nonlinear device causes unwanted band distortion and spectral fading [1]. In an OFDM signal, PTS is the most effective technique with least distortion for the reduction of PAPR.

In PTS, every input block of data is divided into a number of disjoint sub-blocks that are further multiplied by the phase factors and summed up together to yield the transmitted sequence [2, 3]. The inverse fast Fourier transform of every sub-block is joined to form a small PAPR OFDM signal [4].

Many evolutionary PTS-based optimizations algorithms are proposed to reduce the number of searches including Genetic Algorithm (GA), Particle Swarm Optimization (PSO), Artificial Bee Colony (ABC), and Biogeography-Based Optimization (BBO).

The paper is structured in the subsequent ways: Sect. 2 describes the OFDM systems and PAPR. Section 3 corresponds to the PTS technique. Section 4 accounts for the major drawbacks of the PTS technique. All the PTS-based algorithms are described in Sect. 5. Section 6 gives the comparison of all the algorithms and Sect. 8 provides us with the conclusion.

2 OFDM System and PAPR

An OFDM transmitted signal is the addition of orthogonal subcarriers [5]. For N subcarrier OFDM system, the signal can be inscribed as

$$y(t) - \frac{1}{\sqrt{N}} \sum_{n=0}^{N-1} Y_n e^{j2\Pi n \Delta f t} \tag{1}$$

where Y_{n} represents the n-th subcarrier data symbol and Δf represents the frequency spacing between the subcarriers.

The OFDM transmitted signal has high peak values because all the subcarriers are added during the IFFT operation. So, multi-carrier systems have high peak-to-average power ratio than a single-carrier system. This reduces the efficiency of power amplifier and makes it work in the nonlinear region. PAPR is demarcated as the ratio of the extreme power of the OFDM signal to its average power [2–5]. Thus, Eq. (1) defines the PAPR of the OFDM signal:

$$PAPR(y(t)) = \frac{\max\limits_{0 \le t \le N-1} |y(t)|^2}{E\left(|y(t)|^2\right)} \tag{2}$$

where E{.} represents the estimated value or the average power of the OFDM transmitted signal. Moreover, the probability of PAPR of the OFDM symbol surpassing the given threshold $PAPR_0$, is defined as Complementary Cumulative Distribution Function (CCDF). This can be stated as

$$CCDF = \Pr(PAPR > PAPR_0) \tag{3}$$

3 The Partial Transmit Sequence Technique

In the PTS technique, the N symbol input block of data is divided into disjoint sub-blocks, which is then multiplied by the phase factor. Phase factor value is selected in such a manner so that PAPR value of the transmitted OFDM signal is lessened. Figure 1 demonstrates the block diagram of the PTS technique [6]. In PTS, an input block of information is divided into M disjoint sub-blocks X_m where $X_m = \left[X_{m,0}, X_{m,1}, X_{m,2}, \ldots\ldots\ldots X_{m,N-1}\right]^T$, $m = 1, 2 \ldots\ldots\ldots, M$. Therefore,

$$X = \sum_{m=1}^{M} X_M \tag{4}$$

By taking the inverse fast Fourier transform, these M sub-blocks are converted into time domain signal and are expressed as [7]

$$x_m = IFFT(X_m) \tag{5}$$

$$x_m = \frac{1}{\sqrt{N}} \sum_{m=0}^{N-1} X_m e^{j2\Pi n \Delta f t},\ m = 1 \ldots\ldots\ldots M \tag{6}$$

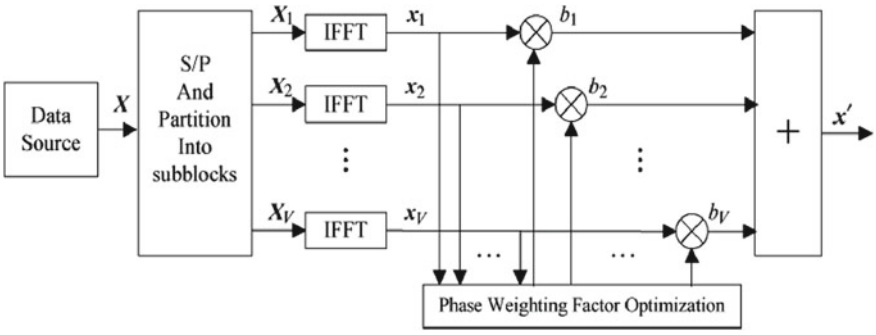

Fig. 1 Block diagram of PTS

The output of IFFT in the time domain is multiplied by the phase factor. This phase factor is given as

$$b_m = e^{j\Phi_m} \tag{7}$$

In the time domain, the resulting signal after combination is

$$X = \sum_{m=1}^{M} x_m b_m \tag{8}$$

where $\Phi_m = \frac{2\Pi w}{W}$, w $= 1, 2, \ldots\ldots\ldots\ldots\ldots$, W - 1. W is the maximum figure of allowed phase angles. As the number of sub-blocks and phase weights increase it leads to higher complexity. Our main objective is to discover the phase factor conforming the least PAPR value.

The following graph in Fig. 2 demonstrates the CCDF of PAPR, corresponding to their PAPR values where V symbolizes the quantity of sub-blocks and W signifies the numeral phase factors allowed [7].

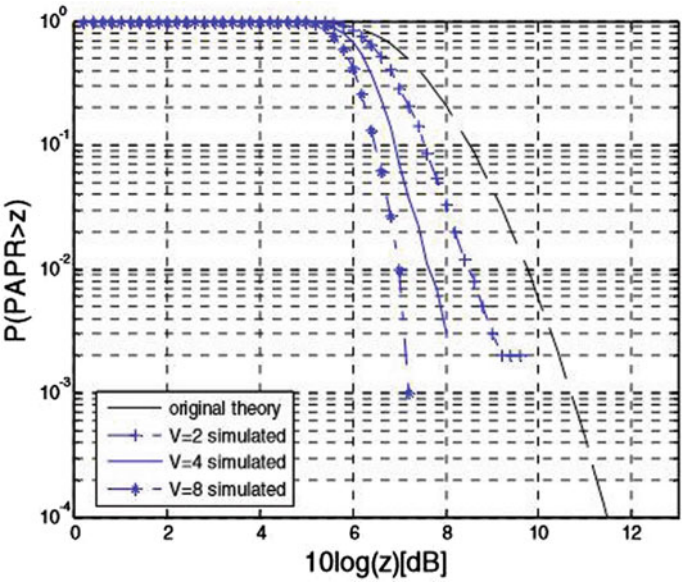

Fig. 2 CCDF of the PAPR by PTS

4 Drawbacks of PTS Technique

PTS being one of the successful PAPR reduction techniques have a major drawback of "space complexity" [8]. The generation of phase factors in PTS technique is the root cause of the phase complexity as it produces an extreme number of combinations, which in turn increases the "computational complexity" of the entire process [9]. As the computational complexity increases, the time requirement for the accomplishment of the process will further increase to a great extent, thus leading to "time complexity" [10].

Thus, in order to reduce these complexities and make the system well optimized, various optimization algorithms have been stated and discussed in detail in the next section.

5 Optimization Algorithms for PAPR Reduction Using PTS Technique

In this section, optimization algorithms for PAPR reduction are discussed.

5.1 Genetic Algorithm

Genetic Algorithm was introduced by John Holland in the 1970s, in the United States. Natural Selection and Genetic Inheritance are the key concepts of the algorithm. The stages in the algorithm are shown in Fig. 3. The focal objective is to find the appropriate phase factor so that the PAPR can be minimized. Initially, this algorithm selects the random population known as chromosome which is then multiplied by a set of phase factors which further lead to PAPR calculation. The value of fitness of each chromosome can be computed by

$$F(y_a(t)) = \frac{1}{10 \log_{10} PAPR(y_a(t))} \tag{9}$$

According to the calculated value of fitness of each chromosome, candidates are selected for the generation of further chromosomes for the next population [11, 12]. The crossover operation is performed by choosing a crossover point for the parent's chromosomes. The entire process is repeated for both the chromosomes and hence, a new offspring is added to the population. In certain new offspring formed, some of their genes are subjected to mutation, i.e., some of the bits in the bit stream are inverted. The chromosome that best fits the desired object amongst the current survivors is selected.

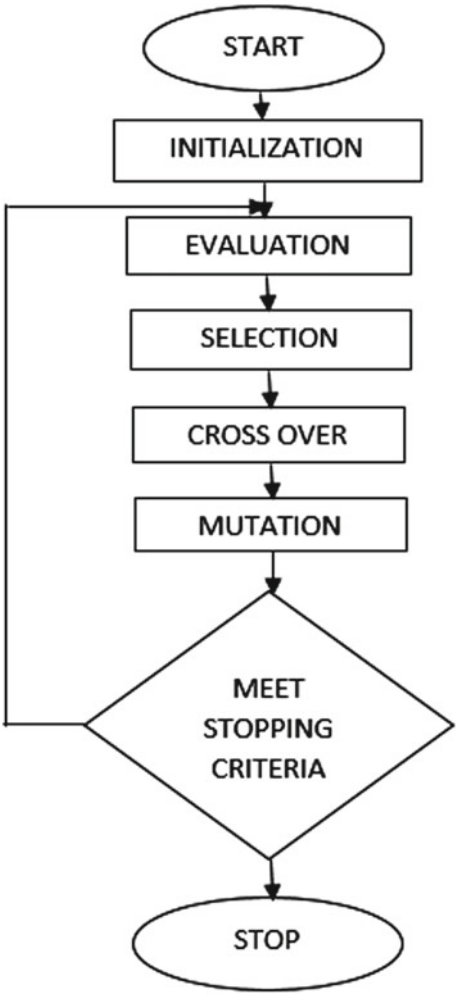

Fig. 3 Flowchart of GA-PTS

Table 1 Performance analysis of GA-PTS

Generation	Population	PAPR (dB)
5	50	6.865
10	50	6.79
20	50	6.72

- **Result of GA-PTS**

It is observed that, while CCDF = 0.001, the PAPR value of the original OFDM are 10.26 dB, 6.346 dB, Table 1 shows the performance analysis of GA-PTS [13].

From Table 1, we can conclude that by increasing the value of generation, the PAPR value gets reduced [13].

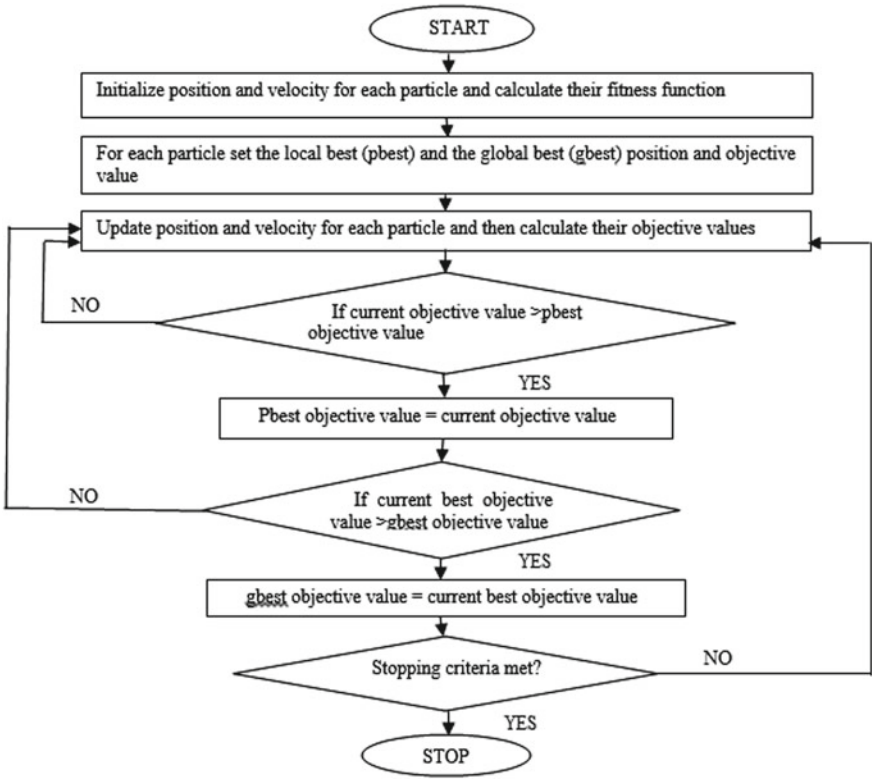

Fig. 4 Flowchart of PSO algorithm

5.2 Particle Swarm Optimization (PSO)

In 1995, the PTS-based Particle Swarm Optimization technique was proposed by Kennedy and Eberhart based on Swarm behavior in nature such as fish schooling, etc. The idea behind the PSO algorithm is to simulate bird's behavior in finding food by observing the behavior of other birds who appeared to be nearby food source [14]. PSO uses a population of individuals to search for the best suitable region in the functional space. In this framework, the population is termed as swarm and individuals as particles [15]. The procedure for the PSO algorithm is explained with the help of flowchart shown in Fig. 4 [5].

- **Result of PSO-PTS**

For a 128 subcarrier OFDM system having generation number = 40, M = 8 sub-blocks, and W phase weighting factors, uniformly distributed random variables are used. Table 2 shows the performance analysis of PSO-PTS [5] with CCDF = 0.001.

It is perceived that with upsurge in the figure of sub-blocks, PAPR value becomes better but computational time is increased.

Table 2 Performance analysis of PSO-PTS

No. of sub-blocks (M)	No. of phase weighting factors (W)	PAPR (dB)
4	2	9
4	4	7
8	4	6.5

5.3 Artificial Bee Colony Algorithm

The algorithm was recently proposed by Karaboga as a bee swarm algorithm for the generation of the most optimized solution by reducing the number of search cycles. The algorithm comprises of three different groups of bees: "employed bees", "onlooker bees," and "scout bees." The best food source with the highest nectar amount is selected to be optimized. The food source here represents one of the possible solutions and the nectar amount goes for fitness of the solution given by [12]

$$fit(x_j) = \frac{1}{1 + f(x_j)} \tag{10}$$

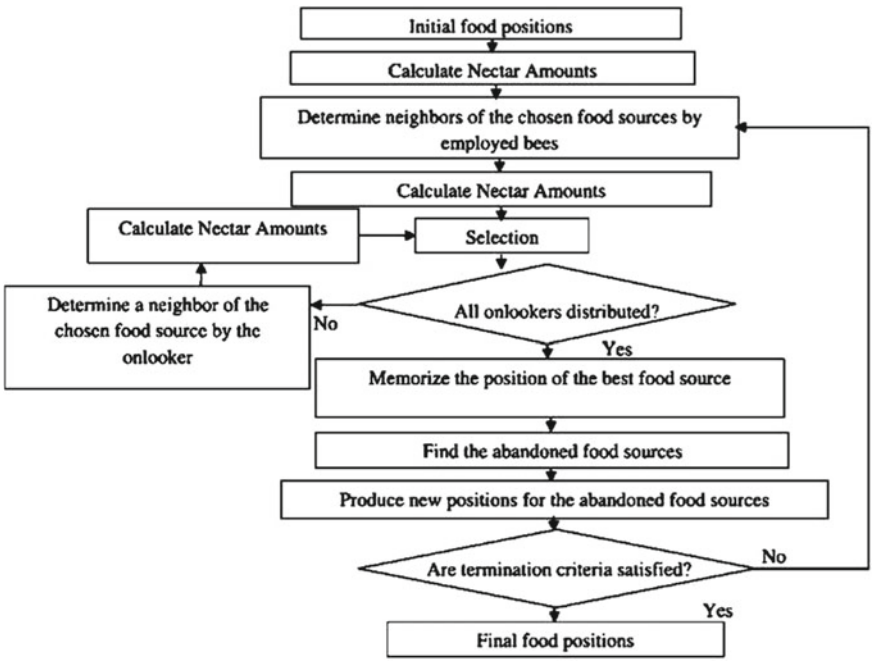

Fig. 5 Flowchart of ABC algorithm

Table 3 Performance analysis of ABC-PTS

Population size (SN)	Maximum cycle number (MCN)	Search number (S = MCN*SN)	PAPR
4	4	16	7.49
4	16	64	6.84
4	64	256	6.44
4	256	1024	6.18

where x_j is the solution and $f(x_j)$ is the PAPR value of the solution. The entire process of ABC is explained in Fig. 5.

- **Result of ABC-PTS**

Table 3 represents the PAPR lessening performance of the ABC-PTS by diverse search numbers (S) and CCDF = 0.001. Here, SN represents the population size, MCN is maximum cycle number, and LV (limit value) = 10 [16].

In the ABC-PTS, as the MCN value increases, the number of searches increases, and the PAPR value decreases.

5.4 Biogeography-Based Optimization

Biogeography-Based Optimization is an evolutionary algorithm, grounded on the distribution and migration of biological species in space and time, using a mathematical model initially proposed in 2008. For the biological survival, important factors like temperature, moisture, etc., are linked with suitability index variable and habitat suitability index to receive an optimal solution. Here, SIV corresponds to the solution vector's components, whereas HSI is used to measure the value of SIV. At first, the SIVs of the habitat is initialized [17]. The feasibility of habitats is checked and HSI is calculated. Elite habitats are identified in the next step based on the HSI value. The main steps of the algorithm are population migration and mutation. Migration is basically used to interchange data with other groups of species. There are more species and a higher immigration rate in the habitats with a high HIS [18]. The degree of population migration depends on their immigration and emigration rate. Cosine model is used for the calculation of these rates. The species with high HSI value correspond to low immigration rate and vice versa. Calculation of HSI is the final step towards the suitability of the entire population. In emergency conditions, even the suitability of groups is changed using the concept of mutation. The species count probability and the mutation rate of all habitats are calculated [19].

6 Comparison

A distinctive comparison can be made between the working of algorithms, to reduce the complexity and computational time for the minimum PAPR calculation. For combinatorial problems, like here, to reduce the number of searches, a discrete technique like GA, is highly suitable. PSO, on the other hand, is a continuous technique that is very poorly suited, in this case. In both algorithms, new solutions are generated in the neighborhood of two parents, via crossover in GA and via attractions toward the pbest positions in PSO. PSO and GA share many similarities, the most common being the generation of the random population and evaluating the population using a fitness value. Compared to GA, PSO is easier to implement and has fewer components. The results generated by deploying ABC algorithm yields great accuracy as compared to other algorithms but the calculation period is longer. In BBO, on the termination of generation of each group, there is no grouping of habitats constituting similar characteristics, whereas, in PSO, the grouping of similar characteristics is done. However, in both the algorithms, the solutions remain intact and in GA, they are ruled out [20]. There are several advantages of BBO which include lesser parameters, faster convergence and simpler calculations.

7 Conclusion

On the generation of multi-carrier transmission systems, high PAPR is one of the foremost problems. In the paper, we have described various optimization techniques for the reduction of the PAPR values. There are number of advantages in using these optimization algorithms, which include solving of multi-parameter. They are robust and not problem-specific. Algorithms like these are time reasonable as they comprise of exploration and exploitation capabilities.

References

1. Abbas, M., Gasser, S., Aziz, A., Khedr, M.: A new approach for PAPR reduction of OFDM signal based on SLM and PTS. IEEE. (2014). ISBN 978-1-4799-3166-8
2. Ku, S., Wang, C., Chen, C.: A reduced-complexity PTS-based PAPR reduction scheme for OFDM systems. IEEE Trans. Wirel. Commun. 9(8) (2010). IEEE
3. Gao, J., Wang, J., Wang, B.: PAPR reduction with phase factors sub optimization for OFDM systems. In: International Conference on Automation and Logistics. IEEE (2010)
4. Ding, S., Li, S., Liu, J., Wang, H., Gu, Z., Gu, L.: A low complexity PTS algorithm for PAPR reduction in OFDM system based on hamming distance. In: International Symposium on Communication and Information Technologies (ISCIT) (2014)
5. Hung, H., Hung, Y., Yeh, C., Tan, T.: Performance of particle swarm optimization techniques on PAPR reduction for OFDM systems. IEEE (2008)

6. Han, S., Lee, J.H.: Modulation, coding and signal processing for wireless communications - An overview of peak-to-average power ratio reduction techniques for multicarrier transmission. IEEE Wirel. Commun. (2005)
7. Wang, X., He, S., Zhu, T.: A genetic-simulated annealing algorithm based on PTS technique for PAPR reduction in OFDM system. In: 2014 Symposium on Computer Applications and Communications IEEE (2014)
8. Ku, S.-J., Wang, C.-L., Chen, C.-H.: A reduced-complexity PTS-based PAPR reduction scheme for OFDM systems. IEEE Trans. Wirel. Commun. 9(8) (2010)
9. Das, J., Bansode, R.: Performance evaluation of papr using pts-pso in mimo-ofdm systems for various higher ordermodulation schemes. In: International Conference and Workshop on Electronics and Telecommunication Engineering (2016)
10. Renuka, N., SathyaSaiRam, M., Naganjaneyulu, P.V.: Performance and analysis of PAPR reduction schemes based on improved low complexity four partial transmit sequences and constellation methods. In: Department of ECE, K L UNIVERSITY, SPACES-2015 (2015)
11. Kim, S.-S., Kim, M.-J., Gulliver, T.A.: A new PTS for PAPR reduction by local search in GA. In: 2006 International Joint Conference on Neural Networks in Canada (2006)
12. Lin, C., Yong, F.: A novel PTS scheme for PAPR reduction in OFDM systems using riemann sequence. In: AICI 2011, Part II, LNAI 7003, pp. 554–560. Springer, Heidelberg. (2011)
13. Kaur, P., Singh, M.: Performance analysis of GA-PTS for PAPR reduction in OFDM system. In: IEEE WiSPNET Conference (2016)
14. Wen, J., Lee, S., Huang, Y., Hung, H.: A suboptimal PTS algorithm based on particle swarm optimization technique for PAPR reduction in OFDM systems. EURASIP J. Wirel. Commun. Netw. **2008**, 601346 (2008). https://doi.org/10.1155/2008/601346
15. Hung, H., Hung, Y., Yeh, C., Tan, T.: Performance od particle swarm optimization techniques on PAPR reduction for OFDM systems. IEEE (2008)
16. Taspinar, N., Taraboga, D., Yildirim, M., Akay, B.: Partial transmit sequences based on artificial bee colony algorithm for peak-to-average power ratio reduction in multicarrier code division multiple access systems. IET Commun. (2010). https://doi.org/10.1049/iet-com.2010.0379
17. Ghoshal, S., Maity, D., Banerjee, S., Chanda, C.K.: Solution of multi-objective emission and economic dispatch using bare bones TLBO algorithm and biogeography based optimization algorithm. IEEE (2017)
18. Hong, X., Pu, H.: Hybrid optimization control of reheat steam temperature based on BBO algorithm. In: 7th International Conference on Intelligent Human-Machine Systems and CYBERNETICs. IEEE (2015) https://doi.org/10.1109/ihmsc.2015.165
19. Zheng, Q., Li, J., Dong, B., Li, R., Shah, N., Tian, F.: Multi-objective optimization algorithm based on BBO for virtual machine consolidation problem. In: 21st International Conference on Parallel and Distributed Systems. IEEE (2015) https://doi.org/10.1109/icpads.2015.59
20. Hordri, N.F., Yuhaniz, S.S., Nasien, D.: A comparison study of biogeography based optimization for optimization problems. Int. J. Adv. Soft. Comput. Appl. 5(1) (2013)

An Active Polarization-Insensitive Ultrathin Metamaterial Absorber with Frequency Controllability

Prakash, Mayank Agarwal and Manoj Kumar Meshram

Abstract In this paper, the design and simulated characteristics of the ultrathin square-shaped active metamaterial absorber are investigated. The unit cell of the proposed absorber is a fourfold symmetric structure consisting Jerusalem cross mounted with four pin diodes within the square ring. By switching the four diodes ON/OFF all at a time, the response of absorbance of this metamaterial structure switches from single-band to dual-band with polarization-insensitive characteristic.

Keywords Absorber · Active · FSS · Metamaterials · Polarization insensitive

1 Introduction

From the time of mid-1960s, the metamaterials are very famous due to their unique characteristic of negative refractive index [1,2]. Metamaterials are artificially engineered structures which have various desired properties on the basis of manipulation with the electromagnetic waves [3–5]. The electromagnetic properties of the metamaterial structure (ε and μ) can be altered by just varying the shape parameters of the structure. Due to their vast application in many of the fields like the construction of super lenses, cloaking devices, metamaterial antennas [6], and absorbers or in defense systems like radar cross section signature reduction mechanism, and metamaterials have a greater importance in the field of electromagnetic field theory and electronics engineering [7]. Out of the above, researchers have a very keen interest in the absorption phenomenon of the metamaterial [8–10]. These structures are

Prakash (✉) · M. Agarwal · M. K. Meshram
Department of Electronics Engineering, Indian Institute of Technology (BHU) Varanasi, Varanasi 221005, India
e-mail: prakash.ece16@itbhu.ac.in

M. Agarwal
e-mail: magarwal.rs.ece@iitbhu.ac.in

M. K. Meshram
e-mail: mkmeshram.ece@iitbhu.ac.in

B. S. Rawat et al. (eds.), *Advances in Signal Processing and Communication* ,
Lecture Notes in Electrical Engineering 526,
https://doi.org/10.1007/978-981-13-2553-3_16

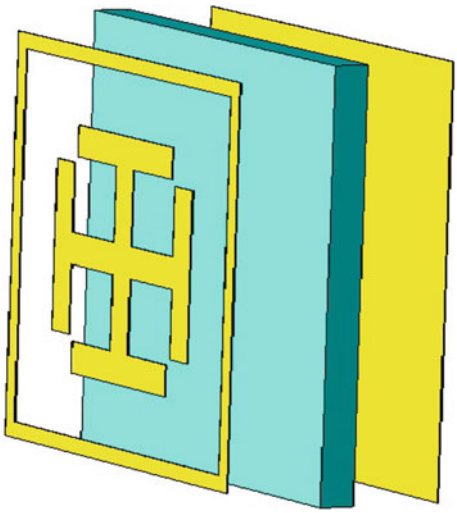

Fig. 1 Three-dimensional structure of the proposed metamaterial unit cell

ultrathin, compact, and easier to fabricate and due to light in weight, they are very much compatible with the other radio frequency devices such as antenna and radar systems.

Basically, a metamaterial absorber is in the form of subwavelength unit cells which is periodically arranged in a plane. The proposed unit cells as shown in Fig. 1 is a three-stage structure which consists of metallic frequency-selective surface at the top, with a metallic plate at the bottom surface in between which a very thin dielectric substrate is sandwiched. The structure has the ability to control its overall electromagnetic parameters by just varying the shape parameters such that the free space impedance is nearly matched to the input impedance of the structure which causes the incident wave to be completely absorbed in the dielectric substrate in the form of loss.

In the past, the research started from the achievement of narrowband to wideband metamaterial absorbers in which polarization insensitivity was the main concern. A number of works have been reported in the field of multiband metamaterial absorbers [11–16]. All the abovementioned work focuses on the conventional passive metamaterial absorbers. In the recent years, there is an increase in research interest in the active metamaterial absorber in which the impedance of the surface is varied to achieve more enhanced properties which make these devices more modern and advance [11,12].

In this paper, an ultrathin active polarization-insensitive metamaterial absorber is proposed. The proposed structure is having single/dual-band absorption characteristics depending on the ON/OFF state of the diode, respectively. The proposed structure is polarization insensitive in both the switching states of the diode. The absorption mechanism of the proposed structure is also discussed with the help of electric field and surface current distribution plots.

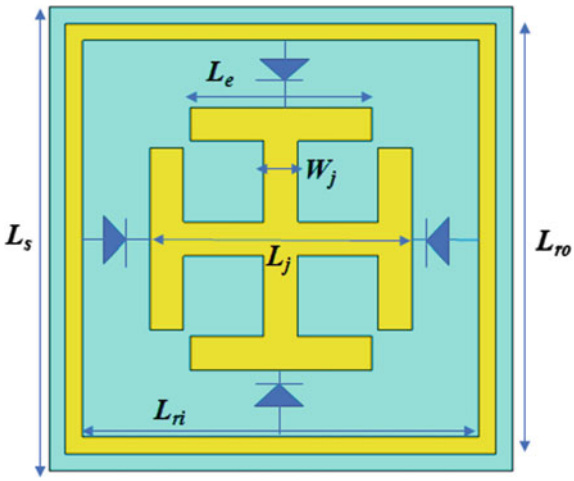

Fig. 2 Top view of the proposed unit cell. (L_s = 13.8, L_{ro} = 12.8, L_{ri} = 11.8, L_j = 7.8, L_e = 5.4, W_j = 1, all dimensions are in mm)

2 Design Specifications of the Proposed Structure

The top view of the unit cell of the proposed structure is shown in Fig. 2. The top side consists of frequency-selective surface (FSS) in the form of the square ring inside which a Jerusalem cross is placed. Four pin diodes of equivalent resistances (10 Ω in ON state and 1 MΩ in OFF state) are mounted in between the edges of the Jerusalem cross and the inner edges of the square ring. A metallic plate is present behind the 1 mm thick FR-4 substrate (ε_r = 4.4 and $tan\delta$ = 0.02). Metallic part of the unit cell is constructed of the 0.035 mm thick copper of finite conductivity of 5.8×10^7 S/m.

3 Results and Discussion

The proposed structure is simulated using CST Microwave Studio 2016 [13] to calculate the *S* parameters of the structure. The diodes mounted in between the edges of Jerusalem cross and the inner edges of the square ring have similar characteristics of the pin diode BAP 70–03 [14] having equivalent resistances of 10 Ω in ON state and 1 MΩ in OFF state. The absorbance of the metamaterial absorber is given by the Eq. 1

$$A(\omega) = 1 - R(\omega) - T(\omega) \tag{1}$$

where $A(\omega)$, $R(\omega)$, and $T(\omega)$ represents absorbance, reflectance, and transmittance of the structure, respectively. Here, $R(w) = |S_{11}|^2$ and $T(\omega) = |S_{21}|^2$. Since the bottom side of the substrate is metal laminated, therefore the transmittance will become zero and the Eq. 1 will be modified as

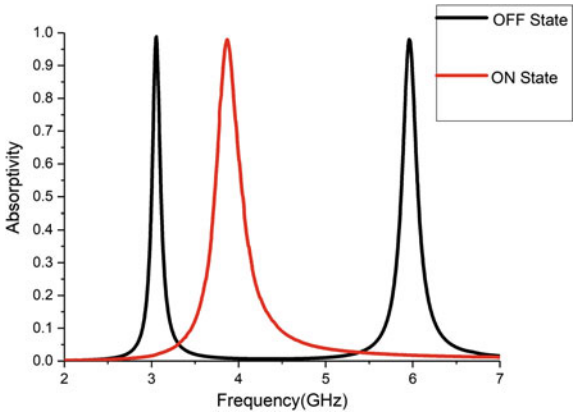

Fig. 3 Absorptivity at ON and OFF states of the diode for normally incident wave

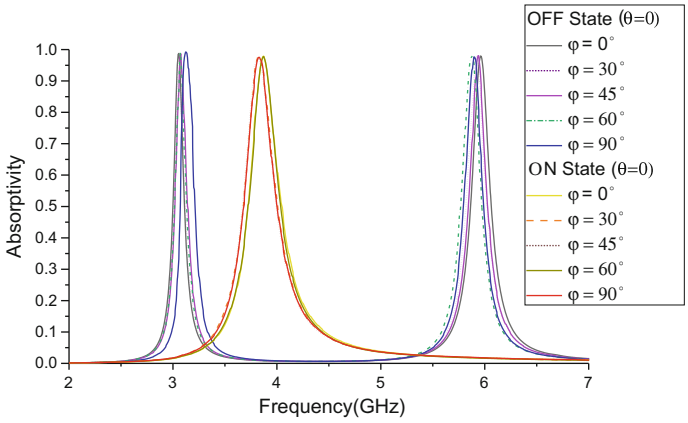

Fig. 4 Simulated absorptivity at different angle of polarization (φ)

$$A(\omega) = 1 - R(\omega) = 1 - |S_{11}|^2 \tag{2}$$

Figure 3 shows the simulated results of the structure for normally incident wave ($\theta = 0^0$) in both ON and OFF conditions of the diode. When all the diodes are in OFF state, the structure behaves as a dual-band absorber resonating at 3.056 and 5.96 GHz with absorptivity of 98.78 and 97.95%, respectively. When all the diodes are in ON condition, the structure is resonating at 3.89 GHz and is having single-band absorption with absorptivity of 97.91%.

Four pin diodes are used in the proposed absorber unit cell instead of two pin diodes [15] to make the structure fourfold symmetric. Therefore, the structure inhibits the characteristics of polarization insensitivity in both ON and OFF conditions of the diode as shown in Fig. 4.

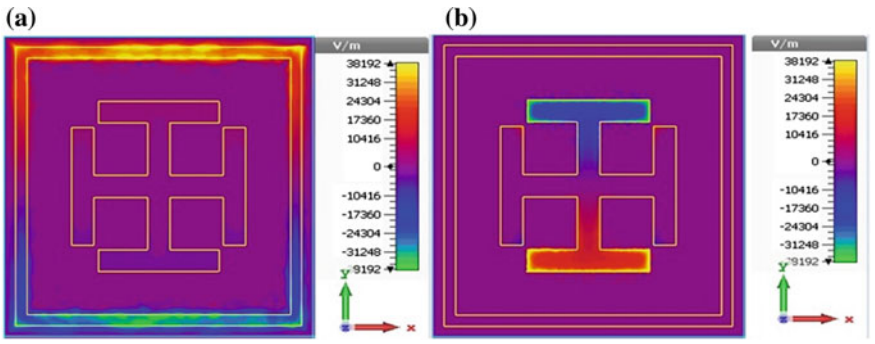

Fig. 5 Simulated electric field distribution at (**a**) 3.056 GHz and (**b**) 5.96 GHz

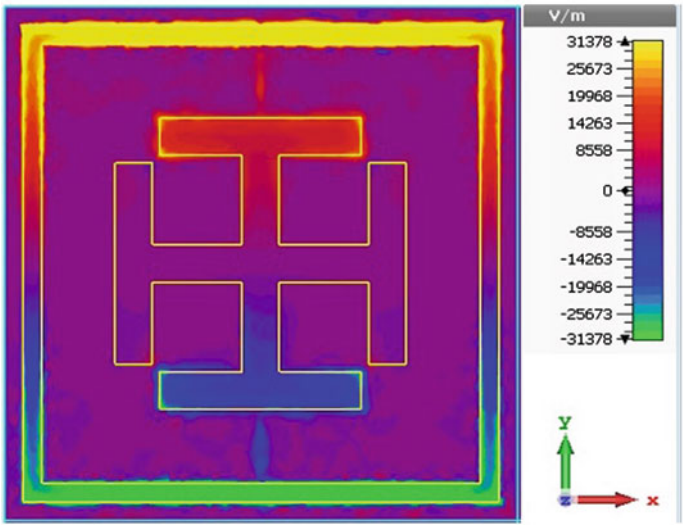

Fig. 6 Simulated electric field distribution at 3.89 GHz

The absorbance mechanism of the proposed structure is based on the simultaneous excitation of electric and magnetic resonance in the structure. For the better understanding of the absorption mechanism, electric field distribution is presented in Figs. 5 and 6 for the OFF and ON states of the diode, respectively. It is clear that when the diodes are in OFF condition, the square ring contributes in resonating at 3.056 GHz and the Jerusalem cross is responsible for the resonance at 5.96 GHz. In the ON state of the diodes, diodes along the *y*-axis are providing a connection path between the edges of Jerusalem cross and the inner edges of the square ring for the *y*-polarized incident wave.

The surface current distributions are plotted on both the FSS and the metallic backplane of the structure at 3.056, 5.96, and 3.89 GHz as shown in Figs. 7, 8, and

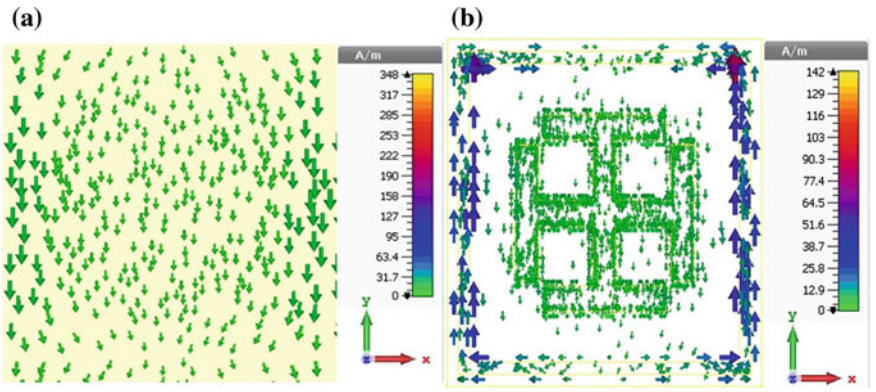

Fig. 7 Simulated surface current distribution on the (**a**) metallic backplane (**b**) FSS at 3.056 GHz

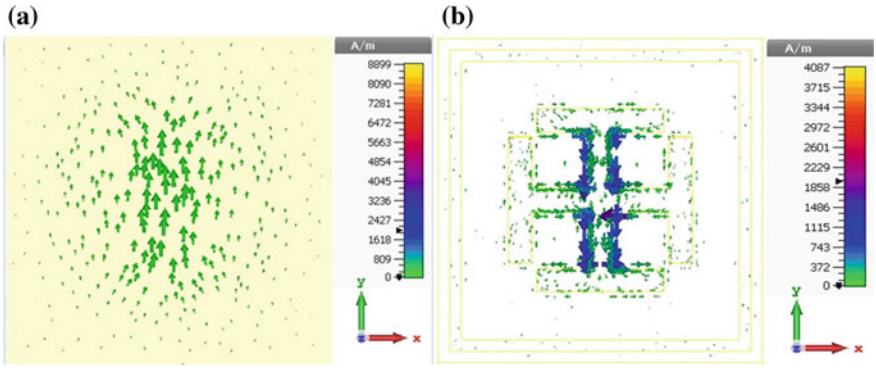

Fig. 8 Simulated surface current distribution on the (**a**) metallic backplane (**b**) FSS at 5.96 GHz

9, respectively. It can be observed that the current in the FSS and metallic backplane are antiparallel to each other and thus forming a current loop which gets energized by a magnetic field oriented perpendicular to the formed current loop, and led to the generation of magnetic resonance in the structure.

4 Conclusion

The proposed absorber structure switches dual-band to single-band absorption behavior depending on the switching state of the diodes. The proposed structure is polarization insensitive owing to the fourfold symmetry in the structure present due to the incorporation of diodes along both the principal polarization direction (x- and y-axis). Furthermore, the absorbance mechanism of the proposed structure is discussed on the basis of simulated electric fields and surface currents distribution plots.

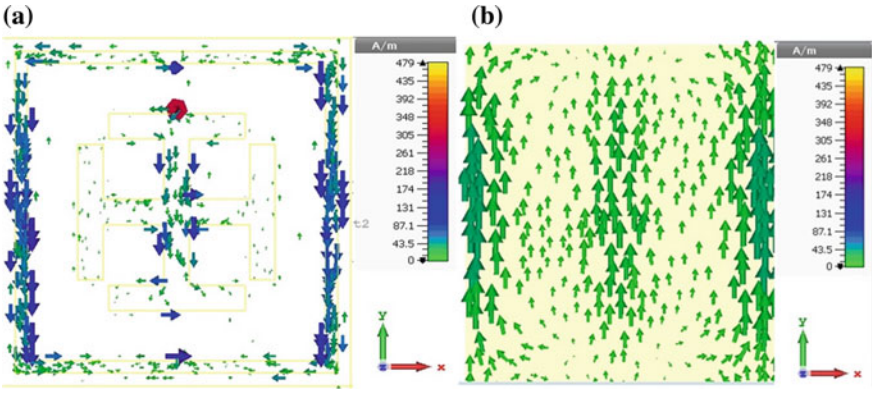

Fig. 9 Simulated surface current distribution on the (**a**) metallic backplane (**b**) FSS at 3.89 GHz

References

1. Vesalago, V.G.: The electrodynamics of substances with simultaneously negative values of ε and μ. Soviet. Phys. Uspekhi. 10(4) (1968)
2. Pendry, J.B., Holden, A.J., Robbins, D.J., Stewart, W.J.: Magnetism from conductors and enhanced nonlinear phenomena. IEEE Trans. Microw. Theory Tech. **47**(11), 2075–2084 (1999)
3. Enghata, N., Ziolkowski, R.W.: Metamaterials: Physics and Engineering Exploration. IEEE press, A John Wiley and sons, inc., publication
4. Lee, Y.P., Rhee, J.Y., Yoo, Y.J., Kim, K.W.: Metamaterials for Perfect Absorption. Springer series in material science, vol. 256
5. Caloz, C.: Itoh T Electromagnetic metamaterial: transmission line theory and microwave. A John Wiley and sons, inc., publication
6. Zhang, H., Cao, X.Y., Gao, J., Yang, H.H., Yang, Q.: A novel dual-band metamaterial absorber and its application for microstrip antenna. Prog. Electromag. Res. Lett. **44**, 35–41 (2014)
7. Watts, C.M., Liu, X., Padilla, W.J.: Metamaterial electromagnetic wave absorbers. Adv. Mater. **24**, 98–120 (2012)
8. Landy, N.I., Sajuyigbe, S., Mock, J.J., Smith, D.R., Padilla, W.J.: Perfect metamaterial absorber. Phys. Rev. Lett. **100**, 207402 (2008)
9. Tuan, S.C.: A practical microwave absorber design based on salisbury screens. In: International Symposium on Antennas and Propagation (ISAP), pp. 944–945. Okinawa, Japan (2016)
10. Ke, L., Xin, Z., Xinyu, H., Peng, Z.: Analysis and design of multilayer jaumann absorbers. In: IEEE International Conference on Microwave Technology and Computational Electromagnetics, pp. 81–84. Beijing, China (2011)
11. Tennant, A., Chambers, B.: A single-layer tuneable microwave absorber using an active FSS. IEEE Microwave Wirel. Compon. Lett. **14**(1), 46–47 (2004)
12. Sanz-Izquierdo, B., Parker, E.A., Robertson, J.B., Batchelor, J.C.: Tuning technique for active FSS arrays. Electron. Lett. **45**(22), 1107–1109 (2009)
13. CST, Framingham, MA, USA, CST Microwave Studio [Online]
14. Datasheet Silicon pin diode BAP 70–03 [Online]
15. Zeng, X., Zhang, L., Wan, G., Gao, M.: Active metamaterial absorber with controllable polarisation and frequency. Electron. Lett. **53**(16), 1085–1086 (2017)
16. Agarwal, M., Behera, A.K., Meshram, M.K.: Wide-angle quadband polarisation-insensitive metamaterial absorber. Electron. Lett. **52**(5), 340–342 (2016)

The Internet of Things: A Vision for Smart World

Brahmjit Singh

Abstract The Internet of Things is a paradigm that involves physical objects with capabilities of sensing, information processing and communication through wireless or wired connection. These physical objects having embedded intelligence and hence decision-making capabilities act as smart things. The paradigm of IoT embraces various domains including sensors, information and communication technology, memory space, data analytics, machine learning and security and privacy mechanisms. The 'things' are constrained in terms of computing power, memory space and data rate and hence need innovative approaches to address the technical challenges present in the real-life implementation of the concept. This work presents a brief introduction to IoT concept, representative discussion on constituent domains and highlights of the technical challenges therein open for research community.

Keywords Internet of things · Security and privacy · Network architecture
Massive connectivity · Communication technologies

1 Introduction

The Internet of Things (IoT) is a new paradigm and probably one of the most important technological revolutions. According to the IEEE IoT initiative [1] IoT is defined as, "A network that connects uniquely identifiable 'things' to the internet." These 'things' have sensing/actuation and programmability capabilities. The word, 'things' in IoT basically refers to smart objects equipped with sensing, storage, data processing, and communication capabilities. The basic concept of IoT is to bring '*anything, anywhere, anytime, anyway, and anyhow'* on a common interconnected networking platform as illustrated in Fig. 1.

The interesting part of IoT is capability of the objects to directly interact with their surroundings. This technology will make the objects, people, processes, machines, environment and infrastructure to interact and communicate with each other. IoT is

B. Singh (✉)
Electronics and Communication Engineering Department, National Institute of Technology Kurukshetra, Kurukshetra 136119, India
e-mail: brahmjit@nitkkr.ac.in

B. S. Rawat et al. (eds.), *Advances in Signal Processing and Communication* ,
Lecture Notes in Electrical Engineering 526,
https://doi.org/10.1007/978-981-13-2553-3_17

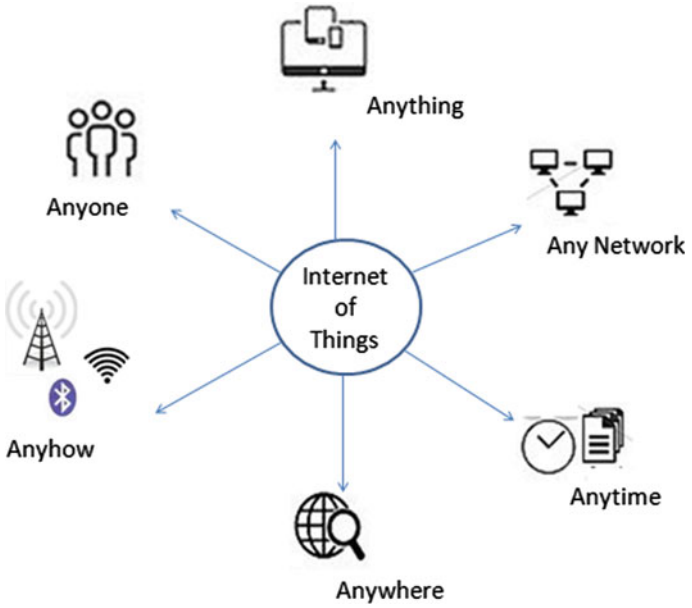

Fig. 1 The basic concept of IoT

indeed being evolved as a global network that will embrace almost all walks of our life. Relative to having less than 1% of the things connected onto the internet today, it is predicted that the advent of IoT will connect more than 24 billion things to the internet by the year 2019 [2]. Projections by Morgan Stanley and Huawei state to have 75 billion by 2020 and 100 billion by 2025 networked devices, respectively [3, 4]. These predictions confirm phenomenal growth and huge impact and influence of IoT on the socio-economic life of the people around the world as depicted in Fig. 2.

IoT enables integration of physical and virtual things through communication technologies, sensors, actuators, Machine-Type Communication (MTC), Device-to-Device Communication (D2D), data analytics and edge computing. Integration of these technologies and supported functionalities results in smart environment, smart transportation, smart home, smart manufacturing, smart health care and so on, which ultimately leads to evolution of the 'Smart World'.

IoT devices are resource constrained in terms of processing power, memory space and data rate support. Conventional communication protocols may not be directly implemented in IoT systems. Moreover, IoT system will generate voluminous data and hence processing, communicating and extracting information from raw data collected from surrounding environment and taking useful action thereupon is a challenging task.

In this paper, a brief introduction to IoT concept, representative discussion on constituent domains and highlights of the technical challenges therein open for research community is presented. Vulnerabilities of the IoT devices to the security breaches are highlighted and research efforts being invested to address those are also presented.

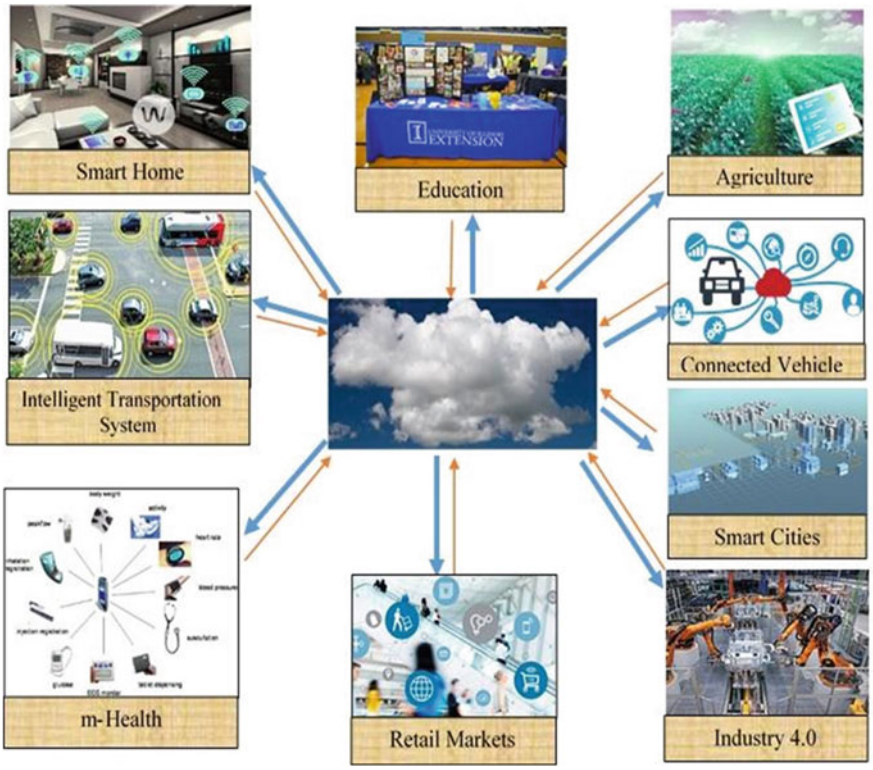

Fig. 2 Ubiquitous growth of networked things

2 Constituent Domains of the IoT System

2.1 Architecture

Given the projection of the trillions of smart things being connected to the internet, the immediate requirement is to decide on an appropriate architecture to handle this scale of connectivity. Primarily, IoT is a network of sensors and actuator envisaged to manifest as utility network similar to electricity type network. This network consists of multiple systems including home automation with energy management system, health care with possible inclusion of wearable medical devices and so on. The architecture must support proper dependencies among such subsystem of IoT.

Integration of subsystems is a very challenging and complicated task. Each system has its own requirements and objectives to accomplish without giving any consideration to others. For example, in healthcare system, wearable particularly critical ones-pacemakers cannot be turned off to save the energy as we can do for home automation. Developing an interacting and powerful architecture supporting interdependencies is indeed an open and challenging research problem. Takno Suganuma

et al. [5] have proposed a flexible edge computing architecture which has the ability to environmental adaptation and user orientation. Though a powerful architecture, its verification is still pending. A hybrid Fi-Wi network architecture has been recently proposed by Hongzhi Guo et al. in [6]. The proposed architecture provides support for the coexistence of centralised cloud and mobile edge computing with collaborative computation offloading feature.

2.2 Communication Technologies for IoT

A number of wireless technologies are being explored for the implementation of IoT systems. Some of the prominent ones are summarised below:

Long-Range (LoRa) WAN is one of the most common technologies for IoT connectivity [7, 8]. Data rate offered ranges from 0.3 to 50 kbits/s in unlicensed frequency band. It offers communication range of up to 20 km. LoRa WAN is equipped with AES encryption for the provisioning of the security.

Z-Wave is a low-power RF communication technology primarily designed for home automation [9]. It operates at 900 MHz frequency band and impervious to interference from Wi-Fi applications. It is optimised for reliable and low latency communication offering data rate of 100 kbits/s and operates on low energy license exempt band. It is equipped with ECDH for key exchange process.

ZigBee is an open standard based on IEEE 802.15.4 protocol for low rate wireless personal area networks. It is an industry standard wireless networking technology providing up to 100 m communication range and supporting data rate up to 31 kbits/s at 868 MHz, which reaches up to 250 kbits/s at 2.4 GHz. This wireless technology is robust, secure and highly scalable and hence found favour for practical implementation in M2 M and IoT applications.

Bluetooth is a short-range communication technology consuming significantly reduced power for its operation. Bluetooth Smart also known as Bluetooth Low Energy (BLE) offers a very promising protocol for IoT applications and considered as the highly promising technology particularly for wearable devices [10]. It offers secure communication equipped with Elliptic Curve Diffie–Hellman (ECDH) in its advanced version BLE 4.2. BLE is simple, open and highly energy-efficient wireless protocol. It is perceived that Bluetooth-enabled smartphones will play a major role in the implementation of IoT paradigm.

Thread [11] is based on IPv6 protocol again optimised for home automation. This technology supports a mesh network based on IEEE 802.15.4 standard. It can handle up to 250 nodes. Simple software upgrades enables users to run threads on the existing IEEE 802.15.4-enabled devices.

Low-Power Wide-Area Networks (LPWANs) has been proposed for IoT systems [12]. The typical LPWAN technologies include SigFox, OnRamp, NB-IoT and Lora. SigFox uses ultra-narrowband frequency spectrum primarily designed to handle low data rate services within 10 to 1000 bits/s. Its power consumption is very low oper-

ating with 50 microwatts and hence may have life cycle of 20 years with a 2.5 Ah battery.

Near-Field Communication (NFC) is specifically designed for two-way communication between the electronic devices like smartphones within proximity of 4 cm [13]. NFC is based on RFID standards—ISO/IEC14443 and FeliCa.

Neul [14] has presented NB-IoT standard for the wireless connectivity of IoT devices. It utilises TV white space as the spectrum to deliver the services. It is highly scalable with larger coverage, low power and cost-effective wireless networking technology. It is also referred to as the weightless technology available at the price of Bluetooth but offering the range of cellular technology and data rate support from a few bits/s to 100 kbps. It is highly energy efficient, consumes 20–30 mA and hence has extended lifetime of 10–15 years.

2.3 Scaling of Connectivity

IoT concept invariability leads to immense connectivity scaling up to 200,000 connections/kM^2. Currently available communication protocols may not work for this scale of connectivity. Centralised server–client model can handle thousands of devices, but it may not work for billions of connected devices. Maintaining servers to handle such large amount of data is very difficult and challenging task. One possible solution may be decentralising the IoT networking. Some of the tasks may be transferred to edge-like fog computing model [6]. IoT hubs can handle mission-critical operations and cloud server can handle collection of data and its analysis. Peer to peer communication may also be explored.

Massive scaling of IoT raises the pertinent issues of maintenance, protection, access authentication, naming and addressing schemes. Again the identification and developing an architecture to support these functionalities is a huge and complex task.

2.4 Real-Time Data Processing

IoT deployment will generate immense amount of data. Knowledge creation through interpretation of the data collected from physical world via an array of sensors is a huge and computationally intensive operation. Drawing the inference from the sensed data through data mining techniques may create knowledge but with finite uncertainty. This may be very risky for actuation and hence may result in lack of trust for the adoption of the IoT technology. It is pertinent to mention that accuracy of the inference drawn from physical data will decide the decision accuracy of the controlling action/actuation.

Further processing and analysing this data in real time will certainly increase load on server by orders of magnitude. This poses new challenges for real-life IoT implantation.

2.5 Security

In this super-connected world, sensitive and private information will flow over wireless channels. As a matter of fact, wireless communication being broadcast in nature lends itself as non-secure medium. It is vulnerable and hence eavesdropper may overhear the confidential messages. Further, the massive scale of connectivity will provide the attacker huge surface area. An attacker can have easy access to these smart but small devices. The things may be used as botnets by the attacker exploiting their security vulnerabilities. Security mechanisms are required which could provide assurances in terms of integrity of the data flow, confidentiality, authentications and non-repudiation of the information flow. In case of no human intervention, the security risk is increased by order of magnitude.

The things in IoT are resource constrained in processing power, memory and battery life and communication capabilities. Conventionally, security mechanisms are implemented at higher layers and these are based on cryptographic approaches, which are intrinsically computationally intensive and demand large memory space. This makes the security in IoT a major and challenging task. Given the limited resources of the IoT devices, the IEEE 802.15.4 standard finds application in IoT scenarios. It is designed with reasonably good energy efficiency, communication range and data rate of the information flow. This standard supports data rate of 250 kbps in a communication range of 10 m. Interestingly, this standard provides security at MAC layer. Hardware platform in IEEE 802.15.4 supports symmetric cryptography using advanced encryption standard [15]. Regarding confidentiality feature of link layer communication, the transmitted data may be encrypted in the counter mode utilising AES-CTR security feature. Data integrity and authenticity may be embedded through cyber block chaining [8].

Though DES is a powerful algorithm and provides strong security cover but it is too heavy to implement in small devices. Lightweight block cipher algorithms [16] are found more suitable for resource-constrained IoT devices. These are efficient and consume relatively less computing resources. For example, KeeLoq [17] is a 32-bit block cipher with 64-bit key size. However, key scheduling being periodic in nature is its weakness. DST is another encryption algorithm with 40-bit block cipher with a 40-bit key size. Unfortunately, small key size leaves it vulnerable for security breaches.

In spite of numerous and serious efforts [18], innovative solutions are needed, which can detect the attacker, can diagnose the attack, can activate the countermeasures and heal/repair the system against the security breaches. One of the major challenges is the real-time response and its promptness. Probably, security provi-

sioning through hardware will ease out the vulnerability to attack problems to the reasonable extent.

2.6 Power Consumption and Energy Efficiency

One of the fundamental requirements of IoT applications is the support for low-power operations. The small devices and sensor nodes are resource-constrained powered by on-board batteries and expected to work for long hours. Particularly in wearable medical devices like pacemakers and in-ear hearing aids, these devices must work without any failure. Standby and sleep mode techniques are used to enhance the battery life. They remain active for brief intervals only to send and receive the data. While in active mode, these draw hundreds of milliamperes but in sleep mode it is only in microamperes. The dynamic range of maximum and minimum current drawn is over 10^6 to 1. Maintaining this large dynamic range of current values is a challenging task.

The most recent trend in IoT paradigm is to integrate Augmented Intelligence (AI) with IoT aiming to augment the performance but not to replace any human power. AI in IoT devices allows those to sense, hear and understand the surrounding environment. Machine learning will extract the information from the vast amount of unstructured data to offer very valuable intelligent insights. It is for sure that the convergence of man and machine will bring the next level of innovation.

3 IoT in India

As per a report from Deloitte (November 2017), the number of IoT devices in India is 60 million and it shall raise to 1.9 billion by the year 2020. Market of IoT-related technology will reach up to $15 billion by 2020 which accounts for 5% of the global market (NASSCOM report). Tata Communications has taken a major and ambitious initiative to setting up an IoT network utilising LoRa WAN technology. This network covers 38 cities and more than 400 million people. These initiatives show huge opportunities for both industry towards enhancing its productivity and efficiency and common user as well for ease of life.

4 Conclusion

IoT may be characterised by ubiquitous connectivity and data collection along with very high level of security risks. Its implementation has myriad of problems and an array of technical challenges. These need to be resolved to realise the vision of smart world through IoT paradigm. Given all the risks and challenges, it is going to become

a reality unleashing plethora of opportunities in all walks of life defence, agriculture, industry, retail, environmental monitoring and automotive industry, urbanisation, health care and business. IoT is evolving as the third in top ten strategic technologies which is expected to grow to $14 trillion business opportunities. The world is indeed transforming into its smart version through a network of connected intelligent things.

References

1. Minerva, R., Biru, A., Rotondi, D.: Towards a definition of the internet of things (IoT), In: IEEE Internet of Things Initiative (2015)
2. Cloud and mobile network traffic forecasting – visual networking Index (VNI) Cisco- (2015)
3. Tony, D., Stanely, M.: 75 Billion devices will be connected to the internet by things by 2020, Business insider (2013)
4. Global Connectivity Index Huawei Technologies Co. Ltd 2015 Wen 06 Sept 2015
5. Suganuma. T., Oide, T., Kitagami, S., Sugawara, K., Shiratori, N.: Multiagent based flexible edge computing architecture for IoT. IEEE Netw. 16–23 (2018)
6. Guo, H., Liu, J., Qin, H.: Collaborative mobile edge computation offloading for IoT over fibre-wireless networks. IEEE Netw. 66–77 (2018)
7. Sornin, N., Luis, M., Eirich, T., Cramp, T., Hersent, O.: LoRaWAN specifications (2015)
8. Centenaro, M., Vangelista, L., Zanella, A., Zorzi, M.: Long-Range Communications in Unlicensed Bands: the Rising Star in the IoT and Smart City Scenarios. IEEE Wirel. Commun. **23**(5), 60–67 (2016)
9. Marksteiner, S., Jimenez, V.J.E., Vallant, H., Zeiner, H.: An overview of wireless IoT protocol security in the smart home domain. In: IEEE Conference on Internet of Things Business Models, Users, and Networks, pp. 1–8 (2017)
10. Hussain, S.R., Mehnaz, S., Nirjon, S., Bertino, E.: Secure seamless bluetooth low energy connection migration for unmodified IoT devices. IEEE Trans. Mobile Comput. (99), 1–17 (2017)
11. Sujin Issa Samuel, S.: A review of connectivity challenges in IoT smart home. In: 3rd MEC International Conference on Big Data and Smart City (2016)
12. Krupka, L., Vojtech, L., Neruda, M.: The issue of LPWAN technology coexistence in IoT environment. In: 17th International Conference on Mechatronics-Mechatronika (2016)
13. Choi, Y., Choi, Y., Kim, D., Park, J.: Scheme to guarantee IP continuity for NFC based IoT networking. In: 19th International Conference On Advanced Communication Technology, pp 695–698 (2017)
14. www.Neul.com, www.silicon.co.uk
15. Miller, F., Vandome, A., McBrewster, J.: Advanced encryption standard (2009)
16. Yap, H., Khoo, K., Poschmann, A., Henricksen, M.: EPCBC- A block cipher suitable for electronic product code encryption. www1.spms.ntu.edu.sg/~kkhoongm/epcbc
17. Indesteege S, Dunkelman NKO, Biham E, Preneel B. A practical attack on KeeLoq. http://www.cosic.esat.kuleuven.be/publications/article-1045.pdf
18. Granjal, Jorge, Silva, Edmundo Monteiro Jorge Sa: Security for the Internet of Things: A Survey of Existing Protocols and Open Research Issues. IEEE Trans. Surv. Tutorials **17**(3), 1294–1311 (2015)

Part II
Signal Processing

Special Pedestrian and Head Pose Detection for Autonomous Vehicles

Sachin Shetty, S. M. Meena, Uday Kulkarni and Harish Basavaraj Hebballi

Abstract Pedestrian safety is a major concern due to increased traffic density and due to driver-pedestrian errors. ADAS (Advanced Driving Assistance Systems) should take different actions for special pedestrians like wheelchair pedestrian. Not much work is done for detecting special pedestrian. In this paper we propose cost effective real-time model for special pedestrian detection and head pose detection. We first detect wheelchair pedestrian and then predict head pose for the Region of Interest (ROI). It is observed that accuracy of wheelchair detection increases considerably by using head pose detection. Our model employs an ensemble of algorithms based on Histogram of Gradient (HOG) for pedestrian features, Modified Census Transform (MCT) for head features and head pose features and SVM for classification. We compare the proposed model against transfer learning approach based on Inception-v3 model.

Keywords Wheel chair pedestrian · HOG · MCT · SVM · ADAS

1 Introduction

ADAS is developed to automate vehicle systems for safe and efficient driving. Research interest in ADAS involves both academia and industry collaborating to reach full autonomy (level 5) [1] from the present systems at conditional autonomy

S. Shetty (✉) · S. M. Meena · U. Kulkarni · H. Basavaraj Hebballi
School of Computer Science and Engineering, KLE Technological University, Hubballi, India
e-mail: sachin.shetty79@gmail.com

S. M. Meena
e-mail: msm@bvb.edu

U. Kulkarni
e-mail: uday.kulkarni@bvb.edu

H. Basavaraj Hebballi
e-mail: harish.hebballi@bvb.edu

B. S. Rawat et al. (eds.), *Advances in Signal Processing and Communication* ,
Lecture Notes in Electrical Engineering 526,
https://doi.org/10.1007/978-981-13-2553-3_18

(level 3) [2, 3]. Anticipation of accidents due to human error; driver/pedestrian is an important feature of ADAS in order to avoid them or mitigate their severity. Counteractive measures need to differ depending on the pedestrian viz., walking pedestrian, pedestrian with wheelchair. Special attention needs to be taken for special pedestrian crossing, due slower response time compared to normal pedestrian.

Pose detection of wheelchair pedestrian is a challenge due to few visual cues available compared to upright walking pedestrian and due to different variety of wheelchair structures leading to variable appearance with different viewing angles. In addition to challenges reported for Head pose estimation of normal pedestrian, the complexity increases with occlusions of wheelchair. Focus of our work is based on head pose detection for three classes (i.e., left, right, front) as it would cover major scenarios for pedestrian at crosswalks. We propose an algorithm for augmenting the ADAS features with wheelchair pedestrian and head pose detection to analyze pedestrian projected actions for behavioral planning. Our paper is organized into following sections: In Sect. 2 we review the existing pedestrian detection algorithms. Section 3 outlines the proposed algorithm. In Sect. 4 implementation details and results are reported. In Sect. 5, we draw conclusions and propose additional improvements.

2 Related Work

Research work has been carried out on normal pedestrian detection at crosswalk and junctions, [4] discusses a Bayesian filtering system for detecting pedestrians at blind spots during turns at junctions. Study was conducted by [5] on driver–pedestrian interaction by examining driver's approaching behavior to understand the different scenarios leading to collisions.

Current approaches are based on normal pedestrian intention detection, most of which evaluate lateral approaching pedestrians considering crossing the street as principal intention of pedestrian [6].

Furthermore, another approach for walking pedestrian pose estimation was reported by [7] using HOG (Histogram of Gradients) and path prediction using MCHOG (Motion Contour Histogram of Gradients) that implicitly encompasses the body language of step initiation, specifically the movement of body of legs, but the absence of any such leg movements in case of wheelchair pedestrian poses challenges.

However, authors of [8] have suggested that head pose contains substantial information to understand the visual attention, because under most circumstances pedestrians turn their head to see a vehicle rather than look away from a vehicle. Thus, it is presumed that patterns exist in head pose that can reveal various intentions.

Haar wavelet features was introduced by [9] to train quadratic support vector machine(SVM) with front and rear-viewed pedestrians. Viola and Jones [10, 11] proposed AdaBoost cascades as learning algorithm for Haar-like features for surveillance-oriented pedestrian detection. The most common features extracted from the raw image files are variants of the HOG structure [12], i.e., local histograms

of gradients, different variants of generalized Haar wavelets, [13, 14], and SIFT [15] designed to capture the overall shape of pedestrians. Sliding window techniques has been used for pedestrian detection, this approach is not robust for scale invariance.

Authors of [16] demonstrated improved performance on ImageNet Large-Scale Visual Recognition Challenge (ILSVRC-2012) based on CNN model consisting of eight layers (five Convolutional and three Fully Connected Layers). Major progress was achieved on subsequent ILSVRC competitions by stacking more CNN layers in different combinations to achieve better performance [17] (22 layers) and [18] (152 layers).

In line with improvisation of CNN on large dataset, [19] research was carried out to utilize the features obtained from one dataset to another distinct dataset. Reference [20] propose DeCAF (A Deep Convolutional Activation Feature for Generic Visual Recognition) based on [16] which show features learnt from ILSVRC to be relevant for recognition on Caltech-101dataset. Also [21] classifies (Extended Cohn-Kanade dataset) based on Inception-V3 [17] architecture trained of ILSVRC.

In this paper we focus towards detection of wheelchair pedestrian as special case of pedestrian since their movement can be predicted to localized region due to directional constraints and also structural occlusions such as wheels and backrest. By using head pose features we focus towards increasing the accuracy of wheelchair pedestrian detection.

We present a work on wheelchair pose detection using an ensemble algorithm which is made of a HOG and MCT for feature extraction and SVM for classification. The results are compared InceptionV3-based transfer learning model.

3 Proposed Work

We illustrate a model which detects pose of wheelchair pedestrian by an ensemble of wheelchair and head features detection. In the first step wheelchair pedestrian is detected, next step will detect head from the observed ROI and the final step classifies head pose based on the previous detected head. Figure 1 depicts the system model.

3.1 Wheelchair Pedestrian Detection

Wheelchair pedestrian image shape can be assumed to be ROI (Region of Interest) with aspect ratio of 1:2, with the wheels and backrest being the prominent features.

HOG proposed by [12] technique tallies occurrences of gradient orientation in localized portions of an image. It is computed on a dense grid of uniformly spaced cells and uses overlapping local contrast normalization for improved accuracy but differs from similar methods such as edge orientation histograms, scale-invariant feature transform descriptors, and shape contexts.

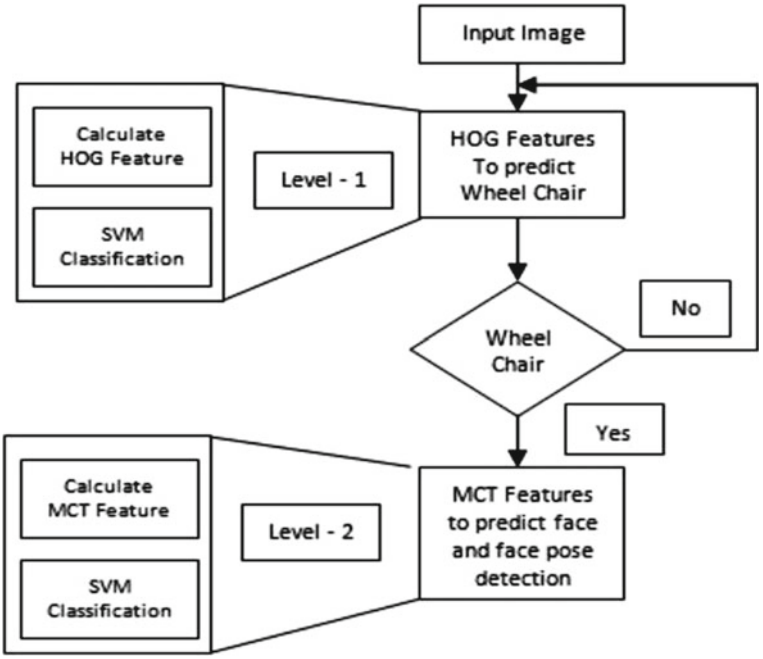

Fig. 1 Ensemble detection model

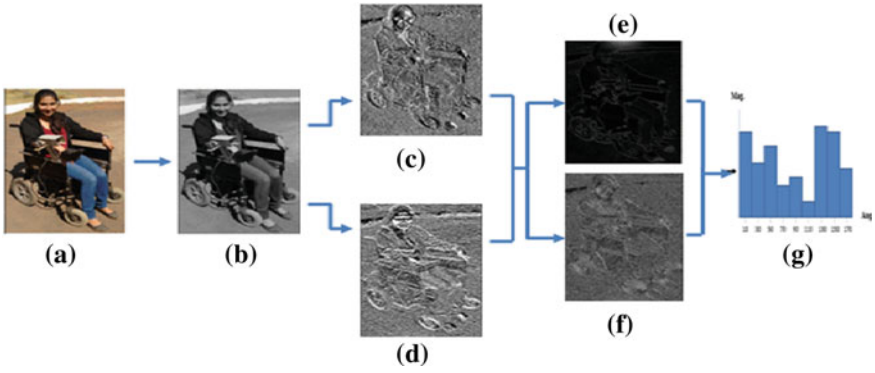

Fig. 2 HOG feature extraction steps for wheelchair pedestrian

3.1.1 Preprocessing

For training, wheelchair pedestrian class is extracted as ROI from an image by cropping only pedestrian region Fig. 2. The images are converted to grayscale Fig. 2b are resized to a resolution of 64 × 128 pixels.

3.1.2 Feature Extraction

1. For the training image, compute x- and y-directional gradients dx(x, y) and dy(x, y) for each pixel using following derivative mask.

$$x - \text{directional gradients} = \begin{pmatrix} -1 & 0 & 1 \end{pmatrix} \tag{1}$$

2. Using the x- and y-directional gradients dx(x, y) and dy(x, y), Gradient magnitude m(x, y) and orientation (x, y) are calculated as

$$y - \text{directional gradients} = \begin{pmatrix} -1 \\ 0 \\ 1 \end{pmatrix} \tag{2}$$

3. Gradient Magnitude image (Fig. 2c, d) is divided into 16 × 16 blocks with 50% overlap. Therefore, we get 105 blocks per image.

$$m(x, y) = \sqrt{\mathrm{d}x(x, y)^2 + \mathrm{d}y(x, y)^2} \tag{3}$$

$$\theta(x, y) = \arctan\left(\frac{\mathrm{d}y(x, y)}{\mathrm{d}x(x, y)}\right) \tag{4}$$

4. Every block has 2 × 2 cells, each cell consists of 8 × 8 pixels.
5. 9-bin histogram is generated by calculating Histogram against each cell. 20 degrees per bin are used (centered at 10, 30,…) with histogram ranging between 0 and 180°. Each pixel votes in histogram according to the magnitude of its gradients.
6. To form block Histogram, concatenate all the cell histogram within block and normalize the block histograms V for improved contrast changes and invariance to illumination, as shown in Fig. 2g.

$$L25\text{qrt} - \text{norm} : f = \frac{v}{\sqrt{\|v\|^2 + \varepsilon}} \tag{5}$$

7. Normalized block histograms are computed to get HOG features descriptors.

3.1.3 Classification

A SVM is a discriminative classifier formally defined by a divided hyperplane. Specifically, given labeled training data, the method outputs an optimal hyperplane which classifies new samples. The process of the SVM algorithm is built upon finding the hyperplane that gives the largest minimum distance to the training samples. Linear SVM machine learning classifier is used to train and classify the feature

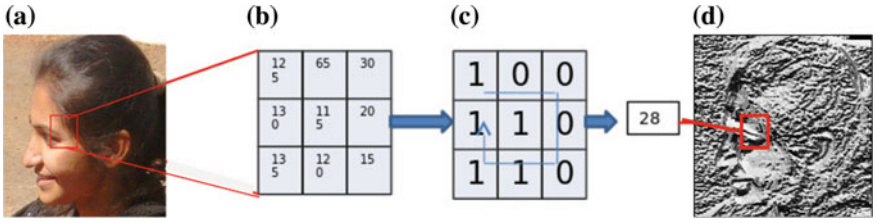

Fig. 3 MCT for head & head pose detection

descriptors as pedestrian/no pedestrian. SVM classifier was sufficient to segregate the objects into wheelchair/non-wheelchair and head pose detection based on the features obtained.

3.2 Head Pose Detection

MCT reported by [8], the transform provides high flexibility against overall luminescence changes and thus is applicable for head detection across broad illumination problems. Given an image, MCT feature extraction is done applying a kernel of 3 × 3. $k(x)$ defines Neighborhood intensity values of central pixel x and $k(x)$ defines Mean intensity values of $k(x)$.

Binary string of each kernel is concatenated using

$$\text{binary} - \text{value} \| f(x) = \begin{cases} 1 & \bar{k}(x) > k(x) \\ 0 \ (\text{binary} - \text{value}) b^{l(q)} + q \end{cases}, \tag{6}$$

where $l(q) = \lfloor \log_2 q \rfloor$ is the number length of q in base b.

MCT value is calculated for each kernel by converting the binary string to base10 number.

$$\text{mct} - \text{image}\,(\text{x}) = \text{binary} - \text{value}_{(10)} \tag{7}$$

For head detection the positive sample contain head images with different orientation and negative sample do not contain any head. Using SVM, bounding square region is classified as either head or not head.

The ROI detected in previous wheelchair detection level, is passed to the ensuing level, which considers a square box of dimensions of 32 × 32 for MCT feature extraction. A kernel of size 32 × 32 is obtained by taking width and size as half of detected rectangle width. Figure 3 depicts calculation of MCT for head detection and head pose detection.

Fig. 4 Describes the different head poses. Three class displays left (0°), front(90°), and right(180°) orientations

SubLevel 1: Head Detection:
Histogram is applied on each MCT block to get 256 bits. Normalization is applied on each bits from each block. The normalized bits are concatenated and L2 normalization is applied to get feature descriptor of 4096 bits. SVM classifier is used to train and classify the feature descriptors as head detected/no head detected. An optimization is achieved by considering only the upper two blocks for head detection, due to head region always present in the top half of wheelchair. This optimization leads to 50% reduction in redundant calculation.

$$\text{facefeaturesize} = 256 * (\text{headW}/yW) * (\text{headH}/xW), \tag{8}$$

where headW and headH are width and height for head image. yW and xW are windowing length in x and y directions.
SubLevel 2: Head Pose Detection:
If ROI in previous level is classified as head, then the headpose detection step does a fine-grained classification into different head pose orientations.

We compare the results of two different models for head pose estimation.

1. MCT—In this model linear SVMs are trained based on yaw angles. Two image classes are trained by extracting MCT features on dataset containing left pose images and right pose images. Based on the max probability provided by SVM, given region is either classified as left pose or right pose image. The MCT features extracted in the previous steps are utilized to get pose direction from SVM.
2. Transfer Learning using Inception-v3—It is the technique of using the features learnt by the Inception-v3 model on the ImageNet dataset, the final classification layer is retrained on our dataset. Using the approach of transfer learning reduces the time taken to optimize the weights of the features (Figs. 4 and 5).

For wheelchair pedestrian, data was collected from ImageNet dataset [22] and locally generated images. Head detection and head pose detection is validated against AFLW [23] dataset. Computations were carried on 3rd Gen i7 processor with 24 Gb RAM with the code written in C++ with OpenCV platform. Figure 6 shows the time taken in seconds for the proposed model. It is seen that there is major difference in time for image sizes with 32 × 32, this due to the local dataset containing head

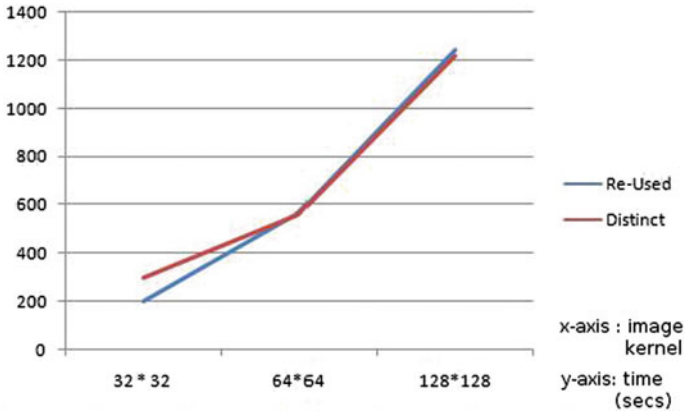

Fig. 5 Time complexity

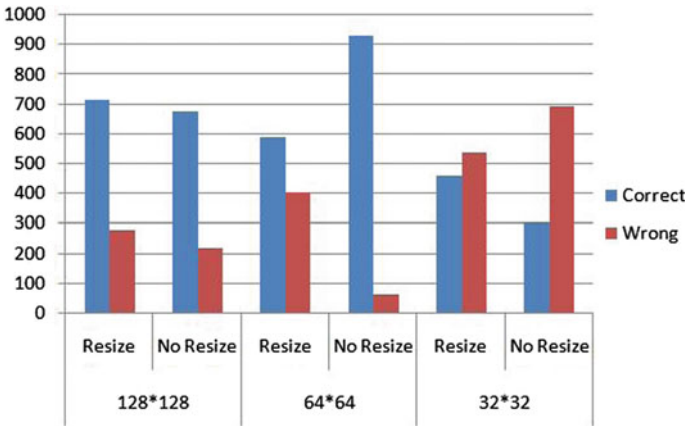

Fig. 6 Left pose detection results

regions with size 32×32. For other image size, there is not considerable change due to entire region being searched without any possible match. The cascading model has demonstrated in 30% reduction in computation costs.

4 Results and Discussions

For wheelchair pedestrian, data was collected from ImageNet dataset [22] and locally generated images. Head detection and head pose detection is validated against AFLW [23] dataset. Computations were carried on 3rd Gen i7 processor with 24 Gb RAM with the code written in C++ with OpenCV platform. Figure 6 shows the time taken

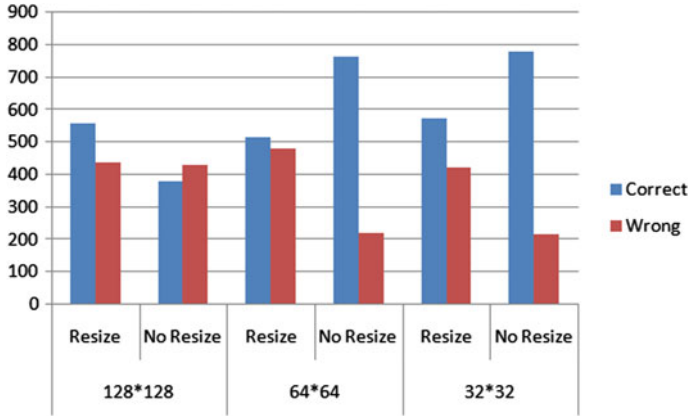

Fig. 7 Right pose detection results

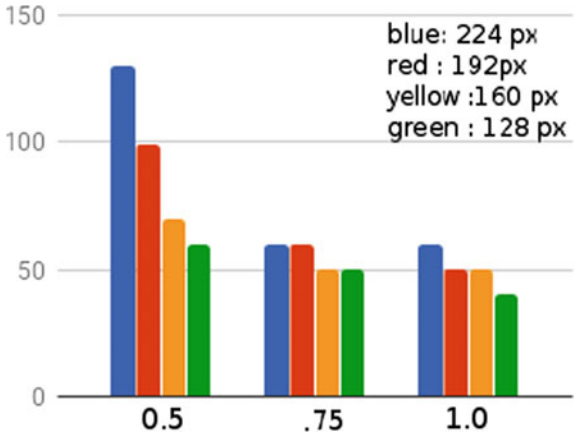

Fig. 8 Iterations required for training using transfer learning

in seconds for the proposed model. It is seen that there is major difference in time for image sizes with 32 × 32, this due to the local dataset containing head regions with size 32 × 32. For other image size, there is not considerable change due to entire region being searched without any possible match. The cascading model has demonstrated in 30% reduction in computation costs.

Head pose detection MCT algorithm has classified AFLW dataset into two different classes with 82% accuracy. From Figs. 7 and 8 which depicts image size vs accuracy on AFLW, it can be observed that kernel 64 × 64 provides better results. Furthermore, we have illustrated the use of Transfer Learning approach using InceptionV3 architecture. InceptionV3 based model classified AFLW dataset into two classes with 98% and three classes with 96% accuracy. Higher accuracy from InceptionV3 model can be attributed to the trained weights from ImageNet (Tables 1 and 2).

Table 1 Time v/s accuracy

Algorithm	Accuracy (%)	Time (sec/image)
HOG + MCT	82	0.8
Transfer learning	96	1.4

Table 2 Dataset Used

Dataset name	Module name	Images
		No. of samples
Local	Wheelchair pedestrian	1194
	Non-wheelchair pedestrian	626
	Head	392
	Non head	400
	Head left	144
	Head right	150
AFLW	Head left	5000
	Head right	5000
ImageNet	Wheelchair pedestrian	350

Figure 8 (*x*-axis: inception model factor, *y*-axis: image kernel) shows that Inception-v3 model optimized to run with kernel 128 × 128 gets better results (80−82%) with less iterations, the original images trained contain five classes (three head poses, wheelchair and non-wheelchair) with varying sizes from 32 × 32 to 224 × 224.

Figure 9 shows output of the detection algorithm, with green bounding box highlighting the special pedestrian region and the red bounding box highlighting the head detection.

5 Conclusion and Future Work

We propose a model to detect wheelchair pedestrian pose detection in real time using HOG for pedestrian, MCT for head feature extraction and SVM for classification. Transfer learning-based approach provides better accuracy compared to MCT for multiclass head estimation but takes additional time. Our future work is to port InceptionV3 model to GPU-based computing to decrease run time using parallel processing. Additional scope is to detect the intention of the pedestrian for tracking and providing feedback to ADAS for further actions by adding road edge detection to get the crosswalk area, such that ROI will be around the crosswalk area, it will reduce the computation costs and also remove the outliers in the image.

Compliance with Ethical Standards

- Conflict of Interest: The authors declare that they have no conflict of interest.

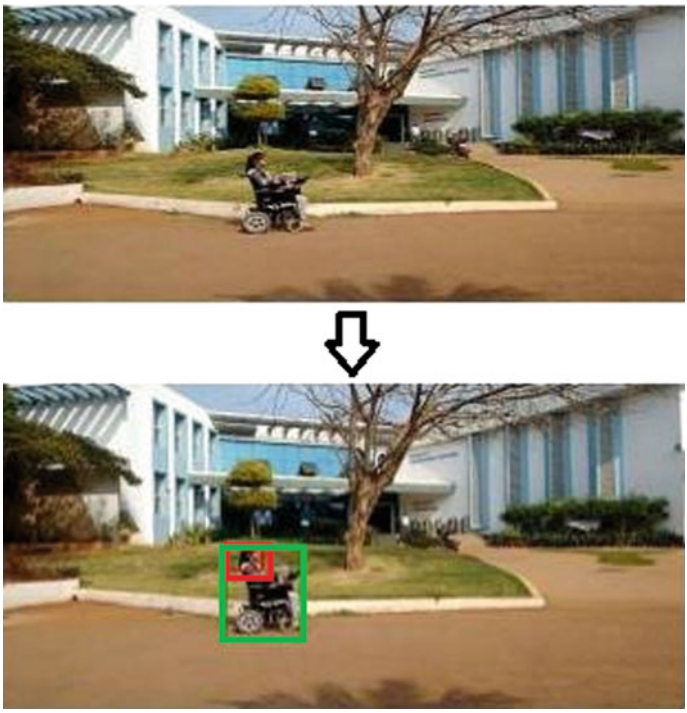

Fig. 9 Sample detected image

- Ethical Approval: This chapter does not contain any studies with animals performed by any of the authors
- Informed Consent: Informed consent was obtained from all individual participants included in the study.

References

1. Taxonomy and Definitions for Terms Related to Driving Automation Systems for On-Road Motor Vehicles - SAE International (2018). https://www.sae.org/standards/content/j3016_201609/. Accessed 27 Feb 2018
2. "Autopilot". Tesla, Inc. (2018). https://www.tesla.com/autopilot. Accessed 23 Feb 2018
3. "Technology – Waymo". Waymo (2018) https://waymo.com/tech. Accessed 23 Feb 2018
4. Hashimoto, Y., Gu, Y., Hsu, L.-T.: Probability estimation for pedestrian crossing intention at signalized crosswalks. In: IEEE Conference on Vehicular Electronics and Safety (2015)
5. Schneemann, F., Gohl, I.: Analyzing driver-pedestrian interaction at crosswalks: a contribution to autonomous driving in urban environments. In: IEEE Intelligent Vehicles Symposium (IV), Gothenburg, Sweden (2016)
6. van de Sande, K., Uijlings, J., Gevers, T., Smeulders, A.: Segmentation as selective search for object recognition. In: ICCV (2011)

7. Khler, S. et al.: Early detection of the pedestrian's intention to cross the street. In: 2012 15th International IEEE Conference on Intelligent Transportation Systems (ITSC). IEEE (2012)
8. Langton, S.R., Watt, R.J., Bruce, V.: Do the eyes have it? Cues to the direction of social attention. Trends. Cogn. Sci. **4**(2), 50–59 (2000)
9. Papageorgiou, C., Poggio, T.: A trainable system for object detection. Int. J. Comput. Vis. **38**(1), 1533 (2000)
10. Viola, P., Jones, M., Snow, D.: Detecting pedestrians using patterns of motion and appearance. In: Proceedings of the International Conference on Computer Vision, vol. 2, pp. 734−741 (2003)
11. Jones, M., Snow, D.: Pedestrian detection using boosted features over many frames. In: Proceedings of the IEEE Conference on Computer Vision and Pattern Recognition (2008)
12. Dalal, N., Triggs, B.: Histograms of oriented gradients for human detection. In: Proceedings of the 2005 IEEE Computer Society Conference on Computer Vision and Pattern Recognition (2015)
13. Dollar, P., Wojek, C., Schiele, B., Perona, P.: Pedestrian detection: a benchmark. In: CVPR (2009)
14. Jarrett, K., Kavukcuoglu, K., Ranzato, M., LeCun, Y.: What is the best multi-stage architecture for object recognition? In: CVPR (2009)
15. Vedaldi, A., Gulshan, V., Varma, M., Zisserman, A.: Multiple kernels for object detection. In: ICCV (2009)
16. Krizhevsky, A., Sutskever, I., Hinton, G.: ImageNet classification with deep convolutional neural networks. In: Advances in Neural Information Processing Systems (2012)
17. Szegedy, C., Liu, W., Jia, Y., Sermanet, P., Reed, S., Anguelov, D., Erhan, D., Vanhoucke, V., Rabinovich, A.: Going deeper with convolutions. In: CVPR (2015)
18. He, K., Zhang, X., Ren, S., Sun, J.: Deep residual learning for image recognition. In: CVPR (2016)
19. Bengio, Y.: Deep learning of representations for unsupervised and transfer learning. In: JMLR (2011)
20. Donahue, J., Jia, Y., Vinyals, O., Hoffman, J., Zhang, N., Tzeng, E., Darell, T.: DeCAF: a deep convolutional activation feature for generic visual recognition. In: ICML (2014)
21. Xia, X.-L., Xu, C., Nan, B.: Facial expression recognition based on TensorFlow platform. In: ITM Web of Conferences (2017)
22. Deng, J., Dong, W., Socher, R., Li, L.-J., Li, K., Fei-Fei, L.: ImageNet: a large-scale hierarchical image database. In: CVPR (2009)
23. Koestinger, M., Wohlhart, P., Roth, P.M., Bischof, H.: Annotated facial landmarks in the wild: a large-scale, real-world database for facial landmark localization. In: Proceedings of First IEEE International Workshop on Benchmarking Facial Image Analysis Technologies (2011)

Sorted Outlier Detection Approach Based on Silhouette Coefficient

Pooja Lodhi, Omji Mishra and Dharmveer Singh Rajpoot

Abstract In this era when data is generated continuously in various domains of machine learning, different algorithms are budding to improve and enhance the learning process. Clustering is one of such machine learning techniques. It is considered to be most important tool of unsupervised learning but it is sensitive to outlier. Thus it is essential to remove the outlier before clustering the data. Most of the outlier detection techniques require some user-defined parameters, which make their accuracy user-dependent. Thus an algorithm which is least dependent on user-defined values is proposed here. The algorithm takes number of cluster in which user want to cluster its data and detect outlier within those clusters using Silhouette Coefficient. The algorithm was compared with some of the existing algorithm in domain of outlier detection. And the experimental analysis is performed on some relevant benchmark dataset presented in UCI repository. Through the experimental results it can be seen that the algorithm we have proposed has performed better than the existing algorithms.

Keywords Outlier detection · k-means · Silhouette coefficient and clustering

1 Introduction

Clustering is considered to be the most important technique/tool of unsupervised learning. Clustering deals with the data structure partition in unknown area [1]. The objective of clustering is to group data objects that are similar into one cluster and to assign the dissimilar data objects to different clusters. Clustering algorithms are

P. Lodhi · O. Mishra (✉) · D. S. Rajpoot
Department of Computer Science Engineering/Information Technology,
Jaypee Institute of Information Technology, A-10 Sector-62, Noida, India
e-mail: omji.mishra@yahoo.com

P. Lodhi
e-mail: poolodhi@gmail.com

D. S. Rajpoot
e-mail: dharmveer.rajpoot@jiit.ac.in

B. S. Rawat et al. (eds.), *Advances in Signal Processing and Communication* ,
Lecture Notes in Electrical Engineering 526,
https://doi.org/10.1007/978-981-13-2553-3_19

used in various domains such as medical, educational, and business, etc. Some of its well-known applications are detection of cancerous data, search engine, wireless sensor actuator networks, etc. In today's world clustering is most commonly used in twitter analysis. Some of the well-known methods are k-means, k-medoids, BIRCH, DBSCAN and SOM, etc. [2]. But unfortunately all the clustering algorithms have some limitations like high time complexity; they need to preset the number of clusters and the clustering result sensitive to the number of clusters. Some of the popular cluster algorithm results are dependent on initial guesses of the seeds and are sensitive to outliers. As clustering algorithms are sensitive to outlier it is essential to cluster data after outlier detection and removal. Outlier detection is also one of the important problems of the fields of machine learning and data mining [3]. An outlier can be defined as an observation or data object which deviates a lot from the other observations present in the dataset that it arouses suspicions that different mechanism or source is cause of its generation [4]. There are various applications of outlier detection like data cleaning, credit card fraud, network intrusion detection, crime detections, stock market, medical data analysis, etc. [3, 4].

A new algorithm to detect outliers and remove them from the dataset is proposed in this paper. The basic idea is to cluster the data using the k-means algorithm into k clusters. Then on basis of intra cluster distance, i.e., distance between the data object and centroid, the objects are sorted within each cluster. Later by using Silhouette Coefficient, we can detect the outliers in the datasets. Experiments were performed and the result has demonstrated that the algorithm we have proposed has performed better in comparison of the existing algorithms.

The organization of various sections in this paper is as follows: Sect. 2, discuss different work related to the outlier detection problem, Sect. 3, contains the background details related to the proposed work, while Sect. 4, present the proposed algorithm, Sect. 5, shows the comparative analysis with experimental results. Finally the last Sect. 6, discuss about the conclusion and future scope of the proposed work.

2 Related Work

We have reviewed various recent clustering-based approaches to detect outlier, in this section. Pre-labeled data is not required to detect outlier when a clustering based outlier detection approach is used. In paper [1], a detailed and comprehensive analysis of various clustering algorithms was discussed. It is essential to analyze the strengths and weaknesses of different clustering algorithm before proposing nay new approach. In this literature clustering algorithms are analyzed from two perspectives, the traditional clustering algorithms and the modern clustering algorithms. Clustering algorithms that are considered to be traditional are K-means, BIRCH, FCM, DBSCAN, CLIQUE and many more. While algorithms like PSO_based, Wavecluster, STREAM, CluStream, etc. are considered to be modern clustering approaches [1].

In literature [5], firstly various application domain of outlier detection were discussed. Later, they proposed a novel approach to detect outliers which uses a

modified k-means clustering algorithm. This method starts with the fundamentals of k-means algorithm of assigning object to the closet centroid, and then SSE that is sum of squared error and SST that is total sum of squares is calculated. This was done with intend to reduce error. Later on the basis of definition they have proposed for outliers, point is judged and removed. Then they recalculated the centroids. The algorithm stops when the objects stop changing their clusters. The results show that their proposed algorithm outperforms existing algorithms used for the detection of outliers. They have also showed that there algorithm had better accuracy on various benchmark datasets. In this paper, authors [3] discussed a k nearest neighbor approach based outlier detection. The data was clustered and then local outliers were detected using LDS algorithm. It had an advantage that its calculation time is 20 times faster than LOF. In paper [6] author presented a classification method which have two-phase. In first phase they clustered the data by k-means. Then in the second phase, they detect outliers using distance-based technique. In the distance-based technique distance of a sample was calculate with all other points in the cluster. A sample was marked as an outlier if at least p fraction of samples in cluster were having distance greater than r. They evaluated there algorithm on 1999 KDD cup dataset. In paper [7] authors presented an Adaptive Rough Fuzzy C-Means clustering algorithm (ARFCM). They have experimentally shown that it outperforms Rough K-Means and fuzzy C-Means clustering method. ARFCM is direct algorithm which aims to assign data object to a cluster by changing the degrees of membership. The membership was used to reflect the degree to which the point is related to that cluster. Literature [8] is about how in high dimensional data it is necessary to remove erroneous data. They proposed two algorithms. One is Distance-Based outlier detection and other Cluster-Based outlier detection algorithm. In their algorithms they were using outlier score for every object and removing all the objects with score less than threshold score. The experiment concluded that cluster-based algorithm to detect outlier produced better accuracy as compared to the distance-based method for outlier detection.

In this paper [9], a method has been proposed to optimize the K-means initial center points. The proposed algorithm has used density-sensitive similarity measure to compute the density of objects. Through computing the minimum distance between the point and any other point with higher density, the candidate points are chosen out. Then, combined with the average density, the outliers are screened out. Ultimately, the initial centers for K-means algorithm are screened out. According to this research paper, experimental results have shown that the algorithm gets the initial center points with high accuracy, and can effectively filter abnormal points. The running time and the iterations of the K-means algorithm are decreased accordingly. The bonus advantage of using the proposed approach is that it has dealt with outliers as well which is another drawback of k-means algorithm. Table 1 shows the analysis of algorithms based on outlier detection.

Table 1 Analysis of outlier detection algorithm

Algorithm	Clustering approach used	Condition of point to be outlier	Disadvantage
Centroid based algorithm [5]	k-means	If the distance between point and the centroid is greater than p times the mean of the distances between centroid and other objects [5]	Requirement of user defined parameters like 'p' Time to calculate mean distance each time
FLDS [3]	k-means	LDS algorithm	–
Distance-based outlier detection [6]	k-means	If at least a fraction 'p' of the samples in cluster lies at a distance greater than 'r' [6]	Requirement of user defined parameters like 'p' and 'r' Execution time
ARFCM [7]	Fuzzy C-means	If object do not have any membership value greater than target value considered as outliers [7].	–
Cluster-based algorithm [8]	k-means	After sorting on basis of distance top ε% of objects forms the outlier objects in the data [8]	Top ε% of objects may not remove outlier present in all the clusters

3 Background

In this section, we discuss about a very popular and basic clustering method, i.e., k-means algorithm and some well-known performance evaluation metric of clustering.

3.1 K-Means Algorithm

In 1976 MacQueen introduced an algorithm known as the k-Means algorithm. It is considered to be one of the simple and effective algorithms for the clustering of data [3]. This algorithm finds a partition in a dataset in such a way that the squared error between the centroid also known as empirical mean of a cluster and the points present in the cluster is minimized [10]. In this algorithm first the k number of cluster is initialized in which we want to partition the data. Then randomly k centroids are selected for each cluster. Later on each data object is assigned to cluster closest to it. This process is repeated until the data objects stop shifting their clusters or centroid stops changing. It has the complexity of O(n*K) where n denoted the number of

data objects and K is used to define number of clusters. The k-means algorithm is described below:

K-Means Algorithm

```
Input: Dataset and K (Number of Cluster)
Output: k cluster
Method:
Step 1: Randomly select k points as initial centroids
of k clusters.
Step 2: Assign each point to its closest centroid to
form clusters.
Step 3: The centroid for each cluster is recomputed on
the basis of the mean value of all the objects present
in the cluster.
Step 4: Repeat step 2-3 till the Centroids stop
changing their cluster.
```

3.2 Cluster Performance Evaluation Metric

The performance of cluster can be determined by knowing how well the cluster is formed. Clustering validity measures helps in determining the quality of created clusters. It is also used to determine the number of clusters which would be optimal. These quality measures are helpful in measuring "goodness" or "badness" of a clustering algorithm. This is done by comparing the results of one algorithm with other algorithms [11]. There are various indices used to evaluate the performance. In this paper we have use Silhouette Coefficient and Calinski–Harabaz Index to measure the quality of cluster formed. These indices are generally used when the ground truth labels are not known.

Silhouette Coefficient: It is a cluster validity measure which determines the consistency within a cluster.

$$S(i) = \frac{b(i) - a(i)}{\max(b(i), a(i))}, \tag{1}$$

where a(i) was the average dissimilarity of "i" with all other data objects within the same cluster and b(i) be the lowest average dissimilarity of "i" to any other cluster, of which "i" is not a member. The S(i) is bounded between -1 and +1. If the S(i) is close to 1 then it is considered as perfect clustering while when it is close to -1 then it considered that the data object is placed in a wrong cluster [12, 13]. On the other hand, if the score is close zero it indicates that there are overlapping clusters. In case of dense and well separated cluster the S(i) is high.

Calinski–Harabaz Index: It evaluates the cluster validity based on the average between-cluster and within-cluster sum of squares.

$$C = \frac{BGSS/(K-1)}{WGSS/(N-K)} = \frac{BGSS(N-K)}{WGSS(K-1)}, \tag{2}$$

where WGSS is the sum of the within-cluster dispersions for all the clusters and BGSS is the between-group dispersion [13]. Higher Calinski–Harabaz index implies that a model defines the clusters very well. The fast computation is an added advantage from this index.

4 Proposed Algorithm

In the field of data mining outlier detection plays a very important role. We found various disadvantages in different algorithms which lead us to propose this method. So, we have proposed a new method to detect outliers. Our algorithm considers a point to be outlier if it is not similar or less similar to the cluster it belongs to. In this algorithm first all the points are clustered using k-means algorithm. Then distance of centroid and all the points present in a cluster is calculated which is considered as intra cluster distance. Then the data points are sorted on the basis of the intra-cluster distance in descending order. After that points are picked one by one, starting from top and tested to be an outlier or not. If after removing that point from cluster the silhouette coefficient increase then that point is considered as outlier. The process stops when the silhouette coefficient stops increasing. The silhouette coefficient was used to decide whether a point is outlier or not because it allows us determine that how similar an object is to its own cluster compared to other cluster present. Thus when the removal of a point increase the coefficients value it implied that after removal of the point the cluster become more similar. And similarity within a cluster is an important property of a cluster. The sorted outlier detection based on silhouette coefficient is described below:

Algorithm: Sorted Outlier Detection Approach based on Silhouette Coefficient

```
Input: N x D Dataset and K number of clusters
Output: Outliers, Dataset after removing outlier
Method:
Step 1: Randomly initialize the K number of initial centers for K
clusters.
Step 2: Place each data objects in one of the K cluster by using k-
means algorithm.
Step 3: Calculate silhouette coefficient S(i) of clusters using
equation (1) of dataset.
Step 4: Calculate the distances between K centroids and all the
objects in cluster/dataset.
Step 5: Sort all the objects on bases of distance within each
cluster.
Step 6: Select the point R with max distance in a cluster.
Step 7: New_SC ← calculate silhouette coefficient for dataset
without point R.
Step 8: If New_SC > SC then
              Remove the point R from cluster.
              Outlier ← append R
              SC ← New_SC
        Else
              Stop detecting outlier for cluster i
Step 9: for each cluster i ϵ N, repeat step 5 to 8.
```

The proposed method will identify the outlier presented in the cluster and dataset. After that, we can remove the outliers to produce efficient clustering of dataset.

5 Experiment and Results

5.1 System Configuration

The experiment was performed on a single machine consisting of Intel core i5 and 2.3 GHz processor. The RAM of the system was 8 GB and the main memory size was 500 GB. OS of system was Windows 7.

Table 2 Dataset description

Dataset	No of features	No of objects	No of clusters
Yeast	8	1484	10
Wine	13	178	3
Iris	4	150	3
Glass	10	214	7

5.2 Dataset

We have used datasets present on UCI Machine Learning Repository to validate our proposed method for outlier detection. The dataset used were Yeast, Iris, Wine, and Glass dataset. These are some of popularly used dataset for clustering and outlier detection. The description of datasets is shown in Table 2.

5.3 Experiment Process

The proposed algorithm was implemented using Python. Similarly, Distance-based, Centroid-based and Cluster-based outlier detection algorithm was also implemented. To analyze the correctness of clusters formed, cluster validity index like Silhouette Coefficient and Calinski–Harabaz index were used.

First, both the cluster validity indexes were calculated for all the existing algorithms and the proposed method. Validity index of a cluster before outlier removal was also calculated. Then all of them were compared with each other. Second, the performance of our algorithm was analyzed by executing it on different dataset by changing the number of cluster. The cluster size was changed from 3 to 15. Then the performance was compared on basis of execution time.

5.4 Result

Cluster validity index: The clustering algorithms were executed and validated by Silhouette Coefficient and Calinski–Harabaz index. (1) In the Fig. 1 shows the analysis of different performance measure. It is essential to calculate these indices because it shows how accurately an algorithm is working.

Figure 1a shows that the proposed algorithm has better silhouette coefficient for different dataset implying that it has better consistency within a cluster. For all the dataset it has performed better than some of the existing algorithms. The removal of outlier through the proposed algorithm has improved the intra-cluster consistency of the dataset if compared to the value before outlier detection and removal.

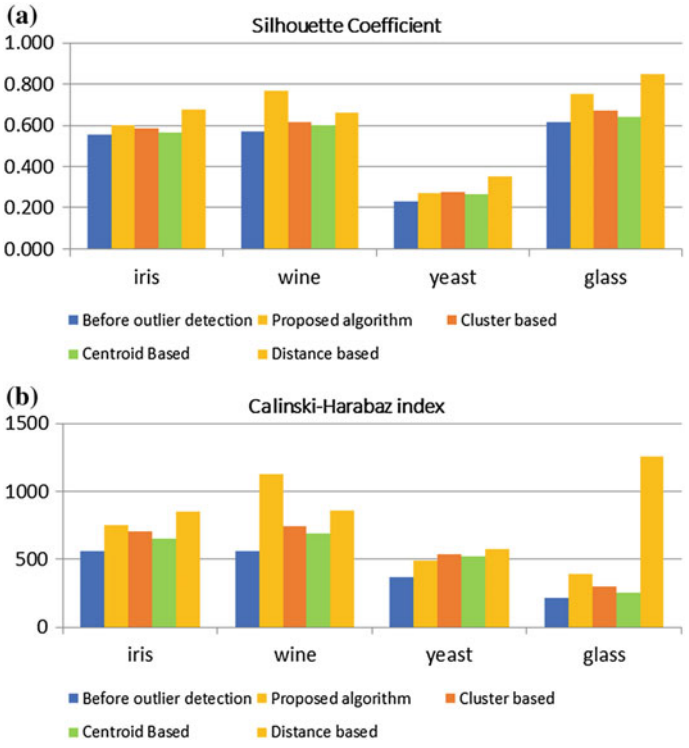

Fig. 1 **a** Silhouette coefficient for the clustering algorithms. **b** Calinski–Harabaz index for the clustering algorithms

On the other hand Fig. 1b shows how the Calinski–Harabaz Index of the dataset varies when different algorithms are executed on them. Our proposed algorithm has performed better than the cluster- and centroid-based algorithms though it was relatively less efficient then distance-based algorithm. The higher the Calinski–Harabaz Index implies that a model defines the clusters very well. And so, according to the results we can conclude that our proposed model defines the cluster very well in different scenarios.

Performance analysis: To determine the performance of the proposed method and other clustering algorithms; these algorithms were executed on different dataset by changing the clusters value. It is essential to analyze an algorithm on basis of execution time because with accuracy an algorithm is required to be fast.

In Fig. 2 we have shown how different algorithms perform when the number of cluster is varied and how much time they take to execute. We have analyzed these algorithms on two dataset, i.e., yeast and glass dataset. It is clear from Fig. 2a, b that our proposed algorithm has performed better compared to the distance base algorithm but when the number of clusters increase its performance decreases. Though our algorithm has more execution time compared to the centroid- and cluster-based

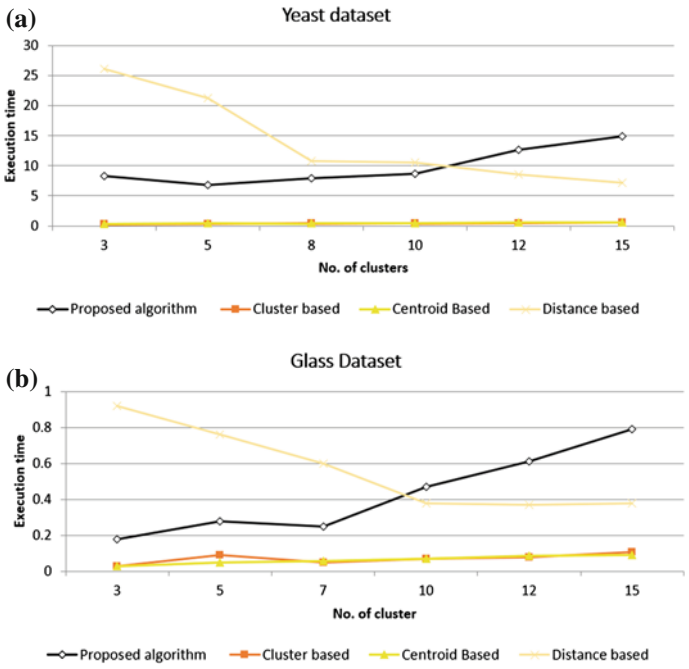

Fig. 2 **a** Silhouette coefficient for the clustering algorithms. **b** Silhouette coefficient for the clustering algorithms

algorithms but its accuracy is far better than them. So, overall we can conclude that it is overall a better algorithm.

6 Conclusion

In this paper an algorithm called Sorted-Outlier Detection based on Silhouette Coefficient was proposed. It used k-means and Silhouette Coefficient to identify an outlier. The proposed method is better than already existing method as it does not require user-defined parameters to decide a point to be outlier. It also reduces the task of comparing all the points that are in cluster to identify an outlier. The algorithm was compared with some of the existing algorithm in domain of outlier detection. And the experiment was performed using some of the benchmark dataset preset on UCI repository. The results show that the proposed algorithm has performed better as compared to some of the existing algorithms in terms of cluster similarity and execution time. In future, the algorithm will be modified to reduce its execution time further.

References

1. Xu, D., Tian, Y.: A comprehensive survey of clustering algorithms. Ann. Data Sci. **2**(2), 165–193 (2015)
2. Ding, S., Wu, F., Qian, J., Jia, H., Jin, F.: Research on data stream clustering algorithms. Artif. Intell. Rev. (2013)
3. Vu Viet Thang, Pantiukhin, D.V., Nazarov, A.N.: FLDS: fast outlier detection based on local density score. In: International Conference on Engineering and Telecommunication, pp. 137–141 (2016)
4. Aggarwal, C.C.: Data Mining: The Textbook. Springer International Publishing, Switzerland (2015)
5. Ahmed, M., Naser, A.: A novel approach for outlier detection and clustering improvement. In: 8th IEEE Conference on Industrial Electronics and Applications (ICIEA), pp. 577–582 (2013)
6. Songma, S., Chimphlee, W., Maichalernnukul, K., Sanguansat, P.: Classification via k-means clustering and distance-based outlier detection. In: Proceedings of Tenth International Conference on ICT and Knowledge Engineering, pp. 125–128 (2012)
7. Ashok, P., Kadhar Nawaz, G.M.: Detecting outliers on UCI repository datasets by adaptive rough fuzzy clustering method. In: Green Engineering and Technologies (IC-GET), Online International Conference (2016)
8. Christy, A., Meera, Gandhi G., Vaithyasubramanian, S.: Cluster based outlier detection algorithm for healthcare data. Procedia Comput. Sci. **50**, 209–215 (2015)
9. Li, X., Lv, K., Xiong, C., Xiong, Z.: An improved K-means text clustering algorithm by optimizing initial cluster centres. In: International Conference on Cloud Computing and Big Data (2016)
10. Jain, A.K.: Data clustering: 50 years beyond K-means. Pattern Recogn. Lett. **31**, 651–666 (2010)
11. Kovacs, F., Legancy, C., Babos, A.: Cluster validity measurement techniques. In: Proceedings of Sixth International Symposium on Hungarian Researchers on Computational Intelligence (CINTI) (2005)
12. Berkhin, P.: Survey of clustering data mining techniques. Technical report, Accrue software (2002)
13. Liu, Y., Li, Z., Xiong, H., Gao, X., Wu, J.: Understanding of internal clustering validation measures. In: Proceedings of IEEE International Conference on Data Mining, pp. 911–916 (2010)

The Terrain's Discrimination Criterion for the Lengthened Objects Identification

Artem K. Sorokin and Vladimir G. Vazhenin

Abstract This paper devoted to the criterion for terrain's discrimination. The proposed criterion is useful for airborne unmanned vehicle's position correction. The criterion is based on the comparison of probability densities, one of them is the reference density and another is the current density. Further it is evaluated the probability of densities intersection. At the next stage it is compared the probabilities for different references, so it was chosen the reference with the largest probability. Then it is described the application of this criterion for the lengthened objects' identification. At last, this criterion is compared with the Kolmogorov–Smirnov's criterion to reveal its strong and weak properties.

Keywords Probability density · Lengthened objects · Autonomous navigation Radar signal processing · Pulse radar signal

1 Introduction

The common challenge for airborne unmanned vehicle's design is creating the stable, trustable, and roughness autonomous navigation system. Nowadays, the normal navigation system is inertial navigation system (NS) which is corrected by satellite NS [1]. This system is enough precise, but in the numerous cases, it cannot be applied for the navigation and it is necessary to implement another, more roughness, but simultaneously less accurate, correctional navigation system. The most usual system for correction of the inertial navigation system is the correlation terrain's NS, but this system works correctly only if the terrain contains enough objects for the on-track correction. In case of insufficient number of navigation objects it is necessary to use

A. K. Sorokin (✉) · V. G. Vazhenin
Institute of Radioelectronics and Information Technologies, Ural Federal University,
Mira Str. 32, 620002 Ekaterinburg, Russian Federation
e-mail: SorokinAK@urfu.ru

V. G. Vazhenin
e-mail: v.g.vazhenin@urfu.ru

B. S. Rawat et al. (eds.), *Advances in Signal Processing and Communication* ,
Lecture Notes in Electrical Engineering 526,
https://doi.org/10.1007/978-981-13-2553-3_20

additional objects, such as the lengthened objects. The lengthened objects are the navigation objects which consist of two types of underlying terrains with different reflection properties and which length in one direction is larger than the exposure spot's size, and which border can be approximated by the straight line. For example, "the river in the forest", "the asphalt road", etc. The recent explorations (for ex. [2, 3]) show the interest to the reflection properties of different terrain's types.

The correction system which is observed in this paper, must work properly in conditions of small evolutions of the vehicle (les 2 degrees in the each direction), the height of flight must be stable, and for the correction we choose "the zones of correction". Also we suppose that flight is horizontal and the velocity is the same during the correction zone. This paper is devoted only to the criterion (not a navigation algorithm) which helps to get the information about the underlying terrain for the navigation algorithm. Also, as the source of and information we used a pulse radar altimeter, which is installed in most of unmanned airborne vehicles.

Following this idea, it were designed a criterion for the discrimination of underlying terrains. The measured parameter used for probability density obtaining is the amplitude of the reflected signal, which counts grouped into a histogram.

In the base of this criterion lies the comparison between probability density of the known homogenous terrain and the current probability density. If we directly find their intersection square we obtain a posteriori probability of the coincidence these signals. Indeed, the probability density shows how much counts of the signal have the same amplitude. So, if we have a number of signals with the same amplitude we can assume that these signals belong to the same distribution. And a posteriori probability shows numerically the degree of densities coincidence.

The next chapter shows the mathematical bases of the suggested criterion.

2 The Description of the Criterion

2.1 The Requirements for the Criterion

At first, we outlined the requirements for the criterion.

The criterion should require following:

- the distribution of incoming signal could be unknown type (really, we do not know are signals normal or not);
- compare two samples of incoming signal, and decide if they are from one distribution, or not;
- after sequential comparison with different reference's samples decide which reference is the best;
- dynamically change decision if terrain changed;
- to define the border position between two typical terrains.

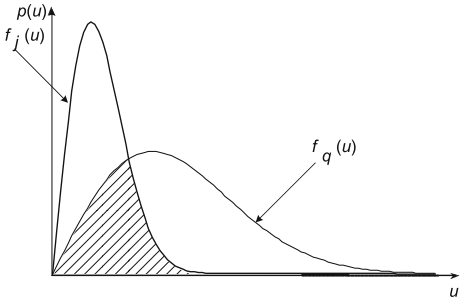

Fig. 1 Reference and current probability densities for Rayleigh densities

Due to the description, not a lot of criteria could be found to relief all requirements. The most suitable is Kolmogorov–Smirnov's criterion, but it cannot be fixed the exact border position because of criterion's accuracy (it can not be detected the smooth border change, it will be shown below).

2.2 The Definitions

Second, it is necessary to make some definitions. In Fig. 1 are implemented the following notations: u is amplitude of the reflected signal (the maximum value of the single pulse), $p(u)$ the dependence of probability from the amplitude; f_j the reference's probability density of the S_j signal for j-type of the underlying terrain; f_q the current probability density of the S_q signal; j-reference's number it changes from 1 to N, where N the number of references; S_j, S_q samples of the reference's and current's reflected signals; the hatched zone shows the intersection between two densities, simultaneously, this square is equivalent to the probability of the densities coincidence. The Rayleigh distribution is natural for reflected signal's amplitude (it is usual for normally reflected signals, which processed in the quadrature channel), but a lot of terrains can be presented by another distributions, such as Rice or lognormal distributions ("asphalt", "concrete", "waved water surface", etc.) [4].

2.3 The Criterion's Mathematical Description

According to other standard criteria we should set the criterion's solving function and the decision rule. This information, as it is mentioned in [5], has no standardized algorithm. So we guided by the requirements for creating these functions.

The solving function defines the numerical result of the comparison between two samples, and it can be presented by the following equation:

$$\Phi_{j,q} = \int_{-\infty}^{\infty} \min\big(f_j(u); f_q(u)\big)du, Z \tag{1}$$

where $\Phi_{j,q}$ criterion's solving function for current probability density and j-reference's probability density.

This function decides which function's ($f_j(u)$ and $f_q(u)$) value for each amplitude is least and this value cumulated into the integral function. So as the result it evaluates the square of the hatched figure in Fig. 1.

The next step is to define the decision rule

$$\Lambda(q) = \arg\min_j \big[\Phi_{j,q}\big], \tag{2}$$

where $\Lambda(q)$ the decision function. It compares values of $\Phi_{j,q}$ for each type of terrain and chooses the smallest value, then it returns the number of the terrain's type with the smallest value of the solving function. As the result it decides which terrain's type is closer to the current sample.

2.4 The Scheme of the Criterion

In previous paragraph it were shown the solving and decision functions, they can be presented in the scheme. Schemes are very common for criterion's presentation, because they show the links between blocks and logic of criterions' work. In Fig. 2 it is shown the process of obtaining the decision by the designed criterion. At first, we have an input signal—the probability density of the reflected signal's amplitude. This signal processed by the series of solving functions (in Fig. 2 it is shown as the parallel processing, but it can be done as the serial processing). As the result we have the probability of coincidence of two functions ($P\big(f_j(u)\big|f_q(u)\big)$, in other words, the hatched square in Fig. 1. Then we filtered values of the solving function by the threshold detector (H), which can be different for each terrain's type. If the value of the solving function is lower than threshold it blocked and instead of it output signal is an empty set. Otherwise, we have the same value as the input value of the threshold detector. The threshold detector allows us to skip the decisions with low probability. The level of the threshold marked as $\Upsilon_1,\ \Upsilon_2,\ \ldots \Upsilon_k$. After this the information collects by the decision function and at the output we have the decision about the terrain which is the most suitable for incoming sample.

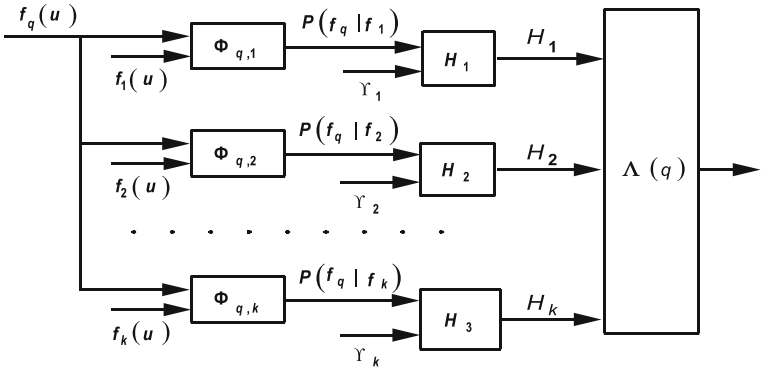

Fig. 2 Scheme of criterion's work logic

2.5 The Samples Preparation

At the beginning it was mentioned about the probability densities of the reflected signal, but this process was not highlighted enough. In this paragraph the description is presented. This algorithm is designed for pulse radar altimeters, but it can be modified for chirp radars or others. First stage is collecting the data-set. As the informational parameter it is suggested to use the maximum value of the reflected pulse. On the one hand, it allows us to work only with the pulse's amplitude without phase information (the pulses processed by the quadrature detector), it is a kind of the restrictions.

On the other hand, we have to work only with positive values, that is why processing becomes simpler and more robustness to the velocity or vehicles evolutions. Another problem is how long the sample size is necessary for our challenge. For the histogram's accuracy measurement Scott designed a formula:

$$\delta \sim \frac{1}{\sqrt[3]{N}}, \tag{3}$$

where N is a number of counts in the data-set; δ – is a fluctuation error.

Formula (1) shows the size of the data-set which is necessary for the fluctuation error limitation. The third degree of the root shows that for the fluctuation error of the histogram in comparison with the normal fluctuation error (the second degree) for data-set it is necessary an additional root's degree for bins. Second stage is organizing data-set into the histogram. Many mathematical packages can easily build a histogram from data-set. And the number of bins should be proportional to $\sqrt[3]{N}$. Then the histogram must be smoothed to decrease the fluctuation error. It can be implemented by the interpolation functions of the low order (first, second, etc.). After that we have the discrete form of the input sample. So, it is necessary to change the solving function to the discrete form, it is presented below

$$\Phi_{j,q} = \sum_i \min\left(f_j(i); f_q(i)\right), \tag{4}$$

where i is the discrete analog of the reflected signal's amplitude.

The decision function will be the same as in the continuous form.

2.6 The References

Another important thing, which is not enough clear yet, is the references' obtaining process. It is closely connected with previous paragraph, because their obtaining is very similar to the samples' preparation process. But the reference's evaluation process has some distinctions.

The reference presented by the probability density of the reflected signal and we exactly know the type of the underlying terrain. The terrain must be homogenous (as far as it is possible for rough terrains, like "forest"). The vehicle's evolutions should be less than a couple of degree in the each direction. The length of the sample connected with the correlation interval, which changes from $0{,}5\lambda$ up to 4λ. It depends on the antenna's pattern width, for more information see [1]. The length of the uncorrelated sample selected in accordance with (3). After all, it is necessary to normalize reference to the flight's height, because the amplitude of the reflected signal depends on the height according to the main radar formula [1]. The inverse operation is necessary for the criterion's work when we prepare the reference for comparison with current sample (we have to know the flight's height). This preparation process we make for each terrain's type, which we can distinct from others. In [6] it is shown which terrains can be discriminated.

3 The Lengthened Objects Identification

The designed criterion can be applied for lengthened objects' (LO) identification. The identification of the lengthened objects consists from the several stages. Here they are presented:

- The estimation of the terrain's type;
- The estimation of the terrain's change moment;
- The estimation of the lengthened object's parameters (the identification).

The designed criterion can be very useful for the identification of the current terrain. In fact the implementation of this criterion returns the terrain's type, if we have appropriate input sample and the proper references.

The previous parts devoted to the static situation, when no changes of the input signal are possible. To empower the criterion it is necessary to add the parameter t (time) to the sample information. The only change will be implemented to the input

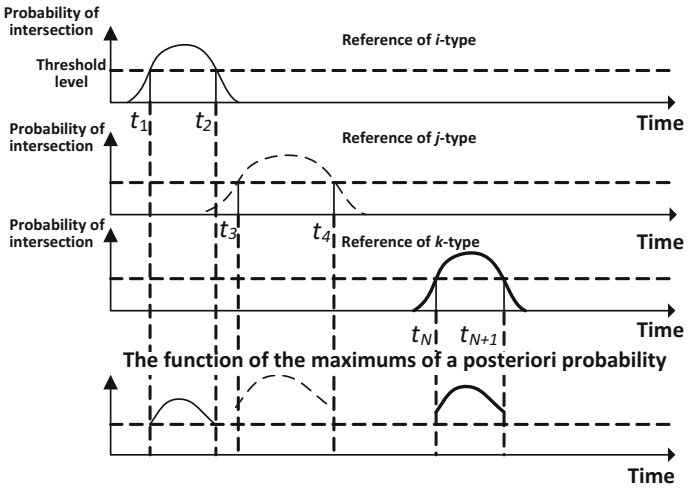

Fig. 3 The function of the maximums of a posteriori probability

sample. It changes each cycle of computation. But all process in the criterion will be the same. To impress the time-dependence we use t-parameter in the solving and decision functions:

$$\Phi_{j,q}(t) = \sum_{i} \min\big(f_j(i,t); f_q(i,t)\big), \tag{5}$$

$$\Lambda(q,t) = \arg\min_{j}\big[\Phi_{j,q}(t)\big]. \tag{6}$$

Formulas (5), (6) present the solving and decision functions in real time. The decision about the underlying terrain changes during the time (see Fig. 3). If probability lies below the threshold, the decision skips. So we can plot the decision function for each reference. And also we choose reference with maximum probability of the intersection. As the result, we have pieces of curve for identified terrain's type. The result function called "The function of the maximum a posteriori probability". It shows the type of underlying terrain, which was detected. Also this function shows the moments of terrain's change. The terrain's change moments allow us to fixate the position of the border between two terrains.

As it was mentioned, the lengthened objects are limited by the borders between two homogenous terrains. Also the length of the lengthened object should be large than an exposure spot and a border between terrains can be approximated by a straight line. So we can select two types of the lengthened objects: "the border" and "the stripe". We separated lengthened objects of "stripe's" type because a lot of industrial objects, such as "asphalt road" or "railway", have width less than the exposure spot's diameter (The standard pulse radar altimeter have the width of the antenna's pattern about 40°.). And the designed algorithm should discriminate such objects as well as

borders. The decision about the type of the lengthened object made in accordance with the formula:

$$\Gamma = \begin{cases} \mu, \text{ if } \Delta t \leq T_0 \\ \eta, \text{ if } \Delta t > T_0 \end{cases}, \tag{7}$$

where T_0 is time, while the vehicle flies the distance which is equivalent to the exposure spot's diameter; Δt is time interval where the decision was accepted; Γ is the decision about the lengthened object's type; μ is the decision about the "stripe" object; η is the decision about the "border" object.

Now we can make a decision about the lengthened object's type ("border" or "stripe"), its width (the second stage) and types of its terrains (the first stage).

4 The Results of the Comparison of Two Criteria

For comparison the designed criterion with known criterion we have to build a mathematical model and implement both criteria to the same flight track. Here the brief results are presented.

4.1 The Model Experiment

The mathematical model is implemented in the frames of the facet-phenomenological paradigm, which is usual for many computer models (for ex. see [7, 8]). This is the common way to model radar signals, when spatial terrain modeling as numerous facet with their own characteristics (the backscattering pattern, the distance, etc.). This model also allows us to model Doppler shift and lengthened objects (see [9]).

The usual result of the model experiment is shown in Fig. 4. Here in bold gray it is marked the lengthened object, which was detected. For comparison here presented two similar cases of "Forest/Asphalt" terrains: "the asphalt road in the forest" and "the separation zone of trees between two roads". Usually, and it is shown in Fig. 4, the detected border between two terrains (the minimum of the function of maximums of a posteriori probability) shifts to the less contrast terrain (to the "Forest" in the example). But as it is shown in [9] it can be compensated for known terrains combination.

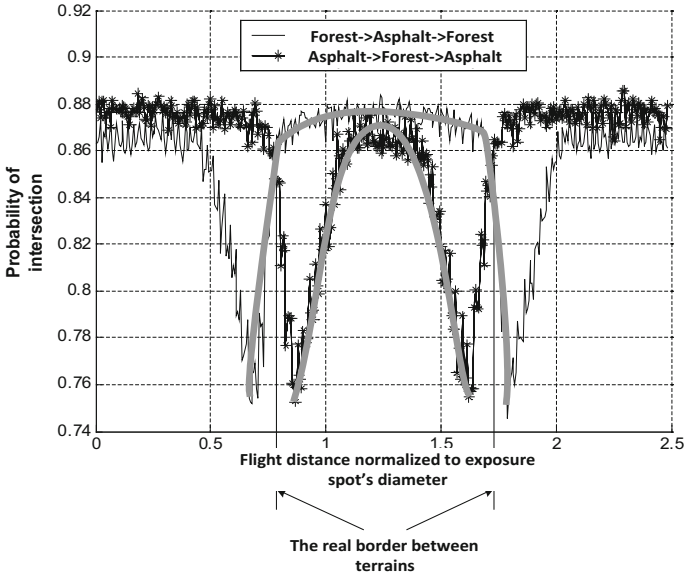

Fig. 4 The results of the model experiment with the designed criterion's application

4.2 The Criterion of Kolmogorov–Smirnov

The usual way of working with two samples of the signal with unknown parameters (which distribution is better approximates the sample signal) is implementation the Kolmogorov–Smirnov's criterion (KS criterion). This criterion answer to the question: "if both samples can be presented by the same distribution". As in the most other criteria we must set the level of the false detection (for example, 0.95). This is the probability of the second order, in other words, it is the probability of the trust to the accepted decision. So, to compare the suggested criterion and the KS criterion we slightly changed the base of the KS criterion by implementation floating level of the false detection. As the result we can compare both criteria, but the meaning of probability will be different. The KS criterion in comparison to the suggested criterion has following the solving and decision functions:

$$\Phi_{j,q}(t) = \sup\left|F_q(t) - F_j(t)\right|, \tag{8}$$

$$\Lambda(q,t) \neq j, \text{ if } \Phi_{q,j}(t) \geq D_{cr}, \tag{9}$$

where "sup" is maximum value of its argument; $F_q(t)$, $F_j(t)$ the integral distribution functions of current and j-reference, respectively; D_{cr} is the function, which can be chosen from the special statistic tables, this function fixed for the known length of the sample and the level of the false detection.

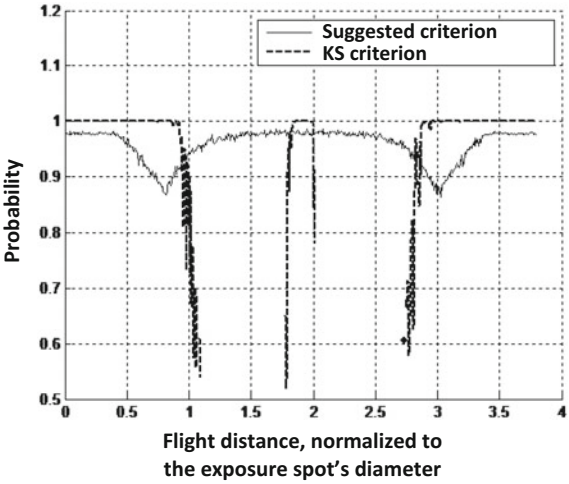

Fig. 5 The results of two criteria comparison

In the model experiment we computed it for any possible level. In other words, we refused the hypothesis about the same distribution for the both samples just in case if we could not set the proper value of D_{cr}. In other cases we accepted this hypothesis.

4.3 The Comparison

Now we can compare these two criteria. The results are shown in Fig. 5. The suggested criterion provides mostly continuous function of the decision, but the KS criterion often does not make any decision if more than one distribution is presented in the sample (the border between two terrains).

It can be explained by following: the KS criterion was specially designed to skip these cases, because probability of the false detection cannot be set. Another point is that the KS criterion has larger value of the probability, but as it was mentioned earlier, these probabilities have different meanings. The last and most interesting distinction is that the designed criterion can detect the exact borders position. It is because of the continuous character of the designed criterion.

5 Conclusion

In this paper it was described the criterion, which allows us to compare the current sample with a number of references and choose, which reference is the best. On the base of this criterion it was designed the algorithm of the lengthened objects identification. This algorithm can be applied for the correction of navigation systems

for the on-track part of the trajectory of the unmanned airborne vehicle. Then it was described the mathematical model for the exploration of the designed criterion. The results of the criterion's implementation are presented in this paper. Also, the designed criterion compared with Kolmogorov–Smirnov's criterion and it was shown that the designed criterion allows us to detect the border position of the lengthened objects. For the natural experiments' results of this criterion's implementation see [9].

Acknowledgements The research was executed by the grant of the Ministry of education and science of the Russian Federation (project № 8.2538.2017/PCh).

References

1. Skolnik, M.I.: Radar Handbook, 3rd edn. The McGraw-Hill Companies (2008)
2. Li, Y., Zhao, K., Ren, J., Ding, Y., Wu, L.: Analysis of the dielectric constant of Saline–Alkali soils and the effect on radar backscattering coefficient: a case study of soda Alkaline Saline soils in Western Jilin Province using RADARSAT-2 data. Sci. World J. **2014** (2014). Hindawi Publishing Corporation
3. Martinez-Agirre, A., Álvarez-Mozos, J., Lievens, H., Verhoest, N.E.C., Giménez, R.: Influence of surface roughness sample size for C-Band SAR backscatter applications on agricultural soils. Geosci. Remote Sens. Lett. IEEE **14**, 2300–2304 (2017)
4. Ulaby, F.T., Dobson, M.C.: Handbook of Radar Scattering Statistic for Terrain. Artech House, USA (1989)
5. Anderson, T.W.: An Introduction to Multivariate Statistical Analysis, 3rd edn. Wiley, New York (2003)
6. Sorokin, A.K., Vazhenin, V.G., Lesnaya, L.L.: The terrain identification by the pulse radar altimeter. In: 5th International Conference on Advances in Computing, Communications and Informatics Proceeding, India, 21–24 August 2016, pp. 2619–2623 (2016)
7. Fung, A.K., Chen, K.S.: Microwave Scattering and Emission Models for Users. Artech House, USA (2010)
8. Soja, M.J.: Electromagnetic Models of Bistatic Radar Scattering from Rough Surfaces with Gaussian Correlation Function. Chalmers University of Technology, Sweden (2009)
9. Sorokin, A.K., Vazhenin, V.G.: The application of pulse altimeter for linear references detection. Procedia Comput. Sci. **58**, 659–664 (2015)

Effective Way to Simulate the Radar's Signal Multi-path Propagation

Alexander S. Bokov, Artem K. Sorokin and Vladimir G. Vazhenin

Abstract The paper is devoted to devices which are designed for hardware implementation of the emitted signal's transformation. Such devices are useful for obtaining signals which are similar to a real radar signal reflected from underlying surface. The implementation of the simulation model can be helpful to form signals for equipment tests. The most challenging problem is to develop the real-time system that generates signals reflected from numerous types of terrain where the signal parameters are variable. This paper shows how this problem can be solved for a radar altimeter with chirp frequency modulation. The methods, the simulator's scheme and some model results are also presented in the paper.

Keywords Simulator · Airborne radar · Altimeter · FMCW signal
Digital signal processing · DRFM

1 Introduction

For indoor radar equipment tests, it is often required to form a carrier frequency signal with noises and distortions occurred by propagation process from a transmitter to terrain and back to the receiver. In many radiolocation challenges the preparatory test signals and their reflection characteristics are obtained from real targets and terrains by high accuracy measurements of radar's, target's and terrain's parameters. Carrier frequency signals can be simulated for numerous types of emitted signals by the suggested digital signal processing methods and algorithms.

For pulse radar systems an emitted signal's form is often constant, so the reflected signal can be written in a "signal" memory with corresponding model parameters

A. S. Bokov · A. K. Sorokin (✉) · V. G. Vazhenin
Institute of Radioelectronics and Information Technologies,
Ural Federal University, Mira str. 32, 620002 Ekaterinburg, Russian Federation
e-mail: sorokinak@urfu.ru

A. S. Bokov
e-mail: a.s.bokov@urfu.ru

B. S. Rawat et al. (eds.), *Advances in Signal Processing and Communication* ,
Lecture Notes in Electrical Engineering 526,
https://doi.org/10.1007/978-981-13-2553-3_21

and can be transmitted to the input of the radar receiver. Time synchronization, for example, can be done by a signal peak detector which also detects the pulse's beginning time. By the detector's complication, it is possible to prepare an array of signals for phase and frequency changing inside pulses.

A large number of modern systems uses long or continuous emitted signals, for example, onboard chirp or frequency-modulated (FM) continuous-wave (FMCW) altimeters. They often operate in the so-called tracking mode which uses changes of emitted signal parameters for each modulation period. Therefore, the reflected signal's computation and its forming must be performed in real time by processing each sample of the emitted signal. This processing will be done with various signal's instabilities and changes of an amplitude, phase and duration for radio transmitter instance of a real radar system.

The above-mentioned method, that is a way of replacing the propagation, reflection and scattering of a real emitted signal by its equivalent processing inside a simulator, is known as the seminatural modeling.

Modern electronic seminatural simulators, for example, Digital Radio Frequency Memory (DRFM) systems [1, 2], are able to simulate radar signals reflected from one or more point targets. They have different implementation, but are often too simple or too expensive to simulate terrain in case of radar evolutions, especially for real-time processing. One of the most important challenges is to develop more realistic simulator's scheme, which can operate in real time.

2 Simulator's Model for Multi-path Propagation

According to the phenomenological modeling approach [3] every terrain or extended object can be presented by a number of discrete reflectors—facets. So, the multi-path signal propagation can be presented by number of elementary signal channels with time-variable parameters and transfer functions $K_i(t, \tau_i)$ (see Fig. 1), which can be specified for each position and speed evolutions. Here K_i—the transmission coefficient for i—channel; t—time; τ_i—the delay-time inside the i-channel; $A(t)$—the transmitted signal; $X(t)$—the received signal.

The transfer function $K_i(t, \tau_i)$ can be randomly changed over all the time (it corresponds to water surface and vegetation waving, radar evolutions, etc.) for each

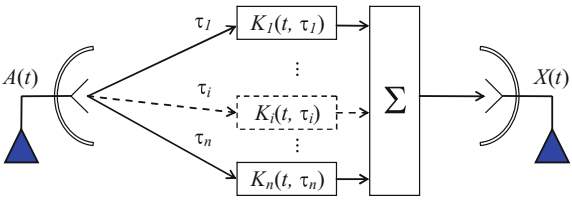

Fig. 1 Phenomenological model of multi-path propagation and reflection

channel. Correlation processes between channels are often neglected to simplify the calculations.

Even nowadays hardware is not enough powerful for real-time processing signal, reflected from large number of reflectors. Consequently, for model simplification it is recommended to group reflectors with similar characteristics, for example, the number of channels is equal to the number of partition area groups with closest values of frequency/delay.

An implementation quality of reflected signals (an equivalency of simulated and real signal parameters and vehicle evolutions in the same conditions) is limited by hardware capabilities of an implementation platform.

For radar applications, we can replace transform of the signal $A(t)$ in each transmission channel, by applying sequential transformations: delays (τ_i), Doppler shifts (Δf_i), and amplitude multiplying (E_i). These variables are sufficient for simulation following parameters: relative speeds of reflectors, radar evolutions, backscattering parameters, parameters of receiving and transmitting antennas, signal attenuation, etc. Therefore, a multiple-channel propagation model "the transmitting antenna – reflectors – the receiving antenna" can be represented by the model with number of delay lines [4, 5] as shown in Fig. 2.

It is difficult to implement a real-time model by using only analog signal processing. This processing may cause some difficulties which are hard to overcome. But it is possible to develop the model by using digital signal processing (DSP) blocks, which include there: a high-speed ADC (analog–digital converter), digital delay line, signal conversion modules and a DAC (digital–analog converter). One of the possible hardware decision is using following blocks: the high-speed ADC, DAC and multiple-input digital adder with low latency as shown in Fig. 2.

It is hard to implement such direct solution at a high carrier frequency, so usual practical decision is to process a signal at an intermediate frequency (within an operation frequency band of DSP blocks).

The solution mentioned above can be too expensive, so, we can use a switch instead of the digital adder in some cases (for signals which instantaneous power spectral density is concentrated in a narrow frequency band, which are applicable to FMCW altimeters). A similar solution is used for multiple-input digitizing ADC in microcontrollers.

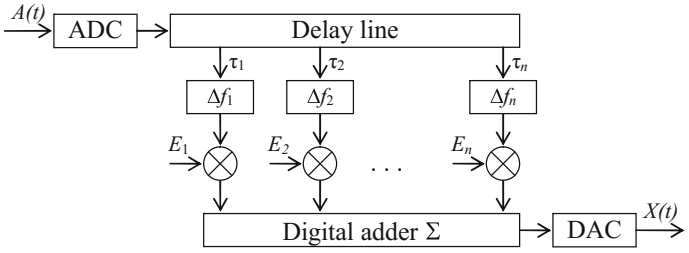

Fig. 2 Signal processing scheme on the base of DSP blocks

In our case, the switch is cyclically connected to one of the n signal's outputs, where signals already transformed in accordance with the specified parameters Δf_i and E_i, as shown in Fig. 3. In other words, we have replaced the adder with the switch.

This switching method could be named "switching in time". This signal transformation can be described by:

$$X(t) = E_i K(A(t - \tau_i),\ \Delta f_i), \quad i = 1 + \mathbf{mod}\left(\mathbf{round}\left(\frac{t}{\Delta t}\right), n\right), \tag{1}$$

where Δt is the mixing interval; **mod** and **round** are known functions used to calculate the reminder and rounded result.

The output signal contains equal time segments from different signals. In the frequency domain it leads to the appearance of additional harmonics corresponded to mixture of the "useful" signals and intermediate mixer's frequency (working frequency of cyclic switch).

If the mixer's frequency is several times higher than the receiver's intermediate frequency band, the resulting signal in the intermediate frequency band becomes similar to the signal formed by the scheme in Fig. 2, but, in our case a signal's amplitude is reduced by n times (it can be compensated by adding an amplifier or increasing the E_i values).

Then, an additional synchronizer can be applied for the previous scheme. It allows us to use segments of each signal with specified duration (see Fig. 4). Consequently, we can replace the set of multipliers by one synchronizer with variable multiplying coefficients $E_1 \ldots E_n$.

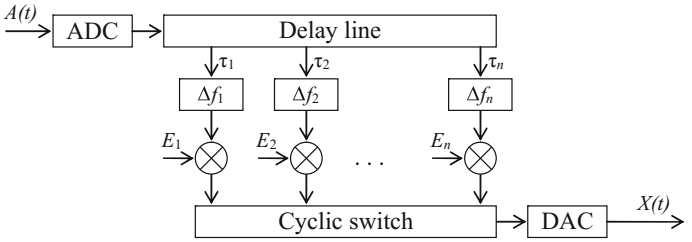

Fig. 3 Signal processing scheme with cyclic switch

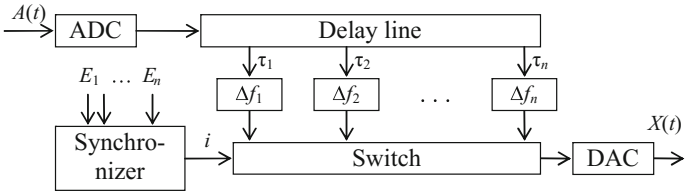

Fig. 4 Scheme with the switch controlled by the synchronizer

This "switching in time" with variable durations of signal pieces can be described by the following expression:

$$X(t) = E_i K(A(t - \tau_i),\ \Delta f_i), \quad i = \mathbf{match}\left(T = \sum_{i=1}^{n} \Delta t_i, t\right), \tag{2}$$

where **match**(T, t) is the matching function of time t (for correct choice of E_i, $\Delta\ t_i$ and $\Delta\, f_i$) inside the repetition interval T; $\Delta\ t_i$—duration interval of the ith signal.

Thus, we proportionally change the duration of each segment instead of amplitude coefficients, in our case it makes no differences (it will be shown below). An exploration mathematical model of the "switching in time" method was designed. We have used typical parameters of FMCW radio altimeter with receiver's frequency band about 60 kHz. An example of a modeling experiment with equal and variable durations of signal segments is shown in Fig. 5.

It allows us to explore the influence of different parameters on a beating signal's spectrum. In Fig. 5a it is shown beating signal and its spectrum shown in Fig. 5b in case of equivalent segment duration.

The "informational" signal's part concentrated in frequency band from 28 to 45 kHz, it is colored in red in Fig. 5b, c. In Fig. 5c all six informational beating signal's harmonics are shown separately, because a corresponded high value of a sampling frequency is chosen.

It is known that spectral peak's amplitude is often used for relative power estimation of signal harmonics. Further, it is necessary to align mixed signal's amplitude to real signal's amplitude. In Fig. 5d it is shown the result of unequal duration segments of sine waves. Here segment durations specified by integer values from 1 to 32. Therefore, the estimation error of harmonic amplitudes is 1/32/2, i.e., $\pm$ 1.6%.

The ratio of harmonics amplitudes in the absence and presence of switching with equal and unequal durations are approximately the same. Consequently, modeled signals are considered to be equivalent by the spectral composition.

Further, the switching signal frequency (F_{sw}) is determined by the following parameters: the minimal switching period dt (which proportional to the ADC quantization interval), the average switching time $<st>$ and the number of channels (N). It can be evaluated by the following expression:

$$F_{sw} = \frac{1}{dt\langle st\rangle N}. \tag{3}$$

The increase of frequency of the beating signal's harmonics and/or reduction of the switching frequency F_{sw}, leads to spectrum interference (overlaying informational and spurious spectral harmonics).

To eliminate the interference effect it is necessary to limit the upper frequency of the bandwidth (F_{b_max}) it should be lower than the first spurious harmonic's frequency ($F_{\mathrm{sw}} - F_{max}$) in accordance with following expression:

$$kF_{b\_max} < F_{sw} - F_{max}, \tag{4}$$

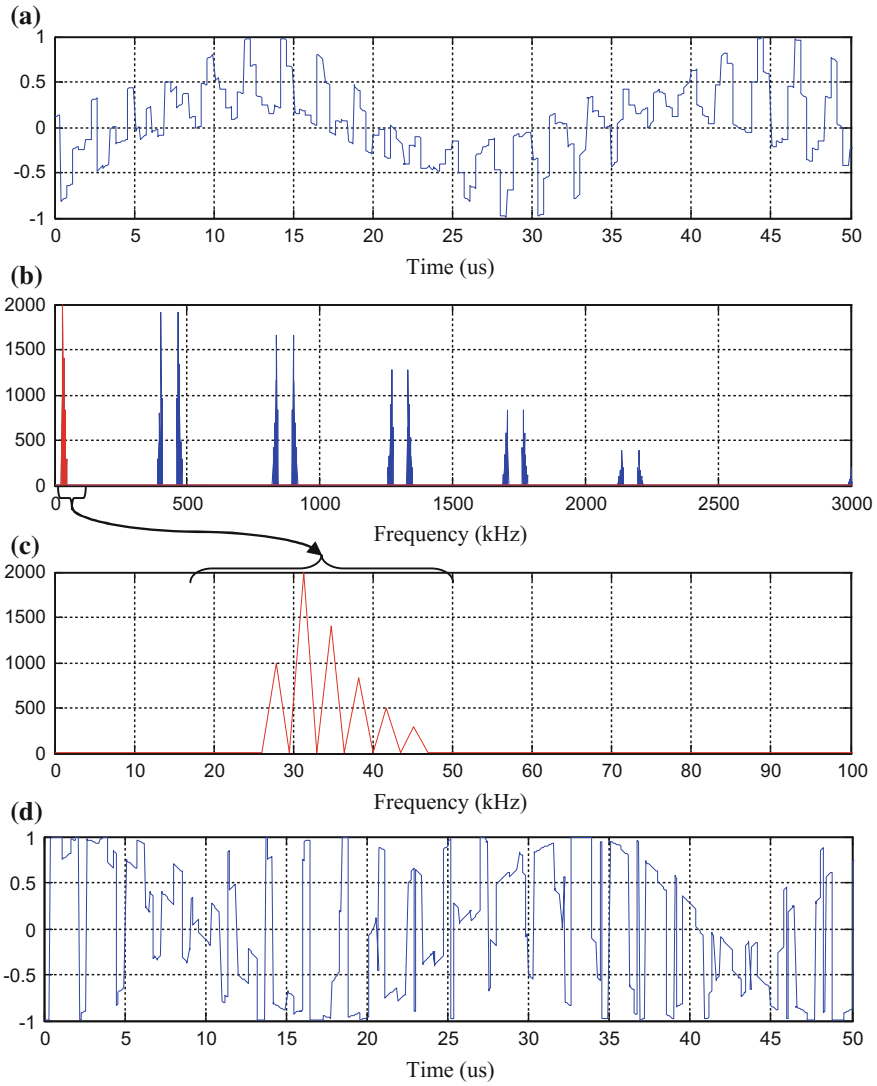

Fig. 5 Model experiment's results: the beating signal is composed from identical duration segments of sine waves (**a**); its spectrum (**b**); "informational part" of the beating signal harmonics (**c**); the beating signal with unequal duration segments of sine waves (**d**)

where F_{max} is maximum frequency of informational signal's part, k is the coefficient (approximately 1.5…2.5). It depends on radio altimeter's parameters.

Further, the maximum number of switching signals can be evaluated by the next expression:

$$N_{max} = \frac{1}{dt\langle st\rangle\left(F_{max} + kF_{b\_max}\right)}. \quad (5)$$

It shows that the number of switching signals depends on altimeter parameters and performance of DSP blocks.

3 The Scheme of the Simulator

Following to the suggested method and information from [6] the simulator of multipath propagation and reflections was designed. It can be applied for altimeters' checking and calibration. The simulator operates with pulse and linear FM modulation emitted signals in frequency band from 4.2 to 4.4 GHz. In case of a typical linear FM radio altimeter, the resulting beating signal's spectrum is statistically equal to a signal's spectrum for terrain with small roughness.

The simplified simulator's structure contains next blocks: attenuators (A1, A2), mixers (Mix1, Mix2) and a local oscillator (LO) (see Fig. 6), digital signal processing blocks: ADC, DAC, the digital signal memory (DSM) based on memory buffer with address counters, and the frequency shift unit. They are designed on a single "system-on-chip" (SoC) 1879BM3(DSM) [7].

All the conversion parameters may be changed by the microcontroller and computer's software. For example, it is able to simulate a flying trajectory over terrain. The simulator's hardware can be extended by 4 PCI-modules MC23.01 with the SoC 1879BM3(DSM) for better simulation of various terrain types. The frequency shift is performed by an arithmetic processing of in-phase and quadrature components of the input signal inside the SoC. These components can be processed in parallel by two internal ADCs [7]. The step for the programmed frequency shift is about 9 Hz. It is enough for simulation Doppler's shifts for most radiolocation decisions.

For instance, as a result for the mentioned implementation, the suggested simulator allows us to simulate discrete delay: for the linear FM modulated signals—less than

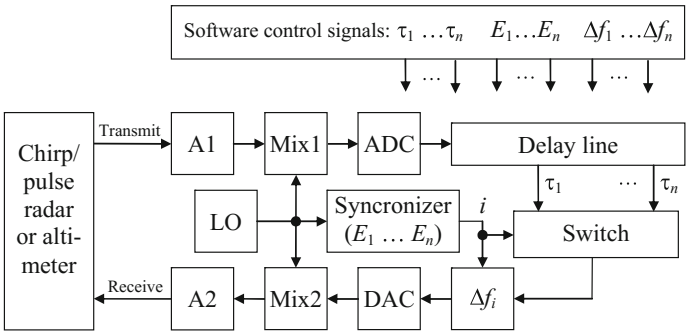

Fig. 6 The scheme of the simulator based on digital signal processing blocks

0.01 m with use of the frequency shift mode [6, 8] for pulse signals—2 m with use of the simple delay mode. The total range of simulated distances (altitudes) is over 20 km. The variable programmed signal's attenuation is up to 157.5 dB which is built on the five digital attenuators inside the block A2.

4 Some Experimental Results

The results of an experiment are shown in Fig. 7. Here the following parameters were used: 7 signal channels with 7 reflectors that are situated from 500 to 555 m; the step between reflectors 9.2 m; the spectrum width 10 kHz; the modulation period 11 ms.

An example of a beating signal in two scales is shown in Fig. 8: there are 3.5 modulation periods in the figure above, and the part of the modulation period in the figure below. In the figure above the falling edges of modulation frequency shown as amplitude's splashes (with duration about 0.3 ms) in time domain at 11, 22, 33 ms. The amplitude modulation has an explicit periodic character, indicating that there are a few strong harmonics.

The number of signal's channels can be increased by various software complications [6, 7] or adding more SoCs. Furthermore, the facet model was designed, which allows us to form reflected signal from various terrains. It also allows us to evaluate software control signals (delays, amplitudes, frequency shifts, as shown in Fig. 6) for

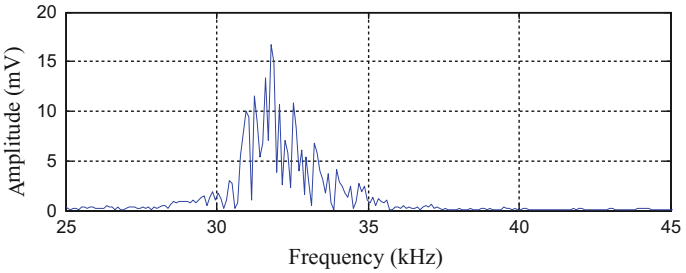

Fig. 7 Spectrum of a beating signal as the result of seven discrete signal's channels switching

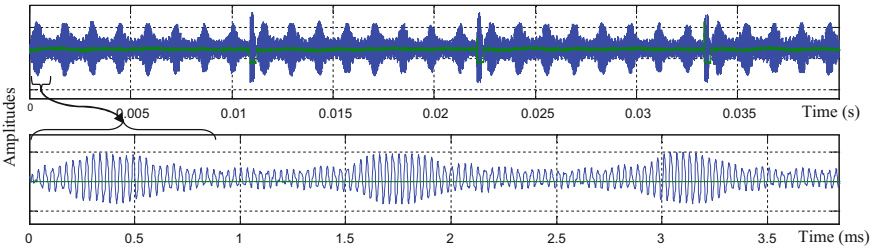

Fig. 8 The beating signal as the result of switching of seven discrete signal channels

the simulator. Obtained characteristics of the simulated signal in time and in spectral domain are close to the theoretical and real flight results in similar conditions for simple natural surfaces.

5 Conclusions

The designed simulator for radar altimeter was described in this paper. At first we concentrated on the method for constructing the multi-path propagation simulator for radar signals. After this we suggested the simulator's scheme, which allows us to simulate the reflected signal by cycle switching of hardware channels. Obviously, these channels have changeable in real-time signal parameters. Thereon, main experimental results were also presented. The obtained results corresponded to known natural and theoretical explorations. Also, we can use and expand resources of SoC for adding more channels or simulating parameters for more complicated terrain types.

The results of this paper could be applied to design of new generation cheap hardware-in-the-loop simulators. These simulators can be proposed for verification and tuning of various autonomous airborne altimeters with frequency modulation.

Acknowledgements The research was executed by the grant of the Ministry of education and science of the Russian Federation (project № 8.2538.2017/4.6).

References

1. Peng, Z.: Realization of DRFM radar target simulator based on general instruments. In: IET International Radar Conference, Hangzhou, China (2015) https://doi.org/10.1049/cp.2015.1470
2. Olivier, K., Gouws, M.: Modern wideband DRFM architecture and real time DSP capabilities for radar test and evaluation. In: Electronics, Communications and Photonics Conference (2013) https://doi.org/10.1109/siecpc.2013.6551019
3. Zubkovich, S.G.: Statistical Characteristics of Radio Signals Reflected from the Earth Surface. Sov.radio, Moscow (1968). (in Russian)
4. Tverskoy, G.N., Terentiev, S.C., Kharchenko, I.P.: Echo Simulators for Marine Radars. Shipbuilding, Moscow (1973). (in Russian)
5. Electronically adjustable delay-simulator for distance-measuring apparatus operating on the frequency-modulated continuous wave principle. Patent application US 4661818 (1987)
6. Bokov, A.S., Vazhenin, V.G., Dyadkov, N.A., Mukhin, V.V., Shcherbakov, D.E., Ponomarev, L.I.: Radar target simulator when probing with primarily long signals (in Russian). Patent application RU 2568899. (2015) http://www1.fips.ru/fips_servl/fips_servlet?DB=RUPAT&DocNumber=2568899
7. Processor 1879BM3 (DSM) (in Russian). http://module.ru/upload/files/vm3.pdf (last Accessed 10 Feb 2018)
8. Bokov, A.S., Vazhenin, V.G., Dyadkov, N.A., Mukhin, V.V., Shcherbakov, D.E., Nagashibaev, D.Zh., Ponomarev, L.I.: Device for imitation of a false radar objective at sensing with signals with linear frequency modulation (in Russian). Patent application RU 2625567. (2017) http://www1.fips.ru/fips_servl/fips_servlet?DB=RUPAT&DocNumber=2625567

Distributed Arithmetic Based Hybrid Architecture for Multiple Transforms

Meghna Nair, I. Mamatha and Shikha Tripathi

Abstract Eight-point transforms play an important role in data compression, signal analysis and signal enhancement applications. Most widely used transforms of size -8 are Discrete Cosine Transform (DCT), Discrete Wavelet Transform (DWT), Discrete Sine Transform (DST), and Discrete Fourier Transform. There have been applications requiring multiple transforms for improving the performance. Unified/Hybrid architectures supporting multiple transforms is a possible solution for such demands as independent architecture for each transform requires more resources and computation power. In this work, a Distributed Arithmetic (DA) based multitransform architecture for supporting 1-D 8-point DCT, DFT, DST and DWT is proposed. A multiplier-less architecture leading to reduced hardware is implemented in 45 nm CMOS technology in Cadence RTL compiler as well as on FPGA using Xilinx ISE. Compared to the standalone transform architectures, there is 51.2% savings in number of adders, 44.34% saving in Look Up Table (LUT) utilization and 54.18% savings in register utilization in the proposed architecture.

Keywords Distributed arithmetic · Discrete Cosine Transform
Discrete Sine Transform · Discrete Fourier Transform · Haar Wavelet Transform
LUT (look up tables)

M. Nair
Department of Electronics and Communication Engineering,
Amrita Vishwa Vidyapeetham, Bengaluru, India
e-mail: meghnanair92@gmail.com

I. Mamatha
Department of Electrical and Electronics Engineering,
Amrita Vishwa Vidyapeetham, Bengaluru, India
e-mail: mamraj78@gmail.com

M. Nair
Amrita School of Engineering, Bengaluru,
Amrita Vishwa Vidyapeetham, Bengaluru, India

S. Tripathi (✉)
Faculty of Engineering, PES University, Bengaluru, India
e-mail: shikha.eee@gmail.com

B. S. Rawat et al. (eds.), *Advances in Signal Processing and Communication* ,
Lecture Notes in Electrical Engineering 526,
https://doi.org/10.1007/978-981-13-2553-3_22

1 Introduction

In modern times, most of the data we access using Internet comprises of video and images. The data is transmitted in compressed form to avoid huge storage space. Different transforms play different roles in data compression. The Discrete Cosine Transform (DCT) gives higher energy compaction properties for lower compression ratio whereas it develops blocking artifacts and false contouring effect at higher compression ratio. Discrete Wavelet Transform (DWT) is multiresolution compression method, i.e., by discarding the detail coefficients and taking only the approximate coefficients an image can be obtained in different resolutions. Discrete Sine Transform (DST) gives better compression ratio for less correlated signals. Discrete Fourier Transform (DFT) is widely used for signal analysis and enhancement and finds application in OFDM-based multi-carrier systems. Owing to these applications, there have been architectures for implementing transforms.

In [1] authors presented a hybrid architecture for addressing a new representation of DCT/DFT/Wavelet matrices using sparse matrix representation. A multiplier-less DCT architecture based on shift-add method resulted in reduced resource utilization [2]. Several DA-based architectures are proposed for transforms [3–8]. Jiang et al. proposed a DWT architecture which is reconfigurable and is adaptable for various kinds of filter banks with various input sets [9].Wahid et al. proposed a hybrid architecture for multiple transforms using matrix factorization and row-permutation algorithm [10, 11]. An efficient DA-based parallel processor architecture to realize 3-D DWT is proposed in [12]. A cyclic convolution based systolic array implementation of 1-D DFT and DCT is presented in [13].

Multitransform architectures are useful for improving the system performance in the applications where several transforms are required and user can select a transform based on the requirement. There have been very few hybrid architectures supporting multiple transforms such as DCT, DST, DFT, and DWT. Hence, a hybrid architecture using DA for 1-D DCT, 1-D DST, 1-D HWT, and 1-D DFT is developed in this work. An 8×8 matrix for DCT, DFT, DST, and Haar wavelet is considered for making the structure. Hardware optimization has been achieved by sharing the common adders and using some unique adders to compute the result. The proposed design has less power and reduced resource utilization compared to the previously reported work.

The paper is organized as follows. Section 2 describes principles of DA. Section 3 discusses implementation of proposed architecture. Results and performance analysis has been presented in Sects. 4 and 5 concludes the work.

2 DA Algorithm

Distributed Arithmetic (DA) is an efficient technique for calculation of product or multiply and accumulate (MAC) operation. DA is an efficient technique that replaces multiplication by LUTs, where LUTs are the main part of the Field Programmable

Gate Arrays (FPGAs). DA technique's mathematical derivation is described below. The summation of products can be given as

$$y = \sum_{K=1}^{K} A_K X_K, \tag{1}$$

Where A_K are fixed coefficients and X_K are input data words which is given as $||X_K| < \mathbf{1}, X_K : \{b_{K0}, b_{K1}, b_{K2}.\ldots\ldots, b_{K(N-1)}\}$. Here, b_{K0} is the sign bit.

We can express, $x_K = b_{K0} + \sum_{n=1}^{N-1} b_{Kn} 2^{-n}$ and $y = \sum_{K=1}^{K} (b_{K0}.A_K) + \sum_{K=1}^{K} \sum_{n=1}^{N-1} (b_{Kn}.A_K)2^{-n}$

Expanding on RHS and simplifying leads to bit level representation. The coefficient corresponding to $2^{-(N-1)}$ is the LSB and that of 2^0 is the MSB. It is clear from the above equation that the output can be obtained by adding LSB bit with left shifted version of the remaining bits by an appropriate units based on the weights assigned to each bits. This results in the architecture being bit-serial in nature.

3 Proposed Architecture

A hybrid architecture is designed for 1-D DCT, 1-D DST, 1-D HWT, and 1-D DFT using DA technique. First step in the algorithm is to calculate the coefficients of the transforms which is put up in the matrix according to the formula. The elements inside the matrix [A] are in binary form comprising of zeroes and ones. The next step is to detect the number of ones in each row and that particular row is represented in the form of adders (considering only ones). In this way each row is represented with some adders which we call as the butterfly structure. By identifying common computations a hybrid architecture is designed leading to sharing of resources. The algorithm for the compression and implementation of the sparse matrix [A] using reduced number of addition operations is discussed here.

3.1 An 8-Point DCT Implementation Using DA

An N point DCT is defined as,

$$Y(u) = \frac{c(u)}{2} \sum_{x=0}^{7} f(x) \cos \frac{(2x+1)u\pi}{16}; \quad 0 \le u \le 7, \quad c(u) = \frac{1}{\sqrt{2}}; u = 0, \quad c(u) = 1; otherwise,$$

where, $N = 8$ is considered.

$$A(x) = \frac{c(u)}{2} \cos \frac{(2x+1)u\pi}{16} \tag{2}$$

Equation (2) can be represented in matrix form as in (3).

$$\begin{bmatrix} Y(0) \\ Y(1) \\ Y(2) \\ Y(3) \\ Y(4) \\ Y(5) \\ Y(6) \\ Y(7) \end{bmatrix} = \begin{bmatrix} A_0(0) & A_0(1) & A_0(2) & A_0(3) & A_0(4) & A_0(5) & A_0(6) & A_0(7) \\ A_1(0) & A_1(1) & A_1(2) & A_1(3) & A_1(4) & A_1(5) & A_1(6) & A_1(7) \\ A_2(0) & A_2(1) & A_2(2) & A_2(3) & A_2(4) & A_2(5) & A_2(6) & A_2(7) \\ A_3(0) & A_3(1) & A_3(2) & A_3(3) & A_3(4) & A_3(5) & A_3(6) & A_3(7) \\ A_4(0) & A_4(1) & A_4(2) & A_4(3) & A_4(4) & A_4(5) & A_4(6) & A_4(7) \\ A_5(0) & A_5(1) & A_5(2) & A_5(3) & A_5(4) & A_5(5) & A_5(6) & A_5(7) \\ A_6(0) & A_6(1) & A_6(2) & A_6(3) & A_6(4) & A_6(5) & A_6(6) & A_6(7) \\ A_7(0) & A_7(1) & A_7(2) & A_7(3) & A_7(4) & A_7(5) & A_7(6) & A_7(7) \end{bmatrix} \begin{bmatrix} f(0) \\ f(1) \\ f(2) \\ f(3) \\ f(4) \\ f(5) \\ f(6) \\ f(7) \end{bmatrix}, \tag{3}$$

Where A_u represents a uth row vector of size 1×8. For A_0(where F_0 is the first row of the matrix), the coefficients are,

$$A_0(0) = A_0(1) = A_0(2) = A_0(3) = A_0(4) = A_0(5) = A_0(6) = A_0(7) = 0.3535$$

The first output sample Y(0) is obtained by multiplying A_0 (first row) with the input sequence. In the above matrix, the coefficients are represented in binary form. The precision of each coefficient is chosen to be 13bits in Q5.8 2's complement format, where, F(4) depicts the sign bit and F(−8) indicates LSB. Hence Y(0) in its bitwise representation can be obtained by converting the coefficients of A0 in binary form and multiplying with the input. In the bitwise representation F(4) represents the signbit and F(−8) represents the LSB which has a weight of 2^{-8}. First row in bitwise form is shown in (4).

The bottom row of A0 consists of the LSB of A0(x), and top row are signed bit of A0(x), for x = 0, 1 ,…, 7. In the above matrix F0, four rows have all 1's, i.e., all eight entries are 1's. When the above matrix is implemented it would only require seven adders as all four rows are same and the computation needs to be done only once. But if it was implemented directly, it would require 28 adders. Similar way, the butterfly structures are obtained for rest of the elements in the matrix too (i.e., from F1 to F7) as shown in Fig. 1. The computation is shared by DA bits of F0(−2), F0(−4), F0(−5), F0(−7). The other outputs are zeros and hence do not require any computation.

$$\begin{bmatrix} F(4) \\ F(3) \\ F(2) \\ F(1) \\ F(0) \\ F(-1) \\ F(-2) \\ F(-3) \\ F(-4) \\ F(-5) \\ F(-6) \\ F(-7) \\ F(-8) \end{bmatrix} = \begin{bmatrix} 0\,0\,0\,0\,0\,0\,0\,0 \\ 0\,0\,0\,0\,0\,0\,0\,0 \\ 0\,0\,0\,0\,0\,0\,0\,0 \\ 0\,0\,0\,0\,0\,0\,0\,0 \\ 0\,0\,0\,0\,0\,0\,0\,0 \\ 0\,0\,0\,0\,0\,0\,0\,0 \\ 1\,1\,1\,1\,1\,1\,1\,1 \\ 0\,0\,0\,0\,0\,0\,0\,0 \\ 1\,1\,1\,1\,1\,1\,1\,1 \\ 1\,1\,1\,1\,1\,1\,1\,1 \\ 0\,0\,0\,0\,0\,0\,0\,0 \\ 1\,1\,1\,1\,1\,1\,1\,1 \\ 0\,0\,0\,0\,0\,0\,0\,0 \end{bmatrix} \begin{bmatrix} f(0) \\ f(1) \\ f(2) \\ f(3) \\ f(4) \\ f(5) \\ f(6) \\ f(7) \end{bmatrix} \tag{4}$$

3.2 8-Point DST Implementation Using DA

The N point Discrete Sine Transform is given by,

$$Y(k) = \frac{2}{N} c(k) \sum_{n=0}^{7} f(n) \sin \frac{\pi(2n+1)k}{2N}; 0 \le k \le 7, c(k) = \frac{1}{\sqrt{2}} if; k = N, c(k) = 1; otherwise$$

When N = 8, considering f(n) as input vector and Y(k) as the output. The butterfly structures for implementing DST coefficients from Y(0) to Y(7) are shown in Fig. 2.

3.3 Eight-Point HWT Implementation Using DA

The Haar Wavelet Transform has a scaling function and a wavelet function. Matrix representation of eight-point Haar wavelet has the entries as 0.5, 0.707, and 0.3536 (readers are suggested to refer [7] for more details). Similar technique is applied to obtain an adder compression structure for HWT. The matrix obtained for A_0 for HWT and DCT are same, therefore the same butterfly structure is shared between them.

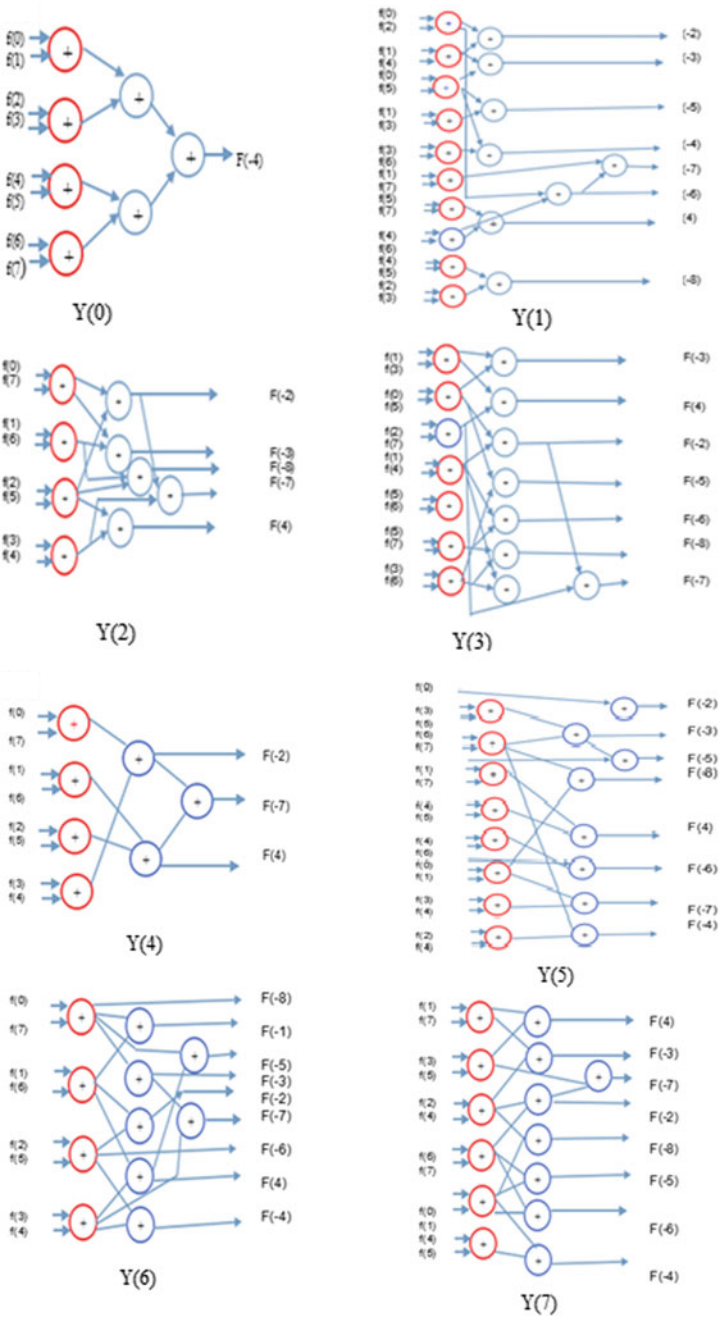

Fig. 1 **a** Butterfly structures for DCT: Y(0) to Y(7) **b** Butterfly structures for DCT: Y(4) to Y(7)

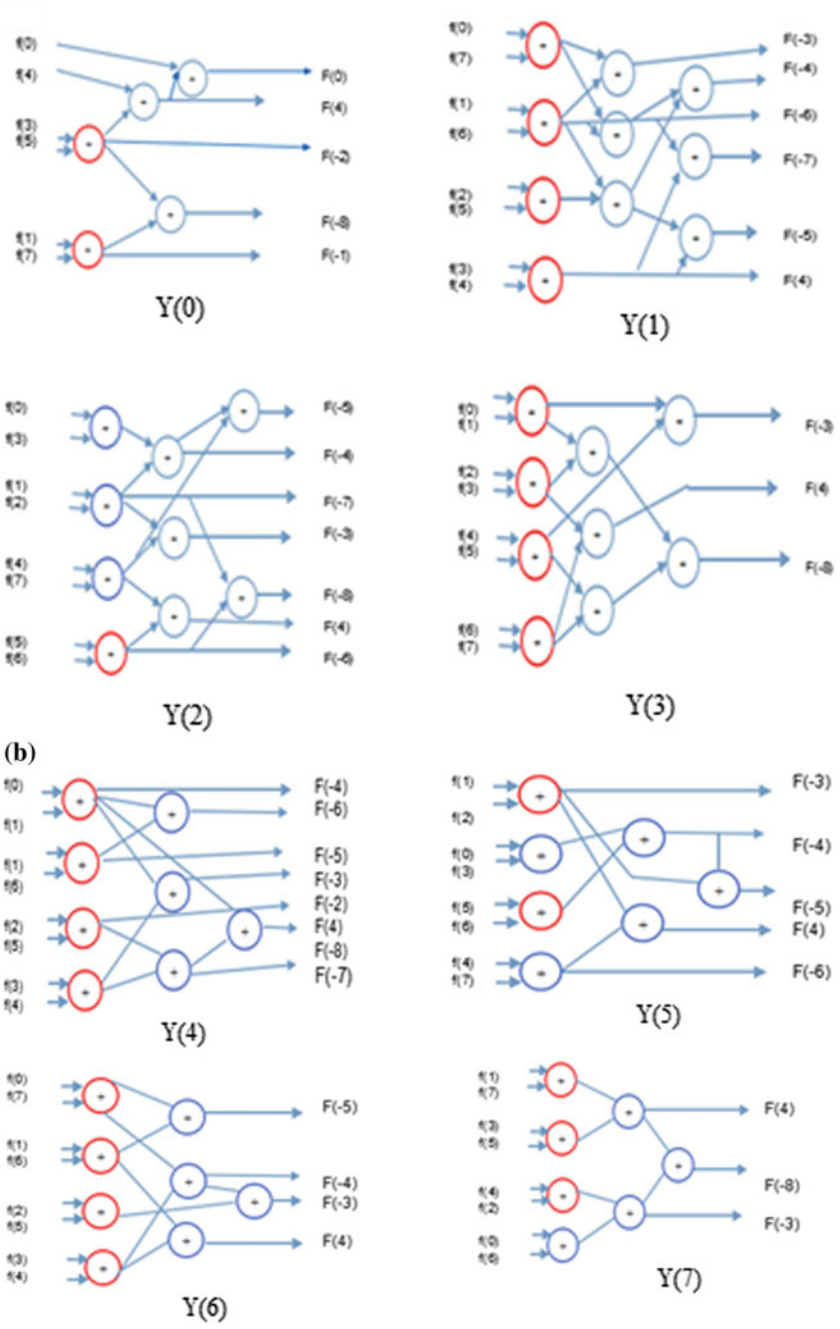

Fig. 2 Butterfly structures for DST: Y(0) to Y(7)

3.4 8 × 8 DFT Implementation Using DA

An N point DFT with N = 8 is defined as in (5), where, f(n) is the input sequence and Y(k) is the output. DFT has real as well as imaginary coefficient. The coefficient matrix for real part of DFT are separated and the butterfly structures for Y(0) to Y(7) are obtained as shown in Fig. 3. Similar structures are drawn for imaginary part as well.

$$Y(k) = \sum_{n=0}^{7} f(n)\, e^{\frac{-j2\Pi kn}{N}}, 0 \leq k \leq 7 \tag{5}$$

Note that the butterfly structure for imaginary part of DFT has structures for Y(1) to Y(7) excluding Y(0) and Y(4) they are zero. From Figs. 1, 2 and 3, the adders highlighted in red are common to all the structures and is shared among all the transforms to reduce the hardware requirement.

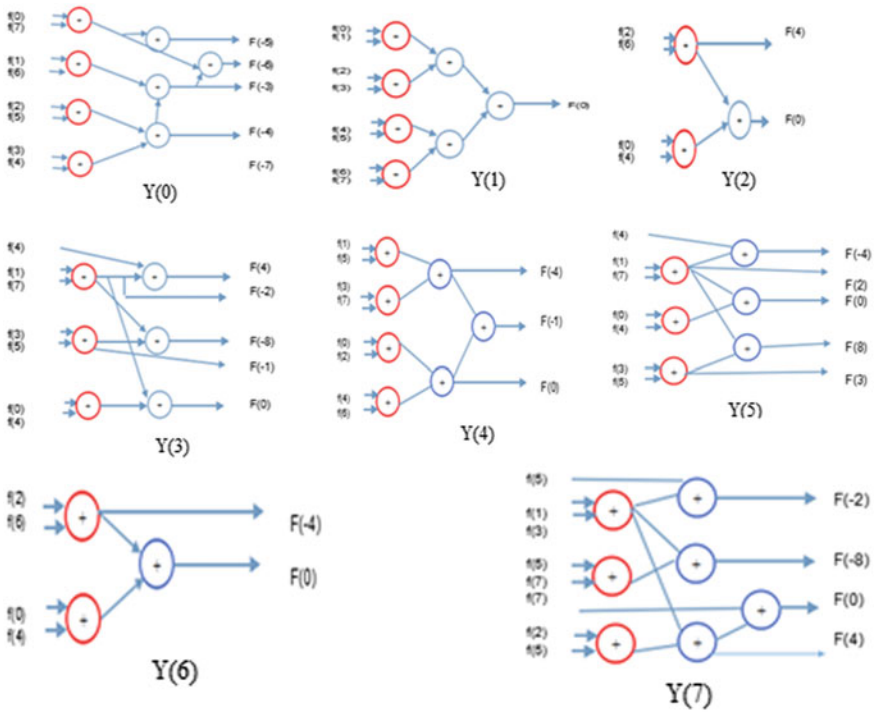

Fig. 3 Butterfly structure for computing DFT (Real Part)

4 Results and Discussions

The complete architecture is designed consisting of the modules which are common and unique among the transforms along with a controller for generating the required control signals. The block diagram of the proposed hybrid architecture is shown in Fig. 4. In this proposed work, an input of 8 KB voice signal is recorded and processed offline. The signal is converted and stored in.hex file using 13 bit representation in Q5.8 format. The first eight samples are stored in the buffer and fed to adder butterfly block for processing. The adder matrix contains number of blocks which are enabled based on the enable signals generated by the controller based on the choice of a transform which is obtained through a 2-bit T_select input. The encoding is as follows: T_select = 00 for HWT, T_select = 01 for DST, T_select = 10 for DFT and T_select = 11 for DCT. RESET, CLK (clock) and T_select are the inputs to the controller. In addition to enable signals, the controller also generates select signals for the multiplexers. Buffer is used to feed input to the adders.

As the DA precision is considered to be 13, there would be 13 single bit outputs which are fed to the 16×1 multiplexers. There are 16 multiplexers to give the 16 outputs where the last eight outputs are high only for DFT (imaginary). The 16×1 multiplexer selects one of the 13 inputs which is fed to the add and shift block where the computations are done and the output is obtained. All the 16 outputs are computed in parallel. The output is obtained at the 13th clock cycle after which the

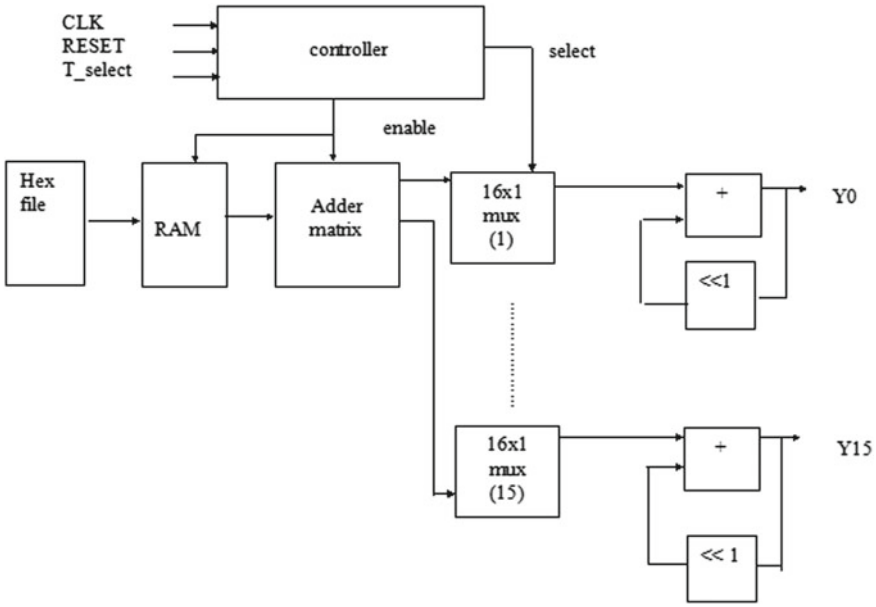

Fig. 4 Proposed hybrid architecture

next set of eight samples are loaded to the buffer. The outputs are available at Y_0 to Y_7 lines for DST, DCT and HWT while Y_8 to Y_{15} lines give '0' outputs. When the chosen transform is DFT, the real part of DFT is obtained through lines Y_0 to Y_7 and imaginary part of DFT is obtained through lines Y_8 to Y_{15}. The simulation of the developed architecture is done in Modelsim SE and the implementation is done using Xilinx ISE environment as well as Cadence RTL compiler. The results obtained from the designed architecture are compared with Matlab results. The mean square error (MSE) between the ModelSim output and Matlab output is calculated and the maximum MSE is found to be 0.0303.

Both the individual and hybrid architectures are synthesized in Xilinx ISE and post synthesis place and route (PAR) report is shown in Table 1. The resource utilization of standalone architectures is compared with the proposed hybrid architecture. It has been observed that the proposed architecture has 51.2% reduction in adders, 44.34% reduction in LUT utilization and 54.18% reduction in number of registers as compared with the standalone architectures.

Table 2 shows comparison among various architectures from previous work and the proposed architecture implemented on FPGA devices. The designed architecture for 1-D DCT,1-D DST, 1-D DFT, and 1-D HWT has 65.6% less register utilization compared to [12] and can operate at twice the frequency. Architectures discussed by Jiang et al. [11] and Abhishek et al. [9] are implemented for single transform. Compared to these approaches, the proposed architecture has almost double the hardware requirement but supports four transforms. The proposed hybrid architecture has two more transforms added to [7] where the number of adders in hybrid architecture has been reduced to 45.5% from [13]. Further, the proposed hybrid architecture is implemented in 0.045 μm CMOS technology using Cadence RTL compiler. Table 3 describes the comparison of the proposed hybrid architecture with various architectures in 0.18 μm CMOS technology. The area requirement of our structure is at par with [13] and [7] and is half as compared to [10] while the power consumption in our approach is least among all the approaches. With this low power consumption, lower area requirement and higher frequency of operation makes the proposed architecture efficient.

Table 1 Comparison of standalone versus proposed hybrid architecture

Topology	Transform	No. of adders	No. of LUTs	No. of registers
Standalone	DCT	82	1142	261
	HWT	41	809	228
	DST	52	930	242
	DFT (real)	43	814	231
	DFT (imag)	20	398	1122
	Total	238	4093	1084
Hybrid	DCT-DST-DFT-HWT	116	2278	508
Overall savings%		51.2	44.34	54.18

Table 2 Comparison of resource utilization of hybrid architecture

Approach	[Shimu et al. 2009]	[Jiang et al. 2013]	[Abhishek et al. 2013]	Proposed
Device used	Virtex4 (xcv4lxi5sf63)	Virtex6 (xc6vlx240t)	Virtex2 (xc2vp307ff896)	Virtex7 (xcv7vx3330tffg1157)
No. of LUTs	2017	29875	1012	2278
Registers	1479	23825	238	508
Maximum frequency (MHz)	95	200	311.944	200
Dynamic power (w)	NA	NA	2.7599	0.169

Table 3 Comparison of area using cadence RTL compiler

Parameters	Liu et al. [10] DA based DCT	Wahid et al. [13]	Vidhya et al. [7] hybrid DCT-DWT	Proposed hybrid DCT- DFT- DST- HWT
Technology used (μm)	0.18	0.18	0.18	0.045
Area (mm^2)	0.601	0.20368	0.36703	0.3867
Frequency (MHz)	20	100	200	125
Power (mw)	15.2	15.38	5.575	5.185

5 Conclusion

A hybrid architecture is developed for 1-D DCT, 1-D DST, 1-DFT, and 1-D HWT and implemented. Compared with individual designed architectures, the proposed hybrid architecture has savings in register utilization by 54.18%, LUT utilization by 44.34 and 51.2% of less adders used. Compared to other structures proposed architecture is efficient in terms of power consumption and resource utilization. Proposed architecture is simulated and implemented using Virtex 7 device where a maximum frequency of operation of 200 MHz is achieved. The hybrid architecture is further implemented in 0.045 μm CMOS technology using cadence RTL compiler. The architecture requires 13 clock cycles to process eight input samples. The technique can be extended for developing 2-D and 3-D architectures.

References

1. Chen, Z., Lee, M.H.: On fast hybrid source coding design. In: IEEE International Symposium on Information Technology Convergence (ISITC), pp. 143147 (2007)
2. El Aakif, M., Belkouch, S., Chabini, N., Hassani, M.M.: Low power and fast DCT architecture using multiplier-less method. In: IEEE Conference on Faible Tension Faible Consommation (FTFC), pp. 63–66 (2011)
3. Sharma, V.K., Mahapatra, K.K., Pati, U.C.: An efficient distributed arithmetic based VLSI architecture for DCT. In: 2011 IEEE International Conference on Devices and Communications (ICDeCom), pp. 1–5 (2011)
4. Pal, N.S., Singh, H.P.: Implementation of high speed FIR filter using serial and parallel distributed arithmetic algorithm. Int. J. Comput. Appl. **25**(7), 26–32 (2011)
5. Chen, Y.H., Chang, T.Y.: A high performance video transform engine by using space time scheduling strategy. IEEE Trans. Very Large Scale Integr. VLSI Syst. **20**(4), 655–664 (2012)
6. Satpute, N.S., Tembhurne, S.B., Bhure, V.S.: LMS algorithm distributed arithmetic based adaptive FIR filter with low area complexity. Proc. Int. J. Adv. Res. Comput. Commun. Eng. **4**(6), 1–7 (2015)
7. Chandran, V., Mamatha, I., Tripathi, S.: NEDA based hybrid architecture for DCT—HWT. In: IEEE International Conference on VLSI Systems, Architecture, Technology and Applications, pp. 1–6 (2016)
8. Mankar, A., Prasad, N., Das, A.D.: FPGA implementation of re-timed low power and high throughput DCT core using NEDA. In: IEEE Students Conference on Engineering and Systems, pp. 1–4 (2013)
9. Jiang, J., Sun, Q., Zhu, Y., Fu, Y.: A reconfigurable architecture for 1-D and 2-D discrete wavelet transform. In: IEEE International Symposium on Field Programmable Custom Computing Machines, pp. 81–84 (2013)
10. Wahid, K.A., Islam, M.A., Shimu, S.S., Lee, M.H., Ko, S.B.: Hybrid architecture and VLSI implementation of the cosine-fourier-haar transforms. Circuits Syst. Signal Process. **29**(6), 1193–1205 (2010)
11. Shimu, S., Wahid, K., Islam, M., Teng, D., Lee, M., KO S.B.: Efficient hardware implementation of hybrid cosine-fourier-wavlet transforms on a single FPGA. In: Proceedings of the IEEE International Symposium on Circuits and Systems, pp. 2325–2328 (2009)
12. Hegde, G., Vaya, P.: An efficient distributive arithmetic based 3-dimensional discrete wavelet transform for video processing. In: International Conference Process Automation, Control and Computing (PACC), pp. 1–6 (2011)
13. Mamatha, I., Raj, J.N., Tripathi, S., Sudarshan, T.S.B.: Systolic architecture implementation of 1D DFT and 1D DCT. In: 2015 IEEE International Conference on Signal Pocessing, Informatics, Communication and Energy Systems (SPICES), pp. 1–5 (2015)

Real-Time Video Surveillance for Safety Line and Pedestrian Breach Detection in a Dynamic Environment

Arjun Prakash, Santosh Verma and Shivam Vijay

Abstract The intended study in light is to emphasize the public safety thereby securing the perimeter of a surrounding, enclosing any pedestrian within the limits broadened by a 'safety line' indicator. The objective to be accomplished is to enhance the detection of said 'safety line' in a dynamic environment. The environment used is of a Train Platform having a maximum priority to the edge of platform limit marked by a distinct yellow line. The colored line intended to be detected can also be treated as an image and thus we can apply object detection techniques for the same. The topic of object detection in image processing is to detect an object within a frame and draw a contour around it. There are various algorithms to detect an object, but we have modified and combined various techniques to produce the desired result. The proposed algorithm works in different phases starting with dividing the given frame in N segments, processing the given segments individually, followed by using the best common result among all the segments to achieve the equation of the colored line. The next phase includes detecting a regular pedestrian using HoG cascades and estimating position with respect to the calculated line to identify whether the line was crossed or not. After implementing this approach, an alarm is successfully generated as soon as any object/person passes the yellow line in order to ensure safety.

Keywords Edge detection · Line detection · Video surveillance · Metro security Image processing · Computer vision

A. Prakash · S. Verma (✉) · S. Vijay
Department of Computer Science and Information Technology,
Jaypee Institute of Information Technology, Noida, UP, India
e-mail: santosh.verma@jiit.ac.in

A. Prakash
e-mail: arjunprakash95@yahoo.com

S. Vijay
e-mail: shivam.vijay95@gmail.com

B. S. Rawat et al. (eds.), *Advances in Signal Processing and Communication* ,
Lecture Notes in Electrical Engineering 526,
https://doi.org/10.1007/978-981-13-2553-3_23

1 Introduction

Digital Image Processing is a technique of digitization of the input image and imposing some operations on it to get an image which is completely enhanced image, or to extract a part of image having some useful information, or to extract the features from it [1]. An Image in Image Processing system is most widely considered as a two dimensional dataset of signals for applying a predefined or some proposed set of signal processing methods to the input. Digital image processing includes following three steps:

(a) Capturing the input image with an optical camera or synthetic image by digital photography.
(b) Preprocessing and postprocessing techniques for analysis and manipulation of the image.
(c) Output is the last step in which result can be a modified image or a report which is based on image analysis at step 2.

Image processing goals can be achieved by implementing many different types of algorithms and techniques. If these algorithms are being imposed on a video, then the best way is to divide the video into frames [1, 2].

The intended study in light is to emphasize the public safety thereby securing the perimeter of a surrounding, enclosing any pedestrian within the limits broadened by a 'safety line' indicator. The objective to be accomplished is to enhance the detection of said 'safety line' in a dynamic environment. Here, dynamic environment can be defined as the continuous change in the ambiance of the platform and the sporadic change in the position of the camera [3]. The environment used is of a Train Platform having a maximum proximity to the edge of platform limit marked by a distinct yellow line. After gathering line information within a frame, algorithm proceeds to identify, mark pedestrians and approximate their location [4]. Algorithm also infers if there is a breach in safety, and timely notifies the system to raise an alarm.

During the literature study of video surveillance, system identified a number of challenges. Challenges faced are usually common to most computer vision implementations of any problem, but during this study we faced some unique and extended versions of common problems, which are listed and explained as below:

(a) *Noise*: The original meaning of noise is any kind of unwanted signal. Noise in images means the random variation of brightness and color information. While implementing this study, Gaussian noise and shot noise were detected. The algorithm gives better result if the noise is removed from the frame [5, 6].
(b) *Time*: Time was also one of the major challenges faced in the implementation because this algorithm needs to be executed in real-time scenario [7, 8]. It was very difficult to generate acceptable output within the given valid time frame of the input. The video frame rate at which we have done this implementation is 10 fps.
(c) *Matching colors in environment*: Complementary colors of the same brightness and hue will always work well together. But, this turned as a challenge in this

study because firstly many other objects got mixed up with the safety line and secondly, the values of the input frame fluctuated as the train entered and left the station.

(d) *Motion Surveillance Camera Issue*: The position of camera is an important thing that has to be kept in mind because the system must be able to handle both stationary and moving objects. In this research project camera is kept at a specific point in order to enhance to productivity of the implemented algorithms [4].

(e) *Indoor and Outdoor Environment*: For the algorithm to work as consistent as possible, it was necessary to maintain the fluctuation in the colors variation of the environment [9].

(f) *Illumination/lighting effect*: It is observed in literature of previous researches that the bonding between the colors, the RGBs or HSIs, in the filtered image after preprocessing and unfiltered images, i.e., original image highly depends on the color of the light and this dependency could be used to estimate the color of the illuminates [3, 4, 7]. A variation in illumination may affect the result of digital image processing.

(g) *Occlusion of object intended to be detected (Safety line and pedestrians occlusion)*: It is a great challenge to segregate the objects or a region which is obscured by the camera point of view. During the research work for the line detection project, SPCPE (Simultaneous Partition and Class Parameter Estimation) algorithm was studied to eradicate occlusion [10]. The said algorithm is used to segregate each pixel in frames into background pixels and foreground pixels. After this, a size-adjustment method is applied that aligns the bounding boxes of the objects.

Proposed Algorithm initially faced many above mentioned challenges but at the end issues were solved and a successful algorithm was delivered.

2 Proposed Algorithm

The Machine vision system detects an object by an image sensor. A computer vision system uses electronic devices and various algorithms that mimic human eyes and brain in order to duplicate the human vision ability. The OpenCV library is the most widely used library in machines to detect, track and understand the surrounding environment captured by image sensors.

2.1 Overview of the Algorithm

The algorithm proposed in this paper starts with a video feed from a static surveillance camera. The study then proceeds to extract frames from video feed, frame skipping may be allowed since the processing has to be in real time and some intermediate frame loss will not affect the efficiency in accurate output. The frame extracted from the video feed is then converted to HSV format from available RGB format [4, 11].

(1) *Obtain Frame from Video*: Videos are imported frame by frame in OpenCV. Once frame have been generated, then they are resized and further processed under various algorithms according to the desired results.
(2) *Convert image to HSV*: Generally in image processing implementations, HSV format is considered over RGB format as HSV separates color information (chroma) from intensity or lighting (luma). As the values are separated, following the thresholding rules become easier by using only the saturation and hue values. It is observed in study that perceiving and classifying colors given clustered data points in HSV color model rather than in RGB color model [12, 13]. And there is a direct correlation between the concentration level and digital colors in both color models. HSV is often used simply due to ease of availability of the code for conversion between RGB and HSV. Figure 4 of Sect. 3 is output after RGB to HSV conversion.
(3) *Blur the HSV image*: In Image processing, blurring is done by passing the HSV image through various low pass filters. There are many filters that can be used in different types of scenarios such as Averaging, Gaussian Blur, Median Blur, and Bilateral Filtering [13]. In this study, blurring was done to remove the noise from the frames by Averaging. A 5×5 kernel was used to average all the pixels under a given area which was calculated by cv2.blur() and cv2.boxFilter() functions.
(4) *Divide image horizontally in N parts*: Adaptive searching in frames to find the best output among available potential results. By dividing the image into frames, it led to an efficient computation with effective O(N) complexity [14].
(5) For each part:
    (a) *Set upper and lower limit of the color to detect the discussed Safety line*: Setting the upper limit and lower limit of the image generated a histogram of the image and eventually calculates a contrast for the generated histogram.
    (b) *Create a mask using the range of colors*: Masking is a technique used to sharpen images and get a better image for further experiments. Unsharp masking is a good tool for sharpness enhancements [15, 16].

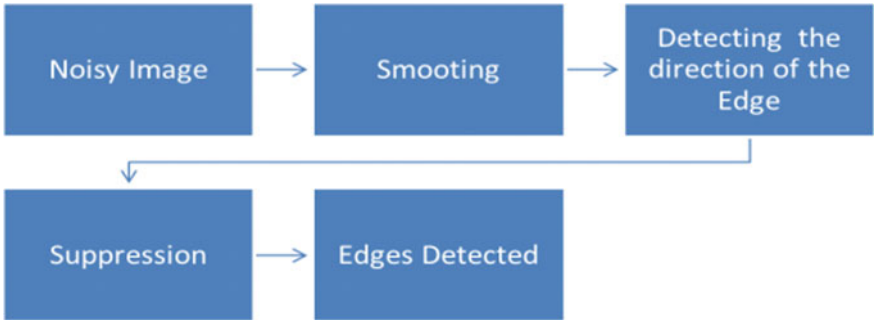

Fig. 1 Steps in canny edge detection algorithm

(c) *Apply morphological opening and closing on the image to smoothen*: The identification of the object can be simplified by restricting each pixel to the value of either 0 or 1. Morphological transformation takes care of this part by implementing morphological operators namely Opening, Closing, Erosion and Dilation. The end result of Opening operator and Erosion operator is similar. This is same for Closing and Dilation operator. (Results can be seen in the section III of this paper. Figure 6 is an output after Opening and Closing Operators).

(d) *Use canny edge detection to detect the colored edges*: Before the edge extraction operation and working on line equations, the noise removal of the original image is important in order to smoothen the image; Gaussian filter was used in this step. After removal of noise, edge strength was computed depending on gradient magnitude. We used Sobel operator for calculation of gradient magnitude. Let the pixel "a" in the sub-image matrix with size 5×5. The resultant image after Canny Edge Detection algorithm is shown by Fig. 7 in the result section. Thereafter, suppression algorithm was applied for non maximum; this eliminates all those values that does not belong to an edge pixel. In final step, hysteresis is plotted. It uses high and the low thresholds. If the pixel value lies between the two thresholds, it will be considered to as an edge pixel, but if this value is lesser than the lower threshold, it will be blocked and if it has a value greater than the higher threshold and has a connection with a pixel that has value between the two threshold, it will be considered an edge pixel. It is implemented by using the following syntax [1, 2, 8, 17, 18]. (Fig. 1)

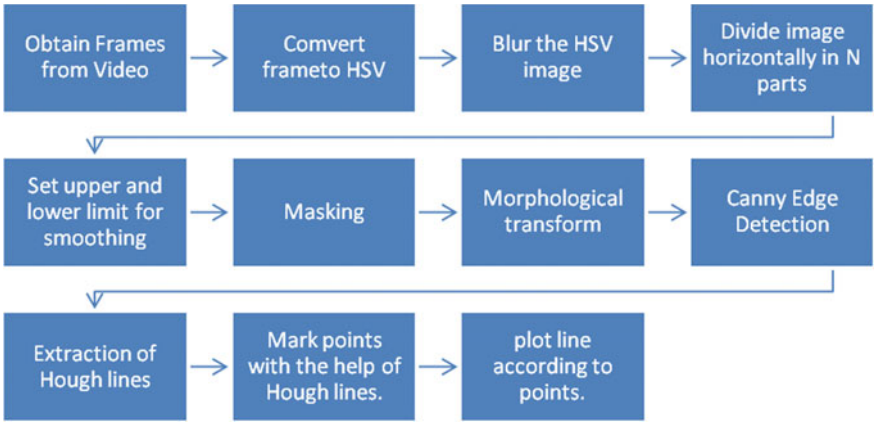

Fig. 2 Flow chart of the proposed algorithm for processing the pedestrian and safety line

(e) *Extract the lines using Hough lines and calculation of line equation*: For detection of line shape one of the known techniques named as Hough Transform is used. During our study, it is observed that it could detect the shapes even if it is broken, small gap in continuity, or distorted a little extent [19–21]. A line can be represented by these two terms, (ρ, $\ominus$). Where, rows are denoted as ρ and columns as $\ominus$. So first it creates an empty 2D array (to hold values of two parameters). Size of array is a subjective choice on the accuracy one need. Consider the first point of the line. One must know its (x, y) values. Now in the line equation, substitute the values $\theta = 0$, 1, 2, 3, …, 180 and validate the ρ you get. For every (ρ, $\ominus$) pair, increment value by one through accumulator in its corresponding (ρ, $\ominus$) cells. So if someone searches the accumulator for maximum votes, there is a line in this frame [17, 18].

(6) *Find the points on the boundary of image lying on the line*: Choose the points on the boundary which have highest frequency within the list of points in all N regions and save them to plot the lines through the saved points. (Fig. 2)

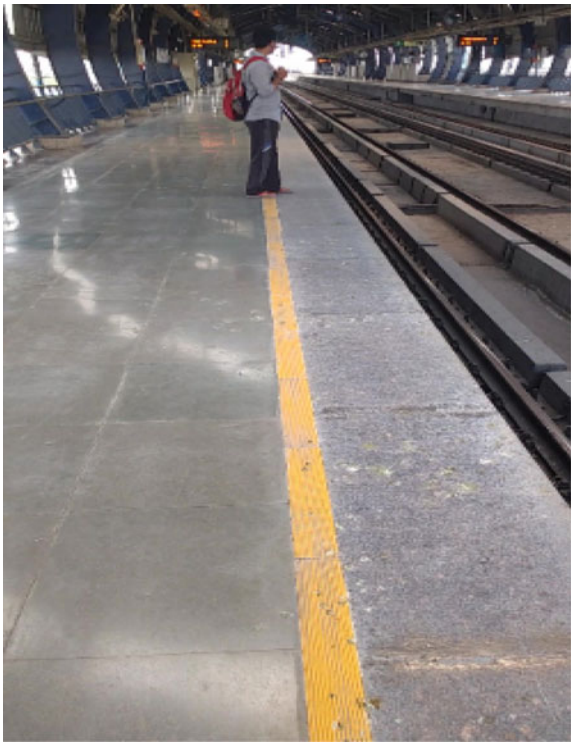

Fig. 3 Original image

3 Experimental Validations and Result

Eclipse was used to implement the line detection algorithm. All the images that were used while implementing this task are listed below. Manual testing was done by implementing different algorithms in various codes, taking some pictures and videos as a set of input to check which algorithm gives better result in respective environment. (Figs. 3, 4, 5, 6, 7, 8, 9 and 10)

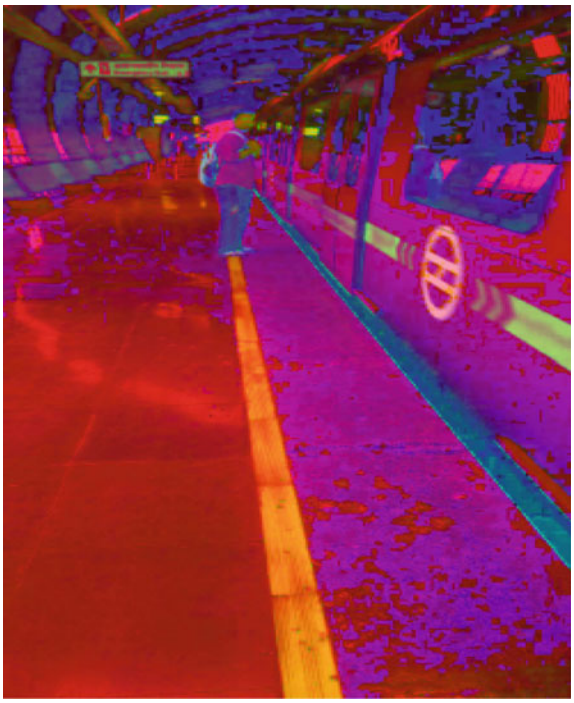

Fig. 4 RGB to HSV converted image

4 Conclusions and Future Work

After implementing the above method, an alarm is raised when an object crosses through the Yellow line on the platform of the metro station while the arrival and departure of metro (see Fig. 9 of Sect. 3 of this paper). Public safety can get enhanced by implementing the proposed algorithm in real time. The study has been done in both noisy and clean environment. The noise has been removed by smoothing and some other techniques that are mentioned in the Sect. 2 of this paper. Among various Edge detection Algorithms, The Canny Operated proved to give the best result. Moreover, Error rate was also calculated by running the code in different set of inputs and values.(Tables 1, 2, 3)

It was proved that the result was better if only 10 frames were being skipped. The Error rate increased as the number of frames that were being skipped increased.

Table 1 Implementation of algorithm

Feature	Expectation	Remark
Convert the BGR image to grayscale	Grayscale image visible	Image visible
Convert the BGR image to HSV	HSV image visible	Image visible
Take picture as an input	Picture should be accepted as an input	Input taken successfully
Take video as an input	Video should be accepted as an input	Video processed by frames
Take live video from web camera as input	Live video should be visible as input	Live video taken as input
Analysis should be performed on all inputs	Border of the object should be visible	Border visible
The yellow line should be recognized	Yellow line should be recognized using color detection	Yellow color recognized
Objects which cross yellow line should be identified	Objects should be identified	Objects identified
Alarm should be raised	Alarm should be generated	Security alarm raised
Convert the BGR image to grayscale	Grayscale Image visible	Image visible
Convert the BGR image to HSV	HSV image visible	Image visible
Take picture as an input	Picture should be accepted as an input	Input taken successfully
Take video as an input	Video should be accepted as an input	Video processed by frames
Take live video from web camera as input	Live video should be visible as input	Live video taken as input
Analysis should be performed on all inputs	Border of the object should be visible	Border visible
The yellow line should be recognized	Yellow line should be recognized using color detection	Yellow color recognized
Objects which cross yellow line should be identified	Objects should be identified	Objects identified
Alarm should be raised	Alarm should be generated	Security alarm raised

Table 2 Error rate without Noise Reduction Algorithms

	10 Frames skipped	20 Frames skipped	50 Frames skipped
Error rate	10%	16%	22%

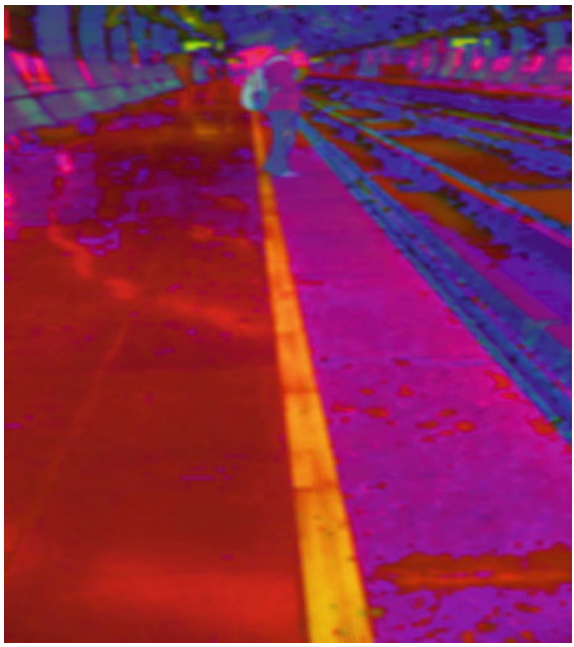

Fig. 5 Noise reduced image for further processing

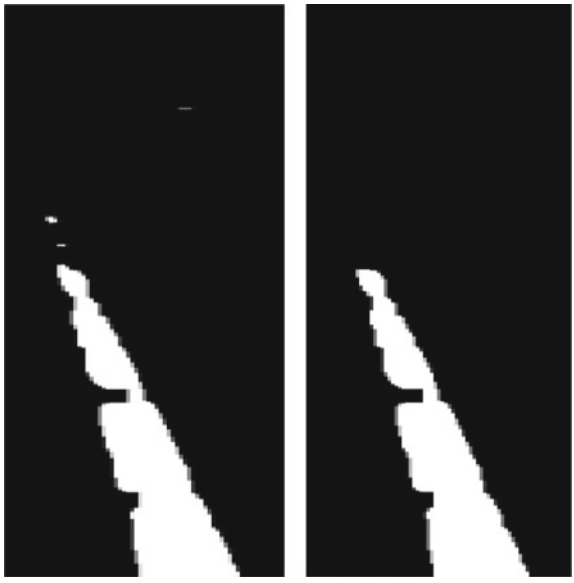

Fig. 6 Closing and opening

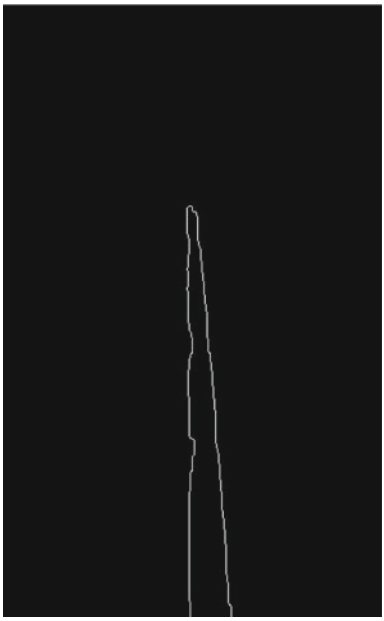

Fig. 7 Canny edge detection

Fig. 8 ROI

Fig. 9 Hough transform (line)

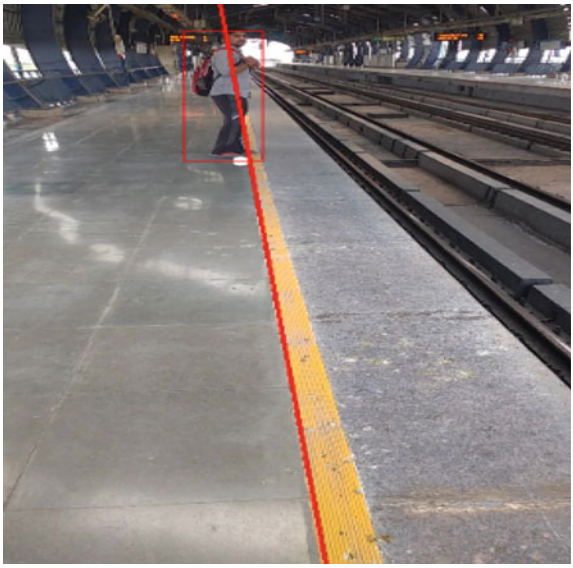

Fig. 10 Final result

Table 3 Error rate after Noise Reduction Algorithms

	10 Frames skipped	20 Frames skipped	50 Frames skipped
Error rate	6%	11%	15%

Finally, some topics could be suggested for future works. In this paper, the experimental results are carried out on Grayscale images only. HSV (Hue Saturation Value) color format that has been used. Other formats may also give us better results. Furthermore, this implementation was done by keeping the camera at one particular angle or at rest. More research needs to be done if the camera is in motion. A case like, if someone crossing the line when train is arrived/arriving at station would also be considered for future implementation with considerable amount of motion blur.

Acknowledgements The author wishes to thank the editor and reviewer of the research paper for their valuable comments, critic, and review. The performance analysis/result, figures, and tabulated data presented in this paper is original and created by the authors only.

References

1. Yang, O.: Moving object detecting method in video. IEEE Aerosp. Electron. Syst. Mag. **1**(23), 18–20 (2008)
2. Yu, Y., Gu, J., Zhang, D.W.: An automatic method for detecting objects of interest in videos using surprise theory. In: 2012 International Conference on Information and Automation (ICIA), pp. 620–625. IEEE (2012)
3. Chen, X., He, Z., Anderson, D., Keller, J., Skubic, M.: Adaptive silouette extraction and human tracking in complex and dynamic environments. In: 2006 IEEE International Conference on Image Processing, pp. 561–564. IEEE (2006)
4. Mahalanobis, A., Cannon, J.L., Stanfill, S.R., Muise, R.R., Shah, M.A.: Network video image processing for security, surveillance, and situational awareness. In: Proceedings of SPIE, vol. 5440, pp. 1–8, (2004)
5. Mahmood, A.M., Maraş, H.H., Elbaşi, E.: Measurement of edge detection algorithms in clean and noisy environment. In: AICT, 2014, pp. 1–6. IEEE (2014)
6. Hsiao, P.Y., Chou, S.S., Huang, F.C.: Generic 2-d gaussian smoothing filter for noisy image processing. In: TENCON 2007–2007, pp. 1–4. IEEE (2007)
7. Wu, D.M., Guan, L., Lau, G., Rahija, D.:. Design and implementation of a distributed real-time image processing system. In: First IEEE International Conference on Engineering of Complex Computer Systems, 1995. Held jointly with 5th CSESAW, 3rd IEEE RTAW and 20th IFAC/IFIP WRTP, Proceedings., pp. 266–269. IEEE (1995)
8. Verma, S., Goel, S.: An empirical evaluation of wavelets based viz-a-viz classical state-of-art to image denoising. In: Contemporary Computing (IC3), 2013, pp. 331–336. IEEE (2013)
9. Pojala, C., Sengupta, S.: Detection of moving objects using fuzzy correlogram based background subtraction. In: 2011 IEEE International Conference on Signal and Image Processing Applications (ICSIPA), pp. 255–259. IEEE (2011)
10. Liu, D., Shyu, M.L., Zhu, Q., Chen, S.C.: Moving object detection under object occlusion situations in video sequences. In: 2011 IEEE International Symposium on Multimedia (ISM), pp. 271–278. IEEE (2011)

11. Mohan, A.S., Resmi, R.: Video image processing for moving object detection and segmentation using background subtraction. In 2014 First International Conference on Computational Systems and Communications (ICCSC), pp. 288–292. IEEE (2014)
12. Ong, P.M.B., Punzalan, E.R.: Comparative Analysis of RGB and HSV Color Models in Extracting Color Features of Green Dye Solutions. In: DLSU Research Congress, pp. 1500–20, (2014)
13. Kulshrestha, R., Bairwa, R.K.: Removal of color blindness using threshold and masking. Int. J. Adv. Res. in Computer Sci. and Soft. Eng **3**, 218–221 (2013)
14. Unser, M.: Multigrid adaptive image processing. In: International Conference on Image Processing, 1995. Proceedings., vol. 1, pp. 49–52. IEEE (1995)
15. Sridhar, S., Meeravali, S.: A generalised unsharp masking algorithm using bilateral filter. Int. J. Eng. Trends Technol. **4**(7), 2896–2902 (2013)
16. Lee, J.S.: Digital image enhancement and noise filtering by use of local statistics. IEEE Trans. Pattern Anal. Mach. Intell. **2**, 165–168 (1980)
17. Yuan, L., Xu, X.: Adaptive image edge detection algorithm based on canny operator. In: 2015 4th International Conference on Advanced Information Technology and Sensor Application (AITS), pp. 28–31. IEEE (2015)
18. Kumar, I., Rawat, J., Bhadauria, H.S.: A conventional study of edge detection technique in digital image processing. Int. J. Comput. Sci. Mob. Comput. **3**(4), 328–334 (2014)
19. Asvadi, A., Peixoto, P., Nunes, U.: Detection and tracking of moving objects using 2.5 d motion grids. In: Intelligent Transportation Systems (ITSC), 2015, pp. 788–793. IEEE (2015)
20. Ghaeminia, M.H., Shokouhi, S.B.: Adaptive background model for moving objects based on PCA. In: MVIP, 2010 6th Iranian, pp. 1–4. IEEE (2010)
21. Mejia, V., Kang, E.Y.: Automatic moving object detection using motion and color features and bi-modal Gaussian approximation. In: 2011 IEEE International Conference on Systems, Man, and Cybernetics (SMC), pp. 2922–2927. IEEE (2011)

Human Activity Recognition in Video Benchmarks: A Survey

Tej Singh and Dinesh Kumar Vishwakarma

Abstract Vision-based Human activity recognition is becoming a trendy area of research due to its broad application such as security and surveillance, human—computer interactions, patients monitoring system, and robotics. For the recognition of human activity various approaches have been developed and to test the performance on these video datasets. Hence, the objective of this survey paper is to outline the different video datasets and highlights their merits and demerits under practical considerations. We have categorized these datasets into two part. The first part consists two-dimensional (2D-RGB) datasets and the second part has three-dimensional (3D-RGB) datasets. The most prominent challenges involved in these datasets are occlusions, illumination variation, view variation, annotation, and fusion of modalities. The key specification of these datasets are resolutions, frame rate, actions/actors, background, and application domain. All specifications, challenges involved, and the comparison made in tabular form. We have also presented the state-of-the-art algorithms that give the highest accuracy on these datasets.

Keywords Human activity recognition · Human–human interaction · RGB RGB-Depth (RGB-D) dataset

1 Introduction

In the present era, human activity recognition [1–5], in videos has become a prominent area of research in the field of computer vision. It has many daily living applications such as patient monitoring, object tracking, threat detection, and security and surveillance [6–9]. The motivation to work in this field is to recognize human

T. Singh (✉) · D. K. Vishwakarma
Department of Information Technology,
Delhi Technological University, New Delhi, Delhi, India
e-mail: tejsingh_2k16phdec05@dtu.ac.in; ttomar07@gmail.com

D. K. Vishwakarma
e-mail: dinesh@dtu.ac.in; dvishwakarma@gmail.com

B. S. Rawat et al. (eds.), *Advances in Signal Processing and Communication* ,
Lecture Notes in Electrical Engineering 526,
https://doi.org/10.1007/978-981-13-2553-3_24

gestures, actions and interactions in videos. The recognition of human activities in video involves various steps such as preprocessing, segmentation, feature extraction, dimension reduction and classification. We can save time if we have accurate knowledge of the publically available datasets [10, 11], so that there is no need to generate new dataset and a researcher's work will be easier to identify the datasets and a key focus will be on developing the new algorithm rather than gathering the information about datasets. With the advancement of labelling algorithm, it becomes an opportunity to label the dense dataset videos for activity recognition, object tracking, and scene reconstruction [12–14]. This work covers gesture recognition, daily living actions or activity, sports actions, human–human interactions and human–object interaction datasets. This paper consists of both RGB and RGB-D publically available datasets. This work provides datasets specifications such as year of publication, frame rates, spatial resolution, the total number of action and number of actors (subjects) performing in videos and state-of-the-art solutions on existing benchmarks. Tables 1 and 2 provides the details of RGB and RGB-D datasets, respectively. Before 2010, a large number of RGB video dataset was available to this community [15–17]. After the advancement of low-cost depth sensor, e.g. Microsoft Kinect, there has been a drastic increase in 3D, and multi-modal videos datasets. Due to low cost and lightweight sensors datasets are recorded with multiple modalities such as depth frames, accelerometer, IR sensors frames, acoustical data, and skeleton data information. The RGB-D datasets having multiple modalities reduce the chance of loss of information in videos as compared to traditional RGB datasets at the cost of increased complexities [18, 19].

2 Related Work

Chaquet et al. [20], focused on 28 publically available RGB datasets of human action and activity. The dataset characteristics are discussed such as ground truth, numbers of action/actors, views and area of applications. Their work does not cover RGB-depth dataset available at that time. Edwards et al. [3], focused on pose-based methods and presented a novel high-level activity dataset. Their work gives no information about state-of-the-art accuracies on existing dataset. Wang et al. [21], discussed specific novel techniques on RGB-D-based motion recognition. T. Hassner [22], focused on action recognition and accuracy of most of the RGB datasets. The very limitation of this work is the action in depth datasets and area of applications. M. Firman [23], analysed the depth dataset such as semantics, identification, face/pose recognition and object tracking. Borges et al. [24], discussed advantages and shortcomings of various methods for human action understanding. Zhang et al. [25], engrossed in action RGB-D benchmarks and lack of considered pose, human interaction activities. Besides, they intended to cover state-of-the-art accuracy and classification techniques on specific benchmarks. Compared with the existing surveys, the primary aim of this work will provide an accessible platform to the readers.

Table 1 RGB (2D) video dataset

Dataset	Year	Modality	Application domain
KTH	2004	Grey	Human action recognition in real outdoor conditions
Weizmann	2005	RGB	Human action recognition
IXMAS	2006	RGB	Multi-view-invariant action recognitions
CASIA Action	2007	RGB	Human behaviour and human–human interaction
UCF Sports	2008	RGB	Sports actions recognition
Olympic Games	2008	RGB	Sports actions recognition
Hollywood	2008	RGB	Realistic actions recognition from movies
UT- Interaction	2009	RGB	Human–Human interaction activity recognition
BEHAVE	2009	RGB	Human Group behaviour activity analysis
HMDB51	2011	RGB	human–human interaction, human – object interaction
UCF50	2011	RGB	Human Sports activity recognition
BIT-Interaction	2012	RGB	Human–human interaction in realistic scenarios
UCF101	2013	RGB	Human Sports activity recognition
YouTube Sports 1 M	2013	RGB	Human Sports activity recognition
ActivityNet	2015	RGB	Human activity understanding
THUMOS'15	2015	RGB	Action recognition in wild video
ChaLearn: Action/Interaction	2015	RGB	Automatic learning of human action and interactions
FCVID	2015	RGB	Human activity understanding
YouTube 8 M	2016	RGB	Human activity recognition, human interaction
Okutama Action	2017	RGB	Concurrent human action recognition form aerial view

3 Challenges in HAR Dataset

In this section, we discuss challenges involved in RGB and RGB-D dataset. It can be noticed that dataset videos are facing limitations in at least one of aspects such as similarity of actions, cluttered background, viewpoints variations, illuminations variations and occlusions.

Table 2 RGB-D (3D) video dataset

Dataset	Year	Modality	Application Domain
MSR Action 3D	2010	Depth + skeleton	Sports Gesture recognition
CAD-60	2011	RGB, Depth, skeleton	Daily activity recognition
RGB-D HuDaAct	2011	RGB, Depth	Daily activity recognition
Berkeley MHAD	2013	RGB, depth, skeleton	Human behaviour Recognition
CAD-120	2013	Depth, skeleton	Action labelling, human and object tracking
Hollywood 3D	2013	RGB, Depth	Natural action recognition in movies
MSR Action Pairs	2013	Depth	Action pairs recognitions
UWA3D Multi-View	2014	RGB, Depth, skeleton	Similar and cross-view action recognition
Northwestern UCLA	2014	RGB, Depth, skeleton	Cross- view action recognition
LIRIS	2014	RGB, Depth, grey	Human activity recognition
UTD-MHAD	2015	RGB, Depth, skeleton	View- invariant human action recognition
M^2I	2015	RGB, Depth, skeleton	Human–human, human–object interaction
SYSU-3D HOI	2015	RGB, Depth, skeleton	human–object interaction
G3Di	2015	RGB, Depth, skeleton	Gaming interaction activity
NTU RGB + D	2016	RGB, Depth, skeleton, IR sequences	Human Action Recognition
PKU-MMD	2017	RGB(image and video), Depth, skeleton, IR sequences	Multi-modal action recognition

3.1 Background and Environmental Conditions

The background in videos may be different types such as slow/high dynamic, static, occluded, airy, rainy and dense populated. It can be observed that KTH dataset is more challenging due to changing the background as compared to Weizmann dataset. The UT-Interaction, BEHAVE, BIT Interactions datasets recorded in the larger outdoor area and changing natural background conditions. The various datasets such as UCF sports activity, UIUC, Olympic sports, hollywood1, HMDB51, THUMOS, ActivityNet and YouTube 8 M recorded from online sources YouTube, Google, and various movies, are challenging due to having both dynamic objects and backgrounds conditions.

3.2 Similarity and Dissimilarity of Actions

The similarity between the actions classes in the datasets provides a fundamental challenge to the researcher. There are many actions which seem to be similar in videos such as jogging, running, walking, etc. The accuracy of classification is affected by the same type of actions. The same actions performed by different actors increase the complexity of the dataset such as YouTube Sports 1 M dataset having thousands of videos of same action class.

3.3 Occlusion

Occlusion is a thing where another object hides the object of interest. For the human action and activity recognition, occlusion can be categorized as self-occlusion and occlusion of another object/partial occlusion. The depth sensor is severely affected by internal noise data and self-occlusion by performing users such as in CAD-60, 50 salad, Berkeley MHAD, UWA3D activity, LIRIS, MSR Action pair, UTD-MHAD, M2I, SYSU-3D HOI, NTU RGB + D and PKU-MMD datasets.

3.4 View Variations

The viewpoint of any activity recorded inside the video dataset is a key attribute in the human activity recognition system. The multiple views have more robust information than single view and independent of captured view angle inside the dataset. However, multiple views increase the complexity such as more training as well as test data is required for classification analysis. Here, KTH, Weizmann, Hollywood, UCF Sports, MSR Action 3D, and Hollywood 3D, are single view datasets. The multi-view datasets are CAD-60, CAD-120, UWA3D, Northwestern-UCLA, LIRIS, UTD- MHAD, NTU RGB-D, IXMAS, CASIA Action, UT-Interaction, BEHAVE, BIT-Interaction, Breakfast Action.

4 Approaches for Human Action Recognitions

Based on the methodologies used in recent years to recognize human action and activities we can categorize the existing solutions to two major categories such as handcrafted features descriptor and deep learning approaches.

4.1 Local and Global Approaches

The initial work of human action recognition is limited to pose somewhat or gesture recognition. The first step to recognize the human action in videos was introduced by Bobik and Davis [26]. They simplified human action using Motion History Images (MHI) and Motion Energy Images (MEI). The global MHI template is given by

$$(x, y, t) = \sum_{\tau=0}^{i-1} B(x, y, t-i), \tag{1}$$

where E_τ is obtained MEI at particular time instant τ, while $B(x, y, t-i)$ is binary image sequences represents detected objects pixels.

The local representation STIPs for action recognition introduced by Laptev et al. [27]. A local 3D Harris operator [23] show a good performance to recognized 3D data objects with less number of interest points and widely used in computer vision applications. It is based on local autocorrelation function and defined as

$$e(x, y) = \sum_{x_i\, y_i} W\left(x_{i,} y_i\right)[I(x_i + \Delta x + y_i + \Delta y) - I(x_i, y_i)]^2, \tag{2}$$

where, $I(\cdot,\cdot)$ is defined as the image function and x_i, y_i are the points in the Gaussian function W centred on (x, y), which defines the neighborhood area in analysis.

4.2 Deep Learning Approaches

After 2012, these architecture received initial successes with supervised approaches which overcome vanishing gradient problem by using ReLU, GPUs (reduced time complexities). Deep learning technique is data driven it lacks when training samples are less, so in the case of small activity dataset local and global feature extractors are good and efficient for classification purpose.

Li et al. [28] showed that 3D convolutional networks outperform the 2D frame based counterparts with a noticeable margin. The 3D convolution value at position (x, y, z) on the j^{th} feature map in the i^{th} layer is defined as,

$$v_{ij}^{xyz} = \tanh\left(b_{ij} + \sum_{m} \sum_{P=0}^{P_{i-1}} \sum_{Q=0}^{Q_{i-1}} \sum_{R=0}^{R_{i-1}} w_{ijm}^{pqr} v_{(i-1)m}^{(x+p)(y+q)(z+r)}\right), \tag{3}$$

where, R_i is the size of the 3D kernel along the temporal dimension while w_{ijm}^{pqr} is the $(p, q, r)^{\text{th}}$ value of the kernel connected to the m^{th} feature map in the previous layer. Karpathy et al. [29] proposed the concept of slow fusion to increase the temporal awareness of a convolutional network. Donahue et al. [30] addressed the problem of

action recognition through the cascaded CNN and a class of recurrent neural network (RCNN) which is also known as Long Short Term Memory (LSTM) networks is given as

$$h^t = \sigma\left(w_x x^t + w_h h^{(t-1)}\right) \tag{4}$$

$$z^t = \sigma\left(w_z h^{(t)}\right) \tag{5}$$

$$w_x \in \mathbb{R}^{r\times d},\ w_h \in \mathbb{R}^{r\times r},\ w_z \in \mathbb{R}^{m\times r} \tag{6}$$

Here, $x^{(t)} \in \mathbb{R}^d$ (external signal), $z^{(t)} \in \mathbb{R}^m$ (output signal), and $h^{(t)} \in \mathbb{R}^r$ (hidden state). The recurrent neural network is found to be best model for video activity analysis.

5 Discussion

In this section, we briefly discuss the advantages and disadvantages of both types of 2D and 3D datasets.

5.1 Advantages of RGB and RGB-D Dataset

It can observe that from Tables 3 traditional human activity datasets are recorded with a small number of actions recognition from segmented videos under somewhat controlled conditions. Some benchmarks downloaded from online media such as YouTube, movies and social videos sharing sites represent a realistic action scene which is more practical for real-life applications. UCF 101 dataset is the largest dataset in the context of some classes, video clips than UCF 11, UCF 50, Olympic sports and HMDB51 datasets. ActivityNet is large-scale RGB video dataset captured with complete annotated labels and bounding box. The 3D datasets have advantages over visual 2D dataset as they are less sensitive to illuminations because they are captured with multiple sensors system such as visual, acoustical, and inertial sensors systems. It can be observed that from Table 4, that the fusion of information using different sensors increases the recognition accuracy on depth dataset at the cost of increased complexities. The 3D Online RGB-D action dataset was recorded in a living room environment used for cross-action environment and real online action recognition. The NTU RGB + D dataset is having a large number of actions/actors among existing datasets and was captured with multiple modalities and different camera views. PKU-MMD is large scale benchmark focused on continuous multi-modalities 3D complex human activities with complete annotation information, and it is suitable for deep learning methods.

Table 3 Technical specification RGB and RGB-D dataset

Dataset	Resolution	FPS	Actions	Actors	Videos
KTH	160×120	25	6	25	600
Weizmann	180×144	50	10	9	90
IXMAS	390×291	23	13	11	1650
CASIA Action	320×240	25	8	24	1446
UCF Sports	720×480	10	10	–	150
Olympic Games	–	–	16	–	783
Hollywood	400×300 300×200	24	8	–	233
UT- Interaction	720×480	30	6	–	160
BEHAVE	640×480	25	6	5	163
HMDB51	320×240	30	51/-	–	6766
UCF50	320×240	25	50	–	6681
BIT-Interaction	320×240	30	8	–	400
UCF101	320×240	25	101	–	13320
YouTube Sports 1 M	–	–	487	–	1133158
ActivityNet	1280×720	30	203	–	27801
THUMOS'15	–	–	101	–	5600
ChaLearn: Action/Interaction	480×360	15	235	14	235
FCVID	–	–	239	–	91223
YouTube 8 M	–	–	4716	–	~800, 000
Okutama Action	3840×2160	30	12	9	44
MSR Action 3D	640×480	15	20	7	567
RGB-D HuDaAct	640×480	30	12	30	1189
CAD-60	640×480	25	12	4	60
Berkeley MHAD	640×480	30	11	12	
CAD-120	640×480	25	10	4	120
Hollywood 3D	1920×1080	24	14	*	650
MSR Action Pairs	320×240	30	10	6	180
UWA3D Multi-view	640×480	30	30	10	900
Northwestern-UCLA	640×480	30	10	10	1475
LIRIS	640×480, 720×576	25	828	21	*
UTD-MHAD	512×424	30	27	8	861
M^2I	320×240	30	22	22	1784
SYSU- 3D HOI	640×480	30	40	12	~ 480
G3Di	640×480	30	12	15	574
NTU RGB + D	512×424, 1920×1080	30	60	40	56880
PKU-MMD	512×424, 1920×1080	30	66/60	51/40	1076

Table 4 RGB and RGB-D dataset with state-of-the-art accuracy and techniques

Dataset	Classification technique	Max avg. accuracy (%)	Evaluation protocol	Reference year
Weizmann	Hybrid (SDGs + AESIs)	100	LOOCV	2016
KTH	Interest points (IP) with differential motion information	98.20	3-fold cross-validation	2016
IXMAS	HC-MTL + L/S Reg	94.7	Cross-View	2017
CASIA Action	Hierarchical Spatio-Temporal model (HSTM)	95.24	–	2017
Olympic Games	Motion Part Regularization	92.3	leave-one-group-out cross-validation	2015
Hollywood	Joint max margin semantic features, DCNN	48.58	Cross-View	2016
UT- Interaction	Hierarchical Spatio-Temporal Model (HSTM)	94.17	leave-one-out cross-validation (LOOCV)	2017
UCF-YouTube	Interest points (IP) with differential motion information	91.30	3-fold cross-validation	2016
BEHAVE	Group interaction zone(GIZ), (ARF + GCT + AF)	93.74	3-folds-cross-validation	2014
HMDB51	Multi-Stream Deep Network	67.8	–	2017
UCF50	HC-MTL + L/S Reg	80.63	LOGO (Cross-View)	2017
BIT-Interaction	4-level, Pachinko Allocation Model	93	10-fold cross-validation	2016
UCF101	Multi-Stream Deep Network	93.3	–	2017
YouTube Sports 1 M	HC-MTL + L/S Reg	89.7	LOGO (Cross-View	2017
ActivityNet	Spatial CNN + Motion features	53.8	–	2017

(continued)

Table 4 (continued)

Dataset	Classification technique	Max avg. accuracy (%)	Evaluation protocol	Reference year
THUMOS'15	Pyramid of Score Distribution Feature (PSDF)	40.9(0.1)	–	2016
ChaLearn: Action/Interaction	Fisher vector + iDT features	53.85	cross-validation	2015
FCVID	rDNN	76.0	–	2017
YouTube 8 M	NetVLAD + CG after pooling and MoE	83.0	–	2017
Okutama Action	SSD(RGB)	18.80	Cross-validation	2017
MSR Action 3D	ConvNets	100	cross-subject	2015
RGB-D HuDaAct	BoW with χ^2 kernel SVM	82.9	Cross-subject validation	2014
CAD-60	Decision-level fusion	96.4	cross-subjects	2015
Berkeley MHAD	Hierarchy of LDSs, HBRNN-L	100	–	2013
CAD-120	QQSTR with feature selection	95.2	4-fold cross-validation	2015
Hollywood 3D	Bag of features (BoF) with Disparity Pyramids	36.09	cross-validation	2014
MSR Action Pairs	HON4D + Ddisc	96	cross-validation	2013
UWA3D Multi-view	MSO-SVM	91.79 (0 degree)	Cross-view	2015
Northwestern –UCLA	CNN + Synthesized + Pre-trained	92.3	Cross-view	2017
LIRIS	Pose + Appearance + context	74 (recall)	–	2014
UTD-MHAD	Depth plus RGB using product rule	91.2	Cross-subject	2016
M^2I	FV/BoVW	92.33	Cross –view	2017
SYSU- 3D HOI	Joint heterogeneous features learning (JOULE)model	84.89 ± 2.29 (S2)	Cross-subject	2016

(continued)

Table 4 (continued)

Dataset	Classification technique	Max avg. accuracy (%)	Evaluation protocol	Reference year
G3Di	Hierarchical Transfer Segments (HiTS)	the average latency time 2 frames (66 ms)	Cross-subject	2016
NTU RGB + D	CNN + Synthesized + Pre-trained	87.21	Cross-view	2017
PKU-MMD	Joint Classification Regression RNN	64.20	Cross-view	2017

5.2 Disadvantages of RGB and RGB-D Dataset

Currently, there are many video datasets, despite this, there are limitations in automatically recognize and classify the human activities. The main reasons of such limitations in at least one of the form are the number of samples for each action, the length of clips, capturing environmental conditions, background clutter and viewpoints changes and some activities. The 2D datasets were recorded with a small number of actions to complex actions with a broad range of applications. The 2D datasets are faced more challenges like view variations, intra-class variations, cluttered background, partial occlusions, and camera movements than depth datasets. The RGB-D dataset is facing limitations of low resolutions, less training samples, the number of camera view, different actions, various subjects and less precision. Initial RGB-D datasets captured single actions videos frames under controlled indoor or lab environments. MSR Action 3D is restricted to gaming actions depth frames only. Northwestern-UCLA dataset was recorded with more than one Kinect sensors at the same time to collect multi-view representations. It becomes a challenge to handle and synchronize all sensors data information simultaneously.

6 Conclusion

A review of the various state-of-the-art datasets on human action has been presented. Human action datasets have been categorized into two major categories: RGB and RGB-D datasets. The challenges involved and specifications of these datasets have been discussed. The conventional RGB dataset faces the problems of a cluttered background, illumination variations, camera motion, viewpoints change and occlusions. It is a challenge for feature descriptors in activity recognitions datasets that meets the changing real-world environments. It is required robust evaluation techniques for cross-dataset validation, which will be useful for realistic scenarios applications.

References

1. Aggarwal, J.K., Ryoo, M.S.: Human activity analysis: a review. ACM Comput. Surv. **43**, 1–43 (2011)
2. Vishwakarma, S., Agrawal, A.: A survey on activity recognition and behavior understanding in video surveillance. Vis. Comput. **29**, 983–1009 (2013)
3. Edwards, M., Deng, J., Xie, X.: From pose to activity: surveying datasets and introducing CONVERSE. Comput. Vis. Image Underst. **144**, 73–105 (2016)
4. Dawn, D.D., Shaikh, S.H.: A comprehensive survey of human action recognition with spatiotemporal interest point (STIP) detector. Vis. Comput. **32**, 289–306 (2016)
5. Bux, A., Angelov, P., Habib, Z.: Vision-based human activity recognition: a review. Adv. Comput. Intell. Syst. **513**, 341–371 (2016)
6. Blank, M., Gorelick, L., Shechtman, E., Irani, M., Basri, R.: Actions as space-time shapes. In: Tenth IEEE International Conference on Computer Vision. Beijing (2005)
7. Dalal, N., Triggs, B., Schmid, C.: Human detection using oriented histograms of flow and appearance. In: Proceedings of the European Conference on Computer Vision (2006)
8. Xu, W., Miao, Z., Zhang, X.P., Tian, Y.: A hierarchical spatio-temporal model for human activity recognition. IEEE Trans. Multimedia **99**, 1 (2017)
9. Heilbron, F.C., Escorcia, V., Ghanem, B., Niebles, J.C.: ActivityNet: a large-scale video benchmark for human activity understanding. In: IEEE Conference on Computer Vision and Pattern Recognition. Boston (2015)
10. Ryoo, M.S., Chen, C.C., Aggarwal, J., Chowdhury, A.R.: An overview of contest on semantic description of human activities. In: Recognizing Patterns in Signals, Speech, Images and Videos. vol. 6388 (2010)
11. Vishwakarma, D. K., Singh, K.: Human activity recognition based on spatial distribution of gradients at sub-levels of average energy silhouette images. In: IEEE Transactions on Cognitive and Development Systems, vol. 9, no. 4, pp. 316–327. (2017)
12. Li, W., Zhang, Z., Liu, Z.: Action recognition based on a bag of 3D points. In: IEEE Computer Society Conference on Computer Vision and Pattern Recognition. San Francisco (2010)
13. Kong, Y., Liang, W., Dong, Z., Jia, Y.: Recognizing human interaction from videos by a discriminative model. IET Comput. Vis. **8**, 277–286 (2014)
14. Ni, B., Moulin, P., Yang, X., Yan, S.: Motion part regularization: Improving action recognition via trajectory group selection. In: IEEE Conference on Computer Vision and Pattern Recognition. Boston (2015)
15. Aggarwal, J., Xia, L.: Human activity recognition from 3D data- a review. In: Pattern Recognition Letters. vol. 48 (2013)
16. Lun, R., Zhao, W.: A survey of applications and human motion recognition with Microsoft Kinect. In: International Journal of Pattern Recognition and Artificial Intelligence, vol. 29 (2015)
17. Presti, L.L., Cascia, M.L.: 3D skeleton-based human action classification: a survey. Pattern Recogn. **53**, 130–147 (2016)
18. Zhang, J., Li, W., Ogunbona, P.O., Wang, P., Tang, C.: RGB-D based action recognition datasets: a survey. Pattern Recogn. **60**, 86–105 (2016)
19. Simonyan, K., Zisserman, A.: Two-stream convolutional networks for action recognition in videos. In: Proceedings of the Advances in Neural Information Processing Systems. (2014)
20. Chaquet, J.M., Carmona, E.J., Caballero, A.F.: A survey of video datasets for human action and activity recognition. Comput. Vis. Image Underst. **117**, 633–659 (2013)
21. Wang, P., Li, W., Ogunbona P.O., Escalera, S.: RGB-D-based motion recognition with deep learning: a survey. Int. J. Comput. Vis. (2017)
22. Hassner, T.: A critical review of action recognition benchmarks. In: IEEE Conference on Computer Vision and Pattern Recognition Workshops. Portland (2013)
23. Firman, M.: RGBD datasets: past, present and future. In: Proceedings of the IEEE Conference on Computer Vision and Pattern Recognition Workshops (2016)

24. Borges, P.-V.K., Conci, N., Cavallaro, A.: Video-based human behavior understanding: a survey. IEEE Trans. Circuits Syst. Video Technol. **23**, 1993–2008 (2013)
25. Bobick, A.F., Davis, J.W.: The recognition of human movement using temporal templates. IEEE Trans. Pattern Anal. Mach. Intell. **23**, 257–267 (2001)
26. Laptev, I.: On space-time interest points. Int. J. Comput. Vision **64**, 107–123 (2005)
27. Li, S., Xu, W., Yang, M., Yu, K.: 3D convolutional neural networks for human action recognition. IEEE Trans. Pattern Anal. Mach. Intell. **35**, 221–231 (2013)
28. Karpathy, A., Toderici, G., Shetty, S., Leung, T., Sukthankar, R., Fei-Fei, L.: Large-scale video classification with convolutional neural networks. In: IEEE Conference on Computer Vision and Pattern Recognition. Columbus (2014)
29. Donahue, J., Hendricks, L., Guadarrama, S., Rohrbach, M.V., Saenko, K., Darrell, T.: Long-term recurrent convolutional networks for visual recognition and description. In: Proceedings of the IEEE Conference on Computer Vision and Pattern Recognition (2015)
30. Sipiran, I., Bustos, B.: Harris 3D: a robust extension of the Harris operator for interest point detection on 3D meshes. In: The Visual Computer, vol. 27 (2011)

SITO Type Voltage-Mode Biquad Filter Based on Single VDTA

Chandra Shankar, Sajai Vir Singh, Ravindra Singh Tomar and Vinay A. Tikkiwal

Abstract A new biquad filter topology realizing three simultaneous voltage-mode filtering responses is reported in the work which employs only single active element in the form of voltage differencing trans-conductance amplifier (VDTA) and three passive elements as two grounded capacitors and one resistor. The realized filtering functions by the filter are lowpass (LP), bandpass (BP), and bandreject (BR). The proposed filter enjoys with reasonable total harmonic distortion, low active/passive sensitivities, and low power consumption. Moreover, the pole frequency can be tuned independent of quality factor by the means of currents. In order to verify the validity of the circuit, the proposed filter is simulated using PSPICE software in 0.18 μm CMOS technology.

Keywords VDTA · Voltage mode · Biquad · Filter · SITO

C. Shankar (✉)
Department of Electronics Engineering, JSS Academy of Technical Education, Noida 201301, India
e-mail: porwalchandra@gmail.com

S. V. Singh · V. A. Tikkiwal
Department of Electronics and Communications, Jaypee Institute of Information Technology, Noida 201304, India
e-mail: sajaivir75@gmail.com

V. A. Tikkiwal
e-mail: Vinay.anand@jiit.ac.in

R. S. Tomar
Department of Electronics and Communication Engineering, Anand Engineering College, Agra, India
e-mail: r_tomar15@rediffmail.com

B. S. Rawat et al. (eds.), *Advances in Signal Processing and Communication* ,
Lecture Notes in Electrical Engineering 526,
https://doi.org/10.1007/978-981-13-2553-3_25

1 Introduction

Nowadays, the current-mode approach is gained a lot of popularity among researchers for developing new analog blocks used in a number of applications of analog signal processing. The current-mode active elements, in which signal state is current rather than node voltages, have many advantageous features as compared to its voltage-mode counterpart such as extended bandwidth without any disturbance in gain part, much higher slew rate, and requirement of low supply voltage and thus consumes less power, etc. [1]. Initially, current conveyors (CCI, CCII, CCIII) and their variants such as DDCCII, DVCCII, FDCCII, etc., were introduced [2–7] as current-mode active elements in the literature. Later on, other active elements with having inbuilt electronic tuning ability such as OTA, CDTA, CCTA, CCCCTA, CFTA, VDTA, DDCCTA, etc. [8–14] were also proposed. Among them, a relatively new current-mode active element named as voltage differencing trans-conductance amplifier (VDTA) was introduced in 2011 [13]. After its inception, the element has been became popular in designing of analog biquad filters [13, 15, 16, 17, 18, 19, 20, 21] operating in different modes. A voltage-mode analog filter (VMBF) is one of the essential building blocks and has been found in many applications of analog signal processing such as audio system, loudspeaker, touch-tone dial telephone system, graphical equalizer system, ECG system, data acquisition systems, etc. [22].

A literature survey reveals that numbers of VMBFs have been reported [15, 16, 22–31] in available research literature. Out of these, few of the VMBFs presented in Refs. [15, 22–29] realize two or more filtering responses, simultaneously, by the use of only single voltage input signal. Remaining VMBFs in Refs. [16, 30, 31] can also realize multiple filtering functions but one at a time (not simultaneously) through appropriate selection of one or more inputs. However, the use of multiple input signals to realize filtering functions which further requires additional hardware to obtain multiple copies. In addition, few of the reported VMBFs among them are single active element based [15, 22, 27–29] while remaining uses more than one active element [23–26]. Since the designing of single element based circuits were always favorable and preferred for reduced cost, space, and power saving point of view, so the research work focuses here on studying and discussion of the VMBFs which realizes multiple filtering functions simultaneously, by the use of only single active element [15, 22, 27–29]. All the reported VMBFs based on single element as well as realizing simultaneous outputs, realize at most three filtering functions (LP, BP, BR [22] or LP, BP, HP [27, 28] or LP, BP [15, 29]). Apart from this, the VMBF circuits reported in Refs. [27, 28] suffers from one or more drawbacks such as (i) use of excess number of passive elements (three- resistors and two-capacitors) (ii) lack of electronic tunability feature (iii) use of more numbers of floating passive elements (two- resistors) not favorable for fabrication of integrated circuits point of view. Moreover, another reported filter in Ref. [22] also provides three filtering responses using two grounded capacitors and one resistor along with the features of electronic tunability. However, this circuit uses an excess number of transistors (33 numbers of MOS transistors), and thus, it may consume more power.

So keeping the above survey of VMBFs in mind, a new VMBF circuit is proposed which uses only single active element and simultaneously realizes three filtering functions namely, LP, BP, and BR, by the use of single input voltage signal. Apart from employing single VDTA as an active element, the proposed VMBF consists of two grounded capacitors and one resistor too. Further, the circuit is also less sensitive due to mismatching in active and passive components and offer electronic tunable feature of pole frequency independent of the quality factor. The functionality of the circuit is proven by PSPICE simulation using 0.18 μm MOS models form TSMC.

2 Voltage Differencing Trans-Conductance Amplifier

The block diagram of VDTA is shown in Fig. 1, whose ideal model can be characterized with the assist of following matrix equation as:

$$\begin{bmatrix} I_z \\ I_{x\pm} \end{bmatrix} = \begin{bmatrix} g_{m1} & -g_{m1} & 0 \\ 0 & 0 & \pm g_{m2} \end{bmatrix} \begin{bmatrix} V_p \\ V_n \\ V_z \end{bmatrix} \tag{1}$$

Where P and N are two high impedance input terminals and ideally draw zero current. The high impedance Z terminal mostly loaded with impedance, receive the current directly proportional to the voltage difference at P and N terminals. Moreover, the voltage across Z terminal is transferred in the form of current at trans-conductance type output terminals X+ and X-.

In above Eqn, the g_{m1} and g_{m2} are two trans-conductance parameters which are controlled by the VDTA biasing currents I_{B1} and I_{B2}, respectively. In Fig. 2, a CMOS implemented circuit of VDTA is also shown for which the mathematical expression of g_{m1} and g_{m2} can be derived and related with I_{B1} and I_{B2}, respectively, as

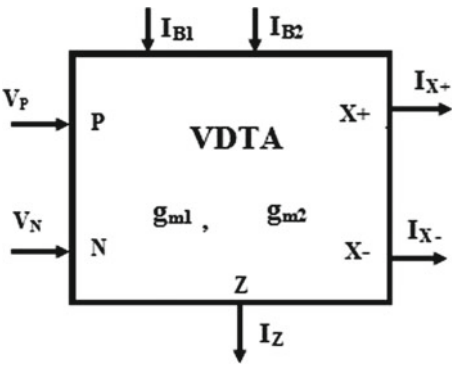

Fig. 1 Block diagram of VDTA

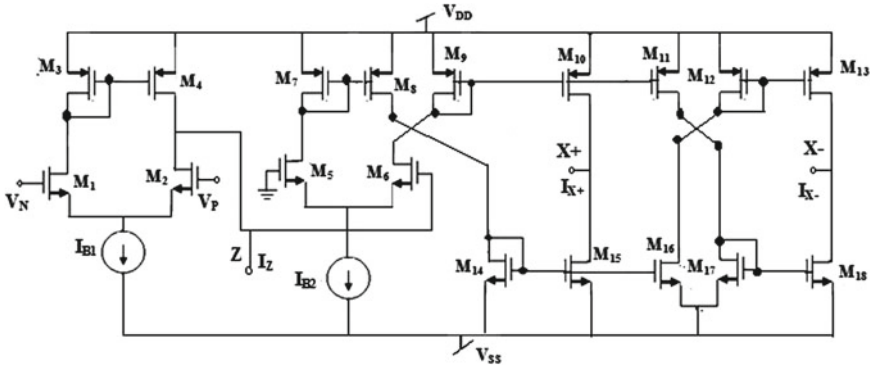

Fig. 2 CMOS realization of VDTA

$$g_{m1} = \sqrt{I_{B1}\mu_n C_{ox}\left(\frac{W}{L}\right)_{M1,M2}} \tag{2}$$

$$g_{m2} = \sqrt{I_{B2}\mu_n C_{ox}\left(\frac{W}{L}\right)_{M5,M6}}, \tag{3}$$

Where μ_n and C_{ox} are the effective carrier mobility of MOS transistors and gate oxide capacitance per unit area of n-MOS transistor, respectively. The $(W/L)_{M1,\,M2}$ and $(W/L)_{M5,\,M6}$ are the aspect ratio of NMOS transistors forming a differential pair in the architecture of VDTA.

3 Proposed VM Filter and Its Analysis

A proposed single input three output (SITO) VMBF employing only single VDTA as active element, two grounded capacitors (C_1 and C_2) and one resistor (R) as passive element is displayed in Fig. 3. On analyzing the VMBF of Fig. 3, the following transfer functions are obtained as:

$$\frac{V_{LP}}{V_{in}} = \frac{g_{m1}g_{m2}/C_1C_2}{D(s)} \tag{4}$$

$$\frac{V_{BP}}{V_{in}} = \frac{sg_{m1}/C_2}{D(s)} \tag{5}$$

$$\frac{V_{BR}}{V_{in}} = \frac{\left(s^2 + g_{m1}g_{m2}/C_1C_2\right)}{D(s)} \tag{6}$$

where

$$D(s) = \left[s^2 + \frac{s g_{m1} g_{m2} R}{C_2} + \frac{g_{m1} g_{m2}}{C_1 C_2} \right] \tag{7}$$

From Eqs. (4)–(6), it is clear that the proposed VMBF is capable of realizing three simultaneous filtering functions such as BR, LP, and BP. The various filter parameters such as the pole frequency (ω_0), the quality factor (Q_0), and bandwidth (BW) (ω_0/Q_0) of each filtering response are obtained as

$$\omega_0 = \sqrt{\frac{g_{m1} g_{m2}}{C_1 C_2}}, \; Q_0 = \frac{1}{R}\sqrt{\frac{C_2}{C_1 g_{m1} g_{m2}}}, \; BW = \frac{g_{m1} g_{m2} R}{C_2} \tag{8}$$

It can be concluded from Eq. (8) that by maintaining condition $g_{m1} = g_{m2} = 1/R = g_m$, ω_0 can be varied electronically without affecting the Q_0.

4 Non-Ideal Errors and Sensitivity Analysis

To visualize the influence of non-idealities on the performance of proposed circuit in Fig. 3, non-ideal gains of the VDTA are taken into consideration. The port depiction of non-ideal VDTA can be re-modeled through following matrix equation:

$$\begin{bmatrix} I_z \\ I_{x\pm} \end{bmatrix} = \begin{bmatrix} \beta_1 g_{m1} & -\beta_1 g_{m1} & 0 \\ 0 & 0 & \pm\beta_2 g_{m2} \end{bmatrix} \begin{bmatrix} V_p \\ V_n \\ V_z \end{bmatrix} \tag{9}$$

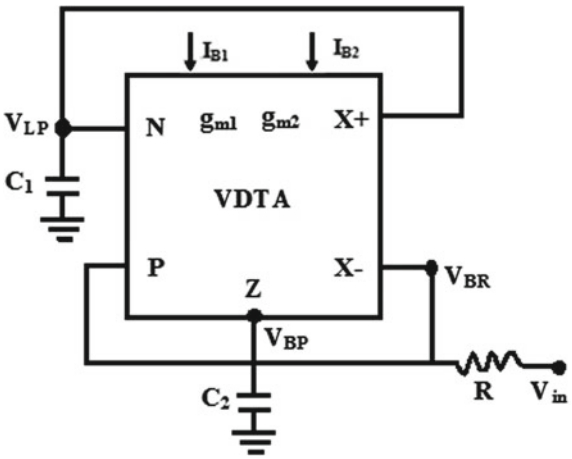

Fig. 3 The proposed VMBF

Where β_1 and β_2 are the trans-conductance gain errors for both stages of the VDTA. With new port descriptions of VDTA in Eq. (9), the proposed circuit has been reanalyzed and the corresponding transfer functions involving non-ideal factors are obtained as

$$\frac{V_{LP}^{'}(s)}{V_{in}} = \frac{\beta_1\beta_2 g_{m1}g_{m2}/C_1C_2}{D^{'}(s)} \tag{10}$$

$$\frac{V_{BP}^{'}(s)}{V_{in}} = \frac{s\beta_1 g_{m1}/C_2}{D^{'}(s)} \tag{11}$$

$$\frac{V_{BR}^{'}(s)}{V_{in}} = \frac{\left(s^2 + \beta_1\beta_2 g_{m1}g_{m2}/C_1C_2\right)}{D^{'}(s)} \tag{12}$$

Where

$$D^{'}(s) = \left[s^2 + \frac{s\beta_1\beta_2 g_{m1}g_{m2}R}{C_2} + \frac{\beta_1\beta_2 g_{m1}g_{m2}}{C_1C_2}\right] \tag{13}$$

With involved non-ideal factors, the ω_o, Q_o, and BW are altered to

$$\omega_0^{'} = \sqrt{\frac{\beta_1\beta_2 g_{m1}g_{m2}}{C_1C_2}},\ Q_0^{'} = \frac{1}{R}\sqrt{\frac{C_2}{C_1\beta_1\beta_2 g_{m1}g_{m2}}},\ BW^{'} = \frac{\beta_1\beta_2 g_{m1}g_{m2}R}{C_2} \tag{14}$$

From Eqs. (10) to (14), it is clear that ω_o, Q_o, BW, and the passband gain of the proposed filter will be obviously deviated from their nominal values due to the appearance of non-ideal factors. However, these deviations are very small and can be minimized and neglected because at the working frequencies transfer errors β_1 and β_2 can be approached to unity. The passive and active sensitivities of the proposed circuit are low, and their absolute values are not larger than unity as depicted in Eqs. (15)–(16). This ensures a low-sensitivity performance of the circuit.

$$S_{\beta_1,\beta_2}^{\omega_0} = \frac{1}{2},\ S_{g_{m1},g_{m2}}^{\omega_0} = \frac{1}{2},\ S_{C_1,C_2}^{\omega_0} = -\frac{1}{2} \tag{15}$$

$$S_{\beta_1,\beta_2}^{Q_0} = -\frac{1}{2},\ S_{g_{m1},g_{m2}}^{Q_0} = -\frac{1}{2},\ S_{C_1}^{Q_0} = -\frac{1}{2},\ S_{C_2}^{Q_0} = \frac{1}{2},\ S_R^{Q_0} = -1 \tag{16}$$

5 Simulation Results

The performance of proposed biquad filter as shown in Fig. 3 has been checked and verified by PSPICE simulations using CMOS model parameters of 0.18 μm form TSMC. The proposed filter circuit was energies with the supply voltages ($V_{DD} = -V_{SS}$) of ± 1.5 V and biasing currents ($I_{B1} = I_{B2}$) of 53 μA which resulted in the trans-conductances values $g_{m1} = g_{m2} \approx 473.5$ μA/V. The passive components were

Table 1 Aspect ratios of transistors for MOS implemented VDTA

Transistor	W(μm)/L(μm) Ratio
M_1, M_2, M_5, M_6	8.28/0.36
M_3, M_4	14.4/0.36
M_7–M_{13}	4.32/0.36
M_{14}–M_{18}	3.6/0.36

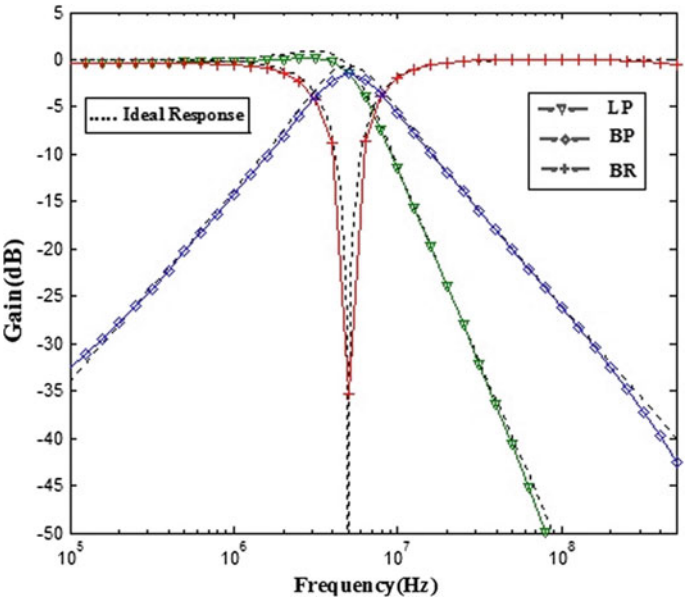

Fig. 4 Simulated and ideal magnitude response of proposed VMBF

taken as: $C_1 = C_2 = 15$ pF, $R = 2.25$ KΩ. The total power consumption of the circuit was found as about 0.816 mW. The transistors aspect ratio of the VDTA as described in Table 1 was determined and used in the simulation. Figure 4 shows the simulated results of magnitude responses of LP, BP, and BR of proposed filter circuit of Fig. 3. For the purpose of comparative study, the ideal magnitude responses of LP, BP, and BR of same filter circuit are also shown in Fig. 4. The measured value of pole frequency from the simulation results is 5.01 MHz which is found nearly same as the calculated or ideal value of 5.02 MHz.

Further to demonstrate the electronic tuning aspects of proposed VMBF in Fig. 3, the circuit was simulated to obtain various BP responses. Corresponding results show the electronic tuning capability of f_0 independent of Q_0, at the different frequency of 2.81, 4.88, 5.40, and 10.19 MHz, are shown in Fig. 5. This behavior was demonstrated by variation of both trans-conductance parameters (g_{m1} and g_{m2}) of VDTAs and resistor in a manner so that $g_{m1} = g_{m2} = 1/R$ as $g_{m1} = g_{m2} = 190.92$, 503.9, 712.62, 920 μA/V ($I_{B1} = I_{B2} = 20$, 60, 120, 200 μA) and resistor values as $R = 3.43$,

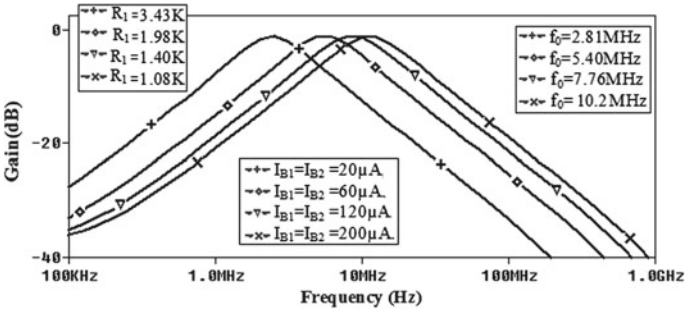

Fig. 5 Electronic tunability behavior of BP filer

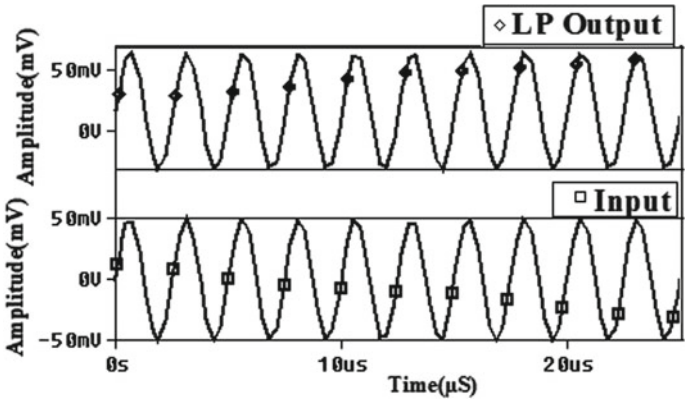

Fig. 6 Transient response of LP filter

1.98, 1.40, 1.08 KΩ, respectively. Lastly, the transient behavior of LP output for the proposed filter circuit is also observed in the circuit by testing it through sinusoidal input voltage signal of the maximum amplitude of 100 mV at the frequency of 400 kHz. Figure 6 shows the simulation results of the large signal transient responses of LP filter without any significant distortion.

6 Conclusion

In this study, the realization of a new VM biquadratic filter is presented. The proposed circuit is designed with only single VDTA, two grounded capacitors, and one resistor and can simultaneously realize three filtering functions, i.e., LP, BP, and BR in the voltage form by the use of single input voltage signal. The VM transfer functions for each filter type have been derived, and different performance characteristics of the circuit such as ω_o, Q_o, and BW have been analyzed with ideal aspects and also

with non-ideal influences. Moreover, the proposed circuit enjoys attractive features, such as (i) lower component sensitivity, (ii) current tunability of pole frequency (f_0) independent of Q_0, (iii) no requirement of inverted and/or scaled inputs for any realized response (s), (iv) consuming less power and (v) canonical structure as employs two grounded capacitors. Using P-SPICE and 0.18 μm CMOS technology, the simulation results have been found to be in good agreement with the theory.

References

1. Toumazou, C., Lidgey, F.J., Marks, C.A.: Extending voltage-mode Op-Amps to current-mode performance. Proc. IEE Pt. G. **137**(2), 116–129 (1990)
2. Smith, K.C., Sedra, A.: The current conveyor: a new circuit building block. Proc. IEEE **56**(3), 1368–1369 (1968)
3. Sedra, A.S., Smith, K.C.: A second generation current conveyor and its application. IEEE Trans. Circuit Theory. **17**, 132–134 (1970)
4. Fabre, A.: Third generation current conveyor: a new helpful active element. Electron. Lett. **31**(5), 338–339 (1995)
5. Elwan, H.O., Soliman, A.M.: Novel CMOS differential voltage current conveyor and its applications. IEE Proc. Circuits Devices Syst. **144**(3), 195–207 (1997)
6. Chiu, W., Liu, S.I., Tsao, H.W., Chen, J.J.: CMOS differential difference current conveyors and its applications. IEE Proc. Circuits Devices Syst. **143**(2), 91–96 (1996)
7. EI-adaway, A.A., Soliman, A.M., Elwan, H.O.: A novel fully differential current conveyor and applications for analog VLSI. IEEE Trans. Circuits Syst. II Analog Digital Signal Process. **47**, 306–313 (2000)
8. Park, C.S., Schaumann, R.A.: High frequency CMOS linear trans-conductance element. IEEE Trans. Circuits Syst. **33**(11), 1132–1138 (1986)
9. Tomar, R.S., Singh, S.V., Chauhan, D.S.: Current-processing current tunable universal biquad filter employing two CCTAs and two grounded capacitors. J. Circuits Syst. **4**, 443–450 (2013)
10. Biolek, D.: CDTA - building block for current-mode analog signal processing. In: Proceedings of the 16th European Conference on Circuit Theory and Design, CCTD'03, pp. 397–400. Krakow, Poland (2003)
11. Singh, S.V., Maheshwari, S., Chauhan, D.S.: Electronically tunable current/voltage- mode universal biquad filter using CCCCTA. Int. J. Recent Trends Eng. Technol. **3**(3), 71–76 (2010)
12. Singh, S.V., Tomar, R.S., Chauhan, D.S.: A new current tunable current input current output biquad using CFTAs. J. Eng. Sci. Technol. **12**(8), 2268–2282 (2017)
13. Yesil, A., Kacar, F., Kuntman, H.: New simple CMOS realization of voltage differencing transconductance amplifier and its RF filter application. Radioengineering. **20**(3), 632–637 (2011)
14. Chen, H.P.: High-input impedance voltage-mode differential difference current conveyor transconductance amplifier-based universal filter with single input and five outputs using only grounded passive components. Circuits Devices Syst. **8**(4), 280–290 (2014)
15. Park, K., Bang, J., Song, J.: A new low voltage tunable CMOS VDTA-based 10 MHz LP/BP filter. Smart Comput. Rev. **4**(4), 287–293 (2014)
16. Prasad, D., Bhaskar, D.R., Srivastava, M.: Universal voltage mode biquad filter using voltage differencing trans-conductance amplifier. Indian J. Pure Appl. Phys. **51**, 864–868 (2013)
17. Gupta, G., Singh, S.V., Bhooshan, S.V.: VDTA based electronically tunable voltage-mode and trans-admittance biquad filter. Circuits Syst. **6**, 93–102 (2015)
18. Shankar, C., Singh, S.V.: A new trans-admittance mode biquad filter using MO-VDTA. WSEAS Trans. Circuits Syst. **14**, 8–18 (2015)
19. Shankar, C., Singh, S.V.: A low voltage operable VDTA based biquad filter realizing band pass and high pass filtering functions in trans-admittance-mode. In: International Conference on Computing, Communication and Automation (ICCCA), pp. 1288–1293 (2015)

20. Shankar, C., Singh, S.V.: Single VDTA based multifunction trans-admittance mode biquad filter. Int. J. Eng. Technol. (IJET) **7**(6), 2180–2188 (2016)
21. Satansup, J., Pukkalanun, T., Tangsrirat, W.: Electronically tunable single-input five output voltage-mode universal filter using VDTAs and grounded passive elements. Circuits Syst. Signal Process. **32**(3), 945–957 (2012)
22. Singh, S.V., Maheshwari, S., Chauhan, D.S.: Single CCCCTA-based SITO biquad filter with electronic tuning. Multimedia, Signal Processing and Communication Technologies (IMPACT), pp. 172–175 (2011)
23. Soliman, A.M.: Kerwin-Huelsman-Newcomb circuit using current conveyor. Electron. Lett. **30**(24), 2019–2030 (1994)
24. Jaikla, W., Biolek, D., Siripongdee, S., Bajer, J.: High input impedance voltage-mode biquad filter using VD-DIBAs. Radioengineering. **23**(3), 914–921 (2014)
25. Tuntrakool, S., Kumngern, M., Sotner, R., Herenscar, N., Jaikla, W.: High input impedance voltage mode universal filter and its modification as quadrature oscillator using VDDDAs. Indian J. Pure Appl. Phys. **55**, 323–324 (2017)
26. Pandey, N., Paul, S.K., Bhattacharyya, A., Jain, S.B.: Voltage mode Tow Thomas universal filter: a current controlled conveyor approach. J. Active Passiv. Electron. Devices. **5**, 105–113 (2010)
27. Chen, H.P., Chien, W., Huang, G.W.: Single DVCC-based voltage-mode multifunction biquadratic filter. In: The International Multi-Conference on Complexity, Informatics and Cybernetics (IMCIC) (2010)
28. Arif, B., Ismail, M.U., Imran, A.: A versatile digitally programmable voltage mode multifunctional biquadratic filter. Int. J. Comput. Appl. **94**(15), 7–13 (2014)
29. Horng, J.W., Hou, C.L., Huang, W.S., Yang, D.Y.: Voltage/current-mode multifunction filters using one current feedback amplifier and grounded capacitance. Circuits Syst. **2**, 60–64 (2011)
30. Mekhum, W., Jaikla, W.: Three input single output voltage –mode multifunctional filter with independent control of pole frequency and quality factor. Theor. Appl. Electr. Eng. **11**(6), 494–500 (2013)
31. Singh, S.V., Tomar, R.S., Chauhan, D.S.: Single CCTA based four input single output voltage mode universal biquad filter. Int. J. Comput. Sci. Inf. Secur. **11**(3), 115–119 (2013)

Despeckling of Medical Ultrasound Images Using Fast Bilateral Filter and NeighShrinkSure Filter in Wavelet Domain

Amit Garg and Vineet Khandelwal

Abstract The diagnostic quality of medical ultrasound (US) images is affected by a multiplicative type of noise known as speckle noise. In this paper, a new denoising scheme based on thresholding of wavelet coefficients in different sub-bands is presented. NeighShrinkSure filter is used for thresholding detail band wavelet coefficients (high pass component). Also, as in medical US images approximation band coefficients (low pass component) also consist of speckle noise so fast bilateral is applied on these coefficients to improve the performance of proposed method. Experiments were performed on synthetic and real US images. The performance of the proposed method with four other existing methods is evaluated objectively and subjectively. Objective evaluation is carried out using parameters PSNR, SNR, SSIM and FOM and for subjective evaluation denoised US images obtained from all methods are inspected visually. The results obtained illustrate the effectiveness of the proposed method over other existing methods.

Keywords Fast bilateral filter · Medical ultrasound image
NeighShrinkSure filter · Speckle noise · Wavelet transform

1 Introduction

Ultrasound (US) images are very effective for diagnosis of a class of diseases related to human internal body parts. US images are popular due to its real-time operation, non-ionization, and non-invasive nature. US are low-resolution images obtained using an US scanning machine. US waves are transmitted inside the human body with a transducer probe and reflected US waves are recorded on a 2-D plane. The

A. Garg (✉) · V. Khandelwal
Jaypee Institute of Information Technology, Sec.62, Noida, India
e-mail: amitstp@gmail.com

V. Khandelwal
e-mail: vineet.khandelwal@jiit.ac.in

B. S. Rawat et al. (eds.), *Advances in Signal Processing and Communication* ,
Lecture Notes in Electrical Engineering 526,
https://doi.org/10.1007/978-981-13-2553-3_26

diagnosis capability of US images is limited due to various noises such as speckle noise, additive noise and system noise, etc. Speckle noise is a multiplicative type of noise which effects more severely than other types of noises in US images. The pattern of speckle noise is a granular type of structure and is generated at low and high acoustic frequencies [1]. Speckle noise in US images occurred due to interference phenomenon between transmitted US signal and returned echo signal obtained after reflection from various body parts viz. blood cells, bones, soft tissues, muscles, etc. Speckle reduction techniques in US images are classified as spatial domain methods; transform domain methods and hybrid methods. In spatial domain techniques, image denoising techniques are directly applied on image pixels using a spatial mask in image neighborhood. Popular filters for US speckle reduction in this category are Lee [2], Frost [3] and Kuan [4] filters. Transform domain methods are applied on transformed coefficients obtained after applying a suitable transform on image pixels. Transform domain techniques are further classified as (i) thresholding methods (ii) Bayesian modeling methods. In thresholding method a suitable threshold value is estimated from noisy wavelet coefficients for the shrinking of wavelet coefficients while Bayesian modeling methods use a prior distribution for the estimation of noise free coefficients. Although, modeling-based methods perform well however the performance is dependent on selection of a suitable prior in lieu of which the results obtained are not accurate. Transform domain techniques are proven to be the popular techniques from last two decades. Wavelet transform is mostly used transform because of its sparse and well localized representation of transformed coefficients. Using wavelet transform noise can be effectively removed and important signal properties can be preserved. Two popular methods of wavelet thresholding are hard thresholding and soft thresholding methods [5]. In hard thresholding methods all coefficients of value less than the threshold value are forced to zero and rest of the coefficients are retained while in soft thresholding methods all coefficients below threshold is set to zero and rest coefficients are scaled to threshold value. VishuShrink [6] is a well known wavelet thresholding technique employs universal threshold for noise estimation. SureShrink [7] is another wavelet based thresholding technique wherein universal threshold and Stein unbiased risk estimator (SURE) [7] technique is combined. In SureShrink method value of threshold is calculated for each of the wavelet sub-band. In BayesShrink scheme [8] the wavelet coefficients are assumed as random variables and threshold value in each sub-band is determined by assuming Generalized Gaussian Distribution (GGD) distribution of wavelet coefficients. Other denoising methods include hybrid methods which provide good denoising results. These methods are realized using combination of two or more filters such as BM3D filter [9]. Another hybrid method based on coefficient of dispersion parameter is presented in [10].

In this paper, a new wavelet based thresholding method is presented. This method exploits the advantages of fast bilateral filter [11] and NeighShrinkSure filter [12] for better denoising performance. Fast bilateral filter is the extension of conventional bilateral filter wherein filtering operation is done very fast as compared to traditional bilateral filter. Each of the, detail sub-band coefficients obtained after 2-D DWT of log transformed image are thresholded using NeighShrinkSure filter. This filter is

the advancement of popularly known NeighShrink filter, generally used for speckle noise reduction. Also, approximation coefficients are filtered using fast bilateral filter as speckle noise still exists in these coefficients after wavelet decomposition.

2 Model of Medical Ultrasound Image

The US echo signal consists of two main parts; reflected signal from human body and the noise component. The reflected signal is of practical use and the noise component consists of mainly two components: additive noise and multiplicative noise or speckle noise. Speckle noise corrupting US images can be modeled as given in Eq. (1) below [13].

$$h(x, y) = f(x, y).n(x, y) + g(x, y), \tag{1}$$

where, h(x,y) is the noisy image and f(x,y) is original image respectively. n(x,y) and g(x,y) represents multiplicative and additive noise components. The effect of additive noise component is less significant and can be ignored in Eq. (1), and the following Eq. (2) is obtained

$$h(x, y) = f(x, y).n(x, y). \tag{2}$$

The multiplicative speckle noise can be converted into additive noise by using log transformation and the model can be represented as given in Eq. (3) below

$$\log(h(x, y)) = \log(f(x, y)) + \log(n(x, y)). \tag{3}$$

3 Speckle Reduction Techniques

3.1 Fast Bilateral Filter

Bilateral filter [14] is yet an effective method for speckle noise reduction in approximation band but because of high complexity involved in these filters the scope is limited for real-time applications. US images are high-resolution images of large size due to which the performance of bilateral filter with US images is not giving promising results. Fast bilateral filters are used to increase the speed of traditional bilateral filter by several times. The output obtained from bilateral filter is given as in Eq. (4)

$$F(i) = \frac{\sum_{j\in\Omega} w(j)\phi(f(i-j) - f(i))f(i-j)}{\sum_{j\in\Omega} w(j)\phi(f(i-j) - f(i))}, \tag{4}$$

where w(i) is the spatial filter and ϕ(t) is the range filter. Ω is the size of spatial window. Spatial filter and range filters are expressed in Eqs. (5) and (6) below

$$w(i) = \exp\left(-\|i\|^2/2\sigma_d^2\right). \tag{5}$$

$$\phi(t) = \exp\left(-t^2/2\sigma_r^2\right), \tag{6}$$

where, σ_d and σ_r are 'geometric spread' and 'photometric spread' parameters respectively [14]. The direct implementation of the traditional bilateral filter given in Eq. (4) is slow and requires $O(W^2)$ number of operations for a single pixel. A fast shiftable bilateral filter [11] based on Fourier kernels are used in the proposed work. This filter is not limited to only Gaussian range filter but can also be applied with any arbitrary range filters having Fourier series convergence.

Finally, the output of fast bilateral filter according to [11] can be expressed as given below in Eq. (7)

$$\hat{F}(i) = \frac{\sum_{j\in\Omega} w(j)\psi_N(f(i-j)-f(i))f(i-j)}{\sum_{j\in\Omega} w(j)\psi_N(f(i-j)-f(i))}. \tag{7}$$

3.2 NeighShrinkSure Filter

NeighShrinkSure [12] is the improved version of the NeighShrink method [15], wherein SURE is incorporated with NeighShrink method. The limitation of NeighShrink method is that the threshold value and window size is fixed in each of the wavelet sub-band. This limitation is overcome in NeighShrinkSure method by estimating an optimal threshold value and window size in image neighborhood for NeighShrink method in each of the wavelet sub-band. Optimal threshold value and window size is estimated using SURE. The risk can be estimated using the below expressions

$$E\left\{\left\|\hat{\theta}_s - \theta_s\right\|_2^2\right\} = N + E\left\{\|h(w_s)\|_2^2 + 2\nabla\cdot h(w_s)\right\}, \tag{8}$$

where,

$$h(w_s) = \{h_n\}_{n=1}^{N} = \hat{\theta}_s - w_s;\ \nabla\cdot h \equiv \sum_n \frac{\partial h_n}{\partial w_n}. \tag{9}$$

$$h_n(w_n) = \hat{\theta}_n - w_n = \begin{cases} -\frac{T^2}{S_n^2}w_n & (T < S_n) \\ -w_n & (otherwise) \end{cases}. \tag{10}$$

$$\frac{\partial h_n}{\partial w_n} = \begin{cases} -T^2\frac{S_n^2 - 2w_n^2}{S_n^4} & (T < S_n) \\ -1 & (otherwise) \end{cases}. \tag{11}$$

$$\|h_n(w_n)\|_2^2 = \begin{cases} \frac{T^4}{S_n^4} w_n^2 & (T < S_n) \\ w_n^2 & (otherwise) \end{cases}. \tag{12}$$

$$SURE(w_s, T, L) = N + \sum_n \|h_n(w_n)\|_2^2 + 2 \sum_n \frac{\partial h_n}{\partial w_n}. \tag{13}$$

Equation (13) represents the estimation of risk in an arbitrary wavelet sub-band. Where, θ_s are unknown noise free wavelet coefficients and $\hat{\theta}_s$ is estimated noise-free wavelet coefficients. T is the optimal threshold value in each sub-band and L is the window size in neighborhood.

4 Speckle Noise Reduction Using Proposed Method

Figure 1 shows the block diagram of the proposed method. The following are the steps involved in the process of US image denoising using the proposed method:

1. Take log transformation of the noisy image to convert multiplicative noise into additive noise.

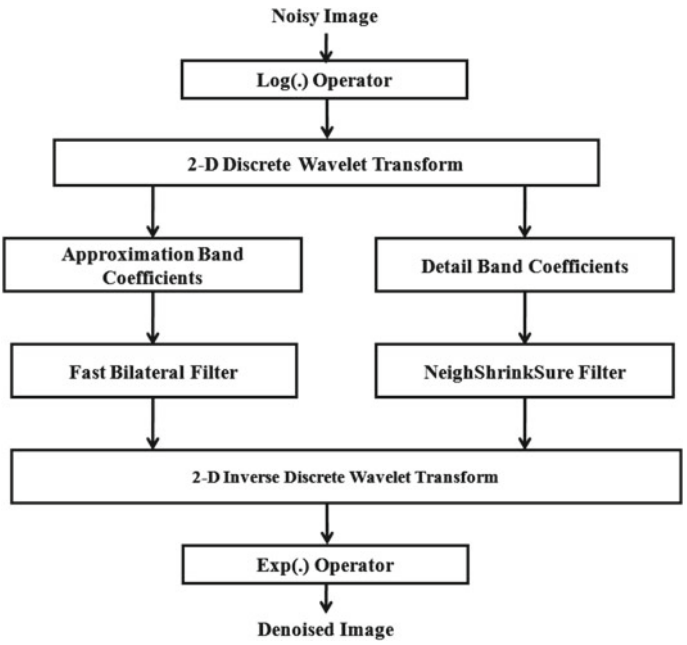

Fig. 1 Block diagram of proposed method

2. Apply 2-D DWT on log transformed image for J levels of decomposition to obtain an approximation band (low pass component) and N no. of detail bands (high pass components).
3. Then fast bilateral filter is applied on approximation band and NeighShrinkSure filter on each of the detail sub-bands obtained after J level decomposition of 2-D DWT.
4. Then denoised coefficients of detail and approximation bands are combined and 2-D IDWT is applied on it to obtain log compressed noise-free image.
5. Finally, exponential operator is applied on the image obtained from step-4 to create final denoised image.

5 Experimental Results

In this work objective and subjective results are presented for proposed method and other existing methods for speckle denoising. Objective evaluation parameters used in the experimentation are Peak Signal-to-Noise Ratio (PSNR) [16], Signal-to-Noise Ratio (SNR) [16], Structure Similarity Index Measures (SSIM) [17] and Pratt's Figure of Merit (FOM) [18]. Subjective evaluation is done by visualizing the denoised images obtained from proposed method and other methods. For synthetic image both objective and subjective evaluation is done while for real images only subjective evaluation is done as reference US image was not available. Synthetic image of kidney (469×522) generated using 'Field-II program' [19] software was taken as test US image. All the experimentation work is performed over MATLAB R2014a. The noisy images of speckle noise variance (σ^2) = 0.1, 0.2 and 0.3 was created using speckle model available with MATLAB. The results are obtained for proposed method and four other methods viz. Wiener [20], BayesShrink [8], Fast Bilateral filter [11], and NeighShrinkSure filter [12]. Wiener filter model used for the comparison purpose is taken from MATLAB and window size chosen is 5×5. In BayesShrink method denoising is performed using db4 wavelet with three levels (J = 3) of decomposition. For fast bilateral filter the value of σ_d are selected as 1, 1.6 and 1.9 for $\sigma^2 = 0.1$, 0.2 and 0.3 and $\sigma_r = 2\sigma$ is chosen for all σ^2 values. In NeighShrinkSure filter results are taken for four levels (J = 4) of decomposition for db1wavelet. Also, for the proposed method four levels (db1, J = 4) of wavelet decomposition is chosen with σ_d values of 11, 14 and 16 for $\sigma^2 = 0.1$, 0.2 and 0.3 respectively. The value of σ_r is chosen as 2σ in all the experiments for all noise variance values.

Table 1 Performance comparison of various image quality metric for synthetic kidney US image (469 × 522) at ($\sigma^2 = 0.1, 0.2, 0.3$)

Noise variance (σ^2)	Denoising methods	PSNR	SNR	SSIM	FOM
0.1	Noisy	20.6811	10.0717	0.3545	0.5853
0.2		17.8353	7.2259	0.2330	0.4483
0.3		16.2502	5.6408	0.1788	0.3732
0.1	Wiener [20]	24.7836	14.1742	0.7611	0.7117
0.2		22.1533	11.5439	0.6993	0.6435
0.3		20.7343	10.1249	0.5543	0.5352
0.1	BayesShrink [8]	24.5694	13.9600	0.6740	0.6732
0.2		22.1739	11.5645	0.5825	0.5756
0.3		20.0081	10.3987	0.5405	0.5673
0.1	Fast Bilateral [11]	26.4173	15.8079	0.6549	0.6255
0.2		23.7214	13.1120	0.5279	0.6129
0.3		20.7479	10.1385	0.4006	0.4409
0.1	NeighShrinkSure [12]	27.9508	17.3415	0.7440	0.6922
0.2		23.2356	12.9885	0.4819	0.4805
0.3		20.9016	10.2922	0.5498	0.4932
0.1	Proposed method	29.0593	18.450	0.7794	0.7326
0.2		24.5358	13.9264	0.6996	0.6720
0.3		21.7982	11.2371	0.5499	0.5921

Table 1 illustrates the performance comparison of proposed method and four other existing methods using objective evaluation criterion. PSNR, SNR, SSIM, and FOM parameter values are obtained at noise variance ($\sigma^2 = 0.1$, 0.2 and 0.3). It can be seen from Table 1 that for proposed method improved values of all assessment parameters are obtained. Although, proposed method performs well for an appropriate range of noise variance ($\sigma^2 = 0.1$–0.3) but improvement is more significant at $\sigma^2 = 0.1$.

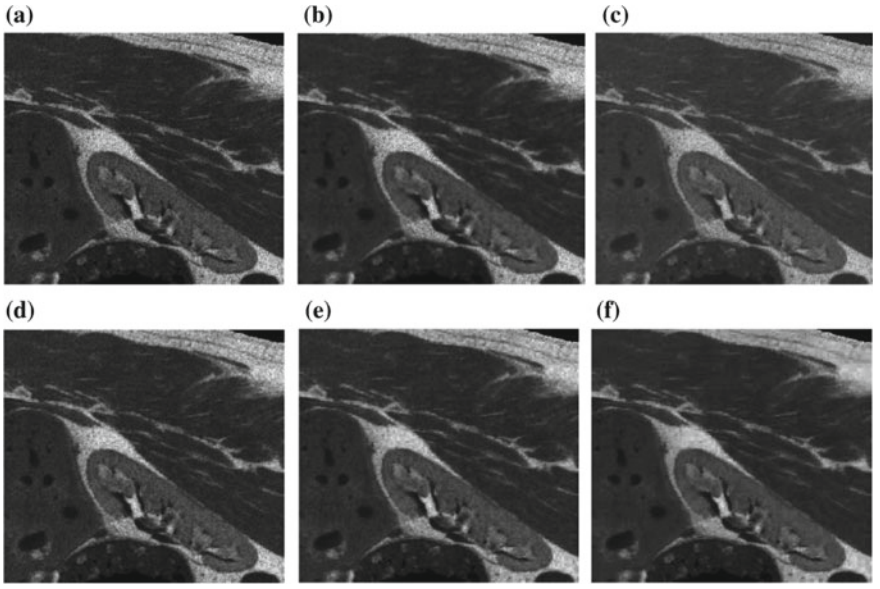

Fig. 2 Synthetic kidney US denoised images obtained from various denoising methods, **a** noisy image $\sigma^2 = 0.1$, **b** using Wiener filter, **c** using BayesShrink filter, **d** using Fast Bilateral filter, **e** using NeighShrinkSure filter, **f** using Proposed method

Figure 2a–f presents the synthetic kidney US images obtained using various denoising methods. From subjective evaluation of the images, it is obvious that the quality of the denoised image obtained using proposed method is better than other denoised images in terms of denoising and edge retention. Almost, similar quality of denoised images is obtained for fast bilateral filter and NeighShrinkSure filter. The performance of Wiener filter is the worst in all the filters used for comparison. The quality of the image obtained using BayesShrink method is better than the one obtained using Wiener filter but is not comparable with the images obtained using fast bilateral filter and NeighShrinkSure filter.

In order to examine the performance in real scenario, experiments are also performed on a set of 50 real US images [21]. For these images denoising results are obtained and compared for all the methods described above. Figure 3a–f shows a real head US images for subjective evaluation of the proposed method and other methods. It is to be noted that the quality of the denoised image obtained using proposed method as compared to other existing methods is better in terms of denoising and edge retention.

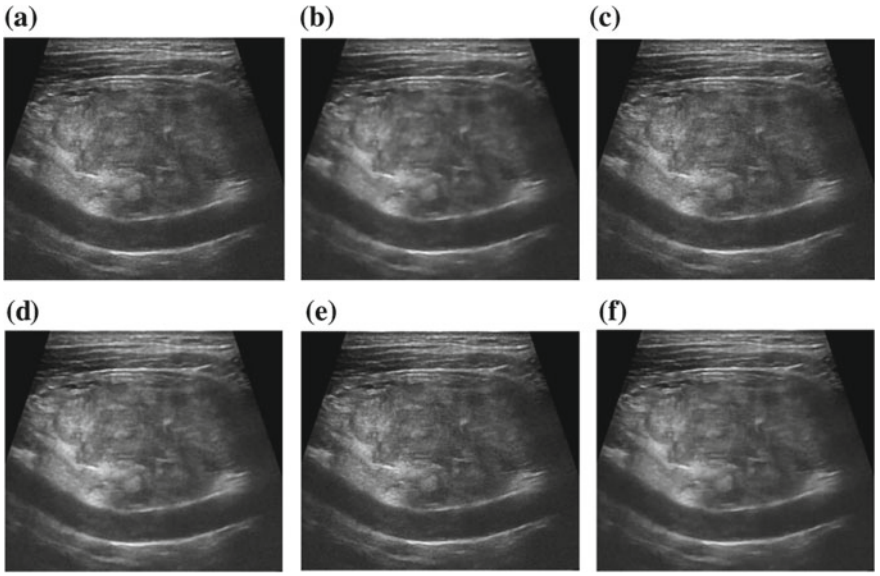

Fig. 3 Real head US denoised images obtained from various denoising methods, **a** noisy image, **b** using Wiener filter, **c** using BayesShrink filter, **d** using Fast Bilateral filter, **e** using NeighShrinkSure filter, **f** using Proposed method

6 Conclusion

A new US image denoising technique in transform domain was presented in this paper. NeighShrinkSure filter was used for filtering of detailed band coefficients and approximation band coefficients were passed through fast bilateral filter for better denoising performance. Synthetic US image of kidney (generated using 'Field-II Program') was used in the experimentation for objective and subjective quality evaluation of proposed method and other existing methods. Experiments were also conducted on a set of 50 real US images for subjective quality evaluation of proposed method and other methods. For visual quality inspection of denoising schemes a real head US image was used. It is evident from the experiments conducted on synthetic and real US images that the quality of denoised image obtained using proposed method is superior to the denoised images obtained from other existing methods.

Acknowledgements The authors would like to thank Jaypee Institute of Information Technology, Noida and Ajay Kumar Garg Engineering College, Ghaziabad for providing the necessary research facilities.

References

1. Wagner, R.F.: Statistics of speckle in ultrasound B-scans. IEEE Trans. Sonics Ultrason. **30**, 156–163 (1983)
2. Lee, J.S.: Digital image enhancement and noise filtering by use of local statistics. IEEE Trans. Pattern Anal. Mach. Intell. **2**, 165–168 (1980)
3. Frost, V.S., Stiles, J.A., Shanmugan, K.S., Holtzman, J.C.: A model for radar images and its application to adaptive digital filtering of multiplicative noise. IEEE Trans. Pattern Anal. Mach. Intell. **2**, 157–166 (1982)
4. Kuan, D.T., Sawchuk, A.A., Strand, T.C., Chavel, P.: Adaptive noise smoothing filter for images with signal-dependent noise. IEEE Trans. Pattern Anal. Mach. Intell. **2**, 165–177 (1985)
5. Burckhardt, C.B.: Speckle in ultrasound B-mode scans. IEEE Trans. Sonics Ultrason. **25**, 1–6 (1978)
6. Donoho, D.L., Johnstone, J.M.: Ideal spatial adaptation by wavelet shrinkage. Biometrika **81**, 425–455 (1994)
7. Chang, S.G., Yu, B., Vetterli, M.: Adaptive wavelet thresholding for image denoising and compression. IEEE Trans. Image Process. **9**, 1532–1546 (2000)
8. Donoho, D.L.: De-noising by soft-thresholding. IEEE Trans. Inf. Theory **41**, 613–627 (1995)
9. Dabov, K., Foi, A., Katkovnik, V., Egiazarian, K..: BM3D Image Denoising With Shape-Adaptive Principal Component Analysis. HAL Saint Malo (2009)
10. Garg, A., Khandelwal, V.: Speckle noise reduction in medical ultrasound images using coefficient of dispersion, pp. 208–212. Noida India, IEEE (2016)
11. Ghosh, S., Chaudhury, K.N.: On fast bilateral filtering using fourier kernels. IEEE Signal Process. Lett. **23**, 570–573 (2016)
12. Dengwen, Z., Wengang, C.: Image denoising with an optimal threshold and neighbouring window. Pattern Recogn. Lett. **29**, 1694–1697 (2008)
13. Goodman, J.W.: Some fundamental properties of speckle. J. Opt. Soc. Am. **66**, 1145–1150 (1976)
14. Tomasi, C., Manduchi, R.: Bilateral filtering for gray and color images, pp. 839–846. Bombay India, IEEE (1998)
15. Chen, G.Y., Bui, T.D., Krzyżak, A.: Image denoising with neighbour dependency and customized wavelet and threshold. Pattern Recogn. **38**, 115–124 (2005)
16. Mateo, J.L., Fernández-Caballero, A.: Finding out general tendencies in speckle noise reduction in ultrasound images. Expert Syst. Appl. **36**, 7786–7797 (2009)
17. Wang, Z., Bovik, A.C., Sheikh, H.R., Simoncelli, E.P.: Image quality assessment: from error visibility to structural similarity. IEEE Trans. Image Process. **13**, 600–612 (2004)
18. Pratt, W.K.: Digital Image Processing, 4th edn. Wiley, New York (2006)
19. Field II.: Ultrasound Simulation Program. http://field-ii.dk/examples/ftp_files/
20. Lim, J.S.: Two-Dimensional Signal and Image Processing. Prentice Hall, Englewood Cliffs (1990)
21. Image Database.: Ultrasound Cases. http://www.ultrasoundcases.info/

Density-Based Approach for Outlier Detection and Removal

Sakshi Saxena and Dharmveer Singh Rajpoot

Abstract This paper represents an algorithm for performing clustering and outlier detection simultaneously. As research says, clustering and outlier (anomaly) detection are not separate problems but they are co-related. So our algorithm provides a generalized solution for outlier detection as per application. It takes some threshold values as input, applies K-means algorithm for initial clustering and based on threshold values, outliers are detected. This approach is not strict to number of clusters k, but applies re-clustering where required. It helps to find local as well as global outliers of dataset. The results can be customized by varying the values of threshold limits. The algorithm works in two phases, first phase provides initial clustering using K-Means and second phase helps to find outliers.

Keywords Outlier · Outlier detection · K-means · Sparse cluster · Cluster density

1 Introduction

Since last decade, the widespread use of data mining applications in various government agencies, banking sector, colleges, universities, and business organizations has been observed. These applications allow us to find observations that cannot be collected manually. The corporations use the data mining apps in predicting the market behavior more accurately. Generally, data mining uses various techniques like association rule mining, classification, clustering, etc., to find the similar patterns in data. However, nowadays, outliers or disturbances or dissimilar patterns are also the area of research. These outliers help to find errors, frauds, or unwanted behavior of the system. Sometimes the presence of outlier may show a new upcoming trend in

S. Saxena (✉) · D. S. Rajpoot
Department of Computer Science Engineering/Information Technology,
Jaypee Institute of Information Technology, A-10, Sector – 62, Noida, India
e-mail: sakshisaxena04@gmail.com

D. S. Rajpoot
e-mail: dharmveer.rajpoot@jiit.ac.in

B. S. Rawat et al. (eds.), *Advances in Signal Processing and Communication* ,
Lecture Notes in Electrical Engineering 526,
https://doi.org/10.1007/978-981-13-2553-3_27

the society. So the outliers or anomalies can help to find the malicious and suspicious activities that cannot be find out otherwise.

1.1 Outlier and Its Types

An outlier is a pattern which seems inconsistent with the other set of data. Outliers may arise due to mechanical faults, human errors, instrumental errors, or some fraudulent behavior in the system [1]. Previously outlier was considered as noisy and useless data, but research proved the outlier detection as an interesting research area.

According to Karanjit et al. [2], outliers can be categorized as follows:

(a) **Point Outliers**- When the occurrence of particular data is as diminished as a single point in comparison to remaining dataset, it is called as Point outlier, these are found in fraud detection cases.
(b) **Contextual Outliers**- These are also known as conditional outliers. They found when any dataset is inconsistent with respect to any context.
(c) **Collective Outliers**- Collective outliers found when a related set of data is inconsistent with the complete dataset. They may not be the actual outliers.

1.2 Outlier Detection Based Techniques

Categorization of outlier detection techniques can be discussed as follows- (Fig. 1)

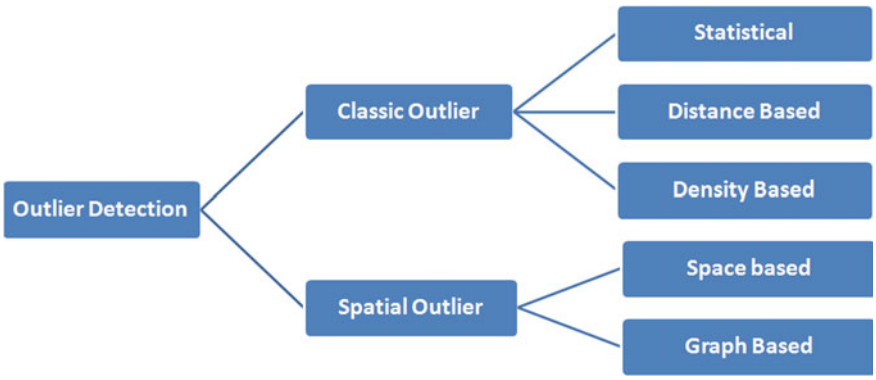

Fig. 1 Classification of outlier detection methods

Statistical-Based Outlier Detection

The Statistical-based approach uses parametric and non-parametric approaches to fit a statistical model on a provided dataset. The parametric approach considers the underlying distributions knowledge and find the parameters values for the outlier detection while non-parametric approach does not consider prior knowledge of given dataset.

Distance-Based Outlier Detection

To improve the above method, Knorr and Ng provided a new method based on Distance to detect and remove outliers. Distance based techniques are generally used to detect land mines with the help to satellite images. This method uses various approaches like k-nearest neighbors, etc., for detection.

Density-Based Outlier Detection

This method declares the objects as normal or anomalous on the basis of density of its neighborhood, i.e., if the density of the nearer block is less, the objects may be anomalous else treated as normal. To calculate the anomaly score Local Outlier Factor (LOF), Connectivity based Outlier Factor (COF), etc., are used.

Space-Based Outlier Detection

Space-based approach helps to find spatial subjective outliers. It uses midpoint space and widespread boundary space concept for outlier detection. The method uses Euclidean distances for distance calculations.

Graph-Based Outlier Detection

Graph-based approaches uses the concept of spatial outliers, spatial domain, and graph connectivity. This approach also helps to find spatial outlier. The connected graph is created for given dataset on the basis of K-nearest association. In next step, the mass boundaries are cut to find the spatial outliers.

1.3 Motivation and Contribution

The motivation for this research is as follows:-

1- Clustering is the process of finding patterns of similar pattern or properties. K-means is most popular clustering algorithm used for clustering. But restricted numbers of cluster ‘k’ may not provide efficient clusters, as sometimes it may have sparse clusters or overloaded (very large) clusters, so actual purpose of clustering to find chunks of similar data may not fulfill.
2- Clustering and outlier detection are co-related process, so we can propose an algorithm which can perform both the task simultaneously.

Our contribution is based on following factors:-

1- The proposed algorithm takes threshold values and no of clusters as input. It applies k-means clustering algorithm for clustering.
2- The very large and sparse clusters are re-clustered to find outliers and exact clusters.

2 Related Work

Outlier detection is a well known process of detecting anomalous observations from the data. These anomalies may occur due human error, technical or mechanical fault, noise, change in system, fraudulent behavior etc. This may also occur due to instrumental error and natural deviations. Outlier detection system helps to find system errors and fix them. The frauds can also be detected with outliers over the given datasets. Another benefit of outlier removal is to preprocess/purify the dataset for the further process. Computer Science and Statistical branch has provided various systematic detection methods that we have discussed in previous section. This paper also provides a concise survey of outlier detection approaches.

K-means is one of the best clustering algorithms of unsupervised learning; it is highly used in various data mining applications. The algorithm takes dataset having 'n' points and no of cluster 'k' as input and provides the set of centroids and 'k' clusters as output. The process grows iteratively and divides the whole dataset into 'k' disjoint sets of points that are named as clusters. The set of centroids contains mean of each cluster. As these clusters are disjoint in nature so every point belongs to only one cluster.

Data Set = Set of 'n' data Points
K = No of clusters
Size of dataset = n
Size of cluster = Points belongs to that cluster
Centroids = mean of respective cluster points

The K-means algorithm initializes a set of clusters and partition P. Now it iterates for convergence, if the initial partition is done correctly, the algorithm provides more dense clusters. K-means algorithm is an example of non-parametric estimator and provides 'k' locally dense clusters (Fig. 2).

Jiang et al. [3], presented a two phase algorithm for outlier detection and removal. To face the NP hard problem of outlier detection, author modified the K-Means algorithm. This algorithms works assigns the points to the clusters one by one and applies the concept that if the new point is far away from all the clusters and assign it to a new cluster. So the first step uses the updated K- Means to find clusters. In the second step, the Minimum Spanning Tree (MST) is created for above clusters. The outliers are detected by removing longest edges in the MST.

Ville et al. [4] presented a threshold-based approach for detecting outliers in given datasets. This approach initially creates clusters according to K-means algorithm. The ORC (Outlier Removal and Clustering Algorithm) helps to create clusters and detect outliers simultaneously. The algorithm removes the data points that are far away from their respective centroids based on threshold values. This method has lower error rate on datasets.

Sanjay et al. [5], presented an approach for outlier detection and removal and named it as "K-means- -", This algorithm uses K- Means as a initial step to find out clusters. The algorithms takes (k, l) as inputs and provides 'k' clusters and 'l' outliers as output. Runtime complexity of this algorithm is in linear in terms of no of data points. It tries to converge to local optima. This iterative algorithm is tested on both real and synthetic datasets.

3 Proposed Method

This research represents an algorithm for performing clustering and outlier detection simultaneously. As research says, clustering and outlier (anomaly) detection are not separate problems but they are co-related. So our algorithm provides a generalized solution for outlier detection as per application. It takes some threshold values as input, applies K-means algorithm for clustering and based on threshold values, outliers are detected according to density of the clusters. This approach is not strict to k clusters only, but applies re-clustering when required.

The analysis is based on following factors:

1. Clustering is the process of finding patterns of similar pattern or properties. K-means is most popular clustering algorithm used for clustering. But restricted numbers of cluster 'k' may not provide efficient clusters, as sometimes it may have sparse clusters or overloaded (very large) clusters, so actual purpose of clustering to find chunks of similar data may not fulfill.

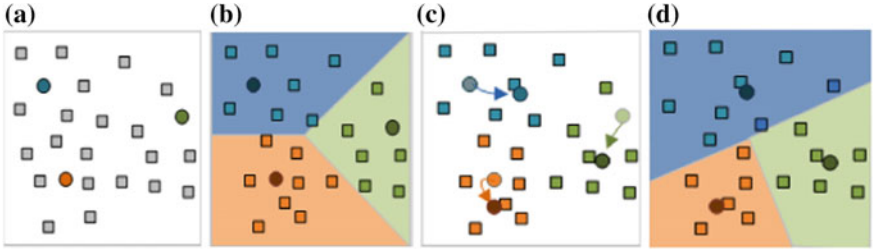

Fig. 2 **a** shows initial dataset, **b** shows initial partitioning, **c** shows iteration process, **d** shows final partitioning

2. Clustering and outlier detection are co-related process, so we can propose an algorithm which can perform both the task simultaneously.

The proposed algorithm takes some inputs from users, so that the results can be obtained as per the requirements. Some Important terms of algorithm are discussed as follows:

- Minimum (T_{min}) – Minimum Threshold value, a factor to determine a maximum no of objects in cluster that can be filtered as outlier. For example, In a dataset of 1000 records, if a cluster of 4–5 points is at a remarkable distance from the rest of data, then it can be termed as outlier, otherwise it will affect the quality of nearest cluster.
- Maximum (T_{max}) – The maximum no of objects any cluster can contain, as very large clusters may not provide better solutions for business applications.
- Density (T_{dense}) – Sometimes, a cluster has some outlier's points that make it sparse and change its quality. So the T_{dense} will contain the minimum density allowed for a cluster. As K-Means provides clusters of spherical shape. So density can be defined as the number of objects in cluster or volume of cluster.

Algorithm
Input: Dataset, k, T_{min}, T_{max}, T_{dense}
Output: Set of clusters, and set of outlier points

Step 1. Apply K-Means on dataset

Get the initial cluster centers
Find the nearest cluster for each data point
Recalculate the mean of all clusters
Repeat last two steps until convergence

Step 2. Examine each cluster,

Calculate no of objects, max distant point and cluster density for each cluster
Repeat Step 3, 4, 5 for all clusters

Step 3. If cluster has more than (Tmax*n) objects,

i. break it into small cluster
ii. Apply K-means locally
iii. Update cluster list
iv. Increase count

Step 4. If cluster has less than (Tmin*n) objects,

i. Outlier<-cluster
ii. Decrease count

Step 5. If cluster density<Tdense,

i. Recluster
ii. Selects the Fartherest Points from cluster center
iii. Remove the outlier Points from cluster
iv. Outlier<-Points

End

Step 1: This step applies K-Means algorithm on the dataset for initial clustering. K-Means is well defined clustering approach which divides dataset into k clusters according to the distance from their centroids.
Step 2: In this step clusters are examined and their attributes (No. of objects/points, point having maximum distance from mean and cluster density, etc.) are calculated for further steps.
Step 3: This step finds all the overloaded clusters (having data objects more than the threshold) and breaks them into two clusters.
Step 4: This step detects the clusters having very less data objects that can be neglected or termed as outliers.
Step 5: Fifth step finds the most distant points of the cluster that increase the error and declare them as outliers.

4 Results and Analysis

The Experiments were run on the PC with following specifications:

- Intel core i5 CPU
- 8 GB RAM
- Windows 7 Ultimate

The algorithm for testing running time is implemented in Python 3.6 on Spyder 3 IDE.

The analysis is based on the consideration that this algorithm does not follow the conventional clustering but updates the clusters (even no. of clusters) if required. It tries to provide the efficient data set to get the better analysis results by removing outliers (or anomalies that creates disturbances in data). The comparison results can be shown as follows in Table 1.

Table 1 Comparison of algorithms

Outlier detection algorithm	Types of outliers	Simultaneous clustering
Two phase clustering	Global	No
Improving K-means by outlier removal	Local	Yes
Density based approach	Global and local both	Yes

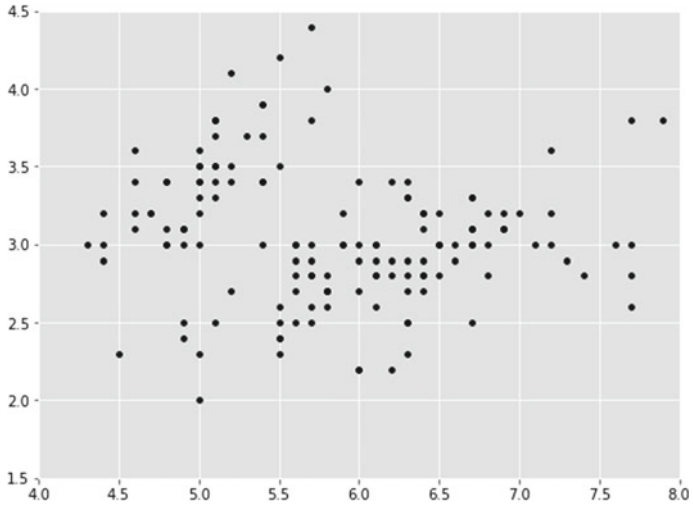

Fig. 3 Initial data set

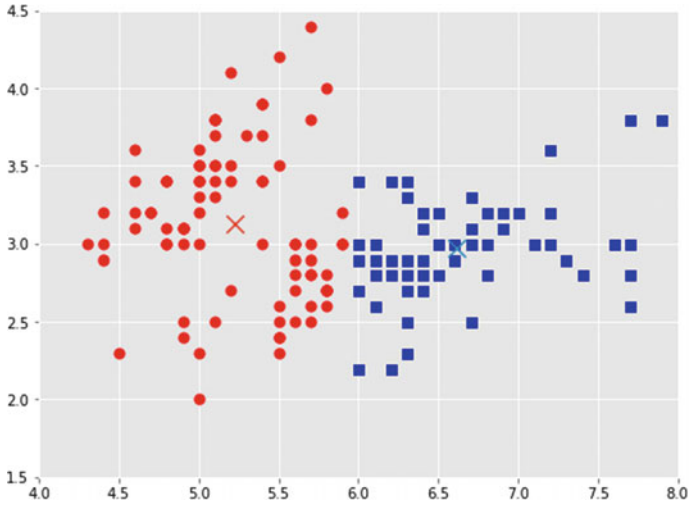

Fig. 4 Initial clustering k = 2

Above table shows that the proposed algorithm is able to find out local as well as global outliers along with clustering process. The quality of the clusters is measured with the help of density and mean square error of each cluster. The observations show that the final clusters have better density index and less mean square error.

This algorithm is implemented on **Iris 2-D data set**. Following images show the results of various stages of algorithm. Figure 3 shows the actual implementation of data set. After first stage, data set is divided into two clusters as shown in Fig. 4.

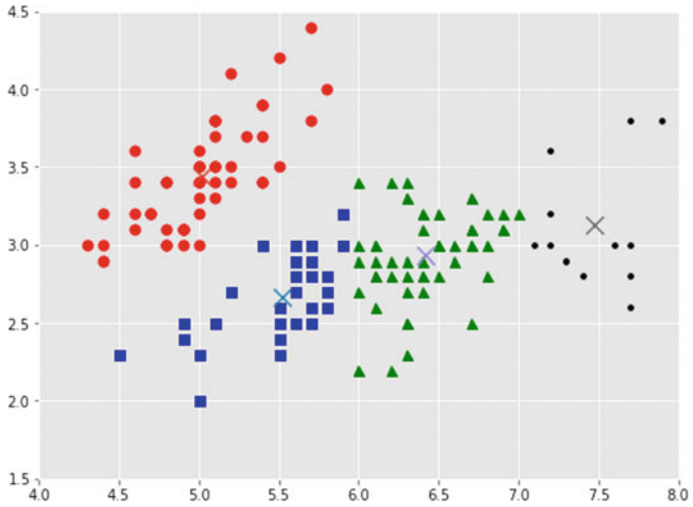

Fig. 5 Both overloaded clusters are broken

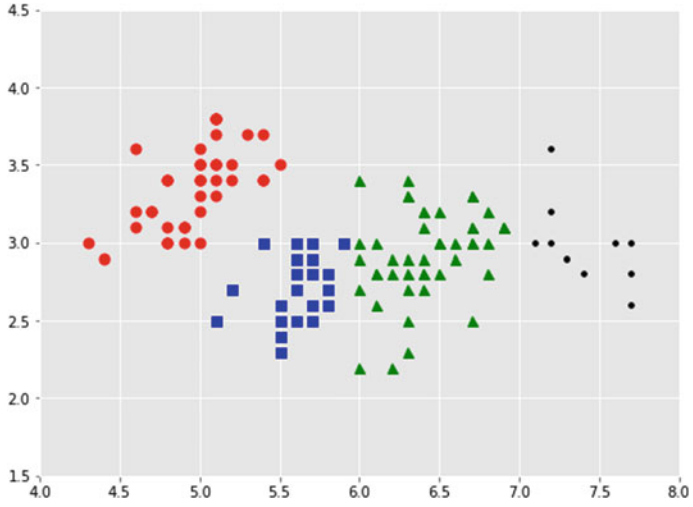

Fig. 6 Outliers removed via Threshold value 1.2

The implementation of clusters (in Fig. 5) shows that these clusters do not combine all the points of same region. As per proposed algorithm, these clusters are sparse (according to threshold value), so further re-clustered; now the dataset has four clusters as shown in Fig. 6.

Now, observing these clusters, we can observe the outliers, the points lying on a measurable distance from the cluster center. So now, Fig. 7 shows the better clusters by removing distant points (1.2 times more distant than average distance from cluster

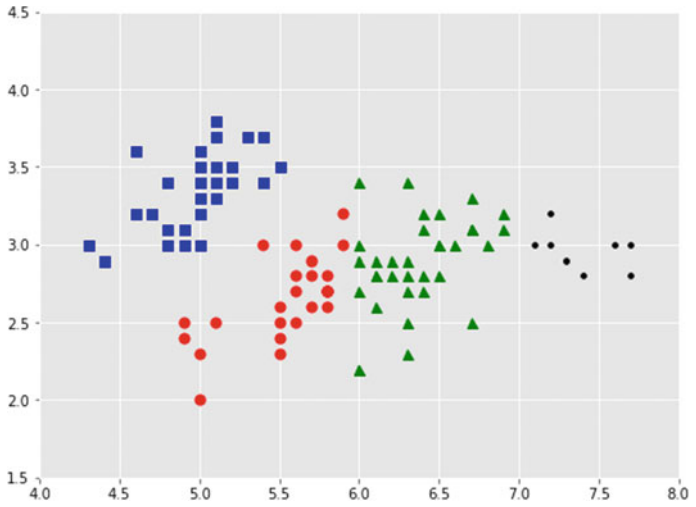

Fig. 7 Outliers removed via Threshold value 1.4

centroid). More dense clusters can be obtained by changing the threshold value from 1.2 to 1.4 or any other.

So, the algorithm as well as results can be customized as per application requirements. From the above figures, it is clear that global as well as local clusters are removed.

5 Conclusion

This algorithm provides a novel approach for finding outliers (global and local both types) and clusters simultaneously. Again the algorithm does not compromise with fixed number of clusters and breaks larger clusters into smaller if required. The proposed approach is compared with some other existing methods and comparison results are discussed. Proposed algorithm allows the users to analyze their results by just changing the threshold values as different threshold values may be required for different application.

References

1. Hodge, Victoria, Austin, Jim: A survey of outlier detection methodologies. Artif. Intell. Rev. **22**(2), 85–126 (2004)
2. Singh, Karanjit, Upadhyaya, Shuchita: Outlier detection: applications and techniques. Int. J. Comput. Sci. Issues **9**(1), 307–323 (2012)

3. Jiang, Mon-Fong, Tseng, Shian-Shyong, Chih-Ming, Su: Two-phase clustering process for outliers detection. Pattern Recogn. Lett. **22**(6), 691–700 (2001)
4. Hautamäki, V., Cherednichenko, S., Kärkkäinen, I., Kinnunen, T., Fränti, P.: Improving k-means by outlier removal. In: Scandinavian Conference on Image Analysis, pp. 978–987. Springer, Berlin (2005)
5. Chawla, S., Gionis, A.: k-means–: a unified approach to clustering and outlier detection. In: Proceedings of the 2013 SIAM International Conference on Data Mining, pp. 189–197. Society for Industrial and Applied Mathematics (2013)
6. Niu, Z., Shi, S., Sun, J., He, X.: A survey of outlier detection methodologies and their applications. In: Artificial Intelligence and Computational Intelligence, pp. 380–387 (2011)
7. Bansal, R., Gaur, N., Narayan Singh, S.: Outlier detection: applications and techniques in data mining. In: 2016 6th International Conference Cloud System and Big Data Engineering (Confluence), pp. 373–377. IEEE (2016)
8. Radovanović, Miloš, Nanopoulos, Alexandros, Ivanović, Mirjana: Reverse nearest neighbors in unsupervised distance-based outlier detection. IEEE Trans. Knowl. Data Eng. **27**(5), 1369–1382 (2015)
9. Tang, G.: New Methods in Outlier Detection. Ph.D. diss. Simon Fraser University (2015)

An Improved Design Technique of Digital Finite Impulse Response Filter for Notch Filtering

Anil Kumar, Kuldeep Baderia, G. K. Singh, S. Lee and H.-N. Lee

Abstract In this paper, an improved method for the design of finite impulse response (FIR) filter for notch filtering is devised using fractional derivative (FD). Optimal design of FIR notch filter is formed as minimization of mean squared error with respect to filter coefficients, subjected to fractional constraint imposed at notch frequency. Solution of this problem is computed using the Lagrange multiplier method. On experimental analysis, it is observed that the fidelity parameters like passband error (Er_p), notch bandwidth (BW_N), and maximum ripple (δ_p) varies nonlinearly with respect to FD values. Also, the exploration of suitable FD value is computationally costly. Thus, to acquire the best solution, modern heuristic methods known as hybrid particle swarm optimization (Hybrid-PSO), which is stimulated by the intelligence of some biological species, is employed. An exhaustive analysis results reveals that second-order FDCs approach results in drop of Er_p by 50%, and BW_N is improved by more 12%, while it is increased for only certain cases. It is also observed that the proposed methodology for convergence requires 100 iterations at most. The designed notch filter is tested for elimination of power line interference introduced in an electrocardiography (ECG) signal and efficient response is observed.

A. Kumar
PDPM Indian Institute of Information Technology,
Design and Manufacturing Jabalpur, Jabalpur 482005, Madhya Pradesh, India
e-mail: anilkdee@gmail.com

K. Baderia (✉)
Jaypee Institute of Information Technology, Noida 201309, Uttar Pradesh, India
e-mail: kuldeep.baderia@jiit.ac.in; kuldeep_gec2000@yahoo.co.in

G. K. Singh
Indian Institute of Technology Roorkee, Roorkee 247667, Uttarakhand, India
e-mail: gksngfee@gmail.com

S. Lee · H.-N. Lee
School of Electrical Engineering and Computer Science,
Gwangju Institute of Science and Technology, Gwangju, South Korea
e-mail: seungchan@gist.ac.kr

H.-N. Lee
e-mail: heungno@gist.ac.kr

B. S. Rawat et al. (eds.), *Advances in Signal Processing and Communication* ,
Lecture Notes in Electrical Engineering 526,
https://doi.org/10.1007/978-981-13-2553-3_28

Keywords Notch filter · Fractional derivative (FD) · Swarm intelligence Hybrid-PSO · Lagrange multiplier

1 Introduction

Signal filtering is the essential task in signal processing applications and that makes digital filters as a vital element. These digital filters have been classified as the finite impulse response (FIR) and infinite impulse response (IIR) filters. FIR filter consists of transfer function having all zero's, which makes them always stable system functions, and is used widely in filtering and filter banks [1–3]. FIR based notch filters are highly employed in the removal of interference due to individual frequency element. Literature review briefs three methods named as (i) windowed Fourier series approach; (ii) frequency sampling approach, and (iii) optimized FIR filter design approach, which were used for notch filter design [4, 5].

In an optimized FIR notch filter design approach, an equitable passband ripples get introduced, while the frequency sampling method takes to quit high interpolation error, because frequency response changes drastically through the notch point. Other familiar methods put forward for minimization of maximum error in frequency response are McClellan–Parks–Rabiner (MPR) computer program and standard linear programming technique. Equiripple FIR filters are generally designed using MPR algorithm, while standard linear programming is employed for the design of Equiripple FIR notch filter. However, this method requires vast memory and eats more computational time. Multiple exchange algorithm method is another approach, which is used to design the notch FIR filter with equiripple ripple content (Equiripple FIR notch filter) [6]. The authors also developed two modified versions to reduce the ripple content in lower frequency band, because most of the energy of biomedical signals lay in lowpass region [6]. Recently, a new method has been proposed, in which notch bandwidth is controlled by selecting odd order derivative constraints so that maximally flat, linear phase FIR notch response may be obtained [7].

Fractional derivative (FD) has emerged as a performance booster in numerous signal processing problem solutions like event detection in biomedical signals [8], image sharpening [9, 10], and accurate passband filter design [11]. FD inherits the memory effect of electrical circuits and chemical reaction, which helps in smooth pursuing. Therefore, fractional derivatives are exhaustively tested by researchers [12–20]. In [12–15], authors put forward a new scheme for designing simple digital FIR filters with improved passband (PB) response, wideband fractional delay filters using fractional derivatives. However, the value of suitable FD is determined by the chain of series of experiments with different values, thus eats to much computational time. To overcome this problem, the authors proposed a unique solution to determine the suitable FD order along with respective value using evolutionary techniques (ETs) like particle swarm optimization (PSO), artificial bee colony (ABC) algorithm, cuckoo search (CS) optimization, etc., to determine optimal value of order of FD for designing FIR filters and filter banks [16–20]. Recently, FD with ET-based approach

has been devised in optimization of IIR filters response in passband along with linear phase [21]. It has been observed that in the expression of a fractional integration, there is a nonlocal operator, which suffices that fractional derivative is also a nonlocal operator. Thus, FD consists of a unique property of apprehending the history of a variable, which is not simply conquerable by integer order derivative only [22].

Therefore, the literature review reflects that designing of FIR notch filters have been performed either as equiripple or improved notch response. The authors in [11], have proposed a method to satisfy the simultaneously notch attenuation and with notch bandwidth using FD constraint approach. However, in this approach, FD term is found by executing series of experiment with different fractional values, and then the best value of FD is picked up by sorting the corresponding solution, which has least value of error. Therefore, in this paper, a new improved ET known as Hybrid-PSO has been modeled to find the best FD order and its value.

2 Overview of Hybrid Particle Swarm Optimization

PSO is one of the most practiced swarm intelligence-based ET, which has been devised for solving numerous optimization problems [23]. PSO has simple structure of exploration with efficient exploitation of search space ($\boldsymbol{X}$), which makes this algorithm faster to converge [24]. Although PSO may be trapped in local minima during the course of exploration; and therefore, the authors in [25], have proposed Hybrid-PSO, which consist of search mechanism of PSO with replacement strategy of artificial bee colony (ABC) algorithm. Exploration of optimal solution is conquered using the following principle equations [24]:

$$\boldsymbol{V}_{a,b}^{k+1} = \chi\left\{w \cdot \boldsymbol{V}_{a,b}^{k} + c_1^k \cdot \varphi_1 \cdot (\boldsymbol{PB}_{a,b}^{k} - \boldsymbol{X}_{a,b}^{k}) + c_2^k \cdot \varphi_2 \cdot (\boldsymbol{gb}_{1,b}^{k} - \boldsymbol{X}_{a,b}^{k})\right\} \quad (1)$$

and

$$\boldsymbol{X}_{a,b}^{k+1} = \boldsymbol{V}_{a,b}^{k+1} + \boldsymbol{X}_{a,b}^{k}, \text{ where } a, b \in i, j. \quad (2)$$

In Eqs. (1) and (2), $k+1$ is the current iteration cycle, $\boldsymbol{V}$ is the velocity matrix, and $\boldsymbol{X}$ is search space matrix of dimension $i \times j$, such that each element of $\boldsymbol{V}$ is associated updated factor of respective element of $\boldsymbol{X}$, and χ is the constraint factor. This allows to be explored in multiple dimension using two guiding components namely; personal best solution matrix ($\boldsymbol{PB}$) and global best solution vector ($\boldsymbol{gb}$). To control the exploration and exploitation, c_1 and c_2 are associated and φ_1 and φ_2 are randomly disturbed number in range of [0, 1). In Hybrid-PSO, during the course of exploration, if any solution of $\boldsymbol{X}$ is not able to progress when compared with the corresponding solution of $\boldsymbol{PB}$, then associated count value is incremented by 1. If this count value reaches the threshold limit (*limit*), then corresponding $\boldsymbol{X}$ solution is replaced by current $\boldsymbol{gb}$, and supports efficient utilization of $\boldsymbol{X}$, which results in overcoming local minima trapping [23].

3 Overview of Fractional Derivatives

In recent decade, immense use of fractional calculus in numerous problems of signal processing has been tested [12–20]. Three prominently established expression for evaluation of fractional derivative (FD) named as Riemann–Liouville (RL), Grünwald–Letnikov (GL), and Caputo are widely accepted. GL FD is mostly used, because it is established on the standard differential operator, however, it is applicable to uninformed order with a discrete summation and binomial coefficient term [26]. GL FD is computed as [11]

$$D^u f(t) = \frac{d^u f(t)}{dt^u} = \lim_{\Delta \to 0} \sum_{l=0}^{\infty} \frac{(-1)^l I_l^u}{\Delta^u} f(t - l\Delta), \tag{3}$$

and the coefficient I_l^u is computed as

$$I_l^u = \frac{\Gamma(u+1)}{\Gamma(l+1)\Gamma(u-l+1)} = \begin{cases} 1, & l = 0 \\ \frac{[u(u-1)(u-2)\ldots(u-l+1)]}{1,2,3,\cdots,l}, & l \geq 1 \end{cases}. \tag{4}$$

4 Design Procedure of Notch Filter Using Fraction Derivative Constraint

The function of filter is to nullify the effect of a particular frequency distinctly, and do not alter the other frequencies. Notch filter response is defined by

$$H_o\left(e^{j\omega}\right) = \begin{cases} 0, & \omega = \omega_{nc} \\ 1, & \omega \neq \omega_{nc} \end{cases}, \tag{5}$$

where ω_{nc} denotes the notch frequency. The notch filter response may be obtained by designing a causal FIR filter with order of N with transfer defined as [11]

$$H_{nc}\left(e^{j\omega}\right) = \sum_{n=0}^{N} h(n) \cdot e^{-j\omega n} \tag{6}$$

The above equation shows that the transfer function with all zero's having a linear phase response. The behavior of impulse response $\{h(n)\}$, whether symmetric or anti-symmetric, categories FIR filters in four types as Type-1 to Type-4 [11]. In this paper Type-1 filter, which has symmetric impulse response with even order (N) is taken for design purpose. Thus, Eq. (6) may be reframed as

$$H_{nc}\left(e^{j\omega}\right) = e^{-j\omega\frac{N}{2}} \left\{ h\left(\frac{N}{2}\right) + 2 \cdot \sum_{n=0}^{N/2-1} h(n) \cdot \cos\left(\omega\left(\frac{N}{2} - n\right)\right) \right\} = H(\omega) \cdot e^{-j\omega\frac{N}{2}}., \tag{7}$$

Let $N/2 = M$ and $H(\omega)$ is the filter response that is computed as

$$H(\omega) = \sum_{m=0}^{M} a(m) \cdot \cos(\omega m), \tag{8}$$

and

$$a(m) = \begin{cases} h(m) & m = 0 \\ 2 \cdot h(M - m) & 1 \leq m \leq M \end{cases} \tag{9}$$

Computation of $H(\omega)$ may be performed in matrix form as

$$H(\omega) = \mathbf{a}^T \cdot \mathbf{C}, \tag{10}$$

where T denotes the transpose and

$$\mathbf{a} = \Big[a(0)\ a(1) \cdots a(M) \Big], \tag{11}$$

and

$$\mathbf{C} = \Big[1\ \cos(\omega) \cdots \cos(M\omega) \Big]. \tag{12}$$

Now, the problem is reduced to find $\boldsymbol{a}$ such that $H(\omega)$ must be close to the desired response $H_o(\omega)$ shown in Eq. (5). For this, an error function is formed and minimized as

$$J(\mathbf{a}) = \int\limits_{\omega \in ROI} (H_{nc}(\omega) - H(\omega))^2 d\omega, \text{ where, } ROI \text{ is the region of interest.} \tag{13}$$

The above form error function on simplification gives

$$J(\boldsymbol{a}) = \left(\boldsymbol{a}^T \cdot \boldsymbol{Q} \cdot \boldsymbol{a}\right) - \left(2 \cdot \boldsymbol{p}^T \cdot \boldsymbol{a}\right) + \alpha, \tag{14}$$

matrix $\boldsymbol{Q}$, vector $\boldsymbol{p}$, and scalar α are given by [11]

$$\boldsymbol{Q} = \int\limits_{\omega \in ROI} \boldsymbol{C} \cdot \boldsymbol{C}^T d\omega, \tag{15}$$

$$\boldsymbol{p} = \int\limits_{\omega \in ROI} (H_o(\omega) \cdot \boldsymbol{C}) d\omega, \tag{16}$$

and

$$\alpha = \int_{\omega \in ROI} \{H_o(\omega)\}^2 d\omega. \tag{17}$$

Now on the differentiation of Eq. (14) with respect to $\boldsymbol{a}$ and equating to zero, it gives conventional least squares design solution as $\boldsymbol{a}_{LS} = \boldsymbol{Q}^{-1} \cdot \boldsymbol{p}$ To get accuracy notch at prescribed frequency with controlled notch bandwidth (BW_N), the following constraints are imposed on the response $H(\omega)$ as [11]:

$$H_{nc}(\omega_{nc}) = H_o(\omega_{nc}) = 0, \tag{18}$$

$$DH(\omega_{nc}) = 0, \tag{19}$$

and

$$D^u H(\omega_{nc}) = \beta(u-1) \tag{20}$$

In Eq. (20), u is the FD of $H(\omega_{nc})$ evaluated at ω_{nc} and β is the prescribed constant, and for this work, it is taken as 30 [11]. By using Eq. (3d) mentioned in [11], $D^u H(\omega)$ is computed as

$$D^u H(\omega) = \frac{d^u\left(\sum_{m=0}^{M} a(m)\cos(\omega m)\right)}{d\omega^u} = \sum_{m=0}^{M} a(m)\frac{d^u \cos(\omega m)}{d\omega^u}$$

$$= \sum_{m=0}^{M} a(m)\cdot m^u \cdot \cos\left(\omega m + \frac{\pi u}{2}\right) = \mathbf{a}^T \cdot \mathbf{c}_{\mathbf{x}}(\omega, u), \tag{21}$$

where the vector $\boldsymbol{c_x}(\omega, u)$ is computed as

$$\boldsymbol{c}(\omega, u) = \left[0 \; 1^u \cos\left(\omega + \tfrac{\pi u}{2}\right) \; 2^u \cos\left(2\omega + \tfrac{\pi u}{2}\right) \cdots M^u \cos\left(M\omega + \tfrac{\pi u}{2}\right)\right]^T. \tag{22}$$

On the basis of the Eqs. (10), (21), and (22), the constraint Eqs. (18)–(20) are represented in matrix form as

$$\boldsymbol{C}_{\mathbf{x}} \cdot \boldsymbol{a} = \boldsymbol{f}_{\mathbf{x}}. \tag{23}$$

Now, $\boldsymbol{C_x}$ is defined as

$$\boldsymbol{C}_{\mathbf{x}} = c(\omega_{nc}, u), \tag{24}$$

whereas

$$\left[\boldsymbol{f}_{\mathbf{x}}\right]^T = \left[\begin{array}{cc} 0 & 0 \ \beta(u-1) \end{array}\right]. \tag{25}$$

Equation (18) is desired magnitude response, while Eq. (19) is used to make first-order derivative equal to be zero [11]. The constraint defined by Eq. (20) helps in gaining the controlled 3-dB notch bandwidth [11]. Thus, it enables to modify the BW_N by alteration of u. The design problem is produced by associating the objective function mentioned in Eq. (14) with constraint defined at Eq. (23) as

$$\min\{J(\boldsymbol{a})\}, \text{ subjected to } \boldsymbol{C}_{\mathbf{x}} \cdot \boldsymbol{a} = \boldsymbol{f}_{\mathbf{x}}, \tag{26}$$

and solution may be computed using the Lagrange multiplier method [11, 19], calculated as

$$\boldsymbol{a}_{\mathbf{opt}} = \boldsymbol{Q}^{-1} \cdot \boldsymbol{p} - \boldsymbol{Q}^{-1} \cdot \boldsymbol{C}_{\mathbf{x}}^T \cdot \left(\boldsymbol{C}_{\mathbf{x}} \cdot \boldsymbol{Q}^{-1} \cdot \boldsymbol{C}_{\mathbf{x}}^T\right)^{-1} \left[\boldsymbol{C}_{\mathbf{x}} \cdot \boldsymbol{Q}^{-1} \cdot \boldsymbol{p} - \boldsymbol{f}_{\mathbf{x}}\right]. \tag{27}$$

The above expression is a closed-form solution having easy computability The computational complexity involved in the above expression includes two terms, first term is the computation of conventional solution $\left(\boldsymbol{Q}^{-1} \cdot \boldsymbol{p}\right)$. Second term consists of the product of $\boldsymbol{Q}^{-1} \cdot \boldsymbol{C}_{\mathbf{x}}^T \left(\boldsymbol{C}_{\mathbf{x}} \cdot \boldsymbol{Q}^{-1} \cdot \boldsymbol{C}_{\mathbf{x}}^T\right)^{-1}$ and $\left[\boldsymbol{C}_{\mathbf{x}} \cdot \boldsymbol{Q}^{-1} \cdot \boldsymbol{p} - \boldsymbol{f}_{\mathbf{x}}\right]$. Since, the dimension of $\boldsymbol{C}_{\mathbf{x}} \cdot \boldsymbol{Q}^{-1} \cdot \boldsymbol{C}_{\mathbf{x}}^T$ is small $L \times L$, where $L =$ (integral order) + (order of FD terms). Therefore, the computational complexity of second term is on smaller scale.

5 Proposed Design Method

The authors in [11], designed a FIR notch filter exploiting only a single FD term (L=2) and demonstrated the effect of u on BW_N. The appropriate FD value was tracked down by first evaluating the filter coefficients followed by the filter response for different FD values from 1.1 to 1.9. For each response obtained, error (Er_p) is defined as

$$Er_p = \frac{1}{\pi}\left(\int_0^{\omega_c^1} \left(H_o\left(e^{j\omega}\right) - H\left(e^{j\omega}\right)\right)^2 d\omega + \int_{\omega_c^2}^{\pi} \left(H_o\left(e^{j\omega}\right) - H\left(e^{j\omega}\right)\right)^2 d\omega\right), \tag{28}$$

where ω_c^1 and ω_c^2 are cutoff frequencies, and BW_N were computed. Then, depending on the requirement, the value of FD was selected. However, this approach depends

on the step size, and track time increases with small value of step size. Moreover, one has to wait till all values of FD are exploited, and it will increase if more than one FD term is used in design. Therefore, in this paper, a methodical approach using swarm intelligence is presented.

5.1 Formulation of Hybrid-PSO for Exploration of FD

In Hybrid-PSO, the optimized solution is obtained by exploring and exploiting the search space ($\boldsymbol{X}$) that is constructed at very initial step. Now, $\boldsymbol{X}$ is formed by uniformly distributed number in the range of lower (X_l) and upper (X_u) bound as

$$\mathbf{X} = X_l - (X_u) \oplus rand\,(0, 1). \tag{29}$$

Each row of $\boldsymbol{X}$ is the set of FD values for the evaluation of filter coefficients using Eqs. (23) and (25). The improved solutions during iterative computation are incorporated in ***PB***, while solution with least value of Er_p from ***PB*** is considered in ***gb***. Thus, at the end of the iterative computation, ***gb*** hold the optimal FD values. The complete design procedure may be conducted as:

1. Specify the notch filter parameters such as N, ω_{nc}, and the desired response $H_o\left(e^{j\omega}\right)$.
2. Set the control parameters of Hybrid-PSO such as χ, c_1 and c_2, w, maximum iteration count (k), upper and lower limits of $\boldsymbol{V}$ and $\boldsymbol{X}$.
3. Initialize the search space ($\boldsymbol{X}^{[k=0]}$) and associated velocity ($\boldsymbol{V}^{[k=0]}$) by uniformly distributed random numbers.
4. Compute notch filter coefficients using Eq. (27), followed by the fitness evaluation using Eq. (28). Store the solutions as ***PB***.
5. ***PB*** with best minimum value of error is picked as ***gb***.
6. Update $\boldsymbol{V}$ using Eq. (1), and then update $\boldsymbol{X}$ using Eq. (2), and confirm that all newly formed elements are in the bounded limit; otherwise assign new values for those, which are not in limits.
7. Again compute the notch filter coefficients using Eq. (27) for new FD values, followed by the fitness evaluation using Eq. (28). Store these fitness values as ***new fitness***.
8. Replace the earlier solutions from ***PB*** with the new solutions that have less error values, respectively.
9. Compare the current error of ***gb*** with new ***PB*** solutions, and check if any ***PB*** is better than ***gb***, then replace ***gb*** with improved ***PB***.
10. Repeat the steps from 6 to 10 until iteration cycle are not over or the desired fitness is achieved.
11. At the end, ***gb*** holds the best FD values.

6 Results and Discussion

In this section, the details of experiments conducted for the optimized design of a FIR notch filter using FD with Hybrid-PSO and their observations are discussed. MATLAB® 2014 is used on Genuine Intel (R) CPU i7 3770 @ 3.40 GHz, 4 GB RAM. The normalized digital frequency with 500 equally spaced sample is considered during the experiments. The control parameter is set as; $c_1 = 2.05$, $c_2 = 2.05$, $\chi = 0.7213$, $limit = 25$, maximum iteration count $(k_{\max}) = 500$, and $w = 1$ as given in [27].

6.1 Experimental Analysis of Proposed Method

In PSO, the optimal solution is tracked by updating $\boldsymbol{X}$, and therefore its size is the key factor. If $\boldsymbol{X}$ consisted of too many solution vectors, then computation time (t) would be very high; and if it is too small, then PSO might get stuck in local minima. In this section, the experimental analysis is made to find the suitable best size of $\boldsymbol{X}$. For experiments, the number of FDs is varied from 1 to 5 and number of solution (Ix) raising gradually from 5 to 40 with increment of 5. For each individual combination of number of FD and Ix, 30 trials are performed. On the examination, it is observed that 2 FD terms with Ix equals to 30 have obtained consistent performance as shown in Figs. 1 and 2. Er_p is least when 2 FD are deployed and BW_N is almost same as observed from Figs. 1 and 2 respectively. It has been found convincing from Figs. 1 and 2 that the proposed method is statically stable, since least, median, and worst lies close with indistinguishable variation. The convergence of the proposed method is depicted in Fig. 3a, in which Er_p as function of k is plotted along with its derivative plotted in dash line. It can be observed that 2-FDC method converges to the optimal point within 100 iterations, and therefore it would be best choice to execute it the same time. Whereas in Fig. 3b, notch response obtained with different number of FDC is shown, and it was found that 2-FDC has achieved best response measured on the basis of Er_p, BW_N, and maximum passband ripple (δ) measured as maximum value of undershoot or overshoot in passband region. When 2 FD are deployed and BW_N is almost same as observed from Figs. 1 and 2, respectively. It has been found convincing from Figs. 1 and 2 that the proposed method is statically stable, since least, median, and worst lies close with indistinguishable variation. The convergence of the proposed method is depicted in Fig. 3a, in which Er_p as function of k is plotted along with its derivative plotted in dash line. It can be observed that 2-FDC method converges to the optimal point within 100 iterations, and therefore it would be best choice to execute it the same time. Whereas in Fig. 3b, notch response obtained with different number of FDC is shown, and it was found that 2-FDC has achieved best response measured on the basis of Er_p, BW_N and maximum passband ripple (δ) measured as maximum value of undershoot or overshoot in passband region.

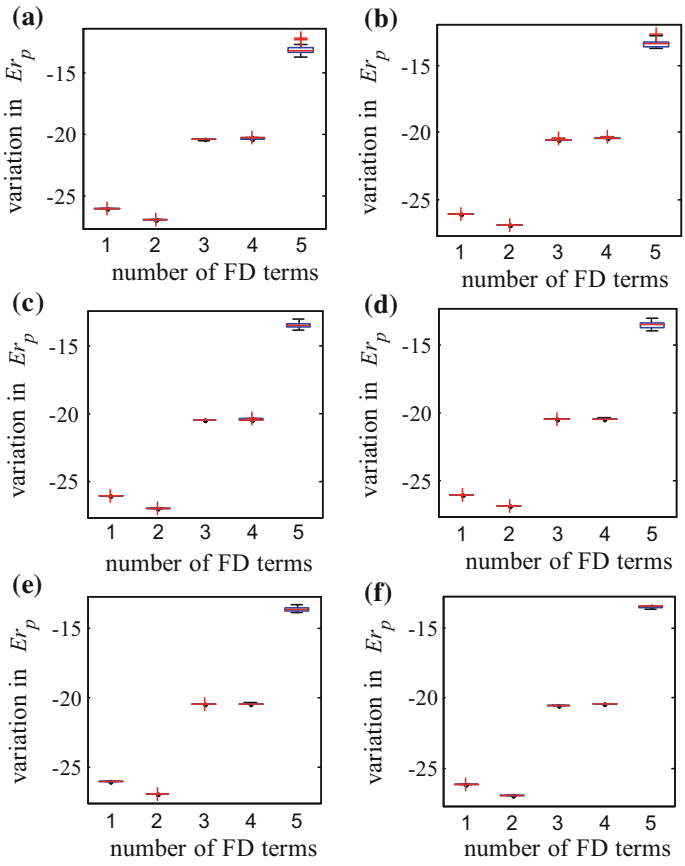

Fig. 1 Variation in Er_p for different numbers of FD constraints with different number of Ix for Hybrid-PSO, **a** $Ix=5$, **b** $Ix=10$, **c** $Ix=15$, **d** $Ix=20$, **e** $Ix=25$, **f** $Ix=30$, **g** $Ix=35$, **h** $Ix=40$

6.2 Comparison with Previous Method

On the basis of experimental analysis performed, it is reflected that the proposed methodology is robust, and in the design methodology, 2-FDC are employed and compared with the 1-FDC strategy proposed in [11]. The fidelity parameters are summarized in Table 1. The obtained filter response is illustrated in Fig. 4a along with the filter response obtained for 1-FDC as produced in [11]. It can be observed that the different values of FD results in different BW_N and Er_p. When $u=1.3$, least BW_N is obtained, which is increased for other three values, $u=1.5$, 1.7, and 1.9.

However, for $u=1.3$, quite high quantity of overshoot is also examined as shown by blue dash line in Fig. 4a. On the basis of quality, it can be perceived that for $u=1.5$ is good choice. While using the proposed technique, the optimal BW_N with least possible value of Er_p is achieved, and shown by solid magenta line of Fig. 4a. The

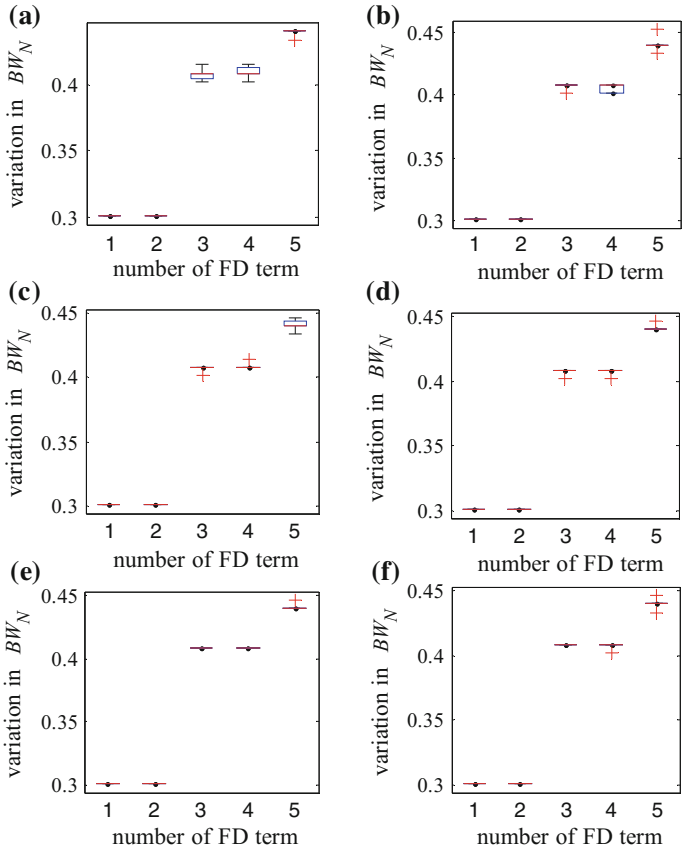

Fig. 2 Variation in BW_N for different numbers of FD constraints with different number of Ix for Hybrid-PSO, **a** $Ix=5$, **b** $Ix=10$, **c** $Ix=15$, **d** $Ix=20$, **e** $Ix=25$, **f** $Ix=30$, **g** $Ix=35$, **h** $Ix=40$

percentage reduction in BW_N and Er_p are shown in Fig. 4b along with positive axis, when compared with the fidelity parameters of individual design examples with the fidelity parameters of the proposed method.

7 Conclusion

In this paper, an improved design approach employing the novelty of fractional derivatives (FDs), with Hybrid-PSO, is demonstrated. First derivative is imposed to obtain the exact null at notch frequency, whereas FDs are used to control the notch bandwidth. The exploration of FDs is computationally expensive, and therefore an exhaustive experimentation is performed, where Hybrid-PSO is modeled to find

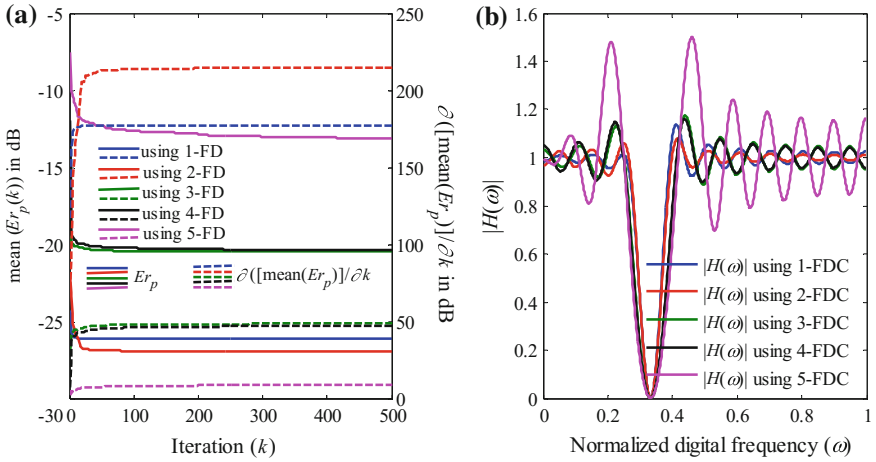

Fig. 3 **a** Convergence of the proposed technique with different FDC, **b** notch response obtained with different numbers of FDC explored by Hybrid-PSO

Table 1 Performance of the proposed method and 1-FDC method

Example (Ex)	u	Er_p in dB	BW_N	ω_c^1	ω_c^2	$\lvert H(\omega_c^1)\rvert$	$\lvert H(\omega_c^2)\rvert$
1 [11]	1.3	−23.7367	0.25761	0.91106	1.16867	0.74673	0.72977
2 [11]	1.5	−24.2661	0.34558	0.85451	1.20009	0.72024	0.70838
3 [11]	1.7	−21.0231	0.40841	0.82310	1.23150	0.72887	0.72545
4 [11]	1.9	−19.6938	0.42097	0.82938	1.25035	0.70722	0.72030
Proposed	1.3925 and 2.9695	−26.9333	0.30159	0.89221	1.19381	0.72231	0.72701

the suitable values of FD to reduce the error-based objective function. About 45% reduction in passband error along with 12% improvement in notch bandwidth has been gained using the proposed technique. The exhaustive experimental analysis confirmed that the swarm size consisting of 30 solutions is the optimal choice, which results in less computation time too. The differentiation of convergence function with respect to iteration, gives maximum required iteration count, which is 100 for two FD-based design using Hybrid-PSO. The designed filter is appropriate for removal of individual frequency interference in biomedical signals like Electrocardiography (ECG) signals.

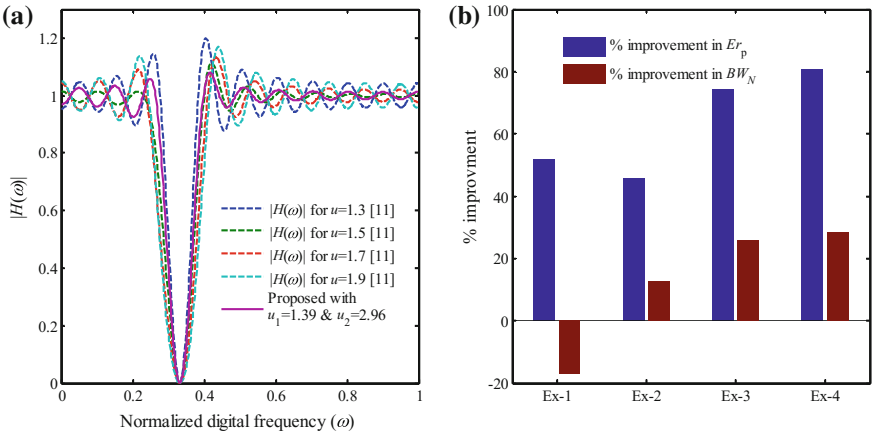

Fig. 4 **a** Frequency response of the FIR notch filter designed using 1-FDC, and proposed method with 2-FDC, **b** reduction in Erp and BWN obtained by the designed filter over the filter response obtained by 1-FDC [11]

References

1. Dutta Roy, S.C., Jain, S.B., Kumar, B.: Design of digital FIR notch filters from second order IIR prototype. IETE J. Res. **43**, 275–279 (1997)
2. Sharma, I., Kuldeep, B., Kumar, A., Singh, V.K.: Performance of swarm based optimization techniques for designing digital FIR filter: a comparative study. Eng. Sci. Technol. an Int. J. **19**, 1564–1572 (2016)
3. Kumar, A., Kuldeep, B.: Design of M-channel cosine modulated filter bank using modified exponential window. J. Franklin Inst. **349**, 1304–1315 (2012)
4. Yu, T.-H., Mitra, S.K., Babic, H.: Design of linear phase FIR notch filters. Sadhana **15**, 133–155 (1990)
5. Hirano, K., Nishimura, S., Mitra, S.: Design of digital notch filters. IEEE Trans. Circuits Syst. **21**, 540–546 (1974)
6. Tsenga, C.-C., Peib, S.-C.: Design of an equiripple FIR notch filter using a multiple exchange algorithm. Sig. Process. **75**, 225–237 (1999)
7. Deshpande, R., Jain, S.B., Kumar, B.: Design of maximally flat linear phase FIR notch filter with controlled null width. Sig. Process. **88**, 2584–2592 (2008)
8. Ferdi, Y., Herbeuval, J.P., Charef, A., Boucheham, B.: R wave detection using fractional digital differentiation. ITBM-RBM. **24**, 273–280 (2003)
9. Tseng, C.-C., Lee, S.-L.: Digital image sharpening using fractional derivative and mach band effect. In: IEEE International Symposium on Circuits and Systems, pp. 2765–2768 (2012)
10. Mathieu, B., Melchior, P., Oustaloup, A., Ceyral, C.: Fractional differentiation for edge detection. Sig. Process. **83**, 2421–2432 (2003)
11. Tseng, C.-C., Lee, S.-L.: Design of linear phase FIR filters using fractional derivative constraints. Sig. Process. **92**, 1317–1327 (2012)
12. Tseng, C.-C., Lee, S.-L.: Fractional derivative constrained design of FIR filter with prescribed magnitude and phase responses. In: IEEE European Conference on Circuit Theory and Design, Dresden, pp. 1–4 (2013)
13. Tseng, C.-C., Lee, S.-L.: Design of wideband fractional delay filters using derivative sampling method. IEEE Trans. Circuits Syst. I Regul. Pap. **57**, 2087–2098 (2010)

14. Tseng, C.-C.: Design of fractional order digital FIR differentiators. IEEE Signal Process. Lett. **8**, 77–79 (2001)
15. Tseng, C.-C., Lee, S.-L.: Designs of fixed-fractional-delay filters using fractional-derivative constraints. IEEE Trans. Circuits Syst. II Express Briefs. **59**, 683–687 (2012)
16. Kuldeep, B., Kumar, A., Singh, G.K.: Design of multi-channel filter bank using ABC optimized fractional derivative constraints. In: IEEE International Conference on Communication and Signal Processing, pp. 492–496 (2015)
17. Baderia, K., Kumar, A., Singh, G.K.: Hybrid method for designing digital FIR filters based on fractional derivative constraints. ISA Trans. **58**, 493–508 (2015)
18. Kuldeep, B., Singh, V.K., Kumar, A., Singh, G.K.: Design of two-channel filter bank using nature inspired optimization based fractional derivative constraints. ISA Trans. **54**, 101–116 (2015)
19. Kuldeep, B., Kumar, A., Singh, G.K.: Design of quadrature mirror filter bank using Lagrange multiplier method based on fractional derivative constraints. Eng. Sci. Technol. an Int. J. **18**, 235–243 (2015)
20. Kuldeep, B., Kumar, A., Singh, G.K.: Design of multi-channel cosine-modulated filter bank based on fractional derivative constraints using cuckoo search algorithm. Circuits Syst. Signal Process. **34**, 3325–3351 (2015)
21. Agrawal, N., Kumar, A., Bajaj, V.: A new design method for stable IIR filters with nearly linear-phase response based on fractional derivative and swarm intelligence. IEEE Trans. Emerg. Top. Comput. Intell. **1**, 464–477 (2017)
22. Charef, A., Djouambi, A., Idiou, D.: Linear fractional order system identification using adjustable fractional order differentiator. IET Signal Process. **8**, 398–409 (2014)
23. Ahirwal, M.K., Kumar, A., Singh, G.K.: EEG/ERP adaptive noise canceller design with controlled search space (CSS) approach in cuckoo and other optimization algorithms. IEEE/ACM Trans. Comput. Biol. Bioinforma. **10**, 1491–1504 (2013)
24. Poli, R., Kennedy, J., Blackwell, T.: Particle swarm optimization. T. Swarm Intell. **1**, 33–57 (2007)
25. Rafi, S.M., Kumar, A., Singh, G.K.: An improved particle swarm optimization method for multirate filter bank design. J. Franklin Inst. **350**, 757–769 (2013)
26. MacDonald, C.L., Bhattacharya, N., Sprouse, B.P., Silva, G.A.: Efficient computation of the Grünwald-Letnikov fractional diffusion derivative using adaptive time step memory. J. Comput. Phys. **297**, 221–236 (2015)
27. Agrawal, N., Kumar, A., Bajaj, V.: Design of digital IIR filter with low quantization error using hybrid optimization technique. Soft Comput. **21** (2017)

Leakage Reduction in Full Adder Circuit Using Source Biasing at 45 nm Technology

Candy Goyal, Jagpal Singh Ubhi and Balwinder Raj

Abstract In this paper, a new technique of source biasing is proposed for leakage reduction in CMOS full adder (FA) circuit. It includes tail transistor between pull-down network and ground (GND). The source terminal of tail transistor is connected to GND during active mode and will be at Vdd in idle mode. High potential at source of tail transistor reduces the potential difference between source and drain of NMOS transistors which reduces gate leakage current. The proposed approach does not have the problem of ground bounce noise (GBN) during idle-to-active mode of transition. The proposed new technique is having reduction in leakage power up to 72% as compared to the existing FA circuit and peak power reduces up to 37% as compared to existing FA circuit while keeping other performance parameters in acceptable range.

Keywords Very large-scale integration (VLSI) · Ground bounce noise (GBN) Power delay product (PDP) · Ground (GND) · Virtual ground (VGND) Full adder (FA)

1 Introduction

Adders are one of the prime components in all the arithmetic circuits. All the DSP algorithms use addition as a primary operation. So, any optimization in the adder circuit can optimize the whole system [1]. With each technology generation, leakage

C. Goyal (✉)
E.C.E. Section, Yadavindra College of Engineering, Talwandi Sabo, Punjab, India
e-mail: candygoyal@pbi.ac.in

J. Singh Ubhi
Department of E.C.E, S.L.I.E.T, Distt. Sangrur, Longowal, India
e-mail: js_ubhi@yahoo.com

B. Raj
Department of E.C.E, N.I.T, Jalandhar, India
e-mail: balwinderraj@gmail.com

B. S. Rawat et al. (eds.), *Advances in Signal Processing and Communication* ,
Lecture Notes in Electrical Engineering 526,
https://doi.org/10.1007/978-981-13-2553-3_29

current is increasing exponentially [2]. Leakage power has become the biggest challenge in nanoscale VLSI design because battery-operated electronic devices have the problem of sharp battery discharge in idle mode [3]. There are the three major types of leakage mechanisms which occur in CMOS technology, subthreshold leakage, gate oxide leakage, and reverse bias p–n junction leakage. Out of these, subthreshold and gate leakage are the major concerns while reverse bias leakage is generally negligible. As the technology is approaching, nanoscale node gate leakage has become the major challenge in circuit designing. Most of the researchers have optimized the adder circuits for leakage power dissipation by using power gating [4] techniques which provide high impedance between Vdd and GND during standby mode but having disadvantages of large GBN peaks. GBN is a serious issue in deep submicron technology.

A new hybrid technique [5] for FA is used feedback of Cout signal, although average power and number of transistors reduce but leakage power increases. Another structure of sleep circuit [6] named gbonor is presented. Although GBN reduces but one sleep circuit require five transistors and an inverter which increases average power and area of circuit. A new low leakage 10T adder circuit [7] is presented in which sum is calculated using PTL logic and carry is propagated using 2:1 mux. However, output voltage does not have full voltage swing and noise margin is lesser as compared to conventional FA. Another leakage reduction technique [8] is presented which uses two sleep transistors and one capacitor. It reduces the leakage current due to the stacking effect but having two GBN peaks and requirements of extra buffers increases area of the circuit. Body biasing is another effective technique used recently for leakage power reduction. A gate level body bias controller [9] is used which dynamically increases the threshold voltage of all the NMOS transistors in an idle state. Although leakage power reduces but accompanying a disadvantages of bias generator which increase silicon area and complexity of the circuit. Another approach [10] used body biasing and semi domino logic in the design of FA. Body bias varies the threshold voltage to achieve the objective of higher speed and lesser energy consumption. However, due to the dynamic operation, leakage is larger in this approach. From the review of literature, it can be concluded that most of the techniques presented so far needs extra circuitry, having problem of GBN and complexity in layout design. An effort is done in this paper in which we have used source biasing in conventional FA circuit to reduce the leakage power dissipation.

2 Proposed Circuit

There are number of circuit styles [11, 12] are available in the literature for CMOS FAs. Conventional FA is having robustness against the noise and provides a stable output with maximum noise margin. So, we have chosen conventional CMOS FA for testing our source basing technique. Figure 1 shows the circuit diagram of conventional CMOS FA and Fig. 2 shows the modified conventional FA using source biasing.

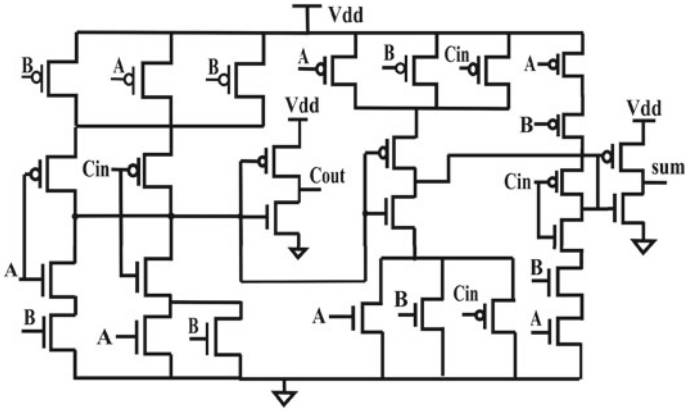

Fig. 1 Conventional CMOS full adder

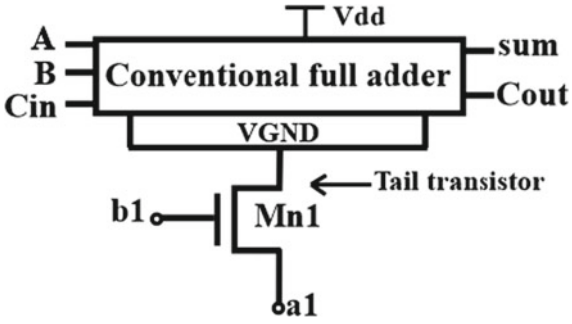

Fig. 2 Modified conventional FA using tail transistor with source biasing

W/L ratio of conventional CMOS FA is chosen in such a way so that the effective width of pull-up network is twice the effective width of pull-down network. Minimum length of all the transistors is fixed at 45 nm to get the maximum speed. Figure 2 shows the block diagram of conventional FA with tail transistor and source basing which is tested by using extensive simulations using H-spice. Working of the modified conventional adder can be explained in two modes which are given as

1. Active mode
2. Idle mode
3. Idle-to-active mode transition.

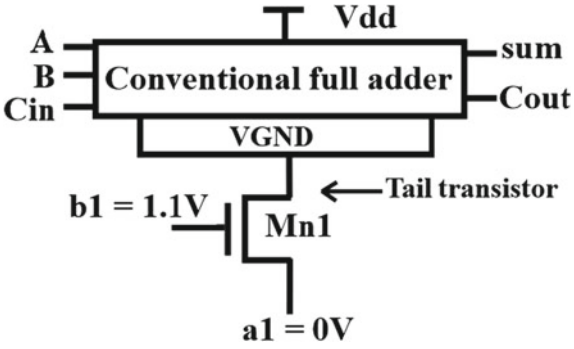

Fig. 3 Modified conventional FA using tail transistor with source biasing in active mode

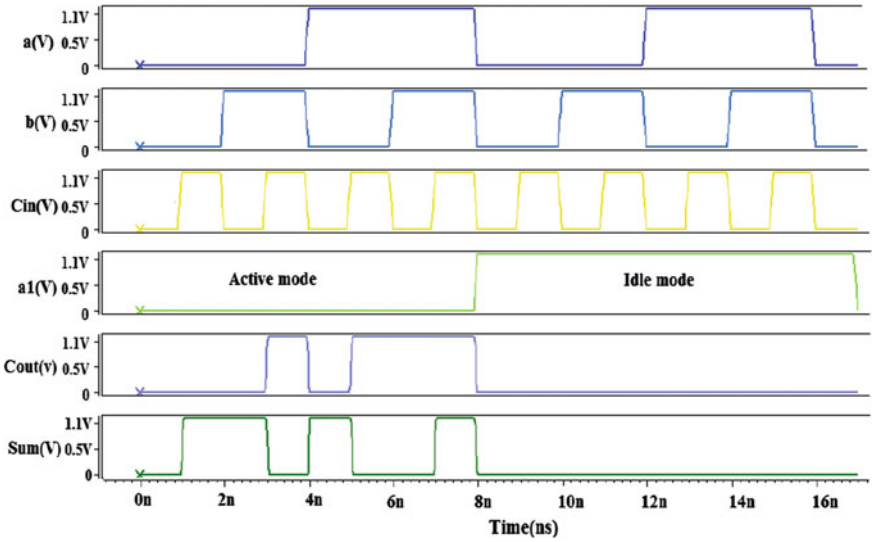

Fig. 4 Input and output waveforms of modified conventional FA using source biasing

2.1 Active Mode

In active mode, voltage at b1 and a1 node of tail Mn1 transistor is shown in Fig. 3.

In active mode, gate of Mn1 will be at logic high which will turn ON Mn1 transistor and source terminal of Mn1 is connected at 0 V. In this mode, Mn1 will offer very less resistance and VGND node will be connected to the real ground. The output, in this case, will be exactly the same as in the conventional FA as shown in Fig. 4. When a1 is at 0 V, then sum and Cout are same as in the conventional adder and when the a1 is at 1.1 V, then there will be no output. The frequency of input data is 500 MHz.

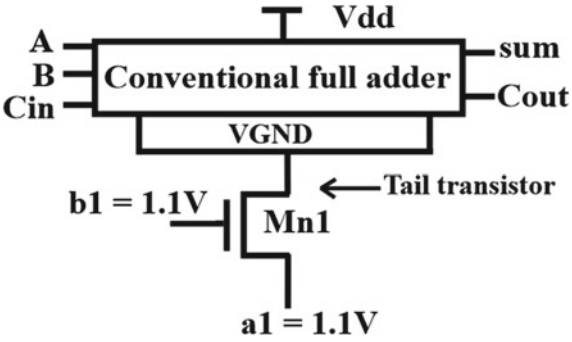

Fig. 5 Modified conventional FA using tail transistor with source biasing in idle mode

2.2 Idle Mode

In idle mode, the source terminal of Mn1 transistor will connected to logic high as shown in Fig. 5.

In this case V_{gs} of the tail transistor (Mn1) will be calculated as

$$\begin{aligned} V_{gs} &= V_g - V_s \\ &= 1.1V - 1.1V = 0V \end{aligned} \tag{1}$$

$V_{gs} = 0$ V will push the Mn1 transistor in cutoff state and VGND node will not connect to real ground. In this condition Mn1 transistor will offer very high resistance. So, there will be almost negligible current flow from Vdd to GND which will reduce the leakage power dissipation. It is well known that if the potential difference between drain and source of the pull-down transistor decreases [13], then gate leakage current can reduce. In modified FA, potential difference between drain and source of pull-down network is 757 mv and in existing hybrid FA this difference is 1100 mv in idle mode. So, leakage current reduces in modified FA using source biasing.

2.3 Idle-to-Active Mode Transition

In idle-to-active mode of transition, voltage at the s**o**urce of tail transistor starts falling from 1.1 V to 0 V. When it reaches to 0 V, Mn1 will switch into conducting state and VGND node will be connected to real GND.

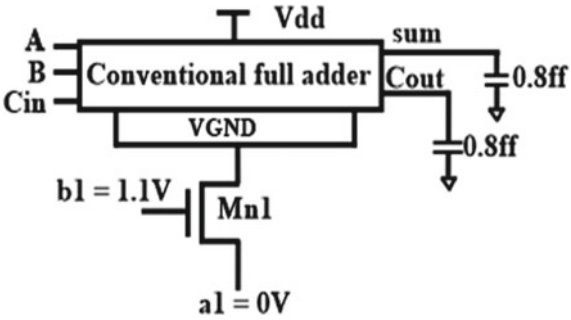

Fig. 6 Simulation setup for modified and existing conventional FA

3 Results and Discussion

All the simulations are performed at 45 nm technology using 1.1 V supply voltage. The simulation setup for extracting all the performance metrics is shown in Fig. 6. An output load of 0.8ff is connected to both the outputs of FAs. For fair comparison, all the FAs under consideration in this paper are simulated under the same environment condition.

All the FA circuits under consideration in this paper are tested by using extensive input test patterns [5] which cover all the possible worst case. Average power dissipation is measured using H-spice EDA tool using test patterns [5] which covers all the switching nodes of the circuit. Average power dissipation is a measure of total power dissipation of the circuit during the particular period of time, mathematically, it is given as

$$P_{avg} = P_{switching} + P_{shortcicuit} + P_{static} \quad (1)$$

where P_{avg} is the average power dissipation in the circuit in active mode. $P_{switching}$ is total switching power loss due to the charging and discharging of all the active node of the circuit, $P_{shortcircuit}$ is the power loss in the circuit due to the simultaneous turn ON pull-up and pull-down network for very short duration of time, P_{static} is the static power dissipation of the circuit.

The propagation delay is calculated for 50% change in input signal from 0 to 1 or 1 to 0 corresponding 50% change in output signals, from either 0 to 1 or 1 to 0. The new design is having the following advantages as compared to the conventional FA circuit.

Table 1 Comparison of average power, delay, PDP, leakage power and peak power between existing and proposed FA at 1.1v 27°C temp

Type of adder	Average power dissipation (μW)	Propagation delay (ps)	PDP (aj)	Leakage power dissipation (nW)	Peak Power (μw)
Conv_adder	7.7	79.7	614	1291	243
Conv_adder_body_bias	7.6	81	616	916	269
Hybrid_FA	5.7	103	587	1943	191
Modified_conv_adder	7.4	83.8	620	547	168

1. Source biasing is having advantages over body biasing technique because layout design of source biasing is very simple and compact as compared to the body biasing technique.
2. In source biasing, gate of NMOS tail transistor remains at high logic in active and idle mode. There is no transition in gate terminal which eliminates the problem of GBN which occurs in conventional sleep circuits.
3. In source biasing, maximum number of transistors remained in cutoff state in idle mode because source terminal of pull down transistors is having high potential.

Table 1 shows the comparison of various performance parameters of modified and existing FAs. Modified FA is having a slight increase in delay as compared to conventional FA, this is due to the stacking effect of transistor which is added at the tail end of the circuit. Similarly, energy consumption of modified FA is almost the same as compared to the existing conventional FA. In modified FA leakage power reduces up to 72% as compared to existing FA which is the biggest achievement of this approach. This is achieved because of the reduction in gate leakage current in modified FA. Peak power also reduces 37% as compared to existing FA.

3.1 Layout of Modified FA

Layout of modified FA is designed using cadence virtuoso layout editor at 45 nm technology as shown in Fig. 7 and post-layout netlist is extracted using RCX extraction. The comparison between pre- and post layout of modified FA is shown in Table 2. There is 13% increase in average power, 17% increase in delay, 28% increase in PDP, and 12% increase in leakage power in post-layout simulation results. It is because of the parasitics in post-layout netlist.

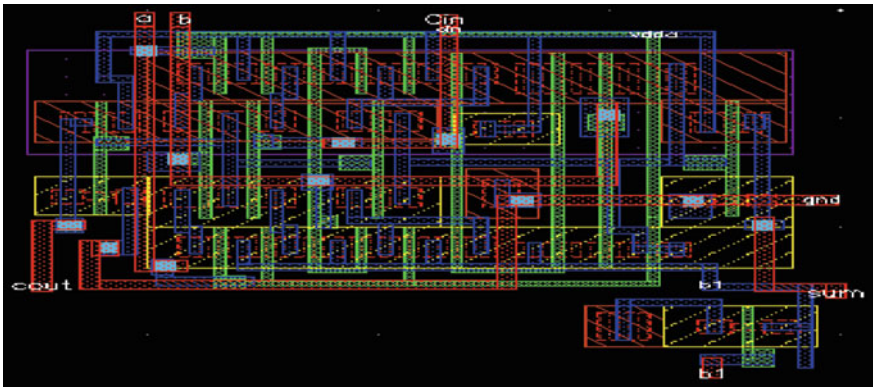

Fig. 7 Layout of modified FA at 45 nm technology using source biasing

Table 2 Comparison of pre- and post-layout simulation results of modified FA

Parameters	Modified_FA (pre layout)	Modified_FA (post layout)	% diff.
Average power (uW)	7.45	8.6	13
Delay (ps)	83.8	101	17
PDP (aj)	620	868	28
Leakage power (nW)	547	624	12

The effects of temperature and voltage variations on the leakage power for modified as well as existing FA are shown in Figs. 8 and 9, respectively. Leakage power increases as the temperature increases, because thermal vibrations of the charge carrier increases and leakage power depend on thermal equivalent of voltage. Increase in leakage power is much steep in conventional FA as compared to the modified FA. Leakage power reduces as the voltage decreases because of the linear relation of supply voltage with respect to leakage power.

4 Conclusion

A source biasing technique is presented to reduce the leakage power in conventional FA. The proposed circuit is analyzed comprehensively and comparatively with existing FAs. The result shows that there is 72% reduction in leakage power and 37% reduction in peak power as compared to existing techniques of leakage reduction in FA. Another advantage of the proposed technique is the elimination of GBN which is a serious issue in all the existing power gating techniques. Use of normal Vth transistor is another advantages feature of the proposed technique. Although the proposed circuit has slight increase in delay and average power dissipation but improvements

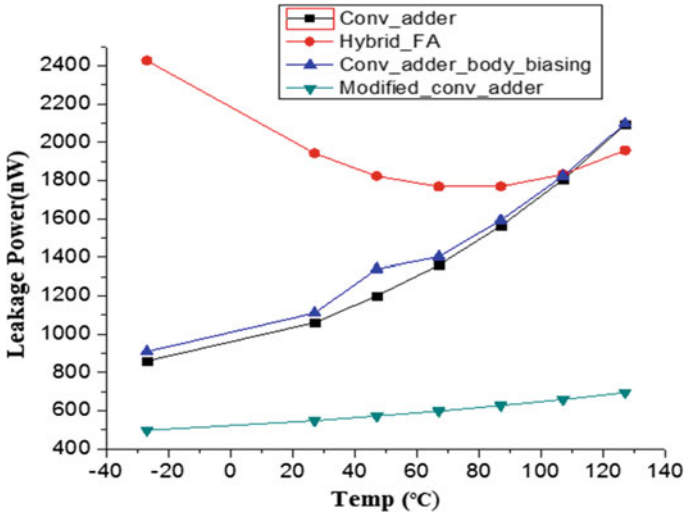

Fig. 8 Effect of temperature on leakage power for modified and existing FAs

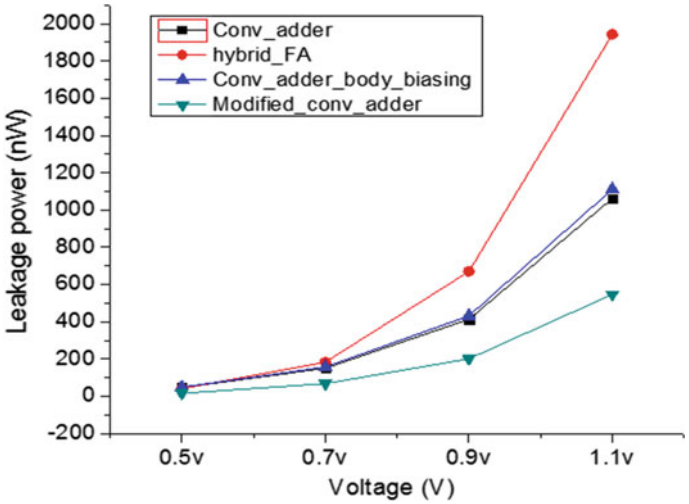

Fig. 9 Effect of voltage variations on leakage power for modified and existing FAs

in leakage power makes this circuit a best choice for circuit design at nanoscale VLSI design. Post-layout simulation results confirm the robustness and reliability of the modified FA circuit.

References

1. Kumar, P., Sharma, R.K.: A new energy efficient full adder design for arithmetic applications. In: 4th International Conference on Signal Processing and Integrated Networks (SPIN), pp. 555–560 (2017)
2. Park, J.C., Mooney, V.J.: Sleepy stack leakage reduction. IEEE Trans. Very Large Scale Integr. Syst. **14**(11), 1250–1263 (2006)
3. Jiao, H., Kursun, V.: Reactivation noise suppression with sleep signal slew rate modulation in MTCMOS circuits. IEEE Trans. Very Large Scale Integr. Syst. **21**(3), 533–545 (2013)
4. Kim, K., Nan, H., Choi, K.: Ultra low-voltage power gating structure using low threshold voltage. Int. Conf. Circuits Syst. II; Express Briefs **56**(12), 926–930 (2009)
5. Parameshwara, M.C., Srinivasaiah, H.C.: Low power hybrid 1-bit full adder circuit for energy efficient arithmetic applications. J. Circuits Syst. Comput. **26**(1), 1750014–1750029 (2017)
6. Sharma, V.K., Pattanaik, M.: A reliable ground bounce noise reduction technique for nanoscale CMOS circuits. Int. J. Electron. **102**, 1852–1866 (2015)
7. Ahmad, M.M.D., Manjunathachari, K., Lalkishore, K.: Analysis of low run-time leakage in a 10 transistors full adder in 45 nm technology. In: International Conference Proceedings/TENCON, pp. 152–156 (2016)
8. Bhanuprakash, R., Pattanaik, M., Rajput, S.S., Mazumdar, K.: Analysis and reduction of ground bounce noise and leakage current during mode transition of stacking power gating logic circuits. In: IEEE International Conference Proceedings/TENCON, pp. 1–6 (2009). https://doi.org/10.1109/tencon.2009.5395850
9. Lorenzo, R., Chaudhury, S.: A Novel low leakage body biasing techniques for cmos circuits. Can. J. Pure Appl. Sci. **10**(1), 3827–3834 (2016)
10. Kumar, A., Srivastava, P., Pattanaik, M.: Design of high-speed power efficient full adder with body biasing. In: Procedding of 2015 Global Conference on Communication Technology, pp. 667–672 (2015)
11. Navi, K., Kavehei, O.: Low-power and high-performance 1-bit full adder. J. Comput. **3**(2), 48–54 (2008)
12. Moaiyeri, M.H., Mirzaee, R.F.: Two new low-power and high-performance full adders. J. Comput. **4**(2), 119–126 (2009)
13. Guindi, R.S., Najm, F.N.: Design techniques for gate-leakage reduction in CMOS circuits. In: Proceeding International Symposimum Qual. Electron. Des. ISQED 2003, pp. 61–65 (2003)

Dual-Mode Quadrature Oscillator Based on Single FDCCII with All Grounded Passive Components

Bhartendu Chaturvedi, Jitendra Mohan and Atul Kumar

Abstract A fully differential second-generation current conveyor (FDCCII) based dual-mode quadrature oscillator with all grounded passive components is presented in this chapter. It comprises one FDCCII, three resistors, and two capacitors. The proposed circuit of quadrature oscillator has the capability to provide two quadrature outputs in voltage mode and four quadrature outputs in current mode, simultaneously. The oscillation frequency and condition of oscillation of the proposed circuit are orthogonally adjustable. Moreover, total harmonic distortion of the outputs is low and power dissipation is also low. The effects of nonidealities of FDCCII on the proposed circuit are also studied. Simulations results are carried out using HSPICE simulation tool with 0.18 μm technology to validate the theoretical analysis.

Keywords Dual-mode · FDCCII · Orthogonal controllability
Quadrature oscillator

1 Introduction

Quadrature oscillators which provide sinusoidal signals at the output with 90° phase difference are important building cells which are used in a large number of applications such as single sideband modulation, selective voltmeters, and vector generators. A quadrature oscillator may be of voltage mode type which provides only voltage outputs or current-mode type which provides only current outputs or dual-mode type which provides both voltage and current outputs simultaneously. A variety of cir-

B. Chaturvedi · J. Mohan · A. Kumar (✉)
Department of Electronics and Communication Engineering, Jaypee Institute of Information Technology, Noida 201304, UP, India
e-mail: atul.nit304@gmail.com

B. Chaturvedi
e-mail: bhartendu.prof@gmail.com

J. Mohan
e-mail: jitendramv2000@rediffmail.com

B. S. Rawat et al. (eds.), *Advances in Signal Processing and Communication* ,
Lecture Notes in Electrical Engineering 526,
https://doi.org/10.1007/978-981-13-2553-3_30

cuits of quadrature oscillator based on various type of current conveyors which fall in one of the above mentioned categories are presented in the literature [1–20]. The circuits presented in [1–4] are voltage mode type, the circuits of [5–9] are current-mode type, and the circuits presented in [10–20] are dual-mode type. The circuits presented in literature [1–20] are benefited with few unique features. However, the circuits presented in [1–6, 9, 11, 12, 14, 17–20] do not provide orthogonal control of oscillation frequency and CO and circuits presented in [1, 2, 4, 7, 9–11, 15, 16, 18] use ungrounded passive components.

This chapter introduces a dual-mode quadrature oscillator (DMQO) which simultaneously provides two voltage outputs and four current outputs. The presented DMQO is realized using one FDCCII, three resistors, and two capacitors. All grounded passive components have been utilized in the realization of presented DMQO. Additionally, output currents can be used to drive any current input circuit without need of additional circuitry as they are available from high impedance terminals. Moreover, the presented DMQO enjoys the following simultaneous features: low total harmonic distortion (THD) of each voltage and current outputs, good active and passive sensitivity performance, and low power dissipation. Furthermore,

Table 1 Comparison of the proposed DMQO circuit with some relevant earlier reported DMQO circuits

Ref.	Active Element/Count	Passive component counts	All-grounded passive components	Orthogonal control of f_0 and CO	Number of current outputs	Number of voltage outputs
[10]	CIDITA/1	3	No	Yes	2	2
[11]	FDCCII/1	4	No	No	4	2
[12]	DVCC/2	4	Yes	No	4	4
[13]	DD-DXCCII/1	5	Yes	Yes	2	3
[14]	DVCC/2	4	Yes	No	4	4
[15]	CDBA/2	5	No	Yes	2	2
[16]	CCCII/3	2	No	Yes	2	2
[17]	DV-DXCCII/1	5	Yes	No	2	3
[18]	DXCCTA/1	2	No	No	3	3
[19]	DVCC/2	4	Yes	No	3	2
[20]	DD-DXCCII/1	5	Yes	No	2	2
Proposed	FDCCII/1	5	Yes	Yes	4	2

Abbreviations: CIDITA: current inverting differential input transconductance amplifier, FDCCII: fully differential second generation current conveyor, DVCC: differential voltage current conveyor, DD-DXCCII: differential difference dual-X second generation current conveyor, CDBA: current differencing buffered amplifier, OTA: operational transconductance amplifier, CCCII: current controlled current conveyor, DV-DXCCII: differential voltage dual-X second generation current conveyor, DXCCTA: dual-X second generation current conveyor transconductance amplifier, f_0: oscillation frequency, CO: condition of oscillation

a comparison of the proposed circuit with some earlier reported circuits of DMQO is given in Table 1. The nonideal analysis of the presented DMQO is also included.

2 Proposed Dual-Mode Quadrature Oscillator

The circuit diagram of the proposed DMQO is shown in Fig. 1. It employs one FDCCII, three resistors, and two capacitors. The active element, FDCCII has been extensively utilized in the realizations of numerous analog signal processing applications [11, 21–25]. The following matrix gives the port relationships of FDCCII.

$$\begin{bmatrix} I_{Y1} \\ I_{Y2} \\ I_{Y3} \\ I_{Y4} \\ V_{X+} \\ V_{X-} \\ I_{Z+} \\ I_{-Z+} \\ I_{Z-} \\ I_{-Z-} \end{bmatrix} = \begin{bmatrix} 0 & 0 & 0 & 0 & 0 & 0 \\ 0 & 0 & 0 & 0 & 0 & 0 \\ 0 & 0 & 0 & 0 & 0 & 0 \\ 0 & 0 & 0 & 0 & 0 & 0 \\ 0 & 0 & 1 & -1 & 1 & 0 \\ 0 & 0 & -1 & 1 & 0 & 1 \\ 1 & 0 & 0 & 0 & 0 & 0 \\ -1 & 0 & 0 & 0 & 0 & 0 \\ 0 & 1 & 0 & 0 & 0 & 0 \\ 0 & -1 & 0 & 0 & 0 & 0 \end{bmatrix} \begin{bmatrix} I_{X+} \\ I_{X-} \\ V_{Y1} \\ V_{Y2} \\ V_{Y3} \\ V_{Y4} \end{bmatrix}, \tag{1}$$

where V_{Y1}, V_{Y2}, V_{Y3}, V_{Y4}, V_{X+}, and V_{X-} are the voltages at Y_1, Y_2, Y_3, Y_4, X+, and X− terminals, respectively. The currents, I_{Y1}, I_{Y2}, I_{Y3}, I_{Y4}, I_{X+}, I_{X-}, I_{Z+}, I_{-Z+}, I_{Z-}, and I_{-Z-} appear at Y_1, Y_2, Y_3, Y_4, X+, X−, Z+, −Z+, Z−, and −Z− terminals, respectively.

It is observed from Fig. 1 that all external resistors and capacitors are grounded; therefore, the presented DMQO is suitable to the modern IC technology. Moreover, the availability of output currents from high impedance terminals allows the presented

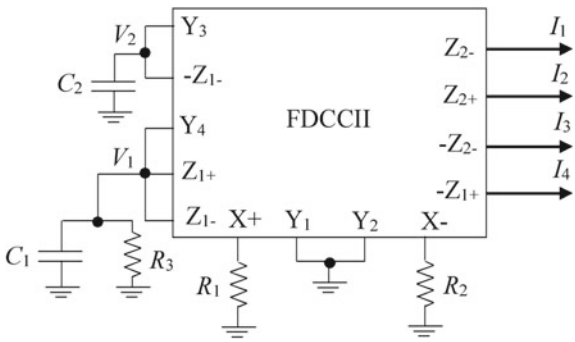

Fig. 1 Proposed dual-mode quadrature oscillator

DMQO to derive any current input circuit easily. After analyzing the DMQO circuit of Fig. 1, the following characteristic equation is achieved.

$$s^2 + \frac{(R_2 - R_3)}{R_2 R_3 C_1} s + \frac{1}{R_1 R_2 C_1 C_2} = 0. \tag{2}$$

From (2), the following oscillation frequency, f_0 and condition of oscillation (CO) are obtained.

$$f_0 = \frac{1}{2\pi}\sqrt{\frac{1}{R_1 R_2 C_1 C_2}}, \tag{3}$$

$$\text{CO: } R_3 \geq R_2. \tag{4}$$

It is to be observed from (3) and (4) that f_0 can be tuned without affecting CO by R_1, whereas CO can be controlled independent of oscillation frequency by R_3. Thus, f_0 and CO are orthogonally controllable by R_1 and R_3 in that order.

The output voltages are related according to (5), whereas output currents are related according to (6).

$$V_1 = -jK_1 V_2, \tag{5}$$

$$I_1 = -jK_2 I_2 = -I_3 = jK_2 I_4. \tag{6}$$

where $K_1 = \omega R_3 C_2$ and $K_2 = \omega R_2 C_2$. It is observed from (5) and (6) that V_1 and V_2 are in quadrature relationship and I_1, I_2, I_3, and I_4 are also in quadrature relationship, respectively. Additionally the phasor diagrams showing the relationships between voltages, V_1 and V_2 are between currents, I_1, I_2, I_3, and I_4 are shown in Fig. 2.

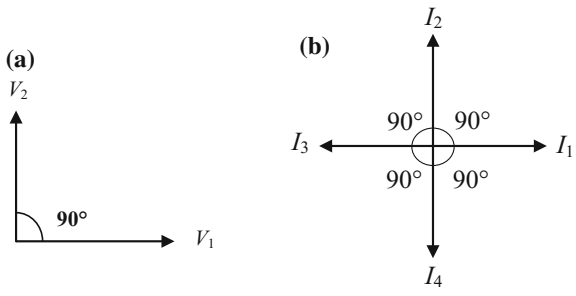

Fig. 2 **a** Relationships between voltages, V_1 and V_2 **b** Relationships between currents, I_1, I_2, I_3 and I_4

2.1 Nonideal Analysis

In nonideal case, the port relationships of FDCCII are expressed as follows:

$$\begin{bmatrix} I_{Y1} \\ I_{Y2} \\ I_{Y3} \\ I_{Y4} \\ V_{X+} \\ V_{X-} \\ I_{Z+} \\ I_{-Z+} \\ I_{Z-} \\ I_{-Z-} \end{bmatrix} = \begin{bmatrix} 0 & 0 & 0 & 0 & 0 & 0 \\ 0 & 0 & 0 & 0 & 0 & 0 \\ 0 & 0 & 0 & 0 & 0 & 0 \\ 0 & 0 & 0 & 0 & 0 & 0 \\ 0 & 0 & \beta_1 & -\beta_2 & \beta_3 & 0 \\ 0 & 0 & -\beta_4 & \beta_5 & 0 & \beta_6 \\ \alpha_1 & 0 & 0 & 0 & 0 & 0 \\ -\alpha_2 & 0 & 0 & 0 & 0 & 0 \\ 0 & \alpha_3 & 0 & 0 & 0 & 0 \\ 0 & -\alpha_4 & 0 & 0 & 0 & 0 \end{bmatrix} \begin{bmatrix} I_{X+} \\ I_{X-} \\ V_{Y1} \\ V_{Y2} \\ V_{Y3} \\ V_{Y4} \end{bmatrix}, \tag{7}$$

In (7), α_1, α_2, α_3, and α_4 are current transfer gains from I_{X+} to I_{Z+}, I_{X+} to I_{-Z+}, I_{X-} to I_{Z-}, and I_{X-} to I_{-Z-}, respectively, whereas β_1, β_2, β_3, β_4, β_5, and β_6 are voltage transfer gains from V_{Y1} to V_{X+}, V_{Y2} to V_{X+}, V_{Y3} to V_{X+}, V_{Y1} to V_{X-}, V_{Y2} to V_{X-}, and V_{Y4} to V_{X-}, respectively. Taking these nonideal gains into consideration, the presented DMQO is reanalyzed. The characteristic equation given in (2) is now modified as follows.

$$s^2 + \frac{(R_2 - \alpha_3\beta_6 R_3)}{R_2 R_3 C_1} s + \frac{\alpha_1\alpha_4\beta_3\beta_6}{R_1 R_2 C_1 C_2} = 0. \tag{8}$$

The modified f_0 and CO are now expressed as follows.

$$f_0 = \frac{1}{2\pi}\sqrt{\frac{\alpha_1\alpha_4\beta_3\beta_6}{R_1 R_2 C_1 C_2}}, \tag{9}$$

$$\text{CO: } \alpha_3\beta_6 R_3 \geq R_2. \tag{10}$$

The active and passive sensitivities of f_0 are expressed in (11).

$$S^{f_0}_{\alpha_1,\alpha_4,\beta_3,\beta_6} = -S^{f_0}_{R_1,R_2,C_1,C_2} = \frac{1}{2},\ S^{f_0}_{\alpha_2,\alpha_3,\beta_1,\beta_2,\beta_4,\beta_5} = S^{f_0}_{R_3} = 0. \tag{11}$$

Equation (11) reveals the good sensitivity performance of the presented DMQO as magnitudes of all sensitivities are fewer than unity.

Table 2 MOS transistors aspect ratios

MOS transistors	W(μm)/L(μm)
M_7–M_9, M_{13}–M_{19}, M_{22}–M_{26}	10/0.7
M_1–M_6, M_{10}–M_{12}, M_{20}–M_{21}, M_{27}–M_{40}	5/0.7

3 Simulation Results

The simulations of proposed DMQO are done using HSPICE simulation tool with 0.18 μm TSMC CMOS technology. The CMOS realization of FDCCII depicted in Fig. 3 is used to implement the proposed DMQO. Table 2 gives the aspect ratios of MOS transistors utilized in CMOS realization of FDCCII. The supply voltages of ± 0.9 V along with bias currents of $I_B = 35$ μA and $I_{SB} = 5$ μA are used in simulations. The presented DMQO is designed for $f_0 = 159$ kHz for which the passive components used are $R_1 = R_2 = 1$ kΩ, $R_3 = 1.1$ kΩ, $C_1 = 1$ nF and $C_2 = 1$ nF. The simulated waveforms of voltages, V_1 and V_2 are depicted in Fig. 4a. The frequency spectrums corresponding to Fig. 4a are depicted in Fig. 4b. The simulated waveforms of currents, I_1, I_2, I_3, and I_4 are depicted in Fig. 5a. The frequency spectrums of Fig. 5a is shown in Fig. 5b. The simulated frequency in Figs. 4 and 5 is 148 kHz. Next, the Monte Carlo simulation results are carried out to check the performance of the presented DMQO for mismatch between capacitors. Figure 6 shows the simulated waveforms of voltages, V_1 and V_2 for 20 multiple runs when Gaussian deviations of 5% are introduced to both the capacitors. It is observed from Fig. 6 that f_0 is affected a little, however, the CO is not affected. THDs for the voltages, V_1 and V_2 are 2.3 and 2.4%, respectively. THDs for the currents, I_1, I_2, I_3, and I_4, are 2.4, 2.3, 2.4 and 2.3%, respectively. Thus, THD for output voltages and output currents is less than 3%. The power dissipation of the presented DMQO is 1.63 mW only.

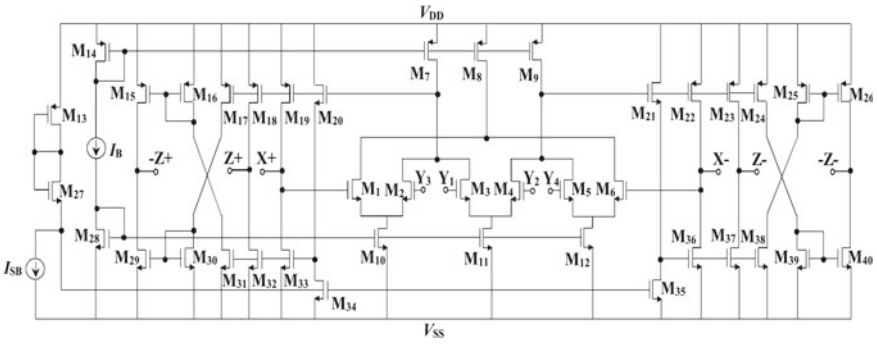

Fig. 3 CMOS realization of FDCCII

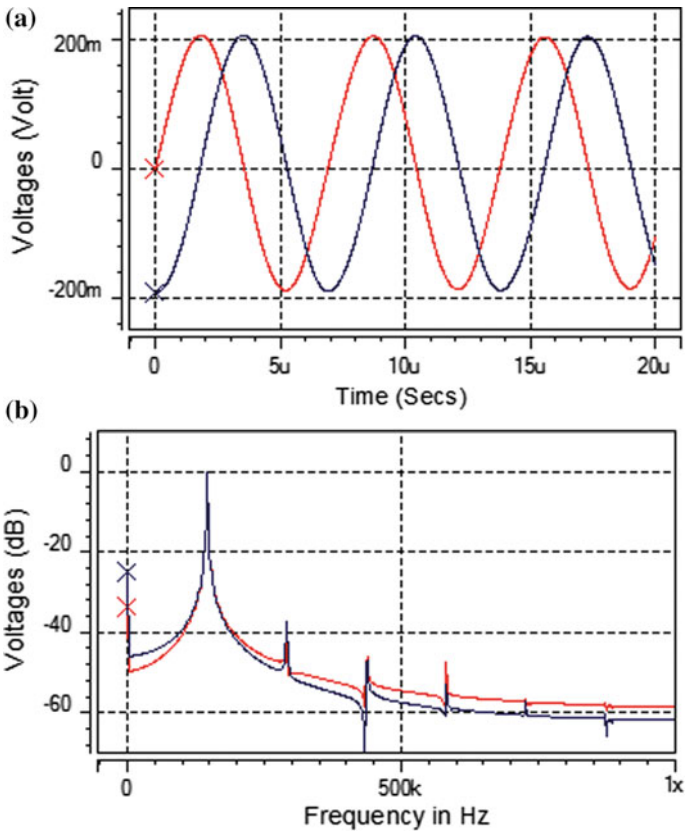

Fig. 4 **a** Simulated waveforms of voltages, V_1 and V_2 at 148 kHz **b** Frequency spectrums of voltages, V_1 and V_2

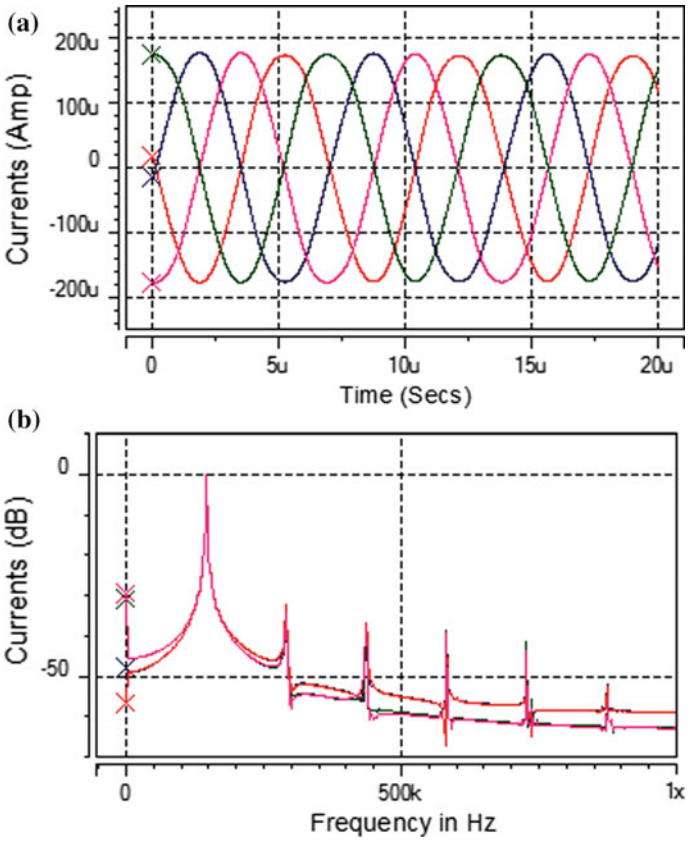

Fig. 5 **a** Simulated waveforms of currents, I_1, I_2, I_3, and I_4 at 148 kHz **b** Frequency spectrums of currents, I_1, I_2, I_3 and I_4

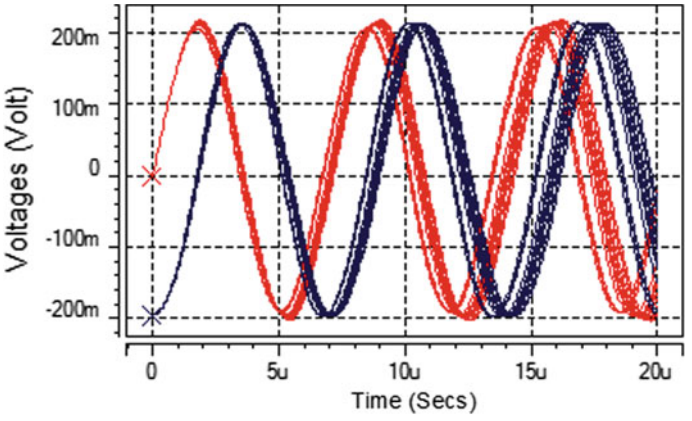

Fig. 6 Monte Carlo simulations for the waveforms of voltages, V_1 and V_2 for 20 multiple runs

4 Conclusion

A DMQO consisting of one FDCCII, three resistors, and two capacitors have been introduced in the paper. The presented DMQO simultaneously provides two voltage signals and four current signals at the outputs. All the output currents are obtained from high impedance terminals, thus it is available for practical applications. The presented DMQO enjoys the features of orthogonal control of f_0 and CO, good sensitivity performance, low THD of each output, and low power consumption. The nonideal effects of FDCCII on presented DMQO have been investigated. For the verification of the proposed circuit, HSPICE simulation results are shown.

References

1. Abaci, A., Yuce, E.: Modified DVCC based quadrature oscillator and lossless grounded inductor simulator using grounded capacitor (s). AEU-Int. J. Electron. Commun. **76**, 86–96 (2017)
2. Maheshwari, S., Chaturvedi, B.: High-input low-output impedance all-pass filters using one active element. IET Circuits Devices Syst. **6**, 103–110 (2012)
3. Maheshwari, S.: High input impedance VM-APSs with grounded passive elements. IET Circuits Devices Syst. **1**, 72–78 (2007)
4. Minaei, S., Yuce, E.: Novel voltage-mode all-pass filter based on using DVCCs. Circuits Syst. Signal Process. **29**, 391–402 (2010)
5. Kumar, A., Paul, S.K.: Current mode first order universal filter and multiphase sinusoidal oscillator. AEU-Int. J. Electron. Commun. **81**, 37–49 (2017)
6. Maheshwari, S., Chaturvedi, B.: High output impedance CMQOs using DVCCs and grounded components. Int. J. Circuit Theory Appl. **39**, 427–435 (2011)
7. Minaei, S., Ibrahim, M.A.: General configuration for realizing current-mode first-order all-pass filter using DVCC. Int. J. Electron. **92**, 347–356 (2005)
8. Maheshwari, S.: Electronically tunable quadrature oscillator using translinear conveyors and grounded capacitors. Act. Passiv. Electron. Compon. **26**, 193–196 (2003)
9. Kumar, A., Chaturvedi, B.: A novel current-mode quadrature oscillator operated at low voltage. In: 6th International Joint Conference on Advances in Engineering and Technology, pp. 201–208 (2015)
10. Kumar, A., Chaturvedi, B.: Novel CMOS current inverting differential input transconductance amplifier and its application. J. Circuits Syst. Comput. **26**, 1750010 (2017)
11. Mohan, J., Chaturvedi, B., Maheshwari, S.: Low voltage mixed-mode multi phase oscillator using single FDCCII. Electronics **20**, 36–42 (2016)
12. Maheshwari, S.: Sinusoidal generator with π/4-shifted four/eight voltage outputs employing four grounded components and two/six active elements. Act. Passiv. Electron. Compon. **2014**, 7 (2014)
13. Chaturvedi, B., Mohan, J.: Single active element based mixed-mode quadrature oscillator using grounded components. IU-J. Electr. Electron. Eng. **15**, 1897–1906 (2015)
14. Maheshwari, S.: High output impedance current-mode all-pass sections with two grounded passive components. IET Circuits Devices Syst. **2**, 234–242 (2008)
15. Maheshwari, S., Khan, I.A.: Novel single resistor controlled quadrature oscillator using two CDBAs. J. Act. Passiv. Electron. Devices **2**, 137–142 (2007)
16. Maheshwari, S.: New voltage and current-mode APS using current controlled conveyor. Int. J. Electron. **91**, 735–743 (2004)
17. Mohan, J., Chaturvedi, B.: Load insensitive, low voltage quadrature oscillator using single active element. Adv. Electr. Electron. Eng. **15**, 408–415 (2017)

18. Kumar, A., Chaturvedi, B.: Novel CMOS dual-X current conveyor transconductance amplifier realization with current-mode multifunction filter and quadrature oscillator. Circuits Syst. Signal Process. 1–28 (2017)
19. Chaturvedi, B., Maheshwari, S.: Second order mixed mode quadrature oscillator using DVCCs and grounded components. Int. J. Comput. Appl. **58**, 42–45 (2012)
20. Chaturvedi, B., Mohan, J.: Single DD-DXCCII based quadrature oscillator with simultaneous current and voltage outputs. Electronics **19**, 94–100 (2016)
21. Mohan, J., Chaturvedi, B., Maheshwari, S.: Single active element based voltage-mode multifunction filter. Adv. Electr. Eng. **2014** (2014)
22. Maheshwari, S., Mohan, J., Chauhan, D.S.: Novel cascadable all-pass/notch filters using a single FDCCII and grounded capacitors. Circuits Syst. Signal Process. **30**, 643–654 (2011)
23. Maheshwari, S., Khan, I.A., Mohan, J.: Grounded capacitor first-order filters including canonical forms. J. Circuits Syst. Comput. **15**, 289–300 (2006)
24. Maheshwari, S., Mohan, J., Chauhan, D.S.: Voltage-mode cascadable all-pass sections with two grounded passive components and one active element. IET Circuits Devices Syst. **4**, 113–122 (2010)
25. Mohan, J., Maheshwari, S., Khan, I.A.: Mixed-mode quadrature oscillators using single FDCCII. J. Act. Passiv. Electron. Devices **2**, 227–234 (2007)

Hybrid Color Image Watermarking Algorithm Based on DSWT-DCT-SVD and Arnold Transform

Palak Garg, Lakshita Dodeja, Priyanka and Mayank Dave

Abstract With emergence of new technologies it is now easier to communicate through multimedia like image, audio, video and text. But at the same time the problem of unauthorized access and copyright protection has also emerged. In order to handle these problems digital image watermarking is one of the best technique. In this paper we present an optimized color image watermarking technique to protect an image data from any unauthorized access. The technique presented in the paper uses a combination of Discrete Stationary Wavelet Transform (DSWT), Singular Value Decomposition (SVD), Discrete Cosine Transform (DCT) and Arnold Transform. In this technique we hide a color image watermark into a colored cover image without hampering the perceptibility of the cover image. Peak-signal-to-noise-ratio (PSNR) and Normalized Correlation (NC) are used to analyze the proposed watermarking technique for the imperceptibility and robustness measures.

Keywords Watermarking · Discrete stationary wavelet transform (DSWT) Discrete cosine transform (DCT) · Singular value decomposition (SVD) Arnold transform

P. Garg · L. Dodeja (✉) · Priyanka · M. Dave
Department of Computer Engineering, National Institute of Technology, Kurukshetra, Kurukshetra, India
e-mail: lakshita.dodeja@gmail.com

P. Garg
e-mail: palak.garg2107@gmail.com

Priyanka
e-mail: pdogra66@gmail.com

M. Dave
e-mail: mdave@nitkkr.ac.in

B. S. Rawat et al. (eds.), *Advances in Signal Processing and Communication* , Lecture Notes in Electrical Engineering 526,
https://doi.org/10.1007/978-981-13-2553-3_31

1 Introduction

The ease of sharing digital media like audio, video, images and text with the rising information technology has also increased the demand for security, copy control, copyright authentication etc. of the information in digital form. Watermarking is one such technique to tackle with these issues along with others. Digital image watermarking hides ownership data known as watermark into the multimedia data that can be extracted when required to provide the proof of authenticity [1]. The watermark either visible or invisible does not hamper the original use of the multimedia content. Watermark can be inserted either by modifying the pixel values of the image known as spatial domain technique which is computationally efficient but low in robustness and imperceptibility or transform domain techniques that are more popular nowadays because they embed the watermark into the coefficients of transform domain [2]. Discrete cosine transform (DCT), discrete stationary wavelet transform (DSWT) and singular value decomposition (SVD) are popular transformation techniques. Each of these is highly efficient against some of the attacks but not all. The proposed algorithm withstands majority of the attacks by combining various techniques. Robustness, imperceptibility and capacity are the three requirements of any watermarking scheme [3]. In this algorithm, discrete stationary wavelet transform (DSWT) provides protection against geometric attacks and robustness, singular value decomposition (SVD) provides imperceptibility, discrete cosine transform (DCT) provides protection against compression and Arnold transform provides watermark security. Using DSWT also enables us to keep the same size of watermark as the cover and hence the capacity of information to be hidden remains the same.

2 Literature Review

2.1 Discrete Stationary Wavelet Transform (DSWT)

Discrete Wavelet Transform (DWT) transforms an image using wavelets having varying frequency and short time interval. It has an advantage over other transforms as it is able to capture location information in both time and frequency. DWT performs down sampling of the signal after passing it through high pass and low pass filters to give the approximation and detail coefficients.

Discrete Stationary Wavelet Transform (DSWT) is similar to DWT [4] but it does not involve down sampling of signal after decomposing it by applying high pass and low pass filters. This attributes DSWT with the additional property of translation invariance

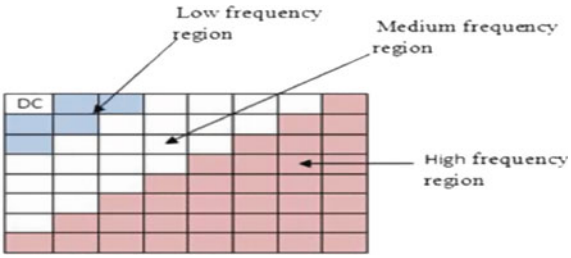

Fig. 1 Separation of an image into 3 frequency regions by DCT

2.2 Discrete Cosine Transform (DCT)

Discrete Cosine Transform is the most popular transform in spectral domain and transforms data points into sum of cosine functions oscillating at different frequencies that can be grouped into three categories low, medium and high frequency. Embedding the image into middle frequencies provide protection against JPEG compression as only high frequencies are lost in the lossy JPEG compression and our eyes being susceptible to low frequency using middle frequency provides imperceptibility (Fig. 1).

2.3 Singular Value Decomposition (SVD)

Singular value decomposition (SVD) is an arithmetical method that is used to covert a matrix into three diagonal matrixes [6]. In image processing an image can be seen as a matrix with non-negative scalar values. The SVD of an image A of size M x N is defined as

$$A = USV^T. \tag{1}$$

where U and V are orthogonal matrices that means multiplication of U and V with their transpose results in identity matrix, $UTU = I$, $VTV = I$, and $S = \text{diag}(\lambda 1, \lambda 2, \lambda 3, \ldots, \lambda r)$. The diagonal entries of S depict the luminance of A where r is the rank of A and they are known as singular values of A. The columns of U and V are used to retain the geometrical properties of the image and they are called the left and right singular vectors of A. US are called the principal components of A. UV together called as the SVD subspace of A. SVD is beneficial for watermarking as modification in singular values of images do not disturb the perceptibility of the cover image.

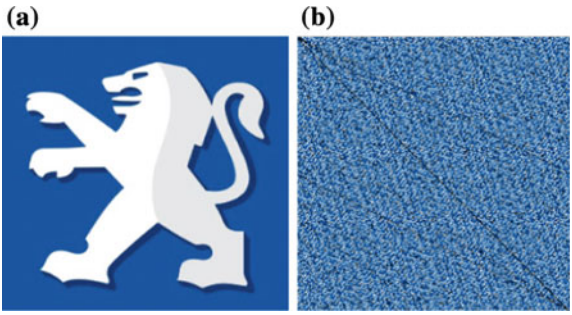

Fig. 2 **a** Original image **b** Scrambled image using Arnold transform

2.4 Arnold Transform

This transform is a splicing and clipping process that realigns the pixel matrix of digital image. It is applied to the watermark before embedding it in host image. A two dimensional Arnold transform [6] is shown as follows

$$\begin{pmatrix} x' \\ y' \end{pmatrix} = \begin{pmatrix} 1 & 1 \\ 1 & 2 \end{pmatrix} \begin{pmatrix} x \\ y \end{pmatrix} mod\ N \tag{2}$$

where x and y are the coordinates of the original image, N is the height or width of the image and x′ and y′ are the coordinate of the scrambled image. The transform changes the position of pixels, and a scrambled image can be obtained by applying the algorithm several times. The disordered image can be converted back to the original image after certain number of permutations due the periodicity of the Arnold transform. For a 256 × 256 image, this period is 192, after which the scrambled image becomes equal to the original image. Due to scrambling the pixels of image get evenly distributed which helps in enhancing the robustness of algorithm (Fig. 2).

3 Proposed Algorithm

The embedding process is as follows-

Step 1: Read the cover and watermark each of 'N x N' pixels in RGB format.
Step 2: Split both the images in three channels, namely Red, Green and Blue.
Step 3: Apply Arnold transform on the watermark with the secret key 10 and 1-level DSWT on the cover image.
Step 4: Apply DCT on the scrambled watermark and LL sub-band of 1-level DSWT.
Step 5: Apply SVD to the DCT coefficients of both the images.
Step 6: Embed the watermark.
Step 7: Apply Inverse SVD.
Step 8: Apply Inverse DCT.

Step 9: Apply Inverse DSWT that gives the watermarked image in one channel.
Step 10: Repeat steps 3–9 for the other two channels.
Step 11: Merge all the three channels to get the watermarked image (Fig. 3).

The extraction process is as follows-

Step 1: Read the cover, watermark and watermarked images in RGB format.
Step 2: Split all the images in three channels, namely Red, Green and Blue.
Step 3: Apply Arnold transform to the watermark and 1-level DSWT on the cover and watermarked images.
Step 4: Apply DCT on the scrambled watermark and LL sub-band of cover and watermarked images.
Step 5: Apply SVD on the DCT coefficients.
Step 6: Extract the watermark.
Step 7: Apply Inverse SVD.
Step 8: Apply Inverse DCT to get the scrambled watermark back.

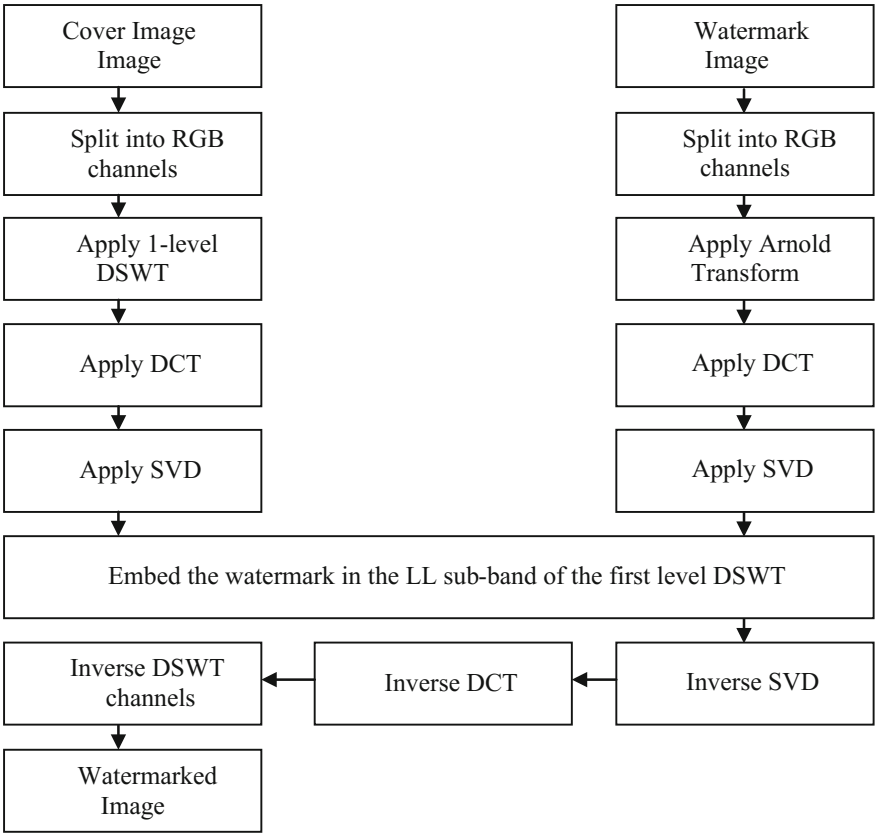

Fig. 3 Embedding process

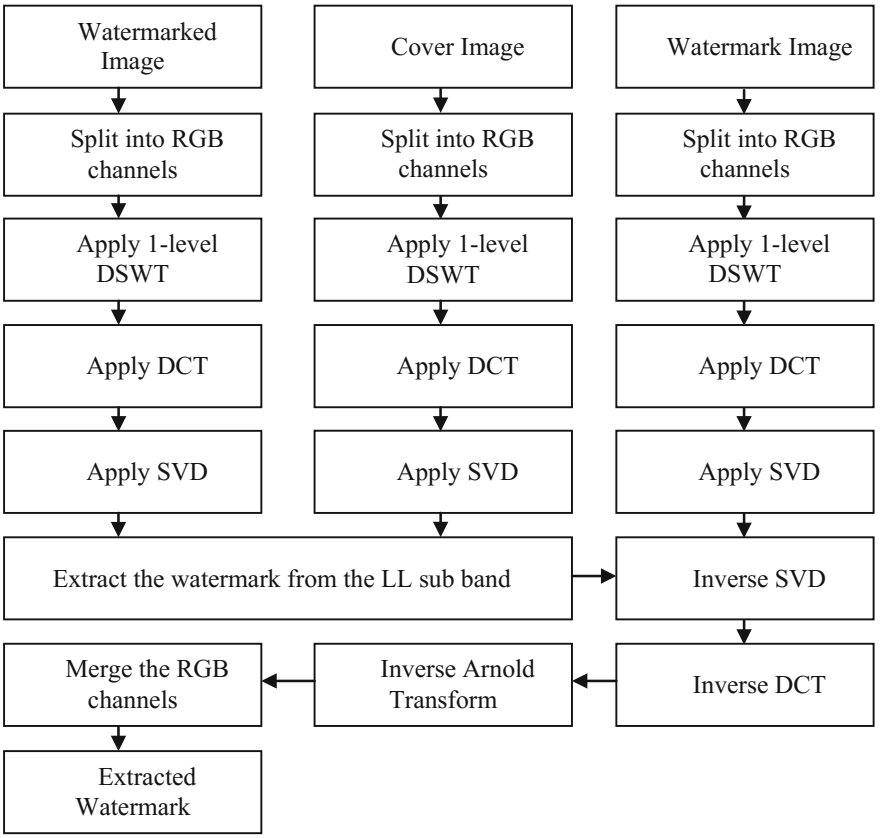

Fig. 4 Extraction process

Step 9: Apply Inverse Arnold transform to get one channel of the watermark.
Step 10: Repeat steps 3–9 for the other two channels.
Step 11: Merge all the three channels to get the final extracted watermark image (Fig. 4).

4 Experimental Results

We tested our proposed algorithm using Lena as the cover image (Fig. 5a) and Peugeot logo as the watermark image (Fig. 5b). The size of cover image and watermark image is 256×256. Both the images used are colored having 24 bit depth.

Where x and y are the coordinates of the original image, N is the height or width of the image and x' and

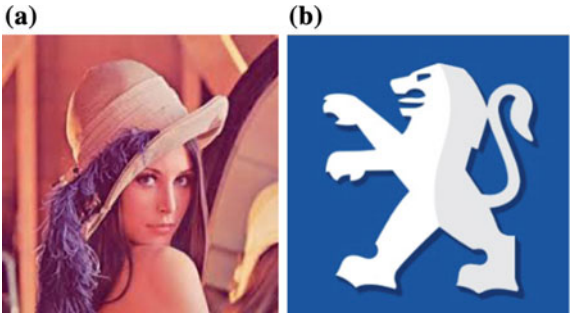

Fig. 5 **a** Cover Image **b** Watermark image

We used PSNR (Peak Signal to Noise Ratio) and NC (Normalised Correlation) to measure the imperceptibility of the watermarked image and to measure the similarity between the extracted watermark and original watermark respectively. PSNR [7] was calculated using the formula

$$PSNR = 10 \log \frac{255^2}{MSE} \tag{3}$$

where MSE is the mean Square error given by

$$MSE = \frac{1}{\mathrm{MN}} \sum_{\mathrm{i}=0}^{\mathrm{m}-1} \sum_{\mathrm{j}=0}^{\mathrm{n}-1} (\mathrm{C} - \mathrm{WM})^2 \tag{4}$$

where C is the Cover Image and WM is the Watermarked Image. Higher the value of PSNR, more imperceptible the algorithms is. We have recorded the highest PSNR value for our proposed algorithm as 79.1674 for 0.1 as α.

Normalised Correlation [8] was evaluated using the formula

$$NC = \frac{\sum_{\mathrm{i}=0}^{\mathrm{m}-1} \sum_{\mathrm{j}=0}^{\mathrm{n}-1} (\mathrm{E} \times \mathrm{W})}{\sqrt{\sum_{\mathrm{i}=0}^{\mathrm{m}-1} \sum_{\mathrm{j}=0}^{\mathrm{n}-1} \mathrm{E}^{\,2} \times \sum_{\mathrm{i}=0}^{\mathrm{m}-1} \sum_{\mathrm{j}=0}^{\mathrm{n}-1} \mathrm{W}^2}} \tag{5}$$

where E is the Extracted watermark and W is the Original watermark. We got 0.9488 as the highest NC value for our proposed algorithm for 0.8 as alpha. The values of PSNR and NC for different values of α are shown in Table 1. The results have been calculated when there are no attacks but in practical implementation the watermarked image can be attacked. We have compared our result with Azadeh et al.'s [9] method under various common attacks such as JPEG Compression, salt and pepper noise, median filter, wiener filter and rotation. We have taken the value of α as 0.5 for comparison.

From Table 2 we can observe that when there is no attack, the proposed method gives a better PSNR by 21.75%, this is because the proposed method contains SVD which makes the algorithm imperceptible whereas Method [9] contains only DWT.

Table 1 Experiment results of proposed method for different α values

A	PSNR	NC
0.1	79.1674	0.9083
0.2	73.1470	0.9328
0.3	69.6251	0.9371
0.4	67.1264	0.9383
0.5	65.1882	0.9419
0.6	63.6045	0.9397
0.7	62.2656	0.9397
0.8	61.1058	0.9488
0.9	60.0827	0.9424

Table 2 Comparison of proposed method with DSWT, DCT and SVD

Attack	DSWT	DCT	SVD	Proposed method
No attack	58.5137	31.6187	5.7790	65.1882
JPEG compression	58.2266	5.7538	5.7570	60.8265
Salt and pepper	58.4197	28.6493	5.7789	65.0423
Rotation	55.8512	11.9222	5.7711	57.6388
Cropping	56.6978	12.1125	5.7664	59.0375
Gaussian noise	58.2143	31.6181	5.7790	63.9163
Median filter	58.5105	30.2074	5.7789	65.4643
Averaging filter	58.5254	29.3464	5.7787	65.6652
Sharpening filter	56.7147	17.6405	5.7813	55.9165

Fig. 6 Attacked images for **a** No attack **b** JPEG compression 90% **c** JPEG compression 80% **d** JPEG compression 50% **e** Salt and pepper 0.002 **f** Salt and pepper 0.003 **g** Wiener filter **h** Median filter **i** Rotation 90 deg

We can also see that even under various attacks the PSNR values of the proposed method remains quite high whereas the PSNR values of Method [9] becomes significantly low, especially during the rotation attack (Figs. 6, 7 and Table 3).

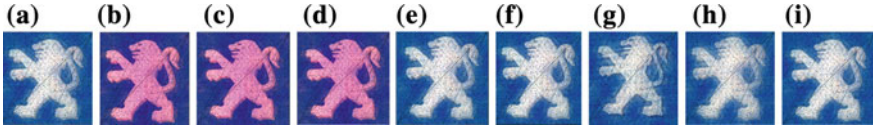

Fig. 7 Extracted images for **a** No attack **b** JPEG compression 90% **c** JPEG compression 80% **d** JPEG compression 50% **e** Salt and pepper 0.002 **f** Salt and pepper 0.003 **g** Wiener filter **h** Median filter **i** Rotation 90 deg

Table 3 Experimental results of proposed method and Method [9] under different attacks

Attack	Proposed method		Method [9]	
	PSNR	NC	PSNR	NC
No attack	65.1882	0.9419	53.5404	0.9986
JPEG compression 90	60.8718	0.9300	34.5933	0.9988
JPEG compression 80	60.8265	0.9303	33.2654	0.9988
JPEG compression 50	60.8691	0.9291	31.4634	0.9988
Salt and pepper 0.002	65.0857	0.9423	32.0912	0.9989
Salt and pepper 0.003	65.0423	0.9427	25.1745	0.9988
Wiener filter	65.5027	0.9304	37.3339	0.9980
Median filter	65.4643	0.9304	35.3360	0.9988
Rotation (90 deg)	57.6388	0.9414	11.7095	0.9986

5 Conclusion

In this research paper we have presented an imperceptible, robust and secure algorithm for Image Watermarking of colored images. All the advantages of DSWT, DCT and SVD are combined to generate this hybrid algorithm and Arnold Transform is added to make it even more secure. The data hiding capacity of the cover image, generally lesser has been equal to its size. Using this method, we are able to get higher values of PSNR by a percentage of 21.75% and hence the proposed algorithm is very imperceptible. The values of NC though less but are comparable to that of Method [9]. Future work can be done towards increasing NC values.

References

1. Lala, H.: Digital image watermarking using discrete wavelet transform. Int. Res. J. Eng. Technol. (IRJET). **04**(01), 1682–1685 (2017)
2. Tyagi, S., Singh, H.V.: Agarwal, R., Gangwar, S.K.: Digital watermarking techniques for security applications. In: International Conference on Emerging Trends in Electrical, Electronics and Sustainable Energy Systems (ICETEESES-16), pp. 379–382. IEEE (2016)
3. Ramamurthy, N., Varadarajan, S. Dr.: Effect of various attacks on watermarked images. Int. J. Comput. Sci. Inf. Technol. (IJCSIT), **3**(2), 3582–3587 (2012)

4. Al-Afandy, K.A., Faragallah, O.S., EL-Rabaie, El.-S.M., Abd El-Samei, F.E., ELmhalawy, A.: A hybrid scheme for robust color image watermarking using DSWT in DCT domain. In: 2016 4th IEEE International Colloquium on Information Science and Technology (CiSt), pp. 444–449 (2016)
5. Barni, M., Bartolini, F., Cappellini, V., Piva, A.: A DCT domain system for robust image watermarking. Signal Process **66**(3), 357–372 (1998)
6. Gaur, S., Srivastava, V.K.: A hybrid RDWT-DCT and SVD based digital image watermarking scheme using arnold transform. In: 4th International Conference on Signal Processing and Integrated Networks (SPIN), pp. 399–404 (2017)
7. Qianli, Y., Yanhong, C.: A digital image watermarking algorithm based on discrete wavelet transform and discrete cosine transform. In: International Symposium on Information Technologies in Medicine and Education, pp. 1102–1105. IEEE (2012)
8. Saravanan, P., Sreekara, M., Manikantan, K.: Digital image watermarking using daubechies wavelets. In: 3rd International Conference on Signal Processing and Integrated Networks (SPIN), pp. 57–62. IEEE (2016)
9. Karimian, A., Vahidi, J.: A new color image watermarking algorithm using 3-level discrete wavelet transform. Int. J. Mechatron. Electr. Comput. Technol. (IJMEC), **7**(26), 3633–3643 (2017)

A Brief Study and Analysis to Investigate the Effect of Various Dielectric Materials on Substrate-Integrated Waveguide

Fatima Haider and Megha Dade

Abstract Substrate-Integrated Waveguide (SIW) technology is an emerging and promising candidate for the development of circuits and components in upper microwave and millimeter wave region. This paper aims at emphasizing various dielectric substrates for the analysis of SIW to investigate their effect on the characteristic curve and electric field distribution. Certain factors that have been considered for evaluation are electric field, transmission gain, and return loss. High-Frequency Structure Simulator (HFSS) has been used to carry out the designs.

Keywords SIW · Via · Pitch distance · Diameter · Return loss · Transmission gain Bandgap effect

1 Introduction

During the past few decades, Substrate-Integrated Waveguide (SIW) [1] has grabbed many eyeballs for its various distinct attributes. We are well acquainted with conventional transmission lines like coaxial cables for transmission of electromagnetic radiation but because of various losses like dielectric loss, radiation loss, and copper loss and also due to their nonplanar nature they are dropped out. Rectangular Waveguides, apart from their uses, are also characterized by their exorbitant structure, stringent manufacturing precision, and nonplanar geometry. In series of making the most effective use of system integration, an approach to a guided structure known as Substrate-Integrated Waveguide (SIW) has been brought forward. Various exploration and experimentation have been executed to cash in on the burgeoning demand on high-performance millimeter and microwave circuits and components that can be developed using economical technologies. Originally introduced as post-wall

F. Haider (✉) · M. Dade
Department of ECE, BIT Mesra, Patna Campus, Patna, India
e-mail: haiderf786@gmail.com

M. Dade
e-mail: megha.dadel@bitmesra.ac.in

B. S. Rawat et al. (eds.), *Advances in Signal Processing and Communication* ,
Lecture Notes in Electrical Engineering 526,
https://doi.org/10.1007/978-981-13-2553-3_32

waveguide or laminated waveguide, SIW is basically a planar version of rectangular waveguide which is formed by two metal plates joining a dielectric material by densely arranging metallized holes or vias which connects both the metal plates to the substrate [1, 2].

SIW technology secures most of the merits related with conventional rectangular waveguides, citing for few like high power handling capacity, electromagnetic shielding through self-consistence, and strong Q-factor. The most remarkable advantage of SIW structure is its capacity of allowing a complete incorporation of all the elements on the same substrate, including passive elements, active elements, and even antennas as presented in [3, 4]. A noteworthy problem emerging at higher frequency is the confining of surface waves that is a cause of decrease in the antenna efficiency. The circumstance can effectively be controlled by SIW techniques. The rapid development of SIW technology over a decade has resulted in the establishment and innovation of active and passive circuits, antennas and systems at millimeter and microwave and frequencies covering a very broad frequency, ranging from subgigahertz to sub-terahertz. Furthermore, the SIW technique can be incorporated with other Substrate-Integrated Circuits (SICs) to develop multi-functional and multi-format system and devices. Being a new means of transmission of electromagnetic signals, SIWs have been the foundation for the design of many circuits.

2 Fundamental Features of SIW

2.1 Loss Considerations

The energy loss during the transmission may take place through various physical mechanisms that include radiation losses, dielectric losses, and conductor losses. Since SIW structure is synthesized using two lines of metallic vias implanted in the substrate that is electrically united by two parallel conducting plates, an appropriate preference of dielectric substrate and quality of conductor can decrease the effect of the last two loss mechanisms [5].

- Attenuation because of losses from dielectric is associated with loss tangent (tan δ) of the substrate and is given as

$$\alpha_d = \frac{k^2 \tan \delta}{2\beta} \tag{1}$$

- Attenuation due to conductor loss is given by

$$\alpha_c = \frac{R_s}{a^3 b\beta k\eta}\left(2b\pi^2 + a^3 k^2\right) \tag{2}$$

The radiation or the leakage loss arises when the periodic separation between the vias increases as a result of which the EM waves no longer remain limited within the vias. The losses of SIW can be reduced by modifying its structural parameters namely, the substrate thickness *h,* the diameter of the metallic vias *d*, and their geometrical spacing or pitch *p.* The thickness *h* offers a critical role in the significant reduction of conductor loss by an increase in its value. This is because lower electric current density flows on the surface of the metal by increasing the thickness of the substrate. The diameter of the holes and pitch *p,* have a great influence on radiation loss. To ensure negligible leakage loss or for the conventional waveguide to become radiation-less, parametric effects of *pitch (p)* and the *diameter (d)* were taken into account on these issues [6]

$$d < \frac{\lambda_g}{5} \tag{3}$$

$$p < 2d. \tag{4}$$

2.2 SIW Propagation Mode

A three-dimensional structure of SIW is shown in Fig. 1 that consists of top and ground conducting planes of dielectric and two rows of parallel metallic via holes into the substrate. F. Xu and Ke. Wu have shown that the SIW and the standard rectangular waveguide manifest the same guided wave properties. Both of these structures uphold the TE_{m0} modes while TE_{10} remaining the dominant mode. As far as TE_{mn} and TM modes are considered, they do not exist in SIW because of the discontinuous geometry of its sidewalls. When these slots on the sidewalls of SIW cut through the orientation of the flow of current, i.e., TE_{m0} modes, very less amount of radiation will be generated and thus these modes can exist in the waveguide. In a similar fashion, other TE_{m0} modes can also exist in the waveguide as they possess the same surface current patterns on the narrow walls.

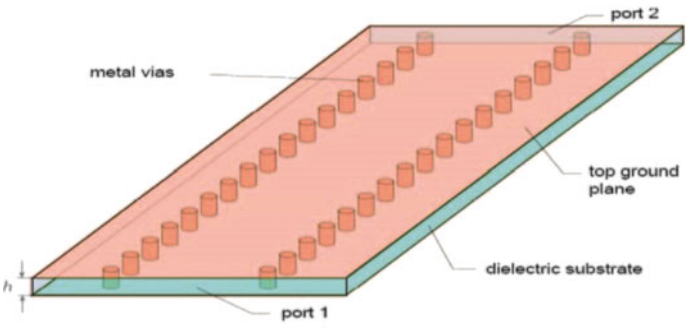

Fig. 1 A geometrical representation of SIW

On the contrary, when the horizontal component of surface current flows on the sidewalls for every TE_{mn} with nonzero n's as well as TM modes, the vias will cut through these paths of current thus resulting in loss due to radiation through the sidewalls.

2.3 SIW Design Rules

The SIW is the integrated planar version of rectangular waveguide form, which can be synthesized and fabricated by making use of two arrays of metallic cylindrical holes or slots lodged in dielectric substrate which is electrically drilled in between two parallel conducting plates. Except for the relative permittivity ε_r and the thickness of substrate *h,* there are three foremost parameters to design an SIW, i.e., a_{siw}, which is known as SIW width, the diameter of the metallic vias d, and the distance between adjoining metalized vias or the pitch p that are used to diminish the radiation loss and the return loss, respectively. The SIW can be considered as a conventional rectangular waveguide with the same dielectric filling just by making use of the SIW equivalent width, a_{eq}, which can be given by

$$a_{eq} = a_{siw} - \frac{d^2}{0.95p} \tag{5}$$

The above equation will become erroneous if d, i.e., the diameter of the vias is increased. Hence, to overcome this shortcoming, a more accurate formula can be stated as under:

$$a_{eq} = a_{siw} - 1.08\frac{d^2}{p} + 0.1\frac{d^2}{a_{siw}} \tag{6}$$

The region where the SIW behaves as a rectangular waveguide with inconsequential leakage loss and presents no bandgap in its operating bandwidth is defined by following equations as discussed in [7]:

$$p < d \tag{7}$$

$$0.05 < \frac{p}{\lambda_c} < 0.25 \tag{8}$$

$$p \leq 2d \tag{9}$$

The condition (7) indicates that the pitch distance in between the vias must be greater than their diameter so that the structure is physically attainable, i.e., there is no overlapping of the vias onto each other. Since SIW is a cyclic structure it is prone to bandgap effects. Hence, while designing SIW components one must make sure that SIW functions in the bandwidth of interest with negligible bandgap effects. The right portion of Eq. (8) is necessary to avert any bandgap in the frequency bandwidth of interest. Finally, an inessential but beneficial condition for the fabrication process is to reduce the number of holes. These holes are usually mechanically drilled and

chemically electroplated, and the manufacturing time is proportional to their number. Therefore, the number of cylinders should not exceed 20 per wavelength as indicated from the left portion of Eq. (8).

3 Design, Simulation and Results

In the manufacturing of high-performance-integrated systems and circuits, low loss material is kept as base. Other parameters which are considered for accurate designing, especially for antenna development, are dielectric nonuniformity, roughness of metallic surface, and thermal effect.

Different dielectric substrates have been taken into account for this report to study their effect on the propagation patterns of SIWs which is shown in the table beneath (Table 1).

The model was designed using HFSS. Frequency of 12 GHz is applied through the waveports to analyze the results. The pitch distance p = 1.9 mm, diameter of the vias are kept as d = 0.8 mm and $W_{siw} = 4$ mm.

The plot shown from Fig. 2a–e indicates characteristic curve between S parameters and the frequency. Return losses (S_{11}) and the transmission gain (S_{21}) was graphed for every dielectric substrate used in the experiment. Figure 3a shows variation between S parameter and frequency for PCB substrate. The first dip in return loss of −34 dB is seen at 10.4 GHz. Transmission gain escalates up to 10 GHz after which it saturates. Figure 2b shows the S_{11} and S_{21} parameter with respect to frequency plot for PTFE substrate. Several dips in the return loss is observed, first being at 12.6 GHz of −27 dB and transmission gain increases up to 12.5 GHz and then saturates. PMMA polymer used in simulation shows that return loss becomes stable after 13 GHz and transmission gain shows dips of −26.61, −48.38, and −45.89 dB at frequencies of 13.1, 14.9, and 17.5 GHz, respectively. Similarly, parametric curve for forward transmission gain as well as return loss is observed in the case for Mica. Return loss increases up to 12 GHz frequency as shown in Fig. 2d. Transmission gain shows several dips of −26.4, −45.65, and −40.63 dB are seen at frequencies 12.4, 13.8, and 15.8 GHz, respectively. Lastly, analysis for Silicon substrate shows several similar numbers of dips at frequencies 11, 13, and 14.8 GHz while the transmission gain remained constant throughout.

The electric field generated while computing the results for different substrates are shown in Fig. 3a−e. Figure 3a shows the simulated result for electric field distribution

Table 1 Properties of different dielectric substrates

Dielectric substrates	Relative permittivity	Relative permeability	Dissipation factor
PCB	4.4	1	0.02
PTFE	2.2	1	0.0009
PMMA	3.7	1	0.01
Mica	5.7	1	0
Silicon	11.9	1	0

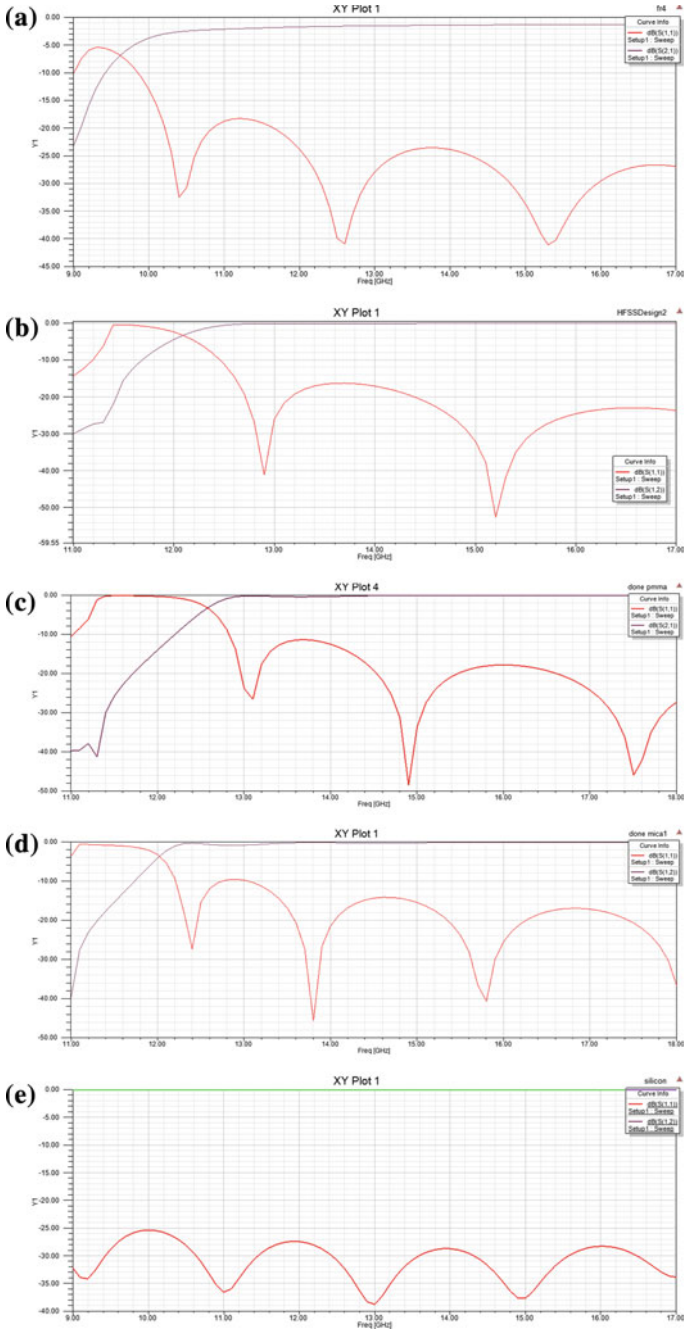

Fig. 2 **a** PCB substrate, **b** PTFE substrate, **c** PMMA substrate, **d** Mica substrate, **e** Silicon substrate

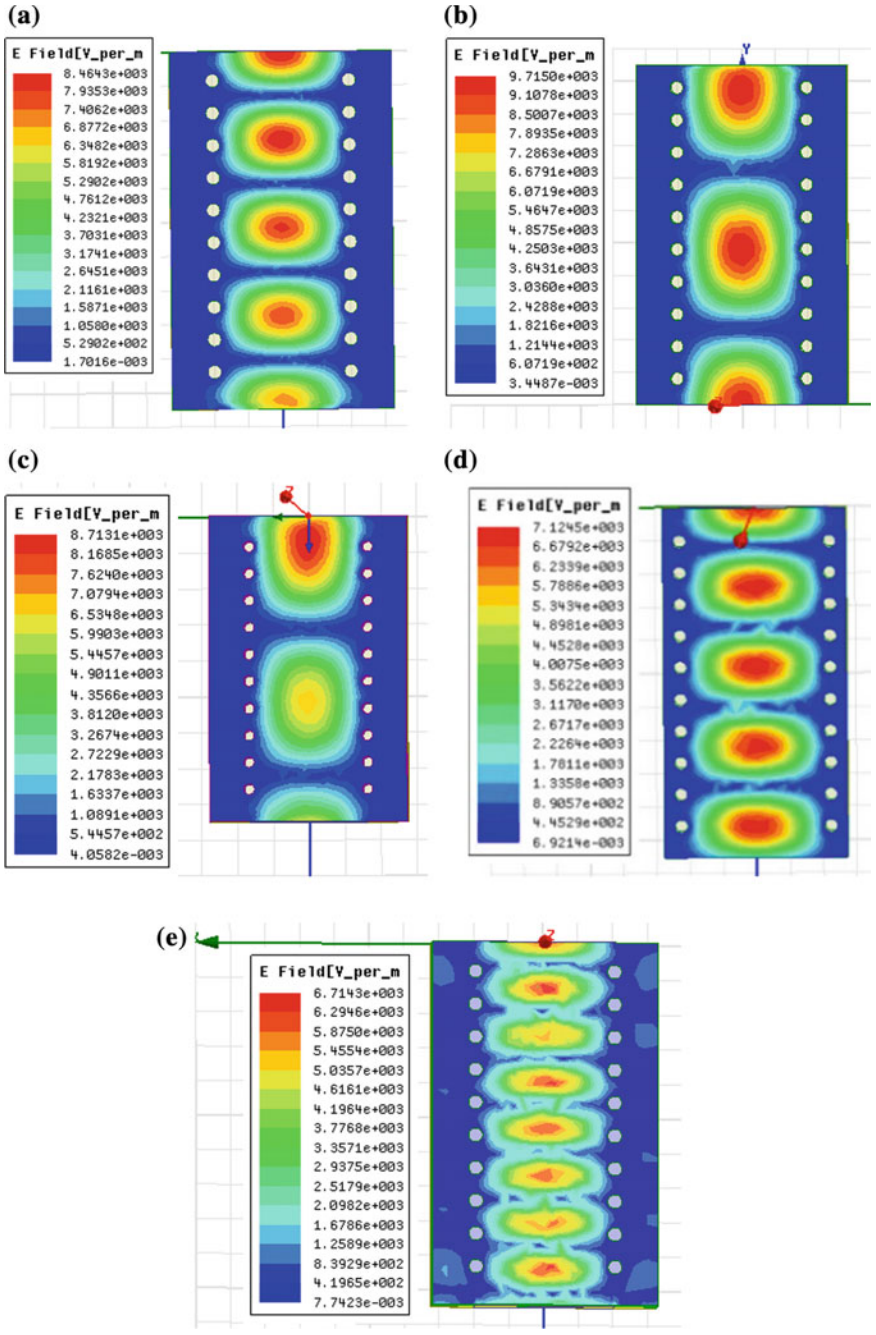

Fig. 3 **a** E-field distribution in PCB, **b** E-field distribution in PTFE, **c** E-field distribution in PMMA, **d** E-field distribution in Mica, **e** E-field distribution in Silicon

generated in PCB as substrate, while Fig. 3b–e shows the electric field which was generated for the substrates taken as PTFE, PMMA, Mica, and Silicon, respectively. From the bar line adjacent to these graphs, it is clear that the maximum value (9.715×10^3 V/m) of electric field is for PTFE while minimum value (6.714×10^3 V/m) is of Silicon. PCB and PMMA showed almost similar results with 8.464×10^3 and 8.713×10^3 V/m, respectively. Electric field distribution of Mica substrate remained at 7.124×10^3 V/m.

4 Conclusion

This reported work has been executed to analyze the outcome of different dielectric substrates on the electromagnetic wave propagation of SIW. In order to access the effect of dielectric substrates, five different substrates such as PCB, PTFE, PMMA, Mica, and Silicon were used in the experiment. S parameters, namely transmission gain and return loss were evaluated for frequency range of 12–18 GHz. Thus, from this analysis, we come to a conclusion that SIWs performance is efficient at around 12–13 GHz. For PMMA and PTFE, the evaluations were found to be appropriate than that of Si and Mica as dielectric substrates. PCB substrate also showed good and acceptable results.

References

1. Uchimura, H., Takenoshita, T., Fuji, M.: Development of a laminated waveguide. IEEE Trans. Microw. Theory Tech. **46**(12) (1998)
2. Hirokawa, J., Ando, M.: Single-layer feed waveguide consisting of ports for plane TEM wave excitation in parallel plates. IEEE Trans. Antenna Propag. **46**(5) (1998)
3. Wu, K., Deslandes, D., Cassavi, Y.: The substrate integrated circuits- a new concept for high-frequency electronics and optoelectronics. In: 6th International Conference on Tele-Communication in Modern Satellite and Cable Broadcasting, TELSIKS 2003, vol. 1 (2003)
4. Wu, K., Cheng, Y.J., Djerrafi, T., Hong, W.: Substrate integrated milli-meter wave and terahertz antenna technology. Proc. IEEE **100**(7), 2219–2232
5. Bozzi, M., Pasian, M., Perregrini, L.: Modelling of losses in substrate integrated waveguide components. In: International Conference on Numerical Electromagnetic Modelling and Optimization for RF Microwave and Terahertz Applications (NEMO), Pavia, 14–16 May 2014, pp. 1–4 (2014)
6. Wu, K., Deslandes, D.: Single substrate integration technique of planar circuits and waveguide components. IEEE Trans. Microw. Theory Tech. **51**, 593–596 (2003)
7. Deslandes, D., Wu, K.: Accurate modelling, wave mechanisms and design considerations of a substrate integrated waveguide. IEEE Trans. Microw. Theory Tech. **54**(6) (2006)
8. Hua, G., Zhou, H.X.H.: Design of an Omni-directional line array with SIW longitudinal slot antenna. In: International Conference on Microwave and Millimeter Wave Technology, 1114–1117 (2008)

Multi-objective Cuckoo Search Algorithm-Based 2-DOF FOPD Controller for Robotic Manipulator

Himanshu Chhabra, Vijay Mohan, Asha Rani and Vijander Singh

Abstract Controller design for effective operation of robotic manipulator is a challenging task due to its highly complex and nonlinear dynamics. This issue may be resolved by incorporating fractional mathematics along with two-degrees-of-freedom PID controller. The fractional mathematics enhances the accuracy of control action, whereas two-degrees-of-freedom controller solves multiple issues like set point tracking and disturbance rejection simultaneously. Therefore, in this paper, a two-degree-of-freedom fractional-order proportional–derivative (2-DOF FOPD) controller is proposed for efficient trajectory control of two-link rigid manipulator. Conventional PID and its integer-order equivalent (2-DOF PD) controllers are also designed for comparative analysis. The parameters of designed controller are tuned using multi-objective cuckoo search algorithm (MOCSA) to minimize two conflicting objectives of robotic manipulator. Simulation study reveals the effectiveness and robustness of 2-DOF FOPD controller, in terms of trajectory tracking and disturbance rejection.

Keywords Robotic manipulator · MOCSA · PID · 2-DOF PD · 2-DOF FOPD

H. Chhabra (✉)
ECE Department, MLV Textile and Engineering College, Bhilwara, Rajasthan, India
e-mail: him08miet@gmail.com

V. Mohan · A. Rani · V. Singh
ICE Division, Netaji Subhas Institute of Technology, New Delhi 110078, India
e-mail: vijay13787@gmail.com

A. Rani
e-mail: ashansit@gmail.com

V. Singh
e-mail: vijaydee@gmail.com

B. S. Rawat et al. (eds.), *Advances in Signal Processing and Communication* ,
Lecture Notes in Electrical Engineering 526,
https://doi.org/10.1007/978-981-13-2553-3_33

1 Introduction

In recent years, robotic manipulators are widely used in various fields like auto assembling, space investigation, waste treatment in nuclear plants, medical surgeries, etc., due to its better performance in terms of precision, accuracy, and durability. Robotic manipulators are highly nonlinear in nature; therefore, researchers have developed different control strategies [1–4] in order to improve its tracking and robust performance.

PID controller has simple structure and may be tuned easily which makes it a good choice for controlling purpose. However, simultaneous control of servo and regulatory problems is not achieved effectively by one-degree-of-freedom PID controllers. This problem motivated the researchers to design 2-DOF control structures. The two-degree-of-freedom controller has two closed-loop transfer functions that can be tuned independently [5]. The 2-DOF PID controller handles the set point tracking and disturbance rejection simultaneously. 2-DOF PID controller and its various structures have been discussed by several authors [4–6]. The performance of 1-DOF PID and 2-DOF PID may be further enhanced by introduction of fractional calculus. Various researchers have also investigated the use of fractional mathematics in control theory [2, 7, 8].

The amalgamation of fractional mathematics with PID controller improves the controller performance but at the same time increases the number of design parameters. Thus, tuning of controller with large number of parameters leads to combinatorial problem. However, optimization techniques provide an alternative for effective tuning of such controllers. Literature reveals the use of various optimization techniques in different fields of engineering [3–5, 9] to reduce the computational effort. Recently, a new metaheuristic technique, *i.e.*, multi-objective cuckoo search algorithm (MOCSA), is proposed [10]. In this optimization technique, less parameters are used for initialization as compared to particle swarm optimization (PSO) and genetic algorithm (GA). Further, selection of parameters does not affect the convergence rate of MOCSA and it is more efficient as compared to other techniques due to its large-step length feature [3, 11].

In this article, a new controller named as two-degree-of-freedom fractional-order PD (2-DOF FOPD) controller is designed for robotic manipulator trajectory tracking control. MOCSA being an effective optimization technique is chosen for evaluating optimum parameters of 2-DOF FOPD controller. MOCSA-tuned PID and 2-DOF PD are also designed for comparative study. The designed controllers are tested for trajectory tracking and disturbance rejection of robotic manipulator.

Rest of the paper is structured as follows: In section II, the mathematical modeling of robotic manipulator is explained. The implementation of proposed control strategy for robotic manipulator is described in section III. Section IV describes the optimization technique, MOCSA. Simulation results are given in section V. Finally, conclusions of the study are drawn in section VI.

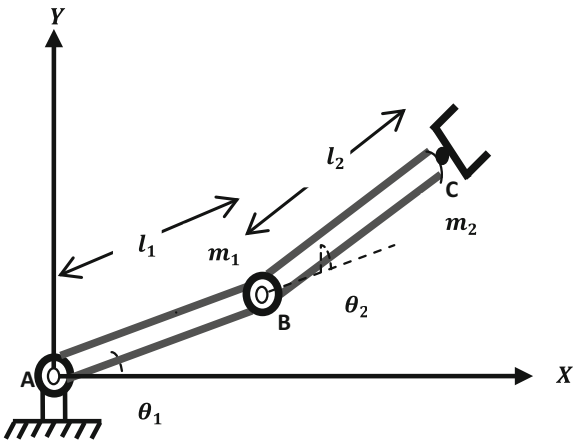

Fig. 1 Schematic diagram of 2-DOF robotic manipulator

2 System Modeling

A robotic manipulator can be described by a set of differential equations. There are various factors that affect the system performance such as varying inertia, centrifugal and Coriolis torques, and load and gravity. The motion of end effector in a defined path with confined speed requires a complicated set of torque functions being applied to actuator link of robotic manipulator. The robotic manipulator under consideration consists of two links and is described by the following equations [3]:

$$\tau_{\theta_1} = m_2 l_2^2\left(\ddot{\theta}_1 + \ddot{\theta}_2\right) + m_2 l_1 l_2 C_2\left(2\ddot{\theta}_1 + \ddot{\theta}_2\right) + (m_1 + m_2) l_1^2 \ddot{\theta}_1 - m_2 l_1 l_2 S_2 \dot{\theta}_1^2 - 2m_2 l_1 l_2 \dot{\theta}_1 \dot{\theta}_2 + m_2 l_2 g C_{12} + (m_1 + m_2) l_1 g C_1 \quad (1)$$

$$\tau_{\theta_2} = m_2 l_1 l_2 C_2 \ddot{\theta}_1 + m_2 l_2^2\left(\ddot{\theta}_1 + \ddot{\theta}_2\right) + m_2 l_1 l_2 S_2 \dot{\theta}_1^2 + m_2 l_1 g C_{12} \quad (2)$$

where $C_1 = cos(\theta_1), C_2 = cos(\theta_2), S_1 = sin(\theta_1), S_2 = sin(\theta_2)$ and $C_{12} = cos(\theta_1 + \theta_2)$. The subscripts 1 and 2 indicate the two links, respectively (Fig. 1).

3 Control Strategy

In the proposed work, order of differentiation for 2-DOF PD controller is modified by considering fractional value rather than integer one. The manipulating variable [6] in time domain is described as

$$\tau_{\theta_i} = \left\{K_{p_i}(1 - \sigma_i) + (1 - \delta_i) K_{d_i} s^{\lambda_i}\right\}(\theta_{id} - y) - \left\{K_{p_i}\sigma_i + \delta_i K_{d_i} s^{\lambda_i}\right\} y \quad i = 1, 2 \quad (3)$$

where (σ_i, δ_i) are set point weight constants and λ_i is fractional-order operator. In this study, Oustaloup's method is used for implementation of fractional operator

"s^p" [12], which is recursive distribution of M_f number of poles and zeros and is characterized as high-order filter.

$$s^p = G_f \prod_{n=-M_f}^{M_f} \frac{s + z_n}{s + p_n} \tag{4}$$

The filter parameters such as gain, zeros, and poles are obtained by the following equations:

$$G_f = (w_2)^b \tag{5}$$

$$z_n = w_1 \left(\frac{w_2}{w_1}\right)^{\frac{n+M_f+\frac{1}{2}(1-b)}{2M_f+1}} \tag{6}$$

$$p_n = w_1 \left(\frac{w_2}{w_1}\right)^{\frac{n+M_f+\frac{1}{2}(1+b)}{2M_f+1}} \tag{7}$$

where b, M_f, and $\left[2M_f + 1\right]$ are order in fraction, Oustaloup's constant, and filter order, respectively. $[w_1, w_2]$ is the frequency range.

4 Multi-objective Cuckoo Search Algorithm

The multi-objective cuckoo search algorithm (MOCSA) is established on the basis of brood parasitic nature of cuckoo along with Levy flight behavior of birds and fruit flies. Certain assumptions are considered in the design of MOCSA. Figure 2 presents the flowchart for implementation of MOCSA. The control effort and error in end-effector position must be minimum for efficient tracking control of robotic manipulator. Minimization of integral square error (f_1) allows the arm to track the desired trajectory, whereas minimization of torque (f_2) applied to joints enables the end effector to follow desired trajectory with minimum wear and tear stress.

Thus, objective functions f_1 and f_2 are defined as

$$f_1 = 0.5 \int \left((\theta_{1d} - \theta_1)^2 + (\theta_{2d} - \theta_2)^2\right) dt \tag{8}$$

$$f_2 = \int \left(\left(\tau_{\theta_1}(t) - \tau_{\theta_1}(t-1)\right)^2 + \left(\tau_{\theta_2}(t) - \tau_{\theta_2}(t-1)\right)^2\right) dt \tag{9}$$

5 Simulation Results

The linearized model of robotic manipulator is simulated in MATLAB on Intel i7 3.40 GHz processor with 4 GB RAM. The system differential equations are solved by fourth-order Runge–Kutta method. Initially, 2-DOF PD and conven-

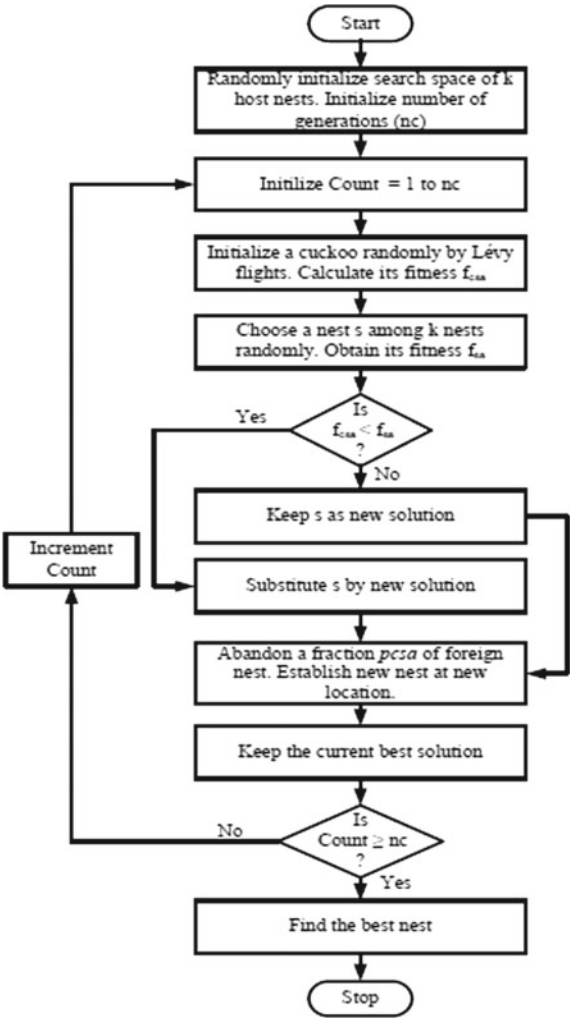

Fig. 2 Flowchart for MOCSA

tional PID controllers are designed and implemented for robotic manipulator. Further, amalgamation of fractional mathematics to 2-DOF PD controller leads to 2-DOF FOPD controller for position control of robotic manipulator. MOCSA is used to optimize parameters of designed controllers in order to follow a time-varying polynomial trajectory of angles θ_1 and θ_2 [1] by minimizing the control effort and integral square error (ISE). The search ranges for controller parameters are $k_{p_i} \in [0, 1000]$, $k_{I_i} \in [0, 300]$, $k_{d_i} \in [0, 50]$, and $\lambda_i, \sigma_i, \delta_i \in [0, 1]$. Figure 3 shows the position tracking, position error, and controller output for 2-DOF FOPD, 2-DOF PD, and PID controllers. The Pareto front obtained during optimization of 2-DOF FOPD controller and the selected solution are shown in Fig. 3d. Table 1 shows the

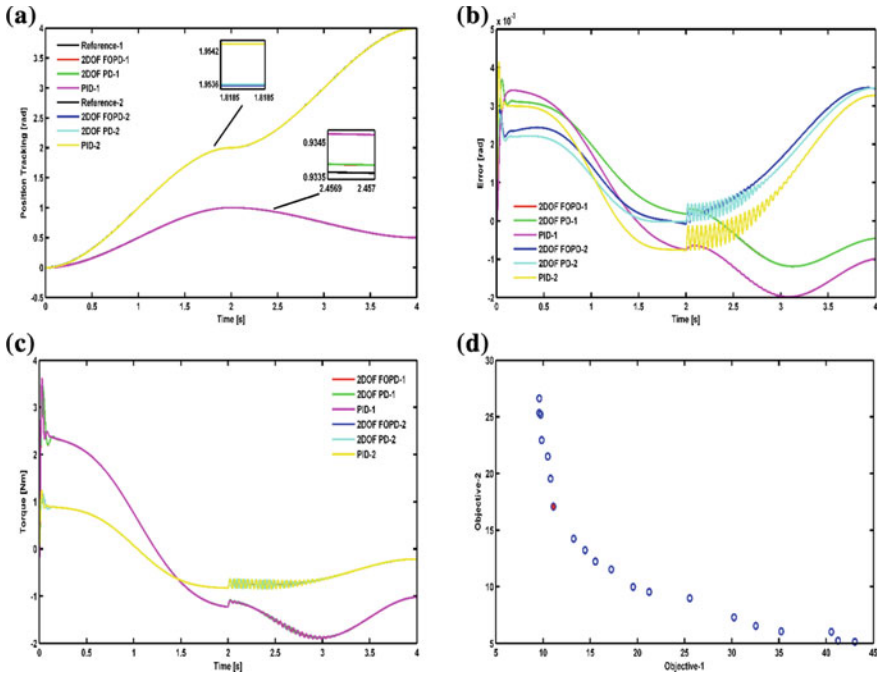

Fig. 3 **a** Position tracking performance, **b** Position error for 2-DOF FOPD, 2-DOF PD, and PID controller **c** Controller output **d** Pareto front for 2-DOF FOPD (selected solution marked as red)

Table 1 Optimized parameters of controllers and fitness function values for link-1 and link-2

For Link-1	2-DOF FOPD	2-DOF PD	PID	For Link-2	2-DOF FOPD	2-DOF PD	PID
K_{P_1}	450.2568	662.4580	782.4170	K_{P_2}	115.2840	129.9310	324.5230
K_{I_1}	–	–	225.2123	K_{I_2}	–	–	119.2450
K_{D_1}	24.5678	26.1275	35.1995	K_{D_2}	5.457	0.2154	20.1025
σ_1	0.0345	0.1235	–	σ_2	0.0547	0.0243	–
δ_1	0.7253	0.1445	–	δ_2	0.9576	0.9248	–
λ_1	0.8546	–	–	λ_2	0.0138	–	–
ISE	$8.235*10^{-5}$	$15.69*10^{-5}$	$11.286*10^{-4}$	ISE	$6.201*10^{-5}$	$11.256*10^{-5}$	$9.875*10^{-4}$
f_1	**0.4219**	12.1637	12.1637			‘	1
f_2	**18.566**	23.002	23.002				

optimized parameter values, integral square error, and objective function values for 2-DOF FOPD, 2-DOF PD, and PID controllers for link-1 and link-2. The simulation results reveal that 2-DOF FOPD is superior to other designed controllers.

Table 2 Quantitative analysis of ISE for sinusoidal disturbance in link-1 and link-2

Disturbance (Nm)	2-DOF FOPD		2-DOF PD		PID	
	Link-1 (10^{-5})	Link-2 (10^{-5})	Link-1 (10^{-5})	Link-2 (10^{-5})	Link-1 (10^{-5})	Link-2 (10^{-5})
In input-1						
$0.2Sin(30t)$	**8.458**	**6.201**	15.785	11.256	113.12	98.75
$0.6Sin(30t)$	**8.578**	**6.201**	15.986	11.256	117.54	98.75
$1Sin(30t)$	**9.152**	**6.201**	16.738	11.256	119.126	98.75
In input-2						
$0.2Sin(30t)$	**8.235**	**6.235**	15.69	11.354	112.86	99.56
$0.6Sin(30t)$	**8.235**	**6.354**	15.691	11.658	112.86	101.246
$1Sin(30t)$	**8.235**	**6.548**	15.691	12.145	112.86	107.548
In both inputs						
$0.2Sin(30t)$	**8.458**	**6.238**	15.785	11.354	113.12	99.56
$0.6Sin(30t)$	**8.579**	**6.354**	15.986	11.658	117.54	101.246
$1Sin(30t)$	**9.169**	**6.548**	16.738	12.145	119.126	107.548

5.1 Robustness Analysis

Robustness analysis of the proposed controller is carried out under various sinusoidal disturbances applied to link-1, link-2, and both links, respectively. Table 2 shows the ISE variation for 2-DOF FOPD, 2-DOF PD, and PID controllers in the presence of sinusoidal disturbance. It is clear from Table 2 that 2-DOF FOPD controller offers less ISE variation in comparison to 2-DOF PD and PID controllers. The results reveal that the proposed controller effectively rejects the disturbance introduced in the system. Therefore, 2-DOF FOPD controller is more robust and provides precise trajectory tracking control.

6 Conclusion

In this work, a 2-DOF FOPD controller is proposed and designed for precise tracking control of robotic manipulator. The results are compared with 2-DOF PD and PID controllers to justify the supremacy of the proposed controller. Extensive simulation study reveals that the proposed controller has better trajectory tracking capability in comparison to 2-DOF PD and PID controllers. Further, robustness analysis of 2-DOF FOPD controller is also carried out for disturbance in the system. It is found that 2-DOF FOPD controller is more robust in comparison to other designed controllers. Hence, it is concluded that MOCSA-based 2-DOF FOPD controller offers robust and tight position tracking control of robotic manipulator.

References

1. Ayala, H.V.H., dos Santos Coelho, L.: Tuning of PID controller based on a multiobjective genetic algorithm applied to a robotic manipulator. Expert Syst. Appl. **39**, 8968–8974 (2012)
2. Bingül, Z., Karahan, O.: Fractional PID controllers tuned by evolutionary algorithms for robot trajectory control. Turkish J. Electr. Eng. Comput. Sci. **20**, 1123–1136 (2012)
3. Chhabra, H., Mohan, V., Rani, A., Singh, V.: Multi objective PSO tuned fractional order PID control of robotic manipulator. In: The International Symposium on Intelligent Systems Technologies and Applications, pp. 567–572 (2016)
4. Mohan, V., Chhabra, H., Rani, A., Singh, V.: An expert 2DOF fractional order fuzzy PID controller for nonlinear systems. In: Neural Computing and Applications, pp. 1–18
5. Pachauri, N., Singh, V., Rani, A.: Two degree of freedom PID based inferential control of continuous bioreactor for ethanol production. ISA Trans. **68**, 235–250 (2017)
6. Araki, M., Taguchi, H.: Two-degree-of-freedom PID controllers. Int. J. Control Autom. Syst. **1**, 401–411 (2003)
7. Pdlubny, I.: Fractional order systems and PIλDμ controllers. IEEE Trans. Autom. Control **44**, 208–214 (1999)
8. Das, S., Pan, I., Das, S.: Performance comparison of optimal fractional order hybrid fuzzy PID controllers for handling oscillatory fractional order processes with dead time. ISA Trans. **52**, 550–566 (2013)
9. Mohan, V., Rani, A., Singh, V.: Robust adaptive fuzzy controller applied to double inverted pendulum. J. Intell. Fuzzy Syst. **32**, 3669–3687 (2017)
10. Gandomi, A.H., Yang, X.-S., Alavi, A.H.: Cuckoo search algorithm: a metaheuristic approach to solve structural optimization problems. Eng. Comput. **29**, 17–35 (2013)
11. Yang, X.-S., Deb, S.: Cuckoo search via Lévy flights. In: Nature and Biologically Inspired Computing, 2009. NaBIC 2009. World Congress on, 2009, pp. 210–214
12. Oustaloup, A., Levron, F., Mathieu, B., Nanot, F.M.: Frequency-band complex noninteger differentiator: characterization and synthesis. IEEE Trans. Circuits Syst. I: Fund. Theory Appl. **47**, 25–39 (2000)

Study of Noise Interfering with Dolphin Clicks

Kapil Dev Tyagi, Rajendar Bahl, Arun Kumar, Shivam Saxena and Sandeep Kumar

Abstract Accurate assessment of dolphin numbers in the Ganga river is crucial for not only conservation but also for the environment. However, the methods used by the government agencies are based on human visualization. These methods are unreliable and also difficult to deploy for continuous monitoring of the dolphins. So, there is a need to develop a system which will be robust, automatic, and reliable to count, track, and analyze the dolphin activities. The dolphin counting system consists of an array of hydrophones which are used to capture dolphin clicks. For counting purpose, this array is required to be mounted on a boat for dragging at a certain speed which is greater than the speed of dolphins. During the movement of the boat, lot of noise is picked up by the hydrophones apart from dolphin clicks. The presence of noise causes the dolphin click detection really a challenging task. In this paper, the various sources of noise and reduction techniques are investigated and presented.

Keywords Dolphin clicks · Cavitation noise · Hydrodynamic flow noise

K. D. Tyagi (✉)
Jaypee Institute of Information Technology, Noida, India
e-mail: kapiltyagiitd@gmail.com

R. Bahl · A. Kumar
Centre for Applied Research in Electronics, Indian Institute of Technology, New Delhi, Delhi, India
e-mail: rbahl@care.iitd.ernet.in

A. Kumar
e-mail: arunkm@care.iitd.ernet.in

S. Saxena · S. Kumar
Delsig Systems Pvt. Ltd., Noida, India
e-mail: shivam@delsig.com

S. Kumar
e-mail: sandeep@voxomos.com

B. S. Rawat et al. (eds.), *Advances in Signal Processing and Communication*,
Lecture Notes in Electrical Engineering 526,
https://doi.org/10.1007/978-981-13-2553-3_34

1 Introduction

Ganges river dolphins are found in freshwater. The population of the Ganga dolphins has decreased sharply in the last few years [1, 2]. One of the main reasons for the reduction in number of dolphins is the extreme pollution of the Ganga water. The chemicals, pesticides, and industrial waste in the water are consumed by the dolphins. These chemicals effect their reproduction capabilities. Also, the pollution has destroyed the fishes which are their natural food. The dolphins are many times trapped in fishing nets where they eventually die. Hunting of dolphins for traditional medicine was a major cause of their population decrement earlier but nowadays with the awareness, this is not a matter of concern.

The dolphins are nearly blind [3]. They use ultrasonic clicks to swim and hunt. The Ganga dolphin uses echolocation to create detailed maps of the scenario around them. The frequency of click is at around 50–60 kHz and duration is of around 50 microseconds. The dolphins are underwater most of the time and to breath, they come out of water for a fraction of second. So, it will be difficult to capture these using still cameras. Also, searching for the dolphins in the video clips is very difficult. However, the detection of dolphins using acoustic clicks is much more easy as dolphins are producing the acoustic clicks continuously while they are underwater [4, 5]. For counting purpose, the array of hydrophones that detects the dolphin click is required to be moved at a faster speed than dolphins, so that the clicks from the same dolphin can be avoided. The typical speed required for this purpose is 10 km/h. The array of hydrophones is normally mounted on a boat for moving it at the required speed. It is observed that the hydrophones also pick noise during the movement. The sources of the noise and the reduction techniques are investigated and presented in this paper.

The next section describes the experimental setup used to capture the dolphin clicks and the description of the noise acquired by the hydrophones. In Sect. 3, the various experiments to detect the source of noise present at the hydrophones are discussed. In Sect. 4, the effect of material used to fabricate the boat and the outboard engines are investigated. Section 5 contains the design of the boat to reduce the cavitation noise at specific speeds. The final section contains the conclusion of the paper.

2 Electronic Hardware and Noise Analysis

2.1 Electronic Hardware

The block diagram of the complete electronic system is shown in Fig. 1. The acoustic pulses of dolphin clicks are picked up by the hydrophones. After digitization and pre-amplification of 60 dB, the signals are fed in the cDAQ for processing and storage purpose. The sampling rate used is 10^6 samples per second. The power supply of ± 9 V is obtained using two batteries of 9 V. The videos are captured from the three

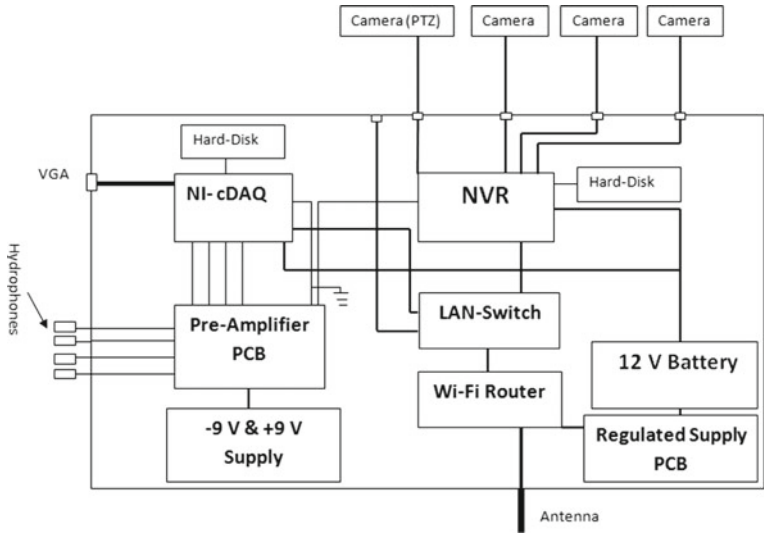

Fig. 1 Block diagram of complete electronic system

cameras using NVR and stored in the external hard disk. The video recording system is not relevant to this experiment. A 12-V battery is used to supply the power to cDAQ and NVR.

2.2 Dolphin Click and Analysis of Noise

Figure 2 shows a hydrophone array mounted on a boat.

The hydrophone and electronic system are able to detect the dolphin clicks in static conditions. One such dolphin click and noise samples around click is shown in Fig. 3. It is observed that the noise amplitude is very low for the order of few millivolts only when the hydrophone is in static condition.

Figure 4 shows the noise samples of 10 ms duration recorded at a speed of 5 km/h. It is observed from the figure that the peak amplitude is around 100 mV. The DFT of noise as shown in Fig. 5 reveals that the recorded noise is broadband in nature. We have used a low-pass filter with 3 dB cutoff frequency of 10 kHz and a high-pass filter with 3 dB cutoff frequency of 100 kHz before and after pre-amplification, respectively, to reduce the noise outside the band of interest. There are few dolphin clicks embedded in the data because of this the DFT plot shows higher magnitude at around 50 kHz.

The cross-correlation is performed between the noise and the dolphin click in an attempt to find a way to get rid of the noise. The correlation plot of the noise samples shown in Fig. 4 with the dolphin click is shown in Fig. 6. It is observed from

Fig. 2 Hydrophone array mounted on a boat

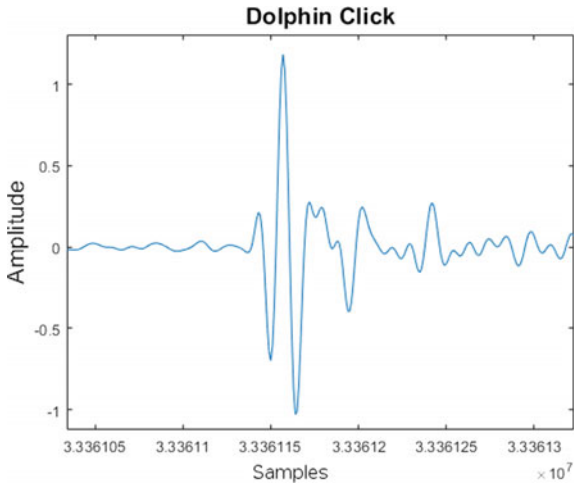

Fig. 3 Dolphin click

the plot that the dolphin clicks are highly correlated with the noise. The duration of the dolphin clicks is around 50 ms. So, any kind of filtering operation does not help much in recovering the dolphin clicks from the noise.

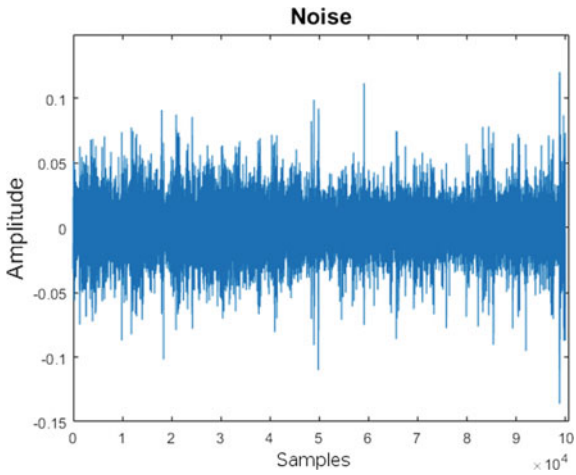

Fig. 4 Noise samples

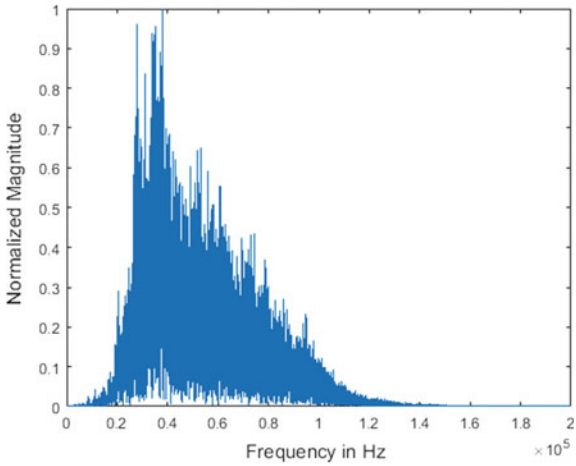

Fig. 5 DFT of noise

3 Experiment to Detect the Source of Noise During Movement of Hydrophones

3.1 Relation of Noise with Speed of Boat

It is observed that the noise picked up by the hydrophones increases as the speed of boat increases. The relation of the speed of boat and mean square value of noise picked up by the hydrophone is summarized in Table 1. It is confirmed from Table 1 that the noise picked with the hydrophones is a function of speed. The noise source could be from electronic coupling or from the coupling from underwater path from

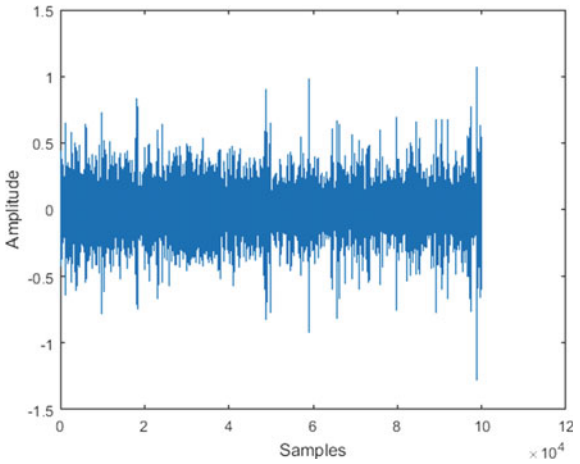

Fig. 6 Cross-correlation of noise and dolphin click

Table 1 Noise recorded at different speeds

Speed in km/h	Noise (rms) mV
3	150
5	250
8	500
10	900

the engine. There is also a possibility of hydrodynamic flow noise. The following experiments are conducted in order to find out the exact source of the noise.

3.2 Experiment to Detect the Noise Source Path

As shown in Fig. 7, the hydrophone is kept in a water-filled bucket and the boat is moved at different speeds. It is observed that the engine and boat speed have no impact on the performance and the noise levels are the same as obtained in the stationary boat. The result of this experiment have lead us to conclude that the noise picked up by the hydrophones is not due to the coupling of the engine generated noise with the electronic circuit.

3.3 Experiment to Study the Effect of Hydrophone Clamps

The hydrophones are mounted using metal clamps. The metal rods holding the hydrophones vibrate whenever the boat is moved. So, there is a possibility that these vibrations are causing noise in the hydrophones. To test this kind of coupling,

Fig. 7 Hydrophone placed in a bucket

the hydrophones are placed in the water at the same depth without metal frames. The boat is moved at different speeds and the noise levels are compared as recorded when the hydrophones were clamped with metal rods. The recorded noise levels in both the cases are observed to be the same at same speeds. This experiment leads us to conclude that the noise is not induced due to the vibrations of the metal frames holding the hydrophones.

3.4 Experiment to Find the Possibility of Hydrodynamic Flow Noise

There is a possibility of non-acoustic pressure fluctuations are induced in the hydrophones. This is primarily due to turbulent water flowing around the hydrophones. To test the amount of hydrodynamic flow noise, the boat is moved at higher speeds above 12 km/h and the engine is switched off. The boat keeps on moving at speed of 5 km/h and above for few minutes. The signal picked up by the hydrophone is analyzed. It is observed that after switching off the engine within few seconds, the noise level is dropped significantly almost to a level recorded in static condition. This experiment was repeated three times. So, it is concluded that the hydrodynamic flow noise was not significant to interfere with the dolphin clicks.

4 Effect of Engine Power and Boat Material on Noise

It is evident from the above experiments that the only source of noise is the engine and the coupling path is water. The source of noise is cavitation noise. When the propeller rotates to obtain the required thrust, the blades cut the water. During this process, a very low-pressure region is built around the blade edges. At low pressure, the water starts boiling at low temperatures. This results in the formation of water bubbles. As the bubbles pop, they make a lot of noise. The noise is broadband in nature. So, a study is carried out to find the effect of different engines.

4.1 Effect of Outboard Engine

Noise acquired by the hydrophones are primarily due to cavitation. The noise level is recorded with three different engines with 15, 20, and 40 HP. The size of the propeller is largest with 40 HP engine. The two propellers attached with 15 and 20 HP engine are shown in Fig. 8. The noise level recorded with 40 HP engine is significantly lower compared to the other two engines. The acquired noise is observed to be dependent on the engine horsepower. This further validates that the noise is mainly due to cavitation.

(a) Propeller of 15 HP engine. (b) Propeller of 20 HP engine.

Fig. 8 Propellers

Table 2 Noise recorded using for metal and wooden boats at different speeds

Speed in km/h	Noise in mV (rms) of metal Boat	Noise in mV (rms) of wooden boat
5	30.4	30.7
8	34.3	65.6
9	42.3	67.2
12	51.2	68.8

4.2 Experiment to Study the Effect of Boat Material

An experiment is conducted to study the effect of material used for fabricating the boat. A metal boat and a wooden boat are used for this experiment. The same 40 HP engine is used for both the trials. The noise is recorded on both the boats at different speeds. The mean square value of noise is calculated for both the boats and summarized in Table 2. It is concluded from the Table 2 that the metal boat is slightly superior compared to the wooden boat in terms of lowering cavitation noise effect.

5 Design of Boat to Reduce Cavitation Noise

The main source of noise acquired by the hydrophones during movement of the boat is the cavitation noise. As the noise is highly correlated with the dolphin click, the cross-correlation operation has not helped to overcome the effect of noise in recovering the dolphin clicks. The dolphin click is very narrow in time and a broadband signal, so any filtering operation will not going to help much. Therefore, one must restrict the noise from entering the system rather than relaying on post-processing for noise removal. We are required to design a proper combination of boat and engine in order to reduce cavitation noise. There is a relation between the hull speed, horsepower, and the length of a boat [6].

The speed of a displacement boat with maximum fuel efficiency is known as hull speed [7]. At hull speed, two distinct waves are formed in the water by the movement of the hull, first one in front at the bow, and second one at the stern, with a distinct crests of two adjacent waves running along the hull without interference. To move a boat faster, one needs higher hull speed and for that, a longer waterline of boat is required. The hull speed HS occurs at the speed/length ratio of 1.34, where the speed of boat is given in knots and the length is the square root of the Length Water Line (LWL) in feet. The LWL of a boat is the length from the front to the back along the waterline at rest on a calm water. The hull speed HS in knots is given as [6]:

$$HS = 1.34 \times sqrt(LWL) \tag{1}$$

A boat approaches maximum efficiency and minimum drag at 75% of hull speed. To achieve the speed for dolphin counting at 10 Km/hr (5.39 knots) of boat with minimum drag and consequently minimum cavitation, one needs the hull speed of 13.33 km/hr or 7.19 knots. For this speed, the required LWL of the boat is around 28 feet as given by (1). The engine power required for the boat with LWL of 28 feet is 20 HP and above [6]. A boat with proper design and adequate power of the engine will generate much less cavitation noise.

6 Conclusion

The study of the noise received by the hydrophones during the measurement of dolphin clicks has been carried out. It is observed that the cavitation noise is the major source of noise interfering with dolphin clicks. It has been demonstrated that the cavitation noise can be reduced significantly by appropriately choosing the engine power. The effect of boat material on noise is also studied. It has been demonstrated that the boat with metal body is a better choice in terms of noise reduction. The design of boat and selection of engine power to reduce cavitation noise at a specific speed is also discussed.

Acknowledgements This research is financially supported by NTT Data under CSR. We thank our colleagues from GANGA who provided the support for the field experiments.

References

1. Akamatsu, T., Ura, T., Sugimatsu, H., Bahl, R., Behera, S., Rupak, D., Panda, S., Khan, M., Kar, C.S., Kar, S.K, Kimura, S., Sasaki-Yamamoto, Y.: Abundance estimation of Ganges river dolphins by acoustic-visual mark recapture method. In: J20th Biennial Conference on the Biology of Marine Mammals. Dunedin, New Zealand (2013)
2. Akamatsu, T., Ura, T., Sugimatsu, H., Bahl, R., Behera, S., Panda, S., Khan, M., Kar, S.K., Kar, C.S., Kimura, S., Sasaki-Yamamoto, Y.: A multimodal detection model of dolphins to estimate abundance validated by field experiments. J. Acoust. Soc. Am. **134**(3), Pt. 2, 2418-2426 (2013)
3. Akamatsu, T., Ura, T., Sugimatsu, H., Bahl, R., Behera, S., Panda, S., Khan, M., Kar, S.K., Kar, C.S., Kimura, S., Sasaki-Yamamoto, Y.: Counting animals using vocalizations; a case study in dolphins. In: Proceedings of the International Symposium Underwater Technology, Tokyo (2013)
4. Sugimatsu, H., Ura, T., Mizuno, K., Asada, A., Kojima, J., Bahl, R., Behera, S., Singh, H., Sagar, V.S.: Study of acoustic characteristics of Ganges river dolphin calf using ehcolocation clicks recorded during long-term in-situ observation. In: Proceedings of the IEEE Oceans'12, pp. 14–19. Hampton Roads, USA (2012)
5. Sugimatsu, H., Ura, T., Kojima, J., Bahl, R., Behera, S., Sakamaki, T.: Long-term Real time monitoring of the Ganges river dolphins(Platanista gangetica)using Integrated Acoustic Observation System. In: Proceedings of the 21st Ocean Engineering Symposium. Tokyo, Japan (2009)
6. http://www.youboat.net/boatpower3.aspx
7. http://www.youboat.net/dictionary.aspx#hullSpeed

Optical Flow Estimation in Synthetic Image Sequences Using Farneback Algorithm

Shivangi Anthwal and Dinesh Ganotra

Abstract Perspective motion corresponding to the real world motion between observer and scene can be characterized by a dense field corresponding to the inter-frame displacement of each pixel, known as *optical flow*. The analysis of optical flow has been an active research domain in the last couple of decades and tremendous progress has been attained by diverse approaches for its estimation. This paper demonstrates the implementation of Farneback method for optical flow determination. Various synthetic image sequences and their ground truth flow images from benchmark datasets are examined. Resultant flow fields, depicted as color-coded images, are compared with ground truth optical flow images by using Structural Similarity Index Measure whereas the flow vectors are compared with ground truth by estimating Angular Error and Endpoint Error.

Keywords Optical flow · Farneback method · Ground truth
Structural similarity index · Angular error · Endpoint error

1 Introduction

Optical flow, the apparent motion of image objects arising due to relative motion between the observer and the scene, is quintessentially considered as a convenient representation of image motion [1]. Computing and investigating flow for given image sequences may provide meaningful and pertinent information about the objects in the scene. Two consecutive frames of *Hamburg Taxi Sequence* are shown in Fig. 1a, b and the optical flow due to motion between them are illustrated in Fig. 1c. At each

S. Anthwal (✉) · D. Ganotra
Department of Applied Science and Humanities, Indira Gandhi Delhi Technical University for Women, New Delhi, Delhi, India
e-mail: shivangianthwal@hotmail.com

D. Ganotra
e-mail: dinesh_ganotra@hotmail.com

B. S. Rawat et al. (eds.), *Advances in Signal Processing and Communication* ,
Lecture Notes in Electrical Engineering 526,
https://doi.org/10.1007/978-981-13-2553-3_35

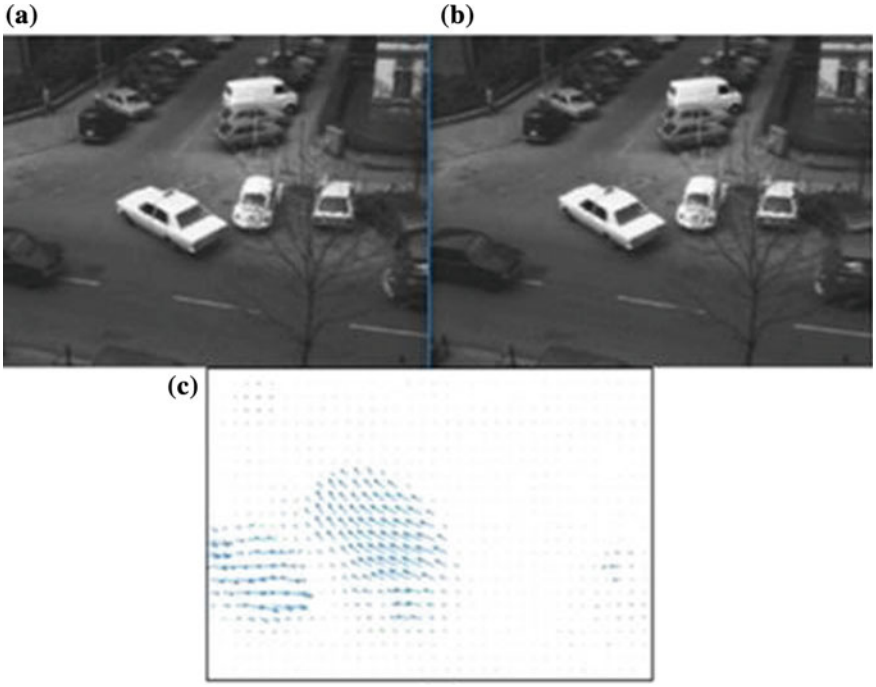

Fig. 1 Optical flow illustration

pixel, the optical flow is depicted by a vector, where the vector points towards the direction of the flow and its length represent the magnitude of the flow.

Optical flow finds application in realms of image stitching and panoramic imaging [2, 3], motion segmentation [4, 5], obstacle detection and avoidance [6–8], fluid velocimetry [9], medical imaging [10], shape tracking [11], image registration [12], structure from motion [13, 14], etc.

2 Optical Flow Equation and Methods

This section briefly characterizes some of the traditional methods to determine optical flow and the fundamental assumption used by them.

Table 1 Quintessential taxonomy of optical flow computation methods

Intensity based methods	Frequency based methods	Region based methods
Compute flow using spatiotemporal derivatives of image intensity. Derivatives can be of first order for simplicity or higher order in complex cases	Estimate flow using energy output of velocity tuned orientation sensitive filters in the Fourier domain	Match features from two frames by maximizing similarity measure or minimizing distance measure to obtain the optical flow field
Lucas B.D. and Kanade T. [16], Horn B.K.P. and Schunck B.G. [17]	Heeger D.J. [18]	Anandan P. [19], Singh A. [20]

2.1 Brightness Constancy

Most of the optical flow computation methods are based on the premise of brightness constancy, i.e., the pixel intensity in the image remains unaltered over time [15]. If f(x, y, t) is the intensity of pixels of a point at location (x, y) and time "t", then at time "t + dt" when the point translates to (x + dx, y + dy), the intensity remains unchanged. Mathematically,

$$f(x, y, t) = f(x + dx, y + dy, t + dt) \tag{1}$$

On expanding (1) and using Taylor series, the *optical flow equation* given below is obtained.

$$f_x u + f_y v + f_t = 0 \tag{2}$$

where u and v are the horizontal and vertical components, respectively, of optical flow. f_x, f_y, and f_t are the first-order spatial and temporal derivatives of pixel intensity.

Different optical flow evaluation methods use various constraints to find the solution of (2).

2.2 Methods to Determine Optical Flow

An expansive compendium by Beauchemin et al. [15] gave an outline and taxonomy of multifarious classical flow determination methods and categorized them as intensity-based, frequency-based, and region-based methods described in Table 1.

2.3 Farneback Method

This novel technique for two-frame motion estimation based on polynomial expansion in an image was proposed by Farneback G. [21]. As per this method, neighborhood of each pixel can be approximated by a quadratic polynomial given as

$$f_1(\mathbf{x}) = \mathbf{x}^T \mathbf{A}_1 \mathbf{x} + \mathbf{b}_1^T \mathbf{x} + c_1 \tag{3}$$

where $\mathbf{A}_1$ is a symmetric matrix, $\mathbf{b}_1$ is a vector, and c_1 is a scalar. This gives a local signal model, expressed in a local coordinate system. The coefficients may be estimated by applying the weighted least square approach by matching with the neighborhood signal values. After a global displacement $\mathbf{d}$, the new signal obtained is given as

$$f_2(\mathbf{x}) = \mathbf{x}^T \mathbf{A}_1 \mathbf{x} + (\mathbf{b}_1 - 2\mathbf{A}_1 \mathbf{d})^T \mathbf{d}^T \mathbf{A}_1 \mathbf{d} - \mathbf{b}_1^T \mathbf{d} + c_1 \tag{4}$$

$f_2(\mathbf{x})$ can be written in a form compatible with (3) as

$$f_2(\mathbf{x}) = \mathbf{x}^T \mathbf{A}_2 \mathbf{x} + \mathbf{b}_2^T \mathbf{x} + c_2 \tag{5}$$

To find the value of $\mathbf{d}$, the coefficients of quadratic polynomials (4) and (5) shall be equated

$$\mathbf{b}_2 = \mathbf{b}_1 - 2\mathbf{A}_1 \mathbf{d} \tag{6}$$

$$2\mathbf{A}_1 \mathbf{d} = -(\mathbf{b}_2 - \mathbf{b}_1) \tag{7}$$

$$\mathbf{d} = -\frac{1}{2} \mathbf{A}_1^{-1} (\mathbf{b}_2 - \mathbf{b}_1) \tag{8}$$

These are the basic equations for the Farneback method. Further refinements might be applied by considering the displacement field to be spatially varying or parameterizing it according to the motion model. Apart from that, an iterative and multi-scale displacement estimation approach might be used.

3 Evaluation Methodology

Ever since the Yosemite Sequence was introduced for studying optical flow [1], image sequences generated synthetically have been used time and again in place of natural images primarily due to the associated ease in controlling the scene properties such as illumination, blurring, occlusion, etc. Moreover, it can be intensely challenging to measure ground truth optical flow in real scenes that contain natural motion.

Fig. 2 Middlebury color coding [22]

Three popular synthetic image datasets namely Middlebury dataset [22], MPI Sintel dataset [23], and the UCL-Flow dataset [24] are explored in this work for optical flow computation using Farneback Algorithm (Number of Pyramid Levels used: 2).

The Middlebury dataset is a widely examined optical flow dataset and the first to introduce ground truth for colored image sequences containing complex but small nonrigid motions that were eventually used for testing the performance of multiple optical flow algorithms. MPI Sintel dataset has presented image sequences with large displacement between consecutive images and challenges such as occlusion, blurring, specular reflections, etc. UCL-Flow dataset comprises of image pairs with complex ambient lighting and rigid but strong object motion.

The most extensively used color coding of optical flow vectors introduced in [22] is portrayed in Fig. 2 and is used for visual depiction of flow in this paper. Here, the vector direction is coded by the color hue value and the vector magnitude by the color saturation. A color-coded optical flow image apparently gives a finer, enhanced, and convenient to analyze visual representation of the motion field.

For analyzing the resemblance between the resultant optical flow color-coded image and the ground truth flow image, a unitless image comparison metric Structural Similarity Index Measure (SSIM) introduced in [25] is used.

SSIM is a reference metric to analyze similarity between two images. The reference image is the color-coded ground truth image while the test image is color-coded image corresponding to Farneback optical flow field. For identical images, the value of SSIM is 1. The formula for SSIM for two images $\mathbf{X}$ and $\mathbf{Y}$ is given as

$$\mathrm{SSIM}(\mathbf{X}, \mathbf{Y}) = \frac{(2\mu_{\mathbf{X}}\mu_{\mathbf{Y}} + c_1)(2\sigma_{\mathbf{XY}} + c_2)}{\left(\mu_{\mathbf{X}}^2 + \mu_{\mathbf{Y}}^2 + c_1\right)\left(\sigma_{\mathbf{X}}^2 + \sigma_{\mathbf{Y}}^2 + c_2\right)} \tag{9}$$

$\mu_{\mathbf{X}}, \mu_{\mathbf{Y}}$ are average intensity values of $\mathbf{X}$ and $\mathbf{Y}$
$\sigma_{\mathbf{X}}, \sigma_{\mathbf{Y}}$ are the standard deviations of $\mathbf{X}$ and $\mathbf{Y}$
$\sigma_{\mathbf{XY}}$ is the covariance of $\mathbf{X}$ and $\mathbf{Y}$

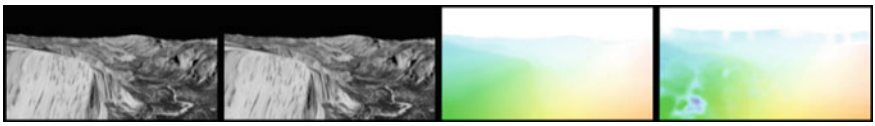

Fig. 3 (From left to right) 015_YosemiteSun sequence: (i) Frame 1 (ii) Frame 2 (iii) GT (iv) FB flow

$c_1 = (k_1 L)^2$ and $c_2 = (k_2 L)^2$ are variables with $k_1 = 0.01$ and $k_1 = 0.03$ and L is the dynamic range of pixel values

For evaluating the error between ground truth and resultant Farneback flow field, performance measures used in [22], namely Angular Error (AE) and Endpoint Error (EE) are used. Barron et al. [1] were pioneers in accentuating the important performance measures or precision with which flow was measured. They computed angular error for numerous real and synthetic image sequences and compared results obtained by different methods. They remarked that AE was convenient as an error measure as it could handle large as well as small velocities without the inherent amplification in the relative measure of velocity vector differences.

AE between the flow vector (u, v) and the ground truth flow (u_{GT}, v_{GT}) is the angle in 3D space between (u, v, 1.0) and $(u_{GT}, v_{GT}, 1.0)$. A low AE would imply that the resultant optical flow's direction is well matched with the actual direction, i.e., the direction of ground truth flow vector.

$$AE = \cos^{-1}\left(\frac{(1.0 + u \times u_{GT} + v \times v_{GT})}{\sqrt{1.0 + u^2 + v^2}\sqrt{1.0 + u_{GT}^2 + v_{GT}^2}}\right) \tag{10}$$

EE gives a measure of the absolute difference between the magnitudes of ground truth flow and resultant optical flow field. A low EE signifies that their magnitudes are comparable.

$$EE = \sqrt{(u - u_{GT})^2 + (v - v_{GT})^2} \tag{11}$$

4 Results

The values of SSIM, AE, and EE obtained by implementing Farneback method for various image sequences are given in Table 2.

Resultant color-coded flow fields for some of the sequences can be seen in Figs. 3, 4, 5, 6, 7. The first two images in the left half are two successive frames of the image sequences that are analyzed. GT refers to the ground truth optical flow color image and FB flow displays the image obtained after finding optical flow by employing Farneback algorithm and then using Middlebury color coding.

Table 2 SSIM, AE and EE values for the image sequences on using Farneback method

Dataset	Image sequence	SSIM (no units)	AE (degrees)	EE (pixels per frame)
Middlebury	Dimetrodon	0.862	5.158	0.242
	Grove 2	0.887	5.238	0.343
	Urban 2	0.944	9.642	4.056
	Urban 3	0.972	18.695	2.174
	Venus	0.898	13.720	0.938
	Rubber Whale	0.831	9.758	0.298
	Hydrangea	0.659	8.005	0.599
UCL-flow	015_YosemiteSun	0.959	4.916	0.232
	019_Sponza2	0.876	7.060	1.431
	051_blow1Txtr1	0.879	7.445	0.285
	089_drop1Txtr1	0.887	13.459	0.794
	107_roll1Txtr1	0.939	0.671	0.011
	124_roll9Txtr2	0.936	2.834	0.071
MPI sintel	alley_1	0.922	7.320	0.726
	alley_2	0.977	5.369	0.240
	bamboo_1	0.970	7.031	0.396
	bamboo_2	0.958	6.588	0.270
	sleeping_1	0.928	7.723	0.541
	sleeping_2	0.976	3.763	0.167
	bandage_2	0.937	12.893	1.034
	Mean value	0.910	7.864	0.742

Fig. 4 (From left to right) Grove2 sequence: (i) Frame 1 (ii) Frame 2 (iii) GT (iv) FB flow

Fig. 5 (From left to right) Dimetrodon sequence: (i) Frame 1 (ii) Frame 2 (iii) GT (iv) FB flow

Fig. 6 (From left to right) Urban 3 sequence: (i) Frame 1 (ii) Frame 2 (iii) GT (iv) FB flow

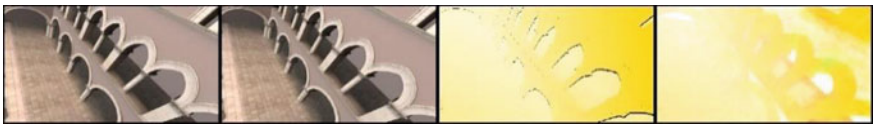

Fig. 7 (From left to right) 019_Sponza2 sequence: (i) Frame 1 (ii) Frame 2 (iii) GT (iv) FB flow

5 Conclusion

This paper discusses the implementation of Farneback method for optical flow determination by examining various synthetic image sequences from benchmark datasets. The resultant color-coded optical flow fields are compared with the ground truth flow fields using SSIM. With an average SSIM value of 0.910, it may be inferred that the resultant optical flow color-coded image bears satisfactory similarity to the ground truth image. For the image sequences considered, an average EE of 0.742 pixels per frame and an average AE of 7.864 degrees imply that the resultant optical flow vectors are comparable with the ground truth flow vectors in terms of magnitude as well as direction. This, in turn, signifies a decent performance by the Farneback algorithm.

Acknowledgements The authors would like to express their most sincere gratitude to the anonymous reviewers for conscientiously reading the manuscript and for giving valuable suggestions.

References

1. Barron, J.L., Fleet, D.J., Beauchemin, S.S.: Performance of optical flow techniques. Int. J. Comput. Vis. **12**, 43–77 (1994)
2. Szeliski, R.: Image alignment and stitching: a tutorial. Found Trends Comput. Graph. Vis. **2**, 1–104 (2006)
3. Rebiere, N., Flavie, M., Fortier, A.: Image mosaicing using local optical flow registration. In: 19th IEEE International Conference on Pattern Recognition, pp. 1–5 (2008)
4. Zappella, L., Llado, X., Salvi, J.: Motion segmentation: a review. In: Proceedings of 2008 Conference on Artificial Intelligence Research and Development, pp. 398–407 (2008)
5. Klappstein, J., Vaudrey, T., Rabe, C., Wedel, A., Klette, R.: Moving object segmentation using optical flow and depth information. In: Wada, T., Huang, F., Lin, S. (eds.) PSIVT 2009. LNCS, vol. 5414, pp. 611–623. Springer, Heidelberg (2009)
6. Souhila, K., Karim, A.: Optical flow based robot obstacle avoidance. Int. J. Adv. Robot. Syst. **4** (2007)

7. Yoo, D.W., Won, D.Y., Tahk, M.J.: Optical flow based collision avoidance of multi-rotor UAVs in urban environments. Int. J. Aeronaut. Space Sci. **12**, 252–259 (2011)
8. Sazbon, D., Rotstein, H., Rivlin, E.: Finding the focus of expansion and estimating range using optical flow images and a matched filter. Mach. Vis. Appl. **15**, 229–236 (2004)
9. Liu, T., Shen, L.: Fluid flow and optical flow. J. Fluid Mech. **614**, 253–291 (2008)
10. Guo, D., van de Ven, A.L., Zhou, X.: RBC tracking using optical flow methods. IEEE J. Biomed. Health Inf. **18** (2014)
11. Smith, S.M., Brady, J.M.: ASSET 2 real time motion segmentation and shape tracking. IEEE Trans. Pattern Anal. Mach. Intell. **17**, 814–820 (1995)
12. Zitova, B., Flusser, J.: Image registration methods: a survey. Image Vis. Comput. **21**, 977–1000 (2003)
13. Adiv, G.: Determining three-dimensional motion and structure from optical flow generated by several moving objects. IEEE Trans. Pattern Anal. Mach. Intell. **7**, 384–401 (1985)
14. Bruss, A.R., Horn, B.K.P.: Passive navigation. Comput. Vis. Graph. Image Process. **21**, 3–20 (1983)
15. Beauchemin, S.S., Barron, J.L.: The computation of optical flow. ACM Comput. Surv. **27**, 433–467 (1995)
16. Lucas, B.D., Kanade, T.: An iterative image registration technique with an application to stereo vision. In: Proceedings of 7th International Joint Conference on AI, pp. 674–679 (1981)
17. Horn, B.K.P., Schunck, B.G.: Determining optical flow. Artif. Intell. **17**, 185–203 (1981)
18. Heeger, D.J.: Optical flow using spatiotemporal filters. Int. J. Comput. Vis. **1**, 279–302 (1988)
19. Anandan, P.: A computational framework and an algorithm for the measurement of visual motion. Int. J. Comput. Vis. **2**, 283–310 (1989)
20. Singh, A.: An estimation-theoretic framework for image flow computation. In: Proceedings of IEEE International Conference on Computer Vision, Osaka, pp. 168–177 (1990)
21. Farneback, G.: Two-frame motion estimation based on polynomial expansion. In: Proceedings of the 13th Scandinavian Conference on Image Analysis, pp. 363–370 (2003)
22. Baker, S., Scharstein, D., Lewis, J.P., Roth, S., Black, M.J., Szeliski, R.: A database and evaluation methodology for optical flow. Int. J. Comput. Vis. **92**, 1–31 (2011)
23. Butler, D.J., Wulff, J., Stanley, G.B., Black, M.J.: A naturalistic open source movie for optical flow evaluation. Eur. Conf. Comput. Vis. **4**, 611–625 (2012)
24. Aodha, O.M., Humayun, A., Pollefeys, M., Brostow, G.J.: Learning a confidence measure for optical flow. IEEE Trans. Pattern Anal. Mach. Intell. **35**, 1107–1120 (2012)
25. Wang, Z., Bovik, A.C., Sheikh, H.R., Simoncelli, E.P.: Image quality assessment: from error visibility to structural similarity. IEEE Trans. Image Process. **13**, 600–612 (2004)

Development of Self-stabilizing Platform Using MPU-6050 as IMU

Vinayak Tripathi, Aditya Bansal and Richa Gupta

Abstract In this paper, we present the development of self-stabilizing platform using MPU-6050 as the Inertial Measurement Unit (IMU). Using this along with two high torque servo motors and Atmega16 as the main controller, we are able to maintain the platform along the horizontal axis whenever the orientation of the structure changes. IMU is a device which is used to measure positional and angular motion of a body. Here we are using MPU-6050 as an IMU which has an inbuilt accelerometer and gyroscope for providing six degrees of freedom. The logic behind the software part is the conversion of digital data obtained from MPU-6050 to positional acceleration and angular velocities, then filtering the data and computing the orientation of the platform (in the form of angles) using some predetermined mathematical functions, and then converting the orientation to angular rotation and then finally to PWM signals for controlling the motion of the servo motors.

Keywords IMU · Accelerometer · Gyroscope · MPU-6050 · Atmega16
Servo motors

1 Introduction

At present, many single chip microcomputers and sensors exist, which are capable of performing their tasks by utilizing minimum power. One of the technologies used in these devices is MEMS. MEMS stands for Microelectromechanical System. Sensors based on this technology have compliance with the requirement of low power consumption and low cost. MPU-6050 is also based on this technology. It is an Inertial

V. Tripathi (✉) · A. Bansal · R. Gupta
Department of Electronics and Communication, Jaypee Institute of Information Technology, Noida, Uttar Pradesh, India
e-mail: vtvinayak0@gmail.com

A. Bansal
e-mail: aditya474012@yahoo.com

R. Gupta
e-mail: richatayal@gmail.com

B. S. Rawat et al. (eds.), *Advances in Signal Processing and Communication* ,
Lecture Notes in Electrical Engineering 526,
https://doi.org/10.1007/978-981-13-2553-3_36

Measurement Unit (IMU) which tells about the angular and positional motion of the body. This data is required for motion sensored games in cell phones and for stabilization of any unmanned devices such as quadcopters, aeroplanes in autopilot mode, etc. Motivation for developing self-stabilizing platform is to demonstrate the stabilization of any object at a particular orientation using this sensor. Self-stabilizing platforms find real uses in automotive industry, robotics, avionic, etc. This paper describes the implementation of self-stabilizing platform using standard parts available. During implementation, some problems were faced, which were later solved. This will be discussed in detail in later sections. The main components used along with MPU-6050 are servo motors and voltage regulators. The controller part could be an 8-bit AVR or 32-bit ARM. This project has been tested on Atmega16, an AVR series controller.

2 Theoretical Analysis

Before the construction, the following theoretical analysis was done:

A. **Selecting degrees of freedom for motion**

The first aspect into consideration is the degrees of freedom for motion and stabilization [1].

- 1 DOF—for motion and stability in x-direction, y-direction or z-direction.
- 2 DOF—for motion and stability in x and y directions.
- 3 DOF—for motion and stability in x, y, and z directions.

With more degrees of freedom in hand, we can stabilize the platform in the whole space. Here we are considering two degrees of freedom for our stabilization purpose.

B. **Sensor to be used**

The sensor selected for solving the purpose is MEMS-based MPU-6050, an integration of accelerometer and gyroscope into one single chip. We can use accelerometer or gyroscope individually, but individually both are not as capable for stabilizing purpose as integration of both. Advantages are described in the upcoming parts.

C. **Placement of sensor**

Another aspect to be considered is the placement of the MPU-6050 sensor for accurate measurement. There are two main positions where the sensor can be placed.

1. *On the top of the platform*

Advantage: Measuring actual values of angular and positional motion of the platform.

Disadvantage: Noise introduced in the data due to motion of platform.

2. *On the base of the motion mechanism*

Advantage: Readings from the sensor have much less noise.
Disadvantage: The trace of motion is not so perfect.
After comparing the level of noise introduced in both of the cases, we decided to place the sensor on the base of the mechanism.

D. **Motion Mechanism**

For selection of moving parts, the precision, reaction time, and load carrying capacity were considered. After consideration, we selected 13 kg servo motors as their torque is quite high and the reaction time is also fast.

E. **Controller**

The main aspect to be considered was to select the controller for manipulating the readings coming from the sensors and controlling the motion of the motors. We can have two choices—an 8-bit AVR or a 32-bit ARM. We chose AVR series of controllers, Atmega16 in particular as they are simple to understand and cost-effective.

3 About the Sensor

MPU-6050 is an integrated MotionTracking device which integrates a three-axis accelerometer, a three-axis gyroscope, and a Digital Motion Processor (DMP) [1] in a single chip package. It also has a dedicated bus for interfacing an external three-axis magnetometer (compass) [2], providing a complete nine-axis motion output. This sensor is also designed to interface with other multiple inertial sensors, such as pressure sensor, through its auxiliary port. This device communicates through I^2C (Inter IC communication), a two-wire serial interface with a speed of 400 kHz [3].

The sensor has 16-bit analog to digital converters (ADCs) for digitalizing the outputs coming from accelerometer and gyroscope. For tracking the fast and slow motions precisely, the accelerometer is full-scale programmable with full-scale range of $\pm 2\ g, \pm 4\ g, \pm 8\ g$, and $\pm 16\ g$, and so is the gyroscope with full-scale range of $\pm 250, \pm 500, \pm 1000$, and ± 2000°/sec (degrees per second) [4]. The orientation of axes of the sensor is shown in Fig. 1.

4 Block Diagram

The block diagram of the circuit is as shown in Fig. 2. The power supply consists of the 12 V battery along with 7805 Vage regulator for regulating the supply for 5 volts as most of the components work on 5 volt supply. LCD display is used for displaying the orientation angles for verifying the working of the circuit. Communication with

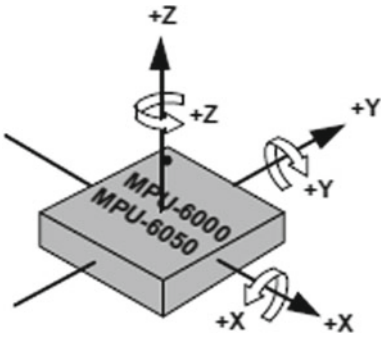

Fig. 1 Orientation of the sensor's axes [1, 2]

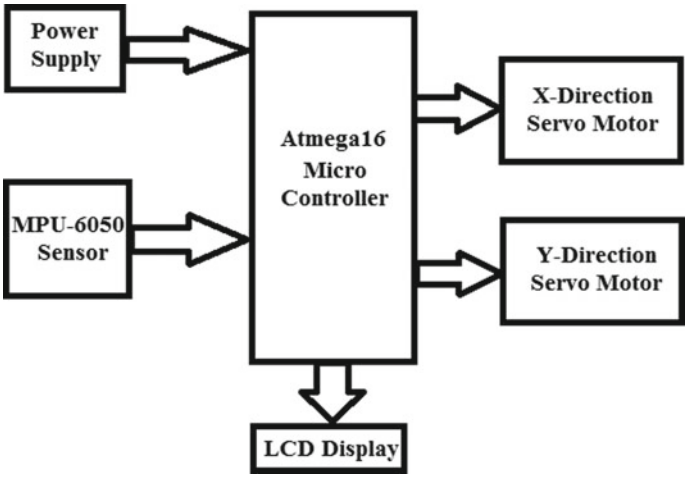

Fig. 2 Block diagram

MPU-6050 is done through I^2C at a speed of 400 kHz. The servo motors used here have a capability of precise rotation up to 180°. They operate on Pulse Width Modulation (PWM) signals. By varying the pulse width of the signal, the rotation of the motor varies from 0 to 180°.

5 Flowchart and Working

The system flowchart is as shown in Fig. 3. For stabilization of any object with two degrees of freedom, two orientation angles are taken into account, roll and pitch. Roll angle tells about the orientation of the object along x-axis, whereas pitch angle tells about the orientation along y-axis. For keeping any object horizontally

stable, the roll and pitch angles have to be maintained close to zero degrees. For measuring them we have to take the help of the data provided by accelerometer and gyroscope which are inbuilt in MPU-6050. An accelerometer usually measures inertial acceleration along a predefined axis in terms of G-forces (g). One G-force is equivalent to an acceleration of 9.8 m/s^2. On the other hand, a gyroscope measures the angular velocity of a body in terms of degrees/s along a predefined axis. But both the information alone are not reliable for accurate prediction of orientation of an object. The readings of accelerometer change drastically with a change in the acting forces on the object and are reliable only on long-term basis. Problem with the gyroscope is that in the long term, it starts drifting. So, its data is reliable only on short-term basis. Therefore, a blend of both of the sensor's data has to be made for predicting the accurate orientation of the object. Also, the data received from them contain a considerable amount of noise due to continuous motion of the sensor. So filtering is also required. Both of these problems were solved by using a control algorithm named complementary filter which we will discuss in detail in the next section. Inputs to the filter are the accelerometer and gyroscope data and it outputs are the roll and pitch angles, i.e., orientation of the object which is accurate and noise free. After getting the roll and pitch angles, the platform has to be adjusted so as the roll and pitch angles reach close to zero degrees, i.e., object returns to its horizontal position. For this, the servo motors are to be rotated accordingly. Servo motors generally work on PWM pulses generated by the controller. The frequency of the generated wave is required to be close to 50 Hz and by varying the width of the pulse, we can rotate its shaft according to the required angle. The width of the pulse varies from 0.5 ms (for 0° rotation) to 2.5 ms (for 180° rotation). Amount of rotation for the motor for both the axes is calculated by the relation.

$$\text{Servo Angle} = 90^\circ - \text{roll/pitch} + \text{offset} \tag{1}$$

This gives the rotational angle in the range 0–180°. The offset value is required for compensation of some error in the orientation and varies from 0 to 2°. In case of no motion, the servo motors maintain an angle of 90° for keeping the platform horizontal. Now for PWM wave generation in Atmega16, Timers are to be initialized. In AVR, there are many timer modes, one of which is PWM mode. For driving servos, we have used Timer1 of Atmega16 in 10-bit fast PWM mode. The frequency of the wave to be generated is decided by the TOP value given to the ICR (Input Capture Register) [5]. This value is calculated according to the requirement of the wave frequency and the frequency of the crystal oscillator. Crystal oscillators are used to provide clock to the controller for their operation. In our case, this value comes out to be 4999. So ICR is initialized with 4999. Now for varying the pulse of the wave, the value of Output Compare Register (OCR) [5] has to be varied. The relation between the OCR value and the rotation angle is given by

$$\text{OCR} = 2.4888 * (\text{Servo Angle}) + 140 \tag{2}$$

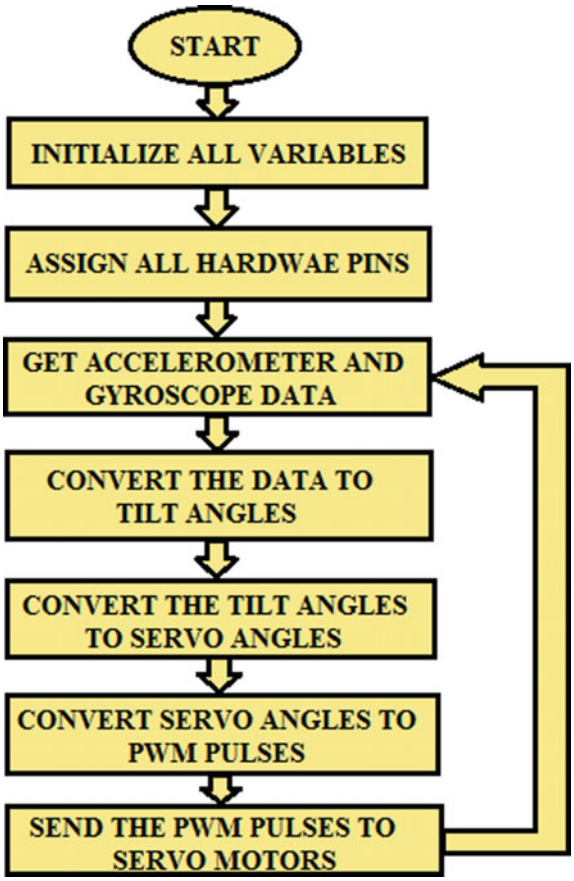

Fig. 3 Flowchart of system flow

So for 0°, OCR = 140 and for 180°, OCR = 588 (approx.). So, by controlling the rotation of the motors through the manipulation done after calculating the roll and pitch angles, the platform's orientation is maintained in horizontal direction.

6 Complementary Filter

As discussed above, the readings coming from accelerometer or gyroscope alone are not able to correctly predict the orientation angles due to their unreliability in short term (accelerometer) and in long term (gyroscope). So both the information have to be combined for making it useful. Some filtering is also required to remove the unwanted noise. There are two solutions to solve these problems: one is using Kalman filter [1] and the other is using complementary filter. Kalman filter gives much

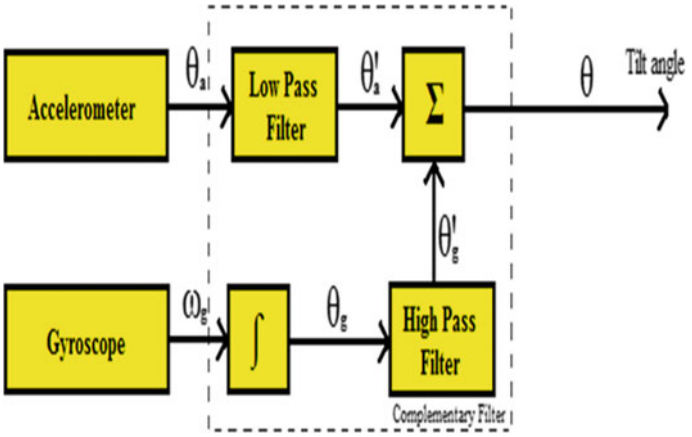

Fig. 4 Flowchart of complementary filter

better results than Complementary, but for an 8-bit processor architecture with a very limited code space, its designing is not possible because many matrix computations are to be made which would make the controller very slow. So the other option left for solution to the problem is to use complementary filter. Complementary filter [6] is basically a simple integration of a high-pass filter and a low-pass filter with some extra mathematical manipulations for calculating the angles. Low-pass filter is used for filtering the data coming from accelerometer and high-pass filter is used for filtering the gyroscope data. The flowchart of our system is as shown in Fig. 4. Inputs to this algorithm are the data coming from the accelerometer and gyroscope. As clearly seen from Fig. 4, the final tilt angle is given as output by the filter.

Its working can be divided into three parts. First part is to calculate the angles from data provided by accelerometer and gyroscope of MPU-6050. As told in previous topics, accelerometer provides acceleration and gyroscope provides angular velocity. So firstly the acceleration and angular velocities have to be converted to roll and pitch angles. Roll and pitch angles [7] from acceleration can be calculated by using the following mathematical equations:

$$\text{Roll} = \tan^{-1}\left(\mathrm{A_y}/\mathrm{A_z}\right) \tag{3}$$

$$\text{Pitch} = -\tan -1(\mathrm{Ax}/\sqrt{A_y^2 + A_z^2}) \tag{4}$$

For calculating the angles from the angular velocities given from gyroscope, the data is integrated by passing it through the integrator. After getting the angles from accelerometer and gyroscope data, the second part of the working is to filter them for removing them. This is done by applying low-pass filter on orientation data calculated from accelerometer and applying high pass filter on the data calculated by gyroscope. Low-pass filter on accelerometer is preferred because its reading is more affected by short-term noise and is reliable for long term. Similarly, high-pass

filtering on gyroscope data is used because it reading drifts after a long time. So after filtering, the main part comes into play, which is combining both data to one. This is done by weighted averaging. So final equation [6] for the filter looks like as shown –

$$\theta = (1 - \alpha) * \theta'_g + \alpha * \theta'_a \tag{5}$$

Here, θ'_g is the angle calculated (after filtering) [1] from the gyroscope data and θ'_a is the angle calculated (after filtering) from accelerometer data. The value of the constant α can vary from 0 to 1. After observing the working of the filter for different values of α, we fix its value as 0.02 for roll and 0.05 for pitch angles.

$$\theta_{\text{roll}} = 0.98 * \theta'_{\text{g roll}} + 0.02 * \theta'_{\text{a roll}} \tag{6}$$

$$\theta_{\text{pitch}} = 0.95 * \theta'_{\text{g pitch}} + 0.05 * \theta'_{\text{a pitch}} \tag{7}$$

For integrating the angular velocity, we have to define the time step "dt". The value of time step depends upon the frequency with which the data coming from MPU-6050 is read by the controller. Since we are reading the data after every 10 ms, the value of time step defined by us is 0.01. We can also calculate the time step every time by taking the time difference between the previous and the current time reading. By doing this, we can increase its accuracy.

7 Results

After implementing all of the above discussed mechanisms and integrating them into one single piece, we get the output in the form of a platform whose position remains horizontal despite any movement or tilt made in the structure of it. The structure of the platform prepared by us is showcased in Fig. 5a.

As can be seen in Fig. 5a, there are two servos placed in a stacked form. The servos are attached with each other using L-shaped clamps. The one below compensates the movement done in x-axis and the one on the top compensates in y-axis. The controller, the sensor unit, and the power supply unit (consisting of battery and regulator circuit) are kept in the box. The LCD is used for displaying the angles calculated by the system, just to make sure that the system is working properly.

In Fig. 5b, the structure is tilted in +x- and +y-directions, but the platform remains horizontal. A mobile phone is kept on the platform for demonstration purpose. The stability can be clearly seen from the figure.

In Fig. 5c, the structure is tilted in –x-direction, but the x-direction servo compensates it by moving in +x-direction, thus making the platform horizontally stable.

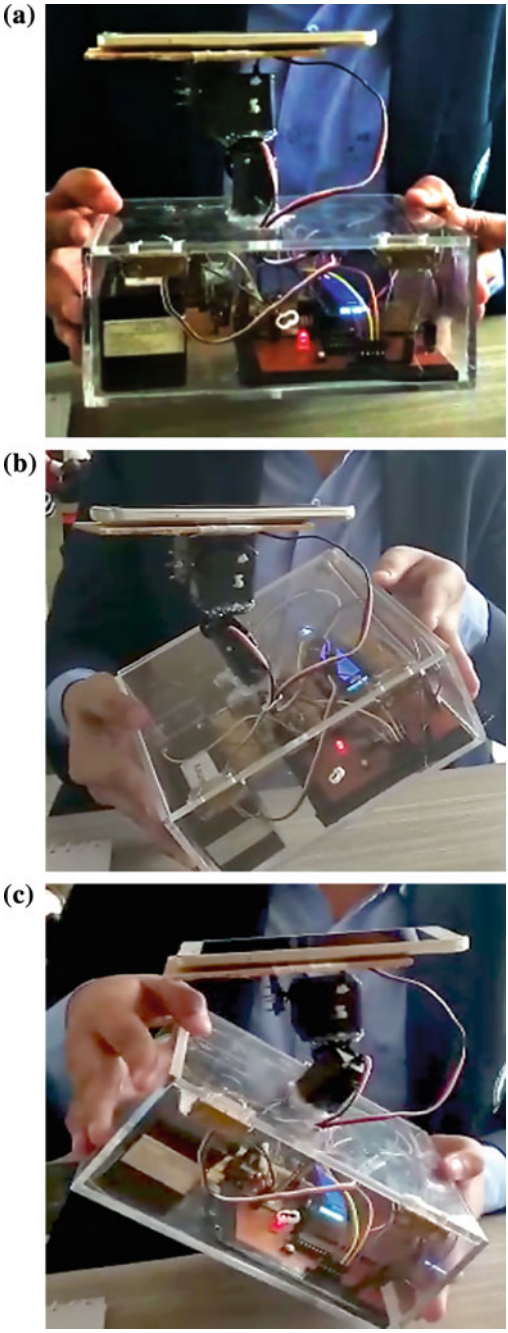

Fig. 5 (a) Final structure of platform and (b) structure tilted in +x- and +y-direction (c). The structure is tilted in –x-direction

8 Conclusion

At this point of time, our structure implementation is able to stabilize the platform in horizontal direction despite any tilt made in the structure in any of the two-dimensional axes. The programming of the controller for this system is done in Atmel Studio 6 and Proteus is used for simulation purpose. The controller and the power supply's circuit board were designed by us on Eagle 7.6.0 software. We are able to stabilize the platform accurately. The objects which were kept for checking the stability include a mobile handset, a half-filled plastic bottle, and a newly bought perfume bottle, and the results were quite satisfactory.

References

1. Popelka, V.: A Self Stabilizing Platform. Int Carpathian Control Conf **15**, 458–462 (2014)
2. MPU-6050 datasheet https://www.invensense.com/wp-content/uploads/2015/02/MPU-6000-Datasheet1.pdf
3. I2C implementation https://www.nxp.com/docs/en/application-note/AN10216.pdf
4. MPU-6050 register map (for programming purpose) https://www.invensense.com/wp-content/uploads/2015/02/MPU-6000-Register-Map1.pdf
5. Atmega16 datasheet http://www.atmel.com/images/doc2466.pdf
6. About Complementary Filter http://www.pieter-jan.com/node/11
7. Calculation of Roll and Pitch angles https://www.nxp.com/docs/en/application-note/AN3461.pdf

Real-Time Mental Workload Detector for Estimating Human Performance Under Workload

Rajesh Singla, Anand Agrawal, Vikas Kumar and Om Prakash Verma

Abstract Brain is often studied for behavioral reasons highlighting various impacts of tasks that intersperse awareness, attention, problem solving, decision-making, etc. It has been a topic of fascination for psychologists. In this work, participant has been asked to perform some primary visual task that is based on cognition process and simultaneously asked to follow some secondary auditory instructions with some predefined relaxation spans in between. The neural response to these stimuli is recorded in the form of EEG signals with the help of RMS EEG-32 Super Spec machine. The EEG frequency bands are being studied for analysis of human behavior. A classification model is designed with the help of support vector machine to test the cognitive processes of human mind, while there are changes in resource allotment in terms of primary and secondary workload. Such a model can further be adopted to depict the type of cognition a participant undergoes. Also, the decrease in efficiency due to involvement in secondary tasks can be alarmed. This alarm may help in avoiding many disasters at places where attention toward a particular primary task is very crucial.

Keywords EEG · Support vector machine · Human–machine interface
One-Against-All (OAA) strategy

R. Singla · O. P. Verma (✉)
Dr B R Ambedkar National Institute of Technology Jalandhar, Jalandhar, India
e-mail: vermaop@nitj.ac.in

R. Singla
e-mail: rksingla1975@gmail.com

A. Agrawal
Jaypee Institute of Information Technology, Noida 201309, Uttar Pradesh, India
e-mail: anand.agrawal@iitg.ernet.in

V. Kumar
Kalinga Institute of Industrial Technology (Deemed to Be University), Bhubaneswar, India
e-mail: vikas.jhafet@kiit.ac.in

B. S. Rawat et al. (eds.), *Advances in Signal Processing and Communication* ,
Lecture Notes in Electrical Engineering 526,
https://doi.org/10.1007/978-981-13-2553-3_37

1 Introduction

Brain handles most of the human thoughts, decisions, behaviors, and emotions. For convening the information from the brain activities, they are studied as electrical signals. The brain activities may be electrophysiological [1] or hemodynamic [2]. Few neuroimaging techniques are electroencephalography (EEG), magnetoencephalography (MEG), electrocorticography (ECoG), intracortical neuron recording, functional magnetic resonance imaging (fMRI), near-infrared spectroscopy (NIRS), computed tomography (CT) scan, positron emission tomography (PET) scan, and diffusion tensor imaging (DTI). The EEG is preferred over others due to its noninvasivity, portability, easy processing of signals, and economic handling. The placement of electrodes over scalp is done based on the international 10–20 system standardized by the American Encephalographic Society [3]. EEG signals can be fragmented into different frequency bands based on frequency limits (Ahirwal 2012) as specified in Table 1. BCI is an artificial intelligence system that identifies particular set of patterns in the brain signals and provides an additional output channel for the applications like control of assistive technology (AT) devices for restoring motor function, communication program, etc. [4, 5]. BCI has also worked on healthy individuals for testing their efficiency under workload conditions in real-time environment. Hampshire et al. [6] had used a similar reasoning task for assessing executive function and found that the patient with some verbal reasoning problem at the onset of every trial. There were two possible answers for every stated problem. The patient was supposed to indicate his response either by imagining a face or by imagining a house depending on his response. It was observed that whenever corresponding to a particular problem, house was correct answer; there was prominently large activation in the areas specified with spatial processing. Kirschner et al. [7] have developed a brain-based battery that involved the participants in some predefined cognitive tasks. On the basis of this study, it was hypothesized that with the help of this battery, individual performance could be easily differentiated using the P300b component. Johnstone et al. [8] and Corballis et al. [9] concluded that the relative delta band power decreased during the stimulation processing with the visual cue. Bagyaraj et al. (2014) proved that during cognitive tasks, cerebral activations were defined by the following factors: (i) Relative band power values during task and relaxing span and (ii) ratio of theta-band power/beta-band power during task and relaxing span. Other than this, statistical paired t-test was done for examining the significant difference between two states: neural excitation and relaxation. In many cases, the operator's primary task was maintained at a particular specified efficiency, while it became difficult to detect the effectiveness of the secondary task that is suffering [10]. During few instances of low workload, operators may feel passive and miss the important signals that need to be responded. Such cases can be very well monitored with the help of workload detector [11].

Table 1 Different frequency bands of EEG signals

S. No	Bands	Frequency range (Hz)	Features
1.	Delta	0.5–4	Seen in babies and adults in deep sleep state
2.	Theta	4–7	Seen in adults in drowsy, meditative, and cognitive state
3.	Alpha	8–12	Establishes relation of memory processing with visual processing
4.	Beta	12–30	Observed during motor activities or imageries desynchronization
5.	Gamma	30–100	Seen in adults during motor functions or perceptions

Fig. 1 Sample of primary visual cue: Spot the difference (*Source* http://elmersunrealsite.com/)

2 Methods

Participants

The complete experimental work was performed in the Human–Machine Interface Laboratory of ICE Department at NIT Jalandhar. Twenty-one subjects had voluntarily participated in this study out of which 9 participants were females. All the participants belonged to an age group of 18–28. All the participants had healthy or corrected to healthy eyesight, and none of the participants had any neurological impairment history.

Stimuli (Primary Visual Cue)

Description: Participants were presented with a not so difficult task: Spot the difference as a primary visual cue. They were asked to mentally spot ten differences in the displayed similar looking images whose sample is being shown in Fig. 1. Three similar trials of such a stimulus were undertaken after a fixed span of time.

Protocols: Every time the task was executed with different images for three trials on a pattern as shown in Fig. 2. In between the trial duration, a ten-second lap of time was given to the participant for relaxation. During the relaxation period, subject was asked to relax with opened eyes and have a fixed gaze on some specific location of the

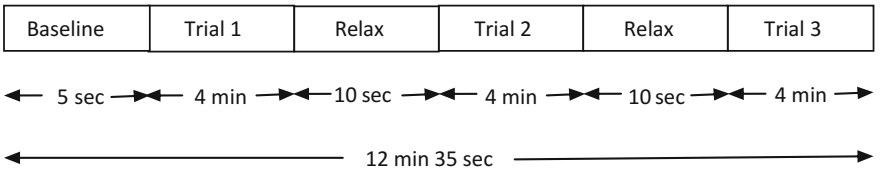

Fig. 2 Organization of the experiment

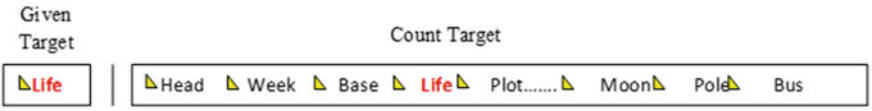

Fig. 3 Sample of secondary auditory cue: auditory task

visual display. The acquisition of EEG signals was performed for all the three tasks out of which trials 2 and 3 were a hybrid of primary visual and secondary auditory cue.

Secondary Auditory Cue

Description: Trials 2 and 3 of the primary visual task were presented along with auditory task in which a specific word (specified before beginning of experiment) was to be counted mentally out of the series of some monosyllabic words. The sequence of 49 words was played with a 5-s gap between every pair of words. Every time the target word was heard, P300 event-related potential (ERP) was evoked, while the nontarget words were simply ignored. The illustration of the sequence of words is shown in Fig. 3.

Protocol: The primary and secondary cue sequences were followed in trials 2 and 3 in which every time the target word fetched the attention of participants from primary to secondary cue. But the cognitive process of every participant varied every time and also from each other. The 5-s gap in between the words was meant for mind relaxation. At the end of the experiment, the count of target words was asked for verification. EEG equipment RMS EEG-32 Super Sec System (Recorders and Medicare Systems, India) was the hardware used for this experiment. Before the experiment, the subjects explained the aim of experiment and also about the procedure that was to be followed for achieving the results. Electrodes were placed at Fp_1, Fp_2, C_z, C_3, C_4, O_z, O_1, O_2, T_7, T_8, T_5, and T_6 with the help of electrode paste as per International 10–20 electrode placement system. The signals were recorded from these locations with respect to reference potential acquired from reference point in scalp. The skin-electrode impedance was kept below 5 kΩ for low noise. The analog EEG data was filtered with cut-off frequency of 0.1 Hz for high-pass filter and 50 Hz for low-pass filter, and a 50 Hz for notch filter. To avoid artifacts interference,

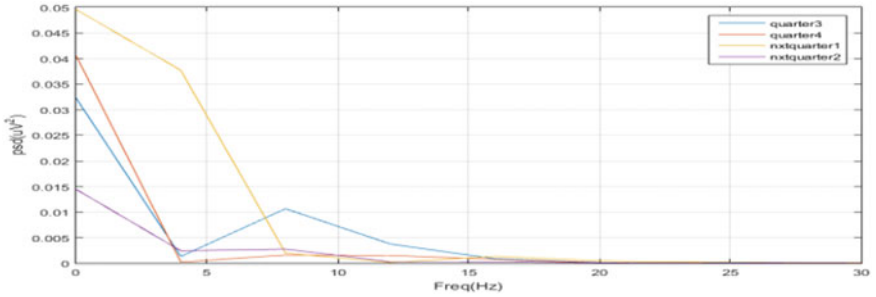

Fig. 4 Quarter-wise spectral analysis

participant was instructed not to undergo any physical movements and have a fixed gaze to avoid blinks artifacts.

EEG Preprocessing

Data was preprocessing using MATLAB for which raw data was exported to excel file from the RMS software. The digital filtering was performed within the band of 0.1–50 Hz. Blinks were removed before normalization of data for making the data more accurate (Delorme 2010).

EEG Feature Extraction

Extraction of required features was the first implicit step for classification of neurophysiologic signals. The EEG signals acquired from electrode placed at Oz-REF were considered for the evaluation to draw out the change in attention with changing resource allocation under workload conditions. The EEG data was analyzed in frequency domain so as to use it further for classification. The span of instance of a particular stimulus was specified and quarter-wise analyzed. Spectral analysis was done to extract specific frequency features [12]. FFT transform was applied on the signal for extraction of different frequencies along powers with their respective. Quarter-wise spectral analysis of one of the stimuli is shown in Fig. 4. The data acquired from the electrode site was recorded in monopolar configuration. Theta- and beta-band analyses were performed on the data extracted after FFT. Ratio of theta-band power to beta-band power during various quarters describes the attention shifted from primary toward secondary task in terms of dip in the ratio. From the theta- and beta-band power analysis, variation in the visual consciousness and active thinking can be done. But for tracing out the shift in attention from visual toward auditory, the ratio of theta-band power to beta-band power is needed. The quarter-wise ratio results of all the stimuli represented as VA have been presented to a particular subject in Fig. 5.

Feature Classification

The process of feature classification in terms of feature vectors helps in recognizing the user's intentions regarding control signals of BCI [13]. In this study, support vector machine (SVM) is used as the classification tool which is a multiclass classifier with

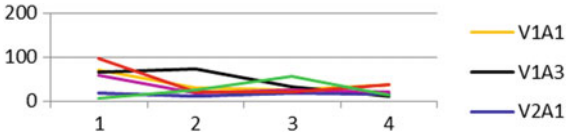

Fig. 5 Theta/Beta-band power ratio analysis of a participant

good accuracy and also has got the ability to find a hyperplane with widest margin that divides the sample into various classes using kernel functions. The aim of the SVM is to design and produce a model that can predict the target value of data instances in the testing set where only attributes are being provided [14].

A model was developed for a multiclass classification with one-against-all (OAA) strategy. The extracted feature vectors were used as the input vectors for the classification step. Each participant was presented with number of stimuli, the acquired data on particularly that instance was processed, and extracted frequency features of 18 subjects were used for training the classifier. Features of three subjects were used for testing the model developed from the training sets. The model generated was able to describe the cognition process of the subjects during change in resource allotment. In this study, the ratios of quarters have been used as the predictors and the stages of trend obtained on a stimulus as responses. The trends used as responses were defined as stages numbering from I to VI.

Choice of Classifier

One-against-all (OAA) strategy was used in the experiment. The formulation of this mode states that a data point gets classified under some class when that SVM class accepts it while all other SVM classes reject it. In this study, we have six SVM classes, all depicting different types of cognition processes in response to the stimuli. Table 2 is the depiction of accuracies with SVMs of different kernel functions with data in non-standardized data and one-against-all (OAA) strategy.

A classifier model was generated after training, with the help of cubic SVM with training accuracy of 96.3%. This model helped in the prediction of classes with test datasets. Figure 6 gives the glimpse of all the scatter plots of support vectors with each color depicting different classes.

Table 2 Comparison of SVMs and their corresponding accuracies

S. No.	Classifier	Accuracy (%)
1.	Linear SVM	50.9
2.	Quadratic SVM	87.5
3.	**Cubic SVM**	**96.3**
4.	Fine Gaussian SVM	51.5
5.	Medium Gaussian SVM	58.1
6.	Coarse Gaussian SVM	89.7

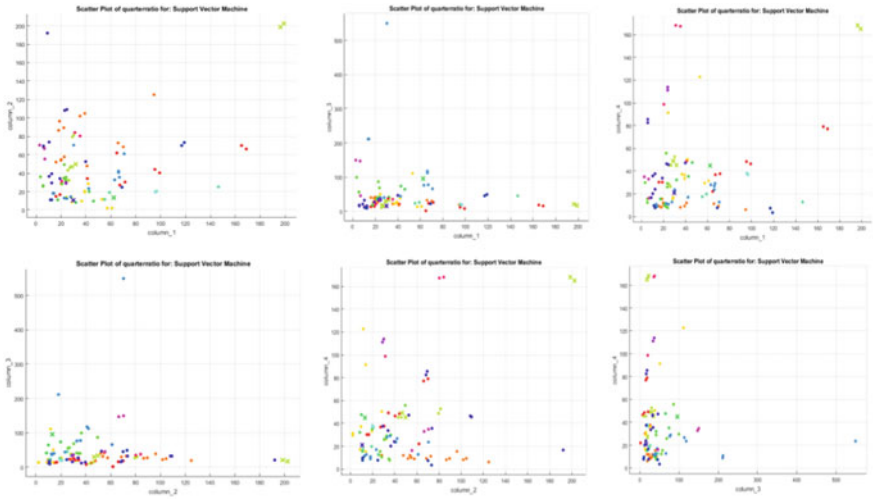

Fig. 6 Scatter plots of support with different predictors as axis variables

3 Results

The main aim of classifier testing is to check whether the relation established between the input and output data with the help the model designed approximates the classification or generalizes as per the requirement. The extent to which classification has been done accurately can be demonstrated in terms of metrics like confusion matrix, receiver operating characteristics (ROC) curve, etc.

SVM Classifier Testing

A total of 136 signals from 18 subjects were used for training of OAA cubic SVM, while a new set of 23 signals from 3 subjects was used for testing purpose. A total of 14.46% of the data was used for testing purpose, while rest of the 85.54% data was used in the training purpose. While classification training was done with 96.3% accuracy after the fivefold cross-validation, the testing process was performed with an accuracy of 86.96%. The results are being shown in various upcoming topics in various forms.

Confusion Matrix

A confusion matrix (error matrix) is a tabular layout that describes the performance of a "Classification Model" in case of a supervised learning. It visualizes the performance of an algorithm on a set of test data for the known true values. Column of matrix represents the predicted class instances, whereas row represented true class instances. The classification was initially done into 14 classes, and then similar classes were combined to form majorly six classes (Stage I–VI). The overall classification error percentage was found as 3.7%, whereas the model developed could test the data with an accuracy of 86.96% only. The various confusion matrices for SVM, as

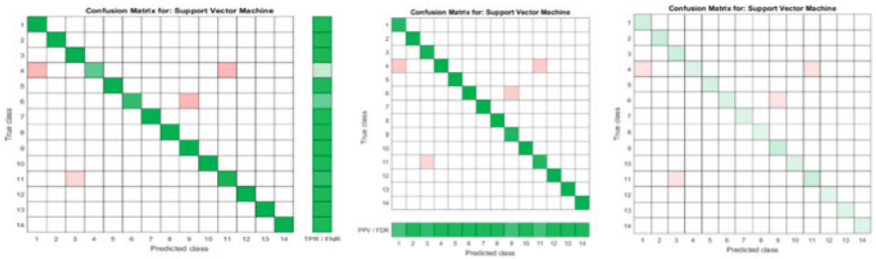

Fig. 7 Confusion matrices for SVM

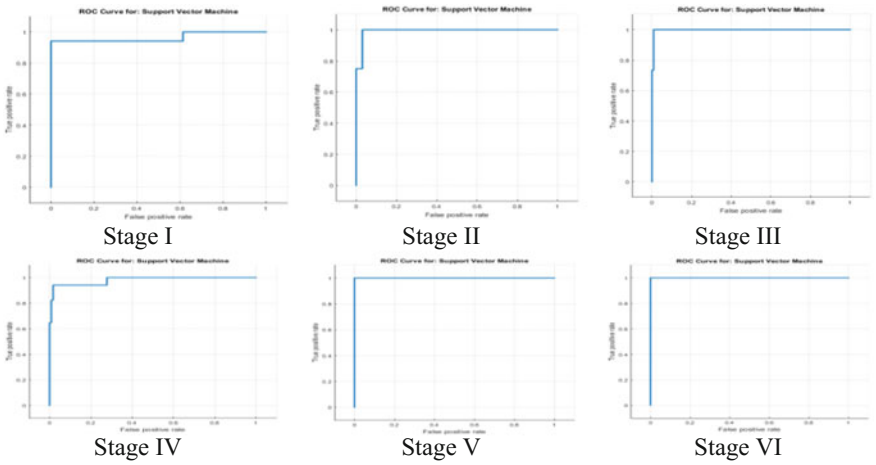

Fig. 8 ROC curve of various stages

shown in Fig. 7, are confusion matrix for SVM depicted/true class, confusion matrix for SVM for predicted class, and overall confusion matrix for SVM.

ROC Curve

The ROC curve is two-dimensional measure of classification performance over all possible thresholds. It is basically a plot depicting the probability of correctly classifying the true positive rate (y-axis) or positive examples against the false positive rate (x-axis) or incorrectly classifying true negative examples as you vary the threshold for assigning observations to a given class. The steepness on the ROC curve is an important factor as it ideally maximizes the true positive rate/sensitivity/recall/hit rate (TPR), whereas minimizing the false positive rate (FPR). Area under the curve (AUC) is the extracted measure from ROC curve for describing the performance. Unit value of AUC signifies that the classifier has got the perfect accuracy for that class if an apt threshold is being chosen. Fig. 8 depicts the stage-wise ROC curve.

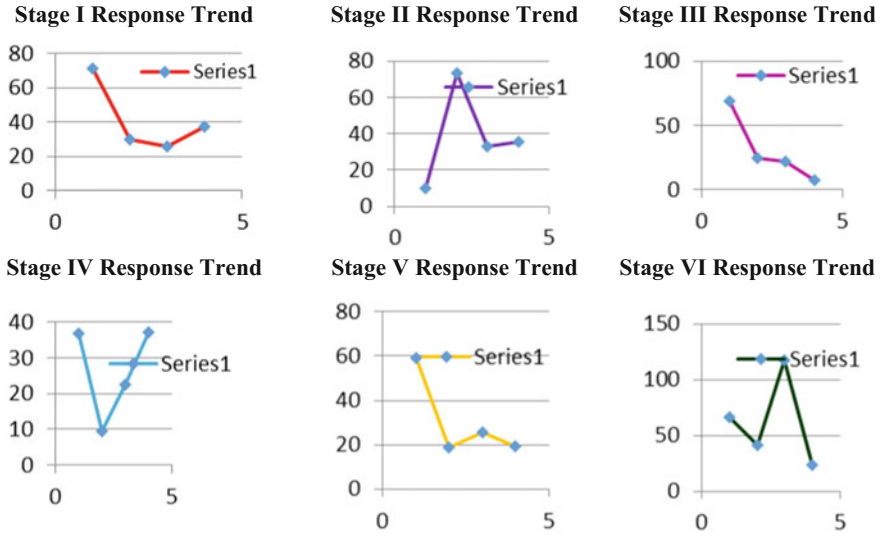

Fig. 9 Respond time

Response Trends

While the resource allocation changed in terms of primary and secondary stimuli, the ratio of theta-band to beta-band power quarter-wise variation of all the instances of stimuli were classified into six stages with the help of cubic SVM: (i) **Stage I**: It signifies a slow transition from high attention in primary visual task to secondary auditory task and then back. (ii) **Stage II**: It signifies a very fast transition of attention to secondary auditory task and then back to high attention in primary visual task. (iii) **Stage III**: It signifies a very slow transition of attention to secondary auditory task from the primary visual task. (iv) **Stage IV**: It signifies a fast transition of attention to secondary auditory task and then back to high attention in primary visual task. (v) **Stage V**: It signifies a fast transition of attention to secondary auditory task and takes time to rekindle the attention back to primary visual task. (vi) **Stage VI**: It signifies about the frequent changes in attention between primary visual and secondary auditory tasks. This may be due to no previous attention in primary visual task or when the secondary auditory task is missed (Fig. 9).

4 Conclusion

The data collected from participants under same primary visual and secondary auditory workload was used to study the cognitive process when more than one workload is present. The frequency responses were studied, and ratio of theta-band power to beta-band power was taken as the parameter to know the shifting of attention from

one to another. The trends of the responses were classified into six stages, and a model was designed with the aid of cubic SVM under OAA strategy that was trained with 96.3% accuracy. The test data from new subjects was classified in those six stages with an accuracy of 86.96%.

Acknowledgements Authors' would like to thank website http://elmersunrealsite.com/ for providing the open-source image for research purpose.

References

1. Baillet, S., Mosher, J.C., Leahy, R.M.: Electromagnetic brain mapping. IEEE Signal Process. Mag. **18**, 14–30 (2001)
2. Laureys, S., Boly, M., Tononi, G.: Functional neuroimaging. In: Steven, L., Giulio, T. (eds.) Neurology of Consciousness, pp. 31–42. Academic Press, New York (2009)
3. Jasper, H.H.: The ten-twenty electrode system of the international federation. Encephalogr. Clin. Neurophiol. **10**, 371–375 (1958)
4. Khalid, M.B., Rao, N.I., Rizwan-i-Haque, I., Munir, S., Tahir, F.: Towards a brain computer interface using wavelet transform with averaged and time segmented adapted wavelets. In: Proceedings of the 2nd International Conference on Computer, Control and Communication (IC4'), Karachi, Sindh, Pakistan, February 2009, pp. 1–4 (2009)
5. Kubler, A., Muller, K.R.: Towards Brain-Computer Interfacing: An Introduction to Brain-Computer Interfacing, pp. 1–25. MIT Press (2007)
6. **H**ampshire, A., Highfield, R.R., Parkin, B.L., Owen, A.M.: Fractioning human intelligence. Neuron **76**, 1225–1237 (2012)
7. Kirschner, A., Cruse, D., Chennu, S., Owen, A.M., Hampshire, A.: A p300-based cognitive assessment battery. Brain Behav. **5**(6), e00336 (2015). https://doi.org/10.1002/brb3.336
8. Johnstone, S.J., Blackmann, R., Bruggemann, J.: EEG from a single-channel dry-sensor recording device. Clin. EEG Neurosci. **43**(2), 112–120 (2012)
9. Corballis, P.M., Funnell, M.G., Gazzanig, M.S.: Hemispheric asymmetries for simple visual judgements in the split brain. Neuropsychologia **40**, 401–410 (2002)
10. Hockey, G.R.J.: Operator functional state: the prediction of breakdown in human performance. In: Duncan, J., Philips, L., Mcleod, P. (eds.) Measuring the Mind: Speed, Control, and Age, pp. 373–394. Oxford University Press, Oxford (2005)
11. Byrne, E.A., Parasuraman, R.: Psychophysiology and adaptive automation. Biol. Psychol. **42**, 249–268 (1996)
12. Moretti, D.V. et al.: Individual analysis of EEG frequency and band power in mild Alzheimer's disease. Clin. Neurophys. **115**, 299–308 (2004)
13. Nicolas-Alonso, L.F., Gomez-Gil, J.: Brain-computer interfaces, a review. Sensors **12**(2), 1211–1279 (2012)
14. Vapnik, V.: Statistical Learning Theory. Wiley, Chichester (1998)
15. Delorme, A., Sejnowski, T., Makeig, S.: Enhanced detection of artifacts in EEG data using higher-order statistics and independent component analysis. Neuro Image **34**, 1443–1449
16. Mitul, K.A., Narendra, D.L.: Power Spectrum Analysis of EEG Signal for Estimating Visual Attention. Int. J. Comp. Appl. **42**(15), 34–40 (2012)

De-seasoning-Based Time Series Data Forecasting Method Using Recurrent Neural Network (RNN) and Tensor Flow

Prashant Kaushik, Pankaj Yadav and Shamim Akhter

Abstract Time series data forecasting is studied by various method until today and has many applications in various fields like stock prediction, contextual chat bots, cognitive search engines, etc. Also till date, many stats models have been developed like ARIMA, ARMA, etc. A new approach is designed for time series data forecasting using RNN with Tensorflow framework, developed by Google for various types of neural networks modelling. De-seasoning of data is also carried out to study and obtains better results in this paper, a comparison chart for the same is presented, helps in aligning the contextual information on chat bot programs, and also is better for other data analysis like context search. This approach also helps us in reducing the training losses to increase in the accuracy of forecasting.

Keywords Recurrent neural networks · De-seasoned data
Time series forecasting · Tensor flow

1 Introduction

Time series forecasting has born again due to the rise of artificial intelligence based framework and applications and the training data for training the neural networks has problems of having the diverse information in them so that the weights of the neural network [1] align themselves well [1]. Google has provided its own framework [1] or designing neural network which requires training them with numerical data and if the numerical data is not available then it is to be generate from various mathematical transformations [2]. Seasoning data is the data which repeats itself after some time

P. Kaushik (✉) · P. Yadav · S. Akhter
Jaypee Institute of Information Technology, Noida, India
e-mail: prashant.kaushik@jiit.ac.in

P. Yadav
e-mail: pankaj.yadav@jiit.ac.in

S. Akhter
e-mail: shamim.akhter@jiit.ac.in

B. S. Rawat et al. (eds.), *Advances in Signal Processing and Communication* ,
Lecture Notes in Electrical Engineering 526,
https://doi.org/10.1007/978-981-13-2553-3_38

duration usually with fixed time duration. Seasoned data has a tendency to add weights to the forecasted data as all the applications which had been designed have many seasons of data be it chat bot of the stock prediction data. Now, neural network are the A neural network is a computational model that is loosely based on the Neural cell structure of the biological nervous system. Given a training set of data, the neural network can learn the data with a learning algorithm; in this research, the most common algorithm, backpropagation, is used. Through backpropagation, the neural network forms a mapping between inputs and desired outputs from the training set by altering weighted connections within the network.

More complex network types, alternative training algorithms involving network growth and pruning, and an increasing number of application areas characterise the state of the art in neural networks. But no advancement beyond feed-forward neural networks trained with backpropagation has revolutionised the field. Therefore, back-propagation based neural network and nowadays is called RNN, A recurrent neural network (RNN) is a class of artificial neural network where connections between units form a directed cycle. This allows it to exhibit dynamic temporal behaviour. Unlike feed-forward neural network, RNNs can use their internal memory to process arbitrary sequences of inputs [3].

Now the datasets are used for training and testing. Stocks data for 5 years which contains many season data the seasoning on stocks values is used. Experimental setups are known to use 80–90% of the data for training and rest of the data for forecasting or testing. Large data is also taken for textural information and have been used the word2vec [4] approach for converting the data from test to numerical value [4].

2 Designing of RNN and Backpropagation Through Time for Time Series Forecasting with De-seasoned Data

The whole project is divided into three parts and worked on them separately so that each module is independent and can be used with another newly developed modules. This also improves the modular approach in the project.

The data set for stocks dataset for 5 years has been taken and has manually detected the seasons in the data which will be de-seasoned using the first module.

2.1 De-seasoning Module

In this module, a mathematical relationship has been developed between seasoned data and de-seasoned data and this mathematical model is programmed in python using Sci-kit [5] library provided in Python. It takes the marked data from all the dataset and converts this into new values and writes them back to csv file. The csv file has three columns and the marking on seasoned data is done as binary 1 and if the

data is not seasoned, it is marked as zero. The output of the de-seasoned module is different for each seasoned signal (s1, s2, ……. sn) and de-seasoned signal (ds1, ds2, ……., dsn), where each ds and s variable is also a vector of time values. Pseudo code for converting the seasoned data to de-seasoned data is mentioned here below.

Pseudo code

1. *Read the csv file and store the signals into a data frame.*
2. *Loop through the column three till end of dataframe.*
3. *IF(val(colmn(3)=1)) then Ec=1/2 SUM(Dc - Oc)(Dc - Oc) where Dc is the current signal value which needs to be de-seasoned and Oc is the last signal value of the de-season and Ec is the new value of the de-season which will be written back to the csv.*
4. *write back the Ec on Dc in data frame.*
5. *write back the data frame to csv file.*

The time taken to do this module is of the order of n (O(n)) as the no. of values which needs to be de-seasoned are there in the data frame already read from the disk and the will be written to disk all together no one by one.

2.2 Setup of TensorFlow with 2 Hidden Layer and Training with Seasoned Data

Initially, four-layer neural network with two hidden layers, one input, and one output layer has been taken. The neural network type is chosen as a recurrent neural network as it uses backpropagation to adjust its weights between the perceptrons. refer to Fig. 1 for the layer structure of the layers of the neural network. The learning rates were kept 0.01 and then lowered down to 0.005 and the no. of epochs was 20,000. The total training time with seasoned data on 64 Gb server was 10 h and the results are to be seen in the result section.

Weight and biases of the neural network are getting changed on every batch of data and in this module, the batch size is taken as 20. Softmax function is used as a firing function as shown in Fig. 1. These figures are generated using the tensor board an inbuilt tool of Tensorflow which allows us to take most of the metrics of the Model out. But after the training, the accuracy is less and only 45% the Fig. 2 has jumped values at the last.

2.3 Setup of TensorFlow with Two Hidden Layers and Execution with De-seasoned Data

Now, the de-seasoned data is used for the same model and the model in the is trained in the exact same way. Now, it took almost 9 h but the results were very promising

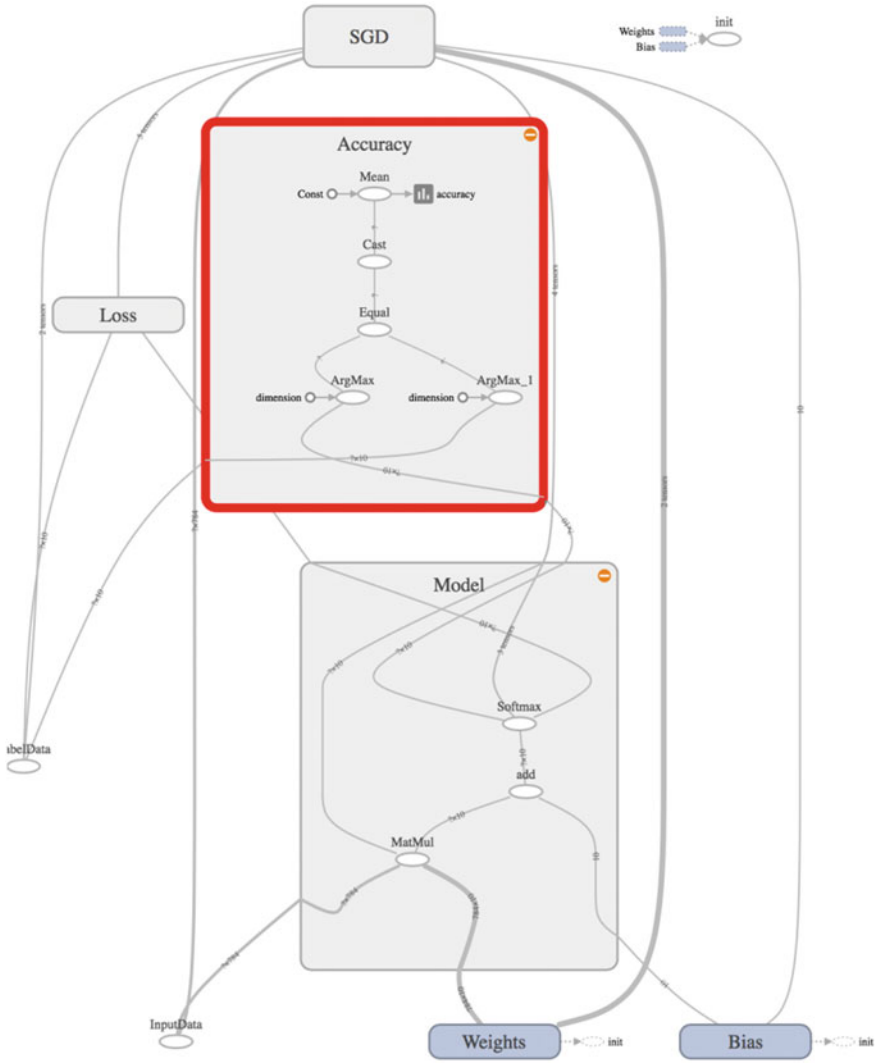

Fig. 1 Four-layer RNN for our model using tensor flow

and the accuracy was 88%. This whole process could be further enhanced in training time if we use the GPU-based training which is currently not available to us so we used CPU-based training only.

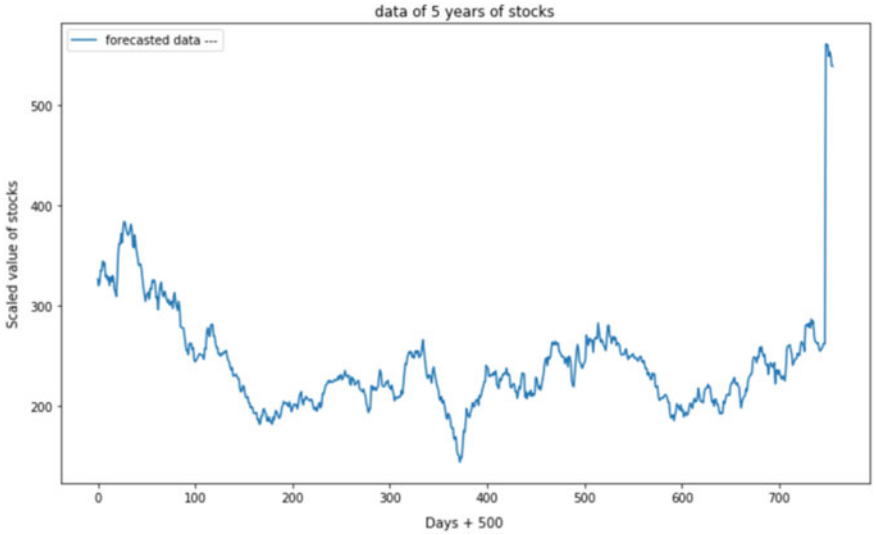

Fig. 2 Forecasting using original data (seasons in data)

3 Experimental Results and Analysis

It is clearly seen that the seasoned data gave the high output but the de-seasoned data follows the tested values with an accuracy of 88% whereas the seasoned data is very inaccurate (Figs. 3, 4 and Table 1).

The ARIMA and ARMA models are classical models and their implementation has been attempted in many areas.

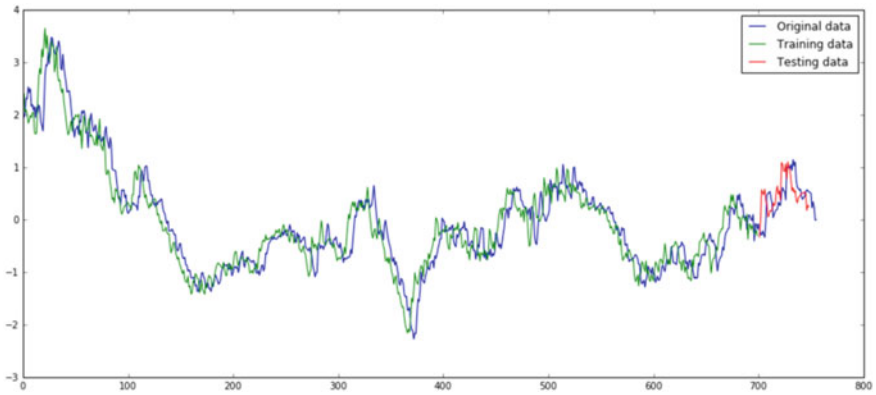

Fig. 3 Results plot with de-seasoned data

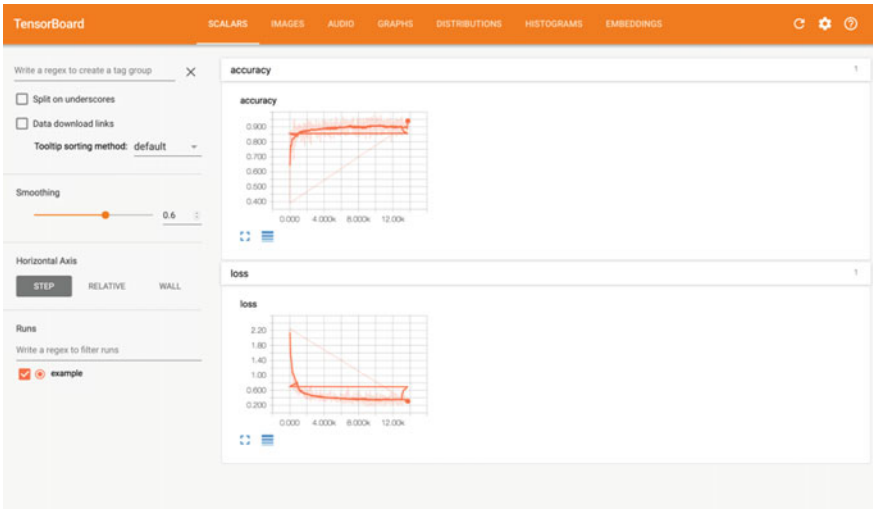

Fig. 4 Tensor board metrics on accuracy and training losses

Table 1 Comparison of results and training time

S. no	Dataset (Signal values)	Model	Training time	Accuracy (%)	Data rows
1	Seasoned	4 layer RNN	10 h	45	1700
2	De-seasoned	4 layer RNN	9 h	88	1700
3	Seasoned	ARIMA	20 min	34	1700
4	Seasoned	ARMA	23 min	35	1700

Table 2 Comparison of results with latest systems

S. no	Model name	Accuracy (%)	Data set size (n*m)
1	RNN with de-seasoned data	88	65*1700
2	RNN	67	65*1700
3	RNN	70	Text data with live features

Below is the table of accuracy comparison with the latest system in the domain [6] and forecasting models [7] (Table 2).

4 Conclusion

After experimenting and getting final results from training, forecasting, and matching them with test results, the following conclusion can be drawn.

a. Recurrent neural network is better than ARIMA model which has been used widely before the invention of neural network frameworks.
b. De-seasoning of data allows better diversity in data which results in better forecasting.
c. Training time and training losses are also reduced a bit by de-seasoning of time series data.

5 Future Works

After getting initial results for single class and one lakh rows, a new plan to carry on our research in diversifying the data in such a way that it contains least season data which helps our neural network to learn and align its weight better. Also, automatic identification of season set in data in big datasets is a limitation as of now and will be a matter of research of ours in near future. Neural network training took 10 h of time for data of 1,00,000 rows with a single class and later for big data training sets the training time will grow, which will be another area of our attention along with more number of classes. Hidden layer increase does not have much effect on the forecasted data but this new direction can also be an area of future work.

Acknowledgements We would like to thank Mr. Vimal Kumar for helping us out in developing the code for neural network in python and supervising the server while the training was in progress.

References

1. https://github.com/tensorflow/tensorflow
2. Wikibooks. Artificial Neural Networks/Error-CorrectionLearning (2013). http://en.wikibooks.org/wiki/Artificial_Neural_Networks/Error -Correction_Learning
3. Allende, H., Moraga, C., Salas R.: Artificial neural networks in time series forecasting: a comparative analysis
4. Sundermeyer, M., Ney, H., Schlüter, R.: From feedforward to recurrent LSTM neural networks for language modeling. IEEE/ACM Trans. Audio Speech Lang. Process. **23**(3), 517–529 (2015)
5. https://github.com/scikit-learn/scikit-learn
6. Fukushima, K.: Neural network model for a mechanism of pattern recognition unaffected by shift in position - Neocogni- tron. Trans. IECE. **J62-A**(10), 658–665 (2012)
7. Sodanil, M., Chatthong, P.: Artificial neural network-based time series analysis forecasting for the amount of solid waste in Bangkok. In: 2014 Ninth International Conference on Digital Information Management (ICDIM) (2014)
8. Shamshiry, E., et al.: Forecasting generation waste using artificial neural networks. In: Proceedings of the 2011 International Conference on Artificial Intelligence (ICAI 2011), Las Vegas, NV, USA, 18–21 July 2011
9. Subrahmanian, V.S., et al.: The Twitter bot challenge (2016). https://arxiv.org/abs/1601.05140
10. Goodfellow, I.J., et al.: Generative adversarial networks. https://arxiv.org/abs/1406.2661. 10 June 2014

11. https://finance.yahoo.com/quote/CSV/history?p=CSV
12. https://www.infoq.com/news/2017/04/microsoft-dataset-chatbots
13. chatterbot.readthedocs.io/en/stable/training.html
14. https://www.kaggle.com/eibriel/rdany-conversations

R-Peaks Detection Using Shannon Energy for HRV Analysis

Om Navin, Gautam Kumar, Nirmal Kumar, Kuldeep Baderia, Ranjeet Kumar and Anil Kumar

Abstract In this paper, a system for R-peak detection in ECG signal is presented that applicable in different heart rate variability (HRV) applications based on S-transform and Shannon energy. The presented technique and system are efficient in R-peak detection as per results illustrated up to 99.80% of sensitivity and positive predictivity. Here, Shannon energy envelope computes sharp peaks that help in the allocation of peak position in ECG signal. The presented technique is evaluated on 27 records of MIT-BIH arrhythmia database of ECG signals. A tool named as SpandanV.1 (Cardiac Rhythm Variability, version 1) also demonstrated for R-peak detection with HRV analysis.

Keywords ECG signal · R-peaks · Shannon energy · S-transform
Heart rate variability

O. Navin · G. Kumar · N. Kumar · A. Kumar
Department of Electronics and Communication Engineering, PDPM Indian Institute of Information Technology, Design and Manufacturing Jabalpur, Jabalpur 482005,, Madhya Pradesh, India
e-mail: omnavin@iiitdmj.ac.in

G. Kumar
e-mail: gautamkumar@iiitdmj.ac.in

N. Kumar
e-mail: nirmal.kumar@iiitdmj.ac.in

A. Kumar
e-mail: anilkdee@gmail.com

K. Baderia (✉)
Department of Electronics and Communication Engineering,
Jaypee Institute of Information Technology, Noida 201309, Uttar Pradesh, India
e-mail: kuldeep_gec2000@yahoo.co.in

R. Kumar
Department of Electronics and Communication Engineering,
Madanapalle Institute of Technology & Science, Madanapalle, India
e-mail: ranjeet281@gmail.com

B. S. Rawat et al. (eds.), *Advances in Signal Processing and Communication* ,
Lecture Notes in Electrical Engineering 526,
https://doi.org/10.1007/978-981-13-2553-3_39

1 Introduction

Cardiovascular decease (CVD) is the major cause of mortality in the world presently and near future as per World Organization and Unites Nations report [1]. Here, heart rate variability (HRV) plays a vital role in the primary screening of cardiac health conditions [2]. It represents the physiological state of an autonomic nervous system (ANS) that is responsible for cardiac rhythm and activity [2, 3]. In this analysis, *QRS* wave complex especially *R*-peak is very important key in electrocardiogram (ECG) signal and its interpretation. Over the years, several researches have been developed in form of algorithms and different systems for screening of HRV based on the *R*-peak analysis [3, 4]. In this context, different techniques have been proposed for *R*-peak detection based on different filtering and morphological operations, derivatives methods, transform techniques, template matching, and many more techniques as reported in literature [5–12]. The basic aim of these techniques is to improve the detection rate/sensitivity of algorithm for *R*-peak detection. Although, these techniques are not up to 100% sensitivity due to different morphology and nonstationary nature of signal that is a challenging and open research problem for the researchers and scientist.

As growing trend of digital monitoring and diagnosis system in healthcare applications is in a growing trend, a wide range of techniques have been proposed in different health screening area. In particular, R-peak or QRS detection algorithms a diverse range of techniques are developed in the last decades [2]. In 1985, Pan Tompkin (PT) has proposed a QRS detection technique that is very popular in the literature based on different filtering and peak finding process [13]. A detailed study of the different algorithm is summarized by Kolher et al. [14]. These techniques have different sensitivity rate in peak detection. Similar to another area of signal processing research [15], wavelet transform based technique gives higher sensitivity and accuracy in peak detection, but it requires the selection of suitable mother wavelet transform. Here, Hilbert transform based R-peak detection technique also popular for higher accuracy but limited cases [16].

In ECG signal, the QRS wave has contained specific band of frequency [13] that can be localized. Several previous works utilized the absolute energy envelope of local spectra for finding the peaks. Here, S-transform and Shannon energy-based R-peak detection technique are presented. Where S-transform offers the frequency-dependent localization; while retaining a direct relationship with the Fourier spectrum. This advantage of S-transform is exploited to isolate the QRS complex in time–frequency domain instead of different filtering operations. Therefore, Shannon energy envelope of QRS spectra in time–frequency domain is exploited for peak localization.

The presented method is evaluated with selected dataset of the MIT-BIH arrhythmia database. The rest of paper is organized as follows with the introduction in Sect. 1, brief details of the methodology are presented in Sect. 2, result and discussion are included in Sects. 3 and 4 followed by a conclusion.

2 R-Peak Detection

In this paper, Shannon energy and s-transform based *R*-peak detection algorithm has been presented as shown in Fig. 1. The basic processes of peak detection are as follows: preprocessing, peak localization, and postprocessing. The performance of *R*-peak detection depends on the efficiency of these processes; although, the dataset is also important for evaluation that helps in performance comparison to other works.

2.1 Materials and Methods

The presented method of *R*-peak detection is based on S-transform and Shannon energy. Where dataset play a big role to evaluate the robustness of algorithms with respect to other techniques performance. These are summarized in subsections as follows.

A. *ECG Dataset*

The MIT-BIH arrhythmia database is utilized for evaluating the presenting technique of *R*-peak detection [17]. The database has conations 48 records of male and female patients. These records having 30-min length of signal from two different channels (modified limb lead II and one of the modified leads V1, V2, V4, or V5) that are recorded with sampling frequency 360 Hz and 11 bits of resolution. In most of the records, lead II is used as a default channel for prominent QTS complexes.

B. *Performance Evaluation Parameters*

The statically parameters are used for evaluating the performance of R-peak detection technique. These are defining as follows:

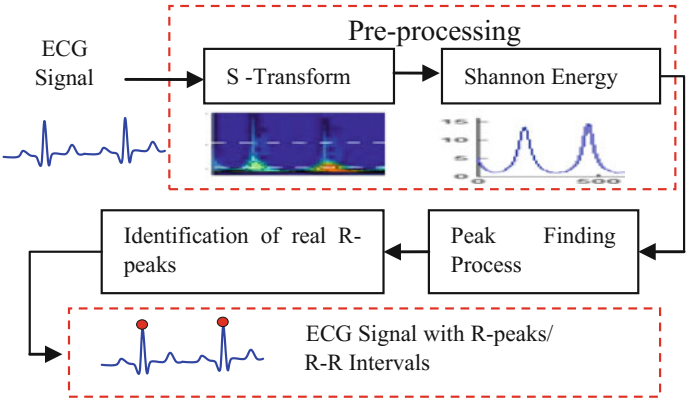

Fig. 1 Block diagram of R-peak detection process based on S-transform and Shannon Energy Envelope

$$\bullet \text{ Sensitivity } (S_e) = \frac{TP}{TP + FN}, \quad \bullet \text{ Positive Predictivity } (P_+) = \frac{TP}{TP + FP}, \quad \bullet \text{ Error } (E_r) = \frac{FN + FP}{TB}$$

where TP, FP, FN, and TB represent the correctly detected beat (True Positive), falsely detected beats (False Positive), the undetected beats (False Positive), and total detected beats, respectively [12].

C. *S-Transform*

In 1996, Stockwell was proposed a time–frequency analysis tool known as S-transform. It is providing the access to various frequency selections without any filtering process. The S-transform also efficient in time–frequency resolution with maintaining a direct relationship with local Fourier spectra [18]. It is derived from short-time Fourier transform (STFT) and wavelet transform (WT) and is defined as for a time-varying signal $x(t)$,

$$S(\tau, f) = \int_{-\infty}^{+\infty} x(t) w(t - \tau) e^{-i2\pi ft} dt \tag{1}$$

where $w(t)$ is a time window that is centred at $t = 0$ and is defined as Gaussian window []. The discrete S-transform is defined as

$$S(j, n) = \sum_{m=0}^{N-1} X(m + n) W(m, n) e^{(i2\pi mj)/N}; \quad n \neq 0 \tag{2}$$

The response of S-transform is called ST-matrix of $N \times M$, where rows are representing the time and columns are frequencies.

D. *Shannon Energy*

The Shannon energy is defined as

$$\text{SE}(j) = -[S(j, n)]^2 \log[S(j, n)]^2 \tag{3}$$

where $[S(j, n)]^2$ is the absolute energy of signal or transform coefficients. In absolute energy process, low and high amplitude of R-peak segment makes difficulty for peak or threshold selection. Therefore, Shannon energy-based approach has been exploited to obtain normalized peaks. It has several benefits over absolute energy approach such as small deviated successive peaks, reduction of low amplitude noise coefficients, produce sharp and smooth local maxima of energy envelop. These advantages help in detection of peak time/sample index in ECG signal using peak finding logic and Shannon energy envelope (SEE) [19].

2.2 R-Peak Detection Methodology

The R-peak detection algorithm is based on S-Transform and SSE has been summarized as follows in different stages as discussed earlier and shown in Fig. 1.

Stage I: Preprocessing

(a) ECG signal is decomposed with ST using Eq. (2), $S(j,n) = \mathrm{ST}[x(t)]$
(b) Compute the Shannon energy envelope $SE(j)$ of ST coefficients using Eq. (3)

Stage II: R-Peak Localization

(a) Find the maxima (peak) of SSE using $SE(j) > SE(j\text{-}1)$ and $SE(j) > SE(j+1)$
(b) Find the minima (valley) of SSE using $SE(j) < SE(j\text{-}1)$ and $SE(j) < SE(j+1)$

Stage III: Identification of Real R-peak

(a) Set threshold value: (maxima-minima)/4
(b) Search again in [–25–25] range of maxima with threshold level.
(c) Store the current maxima and its index value.

Stage IV: ECG signal with R-peaks.

Therefore, detected R-peak helps to identify the heart rate variability, R-R intervals, and maximum amplitude of ECG signals. This analysis helps in preexamination of cardiac health, arrhythmia analysis. Recently, R-peak based temporal modelling of beats has been processed for compression of ECG signals due to its quasi-periodic of nature [15]. The accuracy of detection technique is very important because it causes error during the compression application. It is also important due to clinical accuracy that helps to identify the physiological condition of ANS. In this technique, SEE gives sharp and smooth peaks of selected QRS spectra based on ST that helps in accurate peak detection.

3 Results and Discussion

In this paper, a system is presented for HRV analysis based on the Shannon energy and S-transform. Here, the presented technique is evaluated with 27 different signals from MIT-BIH Arrhythmia records; the system framework gives details of HR as well as average beat duration in term of *R-R* duration.

The performance of presented technique is illustrated in Table 1 in terms of total beat (TB), true positive (TP), false positive (FP), false negative (FN), sensitivity (SE), predictivity (P), and error rate (ER). The analysis presents that R-peak detection technique has 99.8% of sensitivity and predictivity with 27 different subjects

Table 1 Performance analysis for different signals

Signal	TB	TP	FP	FN	SE (%)	P (%)	ER (%)
101	1866	1866	2	0	100	99.89	0.107
102	2187	2187	0	0	100	100	0
103	2084	2084	0	0	100	100	0
104	2255	2255	4	0	100	99.82	0.177
105	2586	2581	5	5	99.8	99.8	0.387
106	2003	2000	5	3	99.85	99.75	0.4
107	2137	2136	0	1	99.95	100	0.046
108	1767	1762	8	5	99.71	99.54	0.737
109	2532	2532	3	0	100	99.88	0.11
112	2539	25339	1	0	100	99.96	0.039
115	1954	1964	6	0	100	99.69	0.307
121	1866	1866	4	0	100	99.78	0.214
122	2476	2476	0	0	100	100	0
123	1520	1520	5	0	100	99.67	0.32
201	1975	1963	2	12	99.3	99.8	0.71
202	2136	2136	8	0	100	99.6	0.37
203	3012	2982	2	30	98.9	96.9	1.07
205	2657	2656	1	1	99.9	99.9	0.05
210	2651	2647	4	4	99.8	99.8	0.15
221	2431	2427	0	4	99.8	100	0.16
222	2504	2484	0	20	99.2	100	0.81
223	2605	2605	0	0	100	100	0
228	2053	2053	4	0	100	99.75	0.24
230	2256	2256	2	0	100	99.91	0.088
231	1571	1571	0	0	100	100	0
232	1780	1780	4	0	100	99.77	0.224
233	3078	3070	2	8	99.74	99.93	0.32
All	**64385**	**64292**	**72**	**93**	**99.80**	**99.80**	**0.25**

of signals. These illustrations have shown the acceptable quality of sensitivity for R-peak detection that helps in HRV analysis. In this context, Fig. 2 represents the variation of sensitivity and positive predictivity of presented technique for different signal. Here, minimum and maximum sensitivity obtained 98.6 and 100%, respectively. Similarly, minimum and maximum positive predictivity is 96.9 and 100% respectively.

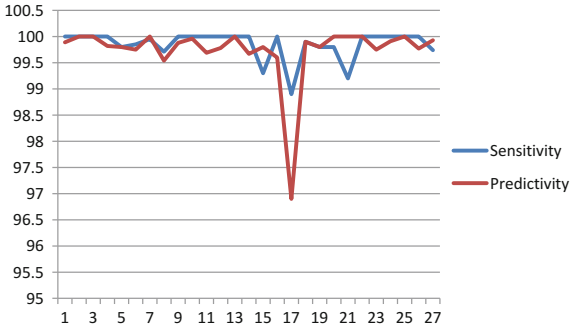

Fig. 2 Sensitivity and positive predictivity of presented technique for different signals

Table 2 Performance comparison with other existing techniques

Techniques	Signal/Database	SE (%)	P (%)
Presented	MIT-BIH-A	99.80	99.80
Zidelmal et al. [9]	MIT-BIH-A	99.64	99.82
N. Arzeno [5]	MIT-BIH-A	99.68	99.63
V. Afonso [6]	MIT-BIH-A	99.56	99.56
B. Abibullaev [8]	MIT-BIH-A	97.20	98.52

Table 2 demonstrates the performance comparison of presented technique with other existing techniques, which clearly indicates the presented technique is suitable for R-peak detection with better efficiency of sensitivity and predictivity as per compared techniques.

4 Conclusion

In this paper, an R-peak detection technique and HRV tool (SpandanV.1) has been presented based on S-transform and Shannon energy envelop (SEE). Here, sharp peak of SSE obtains from transform coefficients that help in the allocation of R-peak position in ECG signal. Obtained results have clearly illustrated the presented technique which is suitable for different subjects of signal to investigate HRV components like HR, R-R duration. In this context, demonstrated tool SpandanV.1 gives details and information of discussed HRV component. Overall, the analysis is concluded with the efficiency of the presented technique is efficient for healthcare systems (Fig. 3).

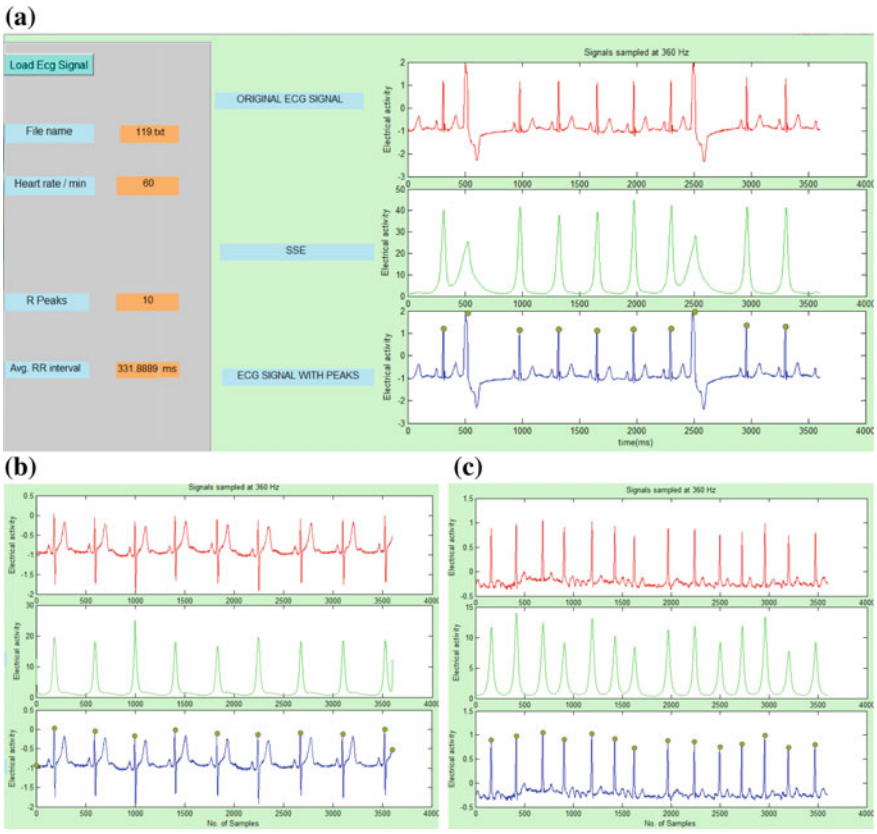

Fig. 3 System framework (SpandanV.1) for HRV analysis based on R-peak: **a** HR with beat duration details for Rec. 119, **b** R-peaks and SEE for Rec. 117, **c** R-peak and SEE for Rec. 201

References

1. Finegold, J.A., Asaria, P., Francis, D.P.: Mortality from ischaemic heart disease by country, regin, and age: statistics from world orgranisation and unites nations. Int. J. Cardiol. **168**, 934–945 (2012)
2. Acharya, U.R., Joseph, K.P., Kannathal, N., Lim, ChM, Suri, J.S.: Heart rate variability: a review. Med. Biol. Eng. Comput. **44**, 1031–1051 (2006)
3. Chen, X., Yang, R., Ge, L., Zhang, L., Lv, R.: Heart rate variability analysis during hypnosis using wavelet transformation. Biomed. Signal Process. Control **31**, 1–5 (2017)
4. John, A.A., Subramanian, A.P., Jaganathan, S.K., Sethuraman, B.: Evaluation of cardiac signals using discrete wavelet transform with MATLAB graphical user interface. Indian Heart J. **67**, 549–551 (2015)
5. Arzeno, N., Deng, Zhi-De., Poon, C.: Analysis of first-derivative based QRS detection algorithm. IEEE Trans. Biomed. Eng. 55(2), 478–484 (2008)
6. Afonso, V.X., Tompkins, W.J., Nguyen, T.Q., Luo, S.: ECG beat detection using filter banks. IEEE Trans. Biomed. Eng. **46**(2), 192–202 (1999)

7. Okada, M.: A digital filter for the QRS complex detection. IEEE Trans. Biomed. Eng. **26**(12), 700–703 (1999)
8. Abidullaev, B., Seo, H.: A new QRS detection method using wavelets and artificial neural networks. J. Med. Syst. **35**(4), 683–691 (2011)
9. Zidelmal, Z., Amirou, A., Adnane, M., Belouchrani, Adel.: QRS detection based on wavelet coefficients. Comput. Method. Program. Biomed. 107, 490–496 (2012)
10. Ruchita, G., Sharma, A.K.: Detection of QRS complex of ECG recording based on wavelet transform using Matlab. Int. J. Eng. Syst. 2(7), 3038–3034 (2010)
11. Chen, S.W., Chen, C.H., Chan, H.L.: A real-time QRS method based on moving-averaging incorporating with wavelet denoising. Comput. Method. Program. Biomed. **82**(3), 187–195 (2006)
12. Moukadem, A., Dieterlen, A., Hueber, N., Brandt, C.: A robust heart sounds segmentation module based on S-Transform. Biomed. Signal Process. Control **8**(13), 273–281 (2013)
13. Pan, J., Tompkins, W.J.: A real-time QRS detection algorithm. IEEE Trans. Biomed. Eng. **32**(3), 230–236 (1985)
14. Köhler, B.U., Hennig, C., Orglmeister, R.: The principles of software QRS detection. IEEE Eng. Med. Biol. Mag. **21**(3), 42–57 (2002)
15. Kumar, R., Kumar, A., Singh, G.K.: Electrocardiogram signal compression based on 2D-transforms: a research overview. J. Med. Imaging Health Inf. **6**(2), 285–296 (2016)
16. Benitez, D., Gaydecki, P.A., Zaidi, A., Fitzpatrick, A.P.: The use of the Hilbert transform in ECG signal analysis. Comput. Biol. Med. **31**(5), 399–406 (2001)
17. Mark, R., Moody, G.: MIT-BIH arrhythmia database. http://www.physionet.org/physiobank/database/mitdb/
18. Stockwell, R.G., Mansinha, L., Lowe, R.P.: Localisation of the complex spectrum: the S-Transform. IEEE Trans. Signal Process. **44**(4), 998–1001 (1996)
19. Zidelmal, Z., Amirou, A., Ould-Abdeslam, D., Moukadem, A., Dieterlen, A.: QRS detection using S-transform and Shannon energy. Comput. Method Prog. Biomed. **116**, 1–9 (2014)

Index Seek Versus Table Scan Performance and Implementation of RDBMS

Akshit Manro, Kriti, Snehil Sinha, Bhartendu Chaturvedi and Jitendra Mohan

Abstract The purpose of this chapter is to make an application which can search the particular piece of information easily within less time. Moreover, it will also show the comparison of two methods that are Table Scan and Index Seek for searching in a database. Table Scan is linear searching method as it traverses each and every row present in the database making the time complexity very large. The objective of this paper is to reduce the problem of the time complexity and it makes indexes to resolve the time complexity issues that are being faced. A seek is the opposite of scan, where a seek uses the indexes to pinpoint the records, which is required to search. Indexing process eliminates the need of unnecessary disk accesses. An UI (User Interface) is made to show user, which searching method is to be used, the time taken in searching, the pages read in total and the complete information of the person who has been searched. This will provide to user, the information of superior method along with whole analysis of time and pages read.

Keywords UI is User Interface which is used to provide a link between user and the machine · SQL is Structured Query Language · RDBMS is Relational Database Management System · GUI is Graphical User Interface

A. Manro · Kriti (✉) · S. Sinha · B. Chaturvedi · J. Mohan
Department of Electronics and Communication Engineering,
Jaypee Institute of Information Technology, Noida 201304, UP, India
e-mail: guptakriti1997@gmail.com

A. Manro
e-mail: akshitmanro@gmail.com

S. Sinha
e-mail: sinha.snehil26@gmail.com

B. Chaturvedi
e-mail: bhartendu.prof@gmail.com

J. Mohan
e-mail: jitendramv2000@rediffmail.com

B. S. Rawat et al. (eds.), *Advances in Signal Processing and Communication* ,
Lecture Notes in Electrical Engineering 526,
https://doi.org/10.1007/978-981-13-2553-3_40

1 Introduction

The paper is about the comparison of two searching methods in the database. The two methods popularly used for searching in database are Table Scan and Index Seek both have their own way to traverse through database. Table Scan searches row by row, which works when data is small but for the huge amount of data the process is very slow. In Index Seek the data is arranged in sorted form, within BTree so the server knows which path will take it to the result. BTree has the ability to go in a certain direction. In SQL data is stored in Relational Database Management system (RDBMS) the data is stored in tabular form. The disk space allocated to a data file is logically divided into pages which is the fundamental unit of data storage in SQL server. A database page is an 8 kB chunk of data. When user inserts any data into a SQL server database, it saves the data to a series of 8 kB pages inside the data file. If multiple data files exist within a file group, SQL server allocates pages to all data files based on a round robin mechanism [1]. So if data is inserted into a table SQL server allocates pages first to data file 1, then allocates to data file 2 and so on, then back to data file 1 again. SQL -server achieves this by an algorithm known as proportional fill. So when it is connected to the Table Scan and Index Seek, in Table Scan the operation will start from the page 1 and will go through each page and each row in it, it will traverse like this till the match of what user asked for is found whereas in Index Seek the time complexity is drastically reduced as the structure of BTree provides well defined path so that the program finds the key and then row within no time [2].

2 Methods of Searching in Database

In SQL, data is stored in tabular form in RDBMS which is different from DBMS (Database management system). The data is divided into pages which is unit of data storage in SQL server.

2.1 Methods Used in Searching

There are 3 methods that can be used for searching and those are:

(1) Table Scan (Linear Searching) – In this process the program searches each and every row in the page and goes through every page until the record is found. A scan works opposite to seek, seek directly points the data that is required to be searched and follow very selective path. The reason for bad performance of scan is it takes more I/O and is long process [3].
(2) Binary Searching – This method is used for sorted arrays it keeps on dividing the array into two parts until the data is found or interval is empty. Initially,

begins with two pointers covering the entire array. If the value of the query is less than the value of data in the middle of the interval, it reduces the interval to the lower half. Otherwise reduce it to the upper half. Binary search is helpful when the input data is small but as the data increases the speed and efficiency decreases [4].

(3) Index Seek – BTree is a self-balancing search tree. It is assumed that everything is in main memory. In order to put light on BTree, it is assumed that large amount of data is stored in main memory. When the number of keys is high or data is very large, the data is read from disk in the form of blocks. Disk access time is very high compared to main memory access time. The purpose of using BTree's to reduce the number of disk accesses. Most of the tree operations (search, insert, delete, max, min, etc.) require O(h) disk accesses where 'h' is height of the tree [5].

2.2 Problems by Using Table Scan

When it comes to the disk access the Table Scan involve the huge amount of access of disk as it is known that disk access time is much more than the main memory access time. The problem with the Table Scan is its time complexity as it doesn't take the extra space for the data allocation but the time complexity is large in Table Scan. The operation will start from the page 1 and will go to the each page and each row in it, it will traverse like this till the match of what user asked for is found. For example if user take millions of data than disk access time will be proportional to it which will take huge amount of time to give the desired output. Hence making it impossible and very long to attain result using Table Scan whereas it works fast for the small amount of data. Binary searching has the same problem of time because it works fast for the small amount of data but when the data is in millions the time complexity is on very higher side also in binary searching the data should be sorted now it comes to load the data onto the memory, it will take lots of uploading process in packets and then applying the merge sorts of rows which is cumbersome process [6].

2.3 Solution Using Index Seek

The problem discussed above are handled by the Index Seek method. Since the Index Seek uses the data structure BTree and it is fat tree [7]. The height for BTree is kept low so as to reduce the disk access time, the height corresponds to the disc accesses, for e.g. for the 8 Millions of data records the height of the BTree will be 3, hence the disc access is also 3, which results in great improvement of the performance. Index Seek uses the seeking mechanism the code starts from the root of the tree and

goes till the leaf where the actual data is contained, by just two comparisons within a single level the code knows where to go further and what to return above [8].

3 Application Development

Java Swing is used to make UI (User interface) for this paper and the layout used in it is group layout.

3.1 Swing (Java)

When it comes to the graphical user interface (GUI) the Java Swing plays a vital role. It is a toolkit which is first used by the Oracle's Java Foundation for java programs. It was developed to provide a more sophisticated set of interface as compared to the earlier version of toolkit that is Abstract Window Toolkit (AWT). Swing provides a native look and feel to the programmer by creating a interface having components such as buttons, check boxes, labels and scroll bars which work for the specific operating system. It also provides several advanced components such as tabbed panel, scroll panes, trees, tables, and lists.

3.2 Layout Description

The role of layout manager is to position all the components that are used in the interface within the container. It is possible to layout the controls manually however it becomes difficult to do so because of the following reasons:

(1) Border Layout – It arranges the components present in the interface to fit in the five regions such as north, east, south, west and center. The programmer will decide in which region the components should be arranged according to the java program.
(2) Card Layout – This layout treats each component in the container in the form of a card. At a time only one card is visible to the programmer respectively.
(3) Flow Layout – It is also known as default layout. It's main purpose is to layout the components present in the interface in directional flow.
(4) Grid Layout – This layout helps to manage the components in the form of a rectangular grid. The programmer can decide whether to opt for this layout or not.
(5) Grid Bag Layout – The key feature of this layout is that it provides great flexibility to the programmer. This layout aligns the component vertically, horizontally or along their baseline without requiring the components of the same size.

(6) Group Layout – In this chapter group layout has been used. It's main feature is that it hierarchically groups the components in order to position them in a container.
(7) Spring Layout – This layout helps to position the children of its associated container according to a set of constraints [9].

3.3 Group Layout

Group Layout is used to position the group components in a container. Group Layout is the best layout to use and can be used by the builders to make the layout, two types of layouts are supported by Group Layout. One of them is sequential group which positions the components sequentially, it places the components horizontally. In four ways the parallel group can align the components. There can be any number of elements in Group Layout. A gap is a component with minimum or maximum size. Group Layout can support a gap which can be defined by the user and then elements can be arranged. Every element in this layout can be defined with a preferred gap which is given by the user by using Layout Style. It can have different axis for all components. There is a group which can be aligned by horizontal axis and a group which can be aligned by vertical axis. The horizontal group is used to define the preferred gap and size along the horizontal axis as well as setting the width of the components. The vertical group is used to define the preferred gap and size along the vertical axis as well as it also sets the height of the component. If components don't exist in both horizontal and vertical group then an IllegalStateException is thrown during layout, or when the preferred size is not given [9].

4 Verification and Simulation Results

An application is built using Java Swing and the layout used is group layout, various actions are implemented on the components present inside the UI using the action listener. The UI basically contains a window with the 4 tabbed panels which are as Home Panel, Data Panel, Indices Panel, and Query Panel.

4.1 Home Panel

Figure 1 shows the Home Panel which is showing the objective of the analysis.

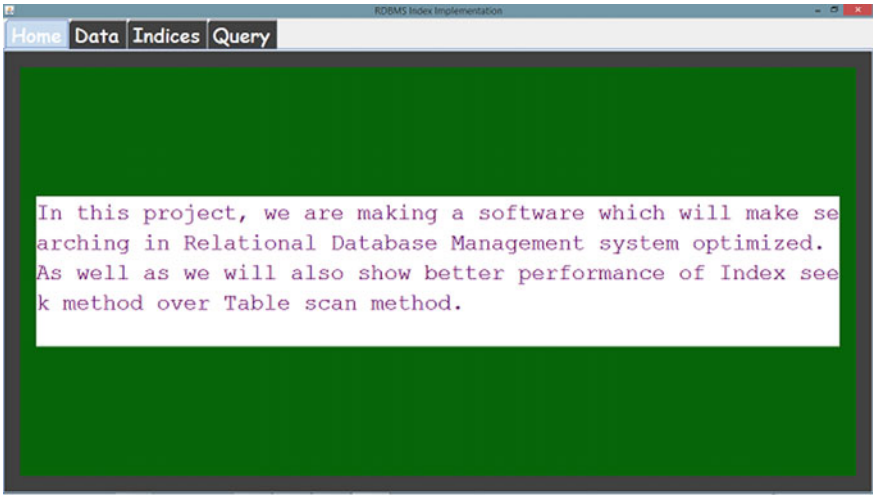

Fig. 1 Home Panel

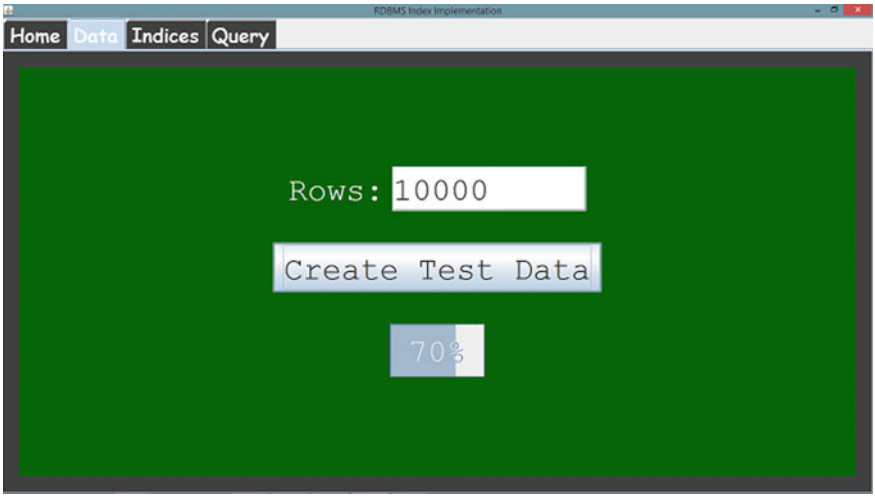

Fig. 2 Data Panel

4.2 Data Panel

When the "Create Test Data" button will be clicked, program will start making data into a source folder which will be assigned to that. To show the progress for the number of rows that have been created there is an area that will show the percentage for that.

Figure 2 shows the Data Panel.

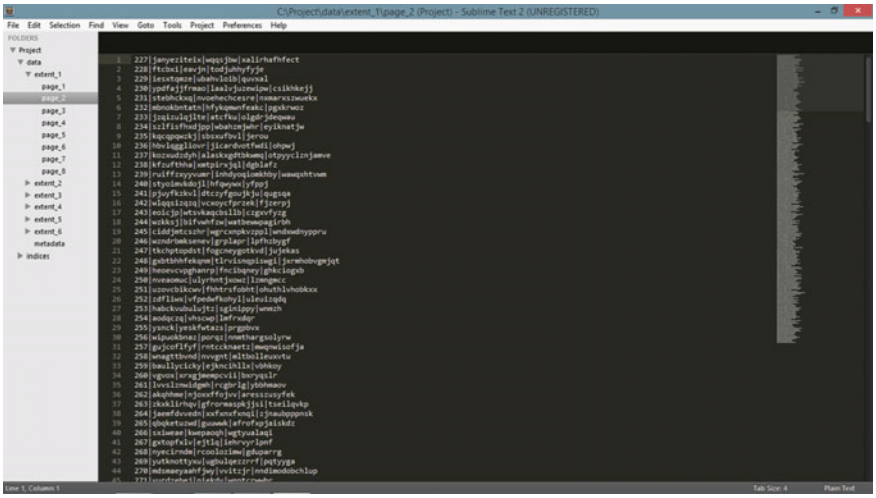

Fig. 3 Sublime Text containing data

Figure 3 shows the database that was created, a software is used "Sublime Text" which will open the folder containing the data. It has metadata folder that consist of the number of rows created and the pages consists of the data and its further information separated by a pipeline.

4.3 Indices Panel

Figure 4 shows the Indices Panel which will make indexes in the data according to column for which user want to make indexes for (Name, Username, Password). Clicking the button "Create Index" will start making indexes and an area will be showing percentage of index created.

Indices created for the database are shown in Fig. 5 using Sublime Text. The folder indices consist of metadata, root and files. The metadata gives the information about the root data and guides to the actual location of the data. The metadata has the indices which points to its lower and higher value indices by the information on either side of pipeline respectively. The files contains the leaves which has the extent number, page number and offset value.

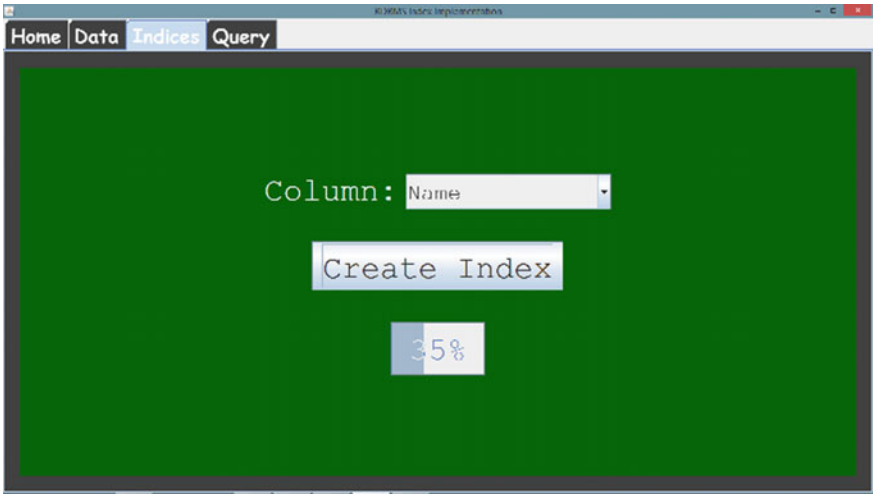

Fig. 4 Indices Panel

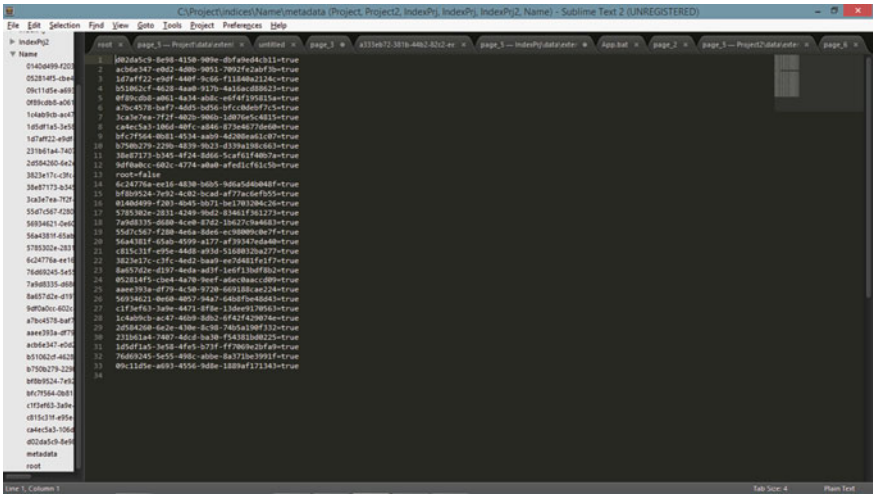

Fig. 5 Indices shown in Sublime Text

4.4 Query Panel

Figure 6 shows Query Panel in which user will enter the query like name, roll number and password and searched result will be shown. (Displaying the details using Index Seek Method).

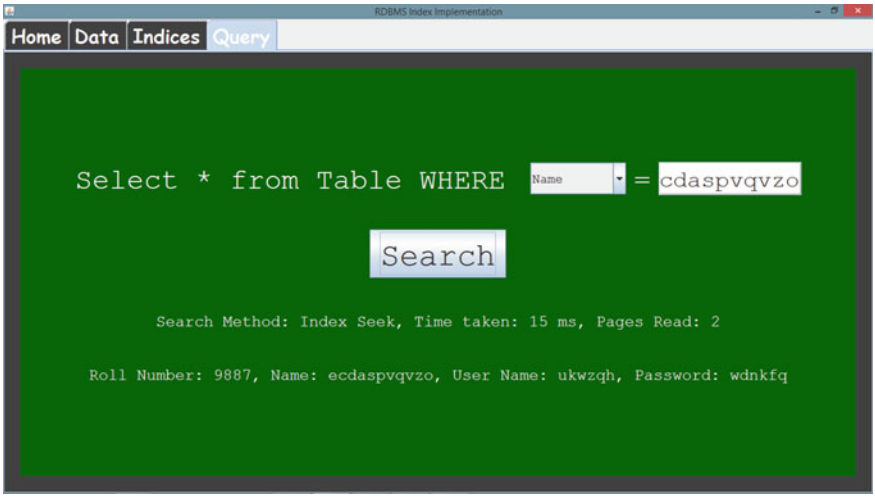

Fig. 6 Result of search using Index Seek

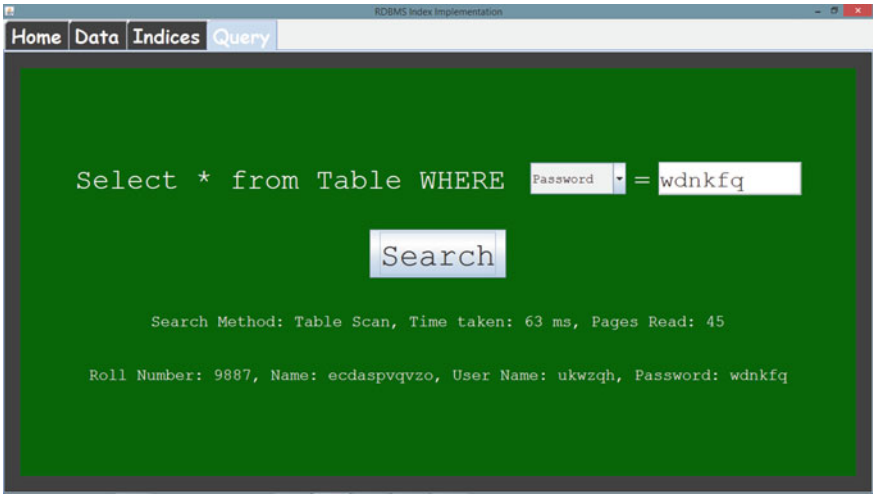

Fig. 7 Result of search using Table Scan

It is Query Panel in which user will enter the query like name, roll number and password and searched result will be shown (Displaying the details using Table Scan Method). Figure 7 is displaying the results after searching.

5 Conclusion and Future Scope

In this chapter, a BTree is used, which will do searching and then creating the indexes and for getting the data, an user interface is made which will do all these things as well as to show the details of searched data. The main motive of this chapter is to reduce the time consumption and in case of huge amount of data, searching can be done faster than the resolute methods. This software will just work as of real database in which a bunch of data will be stored and for certain data details user can search in the database and get what he wants. Real life application of this chapter is that it can be used as the managing software of students in a college, for e.g. A database on student id, username, password and roll number can be made so a database of students using this chapter and this can also be used in offices for maintaining the database of workers just by changing the field names. This application can also be useful in logging into some websites like web kiosk where server can retrieve the data using this software [10].

References

1. Rivest, R.: On the worst-case behavior of string searching algorithms. SIAM J. Comput. **6**, 669–674 (1977)
2. blog.sqlauthority https://blog.sqlauthority.com/2007/03/30/sql-server-index-seek-vs-index-scan-table-scan/ post from 30 March 2007
3. http://searchsqlserver.techtarget.com/definition/database
4. i-manager's J. Inf. Technol. **2l**(11) December 2012–February 2013 Timur Mirosoev and Craig Brockman. Sap Hana and its performance benefits
5. https://www.cs.usfca.edu/~galles/visualization/BTree.html
6. http://searchsqlserver.techtarget.com/definition/SQL
7. Kroenke, D.M., Auer, D.J.: Database Processing: Fundamentals, Design, and Implementation, 12th edn. Pearson, Boston (2012)
8. https://www.geeksforgeeks.org/b-tree-set-1-introduction-2/
9. https://www.tutorialspoint.com/swing
10. Beginning microsoft sql server programming by taul aktinson and robert viera (2012)

Industrial Simulation of PID and Modified-MPID Controllers for Coupled-Tank System

Rajesh Singla, Anand Agrawal, Vikas Kumar, Nikhil Pachauri and Om Prakash Verma

Abstract Most of the chemical industries required to control the liquid or fluid level in many of the processes unit of process industries. Often it becomes more difficult to control when the tanks are cascaded in coupled as the level of one tank influences the level of other one. The present work attempts to investigate and compare the control behavior of level control of two noninteracting coupled-type systems using conventional PID and modified-MPID control action. Usually, PID controller is used for this purpose with certain limitation such as higher overshoot, response time, settling time, etc. In this work, certain modifications in the conventional PID controllers with PID-PD, PI-PD, and I-PD controllers to overcome these limitations have been presented and compared. The modified-MPID controller simulation results yield the better results when it is applied to control the level of noninteracting coupled-tank system.

Keywords Coupled-tank system · Level control · Modified-MPID controllers PID controller

R. Singla · O. P. Verma (✉)
Dr B R Ambedkar National Institute of Technology Jalandhar, Jalandhar, India
e-mail: vermaop@nitj.ac.in

R. Singla
e-mail: rksingla1975@gmail.com

A. Agrawal
Department of Electronics and Communication Engineering,
Jaypee Institute of Information Technology, Noida 201309, Uttar Pradesh, India
e-mail: anand.agrawal@iitg.ernet.in

V. Kumar
School of Electronics Engineering, Kalinga Institute of Industrial Technology (Deemed to be University), Bhubaneswar, India
e-mail: vikas.jhafet@kiit.ac.in

N. Pachauri
Netaji Subhas Institute of Technology Dwarka, New Delhi, India
e-mail: nikhilpchr@gmail.com

B. S. Rawat et al. (eds.), *Advances in Signal Processing and Communication* ,
Lecture Notes in Electrical Engineering 526,
https://doi.org/10.1007/978-981-13-2553-3_41

1 Introduction

Level measurement and its control are critically important in any of the chemical process industries and for the safety of equipment they use. Low level may cause damage to the equipment, whereas high liquid levels might cause overflow and yield safety and environmental problems [1]. Using level controller, level measurements and its control have been ensured accurately and also optimize the performance of the plant and its processes.

A PID controller is widely used usually to control the level in industrial control systems as it is simple and easy to implement [2], while PID controllers do not provide optimal control in general. Therefore, a number of literatures proposed the modifications in the classical PID controller in the recent years [3–5]. Sung and Su Whan have modified the PID controller using a time-variant bias term to achieve high-quality control performance for both tracking of set point change and disturbance rejection in the processes [3]. Alarçin et al. have proposed I-PD controller as a modified version of PID controller and simulate to control the nonlinear roll motion using modified-MPID fin stabilizer system [4]. Kaya has proposed PI-PD controller to overcome the difficulties encountered in PID control for integrating unstable transfer functions [6]. Radaideh and Hayajneh have designed $PII_{\sigma}^{\beta}D$ by modifying the PID controller to improve its performance by changing the length of integration interval and then compared this with conventional PID and $PI_{\sigma}D$ [7]. Haasan has designed I-PD, PD-PI, and PI-PD controllers for second-order systems and tuned them for robust performance [8].

Apart from the various modifications done in the conventional PID controller, many of the literatures studied the different methods of PID tuning parameters for coupled-tank system. Roy and Roy [9] have proposed fractional-order PI controllers with a feedforward control which performs better than the PI/PID/2DOF-PI/3DOF-PI controllers coupled with two-tank MIMO system. The main advantage of the proposed system is its simple design and implementations with better setpoint tracking and disturbance rejection. Hannema and Lina have designed control system based on internal model control (IMC) method for a coupled-tank single-input-single-output (SISO) process which proved to be robust and stable as compared to PID and fuzzy logic controllers (FLC) [10]. It was observed that IMC rejects the disturbance with faster settling time than others. Usually, the conventional industrial controllers, namely, proportional–derivative (PD), proportional–integral (PI) and proportional–integral–derivative (PID), show the linear nature. However, hybrid of industrial controllers with FLC controllers such as PD (FLC-PD), PI (FLC-PI), and PID (FLC-PID) operate on nonlinearity [11]. Duan et al. proposed an effective tuning method for fuzzy PID controllers based on IMC technique which proved to be more robust and achieve better control performance than the conventional PID controllers [12]. Boonsrimuang et al. and Cartes and Wu have used model reference adaptive control (MRAC) technique for a coupled-tank and three-tank system, respectively, and observed that MRAC can adjust the control parameters in response to changes in plant and disturbance [13, 14]. MRAC is an example as its name suggests to adaptive

servo system in which the desired performance is specified in terms of a reference model, which yields the desired response to a command input signal. The parameters are varying with the error, $e = Y_p - Y_m$ based on feedback signal, where Y_p is the plant output and Y_m is the model output. The adjustments of the parameters of MRAC may be obtained using a gradient method mechanism [15]. Chi Chung et al. have developed a web-based laboratory experiment on a coupled-tank apparatus which can be used as virtual laboratory for remotely tuning the important parameters in research [16].

Changing the tuning algorithm can help in better performance of classical PID controllers. Nagaraj et al. [17] have used different heuristics tuning algorithm for PID controller to enhance its performance compared to classical tuning methods like Ziegler–Nichols (Z–N method) method and Cohen–Coon method [18–20] which was laborious and time-consuming. Genetic algorithm was introduced for the first time by Holland in 1970 [21] and has been widely used to evaluate the optimum solution of nonlinear mathematical optimization problem [22, 23] and in control problem, it is used to tune PID parameters [24]. Verma et al. (2016) showed the utility of GA for solving the set of nonlinear algebraic equations and climates the initial point guess dependencies [23]. Another type of heuristic algorithm is particle swarm optimization (PSO) which is more reasonable and effective as compared to GA. Fathi et al. Gaing Zwe-Lee, and Abido have used PSO for tuning of PID parameters using different processes [24–26]. Sivagurunathan and Saravanan have designed a PI controller based on PSO for a nonlinear spherical tank system and compared its performance with that of FLC [27].

On the basis of the pertinent literatures, the present paper has proposed to investigate the modified-MPID controllers such as PID-PD, and tuned the controller parameters using Z-N method and simulated for the noninteracting coupled-tank system.

2 PID-PD Controller

A model-based PID-PD controller design has been proposed in the present work, where the PD controller has been utilized in feedback so that it may shift the location of poles of the plant transfer function to more desirable locations [28, 29]. Hence, the response of the PID-PD controller has been compared with several existing methods to control integrating processes. Finally, it is found that the proposed method is superior to existing ones.

The computed transfer function of the PID-PD closed loop is represented by Eq. 1:

$$\frac{Y(s)}{R(s)} = \frac{G_p K_{p_1}(1 + \frac{1}{\tau_i s} + \tau_{d_1} s)}{1 + [K_{p_1}(1 + \frac{1}{\tau_i s} + \tau_{d_1} s) + K_{p2}(1 + \tau_{d_2} s)]G_p} \tag{1}$$

3 Modeling of Noninteracting Coupled-Tank Systems

When two or more than two tanks are joined together in such a manner that the outflow from the first tank enters the second tank with the contact of air, then it is called noninteracting system and is illustrated in Fig. 1. Consider two tanks of cross-sectional areas, A_1 and A_2. The outlet flow from tank-1 discharges directly into the atmosphere prior to spilling into tank-2, and the flow through R_1 depends only on h_1. The variation in h_2 in tank-2 does not affect the transient response occurring in tank-1. Also, R_1 and R_2 are the flow resistance valves, whereas q_i, q_1, and q_2 are volumetric flow rate to the two tanks. The transfer function of this system is Eq. (2):

$$\frac{H_2(s)}{Q(s)} = \frac{R_2}{(1 + s\tau_1)(1 + s\tau_2)} \tag{2}$$

In the present investigation, various experiments have been performed and acquired the geometrical data to compute the mathematical model of the system and further, transfer function of the model has been evaluated and used to simulate the system. The experimental setup of coupled-tank system with and without interaction of tanks have been carried over in the process control lab, Indian Institute of Technology Roorkee that has been illustrated in Fig. 2a, b. The parameters of the tanks and collected sampled data are represented in Tables 1, 2 for given system.

The calculated transfer function of the noninteracting tank system is given by Eq. (3):

$$\frac{H_2(s)}{Q(s)} = \frac{0.472}{687.553s^2 + 53.2839s + 1} \tag{3}$$

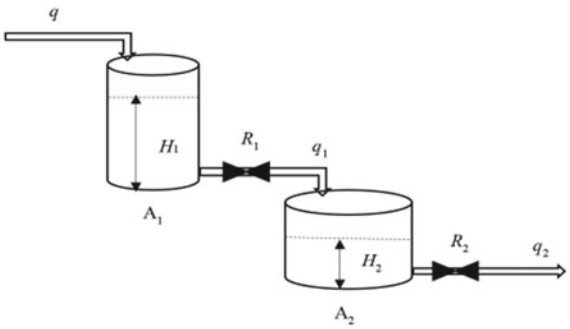

Fig. 1 Noninteracting tank system

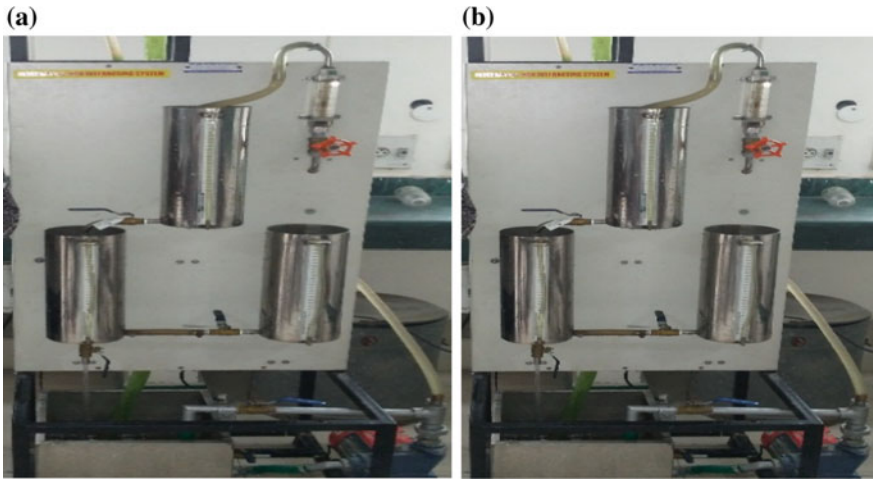

Fig. 2 Illustration of experimental setup of interacting and noninteracting coupled-tank system

Table 1 Parameters of tanks

S. no	Parameter (S)	Value (s)
1	Diameter of tanks	9.2 cm
2	Initial flow rate (LPM)	0
3	Initial steady-state level of tank-1 (cm)	35.007
4	Final flow rate (LPM)	2 or (33.34 cm^3/s)
5	Final steady-state level of tank-2 (cm)	50.76015

4 Simulation Result

The tuning of the implemented controllers is done using Z-N method which is an inbuilt software function in MATLAB. The Simulink model for the noninteracting system has been shown in Fig. 3. However, the step response of all the different types of controllers used here is shown in a combined form in Fig. 4. The compensator formula of a PID-type controller is given in MATLAB as

$$P + I\frac{1}{s} + D\frac{N}{1 + N\frac{1}{s}}$$

It is observed that PID-PD controller improves the transient response control parameters, namely, rise time, overshoot, and settling time for noninteracting system when compared to others. Rise time defined as the time required by the response to reach from 0 to 100% value of final value has also been captured for two cases.

Table 2 Observation of level of tanks

S. no	Time	H_1	H_2	H_1 (observed)	H_2 (observed)
1	0	24	35.0071	0	0
2	15	24.3	36.01	0.3	1.0029
3	30	25.09	36.92	1.09	1.9129
4	45	25.2	37.15	1.2	2.1429
5	60	28.07	37.49	4.07	2.4829
6	75	29.4	40.07	5.4	5.0629
7	90	30.1	42.21	6.1	7.2029
8	105	31.03	44.52	7.03	9.5129
9	120	33.54	45.13	9.54	10.1129
10	135	33.98	49.008	9.98	14.0009
11	150	34.9	50.1	10.9	15.0929
12	165	35.007	50.74	11.007	15.7329
13	180	35.007	50.76015	11.007	15.75305

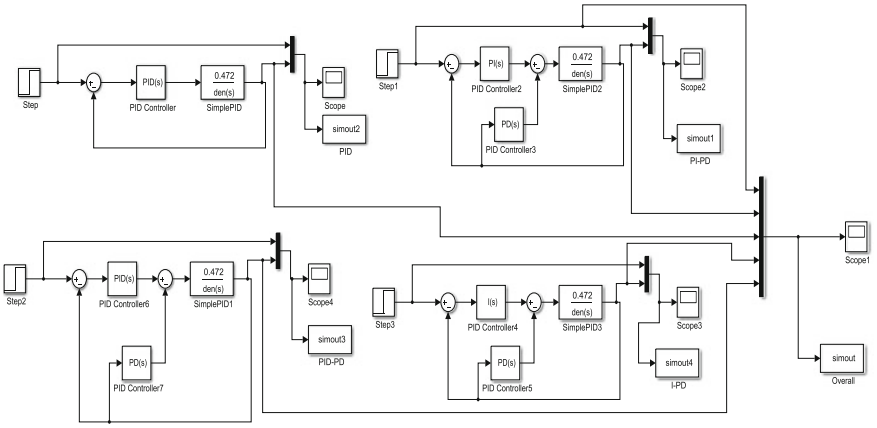

Fig. 3 Simulink model for noninteracting tank system

It is found that PID-PD controller improves the rise time (800%, 337%, and 81% using PID, PI-PD, and I-PD controller, respectively) and settling time (654%, 266%, and 19% using PID, PI-PD, and I-PD controller, respectively). However, in case of overshoot, PID-PD controller shows the improvement marginally with 4.43% when compared to conventional controller PID, whereas I-PD and PI-PD show the reverse.

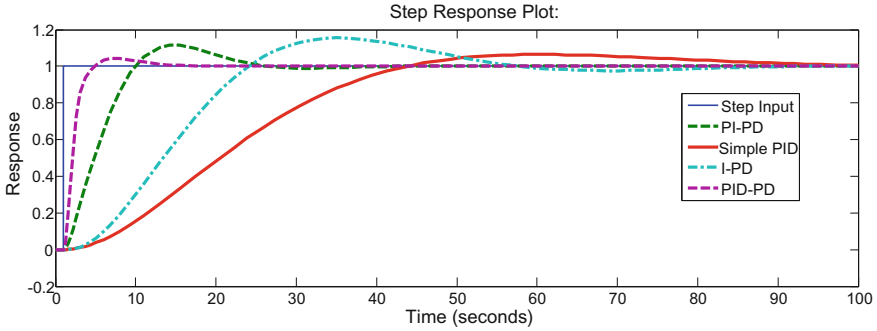

Fig. 4 Step response of PID and modified-MPID controllers for noninteracting tank

5 Conclusion

The modified-MPID controllers like PI-PD, PID-PD, and I-PD designed in this research work offer several advantages. All these control schemes lead to a more general two degrees of freedom control scheme. When compared to the classical PID controller, these new control schemes proved to give better results in terms of settling time, overshoot, and rise time. Also, among the three different modified-MPID controllers, PID-PD is showing the better results.

References

1. Sharma, A.: Mathematical modeling and intelligent control of two coupled tank system in mathematical modeling and intelligent control of two coupled tank system. Imp. J. Interdiscip. Res. **10**, 1589–1593 (2016)
2. Fellani, M.A., Gabaj, A.M.: PID controller design for two tanks liquid level control system using matlab. Int. J. Electr. Comput. Eng. 436–442 (2015)
3. Sung, S.W., Lee, I.B., Lee, J.: Modified proportional-integral derivative (PID) controller and a new tuning method for the PID controller. Ind. Eng. Chem. Res. **11**, 4127–4132 (1995)
4. Alarçin, F., Demirel, H., Su, M.E., Yurtseven, A.: Conventional PID and modified-MPID controller design for roll fin electro-hydraulic actuator. Acta Polytech. Hung. **3**, 233–248 (2014)
5. Verma, O.P., Manik, G.: Comparative analysis of boiler drum level control using advanced classical approaches. Int. J. Eng. Sci. Innov. Technol. **5** (2013)
6. Kaya, I.: A PI-PD controller design for control of unstable and integrating processes. ISA Trans. **1**, 111–121 (2003)
7. Radaideh, S.M., Hayajneh, M.T.: A modified-MPID controller (PII σ β D). J. Franklin Inst. **6**, 543–553 (2002)
8. Hassaan, G.A.: Robustness of I-PD, PD-PI and PI-PD controllers used with second-order processes. Int. J. Sci. Technol. Res. **10**, 27–31 (2014)
9. Roy, P., Roy, B.K.: Fractional order PI control applied to level control in coupled two tank MIMO system with experimental validation. Control Eng. Pract. (2016)
10. Haneema Varghese, K., Rose, L.: Comparitive study of various level control techniques for a two tank system. In: Proceedings of Innovations in Information, Embedded and Communication Systems (ICIIECS), pp. 1–4. IEEE (2015)

11. Verma, O.P., Manik, G., Jain, V.K.: Simulation and control of a complex nonlinear dynamic behavior of multi-stage evaporator using PID and Fuzzy-PID controllers. J. Comput. Sci. (2017)
12. Duan, X.G., Li, H.X., Deng, H.: Effective tuning method for fuzzy PID with internal model control. Ind. Eng. Chem. Res. **47**(21), 8317–8323 (2008)
13. Boonsrimuang, P., Numsomran, A., Kangwanrat, S.: Design of PI controller using MRAC techniques for couple-tanks process. World Acad. Sci. Eng. Technol. **59** (2009)
14. Cartes, D., Lei, W.: Experimental evaluation of adaptive three-tank level control. ISA Trans. **44**(2), 283–293 (2005)
15. Verma, O.P., Kumar, S., Manik, G.: Analysis of hybrid temperature control for nonlinear continuous stirred tank reactor. In: Proceedings of Fourth International Conference on Soft Computing for Problem Solving, pp. 103–121. Springer, New Delhi (2015)
16. Ko, C.C., Chen, B.M., Chen, J., Zhuang, Y., Tan, K.C.: Development of a web-based laboratory for control experiments on a coupled tank apparatus. IEEE Trans. Edu. **1**, 76–86 (2001)
17. Nagaraj, B., Subha, S., Rampriya, B.: Tuning algorithms for PID controller using soft computing techniques. Int. J. Comput. Sci. Netw. Secur. **4**, 278–281 (2008)
18. Jaafar, H.I., Hussien, S.Y.S., Selamat, N.A., Aras, M.S.M, Rashid, M.Z.A.: Development of PID controller for controlling desired level of coupled tank system. Int. J. Innov. Technol. Exploring Eng. **9**, 32–36 (2014)
19. Ziegler, J.G., Nichols, N.B.: Optimum settings for automatic controllers. Trans. ASME **11** (1942)
20. Åström, K.J., Hägglund, T.: Revisiting the Ziegler-Nichols step response method for PID control. J. Process Control **6**, 635–650 (2004)
21. Man, K.F., Tang, K.S., Kwong, S.: Genetic algorithms: concepts and applications. IEEE Trans. Ind. Electron. **5**, 519–534 (1996)
22. Verma, O.P., Manik, G., Jain, V.K., Jain, D.K., Wang, H.: Minimization of energy consumption in multiple stage evaporator using Genetic Algorithm. Sustain. Comput. Inf. Syst. (2017)
23. Verma, O.P., Manik, G.: Solution of SNLAE model of backward feed multiple effect evaporator system using genetic algorithm approach. Int. J. Syst. Assur. Eng. Manage. **1**, 63–78 (2017)
24. Fathi, A.H., Khaloozadeh, H, Nekoui, M.A., Shisheie, R.: Using PSO and GA for optimization of PID parameters. Int. J. Intell. Inf. Process. **1** (2012)
25. Gaing, Z.L.: A particle swarm optimization approach for optimum design of PID controller in AVR system. IEEE Trans. Energy Convers. **2**, 384–391 (2004)
26. Abido, M.A.: Optimal design of power-system stabilizers using particle swarm optimization. IEEE Trans. Energy Convers. **3**, 406–413 (2002)
27. Sivagurunathan, G., Saravanan, K.: Design and Implementation of Controller for a Nonlinear Spherical Tank System using Soft computing Techniques
28. Verma, O.P., Singla, R., Kumar, R.: Intelligent temperature controller for water bath system. Int. J. Comput. Inf. Syst. Control Eng. **6**. World Academy of Science, Engineering and Technology (2012)
29. Gupta, H., Verma, O.P.: Intelligent controller for coupled tank system. Int. J. Adv. Res. Comput. Sci. Softw. Eng. **2**(4)

A VDCC-Based Grounded Passive Element Simulator/Scaling Configuration with Electronic Control

Pranjal Gupta, Mayank Srivastava, Aishwarya Verma, Arshi Ali, Ayushi Singh and Devyanshi Agarwal

Abstract In this research paper, a new circuit configuration which can work like a grounded impedance simulator/grounded impedance scaling circuit has been proposed. The proposed circuit can simulate electronically controllable grounded resistance/capacitance/inductance/FDNC and can also work like a grounded impedance multiplier circuit, which can scale the value of arbitrary grounded impedance with an electronically tunable multiplication factor. The presented circuit employs two voltage difference current conveyors along with four grounded passive elements. The employment of grounded passive elements makes this realization eligible for monolithic integration. The proposed circuit does not require any matched passive elements. Behavior of the proposed configuration under nonideal environment is found un-deviated. The mathematical analysis of the proposed configuration has been verified by simulating under PSPICE TSMC 0.18 μm simulation environment.

Keywords Electronic control · Grounded capacitance · FDNC · VDCC

P. Gupta · A. Verma · A. Ali · A. Singh · D. Agarwal (✉)
Department of ECE, KIET Group of Institutions, Ghaziabad, India
e-mail: devyanshi143105@kiet.edu

P. Gupta
e-mail: Pranjalgupta9838@gmail.com

A. Verma
e-mail: aishwarya.1421017@kiet.edu

A. Ali
e-mail: arshi1431031@kiet.edu

A. Singh
e-mail: ayushisingh3038@kiet.edu

M. Srivastava
Department of ECE, National Institute of Technology, Jamshedpur, Jharkhand, India
e-mail: mayank2780@gmail.com

B. S. Rawat et al. (eds.), *Advances in Signal Processing and Communication* ,
Lecture Notes in Electrical Engineering 526,
https://doi.org/10.1007/978-981-13-2553-3_42

1 Introduction

In the research domain, active realization of floating/grounded passive elements/impedances is very popular for analog circuit designing. Many grounded impedance/passive element simulation circuits using several active devices such as operational amplifiers, differential difference current conveyor, fully differential current conveyor, dual-X current conveyor, current feedback operational amplifiers, four terminal floating nullors, current follower transconductance amplifier, current differencing transconductance amplifiers, voltage differencing differential input buffered amplifiers, operational transconductance amplifiers, operational transresistance amplifiers, voltage differencing transconductance amplifiers, and voltage differencing buffered amplifiers have been proposed by several researchers [1–27]. The circuit configuration proposed in [1–27] suffers with one or more of the following major drawbacks: (1) Employment of floating passive element(s) which is undesirable from the point of view of monolithic integration of circuit [1–25, 27]; (2) unavailability of facility of electronic tunability [1–6, 8–25]; and (3) requirement(s) of active/passive element matching [1–3, 8, 10–12, 18, 21, 24, 25].

Furthermore, no configuration is able to act like an electronically controllable grounded impedance multiplier. Therefore, the important aim of this circuit configuration is to describe a new electronically tunable grounded impedance simulator circuit which can also work as a grounded impedance scaling circuit with electronically tunable scaling factor. The proposed circuit is developed using two voltage differencing current conveyers along with three grounded passive elements. The presented configuration does not need any passive component matching and exhibits excellent behavior under nonideal conditions.

2 VDCC Concept

VDCC a very useful and versatile active building block (ABB) and many VDCC-based analog signal processing/signal generation circuits have been proposed by researchers in recent past. The symbolic representation of VDCC is shown in Fig. 1.

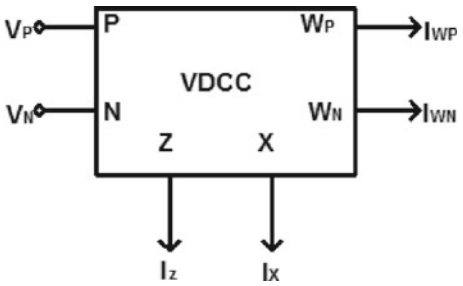

Fig. 1 VDCC ABB

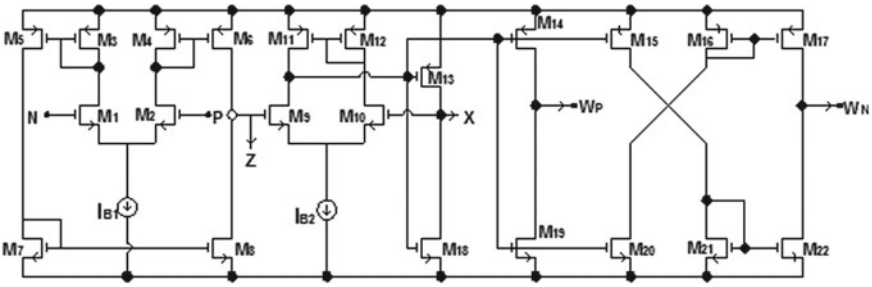

Fig. 2 CMOS transistor-based implementation of VDTA

The voltage–current relationship between the ports of VDCC is given by Eq. 1:

$$\begin{bmatrix} I_N \\ I_P \\ I_Z \\ V_X \\ I_{W_P} \\ I_{W_N} \end{bmatrix} = \begin{bmatrix} 0 & 0 & 0 & 0 \\ 0 & 0 & 0 & 0 \\ g_m & -g_m & 0 & 0 \\ 0 & 0 & 1 & 0 \\ 0 & 0 & 0 & 1 \\ 0 & 0 & 0 & -1 \end{bmatrix} \begin{bmatrix} V_P \\ V_N \\ V_Z \\ I_X \end{bmatrix} \tag{1}$$

where g_{m1} is the transconductance gains of input stage and output stage of VDCC. A popular implementation of VDCC employing CMOS transistor has been shown in Fig. 2 [28].

In recent past, several VDCC-based analog signal generation/signal processing circuits and active impedance simulators [29–34] have been proposed by circuit scientists and researchers.

3 Proposed Configuration

The proposed grounded impedance simulator/impedance scaling circuit employing VDCCs and grounded passive elements have been depicted in Fig. 3.

By mathematical analysis of circuit shown in Fig. 3, the input impedance of the circuit is found as

$$Z_{in} = \frac{V_{in}}{I_{in}} = \frac{Z_3}{g_{m1}g_{m2}Z_1Z_2} \tag{2}$$

where g_{m1} and g_{m2} are the transconductances of VDCC-1 and VDCC-2.

If, $Z_1 = R_1$, $Z_2 = R_2$, and $Z_3 = R_3$

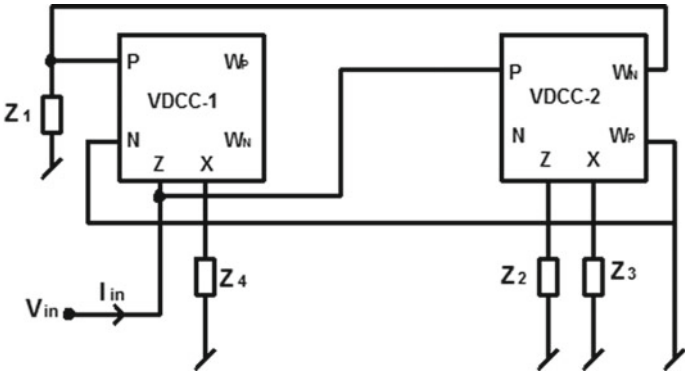

Fig. 3 Proposed configuration

$$Z_{in} = \frac{V_{in}}{I_{in}} = \frac{R_3}{g_{m1} g_{m2} R_1 R_2} \tag{3}$$

Here, the proposed circuit is simulating an electronically tunable grounded resistor of resistance value R_{eq} where

$$R_{eq} = \frac{R_3}{g_{m1} g_{m2} R_1 R_2} \tag{4}$$

The electronic tuning of R_{eq} is found by transconductances g_{m1} and/or g_{m2}.
If $Z_1 = R_1$, $Z_2 = R_2$, and $Z_3 = 1/sC_3$

$$Z_{in} = \frac{V_{in}}{I_{in}} = \frac{1}{g_{m1} g_{m2} R_1 R_2 s C_3} \tag{5}$$

In this case, the proposed circuit is simulating an electronically controllable grounded capacitor of capacitance value C_{eq} where

$$C_{eq} = g_{m1} g_{m2} R_1 R_2 C_3 \tag{6}$$

The electronic control of R_{eq} is obtained by transconductances g_{m1} and/or g_{m2}.
If $Z_1 = 1/sC_1$, $Z_2 = R_2$, and $Z_3 = R_3$

$$Z_{in} = \frac{V_{in}}{I_{in}} = \frac{s C_1 R_3}{g_{m1} g_{m2} R_2} \tag{7}$$

Here, the proposed circuit is simulating an electronically controllable grounded inductor of inductance value L_{eq} where

$$L_{eq} = \frac{C_1 R_3}{g_{m1} g_{m2} R_2} \tag{8}$$

The electronic tuning of L_{eq} is obtained by transconductances g_{m1} and/or g_{m2}. If $Z_1 = R_1$, $Z_2 = 1/sC_2$ and $Z_3 = 1/sC_3$

$$Z_{in} = \frac{V_{in}}{I_{in}} = \frac{s^2 C_1 C_2 R_3}{g_{m1} g_{m2}} \tag{9}$$

In this case, the proposed circuit is simulating an electronically tunable grounded frequency-dependent negative resistance (FDNC) with FDNC value D_{eq} where

$$D_{eq} = \frac{C_1 C_2 R_3}{g_{m1} g_{m2}} \tag{10}$$

The electronic tuning of D_{eq} is obtained by transconductances g_{m1} and/or g_{m2}. The expression given in Eq. 2 can also be written as

$$Z_{in} = \frac{V_{in}}{I_{in}} = \left(\frac{1}{g_{m1} g_{m2} Z_1 Z_2}\right) Z_3 = K_1 Z_3 \tag{11}$$

$$K_1 = \frac{1}{g_{m1} g_{m2} Z_1 Z_2} \tag{12}$$

It is obvious from Eqs. 11 and 12 that proposed configuration is able to scale up or scale down the grounded impedance Z_3 with scaling factor K_1, where values of K_1 can be controlled electronically through transconductances of VDCCs. Hence, the proposed circuit scale up or scale down the value of impedance Z_3.

4 Nonideal Analysis

The current–voltage relationship between VDCC ports, assuming nonideal current/transconductance gains, can be defined by the following equations:

$$I_Z = \alpha g_{m_1}(V_P - V_N),\ V_Z = \beta V_x,\ I_{wp} = \gamma_{wp} I_x,\ I_{wn} = \gamma_{wn} I_x \tag{13}$$

where α β, γ_{wp}, and γ_{wn} are the tracking errors due to nonideal conditions.

The proposed configuration is revisited using Eq. 14–16 to study the behavior of proposed configuration under nonideal environment. The input impedance of the proposed configuration under nonideal environment can be evaluated as

$$Z_{in} = \frac{V_{in}}{I_{in}} = \frac{Z_3 \beta_2}{g_{m1} g_{m2} \alpha_1 \alpha_2 \gamma_{\omega n2} Z_1 Z_2} \tag{14}$$

Hence, from Eq. 17, it can be concluded that in nonideal environment the behavior of the proposed circuit is same as the behavior in ideal environment. Hence, the presented circuit offers excellent behavior under nonideal conditions. The sensitiv-

ities of input impedance of the proposed circuit with respect to active and passive parameters can be found as

$$S_{\beta 2}^{Z_{in}} = S_{Z_3}^{Z_{in}} = 1,\ S_{g_{m1}}^{Z_{in}} = S_{gm2}^{Z_{in}} = S_{\alpha 1}^{Z_{in}} = S_{\alpha 2}^{Z_{in}} = S_{\gamma n2}^{Z_{in}} = S_{Z_1}^{Z_{in}} = S_{Z_2}^{Z_{in}} = -1 \quad (15)$$

So, all the sensitivities are low and not more than unity in magnitude.

5 Application Example

The workability of proposed configuration has been verified by designing some filter functions.

1. The ordinary passive RC high-pass filter has been shown in Fig. 4, and the active realization of this RC filter using the proposed configuration as a grounded resistance has been shown in Fig. 5.

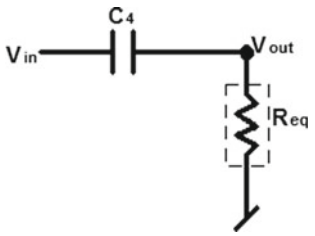

Fig. 4 Passive RC high-pass filter

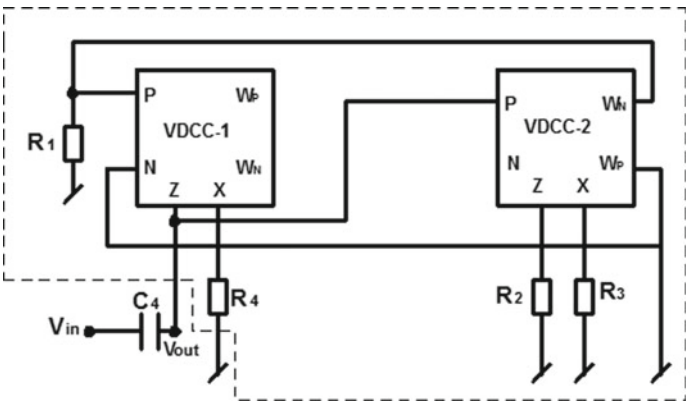

Fig. 5 Active realization of filter shown in Fig. 4

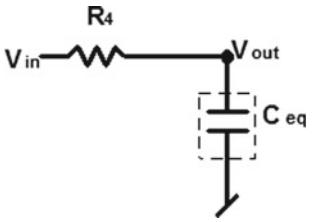

Fig. 6 Passive RC low-pass filter

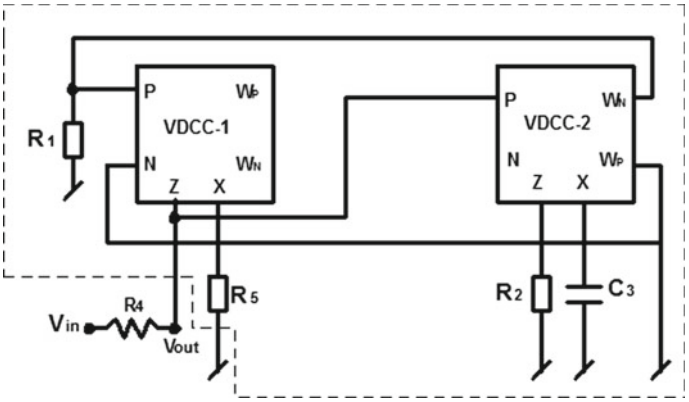

Fig. 7 Active realization of filter shown in Fig. 6

2. The ordinary passive RC low-pass filter has been given in Fig. 6, and the active realization of this RC filter using the proposed configuration as a grounded capacitance has been shown in Fig. 7.

6 Simulation Results

The verification of the mathematical analysis of the proposed configuration has been carried out by performing PSPICE simulations using CMOS VDCC with all the bias currents of all the VDCCs being equal to 150 μA. To show the behavior of proposed circuit as grounded resistance simulator, simulation has been performed with two sets of component values $Z_1 = Z_2 = Z_3 = R_1 = R_2 = R_3 = 1$ kΩ and $Z_1 = Z_2 = R_1 = R_2 = 1$ kΩ, $Z_3 = R_3 = 2$ kΩ. The magnitude response is shown in Fig. 8, which clearly shows that proposed configuration works like an ideal lossless grounded resistance up to 3.94 MHz. Similarly, to verify the working of circuit as a grounded capacitor, the component values for simulation are selected as $Z_1 = Z_2 = R_1 = R_2 = 1$ kΩ $Z_3 = 1/sC_3$ where $C_3 = 0.1$ nF and $Z_1 = Z_2 = R_1 = R_2 = 1$ kΩ $Z_3 = 1/sC_3$ where $C_3 = 0.2$ nF. The simulated magnitude response is shown in Fig. 9. The functioning of

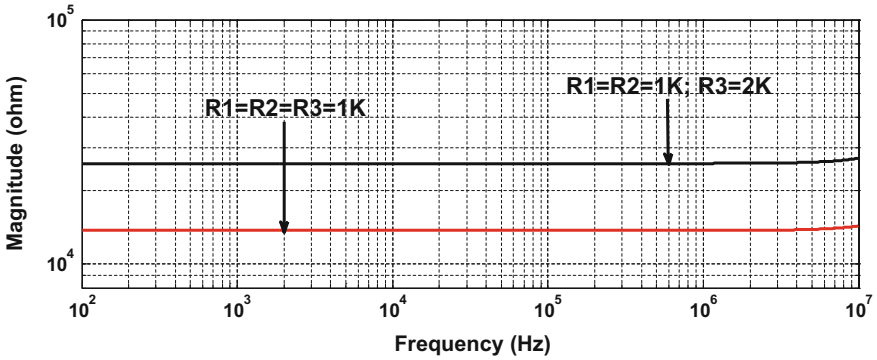

Fig. 8 Magnitude responses of input impedance of the proposed circuit shown in Fig. 3 with component values $Z_1 = Z_2 = Z_3 = R_1 = R_2 = R_3 = 1$ kΩ and $Z_1 = Z_2 = R_1 = R_2 = 1$ kΩ, $Z_3 = R_3 = 2$ kΩ

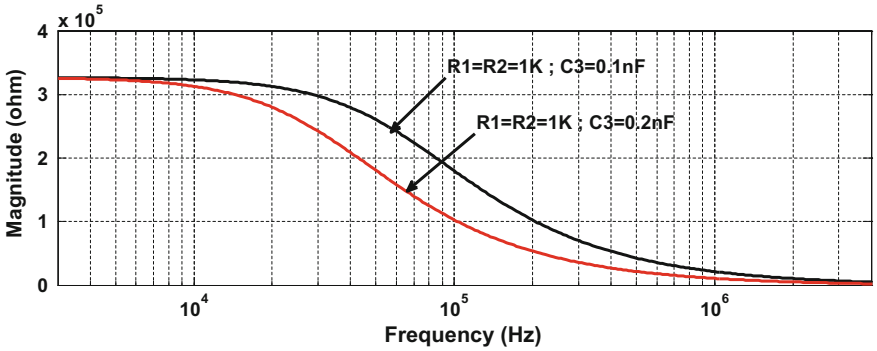

Fig. 9 Magnitude responses of input impedance of the proposed circuit with component values $Z_1 = Z_2 = R_1 = R_2 = 1$ kΩ $Z_3 = 1/sC_3$, $C_3 = 0.1$ nF and $Z_1 = Z_2 = R_1 = R_2 = 1$ kΩ $Z_3 = 1/sC_3$, $C_3 = 0.2$ nF

the proposed simulator as a grounded inductor is shown in Fig. 10 which is found by performing simulation taking component values as $Z_1 = 1/sC_1$ where $C_1 = 0.5$ nF, $Z_2 = Z_3 = R_2 = R_3 = 1$ kΩ. The proposed configuration is also able to simulate a grounded FDNC. The component values for this simulation are selected as $Z_1 = 1/sC_1 = Z_2 = 1/sC_2$ where $C_1 = C_2 = 0.1$ nF and as $Z_1 = 1/sC_1 = Z_2 = 1/sC_2$ where $C_1 = C_2 = 0.2$ nF. The magnitude response of input impedance of FDNC simulator is shown in Fig. 11.

To verify the electronic scaling of input impedance of realized configuration, simulations for different sets of bias currents (Ib_1 and Ib_2) of VDCCs have been performed. Figures 12, 13, and 14 show the electronic scaling in simulated grounded resistance, grounded capacitance, and grounded inductance.

The designed high-pass filter example shown in Fig. 5 is simulated for component values $R_1 = R_2 = R_3 = R_4 = 1$ kΩ and $C_4 = 0.1$ nF. The simulated high-pass

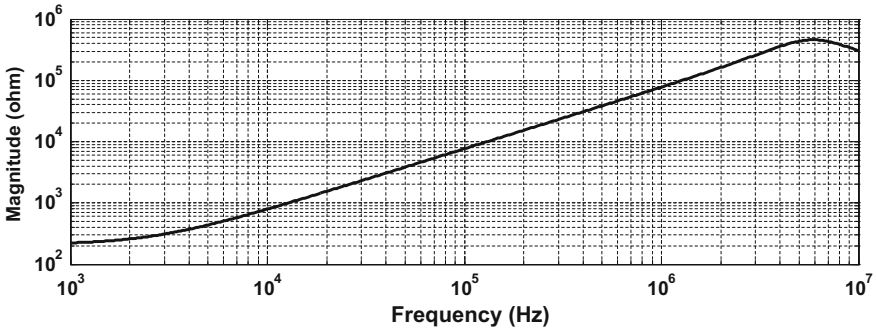

Fig. 10 Magnitude response of input impedance of the proposed circuit with component values $Z_1 = 1/sC_1$, $C_1 = 0.5$ nF, $Z_2 = Z_3 = R_2 = R_3 = 1$ kΩ

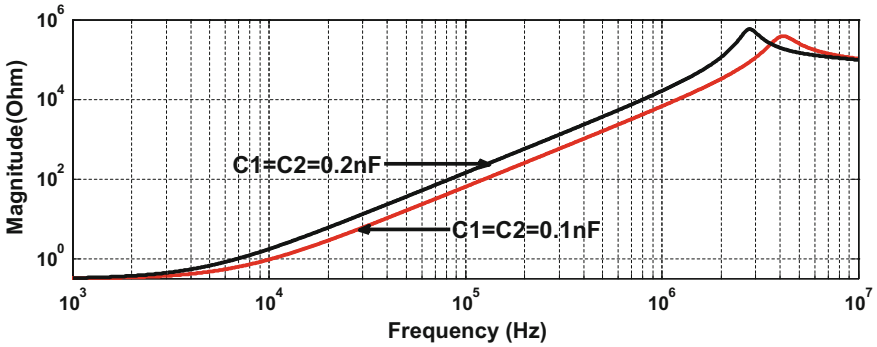

Fig. 11 Magnitude responses of input impedance of the proposed circuit with component values $Z_1 = 1/sC_1 = Z_2 = 1/sC_2$ where $C_1 = C_2 = 0.1$ nF and as $Z_1 = 1/sC_1 = Z_2 = 1/sC_2$ where $C_1 = C_2 = 0.2$ nF

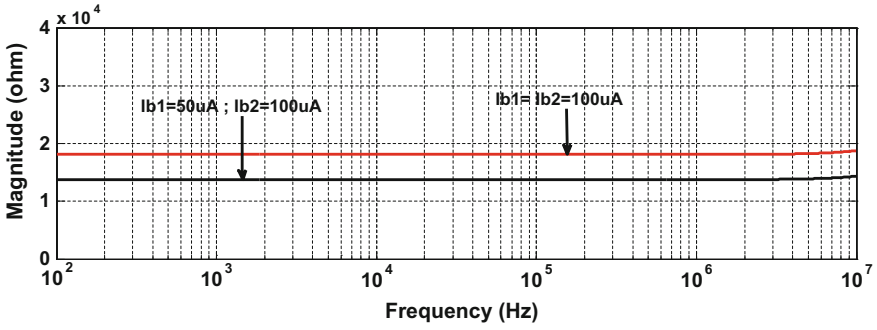

Fig. 12 Magnitude responses with component values $Z_1 = R_1 = Z_2 = R_2 = Z_3 = R_3 = 1$ kΩ and different sets of bias currents (electronic scaling of grounded impedance $Z_3 = R_3$)

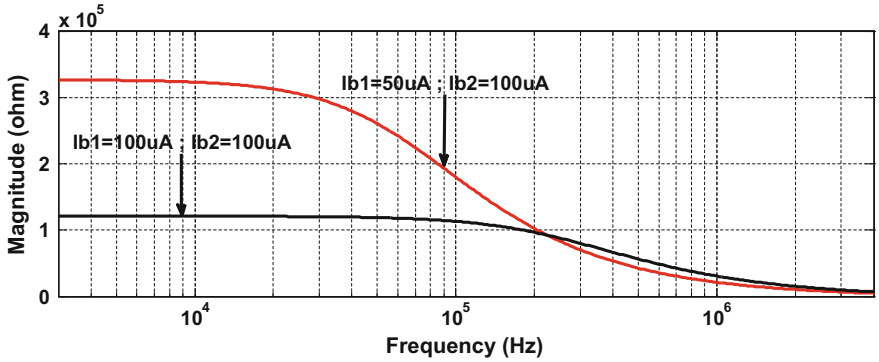

Fig. 13 Magnitude responses with component values $Z_1 = R_1 = Z_2 = R_2 = 1\ k\Omega$, $Z_3 = 1/sC_3$, $C_3 = 0.1$ nF and different sets of bias currents (electronic scaling of grounded impedance $Z_3 = 1/sC_3$)

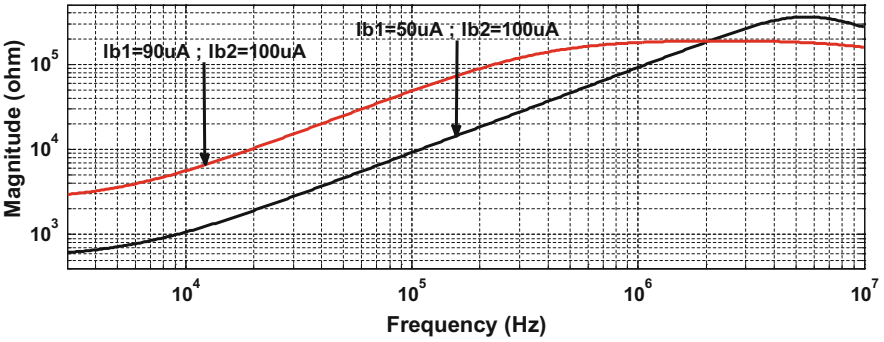

Fig. 14 Magnitude responses with component values $Z_1 = R_1 = Z_2 = R_2 = 1\ k\Omega$, $Z_3 = L_3 = 1$ mH and different sets of bias currents (electronic scaling of grounded impedance $Z_3 = L_3$)

frequency response is shown in Fig. 15. The low-pass filter design example shown in Fig. 7 is simulated for component values $R_1 = R_2 = R_5 = 1\ k\Omega$, $R_4 = 40\ k\Omega$ and $C_3 = 0.1$ nF. The simulated low-pass frequency response is shown in Fig. 16.

7 Conclusion

A new electronically tunable grounded impedance simulator/grounded impedance scaling circuit has been proposed. The proposed circuit employs two VDCCs along with three grounded passive elements. By proper choice of impedances, the proposed configuration can simulate electronically controllable grounded resistance, electronically controllable grounded capacitance, electronically tunable grounded inductance, and electronically tunable grounded FDNC. The circuit is also able to scale up or scale down the value of any arbitrary grounded impedance. The scaling factor can be

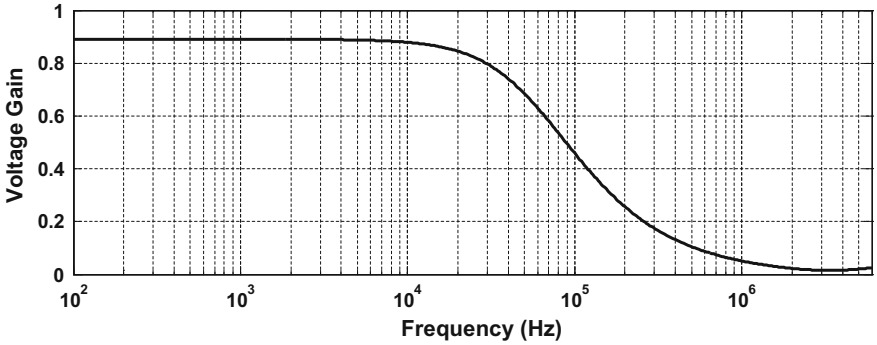

Fig. 15 Frequency response of active high-pass filter shown in Fig. 5 with component values $R_1 = R_2 = R_3 = R_4 = 1\ k\Omega$ and $C_4 = 0.1$ nF

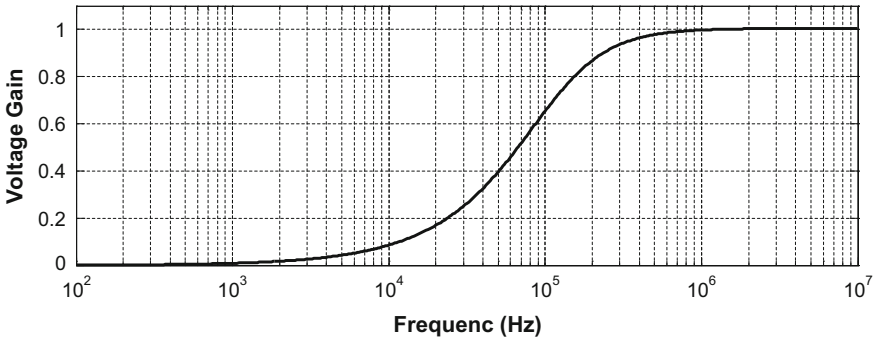

Fig. 16 Frequency response of active low-pass filter shown in Fig. 7 with component values $R_1 = R_2 = R_5 = 1\ k\Omega$, $R_4 = 40\ k\Omega$ and $C_3 = 0.1$ nF

changed electronically through bias currents of VDCCs. The performance of configuration has been verified under nonideal conditions and found un-deviated. To verify the behavior of proposed configuration, some active filter design examples have been demonstrated. PSPICE simulations have been performed to validate all the mathematical analysis.

References

1. Ford, R.L., Girling, F.E.J.: Active filters and oscillators using simulated inductance. Electron. Lett. **2**(2), 481–482 (1966)
2. Prescott, A.J.: Loss compensated active gyrator using differential input operational amplifier. Electron. Lett. **2**(7), 283–284 (1966)
3. Orchard, H.J., Willson, A.N.: New active gyrator circuits. Electron. Lett. **10**(13), 261–262 (1974)

4. Dutta Roy, S.C.: On operational amplifier simulation of grounded inductance. Archiv fuer Elektronik und Uebertragungstechnik **29**, 107–115 (1975)
5. Senani, R.: Active simulation of inductors using current conveyors. Electron. Lett. **14**(15), 483–484 (1976)
6. Nandi, R.: Novel insensitive lossless inductor simulation through inverse function generation. Electron. Lett. **16**(12), 481–482 (1980)
7. Nandi, R.: Lossless inductor simulation: novel configurations using DVCCS. Electron. Lett. **16**(17), 666–667 (1980)
8. Paul, A.N., Patranabis, D.: Active simulation of grounded inductors using a single current conveyor. IEEE Trans. Circuits Syst. **28**(2), 164–165 (1981)
9. Fabre, A.: Gyrator implementation from commercially available trans-impedance operational amplifiers. Electron. Lett. **28**(3), 263–264 (1992)
10. Arslan, E., Cam, U., Cicekoglu, O.: Novel lossless grounded inductance simulators employing only a single first generation current conveyor. Frequenz J. RF Eng. Telecommun. **57**(9–10), 204–206 (2003)
11. Yuce, E., Minaei, S., Cicekoglu, O.: A novel grounded inductor realization using a minimum number of active and passive components. ETRI J. **27**(4), 427–432 (2005)
12. Yuce, E., Minaei, S., Cicekoglu, O.: Limitations of the simulated inductors based on a single current conveyor. IEEE Trans. Circuits Syst. **53**(12), 2860–2867 (2006)
13. Yuce, E.: Grounded inductor simulators with improved low frequency performances. IEEE Trans. Instrum. Meas. **57**(5), 1079–1084 (2008)
14. Pal, K., Nigam, M.J.: Novel active impedances using current conveyors. J. Active Passive Electron. Dev. **3**(1), 29–34 (2008)
15. Yuce, E., Minaei, S.: A modified CFOA and its applications to simulated inductors, capacitance multipliers, and analog filters. IEEE Trans. Circuits Syst. **55**(1), 254–263 (2008)
16. Yuce, E., Minaei, S.: On the realization of simulated inductors with reduced parasitic impedance effects. Circuits Syst. Signal Process. **28**(3), 451–465 (2009)
17. Yuce, E.: Novel lossless and lossy grounded inductor simulators consisting of a canonical number of components. Analog Integr. Circuits Signal Process. **59**(1), 77–82 (2009)
18. Kumar, P., Senani, R.: New grounded simulated inductance circuit using a single PFTFN. Analog Integr. Circuits Signal Process. **62**(1), 105–112 (2010)
19. Ibrahim, M.A, Minaei, S., Yuce, E., Herencsar, N., Koton, J.: Lossless grounded inductance simulation using only one modified dual output DDCC. In: Proceedings of the 34th International Conference on Telecommunications and Signal Processing (TSP2011), Budapest, Hungary, pp. 261–264 (2011)
20. Kacar, F., Kuntman, H.: CFOA-based lossless and lossy inductance simulators. Radioengineering **20**(3), 627–631 (2011)
21. Metin, B.: Supplementary inductance simulator topologies employing single DXCCII. Radioengineering **20**(3), 614–618 (2011)
22. Myderrizi, I., Minaei, S., Yuce, E.: DXCCII based grounded inductance simulators and filter applications. Microelectron. J. **42**(9), 1074–1081 (2011)
23. Geiger, R.L., Sanchez-Sinencio, E.: Active filter design using operational transconductance amplifier: a tutorial. IEEE Circuits Dev. Mag. **1**(2), 20–32 (1985)
24. Ibrahim, M.A., Minaei, S., Yuce, E., Herencsar, N., Koton, J.: Lossy/lossless floating/grounded inductance simulator using one DDCC. Radioengineering **21**(1), 2–10 (2012)
25. Gupta, A., Senani, A.R., Bhaskar, D.R., Singh, A.K.: OTRA-based grounded-FDNR and grounded-inductance simulators and their applications. Circuits Syst. Signal Process. **31**(2), 489–499 (2012)
26. Prasad, D., Bhaskar, D.R.: Grounded and floating inductance simulation circuits using VDTAs. Circuits Syst. **3**(4), 342–347 (2012)
27. Yesil, A., Kacar, F., Gurkan, K.: Lossless grounded inductance simulator employing single VDBA and its experimental band-pass filter application. Int. J. Electron. Commun. (AEU) **68**(2), 143–150 (2014)

28. Kacar, F., Yesila, A., Minaei, S., Kuntmanca, H.: Positive/negative lossy/lossless grounded inductance simulators employing single VDCC and only two passive elements. Int. J. Electron. Commun. (AEÜ) **68**, 73–78 (2014)
29. Prasad, D., Bhaskar, D.R., Srivastava, M.: New single VDCC-based explicit current-mode SRCO employing all grounded passive components. Electron. J. **18**(2), 81–88 (2014)
30. Srivastava, M., Prasad, D.: VDCC based dual-mode quadrature sinusoidal oscillator with current/voltage outputs at appropriate impedance level. Adv. Electr. Electron. Eng. (Czech Republic) **14**(2), 168–177 (2016)
31. .Kacar, F., Yesil, A., Minaei, S., Kuntman, H.: Positive/negative lossy/lossless grounded inductance simulators employing single VDCC and only two passive elements. Int. J. Electron. Commun. (AEU) **68**(1), 73–78 (2014)
32. Srivastava, M., Bhanja, P., Mir, S.: A new configuration for simulating passive elements in floating state employing VDCCs and grounded passive elements. In: IEEE-International Conference on Power Electronics, Intelligent Control and Energy Systems (ICPEICES-2016), pp. 13–18, Delhi, India (2016)
33. Prasad, D., Srivastava, M., Ahmad, A., Mukhopadhyay, A., Sharma, B.B.: Novel VDCC based low-pass and high-pass ladder filters. In: IEEE-INDICON-2015, pp. 1–4, New Delhi, India (2015)
34. Biolek, D., Senani, R., Biolkova, V., Kolka, Z.: Active elements for analog signal processing; classification, review and new proposals. Radioengg. J. **17**(4), 15–32 (2008)

Current Tunable Voltage-Mode Universal Biquad Filter Using CCTAs

Sajai Vir Singh and Ravindra Singh Tomar

Abstract A current tunable voltage-mode biquad filter (VMBF) structure employing two current conveyor transconductance amplifiers (CCTAs) as active elements and three passive elements is described in the paper which has the ability to realizes all the generic responses like low-pass (LP), high-pass (HP), band-pass (BP), band-reject (BR), and all-pass (AP) filters. Thus, the proposed filter is universal. The filter structure is operated at supply rails of ± 1 V. Moreover, the filter's parameters can be controlled electronically and enjoy with reasonable total harmonic distortion and lower passive and active sensitivities. Using CMOS implemented CCTAs, the performance of the proposed circuit has been verified through P-SPICE in 0.18 μm CMOS technology from TSMC.

Keywords Voltage mode · Current tunable · Biquad · Universal · CCTA · Filter

1 Introduction

Filters are key blocks utilized in different signal processing (SP) applications, such as data acquisition systems, speech processing, telephone main switching centers (MSCs), high-frequency transient suppression, phase shifting [1, 2], etc. Behaviorally, analog filters are either current-mode (CM) or voltage-mode (VM) type, and each is categorized into single-input multi-output (SIMO) and multi-input single-output (MISO) filter-type topologies. The filter structures which can realize several filtering functions are multifunction filters. Nowadays, different tunable active build-

S. V. Singh (✉)
Department of Electronics and Communications,
Jaypee Institute of Information Technology, Noida 201304, India
e-mail: sajaivir@rediffmail.com

R. S. Tomar
Department of Electronics and Communication Engineering,
Anand Engineering College, Agra, India
e-mail: r_tomar15@rediffmail.com

B. S. Rawat et al. (eds.), *Advances in Signal Processing and Communication* ,
Lecture Notes in Electrical Engineering 526,
https://doi.org/10.1007/978-981-13-2553-3_43

ing elements (ABEs) are being used to synthesize VM MISO multifunction active filters [3, 4]. In contrast to traditional VM elements, currently the current-mode (CM) elements are highly preferred to synthesize VM filters, and as a corollary several three-input single-output (TISO) VM filter structures were reported in [5–22]. From these circuits, all generic filters can be derived for different combinations of inputs. These structures use nontunable active elements [5–15] and suffer from any one of the following drawbacks such as structures employ floating elements [5–14], some structures [5, 7, 10, 12–14] desire additional external circuitry for inverted/scaled inputs to realize some responses, and some of the structures [5–13, 15] are not offering orthogonal control on pole frequency and quality factor. Some of the filter structures using tunable elements have been reported in the literature, viz., CCCII, CFTA, VDTA, CCTA, etc. These biquadratic VM filters [16–22] employ two CCCIIs [16–18], one CFTA [19], two VDTA [21], and one CCTA [22] along with two capacitors [16–22] and two resistors [19, 22]. However, filter circuit in [20] can realize only LP and BP responses, whereas structures in [17, 18, 22] use four inputs to realize all the generic filter functions at single-output voltage terminal. Although filter structures in [16–19, 21, 22] can realize five filter functions. However, the circuits in refs. [16, 18, 19, 21] need inverted voltage input signal for the realization of some filter function(s). Similarly, VM filter in [22] also lacks with the feature of orthogonal current tunability of ω_o and Q_o. In this paper, a three-input single-output (TISO) VM multifunction filter structure employing two CCTAs, two capacitors and one grounded resistor, is proposed. For different combinations of digitally selected inputs, the filter circuit can realize LP, BP, HP, BR, and AP filter functions one at a time. The filter enjoys attractive features, such as low-sensitivity performance, and filter parameters ω_o and Q_o can be controlled orthogonally without distressing. The workability of the proposed filter is verified through simulations using 0.18 μm CMOS technology from TSMC in P-SPICE.

2 CCTA Descriptions

The CCTA is relatively a recent current-mode active element [15]. An ideal CCTA model can be characterized with the assist of the following set of equations:

$$I_Y = 0, \quad V_X = V_Y, \quad I_Z = I_X, \quad I_{+O} = g_m V_Z, \quad I_{-O} = -g_m V_Z \tag{1}$$

where terminal Y is a high impedance terminal and ideally draws zero current, while terminal X offers low impedance and draws current I_X. An auxiliary Z terminal is a high impedance terminal mostly loaded with impedance and ideally receives a replica of current I_X. The voltage at Z terminal is fed to the transconductance stage of CCTA, and finally, high impedance output terminal of the transconductance amplifier generates I_O current. Depending on the polarity of transconductance (g_m), the I_O may flow in the inward or outward direction. In CCTA, the transconductance (g_m) can

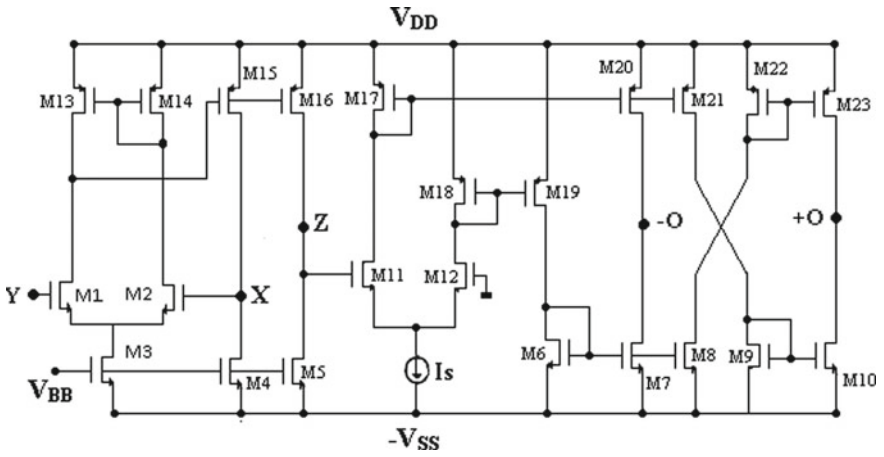

Fig. 1 CMOS implementation of CCTA

be varied through external biasing current I_S. For CMOS implemented CCTA given away in Fig. 1, the transconductance (g_m) can be expressed in terms of I_S as follows:

$$g_m = \sqrt{\beta_n \, I_S} \tag{2}$$

where $\beta_n = \mu_n \, C_{OX}\left(\frac{W}{L}\right)$ and μ_n, C_{OX}, and $\left(\frac{W}{L}\right)$ are correspondingly the electron mobility, capacitance of oxide layer per unit area, and aspect ratio of n-MOS transistors forming a differential pair (DP) in the architecture CCTA.

3 Circuit Descriptions and Analysis

A three-input single-output (TISO) VMBF employing two CCTAs as active element, and two grounded capacitors, one grounded resistor as passive element, are presented as shown in Fig. 2. Here, V_1, V_2, and V_3 are the voltage input signals and V_{out} is the voltage output signal. On analyzing the VMBF in Fig. 2, the following expression at the voltage output node V_{out} can be derived:

$$V_{out} = \frac{C_1 C_2 s^2 V_1 - g_{m1} C_1 s V_2 + (g_{m1}/R) V_3}{C_1 C_2 s^2 + g_{m2} C_1 s + g_{m1} g_{m2}} \tag{3}$$

From Eq. (3), it is apparent that with the appropriate selection of input signals, different generic filtering functions can be received across output voltage node (V_{out}) as depicted in Table 1.

From Table 1, it is clear that the proposed VMBF is capable of realizing all five different filtering responses without requiring inverted or/and scaled version of inputs.

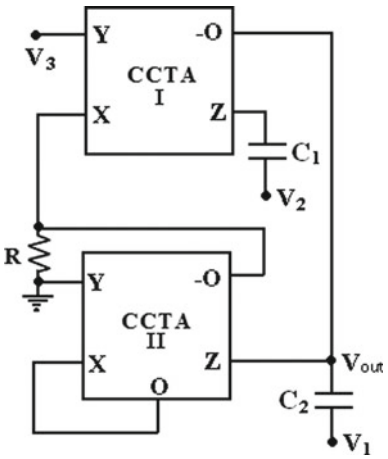

Fig. 2 Proposed TISO VM biquad filter

Table 1 Functionality of the proposed filter

V_1	V_2	V_3	V_{out}	Filter type
V_{in}	0	0	HP	Non-inverted
0	V_{in}	0	BP	Inverted
0	0	V_{in}	LP	Non-inverted
V_{in}	0	V_{in}	BR ($g_{m2} = 1/R$)	Non-inverted
V_{in}	V_{in}	V_{in}	AP ($g_{m1} = g_{m2} = 1/R$)	Non-inverted

However, two of the filtering responses named BR and AP need simple and easily attainable component setting. Furthermore, the filter performance consideration like ω_o, Q_o, and BW for each of the responses can be expressed as

$$\omega_o = \sqrt{\frac{g_{m1}g_{m2}}{C_1C_2}} \tag{4}$$

$$Q_o = \sqrt{\frac{C_2g_{m1}}{C_1g_{m2}}} \tag{5}$$

$$BW = \frac{g_{m2}}{C_2} \tag{6}$$

On substituting the expression of transconductance parameter (g_m) given in Eq. (2), the expressions derived in Eqs. (4)–(6) are modified to

$$\omega_o = \sqrt{\frac{\beta_n(I_{S1}I_{S2})^{1/2}}{C_1C_2}} \tag{7}$$

$$Q_o = \sqrt{\frac{C_2}{C_1}\left(\frac{I_{S1}}{I_{S2}}\right)^{1/2}} \tag{8}$$

$$BW = \frac{\sqrt{\beta_n I_{S2}}}{C_2} \tag{9}$$

From Eq. (7), it is apparent that ω_o can be tuned electronically independent to variation in Q_o simply by keeping the ratio of biasing currents I_{S1} and I_{S2} to be fixed and their product is allowed to vary. Similarly, from Eq. (8) it is also clear that Q_o can be changed by keeping the I_{S1*} I_{S2} to be fixed while changing their ratios.

4 Nonideal Influence and Sensitivity Analysis

To visualize the influence of nonidealities on the performance of the proposed circuit in Fig. 2, nonideal gains of the CCTA are taken into consideration. The port depiction of nonideal CCTA can be modeled through the following set of equations:

$$I_Y = 0, \quad V_X = \beta\, V_Y, \quad I_Z = \alpha\, I_X, \quad I_{+O} = \gamma_1\, g_m\, V_Z, \quad I_{-O} = -\gamma_2\, g_m\, V_Z \tag{9}$$

where α, β, and γ are the current and/or voltage transfer errors between CCTA ports. With new port descriptions of CCTA in Eq. (9), the proposed circuit has been reanalyzed and the output voltage involving nonideal factors is obtained as

$$V_{out} = \frac{\alpha_1 C_1 C_2 s^2 V_1 - \gamma_1 g_{m1} C_1 s V_2 + (\alpha_1 \beta \gamma_1 g_{m1}/R) V_3}{\alpha_1 C_1 C_2 s^2 + \alpha_1 \alpha_2 \gamma_2 g_{m2} C_1 s + \alpha_1 \gamma_1 \gamma_2 g_{m1} g_{m2}} \tag{10}$$

With involved nonideal factors, the ω_o, Q_o, and BW are altered to

$$\omega_o = \sqrt{\frac{\gamma_1 \gamma_2 g_{m1} g_{m2}}{C_1 C_2}} \tag{11}$$

$$Q_o = \frac{1}{\alpha_2}\sqrt{\frac{\gamma_1 C_2 g_{m1}}{\gamma_2 C_1 g_{m2}}} \tag{12}$$

$$BW = \frac{\alpha_2 \gamma_2 g_{m2}}{C_2} \tag{13}$$

From Eqs. (11)–(13), it is clear that ω_o, Q_o, and BW of the proposed filter will be obviously deviated from their nominal values due to the appearance of nonideal factors. However, these deviations are very small and can be minimized and neglected because at the working frequencies current and/or voltage transfer errors α, β, and γ can be approached to unity. The passive and active sensitivities of the proposed circuit are low, and their absolute values are not larger than unity as depicted in Table 2. This ensures a low-sensitivity performance of the circuit.

Table 2 Passive and active sensitivities of ω_o and Q_o for the filter in Fig. 3

Sensitivity of ω_o	Sensitivity of Q_o
$S^{\omega_o}_{\gamma_1,\gamma_2,g_{m1},g_{m2}} = \frac{1}{2}$, $S^{\omega_o}_{C_1,C_2} = -\frac{1}{2}$	$S^{Q_o}_{\gamma_1,g_{m1},C_2} = \frac{1}{2}$, $S^{Q_o}_{\gamma_2,g_{m2},C_1} = -\frac{1}{2}$, $S^{Q_o}_{\alpha_2} = -1$

Table 3 Dimension of MOS transistors

N-MOS	W(μm)/L(μm)
M_1, M_2	8.75/0.54
M_3, M_4, M_5	8.75/0.18
M_6–M_{10}	8.75/0.8
M_{11}, M_{12}	17.5/0.8
P-MOS	W(μm)/L(μm)
M_{13}–M_{16}	17.5/0.18
M_{17}–M_{23}	12/0.8

5 Simulation Results and Discussions

The proposed filter of Fig. 2 has been verified through P-SPICE simulations using CMOS implementation of CCTA as shown in Fig. 1 and 0.18 μm MOS model parameters from TSMC [23]. The dimensions of MOS transistors are obtained as specified in Table 3. For the simulation of synthesized circuit in Fig. 2, the design specifications were used as $I_{S1} = I_{S2} = 45\mu A$, $C_1 = C_2 = 8$ pF, $R = 3.4$ KΩ and $V_{DD} = -V_{SS} = 1$ V, $V_{BB} = -0.45$ V to obtain the f_o of 6.8 MHz. Figure 3 shows the simulated gain and phase responses for each of the filtering functions obtained from the filter circuit in Fig. 2. The simulated f_o is found to be 6.77 MHz which is approaching almost to the calculated value of 6.8 MHz. Further to demonstrate the electronic tuning aspects of the synthesized circuit in Fig. 2, it was simulated to obtain various BP responses at different values of biasing currents I_{S1} and I_{S2}, such as $I_{S1} = I_{S2} = 20$, 45, and 120 μA which resulted into the f_o variation as 3.32, 6.77, and 13.80 MHz, respectively, at $Q_o = 1$.

The simulated results in Fig. 4 show the conception of f_o tuning feature independent to Q_o variation. Similarly, the results in Fig. 5 also illustrate the tuning feature of Q_o independent to f_o variation for the synthesized filter circuit. Here, different Q_o values were obtained as $Q_o = 1$, $Q_o = 1.75$, and $Q_o = 3$, by maintaining the product of I_{S1} and I_{S2} to be fixed as ($I_{S1} = 45$ μA, $I_{S2} = 45$ μA), ($I_{S1} = 90$ μA, $I_{S2} = 22.5$ μA), and ($I_{S1} = 180$ μA, $I_{S2} = 11.25$ μA), respectively. To test the time-domain

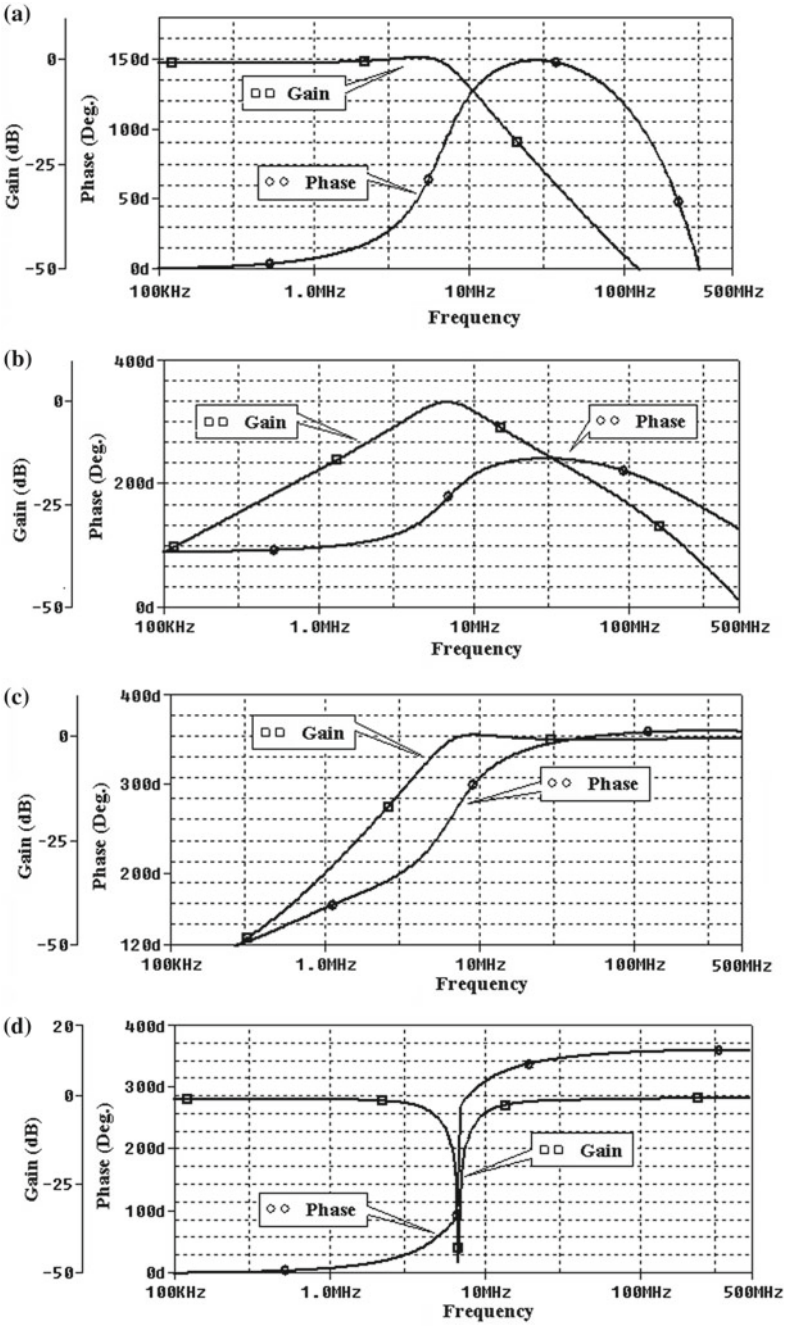

Fig. 3 Simulated gain and phase responses of **a** LP, **b** BP, **c** HP, **d** BR, **e** AP filters of the proposed circuit in Fig. 3

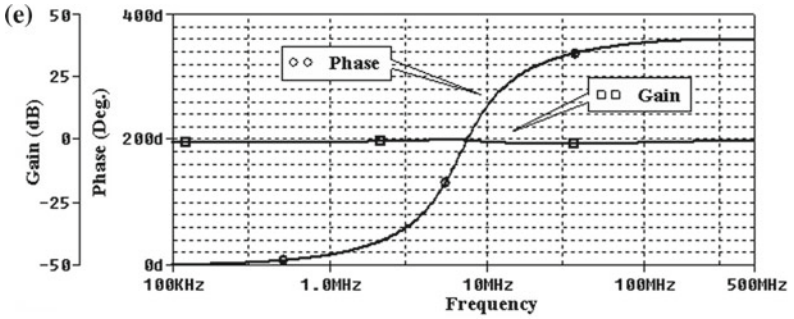

Fig. 3 (continued)

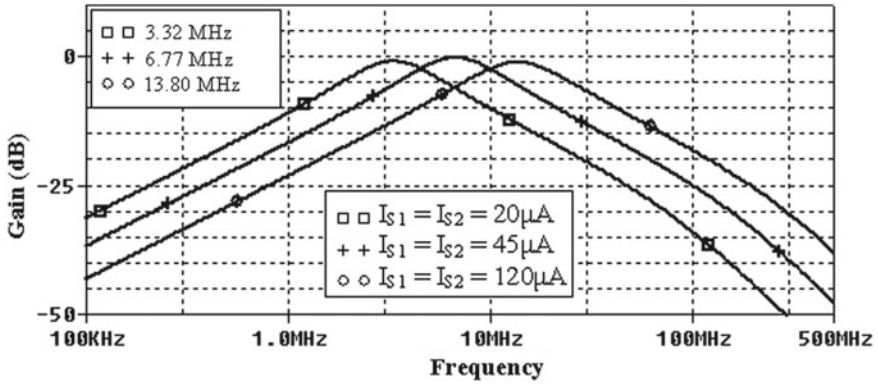

Fig. 4 f_o tunability of BP response of the filter in Fig. 2

behavior of the proposed filter, the simulation of HP response was carried out by applying a sinusoidal input signal of peak-to-peak amplitude 200 mV at 50 MHz and corresponding time-domain HP output result without significant distortion is shown in Fig. 6. Next, in view of the effects such as component mismatching and/or parameter variation on the filter performance, Monte Carlo analysis has been performed. Figure 7 shows the statistical results for 200 simulations for the BP response of the proposed filter with 5% Gaussian deviation in the capacitors value ($C_1 = C_2 = 8$ pF). The simulated mean, median, and standard deviation are obtained 7.463, 7.46 MHz, and 151.8 kHz, respectively. These results indicate that the proposed circuit exhibited reasonably good passive sensitivity performance.

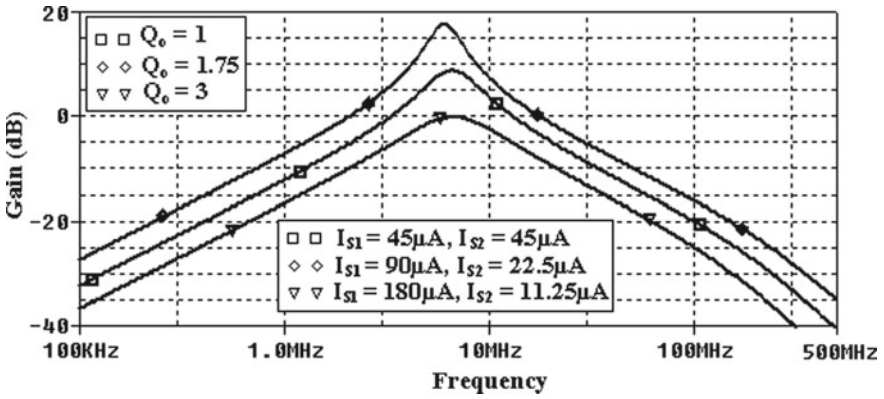

Fig. 5 Q_o tuning for the BP response

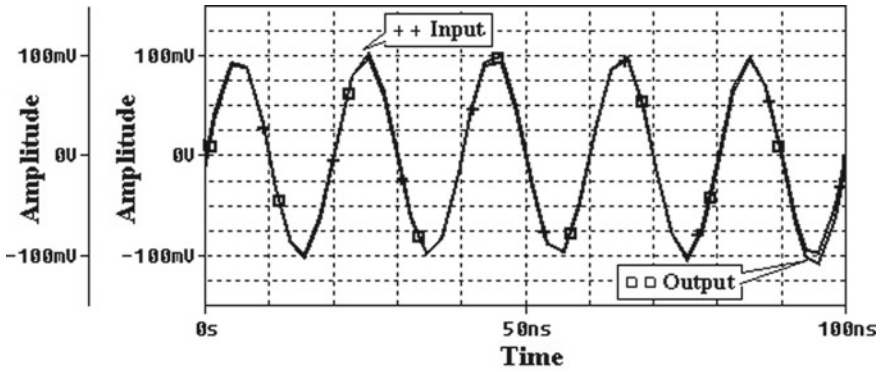

Fig. 6 Time-domain analysis for HP response of the filter in Fig. 2

6 Conclusions

In this study, the realization of a new VM biquadratic filter is presented. The proposed circuit is synthesized with two CCTAs, two capacitors, and one grounded resistor and can realize all the generic filtering functions, i.e., LP, BP, HP, RN, and AP in the voltage form through selection of the input voltages. The VM transfer functions for each filter type have been derived and different performance characteristics of the circuit such as ω_o, Q_o, and BW have been analyzed with ideal aspects and also with nonideal influences. Moreover, the proposed circuit enjoys attractive features, such as (i) lower component sensitivity, (ii) current tunability of characteristic parameters, and (iii) no requirement of inverted and/or scaled inputs for any realized response. Using P-SPICE and 0.18 µm technology, the simulation results have been found to be in good agreement with the theory.

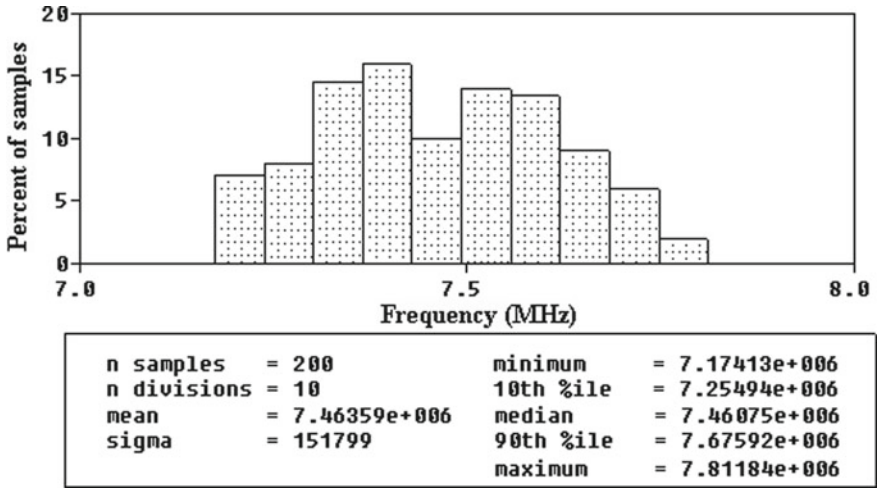

Fig. 7 Monte Carlo 200 runs simulation results for the BP response

References

1. Ibrahim, M.A., Minaei, S., Kuntman, H.A.: A 22.5 MHz current-mode KHN-biquad using differential voltage current conveyor and grounded passive elements. Intl. J. Electron. Commun. (AEÜ) **59**, 311–318 (2005)
2. Maheshwari, S., Singh, S.V., Chauhan, D.S.: Electronically tunable low voltage mixed-mode universal biquad filter. IET Circuits Devices Syst. **5**(3), 149–158 (2011)
3. Senani, R., Singh, V.K.: KHN-equivalent biquad using current conveyor. Electron. Lett. **31**(8), 626–628 (1995)
4. Singh, S.V., Maheshwari, S., Mohan, J., Chauhan, D.S.: An electronically tunable SIMO biquad filter using CCCCTA. Contemp. Comput. CCIS **40**, 544–555 (2009)
5. Horng, J.W.: High-input impedance voltage-mode universal biquadratic filter using three plus-type CCIIs. IEEE Trans. Circuits Syst. II Analog Digital Signal Process. **48**, 996–997 (2001)
6. Chang, C.M., Chen, H.P.: Universal capacitor grounded voltage mode filter with three inputs and a single output. Int. J. Electron. **90**, 401–406 (2003)
7. Horng, J.W.: Voltage-mode universal biquadratic filter using CCIIs. IEICE Trans. Fundam. Electron. Commun. Comput. Sci. **E87-A,** 406–409 (2004)
8. Horng, J.W.: High-input impedance voltage-mode universal biquadratic filter with three inputs using CCIIs. Int. J. Electron. **91**, 465–475 (2004)
9. Chen, H.P.: Single CCII-based voltage-mode universal filter. Analog Integr. Circuits Signal Process. **62**, 259–262 (2010)
10. Kacar, F., Yesil, A.: Voltage-mode universal filters employing single FDCCII. Analog Integr. Circuits Signal Process. **63**, 137–142 (2010)
11. Horng, J.W.: Voltage/current-mode universal biquadratic filter using single CCII+. Indian J. Pure Appl. Phys. **29**, 749–756 (2010)
12. Tangsrirat, W.: Novel current-mode and voltage-mode universal biquad filters using single CFTA. Indian J. Eng. Mater. Sci. **17**, 99–104 (2010)
13. Tangsrirat, W., Channumsin, O.: Voltage-mode multifunctional biquadratic filter using single DVCC and minimum number of passive elements. Indian J. Pure Appl. Phys. **49**, 703–707 (2011)

14. Pushkar, K.L., Gupta, K.: Miso type voltage mode universal biquadratic filter using single universal voltage conveyor. J. Circuits Syst. **8**, 227–236 (2017)
15. Klungtong, S., Thanapatay, D., Jaikla, W.: Three-input single output voltage mode multifunction filter with electronic controllability based on single commercial available IC. Act. Passiv. Electron. Compon. 10 (2017). Article ID 5240751
16. Minaei, S., Yuce, E., Cicekoglu, O.: Electronically tunable multi-input single output voltage-mode filter. In: Proceedings of the 2005 European Conference on Circuit Theory and Design, vol. 3, pp. 401–404 (2005)
17. Parveen, T., Ahmed, M.T., Khan, I.A.: A canonical voltage-mode universal CCCII-C filter. J. Act. Passiv. Electron. Devices **4**, 7–12 (2009)
18. Ranjan, A., Paul, S.K.: Voltage mode universal biquad using CCCII. Act. Passiv. Electron. Compon. 1–5 (2011)
19. Sirirat, J., Tangsrirat, W., Surakampontorn, W.: Voltage-mode electronically tunable universal filter employing single CFTA. In: Proceedings of International Conference ECTI-CON, pp. 759–763. Chaing Mai (2010)
20. Park, K., Bang, J., Song, J.: A new low-voltage tunable CMOS VDTA based 10 MHz LP/BP filter. Smart Comput. Rev. **4**(4), 287–293 (2014)
21. Mekhum, W., Jaikla, W.: Three input single output voltage-mode multifunction filter with independent control of pole frequency and quality factor. Theor. Appl. Electr. Eng. **11**(6), 494–500 (2013)
22. Herencsar, N., Koton, J., Vrba, K.: Single CCTA based universal biquadratic filters employing minimum components. Int. J. Comput. Electr. Eng. **1**(3), 307–310 (2009)
23. Horng, J.W., Hsu, C.H., Tseng, C.Y.: High input impedance voltage mode universal biquadratic filters with three inputs using three CCs and grounded capacitors. Radioengineering J. **21**(1), 290–296 (2012)

Maximum Power Point Tracking Techniques for Photovoltaic System: A Review

Shikha Gupta, Omveer Singh and M. A. Ansari

Abstract As the demand of the electric energy is increasing day by day but conventional energy sources (CESs) like coal, gases, etc., are in the limited amount on the earth. Additionally, they have expanded the pollutions. So that the gap between energy generation by CESs and its fuel can be filled by renewable energy sources (RESs). RESs are abundant and pollution-free sources on the earth. That is why all the research/innovations/implementations are moving toward RESs-based solutions. Solar energy is the prime source among the RESs. Solar energy-based electricity generation is largely reprocessed as it can squarely change solar energy into electrical form with a photovoltaic (PV) cell. Energy generated by PV cell is changing with partially shading conditions, temperature, and environmental condition. In order to select suitable PV cells for a particular area, operators are needed to sensed basic mechanisms and topologies of diverse solar PV with maximum power point tracking (MPPT) methodologies these are checked to a great extent. In this proposed article, researchers reviewed and analyzed a succeeding surge in the solar PV cell probe from one decade to other, and interpreted about their future patterns and characteristics. This article also attempts to emphasize the many experiments and techniques to contribute the perks of solar energy. This article would turn into a convenient reference for future performance for PV-based power creation.

Keywords Renewable energy sources · Solar cell · Photovoltaic
Maximum power point tracking techniques

S. Gupta (✉) · O. Singh · M. A. Ansari
Department of Electrical Engineering, School of Engineering,
Gautam Buddha University, Greater Noida, India
e-mail: shikhagupta247@gmail.com

O. Singh
e-mail: omveers@gmail.com

M. A. Ansari
e-mail: mahmadiitr@gmail.com

B. S. Rawat et al. (eds.), *Advances in Signal Processing and Communication* ,
Lecture Notes in Electrical Engineering 526,
https://doi.org/10.1007/978-981-13-2553-3_44

1 Introduction

With the speed up elevating in electric consumers without pollution and the forever developing composure of current way of life, the extensive energy supply has been dominated by an overpowering strain [1, 2]. Moreover, the distribution of climate change and the requirement of factories, and nations to devote in alternate energy sources, exceptionally the RES, just as the demand of oil is ascending incessantly, the beneficial economic effect of RESs are gradually being identified. The decline of the fossil power and uranium supply make RESs progressively substantial. These energies propose a pleasant contingency to lower the global warming effect. Throughout the world, importance and management of solar energy had to pursue preference amid alternate energy resources owed to its ecological nature and noticeable features [2–17]. Diminish CESs, environmental conditions, amended semiconductors material and long-term benefit are few of the intention inclined to the custom of limitless solar energy, electrical energy acquire is liberating from pollution so the system does not include several machines [18]. With a specific end goal to maintain a strategic distance from this disadvantages, most extreme yield control from sunlight based cell ought to be removed utilizing MPPT Techniques in order to expand the general proficiency of the board [19–32].

Certain approaches and designs have been illustrated for MPPT. The affairs MPPT techniques have been firmly researched by few investigators and in the indicated authors planned to pay attention at on the resolution, these investigators have analyzed.

2 Literature Survey

A lot of MPPT techniques composed of their employment are stated in the literature [4–42]. Investigators consistently felt puzzled while choosing an MPPT technique for a specific function [32]. Unfortunately, only lean techniques were attainable to the range containing, perturb and observe (P&O), incremental conductance (InC), fractional short-circuit current, and fractional open-circuit current. But a lot newly MPPT techniques such as an artificial neural network (ANN), genetic algorithm (GA), modified P&O (M P&O), etc., have been characterized. A review contrasting of the MPPT techniques on the action of benefit, drawback, and control variables elaborate, the category of circuitry, a complication of an algorithm, aggravation level on hardware employment is interpreted. MPPT has been a test for investigators. Many investigators have consigned miscellaneous techniques to MPPT and circulated this work. The reviews of the minute of them are granted below.

2.1 Solar Cell with Different Junction

H. Bellia et al. [12] drawn a detailed model of PV module using MATLAB/Simulink in which irradiance and temperature are taken as input variables and current (I), voltage (V), power (P), or opposed as output variables. Regardless, take after the properties I(V) or P(V) need of three segments i.e. current, voltage and power. The authors selected type was the single diode model alongside the pair of series and parallel resistor for leading certainty. It was simulated gradually overdue to own continual use and their potency, and P. P. Mahajan et al. [16] inclined major characteristics and specification that includes being deliberated modeled a PV module. A 50 W PV module was acquired at constant irradiance and temperature to get the characteristics of I-V and P-V. The investigators also argued for the effect of irresolute environmental status. The outlined model was arranged with user-friendly icons. Then, A. B. Hussain et al. [8] discussed the single and triple-junction solar cells with I-V and P-V curves; described the highest limit of P, I, and V. The researchers also examined the technique of using an object under distinct environment requisite that influences the solar cells for instance temperature and irradiance. The accomplishment of both the cells to the avenue by examining the fill factor, and T. M. Razykov et al. [4] presented like it is beside the forthcoming forecast of the solar PV electricity which criticizes the high-tech advancement past in the preceding certain lifespan in the compass of mono and polycrystalline thin-film PVs.

G. Khajuria et al. [6] reported multi-junction PV Cells and simulation in MATLAB/Simulink platform. The resemblance is made amidst conventional single-junction and multi-junction PV cells to obtain own maximum power point and open circuit voltage. They also reported triple-junction PV cells which concluded InGaP, InGaAs, and Ge sub-cells. For the contour of multi-junction PV cells, diversified judge was used for picking the material. Subsequently, M. S. S. Ashab et al. [5] bespeak involved with the utility of the PV system and intention at becoming economically the theory and catalog of a two distinct system that ventures PV solar systems, and sundry supporting source of energy to furnish heating and air conditioning. A model that produces an air conditioning unit was well built and apt measurements were composed through a data logging logistics as well as plotted that too.

2.2 Different MPPT Techniques

2.2.1 Perturbation and Observation

J. Ahmed et al. [27] proposed an enhanced P&O planted MPPT techniques for PV system. The techniques boost the steady state act of the conventional P&O and the techniques also shrinkage the chance of beating the tracking course, and V. R. Kota et al. [28] conferred a survey on common MPPT algorithms. Common algorithms

endure from reduced efficiency, fluctuation in steady state power and unfortunate dynamic performance an MPPT arrangement proving linear tangents located P&O was proposed. Moreover, M. S. Sivagamasundari et al. [39] written vitality, the particularly elective wellspring of vitality is crucial for the advancement of a nation. In this exploration, the framework execution was upgraded by irritating and watched technique utilizing buck help converter. The execution has been considered by the MATLAB/Simulink and S. Sholapur et al. [40] involved usage of a boost converter for control of PV power utilizing MPPT control component is displayed. To begin with, the PV module prospect exercised in MATLAB programming, and T. Selmi et al. [35] introduced a mathematical analysis of a PV cell for the single diode and double diode cell arrangements. The model of the double diode portrayal was executed utilizing a restrictive calculation. The P&O calculation technique was executed to track the purpose of the maximum power point.

2.2.2 Artificial Neural Network

A. K. Rai et al. [26] developed a refined Simulink model of an ANN occupying MPPT governor. The controller resides of an ANN tracker and the superior control unit. The ANN tracker assessment the currents and voltages associated with a maximum power impact by solar PV array for unstable cell temperature and radiation. The tracker was included to employ a set of 124 arrangements employing the backpropagation algorithm. The ability of the ANN tracker has been approved by engaging distinct test data fixed. Affecting mastery unit's application the appraisal of the ANN tracker to adapt the duty cycle of the chopper to best value wanted for maximum power relocation to the particularized load.

2.2.3 Fuzzy Logic Algorithms

M. Nabipour et al. [25] clarified MPPT arrangement adjust using the arranged novel fix routine thought about along customary direct and indirect fuzzy planted MPPT course of action, show preferred standpoint of the proposed MPPT routine above regular arrangements. In addition with, C. S. Chin et al. [36] introduced fuzzy based P&O maximum power point following in sun-based board. P&O based MPPT and fuzzy based advanced P&O MPPT developed, and the exhibitions of the two controllers were analyzed at variable sun-based irradiances and at various temperatures. C. Larbes et al. [31] implemented a canny control technique for the MPPT of a PV framework under factor temperature and irradiance conditions. A fuzzy logic control (FLC)-based MPPT was then investigated which registered has better advertised contrasted upon the P&O MPPT stationed entrance. The proposition FLC has been too demoted to bestow hereditary reckoning for enrichment. The optimized FL MPPT controller is then reproduced and assessed, which has appeared. Moreover, F. Bouchafaa et al. [37] clarified maximum power point augment the power yield, and along these lines, augment the array proficiency. A near report medially peculiar

controls systems was brought about, concretely, P&O and InC with computerized control by FL were exhibited, and Y. Soufi et al. [38] developed an FL based Mamdani to authority the greatest power point a PV framework. The schemed strategy utilized the FL control to determine the reach of incremental current in the present summon of MPPT.

2.2.4 Incremental Conductance (InC)

K. Vishweswara [3] outlined incremental conductance which is based upon MPPT for a PV system to have the benefits of low-frequency exchange. This article suggested MPPT techniques with an understandable algorithm for PV power system and set down on the application of an InC of the PV to round off a best functioning current for the uppermost output power. After that, R. I. Putri et al. [11] demonstrated MPPT for PV using InC technique with the main plan to seek the accomplishment of a MPPT scheme which doped out InC technique to command the duty cycle of buck–boost converter and to soothe the MPPT realization at its unreserved efficiency and after that, it was correlated to universally used algorithm, i.e., P&O by which it overcomes that InC techniques display a more excellent accomplishment with inferior oscillation.

2.2.5 Modified Perturbation and Observation

V. K. Devi et al. [2] conferred to grab steady state and speedily changeable climatic circumstances. The authors distinguished two techniques in which modified P&O method was projected and P&O method was picked for determination because this method requires to diminish utilization cost with more excellent accomplishment output. The recommended method was judged for accomplishment across the "Hill Climbing" P&O method by examining irradiance, temperature, daily profile, sunny day tests, etc.

2.2.6 Constant Voltage

M. Lasheen et al. [23] designed MPPT for the entire PV applications. The authors intended to retool the potential of the constant voltage approach to exploit proportional integral (PI) controller along gains persistent over the GA. The experimented approaches have been calculated by numerical simulation adopting software covered by the distinct atmospheric condition. For calculation and comparison study, the constant voltage located MPPT techniques with PI gains consumed by the trial and error has been conferred. The efficiency evaluation cover-up time curve and MPPT adeptness. The conclusion displayed efficiency bettering by speedy time response and extreme with gains driven by trial and error.

2.2.7 Open-Circuit Voltage

J. S. Kumari et al. [41] discussed on the design of open-circuit voltage (OCV)-planted MPPT for PV system upon open-circuit voltage algorithm to have the preferences multilevel inverter of underneath frequency switching and retrench integral harmonic distortion. A MPPT control to separate maximum power from the PV arrays at continuous winds up crucial in PV age framework. As of late, countless have been proposed for the following maximum power point. MPPT is utilized as a part of PV frameworks to augment the PV array yield control, independent of the temperature and radiation conditions and of the load electrical attributes, the PV exhibit yield control is utilized to straightforwardly control the DC/DC converter, in this manner decreasing the multifaceted nature of the framework. The ensuing system has high-profitability; cut down cost this paper proposed a MPPT methodology with an immediate calculation for PV control age structures. The technique depends on utilization of an OCV of the PV to decide an ideal working voltage for the greatest yield control.

2.2.8 Genetic Algorithm

M. Lashen et al. [42] implemented constant voltage-planted MPPT methods were regarded as definite in the most usually pre-owned technique in PV systems. The constant voltage (CV)-planted MPPT approach was deliberated single of the better frequently worn capacity in PV systems. The authors intended for reconstructing the potential of the constant voltage approach by applying PI controller along gains persistent by the genetic algorithm. The projected approaches have been calculated by numerical simulation adopting MATLAB covered by the distinct atmospheric condition.

2.3 Comparisons of Different MPPT Techniques

H. Rezk et al. [9] aimed to study the exhaustive similes of distinct MPPT techniques to adjust to PV systems. InC, high climbing, FLC, and P&O were persevering. PSIM and Simulink software were used. To rigid up FLC-MPPT techniques; co-simulation was done in between PSIM and Simulink software package, and K. K. Kumar et al. [14] inclined the simulation of the InC MPPT algorithm worn in solar array power systems along with direct control techniques due to it achieve accurate control beneath speedily changeable atmospheric circumstances.

W. Christopher et al. [15] presented contingent simulation analysis of the two meaningful MPPT algorithms as these algorithms are substantial in PV system that it diminishes the PV array price by lowering the quantity of PV panels requisite to accomplish the want output power while these algorithms were universally pre-owned by reason of its reduced cost and calmness of recognition. Then, S. Neupane

et al. [17] considered a model of solar PV array which is simulated on the equations of single-diode PV cells in MATLAB/Simulink in the form to correlate MPPT techniques. The presenters also discussed the results which were shown that InC was superior to that of the P&O algorithm, and H. Bounechba et al. [33] gave an insightful control technique for the MPPT of a PV framework under which variable temperature and isolation conditions were examined. The MPPT controller for support converter in light of FLC was produced and contrasted with the ordinary calculation by P&O.

2.4 Classification of Different MPPT Techniques

N. Karami et al. [13] pondered the view of intensity following for PV systems, a review of 40 since quite a while ago settled MPPT methodologies. They give a provisional table at the end to clarify the contribution of the distinct way, and Priety et al. [18] presented a literature on various types of techniques which were used in MPPT for PV system. The authors basically talked about the PV system where there is a change of the maximum power point with the temperature and irradiance likewise nonlinear characteristics of I-V and P-V curve which involve the tracking of maximum power point. Z. Salam et al. [20] reviewed on soft computing technique which was positioned PV System MPPT. The researchers also explained distinct effort on MPPT utilizing soft computing techniques from which they prefer nearly 45 published works that were precisely connected to MPPT. The advice on these approaches was spread. This work collected the modern hi-tech and dignity of soft computing MPPT as noted in the miscellaneous literature that also determines an assessment on the efficiency of distinct soft computing approach placed on manifold criteria, especially PV array need, merging time, strength to manage partial shading conditions, the complication of the algorithm, and its application. Subsequently, M. Seyedmahmoudin et al. [19] deliberated a survey in view of MPPT strategies in which maximum power output of PV system exhaustive research into oversight approach for MPPT procedures has been formed. The presented reviews of artificial intelligence-based methods demonstrated an adequate and beneficial to discharge and very typical in literature for MPPT, along with their restraint. Illuminate to control analyzer inaction of the abstracted approach this learning was not clear in criticizing the achievement of the late acknowledged procedure. Slightly debate the scenery assumption operation to MPPT system and generous references disclosing to all method.

2.5 Hybrid MPPT Techniques

O. Celik et al. [21] analyzed direct advancement in functioning I-V of PV panel over directly to the radiation and temperature instability comprise a noticeable difference in the output energy. To assess the straight of the anticipated method, a differentiating

was drifting out by adopting the typical P&O, InC and ANN arranged MPPT methods secured by both speedily changing radiation and partially shaded circumstances by utilizing PSCAD scheme. After that, M. H. Moradi et al. [30] reflected that sun-oriented boards display non-straight I-V attributes producing maximum power at just a single specific working point. The strategy is reenacted in MATLAB/Simulink condition and tentatively confirmed utilizing a research facility model, and A. Mellit et al. [29] discussed the displaying conjointly, a reenactment of a PVPS framework utilizing an adaptive neuro-fuzzy inference scheme (ANFIS) and the suggestion of another master setup PVPS framework. The test was demonstrating that the ANFIS performed superior to the ANN method.

2.6 Real-Time Simulation

H. Bounechba et al. [24] explained real-time simulation of MPPT for PV energy system. In sequence to raise the power drawn out separating the solar panel, it is essential to activate the PV system at the maximum power point. The investigator's projected a method of MPPT founded on current perturbation algorithm (CPA) by means of a changeable perturbation step and fractional short-circuit current algorithm to figure out the most favorable conditions of operating current. The investigators likewise introduced a trial inexact examination of these techniques by utilizing D-space. The capacity of forth put algorithms in limitation of dynamic action and enhanced equilibrium was verified by accurate simulation and preliminary studies.

2.7 Varying Different Parameters

S. Li et al. [22] examined to earn the maximum power point of PV system as fast as attainable and boost the MPPT elasticity to the variable weather circumstances. The presenters projected a MPPT control approach with variable weathers parameter (VWP). The uninterrupted relationship between VWP and control signal were constructed out by the current fitting method which was the essential effort to the appliance this scheduled strategies. Few simulation test demonstration control strategy was achievable and accessible to the track the maximum power point and has superior MPPT work than normal P&O method beneath distinct weather conditions and then FLC method beneath speedy changeful weather conditions.

The above sections are reflecting operating and characteristics behavior of the various MPPT techniques for the solar system. These are also represented in Fig. 1.

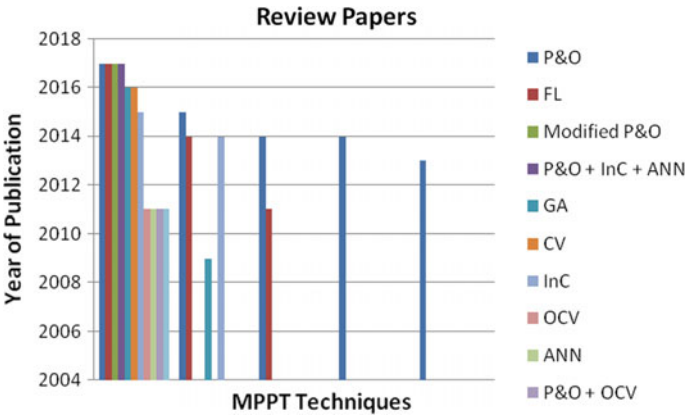

Fig. 1 Bar chart of reviewed techniques in the proposed article

3 Conclusion

The increasing industrialization of democracy and unpredictable green circumstances has influenced us to raise our passion for RESs just as solar energy. The research field of PV framework is still exceptionally dynamic. PV power formation from solar energy is approved by the way of MPPT for adequate tracking. The study article prompts an underlying course of plentiful MPPT systems is laid out. In every class, the different techniques proposed and used by different researchers' cutting edge have been recognized. With this utilization cost, tracking efficiency, PV array need sensors etc. Each MPPT technique is the difference in its owned approach and has earned its owned benefit and drawbacks.

Accordingly, determining the finest of them is a puzzling working so an individual has to select carefully while completing them. From the analysis, the authors achieved that there is a broad opportunity of bettering in the hybrid MPPT algorithms applying miscellaneous other soft computing techniques and developmental calculations which may give better productivity than the present frameworks. Hence, this analysis would absolutely be a very valuable for not exclusively for MPPT consumer but also the engineer and wholesale manufacturer of PV system.

References

1. Rajput, S.K., Singh, O.V.: Reduction in CO_2 emission through photovoltaic system: a case study. In: 3rd IEEE International Conference on Nanotechnology for Instrumentation and Measurement, GBU, India, 16–17 July 2017
2. Devi, V.K., Premkumar, K., Bisharathu Beevi, A., Ramaiyer, S.: A modified perturb & observe MPPT technique to tackle steady state and rapidly varying atmospheric conditions. Solar Energy **157**, 419–426 (2017)

3. Vishweswara, K.: An investigation of incremental conductance based maximum power point tracking for photovoltaic system. In: 4th International Conference on Advances in Energy Research, Energy Procedia, vol. 54, pp. 11–20 (2014)
4. Razykov, T.M., Ferekides, C.S., Morel, D., Stefanakos, E., Ullal, H.S., Upadhyay, H.M.: Solar photovoltaic electricity: current status and future prospects. Solar Energy **85**, 1580–1608 (2011)
5. Ashhab, M.-S.S., Kayline, H., Abdullah, A.: PV solar system feasibility study. Energy Convers. Mange. **65**, 777–782 (2013)
6. Khajuria, G., Kishore, N.: Analysis of multi-junction PV cells. Int. J. Eng. Res. Technol. **5**(03), 344–348 (2016)
7. Singh, O., Rajput, S.K.: Mathematical modelling and simulation of solar photovoltaic array system. In: IEEE International Conference on Research Advances in Integrated Navigation Systems, R. L. Jalappa Institute of Technology, Bangalore, India, 06–07 May (2016). ISBN: 9781509011124
8. Hussain, A.B., Abdalla, A.S., Mukhtar, A.S., Elamin, M., Alammari, R., Iqbal, A.: Modelling and simulation of single and triple junction solar cell using MATLAB/SIMULINK. Int. J. Ambient Energy **38**(6) (2016)
9. Rezk, H., Eltamaly, A.M.: A comprehensive comparison of different MPPT techniques for photovoltaic systems. Solar Energy J. **112**, 1–11 (2015)
10. Gupta, S., Singh, O.V., Urooj, S.: A Review on Single and Multi-junction Solar Cell with MPPT Techniques. In: 3rd IEEE International Conference on Nanotechnology for Instrumentation and Measurement, GBU, India, 16–17 July (2017)
11. Putri, R.I., Wibowo, S., Rifa, M.: Maximum power point tracking for photovoltaic using incremental conductance method. In: 2nd International Conference on Sustainable Energy Engineering and Application, Energy Procedia, Vol. 68, pp.22–30 (2015)
12. Bellia, H., Youcef, R., Fatima, M.: A detailed model of photovoltaic module using MATLAB. NRIAG J. Astron. Geophys. **3**, 53–61 (2014)
13. Karami, N., Moubayed, N., Outbib, R.: General review and classification of different MPPT techniques. Renew. Sustain. Energy Rev. **68**, 1–18 (2017)
14. Kumar, K.K., Bhaskar, R., Koti, H.: Implementation of MPPT algorithm for photovoltaic cell by comparing short- circuit method and incremental conductance method. Procedia Technol. **12**, 705–715 (2014)
15. Christopher, W., Ramesh, R.: Comparative study of P&O and InC MPPT algorithms. Am. J. Eng. Res. **2**(12), 402–408 (2013)
16. Mahajan, P.P., Bhole, A.A.: Modeling of photovoltaic module. International Research. J. Eng. Technol. **02**(03) (2015)
17. Neupane, S., Kumar, A.: Modeling and Simulation of PV array in Matlab/Simulink for comparison of perturb and observe and incremental conductance algorithms using buck converter. Int. Res. J. Eng. Technol. **04**(07) (2017)
18. Priety, Garg, V.K.: A review paper on various types of MPPT techniques for PV system. Int. J. Eng. Sci. Res. **04**(5), 320–330 (2014)
19. Seyedmahmoudian, M., Horan, B., Soon, T.K., Rahmani, R., Oo, A.-M.T., Mekhilef, S., Stojcevski, A.: State of the art artificial intelligence- based MPPT techniques for mitigating partial shading effects on PV systems- A review. Renew. Sustain. Energy Rev. **64**, 435–455 (2016)
20. Salam, Z., Ahmed, J., Merugu, B.S.: The application of soft computing methods for MPPT of PV system: a technological and status review. Appl. Energy **107**, 135–148 (2013)
21. Celik, O., Teke, A.: A hybrid MPPT method for grid connected photovoltaics systems under rapidly changing atmospheric conditions. Electr. Power Syst. Res. **152**, 194–210 (2017)
22. Li, S., Liao, H., Yuan, H., Ai, Q., Chen, K.: A MPPT strategy with variable weather parameters through analyzing the effect of the DC/DC converter to the MPP of PV system. Solar Energy **144**, 175–184 (2017)
23. Lasheen, M., Rahman, A.-K.A., Abdel-Salam, M., Ookawara, S.: Performance enhancement of constant voltage based MPPT for photovoltaic applications using genetic algorithm. In: 3rd International Conference on Power and Energy Systems Engineering, Energy Procedia, Vol. 100, pp. 217–222 (2016)

24. Bounechba, H., Bouzid, A., Snani, H., Lashab, A.: Real time simulation of MPPT algorithms for PV energy system. Electr. Power Energy Syst. **83**, 67–78 (2016)
25. Nabipour, M., Razaz, M., Seifossadat, S.-G.H., Mortazavi, S.S.: A new MPPT scheme based on a novel fuzzy approach. Renew. Sustain. Energy Rev. **74**, 1147–1169 (2017)
26. Rai, A.K., Kaushika, N.D., Singh, B., Agarwal, N.: Simulation model of ANN based maximum power tracking controller for solar PV system. Solar Energy Mater. Solar Cells **95**, 773–778 (2011)
27. Ahmed, J., Salam, Z.: An improved perturb and observe (P&O) maximum power point tracking (MPPT) algorithm for higher efficiency. Appl. Energy **150**, 97–108 (2015)
28. Kota, V.R., Bhukya, M.N.: A novel linear tangents based P&O scheme for MPPT of a PV system. Renew. Sustain. Energy Rev. **71**, 257–267 (2017)
29. Mellit, A., Kalogirou, S.A.: ANFIS- based modelling for photovoltaic power supply system: a case study. Renew. Energy **36**, 250–258 (2011)
30. Moradi, M.H., Reisi, A.R.: A hybrid maximum power point tracking method for photovoltaic systems. Solar Energy **85**, 2965–2976 (2011)
31. Larbes, C., Cheikh, S.-M.A., Obeidi, T., Zerguerras, A.: Genetic algorithms optimized fuzzy logic control for the maximum power point tracking in photovoltaic system. Renew. Energy **34**, 2093–2100 (2009)
32. Lyden, S., Haque, M.E.: Maximum power point tracking techniques for photovoltaic systems: a comprehensive review and comparative analysis. Renew. Sustain. Energy Rev. **52**, 1504–1518 (2015)
33. Bounechba, H., Bouzid, A., Nabti, K., Benalla, H.: Comparision of perturb & observe and fuzzy logic in maximum power point tracker for PV systems. Energy Procedia **50**, 677–684 (2014)
34. Kamarzaman, N.A., Tan, C.W.: A comprehensive review of maximum power point tracking algorithms for photovoltaic systems. Renew. Sustain. Energy Rev. **37**, 585–598 (2014)
35. Selmi, T., Niby, M.A., Devis, L., Davis, A.: P&O MPPT implementation using MATLAB/Simulink. In: 2014 Ninth International Conference on Ecological Vehicles and Renewable Energies (2014)
36. Chin, C.S., Neelakantan, P.,Yoong, H.P., Teo, K.-T.K.: Fuzzy Logic based MPPT for photovoltaic modules influenced by solar irradiation and cell temperature. UKSun In: 13th IEEE International Conference on Modelling and Simulation, Cambridge University, U.K., pp. 376–381 (2011)
37. Bouchafaaa, F., Hamzaouia, I., Hadjammara, A.: Fuzzy logic control for the tracking of maximum power point of a PV system. Energy Procedia **6**, 633–642 (2011)
38. Soufi, Y., Bechouat, M., Kahla, S., Bouallegue, K.: Maximum power point tracking using fuzzy logic control for photovoltaic system. In: 3rd IEEE International Conference on Renewable Energy Research and Applications, Milwakuee, USA, pp. 902–906 (2014)
39. Sivagamasundari, M.S., Mary, P.M., Velvizhi, V.K.: Maximum Power Point Tracking For Photovoltaic System by Perturb and Observe Method Using Buck Boost Converter. Int. J. Adv. Res. Electr. Electron. Instrum. Eng. **2**(6), 2433–2439 (2013)
40. Sholapur, S., Mohan, K.R., Narsimhegowda, T.R.: Boost converter topology for PV system with perturb and observe MPPT Algorithm. IOSR J. Electr. Electron. Eng. **9**(4), 50–56 (2014)
41. Kumari, J.S., Babu, ChS, Kullayappa, T.R.: Design and analysis of open circuit voltage based maximum power point tracking for photovoltaic system. Int. J. Adv. Sci. Technol. **2**(2), 51–86 (2011)
42. Lasheen, M., Rahman, A.-K.A., Salam, M.A., Ookawr, S.: Performance enhancement of constant voltage based MPPT for photovoltaic applications using genetic algorithm. In: 3rd International Conference on Power and Energy Systems Engineering, Energy Procedia, Vol. 100, pp. 217–222 (2016)

Effect of Tonal Features on Various Dialectal Variations of Punjabi Language

Ashima Arora, Virender Kadyan and Amitoj Singh

Abstract Punjabi is tonal as well as under resource language among all the Indo Aryan languages of the Indo-European family. A vast number of variations in language lead to challenges while designing an Automatic Speech Recognition (ASR) system. Therefore, it turned out to be a matter of extreme concern to study the essential features such as tone of the language for designing an effective ASR. This paper lays its focus upon the variation of tonal characteristics of Punjabi dialect. The speech corpus has been collected from native speakers of Punjab (including all the various dialects) and also covering the areas under the Himachali belt of Punjab. The result analysis shows that tonal words and dialectal word information caste a major impact on the information conveyed by the speaker. The analyzed data shows pitch variations in tonal words that vary from region to region. The experiments are performed by using Praat toolkit for calculating F0 value; then depending upon the pitch and frequency variations, we have studied that tonal words show dialectal variations when the similar sentence is spoken by speakers of different regions.

Keywords Accent · Pitch · Tonal variation · Z-score normalization
Dialectal variations · Intensity · Formant frequency (F0)

A. Arora (✉)
Department of Electronics and Electrical Engineering, Chitkara University, Chandigarh, Punjab, India
e-mail: ashima.arora2012@gmail.com

V. Kadyan
Department of Computer Science Engineering, Chitkara University, Chandigarh, Punjab, India
e-mail: virender.kadyan@chitkara.edu.in

A. Singh
Department of Computer Science Engineering, MRSPTU, Bathinda, Punjab, India
e-mail: amitoj.pb@gmail.com

B. S. Rawat et al. (eds.), *Advances in Signal Processing and Communication* ,
Lecture Notes in Electrical Engineering 526,
https://doi.org/10.1007/978-981-13-2553-3_45

1 Introduction

In a land full of diversities, such as India, the various states and provinces follow their respective spoken languages. According to Indian grammarians, there are three grades of recognized accents: **"Udatta"** which means a raise or elevator that indicates the highest pitch. Second, the term **"Anudatta"** stands for unelevated or non-accent pertaining it to a low-pitched syllable. **"Svarita"** the third accent is a mixture of both low and high pitches within a syllable. When this Vedic nomenclature of accents is compared to the tones of Punjabi language in the work done by Grierson, it was found out that, only "Udatta" could be compared to the high tone of Punjabi language, whereas as compared to "Svarita", the low tone of Punjabi language falls for the first syllable but rises for the rest **[**1**]**. The cause for this mismatch became the basic motivation for this study because there are various aspects of Punjabi language which remain uncovered because of it being an under resource language. The variation in these tones is a resultant of the position of the five tonemes (ਘ,ਧ, ਝ, ਢ,ਭ) of Punjabi language **[**2**]**. Other than these tonemes, one of the phonemes 'ਹ' also exhibits tonal characteristics, when placed at the final position, and shows a leveled tone whenever it occurs at the initial position. The differences in the pitch values gathered more interest when it was noticed that the dialectal differences when analyzed exhibit different tonal characteristics. The later part of the paper covers the analyses of pitch variation among most of the dialectal words that have been caused because of the regional variations across the same state. The importance of this study lies in the fact that the correct identification of the lexical is a crucial task while designing any speech processing system.

2 Literature Review

According to ethnologies 2005 estimate, there are 88 million native speakers of Punjabi language which make it 10th most widely spoken language in the world and according to 2001 Census of India, there are 29,102,477 Punjabi speakers in India [3]. But yet the area of research has not been progressive for this language though. The research work/the features of the speech signal in accordance with Tones have been majorly studied for mandarin languages. A tone detection methodology for Mizo language was designed in 2015 that used quantitative analysis of acoustic features of Mizo language [4]. Here, the tone was detected by relying on slope and height due to the availability of a large database. The z- score normalization of the signal is used for eliminating the effects of gender and then the pitch variance results were comparatively analyzed to distinguish whether the tone can be marked as high, low, falling or rising tone. Singh Panday and Aggarwal's (2015) study of Punjabi Tonemes [3] covered the five Tonemes of Punjabi language and their high, low, and mid-tones, and the paper also throws light on the IPA of these high and low tones words. A representation of an experimental study of the tonal characteristics of the laryngeal

phoneme of Punjabi language included the study on words containing phonemes of Malawi dialects carrying tonal effects, as recorded from native Punjabi speakers and then experiments were performed using Praat and Matlab [2]. Tonal analysis of the /h/ phoneme is studied using the (f0) fundamental frequency contour. This study showed that at a syllable level /h/ can reflect tonal occurrences whereas no such thing is observed when /h/ is considered at its initial positions [2]. Analysis of vowel phonemes in Punjabi has been performed but still there persists a twofold interface on acoustic features of vowels in two different languages [1]. The paper throws a lot of light on the fact that the effect of the other non-native languages and changing scenarios has a significant impact on the original Punjabi language, and it is one of the essential features to be kept in mind by designing any ASR system. Furthermore, the detection of Mizo Tones [4] included a lot of technical study over the tonal lexicon in Mizo language. Another paper on the Lexical stress in Punjabi language and its representations in PLS included a lot of linked information with PLS design and a new study about the relation between suprasegmental phonemes such as tone, nasalization, and stress at syllable level [5]. The study made it evident that the nontonal disyllabic words can also carry stress on the second syllable, which can be illustrated through the IPA, which contains the encoded PLS data.

3 Speech Corpus Structure

The regions of undivided Punjabi included the Malwa, Doaba, Majhi, and Puadh regions of Punjab along with the Himachali belt (Rullui, Mandiali, Kangri, and Chambiali). The designed corpus consists of dialectal varieties of undivided Punjab. Thus, the speech corpus was enriched by including the dialectal linguistic differences/varieties from the regions of Undivided Punjab. The sample speech sentences employed in the corpus are shown in Fig. 1.

Kangri:	sɪalkoʈe da ɪk raja tha, səlvan.
	sare sə̃sare cə óda ùkam cəlda tha, pər sɛ phɪri bì udas rɛ̃da tha.
Kullui:	sɪalkoʈara ɪk raja thi, səlvan.
	sare mulkhan teira hukəm cola thi, pər tabɛ bi sɔ udas rɔ́ɑ thi.
Mandiali:	sɪalkoʈara ɪk raja tha, səlvan.
	sári dunia ə̃dər tesra hukm cəlã̃ tha, pər pher bi se udas rã̃ tha.
Chambiali:	sɪalkoʈ vɪc ɪk raja tha, səlvaɳ thia.
	sári duniã̃ usda thia, pər phɪri bì ó udas rɛ̃da thia.
Majhi:	sɪaʟkoʈ da ɪk raja si, səlwan.
	sare jəgət wɪc óda hukəm cəʟda si, pər ó phɪr wì udas rɛ̃da si.
Doabi:	sɪaʟkoʈ da ɪk raja si, səlban.
	sáre jəg c óda hukəm cəlda si, pər ó pher bi udas rɛ̃do si.
Puadhi:	sɪaʟkoʈ ka ɪk raja ta, səlwan.
	sari duniã̃ mã̃ uska hukəm cəle ta, pər pher bi ɔ́ udas rəhe ta.
Malwai:	sɪaʟkoʈ da ɪk raja si səlban.
	sàre jəg c óda hukəm cəlda si, pər pher bi ó ədas rɛ̃da.

Fig. 1 Speech corpus including different dialects of Punjabi language

Table 1 Lexicon variations across the regions of undivided Punjab

Gurumukhi Script	Pronunciation	English Meaning	Native Region
ਸੰਸਾਰੇ/ਦੁਨੀਆਅੰਦਰ/ ਦੁਨੀਆਂ	sə̃sare/ duniaə̃dər/duniə̃	in the whole world	Kangri/Mandiali/Chambiali
ਸੈ/ਸੇ/ਓਹ	sɛ/se/oˊ	he	Kangri/Mandiali/Chambiali
ਥੀਆ/ ਥਾ/ ਥਾ	thia/tha/tha	was	Chambiali/Kangri/Mandiali
ਰਹੇਤਾ/ਰੈਂਦਾ	rəhe ta/rɛ́̃da	remained	Puadhi/Malwai
ਸੇਆਲਕੋਟੇਦਾ/ ਸੇਆਲਕੋਟਾਰਾ	sɹalkoʈe da/ sɹalkoʈara	from Sialkot	Kangri/Mandiali
ਤੇਸਰਾ/ਉਦ੍ਹਾ/ਉਸਦਾ	tesra/úda/usda	his	Mandiali/Kangri/
ਫੇਰਬੀ/ ਫਿਰੀਬੀ/ਫੇਰੀਬ੍ਹੀ	pher bi/phɹri bi/ phɹri bi	yet	Mandiali/Kangri/ Chambiali

The input signal is recorded at 44 kHz using the Sound Forge Software in studio environment. The accuracy and efficiency estimation of pitch of the analyzed dataset is performed on the basis of Tonal and Dialectal variations, through Praat software. The speech corpus includes certain words whose pitch and lexicon vary from region to region; some of the words are depicted in Table 1.

The idea /motive behind this design of the dataset/corpora were to include all the possible dialectal variations of Punjabi language considering its dialect dependent tonal variations. Section 4 shows speech signal would be modeled to conclude the necessity for study of tones while designing a speech system, especially for an under resource language like Punjabi.

4 Speech Signal Modeling

An input signal is studied for the tonal variations caused because of dialectal differences and of position of its vowel. While modeling a speech signal the recorded signal was studied on the base of tonal variations on three grounds (low, high, mid). Figure 2 shows the canonical pitch contour for Punjabi language. The high tone is a rising–falling tone (ਓਹਦਾ = /óda/), low tone is a falling tone (ਹੋਇਆ = /òIa/), and mid-tone has an intermediate pitch between high and low tones [6].

Further analysis of the signal is done as per the block diagram shown in Fig. 3.

The input signal is based on dialectal variations of Punjabi language. The signal is then Z-score normalized over a fundamental frequency (F_0) to immune it to the

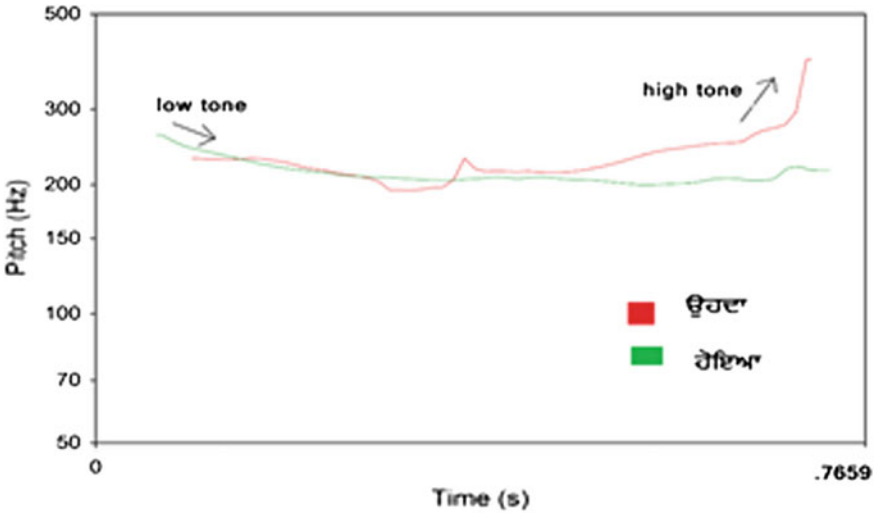

Fig. 2 Canonical pitch contours of Punjabi

Fig. 3 Block diagram of speech modeling

gender effects. The tonal word is identified as per the annotations provided in the Praat software the pitch and intensity contours are analyzed from the given input signal.

Z-Score Normalization

As pitch variation due to gender difference is a factor to be overcome while processing the speech signal, thus the Z-score of the pitch contour is taken to normalize the data to certain frequency that makes it gender independent. The Z-score takes a sample within a set of data and determines the number of standard deviations above or below it. The Z-score of a sample can be calculated using the equation given as [4],

$$p_z(x) = \frac{p(x) - \mu}{\sigma}$$

where μ is mean and σ is standard deviation.

Figure 4 represents the effect of Z-score normalization on the recorded input sound signal by a male and female speaker of the same dialectal region, respectively.

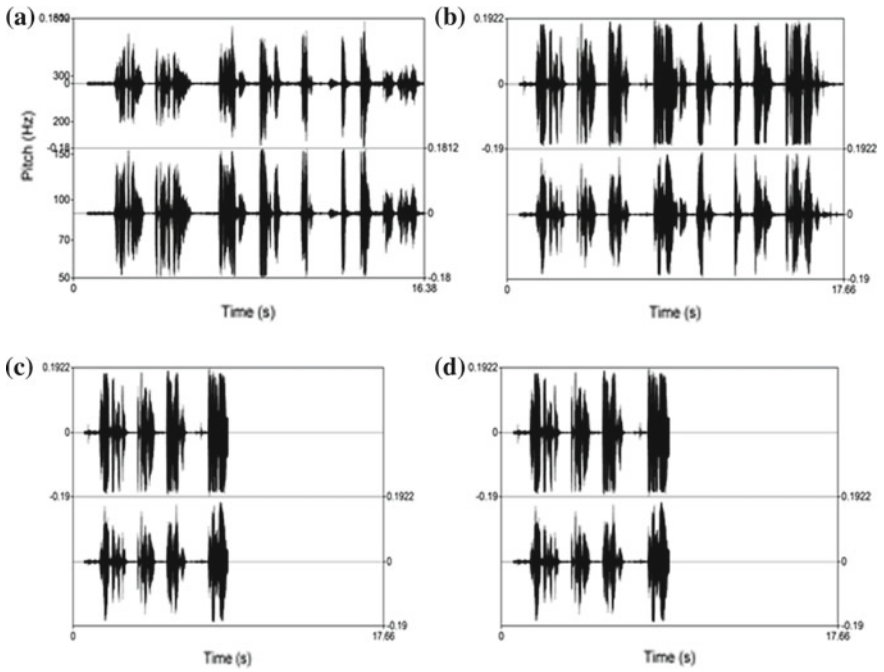

Fig. 4 **a**, **b** Represent recorded voice of the male and female of the same region and **c**, **d** respective Z-score normalized waveform

Role of F_0 frequency

There is a substantial amount of data on the frequency of the voice fundamental (F_0) in the speech of speakers who differ in age and sex [3]. The voice fundamental frequency plays a very important role while differentiating the male and female speakers. Published data on the frequency of the voice fundamental (F_0) in speech shows its range of variation, often expressed in terms of two standard deviations (SD) of the f_0-distribution, to be approximately the same for men and women if expressed in semitones [7]. The male speakers have a low F0 and the female speakers have a high F_0; therefore, only F_0 values cannot be used for the representation of underlying tonal features of a language. Table 2 states the different values of fundamental frequencies (F_0) for the various dialects.

Comparative Lexicon Tonal Analysis (Pitch Contours)

As stated before, the dialectal differences as well as the position of the Toneme determine the variation in the pitch and the intensity contour of the dialectal and tonal words.

The effect of tonemes position on the tone of the signal has already been analyzed in Fig. 2.

The effect of tonemes position on the tone of the signal has already been analyzed in Fig. 2 above. The results of this comparative analysis among the dialectal variations

Table 2 F_0 values of the recorded signals

Regions	Fundamental frequencies (F0)
Majhi	853.10
Doabi	976.21
Puadhi	961.64
Malwai	976.60
Kullui	937.61
Chambiali	770.73
Kangri	860.01
Mandiali	727.20

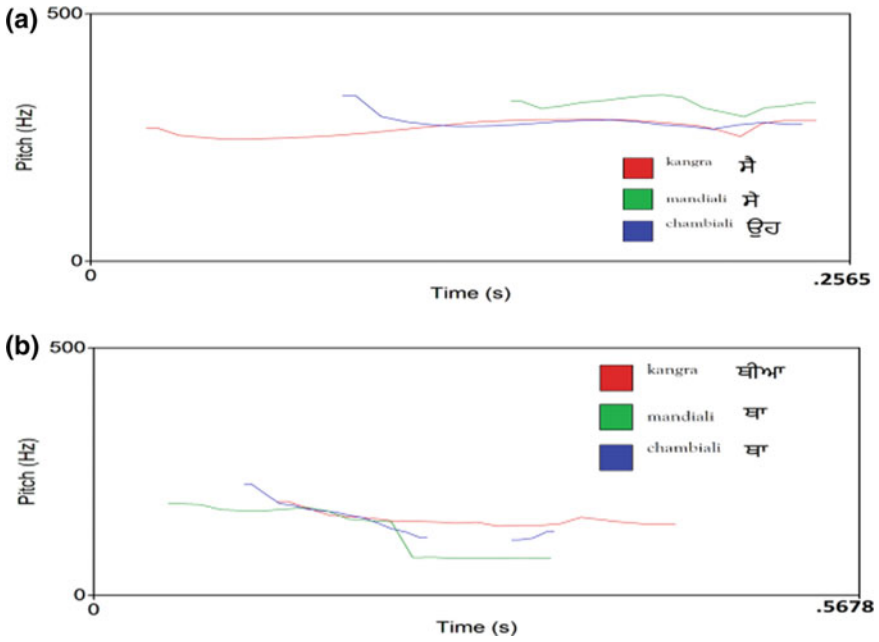

Fig. 5 **a**, **b** Pitch contour variations for dialectal words

are shown through the given Fig. 5. The following graphs are some of the few examples of the pitch contours for the dialectal words in the recorded dataset.

5 Results and Experimental Analysis

The pitch boundaries based on the fundamental frequency of the signal show the dialectal and the tonal variations of the word in different regions. The values of the fundamental frequency (F_0) have already been determined and illustrated in Table 2.

Table 3 Pitch and intensity variations across different regions of undivided Punjab

Dialect name	Value of the pitch			Intensity		
	Mean	Min	Max	Mean	Min	Max
Majhi	250.62	116.21	370.23	64.56	71.23	26.68
Doabi	130.16	86.51	162.23	66.10	71.43	22.14
Malwai	150.61	112.83	194.190	66.81	75.28	20.17
Kullui	124.75	78.31	65.76	58.34	65.76	15.53
Chambiali	238.7	112.60	336.93	64.49	73.41	-9.65
Kangri	199.30	139.27	261.52	58.84	68.32	24.52
Mandiali	248.01	86.39	332.93	59.95	66.64	26.21

Table 3 represents the change in the values of the pitch and corresponding Intensity variation of the dialectal varieties of the input signal. From this experiment, it was analyzed that the values of mean pitch for the Punjabi dialects of the present regions of Punjab range from 130.16 to 250.62 and for the Himachali belt of undivided Punjab it ranges from 124.75 to 248.01. Though the ranges are quite similar to one another, we could easily judge from the table given above that the difference in Pitch variation is minimum in the Punjabi dialect Majhi and Punjabi dialect across Himachali belts (Chambiali and Mandiali). These regions offer higher values of pitch indicating the occurrence of more high tone signals. The regions of Kullui, Malwai, and Doabi offer a similarity with the lower values of mean pitch indicating more of low tones. The intensity though remains as an almost constant value which shows a negligible amount of change when observed for the various Punjabi dialects of the regions of Undivided Punjab. Nevertheless, the Chambiali region reflects the intensity and mean pitch very close to the Modern Punjabi dialectal regions as compared to the others.

6 Conclusions

The paper describes the dialectal variations reflected in the tone of the signal. The pitch, intensity, and fundamental frequency variations of the signal are studied. The pitch boundaries based on the fundamental frequency of the signal show the dialectal and the tonal variations of the word in different regions. The determined values are important because inclusion of tonal information of the words while designing the ASR can show a considerable increase in the efficiency of the designed system.

Acknowledgements The authors would like to present their sincere thanks to the people of Punjab who have extended their support and cooperation in the data collection phase. They would also like to thank the authorities of Linguistics Department Punjabi University and Speech and Multimodal lab, Chitkara University for their extended support in the fulfillment of requirements for data processing.

They would also like to thank Ms. Suman Preet and Mr. Surjit Singh for their help during corpus preparation.

References

1. Singh, A., Pandey, D., Agrawal, S.S.: Analysis of Punjabi tonemes. In: 2015 2nd International Conference on Computing for Sustainable Global Development (INDIACom). IEEE (2015)
2. Lata, S., Samarth A.: Laryngeal tonal characteristics of Punjabi—an experimental study. In: 2013 International Conference on Human Computer Interactions (ICHCI). IEEE (2013)
3. LIU J., HE X., MO F., YU T.:Study on tone classification of chinese continuous speech in speech recognition system
4. Sarma, B.D., et al.: Detection of mizo tones. In: Sixteenth Annual Conference of the International Speech Communication Association (2015)
5. Lata S., Arora, S., Kaur, S.: Lexical stress in Punjabi and its representation in PLS
6. Lata, S.: Challenges for design of pronunciation lexicon Specification (PLS) for Punjabi
7. Traunmüller, H., Eriksson, A.: The frequency range of the voice fundamental in the speech of male and female adults. Consulté le **12**(02), 2013 (1995)
8. Sarmah P., Dihingia, L., Lalhminghlui, W.: Contextual variation of tones in mizo. In: Proceedings of Interspeech (2015)
9. Lata S., Arora, S.: Exploratory analysis of Punjabi tones in relation to orthographic characters: a case study
10. Sarmah P., Dihingia, L., Lalhminghlui, W.: Contextual variation of tones in mizo
11. Bansal, I., Sharan, S., Kilt, A. (n.d.).: Corpus design and development of an annotated speech database for Punjabi. College of Engineering, Gurgaon
12. Dua, M., Aggarwal, R.K., Kadyan, V., Dua, S.: Punjabi automatic speech recognition using HTK. Int. J. Comput. Sci. Issues **9**(4), 359–364 (2012)
13. Kaur, E.A., Singh, E.T.: Segmentation of continuous Punjabi speech signal into syllables. In: The World Congress on Engineering and Computer Science (WCECS), vol. 1, pp. 20–23 (2010)
14. Lata, S., Arora, S. (n.d.).: Exploratory analysis of punjabi tones in relation to orthographic characters : a case study, pp. 3–7
15. Sarma, B.D., Sarmah, P., Lalhminghlui, W., MahadevaPrasanna, S.R.: Detection of mizo tones. In: Proceedings of the Annual Conference of the International Speech Communication Association (Interspeech, 2015), pp. 934–937 (2015)
16. Singh, P., Dutta, K.: Formant analysis of Punjabi non-nasalized vowel phonemes. In: 2011 Proceedings of the International Conference on Computational Intelligence and Communication Systems (CICN 2011), pp. 375–380 (2011). https://doi.org/10.1109/CICN.2011.79
17. Traunmüller, H., Eriksson, A.: The frequency range of the voice fundamental in the speech of male and female adults (Cash Notes 2014). Department of Linguistics, University of Stockholm, vol. 97, pp. 1905–1915 (1994)
18. Kumar, A.: Implementation and performance evaluation of continuous Hindi speech recognition (1) (2014)

Part III
VLSI and Embedded Systems

Optical Functions of Methanol and Ethanol in Wide Spectral Range

Michal Lesňák, Kamil Postava, František Staněk and Jaromír Pištora

Abstract The motivation of this paper is to determinate the precise complex refractive indices dispersion of ethanol, methanol, and their solutions in the wide spectral range from 8 to 40 000 cm^{-1} (wavelength range from 250 nm to 1.25 mm) in coupling to biosensors applications (body liquids analyses, tissue ethanol solutions testing, etc.) because a specification of the complex optical functions consistent with Kramers–Kronig dispersion relations in the whole mentioned spectral range was still missing. A general method combining UV/visible/near-infrared spectroscopy and Mueller matrix ellipsometry, Fourier transform infrared spectroscopy (FTIR), infrared attenuated total reflection (ATR) spectroscopy, and terahertz time-domain spectroscopy (THz-TDS) is proposed. The experimental data are modeled using a dielectric function parametrization based on the Brendel–Bormann oscillators.

Keywords Refractive indices of liquids · Terahertz spectroscopy · ATR Infrared spectroscopy · Ethanol · Methanol

M. Lesňák (✉) · F. Staněk
Institute of Physics, VSB-Technical University of Ostrava, 17. listopadu 15, 70833 Ostrava-Poruba, Czech Republic
e-mail: michal.lesnak@vsb.cz

F. Staněk
e-mail: f.stanek@vsb.cz

M. Lesňák · K. Postava · J. Pištora
Nanotechnology Centre, VSB-Technical University of Ostrava, 17. listopadu 15, 70833 Ostrava-Poruba, Czech Republic
e-mail: kamil.postava@vsb.cz

J. Pištora
e-mail: jaromir.pistora@vsb.cz

B. S. Rawat et al. (eds.), *Advances in Signal Processing and Communication* ,
Lecture Notes in Electrical Engineering 526,
https://doi.org/10.1007/978-981-13-2553-3_46

1 Introduction

Recent progress in terahertz (THz) imaging and spectroscopy has led to intense research and development in biomedical applications, for example, protein–antiprotein interactions, tumor sensitivity, DNA encoding, etc. [1–3]. THz spectral range offers several advantages for biomedical sensing, for example, nonionizing properties, a high sensitivity to vibration–rotation fingerprints of large molecules, a possibility for in vitro testing, or surface plasmon resonance (SPR) sensing [4–6]. Another direction of extensive research is spectroscopy of nanoparticles embedded in liquids [7]. For all the above applications, precise knowledge of optical functions of transporting liquids (water, ethanol, and methanol) in a wide spectral range is essential. The wide spectral range provides the possibility to combine biosensor's advantages in particular spectral regions. Moreover, high absorption and consequent low penetration depth of water in the THz spectral range leads to seeking of appropriate liquid carrier medium. Promising candidates for advanced biomedical sensor applications are ethanol and methanol, the liquids in the focus of this paper.

The most explored liquid material is distilled water. Complex refractive index spectra in the wide spectral range from 50 to 50 000 cm^{-1} were presented in the review paper of Hale and Querry [8]. The paper reported data from various measurements such as the spectral reflectivity and transmission from water surface, and from attenuated total reflection (ATR) spectroscopy. However, a determination of the complex optical functions consistent with Kramers–Kronig dispersion relations in the whole spectral range is still missing.

Moreover, the complex refractive indices of methanol and ethanol have been determined only in a limited visible spectral range [9, 10]. In the infrared, the absorbance spectra and qualitative absorption-peaks spectral positions have been studied and presented in [11], and in the terahertz spectral range in [11–13]. Therefore, there is a need for a systematic study of the complex optical functions in the wide spectral area from the ultraviolet to the terahertz ranges.

This paper focuses on the determination of precise complex refractive indices dispersion of ethanol, methanol, water and their solutions in the wide spectral range from 8 to 40 000 cm^{-1} (i.e., the wavelength range from 250 nm to 1.25 mm).

2 Experimental

2.1 Studied Samples

We describe a general method for a determination of complex refractive indices dispersion of liquids in the case of pure ethanol (C_2H_5OH) and methanol (CH_3OH). The purity of the liquids is 99.9%. The complex refractive indices dispersion (optical functions) of both liquids is of a great practical interest due to their applications in the measurement of biomedical samples.

We compare the optical functions of the liquids with measurements of pure demineralized water. In the following, the solutions of the two liquids, ethanol and methanol, are studied by using the same procedure. Solutions are defined by the mass fractions and measured with a precision of 0.1%. The corresponding volume fraction of solutions can be calculated using the liquid densities.

2.2 Spectroscopic Methods

Optical functions of liquids in the wide spectral range are obtained by combining measurements using three measurement setups: Mueller matrix spectroscopic ellipsometry, Fourier transform infrared spectroscopy (FTIR), and time-domain terahertz spectroscopy (THz-TDS). The Mueller matrix spectroscopic ellipsometer RC2 from Woollam with two rotating compensators was applied in the spectral wavelength range from 193 nm to 1.7 μm (the corresponding photon energy range is from 0.7 to 6.5 eV). The ellipsometer is equipped with a liquid cell with fused silica windows and a crystalline silicon wafer with a 25 nm thick oxide layer to enable reflection from the liquid/silicon–wafer interface at an angle of incidence of 70°.

The infrared spectral range was measured using an FTIR spectrometer Vertex 70v from Bruker. An evacuated cavity space of the spectrometer suppresses the influence of water vapor and CO_2 absorptions. The DLaTGS detectors with KBr and polyethylene windows combined with the KBr and multilayer Mylar beam splitters were used to cover the mid- and far-infrared spectral ranges, respectively. For the mid-infrared spectral range where strong absorption features dominate, the attenuated total reflection (ATR) unit with a diamond prism was applied at an angle of incidence of 45°. The reflection from the prism/vacuum interface was used as a reference. In the far-infrared spectral range, the transmission through 250 μm, 500 μm, and 1.06 mm thick cavities was employed at the normal angle of incidence. The 1 mm thick Topas (cyclic olefin copolymer) window was applied. Combining both FTIR measurements, the optical functions in the spectral range from 100 to 5000 cm^{-1} (the wavelength range from 2 to 100 μm) were obtained.

Optical properties in the terahertz spectral range were obtained using the terahertz time-domain spectroscopy (THz-TDS) TPS Spectra 3000 from TeraView. We have combined both ATR and transmission measurements. The spectral range from 8 to 100 cm^{-1} was studied. The ATR spectra were obtained using a high resistivity silicon prism (35°). The measurement was completed via transmission through 1 mm thick liquid in a cavity defined by z-cut quartz windows. The measurement was performed at the normal incidence.

3 Optical Functions of Methanol and Ethanol

3.1 Model Dielectric Functions Based on Voight Oscillators

The experimental data were modeled by a convolution of a Gaussian function with the dielectric function of the Lorentz damped harmonic oscillator model. The dielectric function fulfilling Kramers–Kronig relations and yielding a variable Gaussian-to-Lorentzian shape of the imaginary part of the dielectric function is chosen in the form [13]

$$X_k(\tilde{\upsilon}) = \frac{1}{\sqrt{2\pi\sigma_k}} \int_{-\infty}^{+\infty} exp\left(-\frac{(x-\tilde{\upsilon}_{0k})^2}{2\sigma_k^2}\right) \times \frac{\tilde{\upsilon}_{pk}^2}{x^2 - \tilde{\upsilon}^2 + i\tilde{\upsilon}_{\tau k}\tilde{\upsilon}} dx, \qquad (1)$$

where $\tilde{\upsilon}$ is the wave number, $\tilde{\upsilon}_{0k}$ is the resonance wave number, $\tilde{\upsilon}_{pk}$ describes the amplitude of the kth oscillator, σ_k is the standard deviation of Gaussian broadening, and $\tilde{\upsilon}_{\tau k}$ is the damping constant related to the Lorentz vibrational mode k. The model describes homogeneously and inhomogeneously broaden oscillations. Depending on the value of $\tilde{\upsilon}_{\tau k}/\sigma_k$, the imaginary part (1) will vary in shape from Gaussian-to-Lorentzian shape. The above parameterization is also called the Voight line profile.

For permittivity consisting of several oscillators, we can write

$$\varepsilon(\tilde{\upsilon}) = \varepsilon_\infty + \sum\nolimits_k X_k(\tilde{\upsilon}) + \frac{\Delta\varepsilon_{DB}}{1 + i\omega\tau}, \qquad (2)$$

where $X_k(\tilde{\upsilon})$ is the contribution of each vibrational mode k and ε_∞ is the constant term describing the high-frequency contribution. The last Debye term $\Delta\varepsilon_{DB}$ describes dipolar absorptions in polar liquids, τ is the characteristic relaxation time. With help of permittivity dispersion, we can express the frequency dependence of index of refraction N $(\tilde{\upsilon})$

$$\varepsilon(\tilde{\upsilon}) = \left[\mathrm{N}(\tilde{\upsilon})\right]^2. \qquad (3)$$

3.2 Refractive Indices Spectra of Studied Liquids

Figure 1 shows obtained spectra of ellipsometric angles ψ and Δ in visible and near-infrared spectral range for the ethanol/silicon–wafer interface. The measurement with liquid cell enables to obtain refractive index dispersion in the range in which the liquid is transparent. Similar dependencies were obtained for water and methanol.

Figure 2 shows mid-infrared ATR spectra of measured liquids. Clear difference in vibration peaks between ATR absorptions of ethanol and methanol in the ranges 800–1600 cm^{-1} and 3000–3300 cm^{-1} was observed. This difference can be used to distinguish both liquids and determines their concentrations in solutions.

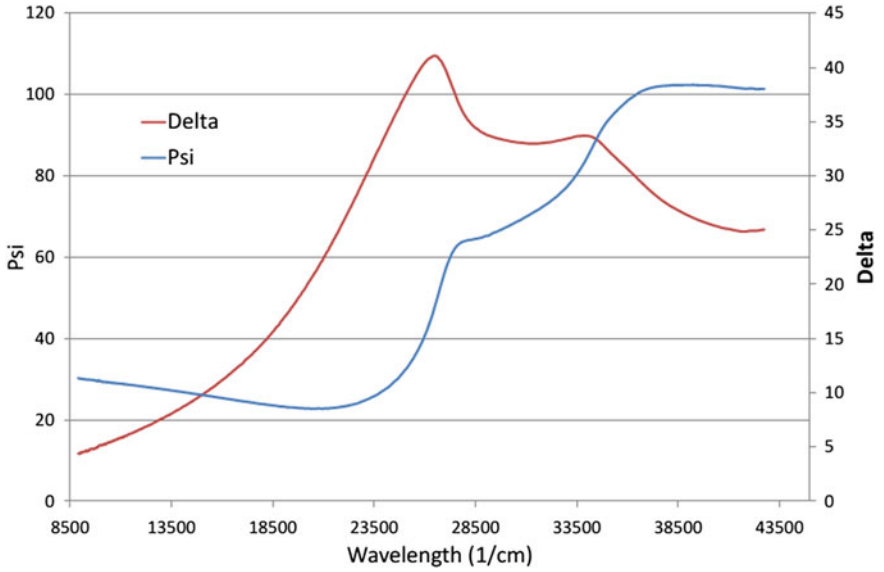

Fig. 1 Spectroscopic ellipsometry data of the ethanol/silicon–wafer interface

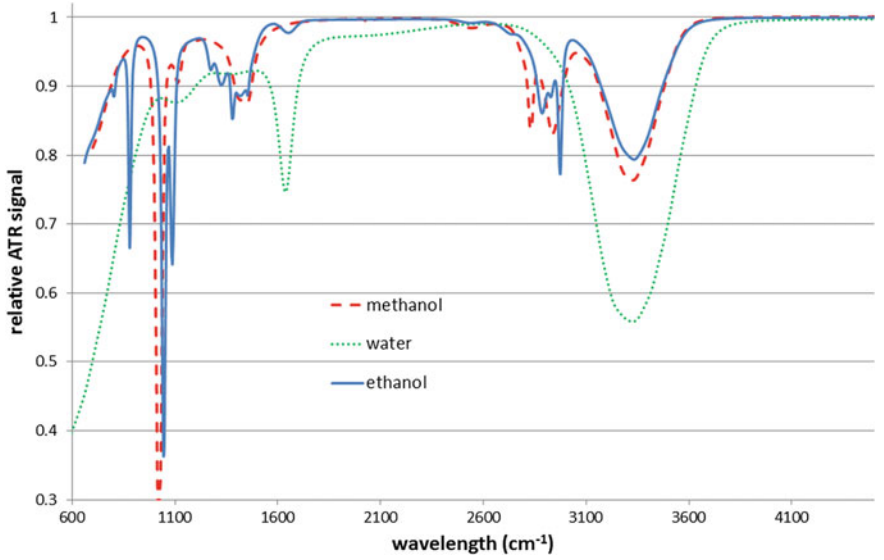

Fig. 2 ATR spectroscopic measurements—clear water, ethanol, and methanol

Figure 3 shows terahertz ATR spectra from the silicon prism/liquid interfaces. In this range, the dipolar Debye absorptions cause reduction of ATR signal. The strongest absorption is obtained in the case of water. Methanol absorbs more than

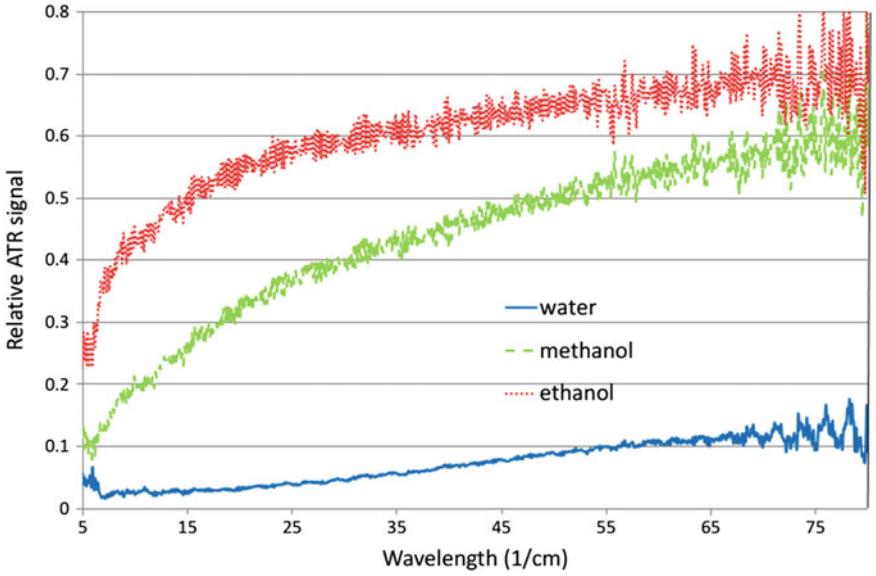

Fig. 3 ATR spectroscopic measurement in the THz region

ethanol particularly for low frequencies. The dependence was also confirmed by transmission measurement in cavity with z-cut quartz windows. The resulting complex refractive indices dispersion from 10 cm^{-1} to 4000 cm^{-1} for methanol and ethanol are depicted in Fig. 4.

All the above-discussed experimental data were fitted simultaneously to a single model. Complex refractive indices dependences on wavelength for ethanol and methanol have been founded using Eqs. (1)–(3). Parameters for each vibrational mode (resonant frequency, oscillator strength, damping, and distribution width) have been computed by Theiss software [14] and they are specified in Table 1 (ethanol) and Table 2 (methanol). The high-frequency permittivity contributions ε_∞ for methanol $\varepsilon_{\infty m} = 1.7790$ and ethanol $\varepsilon_{\infty e} = 1.8736$ have been obtained from critical angle measurement at 589.5 nm (Na arc line). The Debye terms ε_{DB} (2) for methanol and ethanol have been determined as 0.16 and 0.35, respectively. As regards characteristic relaxation time (τ), the following values have been specified: $1/\tau_M = 0.754\ cm^{-1}$ (methanol), $1/\tau_E = 13.812\ cm^{-1}$ (ethanol).

In the visible area, the refractive indices of ethanol and methanol are real numbers, and we can easily compare our achieved results with published data for selective wavelengths. For pure methanol (wavelength 589 nm, temperature 20 °C) our determined value of refractive index is 1.3254 (see Fig. 4). In Refs. [15–17] are described the refractive index dispersion measurements for different temperatures (wavelength and concentration are the same). For 22 °C, the authors declare the methanol index of refraction $n_m = 1.3281$ [15], for 25 °C published result $n_m = 1.3314$ [16], and for 27 °C $n_m = 1.3270$ [17], which is in good agreement with results published in this

Table 1 Parameters describing model dielectric function of ethanol using Brendel–Bormann oscillators

k	$\tilde{\upsilon}_{0k}$ (cm^{-1})	$\tilde{\upsilon}_{pk}$ (cm^{-1})	$\tilde{\upsilon}_{\tau k}$ (cm^{-1})	σ_k (cm^{-1})
1	55.9	25.0	0.000	24.936
2	97.7	14.8	0.000	6.988
3	110.7	45.3	32.334	9.342
4	138.9	29.8	1.978	23.956
5	201.8	63.3	4.887	42.030
6	285.9	31.3	20.703	21.264
7	322.5	42.2	100.712	2.591
8	421.6	62.5	86.559	20.014
9	433.8	33.3	2.534	9.998
10	575.7	167.2	0.011	107.920
11	590.3	73.2	0.744	33.020
12	712.9	56.5	57.951	30.374
13	793.2	71.9	124.928	0.582
14	804.5	14.9	0.019	6.067
15	881.2	58.3	7.320	3.051
16	890.0	16.4	1.875	11.373
17	1048.8	126.7	13.908	0.616
18	1088.8	93.5	11.816	5.842
19	1134.0	54.6	0.000	77.086
20	1274.3	52.0	39.132	1.879
21	1324.4	50.7	0.103	19.853
22	1379.9	31.3	0.284	6.924
23	1420.1	119.4	30.751	43.547
24	1455.2	23.0	10.997	2.115
25	1653.3	36.6	0.005	31.075
26	2534.1	27.3	0.043	46.298
27	2728.8	65.0	104.828	1.854
28	2887.8	77.1	9.475	16.124
29	2889.1	125.6	0.088	63.871
30	2930.1	66.9	32.428	0.022
31	2974.8	104.7	14.305	3.955
32	3078.3	85.3	158.750	1.477
33	3339.6	362.2	0.001	118.637
34	3371.6	62.0	0.000	50.937

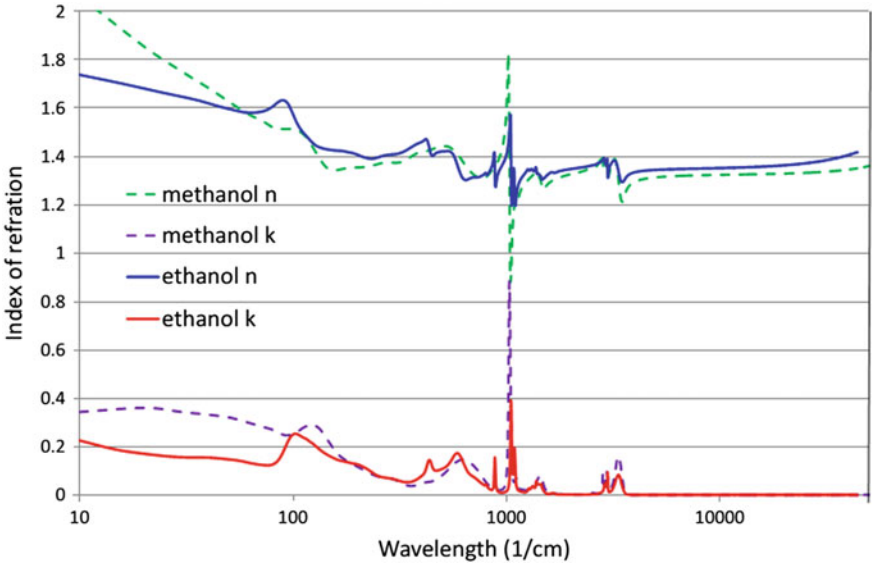

Fig. 4 Dependence of complex refractive index on wavelength for ethanol and methanol in the whole measurable range

paper. As regards pure ethanol, we determined the ethanol refractive index (wavelength 589 nm, temperature 20 °C) $n_e = 1.3589$ (see Fig. 4). In Ref. [20], the authors declare ethanol refractive index value $n_e = 1.3608$, in [18] is specified value of $n_e = 1.3614$, and referred to [19] $n_e = 1.3612$. For the discussed spectral area, the differences of our resulting refractive indices and published data are less than 0.5%. In visible region, the refractive index dispersion of the solution can be described by relatively easy polynomial functions [15–17]. The quality of model approach is demonstrated in Fig. 5. The relative ATR experimental signal and modeled ATR output dependence on wavelength for ethanol–methanol mixture (50:50) is practically coincident. It is evident the possibility to study the influence of intermolecular interactions [20] by the described model.

The interesting frequency band for methanol and ethanol refractive indices dispersion is about 1000 cm^{-1} [19]. For ethanol the vibrational modes $k = 19$ and $k = 20$ (see Table 1) at 1048.8 and 1088.8 cm^{-1} are dominant. The real part and imaginary one of ethanol refractive index dispersion show characteristic peaks (Fig. 4). The damping constants $\tilde{\upsilon}_{\tau k}$ related to the vibrational modes $k = 19$ and $k = 20$ are practically coincident (13.820 cm^{-1}, respectively, 11.431 cm^{-1}). For methanol, we can observe in the area about 1000 cm^{-1} only one expressive peak located at 1028.8 cm^{-1} vibrational mode number $k = 11$ (Fig. 4, Table 2). The damping constant $\tilde{\upsilon}_{\tau k}$ for this mode number is 8.692 cm^{-1}. This damping constant value is near to the damping constants of ethanol for extreme peaks in discussed wavelength area.

Table 2 Parameters describing model dielectric function of methanol using Brendel–Bormann oscillators

k	$\tilde{\upsilon}_{0k}$ (cm^{-1})	$\tilde{\upsilon}_{pk}$ (cm^{-1})	$\tilde{\upsilon}_{\tau k}$ (cm^{-1})	σ_k (cm^{-1})
1	35.1	49.9	121.881	0.000
2	67.0	51.2	94.143	0.065
3	79.0	12.0	21.184	0.000
3	123.5	36.1	0.000	19.292
4	163.3	56.7	103.754	0.000
5	216.9	46.5	108.287	0.011
6	292.3	32.3	8.452	29.550
7	413.5	50.4	102.970	0.157
8	616.0	162.4	0.000	91.532
9	744.1	134.2	213.615	1.622
10	1028.8	168.2	8.561	5.220
11	1025.1	115.3	20.490	8.921
12	1080.6	33.2	39.903	0.943
13	1115.8	55.9	9.182	14.134
14	1180.7	42.7	87.124	12.917
15	1410.0	91.4	50.118	15.161
16	1376.5	118.0	205.146	82.970
17	1460.2	97.1	63.821	0.425
18	1455.6	24.5	8.071	15.947
19	2045.9	19.8	13.475	6.441
20	2538.7	62.6	13.044	60.120
21	2831.8	113.7	26.204	0.345
22	2913.3	191.6	137.991	0.006
23	2937.5	52.9	0.008	15.558
24	2954.7	150.2	15.439	35.465
25	3340.3	457.2	0.006	109.746
26	2794.5	58.0	0.000	28.400
27	3087.4	110.9	97.826	32.986

Moreover, the method was tested on ethanol–methanol mixtures. The solution with mass fractions 50% : 50% has been prepared and characterized. On the base of achieved experimental data, the refractive index dispersion from 500 to 4000 cm^{-1} has been specified. With help of this modeled refractive index distribution, the relevant ATR response has been determined. The comparison of measured and modeled ATR response is shown in Fig. 5.

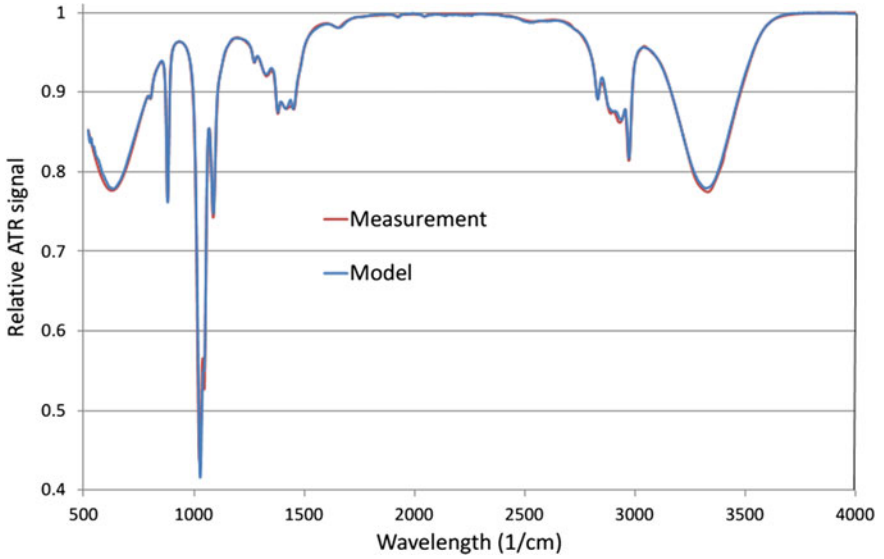

Fig. 5 Comparison of the measured and modeled data for the same amount of mixture of ethanol and methanol

4 Conclusion

In this paper, the optical functions and their parameterization for ethanol and methanol in wide spectral range were presented including terahertz region. Origin of the infrared and terahertz absorptions was discussed. Precise knowledge of the optical functions is essential for modeling and optimization of biomedical sensors in the discussed spectral range. It is also evident that ATR spectroscopic measurement can be used for the specification of concentration dependence of the refractive indices in ethanol–methanol mixtures. This is important for the identification of methanol presence in spirituous liquors.

Acknowledgements This work was partially supported by the Czech Science Foundation (grant #15-21547S), by the Ministry of Education, Youth and Sports: by the National Program of Sustainability (NPU II) project IT4Innovations excellence in science—LQ1602, and "Regional Materials Science and Technology Centre—Feasibility Program" (# LO1203).

References

1. Vance, S.A., Sandros, M.G.: Zeptomole detection of C-reactive protein in serum by a nanoparticle amplified surface plasmon resonance imaging aptasensor. Sci. Rep. **4**. https://doi.org/10.4049/jimmunol.177.8.5129
2. Vance, S., Zeidan, E., Henrich, V.C., Sandros, M.G.: Comparative analysis of human growth hormone in serum using SPRi, nano-SPRi and ELISA assays. Jove-J. Vis. Exp. **107**, e53508 (2016)
3. Chardin, H., Mercier, K., Frydman, C., Vollmer, N.: Surface plasmon resonance imaging: a method to measure the affinity of the antibodies in allergy diagnosis. J. Immunol. Methods **405**, 23–28 (2014)
4. Klein, A.K., Pan, Y., Balocco, C., Zeze, D., Gallant, A.J.: Micro fabricated spoof surface plasmon polariton structures for THz applications. In: 2015 40th International Conference on Infrared, Millimeter, and Terahertz Waves (IRMMW-THz). IEEE, pp. 1–2 (2015)
5. Vollmer, N., Trombini, F., Hely, M., Bellon, S., Mercier, K., Cazeneuve, C.: Methodology to study polymers interaction by surface plasmon resonance imaging. MethodsX **2**, 14–18 (2015)
6. Chochol, J., Postava, K., Čada, M., Vanwolleghem, M., Mičica, M., Halagačka, L., Pištora, J.: Plasmonic behavior of III-V semiconductors in far-infrared and terahertz range. J. Eur. Opt. Soc.-Rapid Publ. **13**(1), 13 (2017)
7. Dupont, J., Meneghetti, M.R.: On the stabilisation and surface properties of soluble transition-metal nanoparticles in non-functionalised imidazolium-based ionic liquids. Curr. Opin. Colloid Interface Sci. **18**(1), 54–60 (2013)
8. Hale, G.M., Querry, M.R.: Optical constants of water in the 200-nm to 200-microm wavelength region. Appl. Opt. **12**(3), 555–563 (1973)
9. Kedenburg, S., Vieweg, M., Gissibl, T., Giessen, H.: Linear refractive index and absorption measurements of nonlinear optical liquids in the visible and near-infrared spectral region. Opt. Mater. Express **2**(11), 1588–1611 (2012)
10. Moutzouris, K., Papamichael, M., Betsis, S.C., Stavrakas, I., Hloupis, G., Triantis, D.: Refractive, dispersive and thermo-optic properties of twelve organic solvents in the visible and near-infrared. Appl. Phys. B-Lasers Opt. **116**(3), 617–622 (2014)
11. Schwager, F., Marand, E., Davis, R.M.: Determination of self-association equilibrium constants of ethanol by FTIR spectroscopy. J. Phys. Chem. **100**(50), 19268–19272 (1996)
12. Kindt, J.T., Schmuttenmaer, C.A.: Far-infrared dielectric properties of polar liquids probed by femtosecond terahertz pulse spectroscopy. J. Phys. Chem. **100**(24), 10373–10379 (1996)
13. Brendel, R., Bormann, D.: An infrared dielectric function model for amorphous solids. J. Appl. Phys. **71**(1), 1–6 (1992)
14. Theiss, W.: http://www.mtheiss.com/docs/scout2/?brendel.htmSCOUT technical manual. http://www.mtheiss.com/docs/scout2/?brendel.htm
15. Kozma, I.Z., Krok, P., Riedle, E.: Direct measurement of the group-velocity mismatch and derivation of the refractive-index dispersion for a variety of solvents in the ultraviolet. J. Opt. Soc. Am. B-Opt. Phys. **22**(7), 1479–1485 (2005)
16. El-Kashef, H.: The necessary requirements imposed on polar dielectric laser dye solvents. Phys. B-Condens. Matter **279**(4), 295–301 (2000)
17. Moutzouris, K., Papamichael, M., Betsis, S.C., Stavrakas, I., Hloupis, G., Triantis, D.: Refractive, dispersive and thermo-optic properties of twelve organic solvents in the visible and near-infrared. Appl. Phys. B-Lasers and Opt. **116**(3), 617–622 (2014)
18. http://www.refractometer.pl/refraction-datasheet-basicRefractive index of some selected substances, refractometer.pl. http://www.refractometer.pl/refraction-datasheet-basic
19. Sani, E., Dell'Oro, A.: Spectral optical constants of ethanol and isopropanol from ultraviolet to far infrared. Opt. Mater. **60**, 137–141 (2016)
20. Rioboo, R.J.J., Philipp, M., Ramos, M.A., Kruger, J.K.: Concentration and temperature dependence of the refractive index of ethanol-water mixtures: Influence of intermolecular interactions. Eur. Phys. J. E **30**(1), 19–26 (2009)

A Novel Method to Detect Program Malfunctioning on Embedded Devices Using Run-Time Trace

Garima Singhal and Sahadev Roy

Abstract Security is an essential part of development in embedded systems. Execution of unknown or malicious program through an unauthorized means of communication on an embedded system can cause unwanted system behavior. To safeguard the sensitive data and devices, presently, sophisticated hardware and software systems based on cryptographic techniques are required which in turn increases the system's cost. In this paper, we proposed a method of securing such embedded devices which cannot afford to have capabilities comparable to conventional computers. This method generates a run-time trace on embedded devices during program execution, using already available hardware circuitry on the board. It observes and analyzes the obtained data using data analysis techniques and detects whether any change is occurred in the program compared to previously obtained data.

Keywords Cycle per instruction [CPI] · Control flow graph [CFG]
Program counter [PC] · Self-organizing map [SOM]

1 Introduction

With emerging new technologies and advancements in a field of embedded systems, the threat of cyberattacks also increases. The embedded devices used in hard real-time systems, e.g., in measurement and instrumentation, defense and navy applications, flight control and automation, medical and healthcare systems, etc., are required to prevent malicious attacks and system failure errors. These applications often possess

G. Singhal (✉) · S. Roy
Department of Electronics and Communication, NIT
Arunachal Pradesh, Papum Pare, Arunachal Pradesh, India
e-mail: garimasinghal.888@gmail.com

S. Roy
e-mail: sahadevroy@gmail.com

B. S. Rawat et al. (eds.), *Advances in Signal Processing and Communication* ,
Lecture Notes in Electrical Engineering 526,
https://doi.org/10.1007/978-981-13-2553-3_47

sensitive data and perform critical operations on various groups of data on daily basis. Security of these embedded systems from cyberattacks and malicious programs becomes more challenging due to limited system resources and cost constraints. Few potentials attacks and need for using separate methods for embedded systems instead of using conventions anti-virus and other methods that are used with computers are described in detail in [1]. Today's advanced security systems use cryptographic encryptions and algorithms [2] which require resources comparable to a computer. But embedded devices have limited amount of memory, computational circuitry, and power constraints which make general-purpose security methods difficult to implement.

This method of analyzing embedded systems through their run-time trace emerges as a new research field in securing the embedded devices. It relies on the feature extraction in programs during run-time and configuring the collected data using a self-learning cluster-based approach. Tracing the internal parameters to detect any variations makes these systems, a very noble and reliable method to detect any abnormal program behavior being it malicious, or system failure. It uses very limited memory space and hardware circuitry and proves to be reliable and robust over the conventional methods used in securing systems. It uses program counter values and cycles per instructions as an input variable to extract on-board features of the circuitry during run-time execution. Then the extracted values are classified and represented into meaningful clumps using a clustering-based analyzer and then finally utilize its behavioral model with a validation module to detect any malicious modification in the program. Safeguarding the data and devices during execution time is a new solution without using external hardware circuitry or expensive cryptographic techniques, thus the overall cost of securing the device decreases.

2 Related Work

Information digitization for providing quick access increases the risk of losing personal data; few relevant risks are described in [3]. A tremendous amount of work has been done to present the potential security threat faced by embedded systems and people have proposed different approaches to solve the problem of limited resources. A method to detect abnormalities in embedded devices using on-chip debug information is demonstrated in [4]. Software watermarks [5], provides a unique method to detect software piracy and protecting software intellectual property rights.

Digital Audio Forgeries is addressed by Yang [6], enlightens an approach to detect modifications in MP3 audio by monitoring its frame offsets. Panagakis and Kotropoulos [7] presented an intrinsic fingerprinting method for device identification using spectral features. Swaminathan [8] proposes the use of information hiding to improve computer system performance without modifying system set architecture. All these papers show that people are working on a single challenge, i.e., to enhance

security systems but all has unique approaches to solve the problem. This is because of the threat to security is itself a growing field with advancements in technology; smarter the devices is, smartest the treats will be. A similar concept of as described in this paper is discussed in [9] using unsupervised SOM, a well-known clustering method to monitor and identify program abnormalities.

Another detection method solely based on systems calls and PC values presented in [10,11] has some limitations and are pointed out in [12]. They claim that these limitations are more severe from embedded system's security point of view. Although some work has been done with similar concepts yet each is unique in a way of its implements part.

3 Threat Model

Attacks that aimed at harming software integrity by trying to modify or inject some malicious code [13] come in a category of code injection attacks. Buffer attack is the most common type of security threat that occurred in absence of proper upper limit check, i.e., when some loopholes are left untreated in programming or designing part. Two common conditions found in Buffer that should be checked are if input length exceeds the certain limit and if any internal variable used in a loop repeatedly checks the overflow condition. The buffer could be exploited easily by an attacker if its stack's address location and return addresses are modified and new return address has been pointed to the malicious code [14]. Sometimes, the return addresses are modified to point it to an existing library function; such attacks are called Return-to-lib attacks. These [15] attacks present a threat to sensitive data by blocking the screen and processing its own task in the background. The saved data in the memory is prone to severe threat since it blocks the screen and can steal the information by running codes in the background.

Since any unexpected code encountered by the embedded device will cause some deviation from original flow of program [16]. Some work is done to utilize characteristic behavior of CPI but none of these utilize it as to enhance the security of the device. The system traces using CPI monitor, execute programs continuously and can trace any behavioral difference uniquely at any instant of time. This algorithm is very promising for monitoring real-time systems which have a high risk of threat and data loss. Another important advantage that system trace provides is, it neither stores user data for unexpected behavior detection, nor does it require support from operating system [17]. Hence, it is capable of providing security benefits to any resource-constrained embedded device, irrespective of the application scenario it supports.

4 Algorithm for Detecting Abnormal Behavior

The implementation of this complete work relies on basic hardware circuitry and architecture of the device. Embedded devices have some specific architectural design based on which its processing speed and complexity are specified. For instance, from a software point of view, the way processors execute the programs can be classified on the basis of function call relationships which occur within the programs. From a hardware point of view, PC register value indicates program location in its code sequence and represents a control flow graph (CFG). By combining both the information; one from software analysis and other from hardware analysis, one can deduce complete architectural and programmable skeleton of the device. An overall featured data can be prepared with function call locations, PC values, and CFG.

Now, this extracted featured data can be utilized to monitor future iterations to validate if the device is compromised or not. Since this method relies only on the device in use and enables verification through both software and hardware trace, hence it provides two-way security to the device. It is highly probable that a device would be exploited either through software side or through hardware side, i.e., exactly by one means. All the new data is continuously monitored and compared with previous iterations to detect if any miss-match has occurred. And if so, it is treated as an attack. Thus, verifying the data in both profiles guarantees that all types of intruder attacks will be detected at an early stage. Hence, the proposed method is proved to be reliable and robust for any malfunctioning detection in the program or device. A common parameter CPI [18] is used to represent system's performance which is an average cycles-per-instruction (CPI) profile, defined as follows.

4.1 CPI Analysis

The average CPI of the processor can be calculated as the ratio of C\I, i.e., No. of cycles C, used for executing total instructions divided by total No. of instructions I, to be executed, in which No. of cycles depends upon time elapsed and processor's maximum clock frequency. CPI values are sensitive to jump and call instructions and shows significant increments with new function calls. If CPI profile shows abrupt changes, it shows the low performance of a processor or the embedded device. Also, No. of executed instructions within each function call defines the resolution of average CPI profile for that event. For instance, the value of I varies from 1 to n with n being a total length of a program so for larger values of I, fewer details of CPI

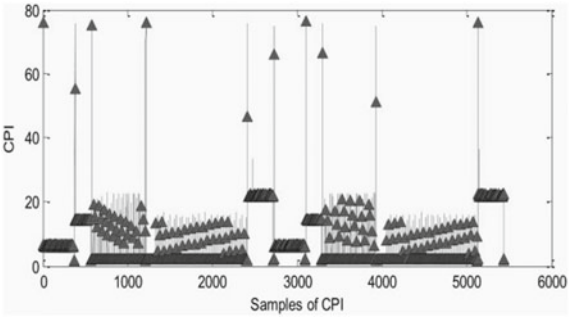

Fig. 1 CPI profile with local peaks

profile are obtained and minute variations are not clearly visible while for smaller values of I, detailed information of CPI profile is obtained and even minute variations are visible. This profile has high resolution to detect any unexpected behavior with small No. of instructions but will increase the computational complexity of the circuit. Hence, there is a trade-off between resolution and complexity and designer has to optimize this system according to the applications requirement.

4.2 Phase and Peak Detector Module

It is identified in two steps. The first is local critical point localizer and the second is global point localizer. The former is used to obtain each and every peak, and later is used to mark only significant peaks that are utilized to observe abnormal behavior in the program.

Local Critical Point Localizer For Peak Detection: First absolute difference d(n) between adjacent elements of CPI profile is calculated as

$$d(n) = |f_{mean}(n+1) - f_{mean}(n)|. \quad (1)$$

where f_{mean} denotes average CPI profile. Now with obtained values of array d(n), the absolute differences between adjacent CPIs; a new array is defined as diff(n) which contains all instantaneous d(n) values. Second, the maximum amplitude of d(n) is observed in diff(n) array. In this way, peak points are obtained for each CPI profile (Fig. 1). This method does not require any fixed threshold to measure the variation and hence is independent of variations scenarios in the program.

Global Critical Point Localizer For Phase Detection: From the array of absolute differences, elements whose value is greater than the mean value of diff[n], i.e., $(max(d)+min(d))/2$ are sorted out. These points represent phase changes at adjacent

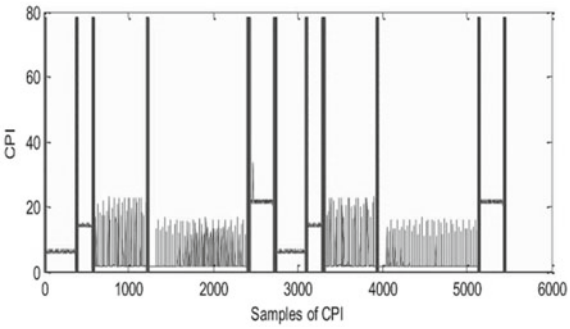

Fig. 2 CPI profile with global peaks

boundaries of average CPI profile and are stored in a phase array *p*. Then, using a similar method as used above absolute differences between phases is calculated and observed for maximum difference or maximum phase length (Fig. 2). These phase changes show major variations in phase at the boundaries along the complete CPI profile. The same global points are used to generate its corresponding PC values. The PC profile obtained is then used to train the similarity analyzer for testing and detecting of compromised programs.

4.3 Clustered Based Analyzer

In this block, a clustering algorithm is developed to partition data and grouped it according to its characteristics. The algorithm is chosen according to the application program. The following two domains are well verified and suitable to be used to cluster CPI data:

An Artificial Neural Network Technique: It includes algorithms like SOM, k-means, LVQ, and winner-take-all [19], etc., are suitable for large data sets, and they grow their clusters in an iterative manner from small size to larger one, use squared error criteria to reduce uncertainty but suffers from complexity of selecting seed for initial iteration. They are relatively less reliable and have stability issues but overall have an optimized performance with very short execution time.

A Fuzzy Logic-Based Fuzzy C-Means Algorithm: This algorithm perfectly removes above disadvantages and is very reliable and flexible to cluster data. It takes care of overlapping and ambiguity in input data by not forming strict boundaries and works well with any type of data. A detailed analysis of fuzzy logic is presented in [20]. It is suitable for applications where the input is highly unstable or uncertain like capturing environmental data through sensors. But it is also equally sensitive to the initial seed. Overall, it outperforms then all other algorithms and is very suitable to cluster CPI profile and detect abnormalities.

A well-known algorithm which is used to find minimum distance is described in [21]. The two arrays obtained above, d(n) and diff(n) are utilized in this block to obtain distance vectors. The points from the input data are grouped into a cluster based on a minimum distance criterion; a point is included in a cluster if it satisfies minimum distance or is associated with other clusters otherwise. The formula to calculate minimum distance D_{min} and maximum distance D_{max} are as follows:

$$D_{min} = \mu - (1+\alpha) * \sqrt{\frac{1}{N-1} \sum_{i=1}^{n} (D_i - \mu)^2}. \tag{2}$$

$$D_{max} = \mu + (1+\alpha) * \sqrt{\frac{1}{N-1} \sum_{i=1}^{n} (D_i - \mu)^2}. \tag{3}$$

Where D denotes an array of distances, i.e., absolute differences of distance measure between the test point and a cluster, α denotes a squared errors term to minimize any error that occurs due to nonlinearity of data, and u is average distance vector. The above equations result in distinct clusters based on their similarity, the most similar points are grouped together and least similar points are placed at a farther distance according to distance criteria defined above. This block is responsible to select an optimize clustering algorithm based on input data sets, and to cluster the data with well defined boundaries. Also, data sets obtained by first time running the program are used as a training set for further iterations in the clustering-based analyzer.

4.4 Validation Module

This stage is developed to validate the results of clustered data obtained from the analyzer. Since programs trace can never be exactly the same with original trace, the results are verified at the end also to improve the overall accuracy and precision. It considers each change which occurs in the output data of analyzer and validates it with original trace to check whether the program or device is compromised or not. The following is an algorithm given for validation of results.

```
Calculating the similarity between program's traces:
Input: A_k and A_k' are matrix arrays where k and k' are
original and testing phases respectively and A is an
array.
Output: To find similarity between phases k and k'.
A_k is sorted in descending order to reduce number of
comparisons in an array.
/* Lookup table for original vectors A_k */
For all elements in A_k do
If j^th element's occupancy rate > 5% then
diff (i) = j; /* save the j^th value in array d */
i ++;
End
End
/* Lookup table for original vectors A_k'*/
For all elements in A_k' do
If j^th element's occupancy rate > 5% then
diff' (i)=j; /* save the j^th value in array d' */
i ++;
End
End
/*generating validation output*/
If length (A_k)/length (A_k') > 85% then
Both phases are similar, validation = 1
Else
Phases are different, validation = 0
end
```

5 Experimental Setup and Observations

In this work, for verification and validation of the work, we simulate it on MATLAB. For the hardware setup, A MDK-ARM-based microcontroller kit is used which comprises Keil MCBSTM32F200 evaluation board and μVision IDE debugger. It is basically an ARM 32-bit Cortex-M3 series microcontroller. To download and debug, a Keil ULINKPro or ULINK2 USB-JTAG Adapter is used. It incorporates both a JTAG interface and a [Cortex Debug + ETM] interface. With the ULINKPro adapter, the Cortex Debug/ETM interface allows flash programming and instruction trace debugging. The Keil and JTAG adapter itself has sufficient features to provide complete hardware support for implementing the above project work. It is a full duplex, serial port to send data in/out from the microcontroller. It has 3 types of external memory, each with different capacity: 2 MB external SRAM, 8 MB external NOR Flash, and 512 MB external NAND Flash.

In the board, there is STM32F207IG chip placed near the peripheral ports. It acts as CPU for the microcontroller and can perform all the controlling and logical opera-

tions. It also provides communication between two or more microcontrollers without the host PC. It enables hardware–software synchronization and advanced embedded applications. The use of an on-board camera, microphone, digital modulation amplifier, antenna, etc., features can be used for networking and communication applications. This chip supports routing, sensors based communication and monitoring applications, IoT-based applications, and low power automation and detection. The board provides the facility of generating the trace. This tracing feature of the board is utilized in such a way as to generate specific trace data of the program. The proposed work is a novel method in a sense that the available resources in embedded devices are utilized to obtain a trace data. Then this obtained data is analyzed and processed in such a way as to detect program ambiguities and functions failure errors.

6 Conclusion

Providing the above architecture with external classifier/analyzer to cluster trace data, this system can work independently without requiring any operating system or high-cost external architecture. Since the device is self-sufficient for tracing system behavior and fulfills the criteria of the resource-constrained device, it can be considered a novel method to provide run-time security against malicious program injection, or other program abnormality. It is also useful in detecting any error, process/part of function failure or even system failure. This proposed work can be implemented in industries on FPGA boards and is highly scalable according to requirements and cost constraints. Few more functionality for wireless or routing applications can easily be added and for cost-effective implementation, it can be designed with minimum complexity without compromising with accuracy, precision, and reliability of the system. This method is self-sufficient, reliable, and robust and has much-added advantages over conventional cryptographic techniques.

References

1. Boufounos, P. and Rane, S.: November. secure binary embeddings for privacy preserving nearest neighbors. In: 2011 IEEE International Workshop on Information Forensics and Security (WIFS), pp. 1–6. IEEE (2011)
2. Hopkins, A.B., McDonald-Maier, K.D.: Debug support strategy for systems-on-chips with multiple processor cores. IEEE Trans. Comput. **55**(2), 174–184 (2006)
3. Deng, M., Wuyts, K., Scandariato, R., Preneel, B., Joosen, W.: A privacy threat analysis framework: supporting the elicitation and fulfillment of privacy requirements. Requirements Eng. **16**(1), 3–32 (2011)
4. Maier, K.D.: On-chip debug support for embedded systems-on-chip. In: Proceedings of the 2003 International Symposium on Circuits and Systems, ISCAS'03. vol. 5, pp. V–V. IEEE (2003)
5. Collberg, C., Carter, E., Debray, S., Huntwork, A., Kececioglu, J., Linn, C., Stepp, M.: Dynamic path-based software watermarking. ACM Sigplan Not. **39**(6), 107–118 (2004)

6. Yang, R., Qu, Z., Huang, J.: Detecting digital audio forgeries by checking frame offsets. In: Proceedings of the 10th ACM Workshop on Multimedia and Security, pp. 21–26. ACM (2008)
7. Panagakis, Y., Kotropoulos, C.: December. Telephone handset identification by feature selection and sparse representations. In: 2012 IEEE International Workshop on Information Forensics and Security (WIFS), pp. 73–78. IEEE (2012)
8. Swaminathan, A., Mao, Y., Wu, M., Kailas, K.: Data hiding in compiled program binaries for enhancing computer system performance. In: Barni, M., Herrera-Joancomartí, J., Katzenbeisser, S., Pérez-González F. (eds.) Information Hiding, vol. 3727. Springer, Berlin (2006)
9. Kohonen, T.: Learning vector quantization. In: Michael, A.A. (ed.) The Handbook of Brain Theory and Neural Networks, pp. 537–540. MIT Press (1998)
10. Arora, D., Ravi, S., Raghunathan, A., Jha, N.K.: Secure embedded processing through hardware-assisted run-time monitoring. In: Proceedings of the Conference on Design, Automation and Test in Europe-Volume 1, pp. 178–183. IEEE Computer Society (2005)
11. Handschuh, H., Schrijen, G.J., Tuyls, P.: Hardware intrinsic security from physically unclonable functions. In: Towards Hardware-Intrinsic Security, pp. 39–53. Springer, Heidelberg (2010)
12. Kolbitsch, C., Comparetti, P.M., Kruegel, C., Kirda, E., Zhou, X.Y., Wang, X.: Effective and efficient malware detection at the end host. In: USENIX Security Symposium, pp. 351–366 (2009)
13. Studnia, I., Nicomette, V., Alata, E., Deswarte, Y., Kaâniche, M., Laarouchi, Y.: Survey on security threats and protection mechanisms in embedded automotive networks. In: 2013 43rd Annual IEEE Dependable Systems and Networks Workshop (DSN-W) (2013)
14. Costin, A., Zaddach, J., Francillon, A., Balzarotti, D., Antipolis, S.: A large-scale analysis of the security of embedded firmwares. In: USENIX Security Symposium, pp. 95–110 (2014)
15. Tran, M., Etheridge, M., Bletsch, T., Jiang, X., Freeh, V., Ning, P.: On the expressiveness of return-into-libc attacks. In: Recent Advances in Intrusion Detection, pp. 121–141. Springer, Heidelberg (2011)
16. Ravi, S., Raghunathan, A., Chakradhar, S.: Tamper resistance mechanisms for secure embedded systems. In: 2004 Proceedings. 17th International Conference on VLSI Design, pp. 605–611. IEEE (2004)
17. Zhai, X., Appiah, K., Ehsan, S., Howells, G., Hu, H., Gu, D., McDonald-Maier, K.D.: A method for detecting abnormal program behavior on embedded devices. IEEE Trans. Inf. Forensics Secur. **10**(8), 1692–1704 (2015)
18. Eyerman, S., Eeckhout, L., Karkhanis, T., Smith, J.E.: A performance counter architecture for computing accurate CPI components. ACM SIGOPS Oper. Syst. Rev. **40**(5), 175–184 (2006). ACM
19. Nowlan, S.J.: Soft competitive adaptation: neural network learning algorithms based on fitting statistical mixtures (1991)
20. Ahmed, M.N., Yamany, S.M., Mohamed, N., Farag, A.A., Moriarty, T.: A modified fuzzy c-means algorithm for bias field estimation and segmentation of MRI data. IEEE Trans. Med. Imaging **21**(3), 193–199 (2002)
21. Davies, D.L., Bouldin, D.W.: A cluster separation measure. IEEE Trans. Pattern Anal. Mach. Intell. **2**, 224–227 (1979)

Performance Analysis of Comparator for IoT Applications

Mansi Jhamb, Tejaswini Dhall and Tamish Verma

Abstract Wearable devices are a boon for uninterrupted real-time monitoring of personal health. Cost, power consumption, and limited device dimensions are the critical issues which need to be handled carefully while designing these battery-powered devices. These devices involve high-end processors dedicated for complex signal processing. The arithmetic units like comparators constitute the core of data path and an addressing unit for these processors. This work exhaustively compares the latest version of comparators pertaining to the application of low-power, high-speed wearables. The analysis is performed using HSPICE environment at 90 nm process technology. The critical path delay of the dynamic version turns out to be 17.63% less than static. The power consumption of static comparator is 66.66% less as compared to dynamic counterpart.

Keywords Asynchronous · Comparators · Power · Delay · Layout area · Process voltage temperature (PVT) · Complementary metal oxide semiconductor (CMOS) Differential cascode voltage switch logic (DCVSL) · Integrated circuit (IC)

1 Introduction

The wireless body area network (WBAN) is a wireless sensor network supporting a wide range of latest wearable devices for healthcare and biomedical applications. These WBAN's [IEEE 802.15.6] comprise sensors, batteries, transceivers, and embedded DSP processor. The core of every digital signal processing is its data path. Hence, designing an area–delay–power efficient system guarantees a high-end

M. Jhamb · T. Dhall (✉) · T. Verma
USICT, GGSIPU, New Delhi, India
e-mail: tejaswini.dhall1994@gmail.com

M. Jhamb
e-mail: mansi.jhamb@ipu.ac.in

T. Verma
e-mail: tamish60@gmail.com

B. S. Rawat et al. (eds.), *Advances in Signal Processing and Communication* ,
Lecture Notes in Electrical Engineering 526,
https://doi.org/10.1007/978-981-13-2553-3_48

performance for wearable [1–5]. The comparator is the most commonly used application in wearable technology [6]. A large conglomeration of algorithms that have been implemented for comparison purposes [7–9]. The rapidly emerging IoT industry strives for low-power, high-speed devices. Comparator acts as an indispensable unit in the analog-to-digital conversion employed in wearables. These comparators are primarily responsible for delay incurred and power consumption of ADC. A high-speed, low-power comparator is highly desired to satisfy the power and delay constraints of future wearables. This work exhaustively compares the latest version of comparators [10, 11]. Asynchronous circuit design are inherently low power due to the absence of a global synchronizing signal [12]. They offer high throughput and are highly immune to PVT variations due to the absence of clock synchronization [13]. Section 2 explains state-of-the-art comparator design. Section 3 explains and compares the simulation and performance analysis of the static and dynamic adders.

2 Conventional Comparators

A comparator compares a given set of input entities, for example, X (X1, X2, X3… Xn, etc.) is a given set that is to be compared with an unknown value such as Y (Y1, Y2, Y3 …. Yn, etc.) and yields an output according to the result of comparison.

2.1 State-of-the-Art Comparators

For comparing a given pair of bits, Exclusive-NOR gates are employed for implementation of comparators. While comparing variables against or binary or BCD values, the "magnitude" of the values, a logic "0" and logic "1" are shown.

A magnitude comparator with (X and Y) inputs of 1-bit will generate three comparing outputs as shown in Fig. 1 [14, 15].

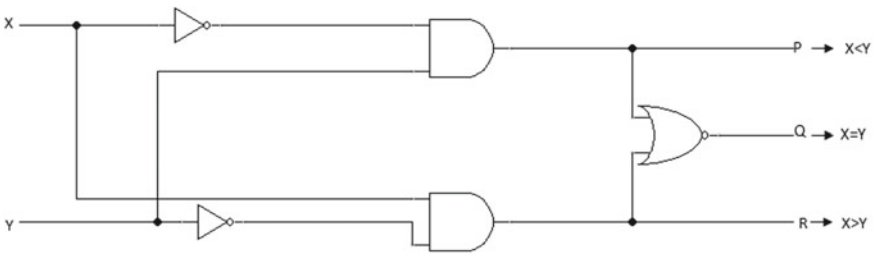

Fig. 1 Basic comparator

2.2 1-Bit Comparator

This combinational circuit comparing two input voltages; it is used in most microprocessors and microcontrollers in the ALU (Arithmetic Logic Unit). It is also used in oscillators, detectors and analog-to-digital converters (ADC). This work exhaustively compares the two latest versions of comparators, i.e., static and dynamic comparators. It is the application which decides which of them will be employed. Figures 2 and 3 show a schematic of static and dynamic comparators [16, 17].

Using 1-bit comparator, we can also implement 3-bit comparator model. The Fig. 4 shows the same.

3-bit comparator circuit works according to Eqs. (1)–(3)

$$\begin{aligned} \text{GREATER} = &\left((A_2 \text{ x or } B_2) + A_1' + B_1\right)' + \left(A_2' + B_2\right)' \\ &+ \left(\left(A_2' \text{ x or } B_2\right) + (A_1 \text{ x or } B_1) + A_0' + B_2\right)' \end{aligned} \tag{1}$$

$$\text{EQUAL} = (A_2 \text{ xnor } B_2) \times (A_1 \text{ xnor } B_1) \times (A_0 \text{ xnor } B_0) \tag{2}$$

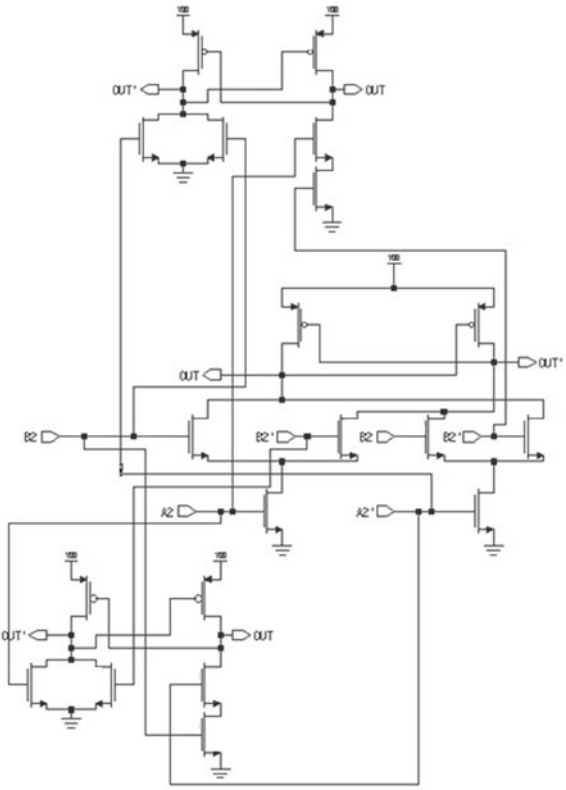

Fig. 2 Bit static comparator circuit implemented using DCVSL

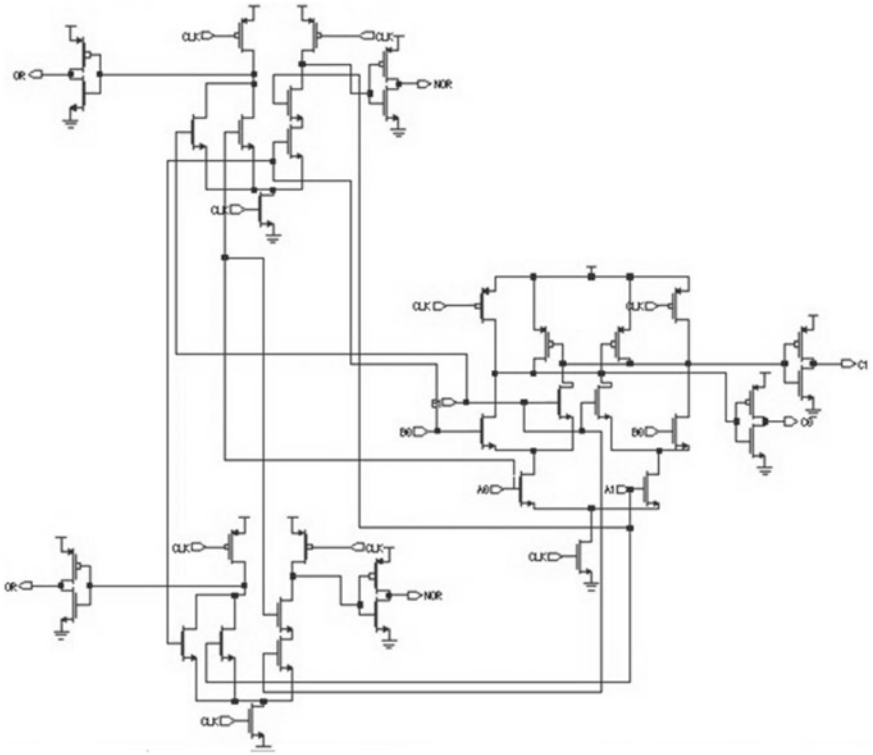

Fig. 3 1-bit dynamic comparator circuit implemented using domino logic

$$\text{LESSER} = \left((A_2 \text{ xor } B_2) + A_1 + B_1'\right)' + \left(A_2 + B_2'\right)' + \left((A_2 \text{ xor } B_2) + (A_1 \text{ xor } B_1) + A_0 + B_0'\right)'. \quad (3)$$

3 Performance Analysis of the Comparators

The asynchronous designs have inherently an advantage over synchronous counterparts. The asynchronous devices consume less power and are quite faster. The clockless system works according to the actual delays of the elements of the system. In asynchronous implementation of the system, we have T_{plh} and T_{phl} which indicate the time for processing the input when the output goes low to high and high to low.

The complete processing time for one cycle is given in Eq. 4.

$$T_{pa} = T_{plh} + T_{phl} \quad (4)$$

where T_{pa} = processing time of the asynchronous device

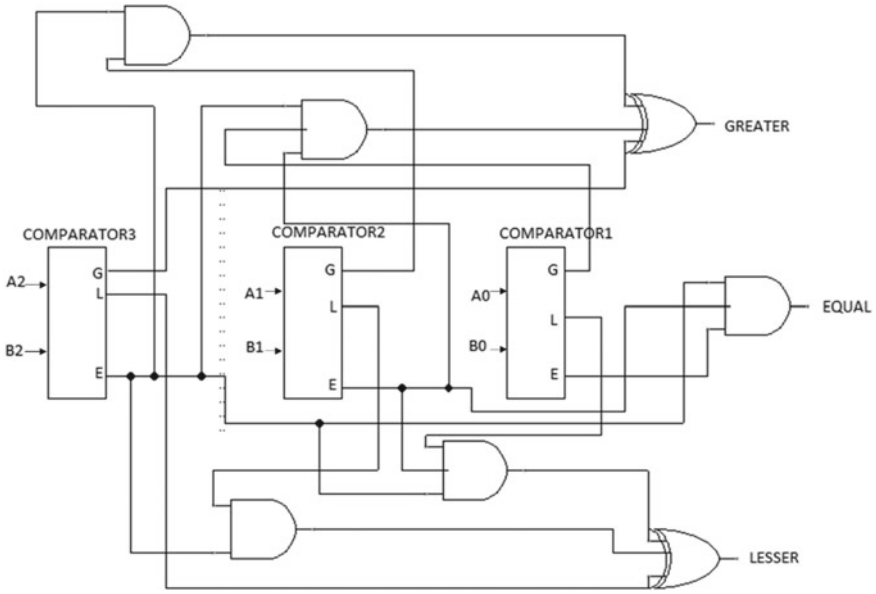

Fig. 4 3-bit comparator model

For synchronous devices, processing time taken for the cycle is given in Eq. 5.

$$T_{ps} = T_{plh} + T_{plh} = 2T_{plh} \tag{5}$$

where T_{ps} = processing time of the synchronous device

The cycle time for asynchronous is less as compared to synchronous.

$$T_{pa} < T_{ps}$$

Static power dissipation basically means the power dissipated during the steady-state condition, whereas dynamic power dissipation means power dissipated during transient state conditions. In static case, a transistor is either on or off as they are not switching from one state to another hence power dissipated is less as compared to dynamic circuits but practically there is a leakage current in static circuits even if the transistor is off.

Whereas if we see dynamic circuit they are faster than static, this also improves the transistor sizing. Since the dynamic circuit is implemented using domino logic parasitic capacitances which are smaller and which further gives high operating speed.

The spice level simulations were carried out on HSPICE using 90 nm TSMC CMOS. All the designs were simulated with extracted wire and layout parasitic. In order to satisfy the delay constraints, the MOSFETs with minimum size are employed

Table 1 Performance analysis of comparators

Implementation style	Power (μw)	Delay (ns)	PDP (watt-s)	Transistor count	Layout area (μm^2)
Static	417.38	288.96	1204.632	25	174.138
Dynamic	848.32	199.63	1693.50	37	324.439

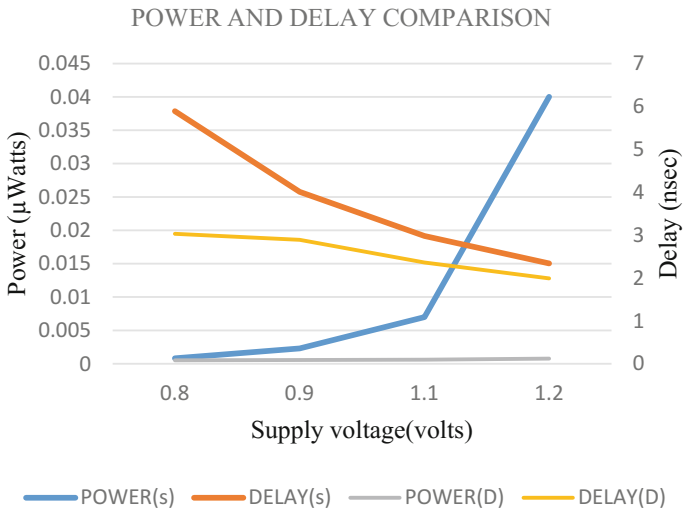

Fig. 5 Power and delay comparison of static and dynamic circuits

in the design. Though increasing the transistor size improves our speed but it also contributes to the increased power dissipation as the load capacitances increases. Thus, we have used the minimum size of TSMC 90 nm CMOS process (W/L = 180/90 nm). Our results show that there exists a trade-off between delay and power consumption. With the results, we may determine the maximum delay is observed at minimum power consumption.

The performance analysis of static and dynamic comparators are shown in Table 1.

The power and delay of static and dynamic circuits are shown in Fig. 5.

The layout of static comparator is presented in Fig. 6.

The dynamic comparator's layout is presented in Fig. 7.

After the physical layout designing, post-layout simulations are performed with the extractions of parasitic. Layout design is a schematic of the integrated circuit(IC) which depicts the accurate position of the PMOS and NMOS for fabrication. Layout designs also tell about the area consumption of a circuit. Area of static circuit is 46.32% less as compared to dynamic circuit which shows that static comparators are more superior in terms of area when compared to dynamic comparators.

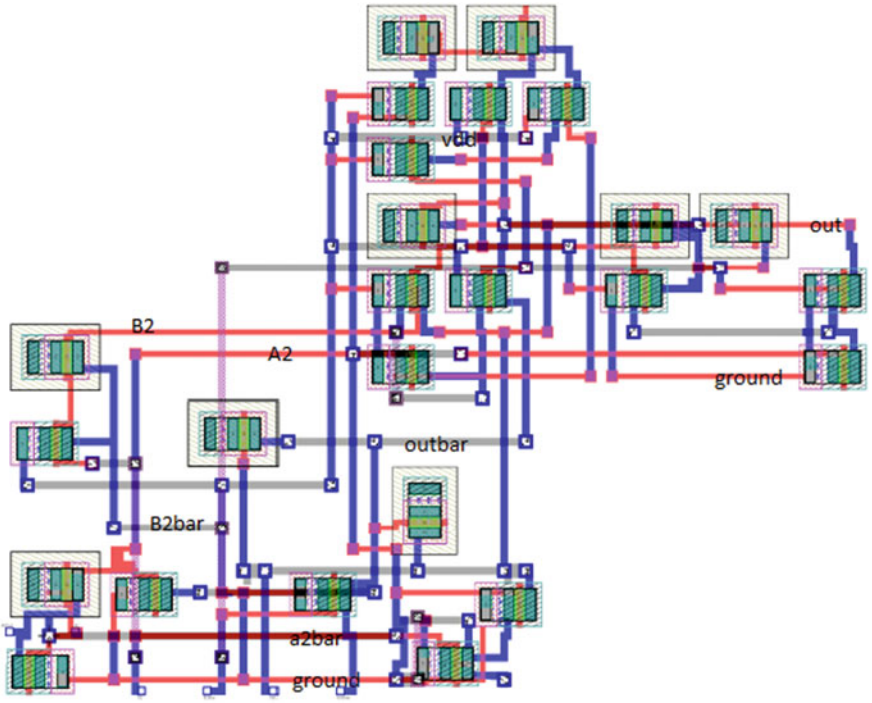

Fig. 6 Layout of static comparator

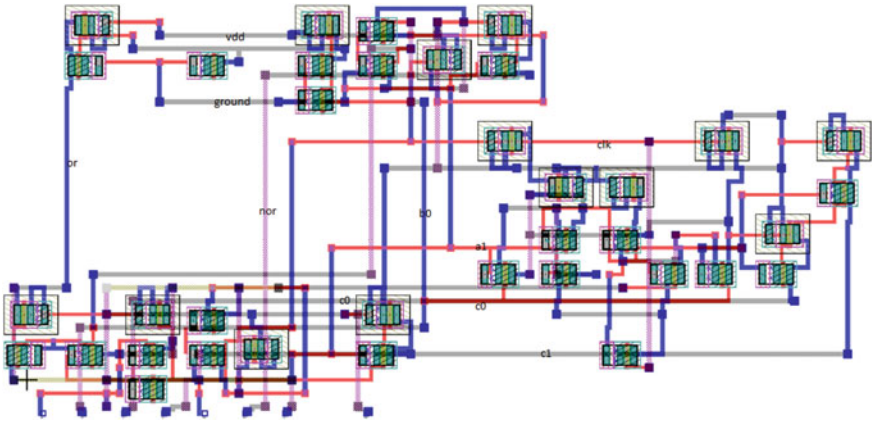

Fig. 7 Layout of dynamic comparator

4 Conclusion

IoT, i.e., Internet of things is an amalgamation of software, communication network and embedded devices. In IoT-based applications, the sensors are used to collect and forward data to system through microcontroller for processing. These microcontrollers use comparators for various computations. Dynamic comparator which offers lesser delay are used in those systems where the time constant of sensor is susceptible to changes in various physical parameters and the performance of the control system depends on the feedback signal measured from the sensors. Also, IoT applications require wireless, remote, or mobile solutions where lower power management is a major challenge. In such applications, static comparators can be used in designing the system as they offer less power consumption. As IoT devices work with timing and power constraints. It is the application which determines which of the comparator needs to be employed in the design. The constraints of cost, power consumption, and limited device dimensions are the critical issues which must be handled carefully while designing these battery-powered devices. For low-power applications, the static comparator is the preferred choice as it provides power savings up to 66.66%. For high-speed applications, the dynamic comparator is the most suitable candidate as it provides speed gain by 17.63%.

5 Future Scope

We plan to further investigate the possibilities of comparators in low-power high-speed wearable devices. By analyzing the relative performance metrics of static and dynamic comparators, the results were obtained in this paper. We can draw some indicative relations for the performance of low-power low-voltage comparators. The existing topologies can be investigated with the topologies mentioned in the paper for future work.

References

1. Sparso, J.: Asynchronous Circuit Design. Technical University of Denmark, A Tutorial (2006)
2. Nagyn, L., Stopjakova, V., Zalusky, R.: Completion detection in dual-rail asynchronous systems by current-sensing. Microelectron. J. **44,** 538–544 (2013). Science Direct
3. Xia, Z., Hariyama, M., Kameyama, M.: Asynchronous domino logic pipeline design based on constructed critical data path. IEEE Trans. Very Large Scale Integr. (VLSI) Syst. **23**, 619–630 (2014). IEEE
4. Jhamb, M., Gitanjali: Efficient adders for assistive devices. Eng. Sci. Technol. Int. J. **20**, 95–104 (2017). Science Direct
5. Wuu, T.-Y., Vrudhula, S.B.K.: A design of a fast and area efficient multi-input Muller C-element. IEEE Trans. VLSI Syst. **1**(2), 215–219. (1993). IEEE Press

6. Yun, K.Y., Dooply, A.E., Arceo, J., Beerel, P.A., Vakilotojar, V.: The design and verification of a high-performance low control- overhead asynchronous differential equation solver. In: Proceedings of the International Symposium on Advanced Research in Asynchronous Circuits and Systems. IEEE, Computer Society Press (1997)
7. Koren, I.: Computer Arithmetic Algorithms. A. K, Peters (2002)
8. Parhami, B.: Computer Arithematic - Alogorithms and Hardware Design, Oxford University Press (2000)
9. Ergecovac, M., Lang, T.: Digital Arithematic, Morgan Kauffman (2003)
10. Krishnan, P.M., Mustaffa, M.T.: A low power comparator design for analog-to-digital converter using MTSCStack and DTTS techniques. In: Ibrahim, H., Iqbal, S., Teoh, S., Mustaffa, M. (eds,) 9th International Conference on Robotic, Vision, Signal Processing and Power Applications. Lecture Notes in Electrical Engineering, vol 398. Springer, Singapore (2017)
11. Rai, A., Venkatesan, B.A.: Analysis and design of high speed low power comparator in ADC. Int. J. Eng. Dev. Res. **2**(1), 103–109 (2014)
12. Cheng, F.-C.: Practical design and performance evaluation of completion detection circuits. In: Proceedings of the International Conference on Computer Design: VLSI in Computers and Processors, ICCD'98, pp. 354–359 (1998)
13. Chung, S.H., Furber, S.: The design of the control circuits for an asynchronous instruction prefetch unit using signal transition graphs. In: Yakovlev, A., Gomes, L., Lavagno, L. (eds.) Hardware Design and Petri Nets, pp. 171–190. Springer, Boston (2000)
14. Nagy, L., Stopjakova, V., Brenkus, J.: Current sensing completion detection in single rail asynchronous systems. In: Computing and Informatics, vol. 33, pp. 1116–1138. Computing informatics (2014)
15. Chengwei, D., Yucchao, N.: 3 bit comparator design. In: Submicron project, SoC (2005)
16. Murotiya S.L., Gupta A., Vasishth S.: Novel design of ternary magnitude comparator using CNTFETs In: 11th IEEE India Conference: Emerging Trends and Innovation in Technology, pp. 1–4. IEEE, INDICON (2014)
17. Anjuli, Anand, S.: 2-Bit Magnitude Comparator Design Using Different Logic Styles, vol. 2, pp. 13–24. IJESI (2013)

Adiabatic Logic Based Full Adder Design with Leakage Reduction Mechanisms

Dinesh Kumar and Manoj Kumar

Abstract In this paper, two-phase clocked adiabatic static CMOS logic (2PASCL), stack effect, and body bias techniques have been used for the optimization of a full adder. Based on the above techniques four designs of a full adder, A1 with adiabatic logic, A2 with stack transistor, A3 with body bias, and A4 with stacking + body bias have been implemented. The performance of optimized and existing designs has been evaluated in 0.18 μm CMOS technology. The optimized designs show a significant improvement in power delay product (PDP) in the range of $(25.33 - 84.49) \times 10^{-24}$ J for A1, $(50.21 - 167.32) \times 10^{-24}$ J for A2, $(52.65 - 109.16) \times 10^{-24}$ J for A3 and, $(36.00 - 81.56) \times 10^{-24}$ J for A4 as compared to $(76.14 - 254.03) \times 10^{-24}$ J of existing 1-bit hybrid full adder with a varying voltage range (1.2–2.8 V), respectively. Simulation results of optimized designs have been compared with the best reported existing designs in literature and optimized designs outperform in terms of PDP with temperature and voltage variations.

Keywords Adiabatic logic body bias · CMOS · Low power full adder
Power delay product · Stack effect

1 Introduction

Ultralarge-scale integrated circuits become the backbone of the modern electronics industry. Portable electronic devices such as personal digital assistants (PDAs), biomedical implantable devices, memories, and high-speed data processors demand prolonged battery life. The demand for battery life for the aforementioned circuit applications can be fulfilled by decreasing the power dissipation. As the feature size

D. Kumar (✉) · M. Kumar
University School of Information, Communication and Technology, Guru Gobind Singh Indraprastha University, New Delhi, Delhi, India
e-mail: dinesh4saini@gmail.com

M. Kumar
e-mail: manojtaleja@ipu.ac.in

B. S. Rawat et al. (eds.), *Advances in Signal Processing and Communication* ,
Lecture Notes in Electrical Engineering 526,
https://doi.org/10.1007/978-981-13-2553-3_49

is decreasing day by day with scaling, the power performance of the system attracts researches attention in both static and dynamic mode of operation. Power dissipation during an idle condition of the circuit is a major concern for researchers due to increased leakages with improved scaling [1, 2]. Full adder has a great importance in arithmetic and logic circuits which are the fundamental building blocks of modern electronic systems. Therefore, the power–delay characteristic of full adder attracts the researcher's attention over the years [3]. Different types of full adders with several logic styles have been implemented in [4–8]. Each logic style has their importance with some bottlenecks such as complementary pass transistor logic (CPL) shows good voltage swing [5, 6]. However, the high transistor count (32) with a low power delay product (PDP) makes it less impressive. Static complementary metal oxide semiconductor (CMOS) based adder is robust against voltage scaling at the cost of high input capacitance [9]. With these conventional designs transmission gate (TG) based full adder [7, 8] is used to design logic circuits. For ultralow power applications, subthreshold adiabatic logic has been reported in [10]. Some adder designs have been implemented with two or more logic style to increase power delay performance and termed as hybrid logic style. Hybrid pass logic with static CMOS output drive (HPSC) is used to design full adder [11]. In this paper, the problem of increasing leakages with improved scaling has been addressed with the stacking of transistors and body biasing techniques. A two-phase clocked adiabatic static CMOS logic (2PASCL) [12] based X-NOR gate has been proposed. Use of adiabatic logic promises the reduction in power without scaling. A 2PASCL X-NOR-based hybrid 1-bit full adder has been presented in this paper. The proposed designs have been compared with existing hybrid 1-bit full adder design [13].

1.1 Fundamental Elements of Adder and Operation

A full adder fundamentally adds three input bits with two output bits as sum and carry. Conventionally, a full adder comprised of three modules as shown in Fig. 1. Two modules consist of X-OR/X-NOR gate and responsible for SUM output. In the third module, generally, multiplexer is used for carry calculation. For a full adder let, the three input bits are *A, B,* and, *C*. The logical expressions for output bits sum and carry are given as follows.

1.2 Adiabatic Logic, Stack Effect, and Body Bias

The term adiabatic is associated with classical thermodynamics in which the state transfer of a system takes place without loss or gain of heat. Conventionally in a CMOS inverter, the total CV_{dd}^2 energy is required during the transition from the supply. Half of this energy ($1/2CV_{dd}^2$) is consumed by PMOS due to its ON state resistance for charging the node capacitance up to the same level of energy ($1/2CV_{dd}^2$).

$$Sum = A \oplus B \oplus C$$
$$Carry = AB + BC + CA$$

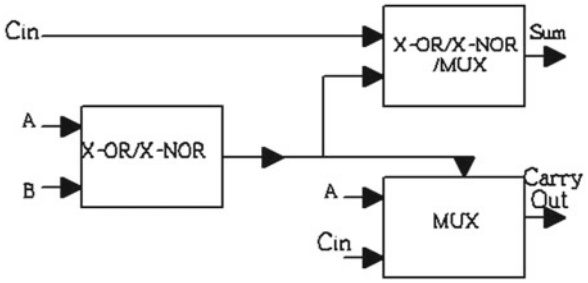

Fig. 1 Full adder

Fig. 2 Stacking of transistors

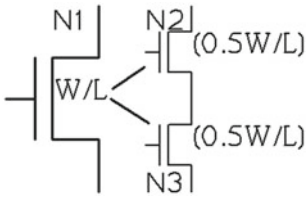

The stored energy in the node capacitance goes to the ground via NMOS during discharging and wasted away. Adiabatic logic utilizes the stored energy by recycling it back to the power supply which increases the power efficiency [12]. Stacking of transistors is used where more than one transistor OFF in a path from the supply voltage to ground. In this technique, two transistors are used instead of one with half W/L of the original one and this combination reduces the leakage power dissipation than a state with only one as shown in Fig. 2 [4]. Body bias technique affects the threshold voltage by changing the source-bulk voltage according to the following equation and reduces the leakages [4].

$$V_{th} = V_{th0} + \gamma\left(\sqrt{|-2\emptyset_F + V_{SB}|} - \sqrt{|-2\emptyset_F|}\right) \quad (1)$$

.

2 Proposed Designs

2.1 2PASCL X-NOR

In this work, a new eight-transistor X-NOR gate, which consists of 2PASCL-based inverter for the implementation of full adder design has been proposed. Operation of this X-NOR gate is based on the functioning of 2PASCL-based inverter, which is demonstrated in Fig. 3. This comprised of two power supply clocks PC and $\overline{PC}$ with

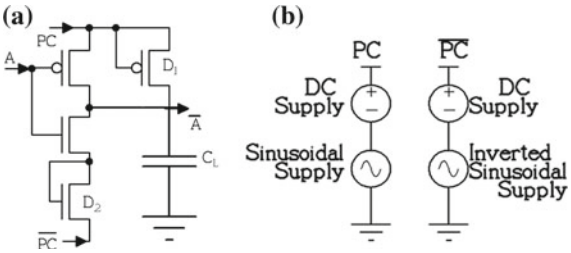

Fig. 3 **a** 2PASCL-based Inverter **b** Power clock supplies

two extra MOS transistors which function as diodes D_1, D_2. These MOS transistors (D_1, D_2) help to recycle the stored energy from load capacitance. Power clock supplies are complementary with the each other and the magnitude of both power clock supplies is determined by (2) and (3) [8].

$$V_{PC} = \frac{V_{DD}}{4}\sin(\omega t + \theta) + \frac{3}{4}V_{DD} \tag{2}$$

$$V_{\overline{PC}} = \frac{V_{DD}}{4}\sin(\omega t + \theta) + \frac{1}{4}V_{DD} \tag{3}$$

It is depicted in (2) and (3) that power performance will be improved with the decreased node voltage difference as the magnitude of V_{PC} is twice of $V_{\overline{PC}}$. In the proposed design, split level clock supply is used which alleviates slow charging/discharging of load capacitance consequently minimizes the energy loss. The functioning of this design can be explained in two steps, i.e., evaluation and hold. During evaluation when output is low and pull-up network turns ON, the charging of load capacitance C_L takes place via PMOS and output goes HIGH. When the output is high and pull-down network turns ON charge transfer takes place to $V_{\overline{PC}}$ via NMOS and D_2. In the hold step, if the input is bound to be stable then there will be no transition at the output node capacitance consequently, reduces switching activity and results in decreased energy loss.

2.2 Results and Performance Evaluation

In this article, 0.18 μm CMOS technology has been used for the simulation of all designs. The results of all designs have been compared and analyzed with varying power supply and temperature. The new 2PASCL-based design of full adder which consists of 20 transistors is shown in Fig. 4a. The stack transistors based full adder design are illustrated in Fig. 4b. Body biasing with the stacking of transistors is given in Fig. 4c. The design of the 1-bit hybrid full adder has been simulated for comparison and shown in Fig. 4d.

Power and delay results have been given in Tables 1 and 3 with temperature and supply voltages variations, respectively. The results of all designs in terms of PDP

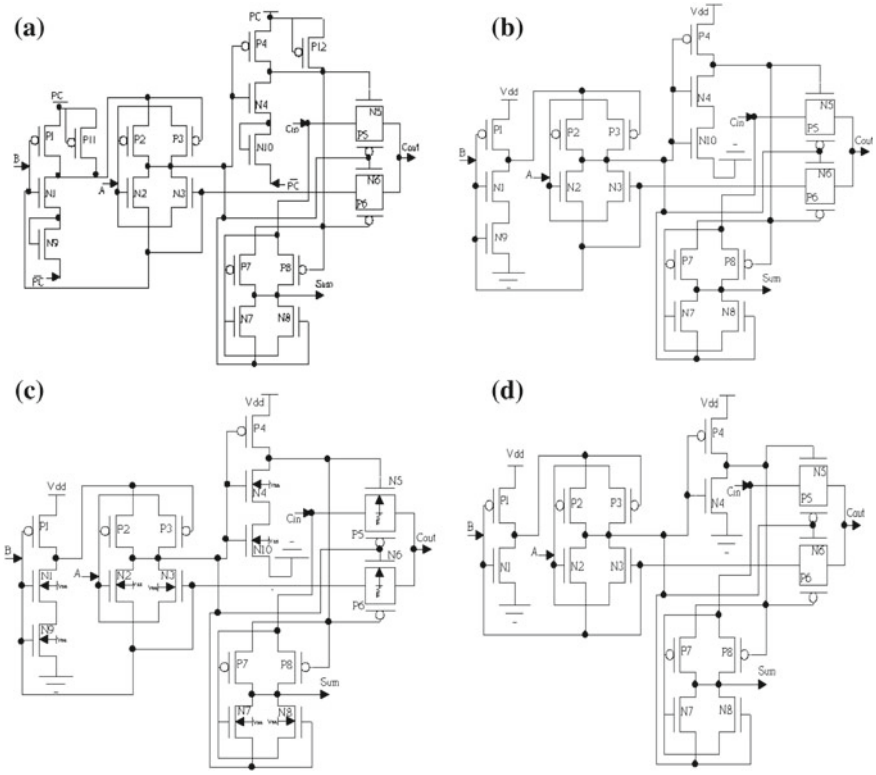

Fig. 4 Full adder designs, **a** A1, **b** A2, **c** A4, **d** Existing

have been computed with the help of Tables 1 and 3 and analyzed in Tables 2 and 4 with temperature and supply voltage variations respectively. The graph in Fig. 5 shows the performance in terms of PDP with existing designs with a temperature range of 10–60 °C, whereas Fig. 6 shows with a supply voltage variation of 1.2–2.8 V.

2.3 Comparison with Existing Designs

The new design which consists of 2PASCL has been compared with the existing design of 1-bit hybrid full adder reported in [13]. Power delay characteristics of this reported design [13] show better performance as compared to other designs which are reported in the literature earlier. Therefore, it is obvious that our proposed designs perform better as compared to existing designs. Table 5 shows the comparison in terms of power delay characteristics.

Table 1 Power (pW) and delay (pS) comparison at varying temperature

	Adiabatic (A1)		Stacking (A2)		Body biasing (A3)		Stacking + body biasing (A4)		Existing	
Temperature (°C)	Power	Delay	Power	Delay	Power	Delay	Power	Delay	Power	Delay
10	47.33	0.72	85.26	0.60	63.94	0.94	66.14	0.62	93.26	0.88
15	52.68	0.73	95.15	0.60	65.93	0.95	68.11	0.63	105.18	0.90
20	59.15	0.75	107.06	0.61	68.39	0.97	70.53	0.64	119.50	0.91
25	66.93	0.76	121.30	0.62	71.43	0.98	73.54	0.65	136.63	0.93
30	76.28	0.79	138.28	0.64	75.24	1.01	77.30	0.66	157.01	0.95
35	87.53	0.82	158.52	0.65	80.08	1.04	82.13	0.68	181.22	0.98
40	101.13	0.86	182.71	0.67	86.44	1.07	88.55	0.70	210.01	1.02
45	117.84	0.91	211.89	0.70	95.18	1.12	97.52	0.73	244.45	1.06
50	138.86	0.96	247.70	0.74	107.87	1.18	110.82	0.76	286.15	1.11
55	166.30	1.01	292.87	0.77	127.38	1.24	131.70	0.81	337.18	1.16
60	203.85	1.06	352.09	0.89	158.95	1.30	166.13	0.84	403.80	1.21

Table 2 PDP ($J \times 10^{-24}$) comparison at varying temperature

Temperature (°C)	Adiabatic (A1)	Stacking (A2)	Body biasing(A3)	Stacking + body biasing (A4)	Existing
10	34.22	51.24	60.23	41.60	82.91
15	38.72	57.85	62.90	43.25	95.08
20	44.36	65.95	66.34	45.35	109.70
25	51.47	76.06	70.64	48.02	127.75
30	60.64	88.50	76.22	51.48	150.42
35	72.39	103.99	83.28	56.09	178.50
40	87.68	123.88	93.10	62.43	214.42
45	108.18	149.59	106.98	71.48	260.33
50	133.58	183.30	127.29	85.11	319.92
55	168.30	226.10	158.08	106.68	392.48
60	217.30	315.82	207.75	140.55	489.41

2.4 Waveforms

The waveform of all three-bit combinations used as input for full adder and output (sum and carry) of simulated designs is shown in Fig. 7. It is evident from the waveform that the proposed designs are functioning properly with output voltage level, above 0.929 V for high logic and below 0.565 V for low logic, which is considerable for adiabatic logic based designs for digital switching as reported in the literature.

Table 3 Power (pW) and delay (pS) comparison with supply voltage variation **(V)***

	Adiabatic (A1)		Stacking (A2)		Body biasing (A4)		Stacking + body biasing (A4)		Existing	
(V)*	Power	Delay	Power	Power	Delay	Delay	Power	Delay	Power	Delay
1.2	32.48	0.78	55.73	0.90	36.64	1.43	38.34	0.93	62.41	1.22
1.3	43.16	0.76	65.18	0.84	41.69	1.38	43.46	0.86	73.10	1.20
1.4	43.22	0.75	75.57	0.80	47.12	1.31	48.96	0.83	84.89	1.18
1.5	43.29	0.74	86.96	0.75	52.95	1.22	54.85	0.78	97.83	1.13
1.6	55.83	0.74	99.41	0.70	59.17	1.14	61.44	0.75	112.05	1.06
1.7	62.89	0.73	112.98	0.66	65.81	1.08	67.83	0.69	127.48	0.99
1.8	70.47	0.73	127.74	0.63	72.85	0.99	74.94	0.65	144.36	0.94
1.9	78.61	0.72	143.76	0.60	80.32	0.94	82.46	0.62	162.72	0.89
2.0	87.33	0.68	161.14	0.57	88.22	0.83	90.41	0.59	182.66	0.81
2.1	96.59	0.64	179.96	0.55	96.56	0.81	98.80	0.57	204.29	0.77
2.2	106.57	0.60	200.30	0.53	105.35	0.77	107.64	0.55	227.70	0.73
2.3	117.24	0.57	222.27	0.52	114.61	0.75	116.93	0.54	253.03	0.70
2.4	128.47	0.54	245.98	0.50	124.33	0.72	126.69	0.52	280.40	0.70
2.5	140.57	0.52	271.54	0.49	134.54	0.70	136.92	0.51	309.93	0.66
2.6	153.37	0.50	299.07	0.48	145.25	0.68	147.65	0.49	341.78	0.64
2.7	166.95	0.48	328.71	0.47	156.47	0.66	158.88	0.48	376.11	0.63
2.8	181.30	0.46	360.60	0.46	168.20	0.64	170.62	0.47	413.06	0.61

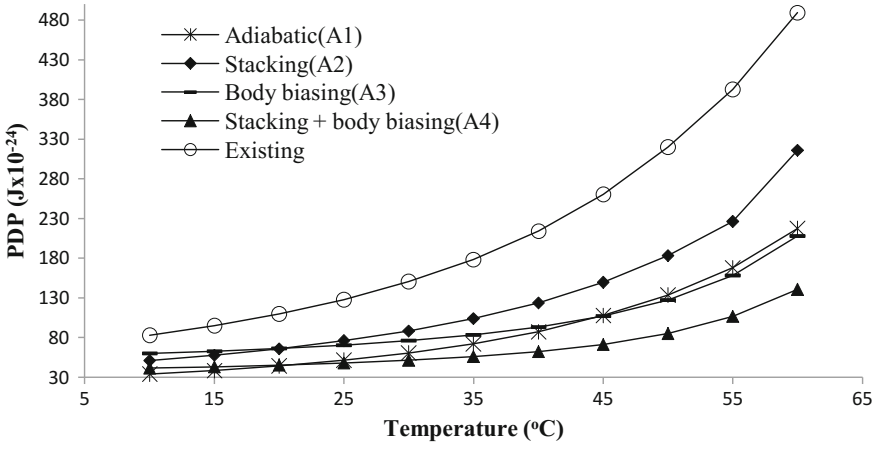

Fig. 5 Comparison of PDP at varying temperature

Table 4 PDP ($J \times 10^{-24}$) comparison at varying supply voltage

Supply voltage (V)	Adiabatic (A1)	Stacking (A2)	Body biasing (A3)	Stacking with body biasing (A4)	Existing
1.2	25.33	50.21	52.65	36.00	76.14
1.3	32.97	54.82	57.62	37.59	87.79
1.4	32.76	60.83	61.96	40.78	100.34
1.5	32.29	65.31	64.70	42.78	110.94
1.6	41.37	69.79	67.81	46.26	119.22
1.7	46.41	75.02	71.07	47.07	126.72
1.8	51.58	80.73	72.56	49.39	136.28
1.9	57.31	86.83	75.74	51.87	145.80
2.0	59.73	92.82	73.84	54.16	149.60
2.1	61.91	99.88	78.21	57.01	157.92
2.2	64.58	107.56	81.96	60.06	167.59
2.3	67.30	115.80	85.96	63.14	179.40
2.4	70.14	124.47	90.26	66.51	196.84
2.5	73.38	134.14	94.72	69.83	206.10
2.6	76.99	144.45	99.50	73.53	220.79
2.7	80.64	155.48	104.05	77.37	236.95
2.8	84.49	167.32	109.16	81.56	254.03

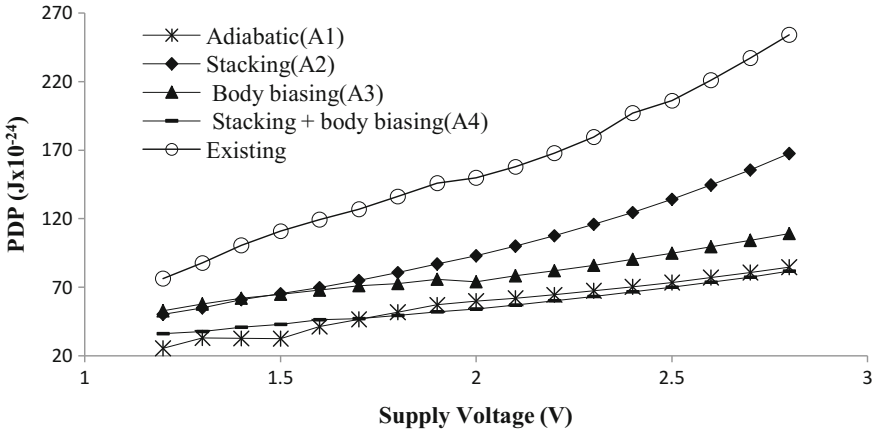

Fig. 6 Comparison of PDP voltage variation

Table 5 Comparison with existing designs at the 1.8 V supply voltage

Technology (μm)	PDP(J)	Design
0.18	51.58×10^{-24}	Adiabatic(A1)
0.18	80.73×10^{-24}	Stacking(A2)
0.18	72.56×10^{-24}	Body biasing(A3)
0.18	49.39×10^{-24}	Stacking + body biasing(A4)
0.18	136.28×10^{-24}	Existing [13]

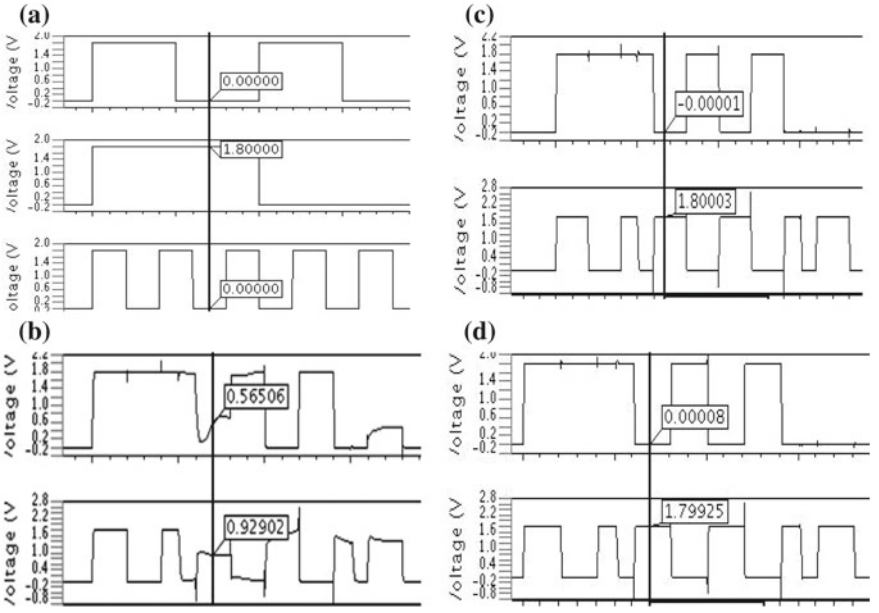

Fig. 7 Waveforms of **a** All three-bit combinations as input, carry and sum of a full adder, with **b** 2PASCL, **c** Stack + body bias, **d** Existing

3 Conclusion

With the consideration of limitations of scaling a new design of full adder using 2PASCL has been reported in this paper. The optimized designs show improved PDP of 51.58×10^{-24}J for A1, 80.73×10^{-24}J for A2, 72.56×10^{-24}J for A3, and 49.39×10^{-24}J for A4 as compared to 136.28×10^{-24}J of 1-bit hybrid full adder with a supply voltage 1.8 V, respectively. The implemented designs outperform in terms of PDP at stringent temperatures conditions. The improved performance of implemented designs as compared to the existing designs makes them a better candidate for low-power applications.

References

1. Taur, Y.: CMOS design near the limit of scaling. IBM J. Res. Dev. **46**(2.3), 213–221 (2002). https://doi.org/10.1147/rd.462.0213
2. Sery, G., Borkar, S., De, V.: Life is CMOS: Why chase life after? In: Proceedings of the IEEE/ACM International Design Automation Conference, pp. 78–83 (2002). https://doi.org/10.1109/dac.2002.1012598
3. Tung, C.K., Hung, Y.C., Shieh, S.H., Huang, G.S.: A low-power high-speed hybrid CMOS full adder for embedded system. In: Proceedings of IEEE Conference, Design Diagnostics Electronic Circuits and Systems, vol. 13, pp. 1–4, Krakow (2007). https://doi.org/10.1109/ddecs.2007.4295280
4. Rabaey, J.M., Chandrakasan, A., Nikolic, B.: Digital Integrated Circuits: A Design Perspective, 2nd edn. Pearson Education, Delhi, India (2003)
5. Radhakrishnan, D.: Low-voltage low-power CMOS full adder. IEEE Proc. Circuits Devices Syst. **148**(1), 19–24 (2001). https://doi.org/10.1049/ip-cds:20010170
6. Zimmermann, R., Fichtner, W.: Low-power logic styles: CMOS versus pass-transistor logic. IEEE J. Solid-State Circuits **32**(7), 1079–1090 (1997). https://doi.org/10.1109/4.597298
7. Chang, C. H., Gu, J. M., Zhang, M.: A review of 0.18-μm full adder performances for tree structured arithmetic circuits. IEEE Trans. Very Large Scale Integr. VLSI Syst. **13**(6), 686–695, NJ, USA (2005). doi: https://doi.org/10.1109/tvlsi.2005.848806
8. Shams, A.M., Darwish, T.K., Bayoumi, M.A.: Performance analysis of low-power 1-bit CMOS full adder cells. IEEE Trans. Very Large Scale Integr. VLSI Syst. **10**(1), 20–29 (2002). https://doi.org/10.1109/92.988727
9. Weste, N.H.E., Harris, D., Banerjee, A.: CMOS VLSI Design: A Circuits and Systems Perspective, 3rd edn. Pearson Education, Delhi, India (2006)
10. Chanda, F., Jain, M., De, S., Sarkar, C.K.: Implementation of Sub threshold adiabatic logic for ultra low-power application. IEEE Trans. Very Large Scale Integr. VLSI Syst. **23**(12), 2782–2790 (2015). https://doi.org/10.1109/tvlsi.2014.2385817
11. Zhang, J. Gu, Chang, C.H.: A novel hybrid pass logic with static CMOS output drive full-adder cell. In: Proceedings of International Symposium on Circuits Systems, pp. 317–320 (2003). https://doi.org/10.1109/iscas.2003.1206266
12. Anuar, N., et al.: Two phase clocked adiabatic static CMOS logic and its logic family. J. Semicond. Technol. Sci. **10**, 1–10 (2010). doi: https://doi.org/10.5573/JSTS.2010.10.1.001. Japan
13. Bhattacharyya, P., Kundu, B., Ghosh, S., Kumar, V., Dandapat, A.: Performance analysis of a low-power high-speed hybrid 1-bit full adder circuit. IEEE Trans. Very Large Scale Integr. VLSI Syst. **23**(10), 2001–2008 (2015). https://doi.org/10.1109/TVLSI.2014.2357057
14. De, V., Borkar, S.: Technology and design challenges for low power and high performance. In: Proceedings of IEEE/ACM International Symposium on Low Power Electronics and Design, pp. 163–168, San Diego, USA (1999). https://doi.org/10.1109/lpe.1999.799433

IP Protection of Sequential Circuits Using Added States Watermark with Property Implantation

Ankur Bhardwaj and Shamim Akhter

Abstract Watermarking is a technique which is used to verify the source of creation of a signal which may be in the form of an image, text, or video. There are many techniques for watermarking an intellectual property (IP) with their merits and demerits. In this paper, a watermarking algorithm is proposed for finite state machines by employing both properties implanting watermarking technique and extra added states watermarking technique in a combined way. This improves the security of intellectual property of a designer. Simulations and synthesis of state transition graph (STG) of FSM are performed on Xilinx ISE tool using Verilog HDL.

Keywords Watermarking · Finite state machines · Intellectual property
State transition graph

1 Introduction

Simulation of circuit designs for checking the execution of the circuit and verifying its functionality before actual synthesis of the circuit has become very useful for designers. At the same time, the availability of such simulation tools has provided a way for the attackers to tamper or attack the intellectual property of a designer. So there must be a way to protect the interest of an IP maker who gave time and put efforts to develop and implement an original design. Watermarking is used to verify the source of creation of a signal which may be in the form of an image, text, or video. A watermarking algorithm protects the original design from various attacks and provides a way to prove the authenticity and source of its creation in court of law.

A. Bhardwaj (✉) · S. Akhter
Department of Electronics and Communication Engineering,
Jaypee Institute of Information Technology, Noida, India
e-mail: bhardwaj.ankur09@gmail.com

S. Akhter
e-mail: shamim.akhter@jiit.ac.in

B. S. Rawat et al. (eds.), *Advances in Signal Processing and Communication* ,
Lecture Notes in Electrical Engineering 526,
https://doi.org/10.1007/978-981-13-2553-3_50

Almost every digital design used nowadays has some memory and a combinational logic like sequential and Finite State Machines (FSM) [1] are inherent part of the design. The FSM is represented with the help of a STG which shows all the states and transitions to and from each state. There are many watermarking algorithm for IP Protection of FSM. Oliviera uses a technique in which the watermark is embedded without affecting the functionality of the FSM [2]. This algorithm was used to watermark a sequence detector [3]. The problem with this technique is the usage of too many redundant states. Another issue is that anyone can use the design freely without any authorization. Lin Yuan et al. proposed a strategy in which extra watermarking states are added before the original FSM. Each state is associated with an input and output sequence as. This sequence is provided as a key to the client to use the FSM. If the client redistributes that key, then it is not possible to stop the unauthorized use of the design. Another algorithm uses a counter instead of adding extra states to the FSM [4]. The watermarking sequence is extracted from the inputs that are provided to the original FSM and a counter is attached to the state which is reached when we input the watermarking sequence. The counter gives a high value when the watermarking sequence is inputted for a certain number of times. This algorithm does not explain the case in which there are more than one path to reach a particular state. A complete survey of various watermarking techniques of FSM is given in literature [5].

In this paper, an algorithm is proposed which uses both property implanting technique [2] and added states technique [3]. Two signatures are embedded in the circuit. Out of two, one signature will be made public, in order to use the circuit and the other signature will be kept private. Paper is divided into four sections. Section 1 explains the watermarking techniques use in FSM. Section 2 explains the proposed algorithm. Simulation results and synthesis report are explained in Sects. 3 and 4 give the conclusion.

2 Watermarking in FSM

Consider a FSM of a sequence detector which detects a sequence “11011” (Fig. 1). The following techniques have been used on the proposed algorithm:

2.1 Property Implanting Watermarking [2]

In this technique, all the states of original FSM with Q states are copied to make a duplicate FSM with V states. Now both original and copied FSM are linked by adding few extra watermarking states {r1, r2, r3} which are traversed only when we input a certain signature sequence as shown in Fig. 2. The strength of watermark can be increased by increasing the length of signature, to check the authenticity, the IP owner needs to input the signature at the initial state of the FSM. If all the R states are

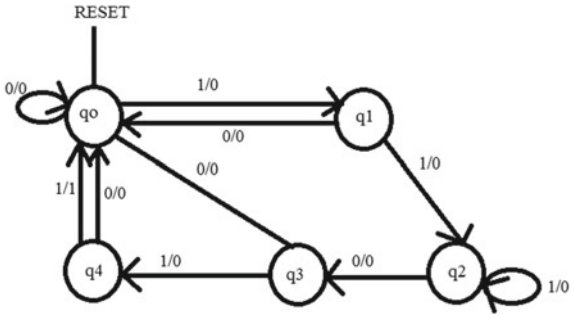

Fig. 1 STG of 5-bit sequence detector for the input 11011

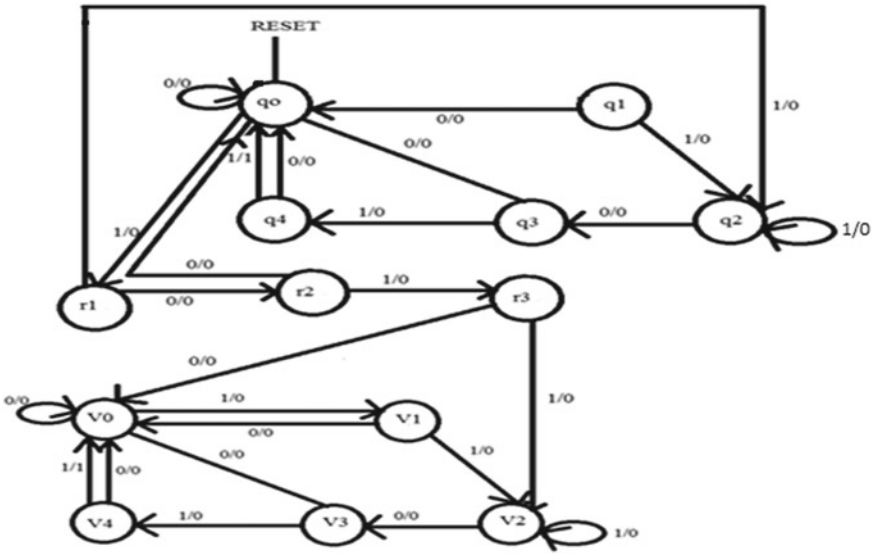

Fig. 2 STG of watermarked sequence detector with signature sequence 101

traversed, a detector circuit will provide a high value and the rightful ownership will be proved. The detector circuit consists of a counter which takes the state variable as input.

The technique suggested by Lin Yuan et al. is divided into two algorithms, namely Front-Added Watermarked States (FAWS) and Back-Added Watermarked States (BAWS) [1].

2.2 *Front-Included Watermarked States (FAWS)*

In this algorithm, extra W states are added before the initial state of the original FSM (Fig. 3.). These states are associated with a certain input/output pair, {0000/001, 1000/011, 0111/101, 0110/111}. This sequence acts as key which must be proved to the client. The client needs to enter this key then only the functionality of FSM can be accessed.

2.3 *Back-Added Watermarked States (BAWS)*

In this algorithm instead of adding states in front of the original FSM, W watermarking states are added between the original states and we duplicate the state which is reached after we input the final bit of the input sequence. In this case we copied w5 whose original state is q0. Now, these watermarking states are added to the original states using watermarking input/output pair (Fig. 4).

The key must be given to client to working of FSM. However, the client cannot be trusted, as he may share the code to other designers and IP of the maker can be re-utilized without consent. Then again, property embedding strategy keeps our IP ensured, however, anybody can utilize the FSM usefulness.

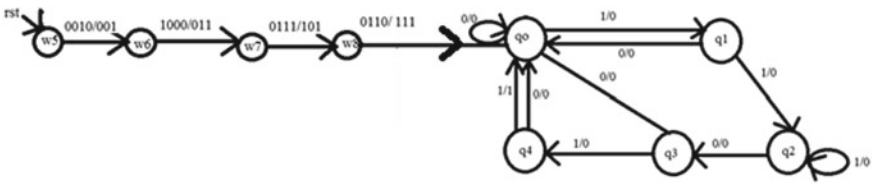

Fig. 3 STG of watermarked sequence detector using FAWS

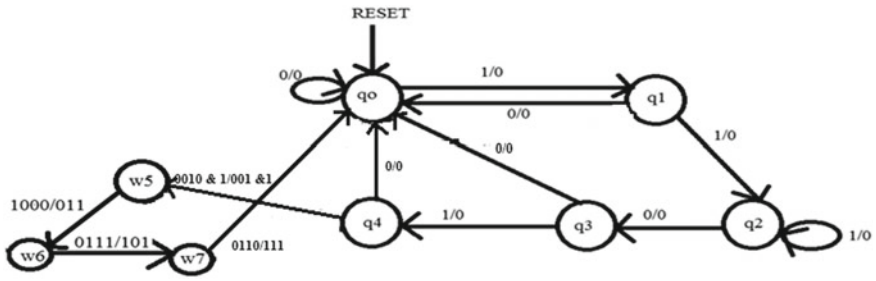

Fig. 4 STG of watermarked sequence detector using BAWS

3 Proposed Algorithm

The proposed model is basically a "dual security lock" in which the owner embeds two keys, in order to protect the STG. One key is made public—in order to use the STG and get the desired output, whereas one key is kept private in order to prove its ownership at the times of need.

Property Implanting with FAWS

This algorithm uses both properties of implanting algorithm and FAWS algorithm. Because of this, the FSM becomes protected by a public key due to FAWS and a private key due to property implanting as shown in Fig. 5. In the similar way we can use a combination of BAWS with property implanting technique and the results will be same as shown in Fig. 6.

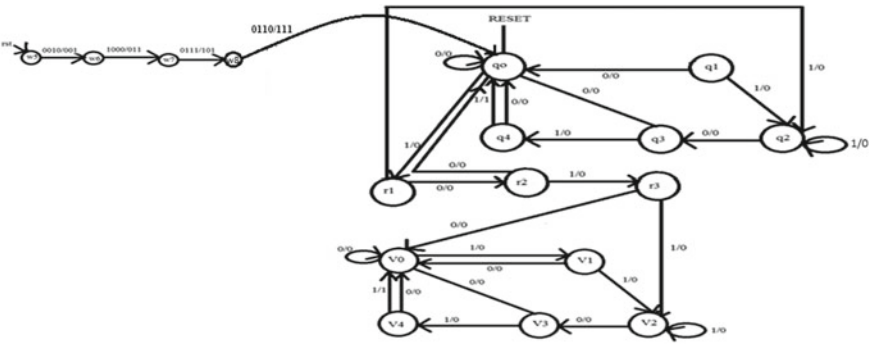

Fig. 5 STG of proposed sequence detector using FAWS

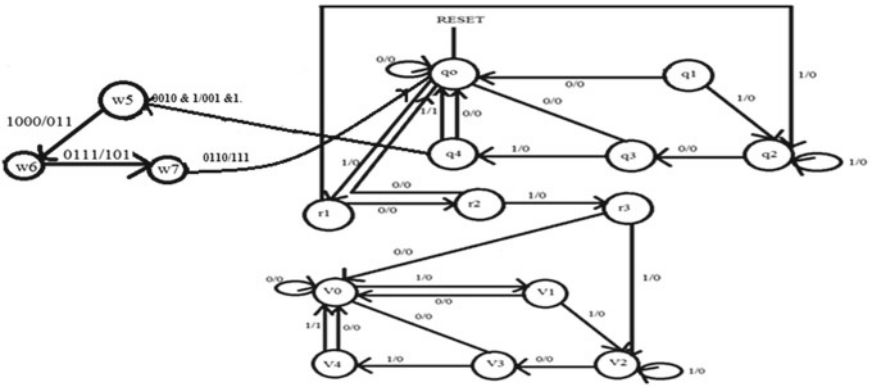

Fig. 6 STG of proposed sequence detector using BAWS

4 Results

The simulation and synthesis are done using Verilog HDL in Xilinx ISE 6.1i EDA tool with its synthesis tool IST and Modelsim 5.4a simulator.

Figure 7 shows the normal operation of a sequence detector without watermark.

Figure 8 shows the FAWS technique applied to the sequence detector the key used here is {0010/001, 1000/011, 0111/101, 0110/111}.

Figure 9 shows the output using the proposed algorithm. As it can be seen from all the simulation results that there is no change in the original functionality of the sequence detector.

As we can see from the synthesis results as shown in Table 1. The number of hardware utilized is more in the case of proposed algorithm as compared to previous algorithms at the cost of better security.

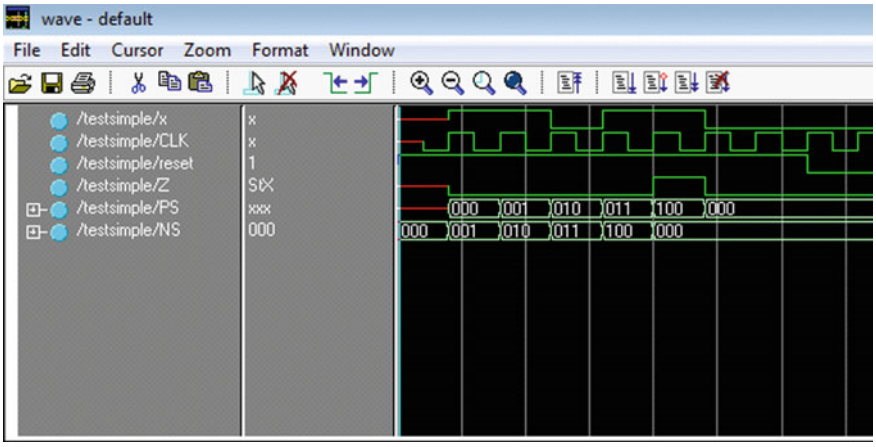

Fig. 7 Sequence 11011 without watermark

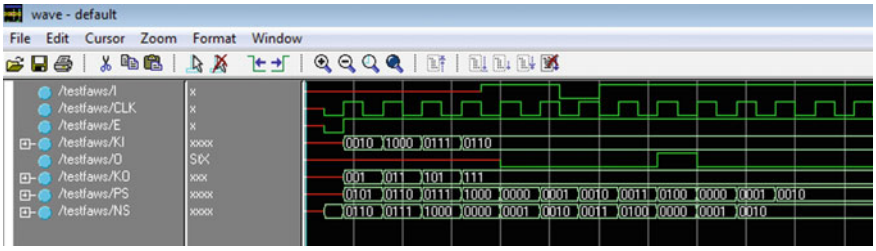

Fig. 8 Front-included Watermarked States (FAWS)

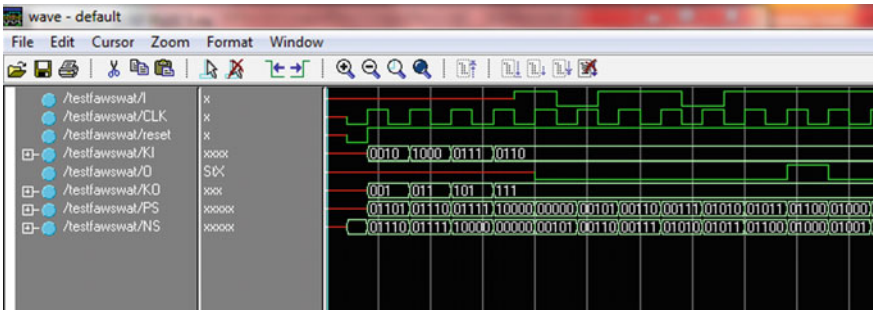

Fig. 9 FAWS watermarking with property implanting

Table 1 Comparison of synthesis results

Parameters	Without watermark	FAWS algorithm	Proposed algorithm
IOs	6	19	21
Cell usage (BELs)	13	48	64
Flip flops/latches used	6	20	24
Clock buffers	1	2	2
IO buffers	5	17	19
IBUF	4	5	5
OBUF	1	12	14

5 Conclusion

The proposed calculation is better as far as security but it utilized more hardware when compared with other algorithms. There is no change in the original functionality of a sequence detector and the IP owner can protect his IP using the advantage of both licence key using FAWS or BAWS and private signature using property implanting algorithm using the proposed technique.

References

1. Nguyen, K.-H., Hoang, T.-T., Bui, T.-T.: An FSM based IP protection technique using added watermaked states. In: The 2013 International Conference on Advanced Technologies for Communications (ATC'13), pp. 218–723
2. Oliveira, A.L.: Techniques for the creation of digital watermarks in sequential circuit design. IEEE Trans. Comput.-Aided Des. Integr. Circuits Syst. **20**(9) (2001)
3. Shaila, S., Nandgawe, P.S.: Intellectual property protection of sequential circuits using digital watermarking. In: First International Conference on Industrial and Information Systems, ICIIS 2006, 8–11 Aug 2006, Sri Lanka

4. Malik, S.: Counter based approach to intellectual property protection in sequential circuits and comparison with existing approach. In: 2014 International Conference on Circuits, Systems, Communication and Information Technology Applications (CSCITA), pp. 48–53 (2014)
5. Abdel-Hamid, A.T., Tahar, S., Aboulhamid, E.M.: IP watermarking techniques- survey and comparison. In: Proceedings of the 3rd IEEE International Workshop on System-on-Chip for Real-Time Applications, Calgary, Alta., Canada, pp. 60–65, July 2003

Design of Low Power and High-Speed CMOS Phase Frequency Detector for a PLL

Nitin Kumar and Manoj Kumar

Abstract High-performance phase frequency detector (PFD) is an integral part of the high-speed phase-locked loop (PLL), and their characteristics have a great impact on the performance of PLL system. The demand for the decreasing of power dissipation in CMOS design is a major challenge to optimize the circuit power consumption. In this paper, the concept of low power techniques namely, stacking and body bias have been utilized for the implementation of the proposed CMOS PFD for high-frequency applications. All the results related to the proposed designs have been obtained using TSMC 0.18 μm CMOS process. The proposed PFD design shows a remarkable reduction in power dissipation up to 172.670 pW which is significantly lower than the conventional PFD. Simulation results also show that the proposed design has wider operating frequency of 1 GHz, making it a suitable circuit for high-performance PLL systems.

Keywords Body bias · CMOS · LCNT · Phase frequency detector
Phase-locked loop · Stack effect

1 Introduction

In recent years, increasing growth in CMOS technology has led to enhancing the demand for low power and high-speed circuits. Low power circuit design is the backbone to extend the battery life. There are three dominant sources of power dissipation in a MOS device, which are responsible for the draining of battery.

N. Kumar (✉) · M. Kumar
University School of Information, Communication and Technology,
Guru Gobind Singh Indraprastha University, New Delhi, Delhi, India
e-mail: nitinkumarvlsi@gmail.com

M. Kumar
e-mail: manojtaleja@ipu.ac.in

B. S. Rawat et al. (eds.), *Advances in Signal Processing and Communication* ,
Lecture Notes in Electrical Engineering 526,
https://doi.org/10.1007/978-981-13-2553-3_51

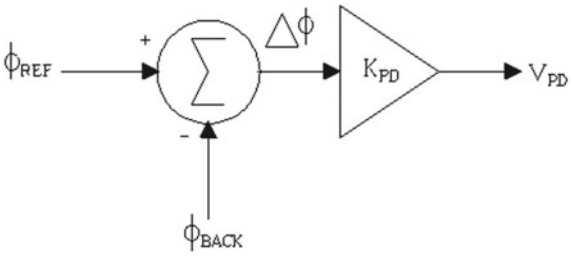

Fig. 1 Simplified model of a PFD

$$P_T = P_D + P_{SC} + P_L \tag{1}$$

P_T is the total power dissipation which takes place in CMOS during the operation. The first component takes place during dynamic switching of the power supply (P_D), second is due to short circuit or by the formation of low impedance path between power and ground rails (P_{SC}), and third is due to leakage currents (P_L). The leakage current is the dominant part of the total power dissipation as MOS geometry size is scaled down [1]. Scaling of the device size, increases the leakage power due to the reduction of threshold voltage. In this paper, leakage control NMOS transistor (LCNT), stacking and body biasing techniques are used to reduce the leakage power dissipation. Phase-locked loop (PLL) is the essential block of the modern communication system. It is widely used in the generation of radio frequencies, data recovery circuits, clock generation and clock synchronization circuit for various high-speed digital and mobile communication systems [2]. The phase frequency detector is the key module of the PLL system. A PFD compares the phase difference between input reference signal and the output signal of PLL. PFD generates either UP signal or DOWN signal depending upon the phase difference between the reference signal (REF) and PLL output signal (BACK) is shown in Fig. 1. Here, $\Delta\Phi$ shows the phase variation between the reference signal, Φ_{REF} and the feedback signal, Φ_{BACK} as per (2)

$$\Delta\phi = \phi_{REF} - \phi_{BACK} \tag{2}$$

The phase frequency detector produces an output signal V_{PD} by multiplying the phase error $\Delta\Phi$ with the gain K_{PD} of PFD.

$$V_{PD} = K_{PD}\,\Delta\phi \tag{3}$$

The phase detector can be categorized into different types according to its function and realization: sinusoidal, combinational, and sequential. Phase recognition interval in the sinusoidal PFD is ($-\pi/2$ to $\pi/2$) where it operates as a multiplier [3]. Analog multiplier has high speed of operation as compared with other implementations nevertheless it suffers from large power consumption. The combinational phase detector has difficulty in detecting the small phase difference between rising/falling edge of REF and BACK signal and suffers from dead zone problem. PLL locks in incorrect phase due to this problem. Sequential PFD has a memory element, and generally used in PLL structure, mainly in frequency synthesis as compared to the combinational phase detector. Sequential PFD has larger input range which enables increasing of locking speed and acquisition range [4]. Sequential PFDs can be constructed with the help of digital circuits and operate with binary input waveform. Hence, they are recognized as digital PFD. In order to reduce the circuit complexity, reduce the power consumption and increase the operating frequency, numerous design techniques have been reported [5–10]. Here, a new design of PFD is proposed which shows low power dissipation and can able to operate at higher frequencies. The major challenge in the design of PFD is to obtain high operating frequency with minimum power dissipation. The overall power consumption of PLL can be reduced mainly by minimizing the power consumption in PFD circuit.

The rest of the paper is structured as follows. Section 2 presents the design description of the conventional and proposed PFD. Simulation results and design comparison of different PFDs are given in Sect. 3. Section 4 summarizes the conclusion of this work.

2 Design Description of Phase Frequency Detector

2.1 Design of Conventional PFD

The conventional phase frequency detector constructs with two identical building blocks having no feedback path are shown in Fig. 2. Each building block of PFD is consists of two stages, p-precharge and n-precharge, attached in cascade driven by a CMOS inverter stage produces an output DOWN and UP signal. The working of conventional PFD is very simple. When input REF and the BACK signal is low, the node Q_1 is connected to V_{dd} through M_1 and M_2 in down block and charge node Q_1 to V_{dd}. The charge at node Q_1 turn off M_4 and turn on M_6; this prevents the node Q_{11} charging and discharging. The DOWN signal maintains the previous value. When input REF signal is low and BACK signal is high then the Q_{11} node connected to ground through M_5 and M_6 and pulled up the DOWN signal. When the REF input

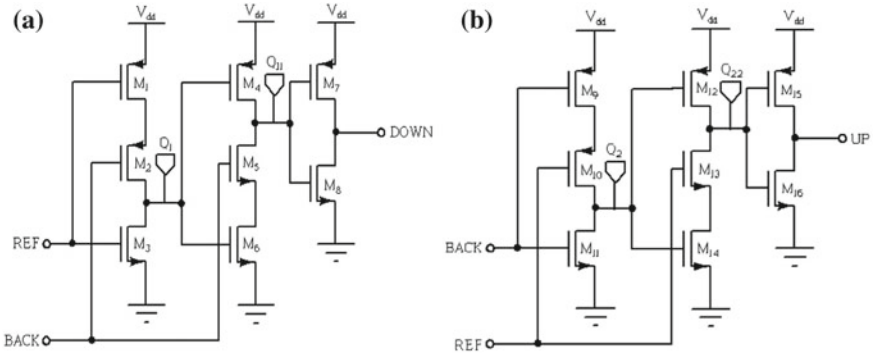

Fig. 2 Schematic of conventional PFD [4] **a** down block **b** up block

signal is high and the BACK signal is low and high, then the node Q_{11} charge to V_{dd} and pulled down the DOWN signal. Similar to DOWN block, UP block will also perform its operation.

2.2 Design of Conventional PFD with LCNT Approach

The conventional PFD with LCNT technique is shown in Fig. 3. The LCNT technique is a circuit level approach for reducing the leakage current in CMOS logic gate [11]. This technique uses two NMOS transistor connected in series between pull up and pull down network. The gate terminal of two NMOS leakage control transistor LCT_1 and LCT_2 for DOWN signal as well LCT_3 and LCT_4 for UP signal are connected to output terminal shown in Fig. 3a, b. The output node voltage controls the switching of both the leakage control NMOS transistor. When node Q_{11} charged to V_{dd} in DOWN block, M_7 is turned OFF in pull up network and M_8 are turned ON in pulled down network. Therefore, both NMOS LCT_1 and LCT_2 enters into their cut off region and offering high resistance to any leakage current that would flow from pull up to pull down network and reduce the leakage current. When node Q_{11} discharged through M_5 and M_6, M_7 is turned ON in pull up network and, M_8 are turned OFF in pulled down network. As a result, both NMOS LCT_1 and LCT_2 turned ON, so there is twice V_{th} drop which will cause a reduced voltage in the path from output node to ground. Moreover, the M_8 transistor is offered more resistance and hence substantially minimizes the leakage current. UP block will also perform a similar operation as DOWN block.

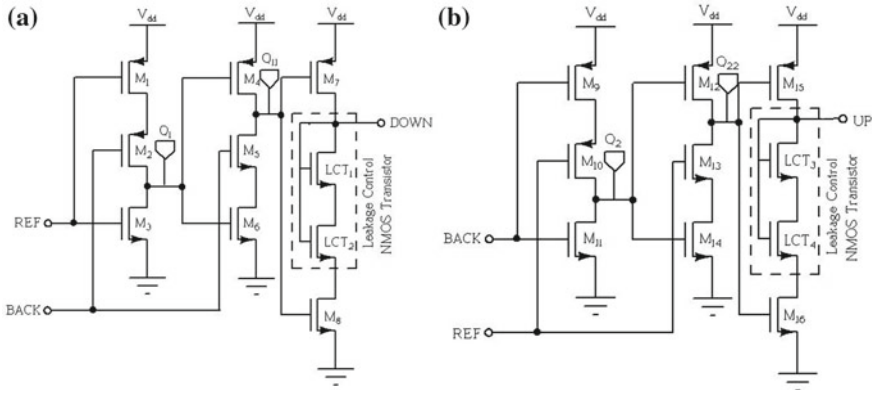

Fig. 3 Schematic of conventional PFD using LCNT **a** down block **b** up block

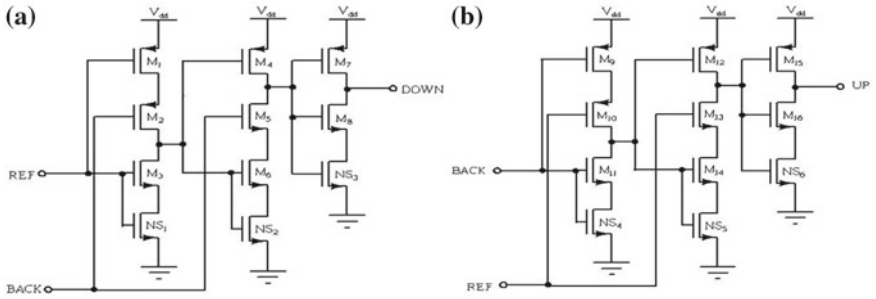

Fig. 4 Schematic of conventional PFD using NMOS stacking **a** down block **b** up block

2.3 Design of Conventional PFD with NMOS Stacking

The conventional PFD with NMOS stacking technique is shown in Fig. 4. Transistor NS_1, NS_2, NS_3 are connected in series with M_3, M_6 and M_8 in DOWN block whereas NS_4, NS_5, NS_6 are added in series with M_{11}, M_{14} and M_{16} in UP block to perform the stacking operation. Stacking mechanism is used where more than one transistor OFF in a path from supply voltage to ground. This technique reduces the subthreshold leakage currents when two transistors are used instead of one with half (W/L) of the original one [12].

2.4 Design of Conventional PFD with NMOS Body Biasing

The conventional PFD with NMOS body biasing is shown in Fig. 5. There are various approaches to increase V_{th}, increase the gate oxide thickness, increase the doping concentration and apply reverse body bias voltage. Increasing the V_{th} is one of the effective techniques to decrease the leakage current. Reverse body bias voltage (Vss) applied on M_3, M_6 and M_8 in DOWN block, whereas M_{11}, M_{14}, and M_{16} in UP block. Reverse body bias voltage ($V_{ss} = -0.5$ V) widens the substrate depletion region and increases the threshold voltage [13] as per (4), resulting reduces the subthreshold leakage currents.

$$\mathrm{V_{th}} = \mathrm{V_{tho}} + \gamma\left(\sqrt{|-2\phi_F + V_{ss}|} - \sqrt{|-2\phi_F|}\right) \tag{4}$$

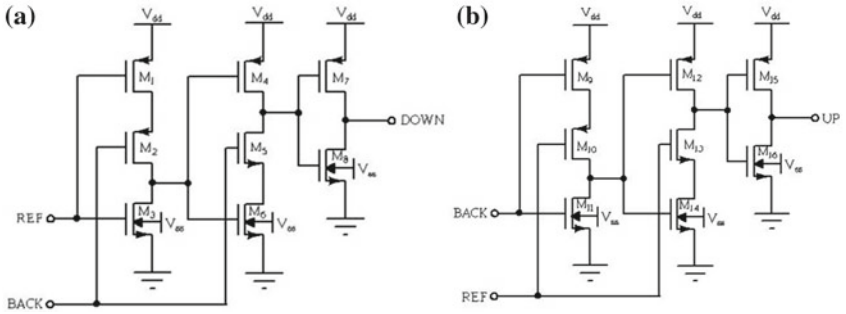

Fig. 5 Schematic of conventional PFD using NMOS body biasing **a** down block **b** up block

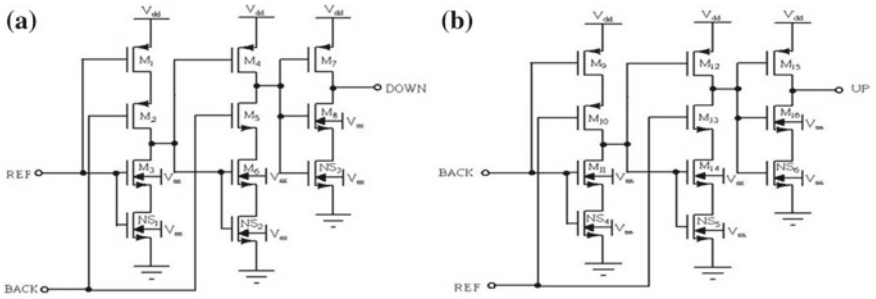

Fig. 6 Schematic of proposed PFD using NMOS stacking with body biasing **a** down block **b** up block

Table 1 Transistor sizing of MOS devices with L = 0.18 μm

Device name	Conventional PFD width (μm)	Conventional PFD with LCNT width (μm)	Conventional PFD with stacking width (μm)	Conventional PFD with body biasing width (μm)	Proposed PFD with both stacking and body biasing (hybrid) width (μm)
M_1, M_2	1.0, 1.0	1.0, 1.0	1.0, 1.0	1.0, 1.0	1.0, 1.0
M_3, M_4	0.5, 1.0	0.5, 1.0	0.25, 1.0	0.5, 1.0	0.25, 1.0
M_5, M_6	0.5, 0.5	0.5, 0.5	0.5, 0.25	0.5, 0.5	0.5, 0.25
M_7, M_8	1.0, 0.5	1.0, 0.5	1.0, 0.25	1.0, 0.5	1.0, 0.25
M_9, M_{10}	1.0, 1.0	1.0, 1.0	1.0, 1.0	1.0, 1.0	1.0, 1.0
M_{11}, M_{12}	0.5, 1.0	0.5, 1.0	0.25, 1.0	0.5, 1.0	0.25, 1.0
M_{13}, M_{14}	0.5, 0.5	0.5, 0.5	0.5, 0.25	0.5, 0.5	0.5, 0.25
M_{15}, M_{16}	1.0, 0.5	1.0, 0.5	1.0, 0.25	1.0, 0.5	1.0, 0.25
LCT_1, LCT_2	–	0.5, 0.5	–	–	–
LCT_1, LCT_2	–	0.5, 0.5	–	–	–
NS_1, NS_2, NS_3	–	–	0.25, 0.25, 0.25	–	0.25, 0.25, 0.25
NS_4, NS_5, NS_6	–	–	0.25, 0.25, 0.25	–	0.25, 0.25, 0.25

2.5 *Design of Proposed PFD with NMOS Stacking and Body Biasing (Hybrid)*

In the proposed PFD, NMOS stacking and body biasing technique is applied simultaneously which is shown in Fig. 6. The operation of proposed PFD is similar to conventional PFD. Both stacking and body biasing technique in a circuit reduces the more subthreshold leakage currents as compare to a single one, as a result, the proposed PFD has power dissipation in pW.

2.6 *Sizing of Transistor*

The aspect ratio of the MOS devices has been optimized for achieving the low power dissipation. Table 1 shows the optimized W/L ratio where channel length has been fixed at 0.18 μm

Table 2 Power consumption of conventional and proposed PFD designs at different V_{dd}

V_{dd} (V)	Conventional PFD (μW)	Conventional PFD with LCNT (μW)	Conventional PFD with stacking (μW)	Conventional PFD with body biasing (μW)	Proposed work (PFD with both stacking and body biasing) (pW)
1.70	1.053	0.785	0.229	0.112	130.286
1.72	1.281	0.954	0.278	0.134	137.235
1.74	1.557	1.156	0.336	0.160	144.848
1.76	1.887	1.399	0.405	0.192	153.248
1.78	2.282	1.689	0.489	0.229	162.451
1.80	2.754	2.036	0.588	0.273	172.670
1.82	3.316	2.449	0.707	0.325	184.018
1.84	3.982	2.939	0.848	0.387	196.657
1.86	4.470	3.519	1.016	0.459	210.776
1.88	5.696	4.203	1.215	0.545	226.587
1.90	6.780	5.006	1.449	0.646	244.333
1.92	8.044	5.946	1.725	0.765	264.291
1.94	9.510	7.039	2.048	0.905	286.772
1.96	11.200	8.306	2.425	1.069	312.127
1.98	13.138	9.766	2.862	1.260	340.753
2.00	15.347	11.440	3.368	1.484	373.107

3 Result and Discussions

In this paper, the proposed and conventional PFD designs have been simulated in 0.18 μm CMOS technology. These designs preserve the circuit stability when operating at low as well as high reference input frequency. Table 2 shows the simulation results of all designs in terms of power consumption when reference input frequency at 1 GHz. The conventional PFD, conventional PFD with LCNT, conventional PFD with stacking, conventional PFD with body bias and proposed PFD design consumes power [1.053–15.347] μW, [0.785–11.440] μW, [0.229–3.368] μW, [0.112–1.484] μW and [130.286–373.107] pW, respectively. The graph in Fig. 7 shows the comparison of power dissipation with existing design at supply voltage of 1.7–2.0 V. The output waveform of conventional and proposed designs have been analyzed in Fig. 8. All the waveforms have been analyzed at $V_{dd} = 1.8$ V and $f = 1$ GHz The proposed design has been compared with conventional PFD with different techniques, shows better performance in terms of power consumption.

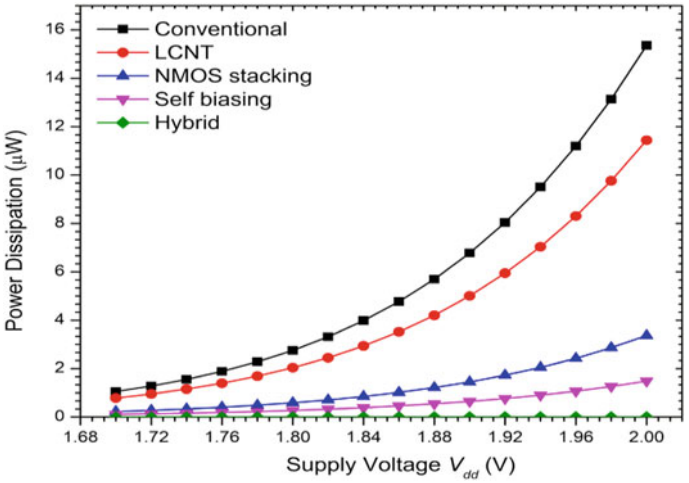

Fig. 7 Variation in power dissipation with supply voltage

4 Conclusion

In this paper, leakage control NMOS transistor (LCNT), stacking effect, and body bias techniques have been utilized to design the proposed PFD in order to reduce the power consumption. The results of conventional and proposed design have been obtained in TSMC 0.18 μm CMOS technology. The conventional PFD designs with LCNT, NMOS stacking, NMOS body bias and proposed PFD with NMOS stacking and body bias approaches consumes power 2.036 μW, 0.588 μW, 0.273 μW and 172.670 pW, respectively, with V_{dd} 1.8 V and reference input frequency of 1 GHz. The result of proposed design has been compared with conventional PFDs with different approaches, demonstrate the significantly improved power consumption performance, and suitable for high-performance PLL system.

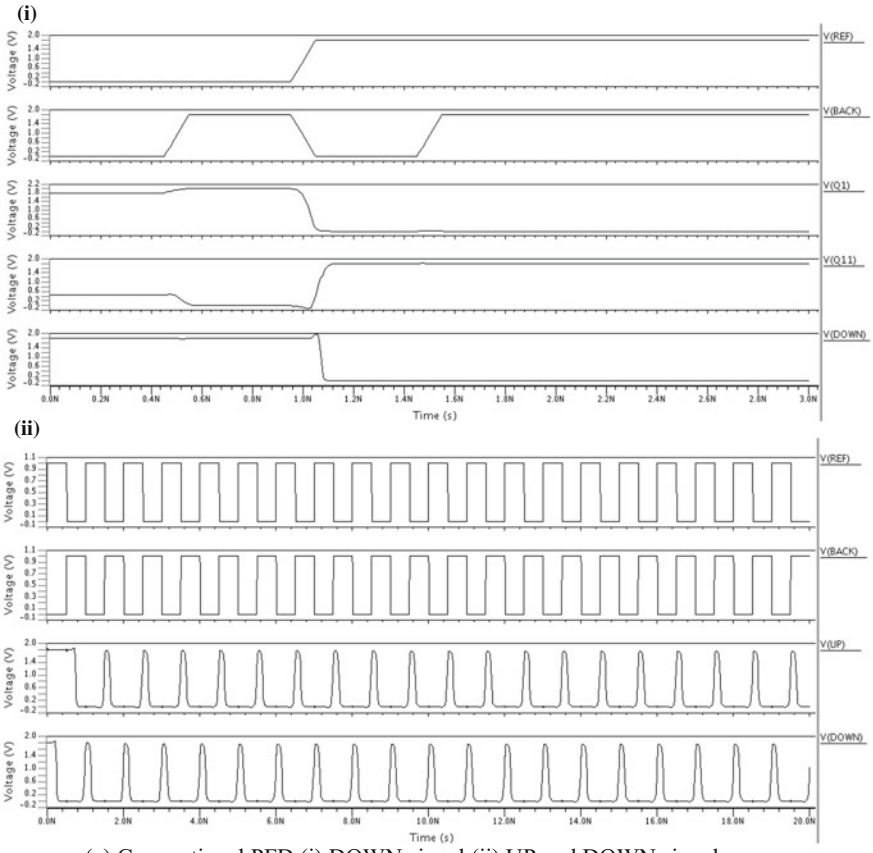

(a) Conventional PFD (i) DOWN signal (ii) UP and DOWN signal

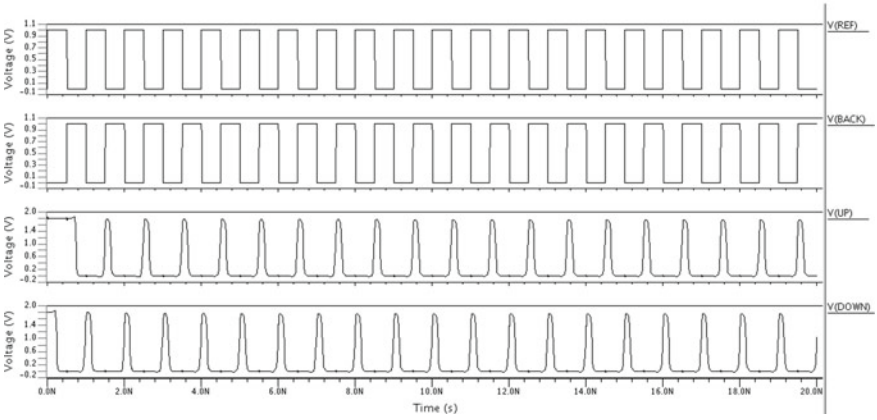

(b) Conventional PFD with LCNT

Fig. 8 Output waveforms of phase frequency detectors at $V_{dd} = 1.8$ V and $f = 1$ GHz

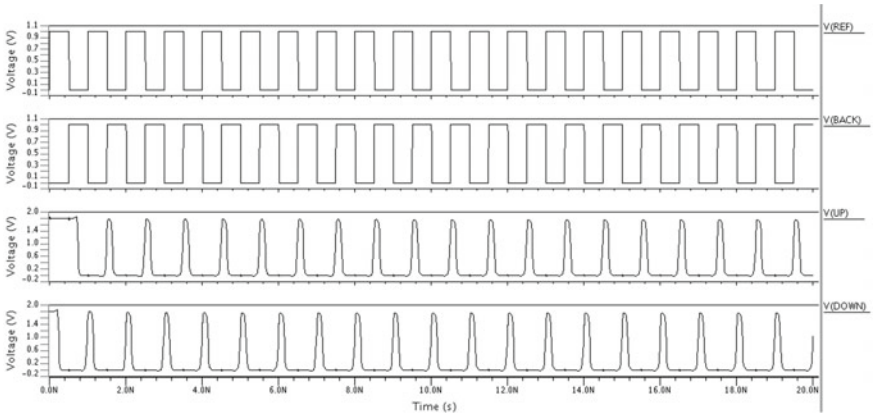

(c) Conventional PFD with NMOS stacking

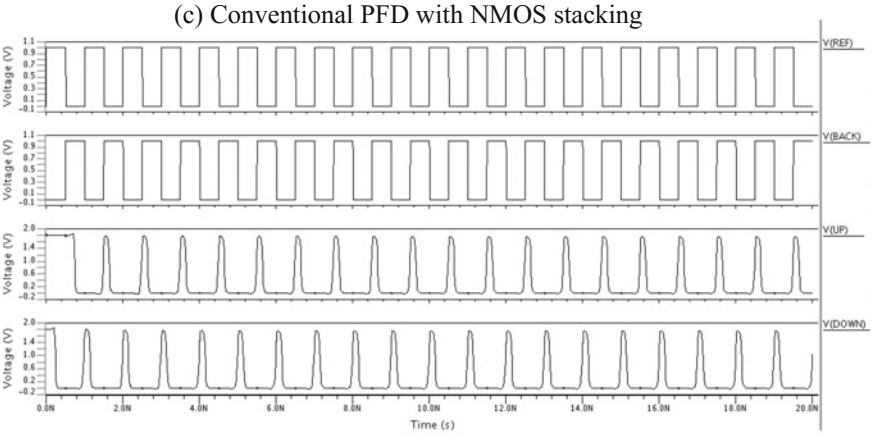

(d) Conventional PFD with NMOS Body biasing

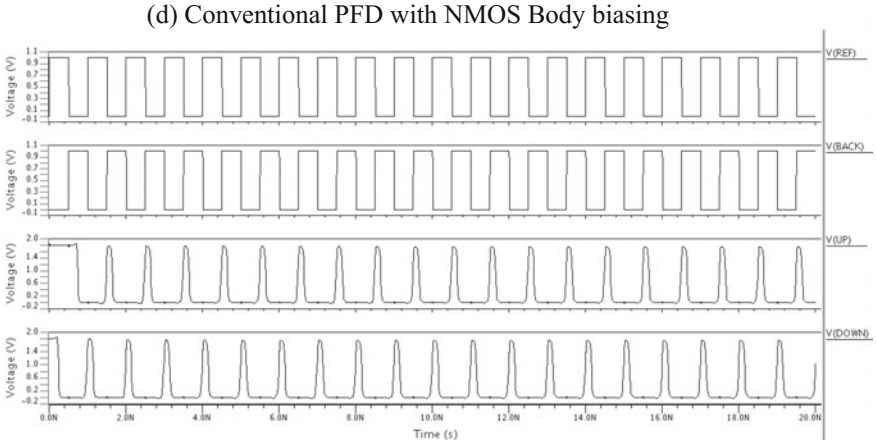

(e) Proposed PFD with NMOS stacking & body biasing (Hybrid)

Fig. 8 (continued)

References

1. Sharma, V.K., Pattanaik, M., Raj, B.: INDEP approach for leakage reduction in nanoscale CMOS circuits. Int. J. Electron. **102**(2), 200–215 (2014)
2. Gholami, M.: Phase detector with minimal blind zone and reset time for GSamples/s DLLs. Circuits Syst. Signal Process. **36**(9), 3549–3563 (2017)
3. Soliman, S., Yuan, F., Raahemifar, K.: An overview of design techniques for CMOS phase detector. In: Proceedings of IEEE International symposium on circuits and systems, pp. V-457–V-460, Phoenix Scottsdale, AZ, USA (2002)
4. Nikolic, G., Jovanovic, G., Stojcev, M., Nikolic, T.: Precharge phase detector with zero dead zone and minimal blind-zone. J. Circuits Syst. Comput. **26**(11), 1750179-1–1750179-15 (2017)
5. Chen, W.H., Inerowicz, M.E., Jung, B.: Phase frequency detector with minimal blind zone for fast frequency acquisition. IEEE Trans. Circuits Syst.-II **57**(12), 936–940 (2010)
6. Mansuri, M., Liu, D., Yang, C.K.K.: Fast frequency acquisition phase-frequency detectors for GSamples/s phase-locked loops. IEEE J. Solid-State Circuits **37**(10), 1331–1334 (2002)
7. Johansson, H.O.: A simple precharged CMOS phase frequency detector. IEEE J. Solid-State Circuits **33**(2), 295–299 (1998)
8. Woo, Y., Jang, Y.M., Sung, M.Y.: PLL with dual PFDs for adjusting the loop bandwidth to input frequency ratio. Int. J. Electron. **90**(1), 43–55 (2003)
9. Babazadeh, H., Esmaili, A., Hadidi, K.: A high-speed and wide detectable frequency range phase detector for DLLs. In: IEEE Proceedings 27th NORCHIP, Trondheim, Norway, pp. 1–3 (2009)
10. Johnson, T., Fard, A., Aberg, D.: An improved low voltage phase frequency detector with extended frequency capability. In: Proceedings of IEEE 47th Midwest symposium on Circuits and Systems, Hiroshima, Japan, Nov 2004, vol. 1, pp. I-181–I-184
11. Lorenzo, R., Chaudhary, S.: LCNT-an approach to minimize leakage power in CMOS integrated circuits. Microsyst. Technol. **23**(9), 4245–4253 (2017)
12. Kumar, M., Hussain, M.A., Paul, S.K: New hybrid digital circuit design techniques for reducing subthreshold leakage power in standby mode. Circuits Syst. **4**, 75–82 (2013)
13. Rabaey, J.M., Chandrakasan, A., Nikolic, B.: Digital Integrated Circuits: A Design Perspective, 2nd edn. Pearson Education, Delhi, India (2003)

Comparative Analysis of Standard 9T SRAM with the Proposed Low-Power 9T SRAM

Balraj Singh, Mukesh Kumar and Jagpal Singh Ubhi

Abstract This paper presents a novel 9T SRAM (static random-access memory) cell design with reduced leakage power and high performance. The design makes use of a sleep transistor so as to curtail the leakage power by eliminating the formation of a direct connection between the supply voltage (V_{DD}) and ground. The results are compared with existing 9T SRAM cell with the same transistor sizing and parameter variations. The designed SRAM cell has decoupled read and write operations and is simulated using Cadence at 45 nm CMOS technology. At 0.8 V, the proposed cell has an improvement of 31.78% and 73.66% respectively in dynamic and static powers when compared with the reported 9T SRAM cell. Also, nearly 36% improvement in power delay product (PDP) is achieved with the proposed design.

Keywords SRAM · Leakage power dissipation · Dynamic power · Static power Transistor sizing · PDP

1 Introduction

In earlier times, the major challenges for the VLSI designer were area, performance, cost, and power consumption. In recent years, however, power consumption is being given comparable weight to area and speed considerations. With the technological developments, Moore's law has led to a much smaller integrated circuit technology. Amid the shrinking of the technology, the performance of the integrated circuits is enhanced but this improved performance comes with the cost of increases in leakage power, process variation, and power density. Today, most of the power systems

B. Singh · M. Kumar (✉) · J. Singh Ubhi
Department of ECE, SLIET, Longowal, India
e-mail: mukeshkumar@sliet.ac.in

B. Singh
e-mail: balraj@gmail.com

J. Singh Ubhi
e-mail: js_uhbi@yahoo.com

B. S. Rawat et al. (eds.), *Advances in Signal Processing and Communication* ,
Lecture Notes in Electrical Engineering 526,
https://doi.org/10.1007/978-981-13-2553-3_52

require high performance when in active state while a very low leakage when in idle/hold state [1]. It is important to note that the power dissipation parameters and some other parameters like propagation delay and PDP (Power Delay Product), all are interrelated. An improvement in one parameter leads to the degradation of other parameters [2]. The motivations for reducing power consumption differ from application to application and circuit to circuit. Downscaling and lower voltage activity are the most critical and supportive approaches to accomplish the low power and superior CMOS logic. Despite the way that the pattern of contracting gate length is exceptionally forceful nowadays and there are a few difficulties associated with having low power activity with gadgets having small dimensions.

An attempt with CMOS technology is used to observe the performance of NAND and NOR gate and conclude NAND gate has more advantages over NOR gate. Static power dissipation is 55.73% less, also having less area and less access time for NAND gate [3]. SRAM is primary memory block implemented in high-performance processors because of its compatibility with the logic. In fact, the biggest area in modern silicon on the chip is possessed with SRAM [4, 5]. SRAM has a vital role in ADC, cache memory, camera, electronic toys, mobile phone, etc. The main advantage of SRAM is that it need not refresh data periodically [6]. The outline of low-power SRAM is itself a monstrous test to manage. Further, scaling and the process variations are huge snags to low power SRAM outline. As the supply voltage diminishes, SRAM must be consistent with the working conditions. However, with low-voltage task in SRAM, designers need to confront a few difficulties like process variations, bit cell stability, detecting and dependability of the entire memory. The upside of SRAM is the low power utilization, yet to configuration low power, planner needs to deal with the area and performance trade-off. For enhancing these areas and execution metrics, additionally makes a challenge to manage leakage current.

A Novel 9T SRAM cell is proposed with less leakage power and high performance. The measurement results of this cell are compared with the standard 9T SRAM cell and concluded it is 31.78% and 73.66% efficient for static power and dynamic power dissipation, respectively.

This paper is sorted out into following segments: Segment I enrolls a short presentation of past work done. Segment II has a talk on the activity of existing 9T SRAM cell. Segment III has centered around the operation of proposed 9T SRAM cell. In segment IV, simulated results are discussed along with graphs. Segment V has the comparison of results of novel 9TSRAM with existing. Segment VI has the conclusion of the paper.

2 Existing 9T SRAM Cell

First, the schematic of 9T SRAM cell with transistors sized for 45 nm CMOS technology is shown in Fig. 1. The SRAM can be thought as consisting of two parts namely upper subsystem and lower subsystem [7].

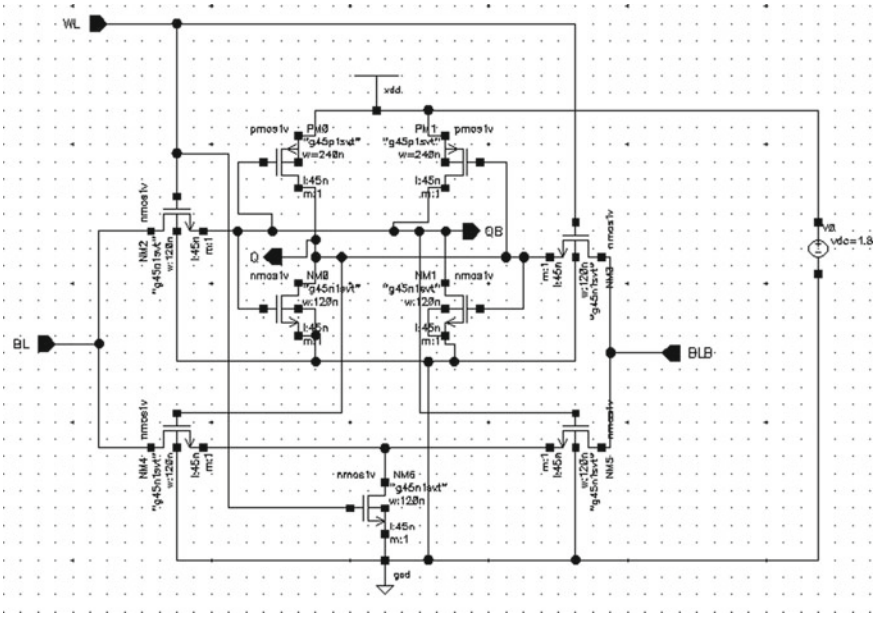

Fig. 1 Schematic of the standard 9T SRAM cell [8]

The upper subsystem is basically a six transistor (6T) conventional SRAM cell consisting of four NMOS transistors from NM0 through NM3 and two PMOS transistors shown as PM0 and PM1 in Figure. The access transistors, named as NM2 and NM3, are controlled by the same word line (WL). The lower subsystem of the 9T SRAM cell consists of transistors NM4 through NM6, in which, NM4 and NM5 transistors act as access transistors for bit lines while transistor NM6 act as the read access transistor. The data stored in the cell control the operations of NM4 and NM5 transistors and a separate read line (RL) signal controls the transistor NM6. The gate of this NM6 transistor can also be connected to the WL instead of connecting a separate RL signal.

Operations of the Cell:

When write operation is performed, WL signal transitions are made HIGH while RL is kept LOW making NM6 OFF, the two access transistors NM2 and NM3 are turned ON. If one wishes to write bit '0' to node Q, then BL is discharged while BLB is charged. Bit '0' is stored in the SRAM cell through NM2. To write '1' at Q, the operations at BL and BLB are reversed, i.e., BL is charged and BLB is discharged.

While performing Read operation, RL is made to go HIGH and maintaining WL at LOW causing NM6 ON and NM2 and NM3 transistors OFF. If stores a '1' then BL is discharged through NM4 and NM6 and if QB stores a '1' then BLB is discharged through NM5 and NM6. Since during the Read it is seen from the operation that accesses transistors NM2 and NM3 are in cut off, the storage nodes Q and QB are

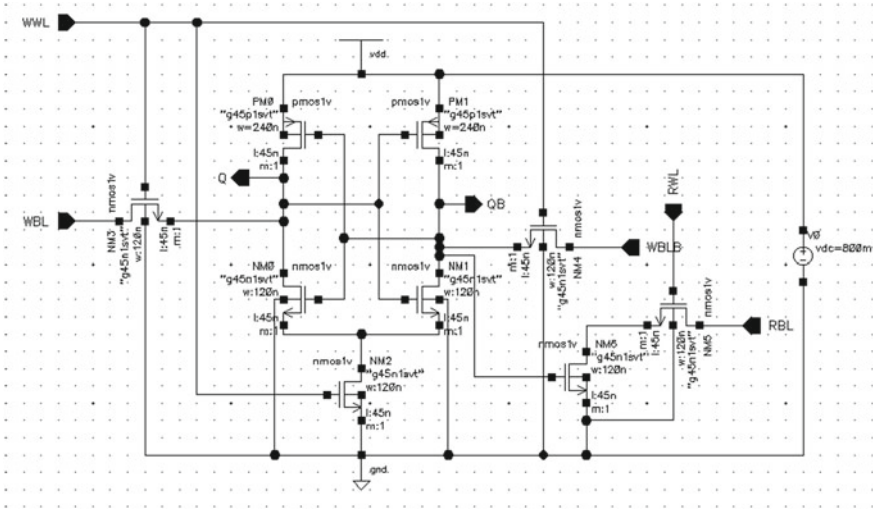

Fig. 2 Schematic of proposed 9T SRAM cell

totally segregated from the bit lines. The read stability of this conventional 9T SRAM cell is improved compared to that of standard 6T SRAM cell as the voltage of the node which stores '0' is stringently kept at the ground during a read operation which is not so in case of standard 6T SRAM cell [7].

3 Proposed 9T SRAM Cell

The schematic of the proposed SRAM cell is shown in Fig. 2 which is supposed to be split into two parts: left sub-circuit of the SRAM cell consists of a traditional 6T SRAM cell with a sleep transistor at the bottom through which the cell is grounded. The right sub-circuit of the proposed cell consisting of two transistors used for Read operation.

In this 9T SRAM cell, read and write are controlled by separate devices within the cell as the two operations are entirely decoupled [9]. The transitions of the read word line (RWL) decide the read operation of the proposed cell. NM3 and NM4 act as the write access transistors which are guarded by the column based write word line (WWL) whose transitions control the write process of the SRAM cell. The bottom transistor NM2 is sized uniformly to that of cross-coupled inverters [10]. This is done as such as to coordinate their current conveying limit. Thus, by employing the extra transistor in the read stable 8T SRAM cell [9], the leakage or static power dissipation can be reduced.

Operations of the Cell:
For read operation, the row-based high going read word line and row-based gnd enable the two-stacked read port, and if QB = '1' the RBL would be discharged and sensing of Q = '0' will be done by the sense amplifier. When '1' is to be read reverse operation is performed. Generally, during read operation, RBL is pre-charged to VDD and WWL is kept LOW or at '0' volt. When WWL, WBL and WBLB are maintained LOW, the cross-coupled inverter get separated from the external interconnect and there is no intrusion effect in the latch [11]. Depending on the data associated in the cross-coupled inverters, RBL discharges or remain at VDD. If RBL discharges, it can be treated as the stored bit is supposed to be '1', otherwise, it is '0'. Therefore, it can be interpreted here that the read stack works indirectly to read the data from the latch.

To execute the write operation, read circuitry is disabled by keeping RWL at LOW level while WWL is asserted. But before asserting the write word line, the data is loaded onto the write bit lines (WBL and WBLB), i.e., write operation is initialized by pre-charging the WBL and WBLB signals. After pre-charging of write bit lines is done the asserting of the WWL signal makes the access transistors NM3 and NM4 to switch ON so as to access or pass the data from word bit line to the cell. Thus, data is placed into the cell at the respective nodes.

4 Simulation Results

The existing as well as the proposed SRAM cell has the width for the NMOS transistor as 120 nm while it is 240 nm for PMOS transistors. The length of each transistor used in the cell is taken as 45 nm. The simulation results for both the SRAMs are obtained for the same transistor sizing and other parameter variations.

A. Transient and DC Responses for Existing 9T SRAM Cell

The combined transient and DC responses are shown in the Fig. 3. The transient response is obtained for a period of 100 ns. The output Q varies with respect to BLB signal and gives the same value as BLB when WL is enabled. The case when WL is disabled/LOW, the output Q holds the previous value. DC response is obtained against the DC voltage applied.

B. Transient and DC Responses for Proposed 9T SRAM Cell

The transient and DC responses obtained for 45 nm node for the proposed 9T SRAM cell are combined together in Fig. 4. A 100 ns period is taken for the transient response. Owing to separate circuitries for write as well as read operation, timing control is an important aspect to obtain a response in this case.

The output Q in transient response follows WBLB and if WWL is HIGH Q changes accordingly as WBLB while it holds the previous state in case the WWL is LOW. The different plots in DC response are with respect to applied voltage.

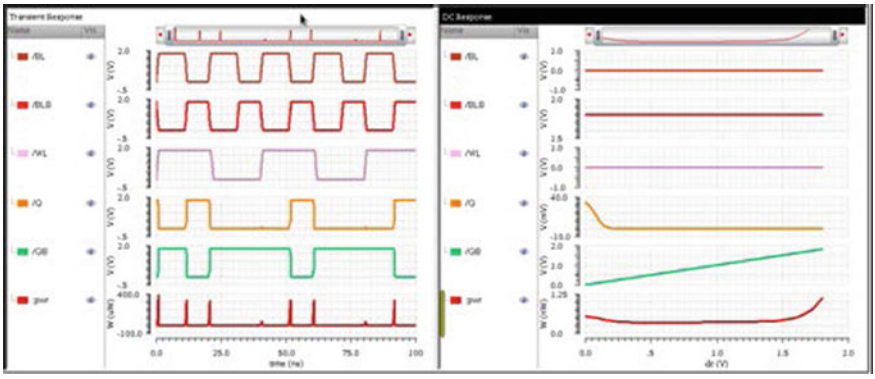

Fig. 3 Transient and DC responses for existing 9T SRAM cell

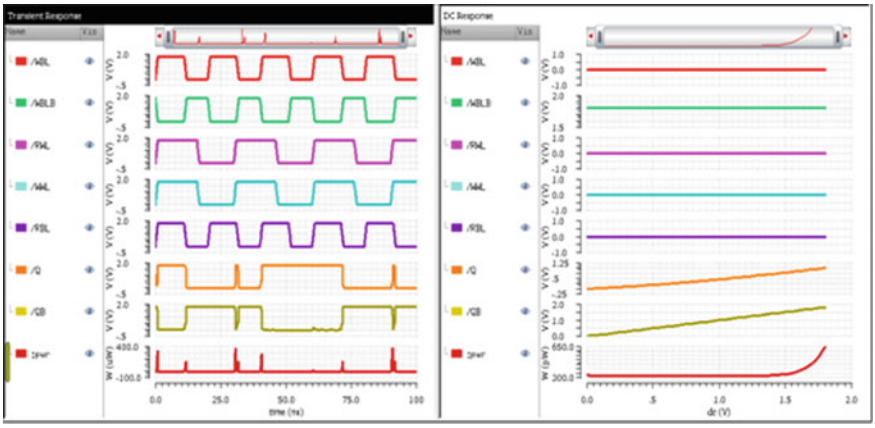

Fig. 4 Transient and DC responses for the proposed 9T SRAM cell

5 Comparison Between the Existing and the Proposed 9T SRAM Cells

Nine transistor SRAM cells are compared with the same transistor features and other parameter variations. The results for both the SRAM cells are obtained at a temperature of 27 °C and with the same technology node of 45 nm.

Dynamic and Static Power Against Applied Supply Voltage

The comparison graph for the reported 9T SRAM cell and proposed 9T SRAM cell are shown in the Figs. 5 and 6.

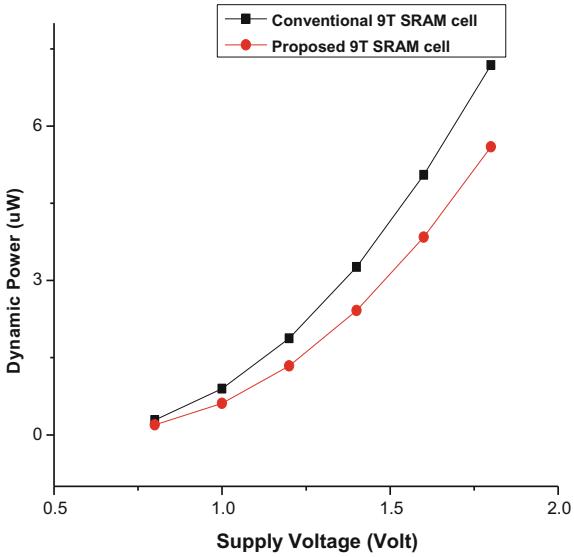

Fig. 5 Dynamic power versus supply voltage

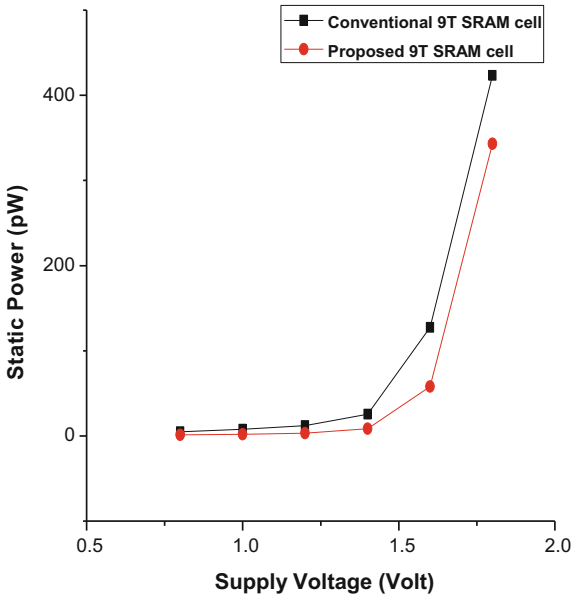

Fig. 6 Static power versus supply voltage

Various Timing Parameters with Voltage

The various timing parameters obtained through simulation results are the rise time, fall time, and delay. From the graphs plotted in Fig. 7, it can be interpreted that the rise time for the signal is higher in the case of proposed SRAM cell to that of

Fig. 7 Time versus voltage

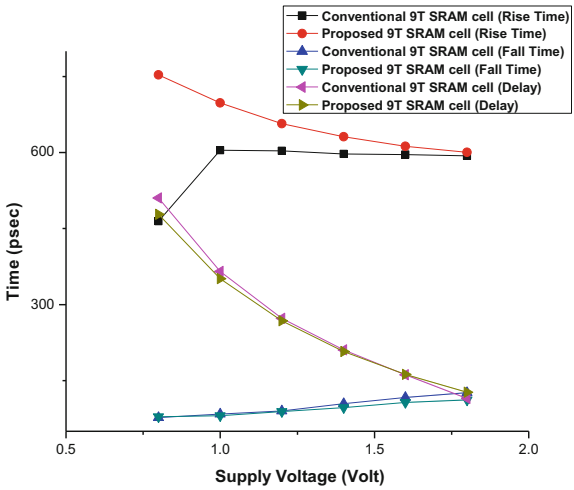

conventional SRAM cell. In other cases, i.e., fall time and delay, the results are better for the proposed 9T SRAM cell when compared with the existing SRAM cell.

Different Parameter Variation with Temperature

The dynamic power for both the SRAM cells is improved with the temperature while the static power and the delay parameters are degraded in case of existing as well as the proposed nine transistor SRAM cells.

From Fig. 8, it can be seen that the dynamic power varies nearly the same for two SRAM cells against the temperature. However, from Fig. 9, it can be observed that leakage power dissipation in reported 9T SRAM cell increases exponentially with the temperature while there is nearly a linear increase in case of proposed SRAM cell making it better in temperature varying environments.

It can be reported from the Fig. 10 that the variation in delay for the proposed cell with respect to temperature is nearly linear. At temperatures above 100 °C, the delay in the case of existing SRAM increases more while this increase for the proposed bit cell is very low.

Comparison Between Power Delay Product (PDP)

The power delay product for the two cells is shown separately in Table 1.

Table 1 PDP comparison at different voltages

Voltage (volt)		1.2	1.0	0.8
PDP (Watt-femtosecond)	Existing 9T SRAM cell	0.511	0.327	0.146
	Proposed 9T SRAM cell	0.359	0.214	0.093

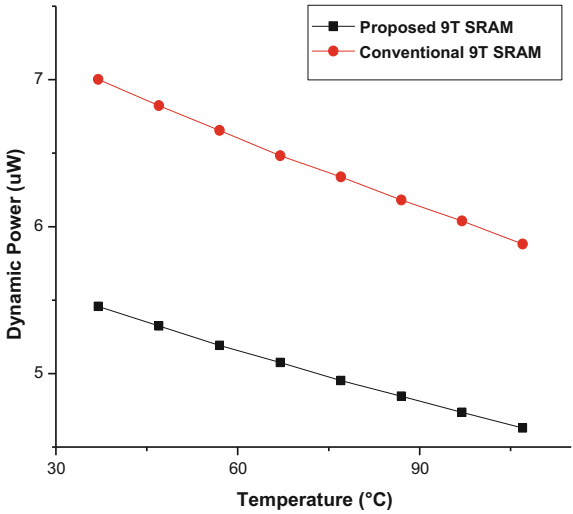

Fig. 8 Dynamic power versus temperature

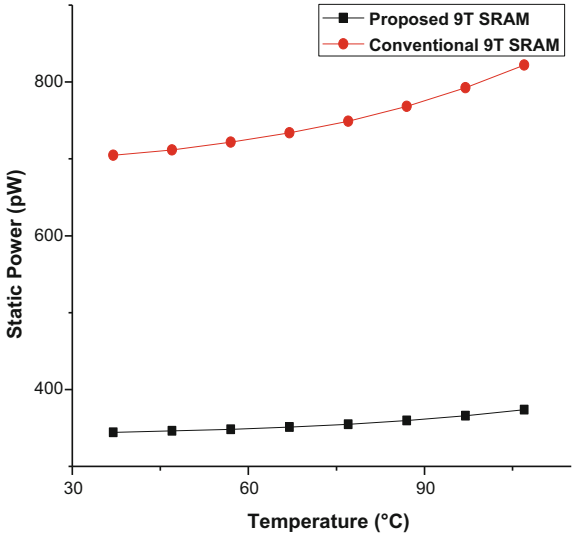

Fig. 9 Static power versus temperature

The power delay product for both the SRAM cells decreases as the voltage decreases. The variation with the voltage can be clearly observed from the combined graphs of power delay product with the voltage as shown in Fig. 11.

From the above Fig. 11, it can be clearly depicted that PDP value against the voltage is higher in case conventional 9T SRAM cell which is further degraded at lower voltages. The simulation results show that at 1.8 V, there is an increase of 13.73% in PDP for the conventional SRAM cell which increases to 36.30% when the applied voltage is reduced to 0.8 V. Therefore, from this, it can be interpreted that

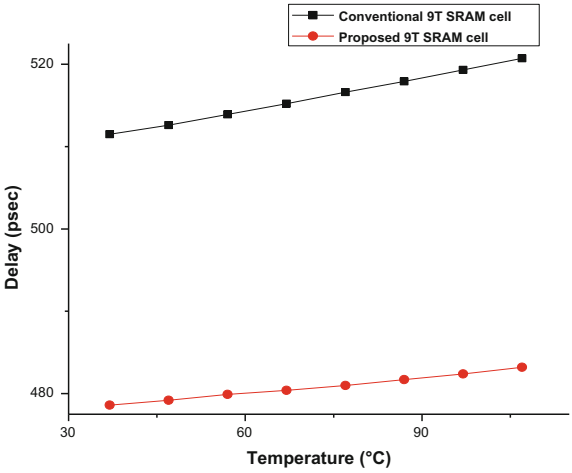

Fig. 10 Delay versus temperature

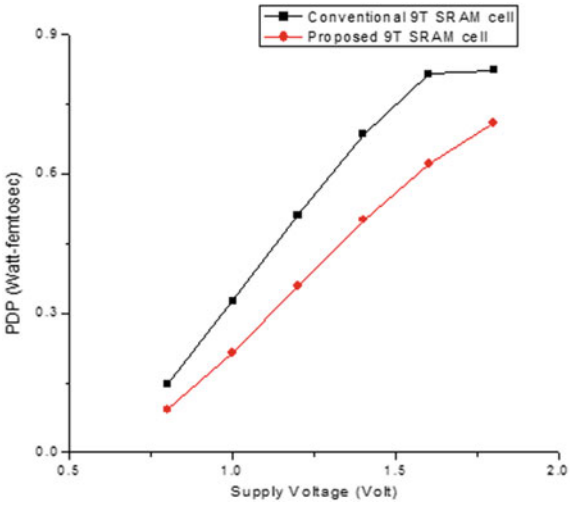

Fig. 11 PDP versus supply voltage

the PDP value increases in case of existing SRAM cell when the voltage is scaled down. This makes the proposed SRAM cell a favorable choice for use over existing SRAM cell.

6 Conclusion

The proposed SRAM cell shows better results at a higher temperature in contrast to the reported bit cell in which the increase in leakage power with the temperature is much higher than the former. The simulation results using Cadence Spectre show that

at 0.8 V the proposed cell has an improvement of 31.78% and 73.66% respectively in dynamic and static power when compared with the reported nine transistor SRAM cell. There is a little degradation of nearly 10.7% in propagation delay which makes the PDP to be improved by 13.73% at 1.8 V for the proposed cell. At a scaled voltage of 0.8 V, it exhibits an improvement of about 36.30% in PDP due to a step up of about 6% in propagation delay. Therefore, with the voltage getting scaled down, this improvement in PDP increases making the proposed SRAM cell better than the reported one at the same technology node.

References

1. Weste, N.H.E., Harris, D., Banerjee, A.: CMOS VLSI Design, 3rd edn. Pearson Education
2. Rabaey, J.M., Kasan, A.C., Nikolic, B.: Digital Integrated circuits: A Design Perspective, 2nd edn
3. Singh, B., Kumar, M., Ubhi, J.S.: Analysis of CMOS based NAND and NOR gates at 45 nm technology. IJEECS **6**(4), 224–227 (2017)
4. Sinangil, M.E., Chandrakasan, A.P.: Application-specific SRAM design using output prediction to reduce bit-line switching activity and statistically gated sense amplifiers for up to 1.9 lower energy/access. IEEE J. Solid-State Circuits **49**(1), 107–117 (2014)
5. Rusu, S., et al.: A 65-nm dual-core multithreaded xeon processor with 16-MB L3 cache. IEEE J. Solid-State Circuits **42**(1), 17–25 (2007)
6. Kumar, M., Ubhi, J.S.: Performance evaluation of 6T, 7T & 8T SRAM at 180 nm technology. In: Presented in IEEE Conference held at IIT Delhi, July 2017
7. Liu, Z., Kursun, V.: Characterization of novel nine transistor SRAM cell. IEEE Trans. Very Large Scale Integr. (VLSI) Syst. **16**, 488–492 (2008)
8. Kao, J.T., Chandrakasan, A.: Dual-threshold voltage techniques for low-power digital circuits. IEEE J. Solid State Circuits, **35**(7), 1009–1018 (2000)
9. Chang, Leland, Montoye, Robert K., Nakamura, Yutaka, Batson, Kevin A., Eickemeyer, Richard J., Dennard, Robert H., Haensch, Wilfried, Jamsek, Damir: An 8T SRAM for variability tolerance and low voltage operation in high-performance caches. IEEE J. Solid-State Circuits **43**(4), 956–963 (2008)
10. Hentrich, D., Oruklu, E., Saniie, J.: Performance evaluation of SRAM cell in 22 nm predictive CMOS technology. In: IEEE International Conference on Electron/Information Technology, pp. 470–475 (2009)
11. Rahman, M.I., Bashar, T., Biswas, S.: Performance evaluation and read stability enhancement of SRAM bit-cell in 16 nm CMOS. In: 5th International Conference on Informatics, Electronics and Vision (ICIEV), pp. 713–718 (2016)

Fabrication and Characterization of Photojunction Field-Effect Transistor

Yogesh Kumar, Hemant Kumar, Gopal Rawat, Chandan Kumar, Varun Goel, Bhola N. Pal and Satyabrata Jit

Abstract In this article, ZnO Quantum Dot (QD)-based photojunction field-effect transistor (photo-JFET) has been fabricated for the detection of ultraviolet (UV) spectrum. The effects of photojunction between the ZnO Quantum Dots (QDs) and deep work function transparent MoO_2 is analyzed under the illumination of UV. The illuminated optical power density acts as a floating gate for the JFET. The device was fabricated on a glass substrate using interdigitated electrodes (Ag) followed by ZnO QDs layer and MoO_2. The dark current between source and drain was found minimum, 2.79 $\mu A/cm^2$, in the case of photojunction as compared to the metal semiconductor metal (MSM)ZnO QDs photoconductor 19.32 $\mu A/cm^2$ at an applied bias of 10 V. The reduction in dark current is attributed due to the effect of the junction formed between ZnO QDs and MoO_2 with the rectification ratio of ~347. The MoO_2 depletes the ZnO QDs channel between the electrodes and reduces the dark current which in turn helps to improved photodetector characteristics.

Y. Kumar (✉) · H. Kumar · G. Rawat · C. Kumar · S. Jit
Department of Electronics Engineering, IIT (BHU) Varanasi, Varanasi, India
e-mail: ykumar.rs.ece13@iitbhu.ac.in

H. Kumar
e-mail: hkumar.rs.ece13@iitbhu.ac.in

G. Rawat
e-mail: grawat.rs.ece13@iitbhu.ac.in

C. Kumar
e-mail: chandank.rs.ece14@iitbhu.ac.in

S. Jit
e-mail: sjit.ece@itbhu.ac.in

B. N. Pal
School of Material Science and Technology, IIT (BHU) Varanasi, Varanasi, India
e-mail: bnpal.mst@itbhu.ac.in

Y. Kumar · V. Goel
Jaypee Institute of Information Technology, Noida, India
e-mail: varun.goel.ece12@iitbhu.ac.in

B. S. Rawat et al. (eds.), *Advances in Signal Processing and Communication* ,
Lecture Notes in Electrical Engineering 526,
https://doi.org/10.1007/978-981-13-2553-3_53

Keywords Photo-JFET · ZnO quantum dots · Schottky junction

1 Introduction

Zinc oxide has played the important role in the various fields of sensing like ultraviolet detection, biomedical, nanogenerators, and gas sensing. It is a versatile compound with strong radiation hardness, high chemical stability, low cost, and large band gap (3.7 eV) [1]. Dark current plays an important role to optimize the performance of the photodetectors [2]. Dark current should be minimized to enhance the fundamental aspects of photodetectors like power consumption and the effectiveness of photoconductor readout process [2]. Researchers have reported very low dark currents <1 nA/cm^2 [3] and <10 nA/cm^2 [4] by increasing the inter-electrode spacing in sandwich-like structures, i.e., the thickness of active layers, so that the optimum results can be achieved. Adinolfi et al. [5] fabricated the photo-JFET by depositing the silver electrodes (source and drain) on glass, PbS quantum dot as an active layer, and MoO_3, respectively.

In this article, we have analyzed the photojunction formed between the ZnO QDs and MoO_2 so the channel has fully depleted in the dark and also optimize the dark current with photojunction and without photojunction. The behavior of the photodetector varies with the variation of photo-generated carriers. The carriers can be collected at electrodes or recombine before reaching the electrode. The probability of recombination decreases when the channel is depleted and then the maximum number of photo-generated charge carriers can be extracted via electrodes.

2 Experimental Details

2.1 ZnO QDs Synthesis and Device Fabrication

For the ZnO QDs thin film deposition, first, the ZnO QDs were synthesized under a nitrogen atmosphere by solution processing method [6]. The Zinc acetate dehydrate (500 mM) was dissolved in 2-methoxy ethanol and stirred continuously under the steady flow of nitrogen gas for 30 min. The temperature was raised up to 60 °C after that 1.5 ml of MEA was quickly injected into the solution. The solution was then further stirred for 24 h under inert atmosphere. The solution is filtered using PVDF membrane (0.22 μm) to filter out the large particles from the solution. The thin film of the prepared solution of the colloidal ZnO QDs was deposited on the glass substrate by spin coating method. The process was repeated multiple times to achieve the desired thickness of ~40 nm. The thickness was measured by Reflectometer (F-20 UV)thin film analyzer provided by Filmetrics. The particle size (~2.69 nm) of the as-grown ZnO QDs were analyzed by transmission electron microscopy (TEM)

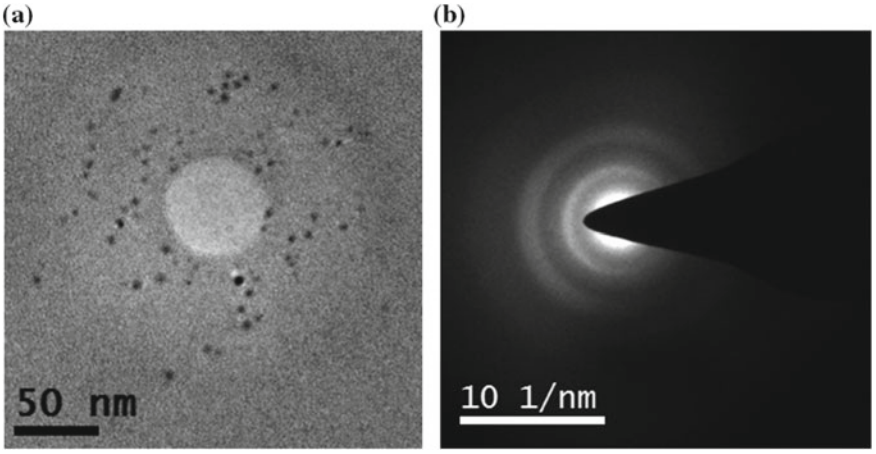

Fig. 1 **a** TEM image of as-grown ZnO QDs and get the particle size ~2.69 nm which is equivalent to its Bohr's radius (~2.87 nm), **b** SAED pattern of ZnO QD

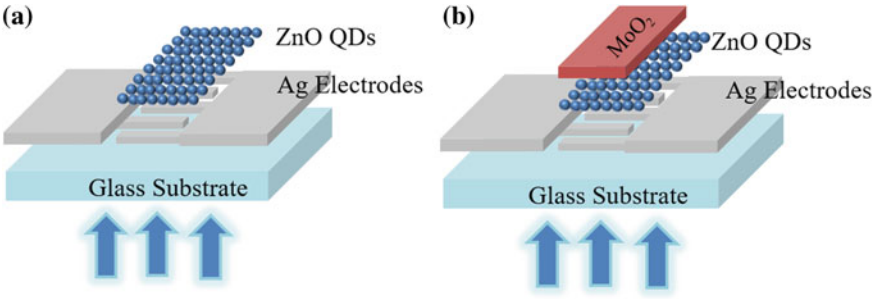

Fig. 2 For the device structure fabricated on the glass with interdigitated electrodes (source and drain) spacing (channel length) of 300 μm **a** device structure of ZnO QD-based photoconductor, **b** device structure of ZnO QD-based photo-JFET, where MoO_2 is used to deplete ZnO QD layer

shown in Fig. 1a. which is equivalent to Bohr's radius (i.e., ~2.87 nm of ZnO) thereby confirming the QD nature of the colloidal ZnO nanoparticles. The diffraction pattern and the concentric ring confirms the crystallinity of the QDs as shown in Fig. 1b.

The High purity Ag and MoO_2 were deposited by thermal evaporation for the thickness of ~50 nm and ~30 nm respectively. The complete device structure of ZnO QD-based MSM photoconductor and ZnO QD-based photo-JFET is shown in Fig. 2a, b.

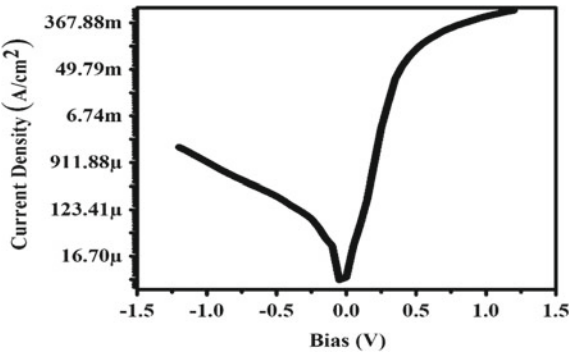

Fig. 3 Rectifying junction between the ZnO QDs and MoO_2 under the dark

3 Results and Discussion

3.1 Junction Characteristics of JFET

Figure 3 shows the rectifying behavior of ZnO QDs and MoO_2 film, which proves that the junction between ZnO/MoO_2 layers important for depleting the ZnO QD layer.

3.2 Source–Drain Current Characteristics of JFET

The comparative study of dark current of both ZnO QDs-based photoconductor and ZnO QDs-based photo-JFET is shown in Fig. 4. One can easily see that for all the similar physical parameters like the thickness of ZnO QDs thin film, the thickness of electrodes, and the interspacing between the interdigitated metal electrodes; the dark current value of photo-JFET is ~20 times lesser than that of photoconductor current.

The applied bias on the Ag electrodes provides an electric field across the depleted ZnO QD layer. The UV light is illuminated from the back side of the device. It is generated the charge pair in the ZnO QDs and collected by the electrodes. The photogenerated charge carriers in the depleted region is higher than comparative to the number of free charge carriers under dark.

The photo-JFET-based on ZnO QDs and MoO_2 has been analyzed with different power densities, where the optical power density is working as a floating gate as shown in Fig. 5. The drain current density versus drain voltage was measured by semiconductor parameter analyzer (B1500, Keysight) under the illumination of the monochromatic UV light at the wavelength of 365 nm from the back side of the

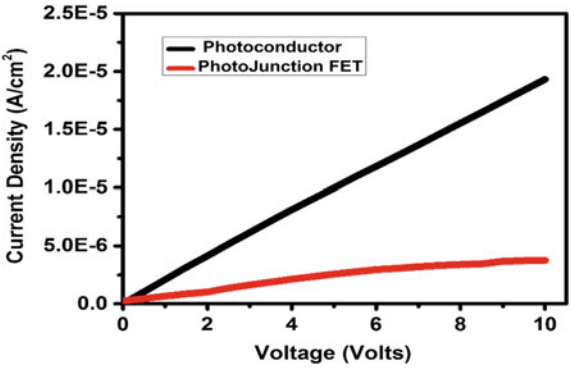

Fig. 4 Current density comparison of MSM and photojunction FET device under the dark condition

Fig. 5 Electro-optical properties of photo-JFET where the photocurrent is the function of the amount of incident monochromatic optical power at wavelength 365 nm and applied bias

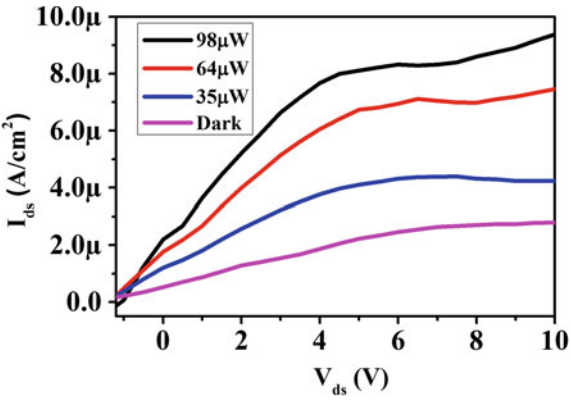

device. The current density versus voltage relationship clearly exhibits the nature of FET under the effect of light intensities as shown in Fig. 5. Nearly, for all intensities and under dark condition saturation is achieved at a low voltage of 4 V comparative to the channel length of 300 μm.

4 Conclusion

Here, we have demonstrated the photojunction FET fabricated on the glass substrate. The photojunction formed between ZnO QDs and MoO_2 under the electric field. The junction behavior like the Schottky junction that limits the dark current flow between the source and drain of the photojunction FET. The device exhibits the transistor characteristics under the illumination of different values of the optical power densities. The optical power densities work as a floating gate for the device.

References

1. Liu, K., Sakurai, M., Aono, M.: ZnO-based ultraviolet photodetectors. Sensors (Basel) **10**(9), 8604–8634 (2010)
2. Baeg, K.-J., Binda, M., Natali, D., Caironi, M., Noh, Y.-Y.: Organic light detectors: photodiodes and phototransistors. Adv. Mater. **25**(31), 4267–4295 (2013)
3. Ng, T.N., Wong, W.S., Chabinyc, M.L., Sambandan, S., Street, R.A.: Flexible image sensor array with bulk heterojunction organic photodiode. Appl. Phys. Lett. **92**(213303), 1–3 (2008)
4. Ramuz, M., Bürgi, L. Winnewisser, C., Seitz, P.: High sensitivity organic photodiodes with low dark currents and increased lifetimes. Org. Electron. Phys. Mater. Appl. **9**(3), 369–376 (2008)
5. Labelle, J., Sutherland, B.R., Hoogland, S., Sargent, E.H., Adinolfi, V., Kramer, I.J.: Photojunction field-effect transistor based on a colloidal quantum dot absorber channel layer. ACS Nano **9**(1), 356–362 (2015)
6. Kumar, Y., Kumar, H., Rawat, G., Kumar, C., Sharma, A.: Colloidal ZnO quantum dots based spectrum selective ultraviolet photodetectors. IEEE Photonics Technol. Lett. **29**(4), 361–364 (2017)

Sarcasm Detection of Amazon Alexa Sample Set

Avinash Chandra Pandey, Saksham Raj Seth and Mahima Varshney

Abstract Sentiment analysis using collection of positive, negative score of a word has been one of the most researched topics in Data Mining. This kind of analysis is more prominent based on the content available on social media like comments on Facebook, tweets on Twitter, and the count goes on. Sarcasm can be understood as irony but it is a text spoken in such a manner that evokes laughter and humor. It is a type of sentiment where people express their negative feelings using positive or intensified positive words in the text. While speaking, people often use heavy tonal stress and certain gestures clues like rolling of the eyes, hand movement, etc., to reveal sarcasm. In this paper, NLTK has been used which is a Python toolkit to harness the power of generating information from the huge text datasets available. Sampled data from Amazon Alexa has been collected which is further processed using SentiWordNet 3.0 and TextBlob to remove noise and irrelevant data. Thereafter, Gaussian naive Bayes algorithm along with TextBlob has been used to detect sarcasm in dataset. The performance of the proposed method is compared with naïve Bayes, decision tree, and support vector machine. From the experimental results, effectiveness of the proposed method is observed.

Keywords SentiWordNet 3.0 · TextBlob · Semi-supervised classification · NLTK POS vector · POS-Tag · Naïve Bayes · Capitalization

A. C. Pandey · S. R. Seth (✉) · M. Varshney
Jaypee Institute of Information Technology, Noida, India
e-mail: saksham2801@gmail.com

A. C. Pandey
e-mail: avinash.pandey@jiit.ac.in

M. Varshney
e-mail: mahimavarshney011@gmail.com

B. S. Rawat et al. (eds.), *Advances in Signal Processing and Communication* ,
Lecture Notes in Electrical Engineering 526,
https://doi.org/10.1007/978-981-13-2553-3_54

1 Introduction

In the present-day world where humans are having conflicting emotions, it is a tedious task to analyze their sentiments. Sarcasm requires shared knowledge between speaker and the listener [1]. Detection of sarcasm in text is difficult because gestural and tonal clues are missing. Many machine learners collect their dataset from social texts to detect sarcasm, especially in tweets [1]. We used the dataset provided by the Amazon Alexa's sample set to apply machine learning algorithms. A machine learning algorithm is attempted to design to detect sarcasm in text. Naive Bayes, one-class SVM and Gaussian kernel are few algorithms commonly used to perform the same task [2].

Semi-supervised sarcasm is identified on two different datasets: a collection of millions of tweets collected from Twitter, and a collection of millions of product reviews from Amazon [3]. On Twitter a common form of sarcasm exists in a form where a positive sentiment contradicted with a negative situation. For example, many sarcastic tweets include a positive sentiment, such as "love" or "enjoy", followed by an expression that describes an undesirable activity or state (e.g., "taking exams" or "being ignored") [4].

Sarcasm changes the polarity of an apparently positive or negative statement into its contradictory statement. A corpus of sarcastic messages on Twitter is created by many authors on whom determination of the sarcasm of each message has been made by its author. These corpuses are used as a reliable benchmark to compare sarcastic expressions in Twitter. Many authors also investigated the impact of lexical and pragmatic factors for discovering sarcastic statements. Sarcastic statements are difficult to identify. Therefore, we compare the performance of machine learning techniques and human judges on this task to find who is performing better. Perhaps unsurprisingly, neither the human judges nor the machine learning techniques [5–7] perform very well [8]. There are many computational approaches for sarcasm detection using lexical cues has been given [9].

Many properties [10–14] were explored while finding sarcasm in text like theories of sarcasm, syntactical properties [15], lexical feature [16, 17], etc. [4, 18, 19]. Model's accuracy can be improved after finding positive and negative works, which can be done using bag-of-words. Accuracy increases for feature extraction by the use of bag-of-words [12]. The experimental results depict that the proposed method outperforms the existing methods. The rest of the paper is organized as follows: Sect. 2 describes the proposed method. Section 3 discusses experimental results and Sect. 4 concludes the paper.

2 Proposed Work

In this research paper, we performed various operations to build our model. SentiWordNet 3.0 dictionary is preprocessed and transformed to form a map, which

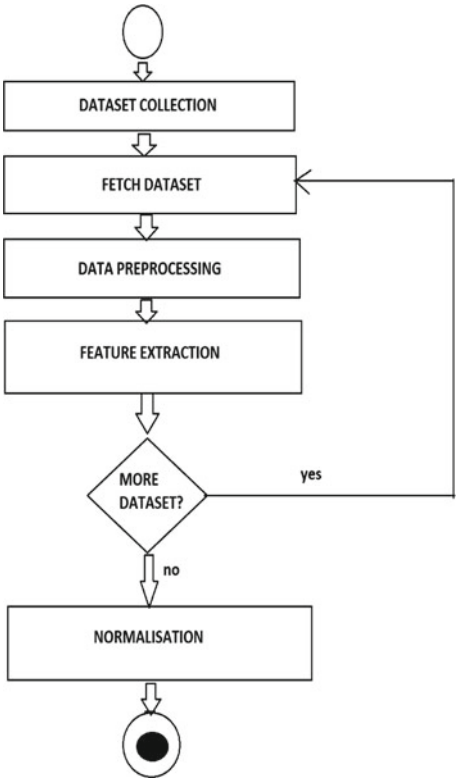

Fig. 1 Flowchart shows the process of data processing, features extraction to detect sarcasm

contains a key and value from the dictionary, where key contains the POS tags and synsets of the SentiWordNet dictionary and value contains the mean of positive and negative values of the respective words in the SentiWordNet dictionary. We used this map to calculate to sentiment of the provided textual data. The complete steps of proposed method have been shown in Fig. 1.

The aim of TextBlob is to provide access to common text processing operations. Polarity and Subjectivity are the main factors of Python library, i.e., TextBlob. TextBlob objects can be treated as Python library to do Natural Language Processing. On the provided textual data, polarity and subjectivity are calculated by the TextBlob objects, to improve the sentiment score. Above two methods were very useful and improvement in accuracy was up to 5–7%. Apart from these two methods, we implemented Vectorization method.

In which a vector was created to store the count of Nouns, Adverbs, Adjectives, and Verbs in the provided textual data. This method was implemented with the help of POS-TAG (Part-Of-Speech Tagging), a very impressive method in the Python library in NLTK (Natural Language Toolkit). NLTK library deals with the textual data and simplifies work for Python programmers. Method POS-TAG returns a list

Table 1 Accuracy of the existing method and the proposed method

Sr. No.	Methods	Accuracy (%)
1	Naive Bayes	65.35
2	Decision tree	65.78
3	SVM	69.37
4	Proposed method	70.96

of each word from the provided textual data, with the tags of Nouns, Verbs, Adverbs, Adjectives, etc.

To improve our accuracy for about 2–3%, we implemented a technique called Capitalization. In which the focus is given on the words which are Capital, so that we can detect the words which are to be focused to be spoken. When we provide a textual data, we have no idea which word is given stress on. This was a very impressive technique to judge the textual data's sense.

A matrix was created for the whole dataset containing the features extracted from the above techniques and final step taken was to apply naive Bayes Algorithm. The naive Bayes is used as a baseline for text categorization. The classifier makes the naïve assumption that the independence occurs between all the features. The classifier is applied from Bayes theorem. Its simplicity makes it a popular machine learning classifier.

$$P(C_k|x) = \frac{P(x|C_k) \cdot P(C_k)}{P(x)}$$

On a whole, after the application of all these great techniques, an accuracy of 70.96% was obtained.

3 Experimental Results

The performance of the proposed method has been tested on sarcasm dataset and its accuracy is also compared with naïve Bayes, decision tree, and SVM. From Table 1, it is easily observed that the proposed method outperforms the exiting method. Moreover, histogram for accuracy is also plotted in Fig. 2. From Fig. 2, the effectiveness of the proposed method can be easily observed.

The above histogram shows the accuracy rate variation for executing the same model for three times.

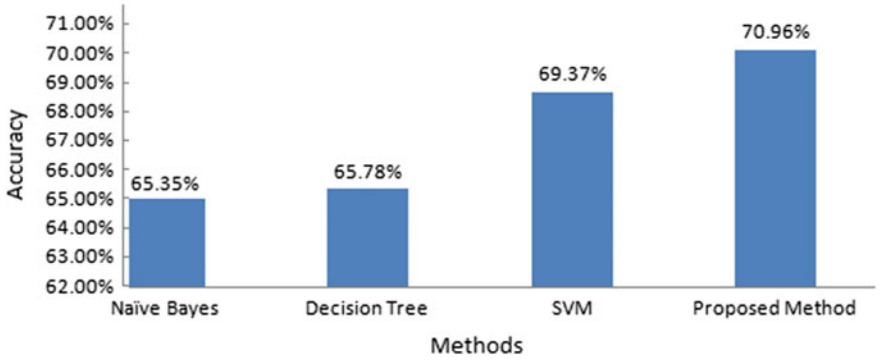

Fig. 2 Comparison of various models on sarcasm dataset

4 Conclusion

Automatic sarcasm detection is a formidable task. This paper offers novel naïve Bayes method to detect sarcasm in Amazon Alexa dataset [20]. The dataset is divided into training and test dataset using cross-validation techniques. The quality of features/attributes extracted from the training dataset affects the performance of the technique. Therefore, SentiWordNet and TextBlob have been used to extract important features from dataset and the model is trained using those features. The test dataset is tested using Gauss-based naïve Bayes method and three baseline methods namely; naïve Bayes, decision tree, and support vector machine. From the experimental results, it is found that the proposed method outperforms the baseline methods.

Sarcasm is closely related to language- or culture-specific traits. Future approaches to identity sarcasm in new languages can benefit to identify such traits.

References

1. Bharti, S.K., Vachha, B., Pradhan, R.K., Babu, K.S., Jena, S.K.: Sarcastic sentiment detection in tweets streamed in real time: a big data approach. Digital Communications and Networks **2**(3), 108–121 (2016)
2. Peng, C.-C., Lakis, M., Pan, J.W.: Detecting Sarcasm in Text: An Obvious Solution to a Trivial Problem (2015)
3. Dmitry, D., Tsur, O., Rappoport, A.: Semi-supervised recognition of sarcastic sentences in twitter and amazon. In: Proceedings of the fourteenth conference on computational natural language learning, pp. 107–116. Association for Computational Linguistics (2010)
4. Ellen, R., Qadir, A., Surve, P., De Silva, L., Gilbert, N., Huang, R.: Sarcasm as contrast between a positive sentiment and negative situation. In: Proceedings of the 2013 Conference on Empirical Methods in Natural Language Processing, pp. 704–714 (2013)
5. Pandey, A.C., Pal, R., Kulhari, A.: Unsupervised data classification using improved biogeography based optimization. Int. J. Syst. Assur. Eng. Manag. 1–9

6. Pandey, A.C., Rajpoot, D.S., Saraswat, M.: Data clustering using hybrid improved cuckoo search method. In: 2016 Ninth International Conference on Contemporary Computing (IC3), pp. 1–6. IEEE (2016)
7. Pal, R., Avinash Pandey, H.M., Saraswat, M.: BEECP: Biogeography optimization-based energy efficient clustering protocol for HWSNS. In: 2016 Ninth International Conference on Contemporary Computing (IC3), pp. 1–6. IEEE (2016)
8. González-Ibánez, R., Muresan, S., Wacholder, N.: Identifying sarcasm in Twitter: a closer look. In: Proceedings of the 49th Annual Meeting of the Association for Computational Linguistics: Human Language Technologies: Short Papers, vol. 2, pp. 581–586. Association for Computational Linguistics (2011)
9. Forslid, E., Niklas, W.: Automatic Irony-and Sarcasm Detection in Social Media (2015)
10. Bamman, D., Smith. N.A.: Contextualized sarcasm detection on Twitter. In: ICWSM, pp. 574–577 (2015)
11. Pandey, A.C., Rajpoot, D.S., Saraswat, M.: Twitter sentiment analysis using hybrid cuckoo search method. Inf. Process. Manag. **53**(4) 764–779 (2017)
12. Wicana, S.G., İbisoglu, T.Y., Yavanoglu, U.: A Review on sarcasm detection from machine-learning perspective. In: 2017 IEEE 11th International Conference on Semantic Computing (ICSC), pp. 469–476. IEEE (2017)
13. Dave, A.D., Desai, N.P.: A comprehensive study of classification techniques for sarcasm detection on textual data. In: International Conference on Electrical, Electronics, and Optimization Techniques (ICEEOT), pp. 1985–1991. IEEE (2016)
14. Rajadesingan, A., Zafarani, R., Liu, H.: Sarcasm detection on twitter: a behavioral modeling approach. In: Proceedings of the Eighth ACM International Conference on Web Search and Data Mining, pp. 97–106. ACM, (2015)
15. Mishra, A., Kanojia, D., Seema N., Kuntal D., Bhattacharyya, P.: Harnessing Cognitive Features for Sarcasm Detection (2017). arXiv:1701.05574
16. Sharada, A., Krishna, P.P.: Sentiment Mining: an approach for Hindi reviews. Algorithms (2017)
17. Forslid, E., Wikén, N.: Automatic Irony-and Sarcasm Detection in Social Media (2015)
18. Detection Ratcliffe, C., Griffith, J., A Machine Learning Approach to Automatic Sarcasm. National University of Ireland, Galway
19. Joshi, A., Kanojia, D., Bhattacharyya, P., Carman, M.J.: Sarcasm Suite: a browser-based engine for sarcasm detection and generation. In: AAAI, pp. 5095–5096 (2017)
20. Amazon Alexa dataset, http://curtis.ml.cmu.edu/w/courses/index.php/Amazon_Dataset_for_Sarcasm

Reducing Efficiency Droop for Si-Doped Barrier Model of GaN/InGaN Multi-quantum Well Light-Emitting Diode by Designing Electron Blocking Layer

Pramila Mahala, Amit K. Goyal, Sumitra Singh and Suchandan Pal

Abstract An InGaN/GaN light-emitting diode (LED) consisting of special Si-doped barrier profile and graded-composition electron blocking layer (EBL) with varying Al composition was designed and simulated. The simulation results show that EBL can enhance the hole injection and electron confinement compared to nongraded EBL. Consequently, the LED with a special Si-doped barrier profile and graded EBL shows improved electrical and optical properties compared to LED with a special Si-doped barrier profile alone. In addition, the efficiency droop is reduced from 56.71% with nongraded EBL LEDs to 30.92% at a high injection current of 1000 A/cm^2.

Keywords Barrier doping · Efficiency droop · Light-emitting diode · GaN/InGaN Graded electron blocking layer

P. Mahala (✉)
Department of Electrical and Electronics Engineering, Birla Institute of Technology and Science (BITS), Pilani, India
e-mail: pramila.mahala98@gmail.com

S. Pal
Opto-Electronics and MOEMs Group, CSIR–Central Electronics Engineering Research Institute (CSIR-CEERI), Pilani, India
e-mail: spal@ceeri.res.in

A. K. Goyal (✉)
ECE Department, Jaypee Institute of Information Technology, Sector-62, Noida, India
e-mail: amit.goyal@jiit.ac.in

A. K. Goyal · S. Singh · S. Pal
Academy of Scientific and Innovative Research (AcSIR), CSIR–Central Electronics Engineering Research Institute (CSIR-CEERI) Campus,
Pilani, India
e-mail: sumitra@ceeri.res.in

S. Singh
Flexible and Non-Silicon Electronics Group, CSIR–Central Electronics Engineering Research Institute (CSIR-CEERI), Pilani, India

B. S. Rawat et al. (eds.), *Advances in Signal Processing and Communication* ,
Lecture Notes in Electrical Engineering 526,
https://doi.org/10.1007/978-981-13-2553-3_55

1 Introduction

GaN-based LEDs offer much scope to reduce energy consumption and enhance the quality of lighting [1]. In recent years, much advancement has been observed in the field of high-power LEDs. Though they have attracted great interest for various applications in the field of optoelectronics, there are still drawbacks that need to be eliminated to further improve LED performance. The efficiency droop is the major factor in LEDs performance. Various reasons for efficiency droop have been accounted which include, the nonradiative carrier loss mechanisms either inside or outside of the active region; which has very little effect at lower currents but become dominant at high currents. Several mechanisms for this effect have been emphasized in recently published works such as Auger scattering [2, 3], carrier delocalization [4], electron overflow [5], and limited hole transport [5, 6]. Works have been reported toward optimizing the performance of GaN-based LEDs in order to overcome the efficiency droop problem by introducing special Si doping in the GaN quantum well barrier (QWB) layers [7]. Although we can find lots of work proposing excellent results for fabricating the InGaN/GaN-based epilayers for high efficient light-emitting diodes, there are very few discussions on the effects of doping in the quantum-well and/or quantum-well barriers [7] along with graded electron blocking layer to increase the LED efficiency. Nowadays, integration of specially graded EBL is the most operative approaches in reducing efficiency droop [8].

Various reasons have been identified for efficiency droop such as carrier overflow, low hole injection, etc. [3, 8, 9]. To improve the carrier confinement, $Al_xGa_{1-x}N$ EBL was used in conventional LEDs. However, the effective barrier height of electrons reduces due to the high polarization effect in $Al_xGa_{1-x}N$ electron blocking layer [10]. As a result, EBL could not be dealt with efficiently with the carrier overflow. On the other hand, it results in valence band offset and band bending at GaN/EBL junction resulting in reduction of hole injection [11]. To address these problems researchers have come up with EBL by using polarization-matched electron blocking layer like AlInGaN or AlInN these are significant in electron confinement [12, 13]. But, it may degrade crystallinity of the subsequent p-GaN layer. Furthermore, EBL cannot enhance hole injection effectively because band offset occurs between the last GaN barrier and electron blocking layer [10].

In this paper, we investigate the effect of special Si-doped barrier profile along with graded EBL in InGaN/GaN MQW LEDs as an attempt to overcome the efficiency droop by simulation. We have simulated InGaN/GaN MQW LED heterostructure using the SiLENSe5.8 module of the SimuLED software. The LED band diagrams simulated by software as a function of bias. It is used for two recombination processes that are nonradiative and radiative and drift-diffusion analysis of electron and hole injection in multi-quantum wells structure [14].

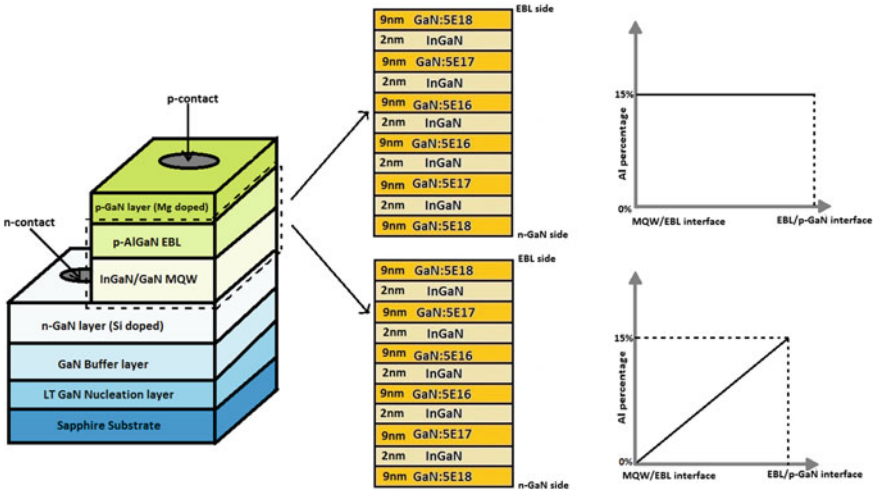

Fig. 1 Schematic of light-emitting diode with and without graded electron blocking layer structure

2 Simulation Parameters and Device Structure

The original structure of LED as a reference is based on the LED designed by Dipika et al. [6]. The LED structure is composed of a 2 μm thick n-GaN layer (n-doping = 5×10^{18} cm^{-3}), five 2-nm thick $In_{0.23}Ga_{0.77}N$ (of doping = 1×10^{15} cm^{-3}) QWs sandwiched by six 9 nm-thick GaN barrier layers, 20 nm-thick EBL with N_A 1.2×10^{19} cm^{-3} and p-GaN layer thickness is 200 nm ($N_A = 1.2 \times 10^{19}$ cm^{-3}). The donor concentration in the six barriers are 5×10^{18}, 5×10^{17}, 5×10^{16}, 5×10^{16}, 5×10^{17}, 5×10^{18} cm^{-3}, successively. Based on the reference structure, we designed LED structure with a linearly graded electron blocking layer and from here on we denote it by GEBL LED. The GEBL LED was simulated with the composition of aluminum vary from 0 to 15% (Fig. 1).

In both these cases electron mobility, hole mobility, were assumed as 150 cm^2/Vs and 10 cm^2/Vs, respectively. While doing simulation operating forward voltage remains constant, i.e., 3 V.

3 Results and Discussions

The band diagram for both the structures for uniform p-$Al_{0.15}Ga_{0.85}N$ EBL and linearly graded P-$Al_{0\text{-}0.15}Ga_{1\text{-}0.85}N$ EBL is illustrated in Fig. 2. The energy gap between the barrier of GaN and EBL is lower in GEBL LED. Thus, enhancement in hole injection can be possible by using GEBL structure in LEDs [8]. As a payable cost to improve the hole injection, we observe a slight reduction in conduction band offset

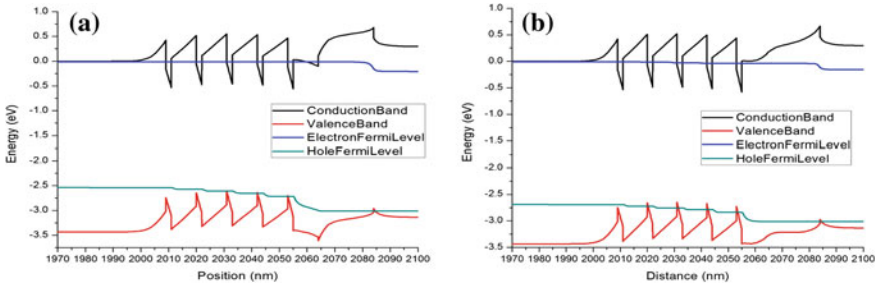

Fig. 2 Band diagram for **a** Reference Structure **b** GEBL LED

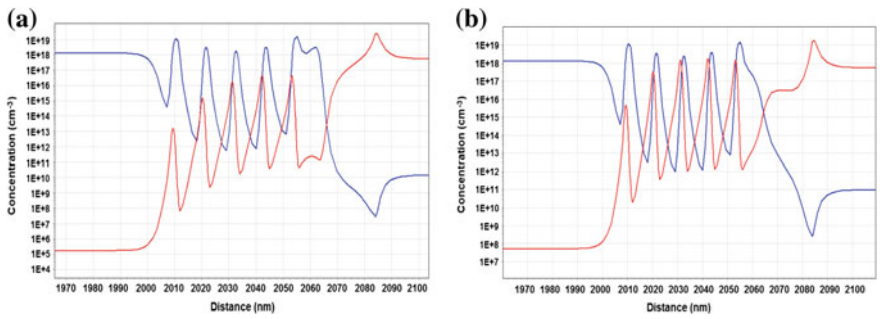

Fig. 3 Concentration profile of holes and electrons in **a** Reference Structure **b** GEBL LED at 3 V

at the interface of GEBL and p-GaN that enhance electron confinement. We can achieve a higher conduction band offset by increasing the Al composition.

The distribution of electron and hole concentration in reference and GEBL light emitting diode at 3 V are shown in Fig. 3a and b, respectively. We have observed that with GEBL, the concentration of injected holes is significantly high and is also uniformly distributed in the EBL region as compared to the reference structure. It signifies that the flatter valence band (as one can see in the band diagram) facilitates the hole transportation across EBL.

Figure 4 reveals that the barriers with graded EBL shows higher and uniform radiative recombination compared to the reference structure because of the higher concentration and uniform distribution of the holes and electrons in the active region. We observed two orders higher radiative recombination in each of the quantum well. This can be ascribed to improved hole injection and transport.

We have studied the nature of emission intensity with respect to the emission wavelength in both the reference structure and with GEBL LED structure. It is observed that the structure with a linearly graded p-$Al_{0\text{-}0.15}Ga_{1\text{-}0.85}N$ electron-blocking layer has significantly higher emission intensity as compared to the reference structure. The peak wavelength in the case of GEBL LED shifted slightly toward the higher wavelength side as illustrated in Fig. 5.

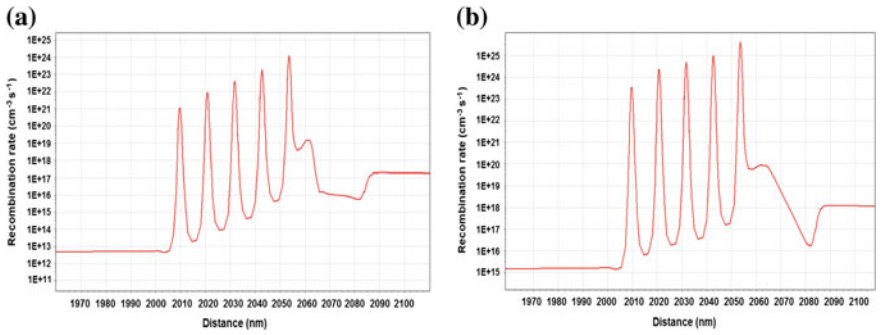

Fig. 4 Radiative recombination in **a** Reference Structure **b** GEBL LED at 3 V

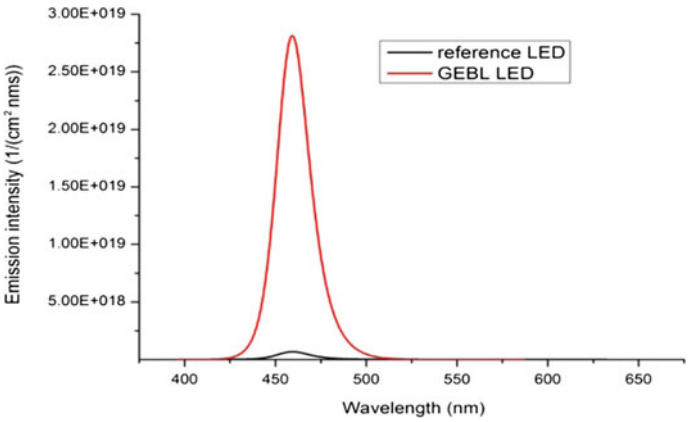

Fig. 5 Emission intensity curve for Reference Structure and GEBL LED structure

Finally, we have studied the internal quantum efficiency of reference and GEBL light-emitting diode structures versus current density. Figure 6 shows the maximum efficiency peak of GEBL light-emitting diode occurs at a current density of 61.4 A/cm^2, which is higher for GEBL LED structure at 20.3 A/cm^2. Moreover, the efficiency sink defined as (peak efficiency – efficiency at X A/cm^2)/peak efficiency, was reduced from 56.71% in reference light-emitting diode to 30.92% in GEBL light-emitting diode.

The improvement in internal quantum efficiency mostly attributed to the enhancement of hole injection, especially at high current density. The insert figure of IQE shows that at a low current density (up to 10 A/cm$^{2)}$ the suggested design having almost no efficiency droops. Therefore, by using the proposed InGaN/GaN MQW LEDs with a linearly graded p-$Al_{0\text{-}0.15}Ga_{1\text{-}0.85}N$ electron-blocking layer the droop problem may be reduced and better internal quantum efficiency may be achieved.

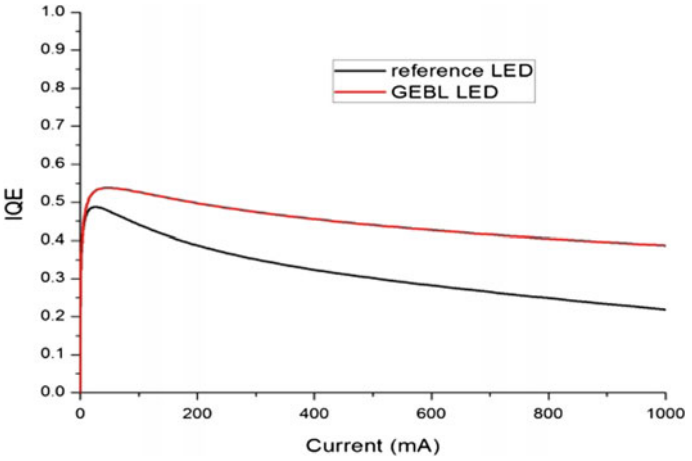

Fig. 6 Internal quantum efficiency versus current density for reference and GEBL light-emitting diodes

4 Conclusions

InGaN/GaN MQW LED structure we have investigated the effects of linearly graded AlGaN electron-blocking layer. We have simulated GEBL LED structured and compared it with the reference structure [7]. The hole concentration in MQWs is enhanced in the GEBL region and p-GaN, showing that the hole transportation across the EBL can be enhanced by GEBL. We observe an increase in radiative recombination by almost two orders in the GEBL LED structure. We observed improvement in internal quantum efficiency and also a reduction in the efficiency droop. At a lower injection current of 100 A/cm^2, the efficiency droop is only 2.63% in GEBL LED whereas, in nongraded EBL LED the efficiency droop is 14.15%. The efficiency droop is reduced from 56.71% in reference LED to 30.92% in GEBL LED when 1000 A/cm^2 current is injected. This work involves that behavior of carrier transportation can be improved by appropriately modifying the composition of the electron blocking layer to achieve enhanced internal quantum efficiency.

Acknowledgements We acknowledge Director, CSIR-CEERI, Pilani for his inspiration in this work. The authors thank all Opto-electronic and MOEMS group members for their help and support.

References

1. U.S. Department of Energy, http://www.energy.gov/
2. Shen, Y.C., Mueller, G.O., Watanabe, S., Gardner, N.F., Munkholm, A., Krames, M.R.: Auger recombination in InGaN measured by photoluminescence. Appl. Phys. Lett. **91**, 141101 (2007)

3. David, A., Grundmann, M.J., Kaeding, J.F., Gardner, N.F., Mihopoulos, T.G., Krames, M.R.: Carrier distribution in (0001) InGaN/GaNmultiple quantum well light-emitting diodes. Appl. Phys. Lett. **92**, 053502 (2008)
4. Monemar, B., Sernelius, B.E.: Defect related issues in the "current roll-off" in InGaN based light emitting diodes. Appl. Phys. Lett. **91**, 181103 (2007)
5. Rozhansky, I.V., Zakheim, D.A.: Analysis of processes limiting quantum efficiency of AlGaInN LEDs at high pumping. Phys. Status Solidi A **204**, 227–230 (2007)
6. Lu, T.P., et al.: Advantages of GaN based light-emitting diodes with a p-InGaN hole reservoir layer. Appl. Phys. Lett. **100**, 141106 (2012)
7. Robidas, D., Arivuoli, D.: Simulation Studies on GaN/InGaN Based Multi Quantum Well Light Emitting Diode for Reducing Efficiency Droop by Imposing Improved Si-Doped Barrier Model. Energy Environ. Focus **1**, 57–63 (2012)
8. Wang, C.H., et al.: Hole injection and efficiency droop improvement in InGaN/GaN light-emitting diodes by band-engineered electron blocking layer. Appl. Phys. Lett. **97**, 261103 (2010)
9. Wang, C.H., et al.: Temperature-Dependent Electroluminescence Efficiency in Blue InGaN—GaN Light-Emitting Diodes With Different Well Widths. IEEE Photonics Technol. Lett. **22**, 236–238 (2010)
10. Han, S.H., et al.: Effect of electron blocking layer on efficiency droop in InGaN/GaN multiple quantum well light-emitting diodes. Appl. Phys. Lett. **94**, 231123 (2009)
11. Kim, M.H., et al.: Design of high-efficiency GaN-based light emitting diodes with vertical injection geometry. Appl. Phys. Lett. **91**, 23510 (2007)
12. Choi, S., et al.: Improvement of peak quantum efficiency and efficiency droop in III-nitride visible light-emitting diodes with an InAlN electron-blocking layer. Appl. Phys. Lett. **96**, 221105 (2010)
13. Kuo, Y.K., Tsai, M.C., Yen, S.H.: Numerical simulation of blue InGaN light-emitting diodes with polarization-matched AlGaInN electron-blocking layer and barrier layer. Opt. Commun. **282**, 4252–4255 (2009)
14. SimuLED online resource, http://www.str-soft.com/products/SimuLED/

Mole Fraction Dependency Electrical Performances of Extremely Thin SiGe on Insulator Junctionless Channel Transistor (SG-OI JLCT)

B. Vandana, Prashant Parashar, B. S. Patro, K. P. Pradhan, S. K. Mohapatra and J. K. Das

Abstract In this paper, the single-gate junctionless (JL) MOSFET with extremely thin silicon germanium (SiGe) device layer on insulator (ETSG-OI) is explored to identify the short channel effects (SCEs) and electrical behavior of the device. The device incorporates various engineering schemes (channel and spacer engineering scheme) with JL topology on SOI platform. The influence of the SiGe device layer with mole fraction (x) variation (x = 0.25, 0.5, 0.75) is investigated to understand the bandgap differences of the device. Depending on the change in Ge mole fraction, the energy potential, electric field, and drain induced barrier lowering (DIBL) performances are analyzed. From the simulation results at x = 0.25, the ETSG-OI JLCT shows reasonable improvement in ON current (I_{ON}) and DIBL at both linear and saturation drain voltages. For different values of x, the energy bandgap tends to vary from 0.6−1.1 eV. It is observed that at x = 0.25 the bandgap is 0.8 eV which is almost near to the bandgap of Si material due to the 25% existence of Ge material.

B. Vandana · B. S. Patro · S. K. Mohapatra · J. K. Das
School of Electronics Engineering, Kalinga Institute of Industrial Technology, Bhubaneswar, India
e-mail: vandana.rao20@gmail.com

B. S. Patro
e-mail: shivalalpatro@gmail.com

S. K. Mohapatra
e-mail: skmctc74@gmail.com

J. K. Das
e-mail: jkdas12@gmail.com

P. Parashar (✉)
ECE Department, Jaypee Institute of Information Technology Deemed to be University, Noida, India
e-mail: pparashar97@gmail.com

K. P. Pradhan
ECE Department, Indian Institute of Information Technology Design and Manufacturing Kancheepuram, Chennai, India
e-mail: kppradhan@iiitdm.ac.in

B. S. Rawat et al. (eds.), *Advances in Signal Processing and Communication* ,
Lecture Notes in Electrical Engineering 526,
https://doi.org/10.1007/978-981-13-2553-3_56

Keywords Drain induced barrier lowering · Junctionless MOSFET · I_{ON}-I_{OFF} Silicon germanium · Electrical performances

1 Introduction

In deep submicron technology, reducing I_{OFF} and improving the device performance are an important parameter for nanoelectronics. The importance of scaling and the factors affecting the device are discussed and reported in [1]. At a particular technology node, international technology road map for semiconductors (ITRS) [2] has given the scaling limits for every technology. This helps the device engineers to involve themselves in developing new ideas on device modeling. Scaling gate length (L_G) below 100-nm will degrade the device performance with an increase in leakage currents. To improvise this, explicit architectures and material properties are added to the classical MOSFET and implemented with various architectures. Few of the architectural representations are DG-MOSFET [3], GAA-MOSFET [4], and CNT-FET [5] that are supported on a nonplanar structure. In nanoscale regime, the devices are well represented through fully depleted body and usually observed with silicon-on-insulator (SOI) technology. The example of fully depleted body includes single gate extremely thin SOI in terms of device processing [6].

Various materials are represented at nanoscale such as high-k dielectric materials for gate stack, strained silicon for channel engineering (high mobility), and compound materials for high electron mobility transistors (HEMT) that improve the channel mobility that depends on the mole fraction value. Hence, these materials are used to formulate new planar structures, which further condense the fabrication cost. To reduce the fabrication cost, again a planar architecture with different device patterns is used in practice. Such as SOI-FET, HEMT devices, Junction Less Transistors (JLTs), FinFETS [7], etc., and other hetero-structures are implemented. For the first time, Lilienfeld transistor [8] proposes a planar device for controlling electric current. The device is constructed with no metallurgical junctions across source/channel and drain/channel (device layer). Further, Colinge et al. explore the device and named it as junctionless transistor (JLT) and fabricated with silicon (Si) [9] on the SOI platform. The first JLT was designed using gate all around (GAA) structure, the nanowire transistors with bulk substrates with planar approximation was performed and demonstrate in [10, 11]. The high-k materials are preferable due to larger bandgap which reduces the leakage currents across junctions and degrades channel mobility slowing down the device speed. The high-k spacer engineering technique establishes lower electrostatic integrity and diminishes impact ionization effect due to gate fringing electric fields [12]. Besides incorporating high-k gate sidewall spacers, the effective approach owning channel controllability through multi-gate architecture induces superior characteristics for small channel length devices. The mole fraction is one way of expressing the composition of a mixture with a dimensionless quantity; mass fraction (percentage by weight) and volume fraction (percentage by volume) are others [13]. The thin epitaxial layer of $Si_{1-x}Ge_x$ layer is grown on

top of a Si, a compressive strain is induced in $Si_{1-x}Ge_x$ layer due to the mismatch between Si and SiGe layer, and the hole mobility increases due to strain effect [14, 15]. Due to this, the V_{TH} decreases as Ge mole fraction increase.

The paper explores the extensive simulation study of JLT with extremely thin silicon germanium (SiGe) device layer on insulator (ETSG-OI) which is a channel engineering technique. The impact of Ge mole fraction on the electrical characteristics investigated for SiGe device layer JLT. The electrical performances and short channel effects (SCEs) are evaluated with the mole fraction variation of the germanium material. Overall, simulations are carried out with TCAD 2D simulator.

Along with the introduction, Sect. 2 discusses the device structure and the physics models activated for the simulation. Section 3 describes the study of the electrostatic integrity and the electrical performances of ETSG-OI JLCT. Finally, the conclusion is drawn.

2 Extremely Thin Silicon Germanium on Insulator Junctionless Channel Transistor (ETSG-OI JLCT)

The paper introduces an ETSG-OI JLCT with high-k spacer and Fig. 1a, b represents the schematic view of ETSG-OI JLCT. The construction details of JLT have no metallurgical junctions along lateral surface. The oxide layer provides isolation across vertical direction at oxide/channel interface. Usually, the device layer is doped (N_D) uniformly with heavy doping of N_D 10^{19} to 10^{22} cm^{-3}depending on the type of the channel formation. The JLTs are well known reduce the short channel effects (SCEs). The device with high doping dependency induces high electric field along vertical direction which makes channel fully depleted below V_{TH} at $V_{GS} = 0$. Above threshold voltage (V_{TH}), the field drops to zero, with the work-function difference ($\phi_m - \phi_s$) of 1.1 eV. The change in work-function makes the band flat at V_{FB} with a positive shift in V_{TH} is observed ($V_{GS} = V_{DS}$), and the conduction takes place at bulk of the SiGe device layer avoiding surface potential. At maximum voltage, the field drops to zero across vertical direction. Therefore, JLTs with different structures (engineering schemes) are preferable to scale SCEs [9, 16]. To avoid self-heating effects buried oxide (BOX) is laid over the substrate, this induces lower parasitic capacitances due to isolation from the bulk silicon.

Both the device utilizes the transistor on insulator technique but with different channel materials. The device layer for SOI JLT is Si and SG-OI JLCT is SiGe. To develop the device design, the parameters listed in Table 1 are used to design ETSG-OI JLCT. The substrate for bulk planar structure is initiated with Si material and doped with N_A. The buried oxide (BOX) as insulator is grown on top of the Si substrate to form SOI topology. An extremely thin SiGe layer is grown epitaxial over BOX forming a device layer. The device layer formation is of S/D and channel with uniform N_D of $10^{19}cm^{-3}$ with no doping gradients and forming a JL topology. The effective oxide thickness (EOT) thickness is taken as 1-nm and a metal gate with the

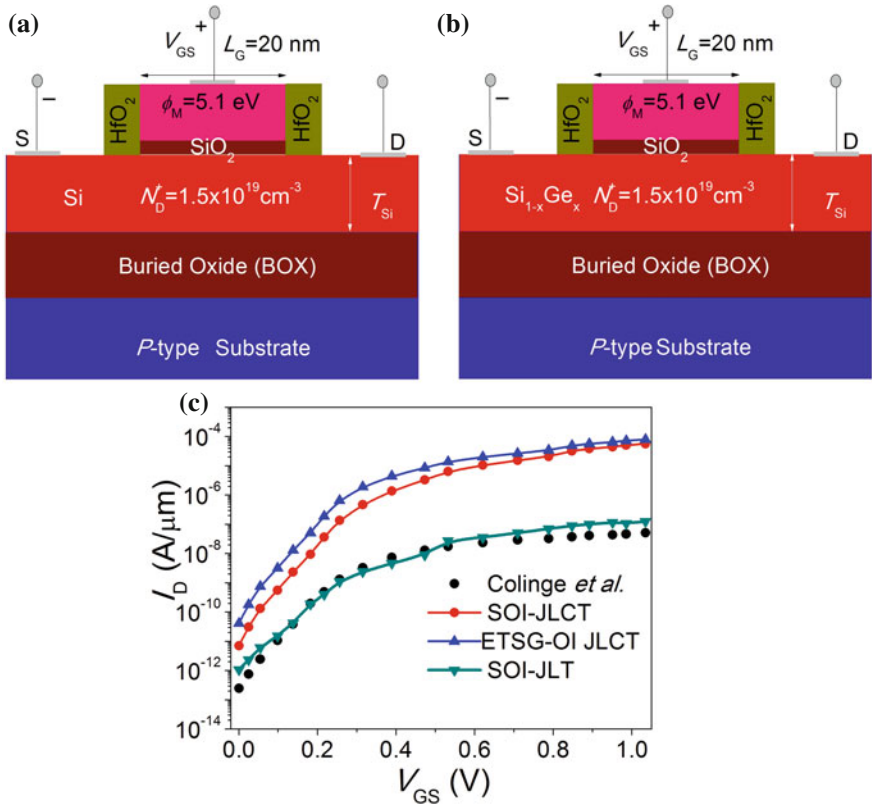

Fig. 1 Cross-sectional view of **a** silicon-on-insulator junctionless channel transistor (SOI JLCT). **b** Extremely thin silicon germanium junctionless channel transistor (ETSG-OI JLCT). **c** I_D as a function of V_{GS}, the plot SOI JLT with no spacers is calibrated with [16]. The plots represent SOI JLCT and ETSG-OI JLCT with high-k spacers. $I_{OFF} = 10^{-11}$ cm^{-3} and $I_{ON} = 10^{-5}$ cm^{-3}

ϕ_m of 5.1 eV is considered. Finally, the contact set using metal is applied to gate source and drain. Introducing the high-k HfO_2 spacers on either side of the gate [17, 18] allows to improve fringing electric field to reduce OFF current.

The conduction mechanism of JLTs is similar to that of conventional MOSFET, but JLT conducts with high ϕ_m that denotes a shift in V_{TH}. The advantage in dealing with the SiGe is compatible with standard Si technology. The compound material SiGe has 4.2% of lattice mismatch and the lattice constant of Si and Ge is given as x = 5.431 Å and 5.658 Å respectively [19, 20]. The variation in x value includes lattice match, lattice constant of $Si_{1-x}Ge_x$ $(5.431 + 0.20x + 0.027x^2)$Å. As the device layer is $Si_{1-x}Ge_x$ material, the device satisfies the channel engineering scheme due to the band gap variation and fulfill in achieving Si bandgap value even. The change in mole fraction (x) results in a change in the bandgap across E_C and E_V [21].

Table 1 Parameters used for simulation [7, 29]

Parameters	ETSG-OI JLCT	SOI JLCT
Device layer (T_{Si})	5-nm	5-nm
Donor doping (N_D)	1.5×10^{19} cm^{-3}	1.5×10^{19} cm^{-3}
EOT gate dielectric (T_{OX})	1-nm	1-nm
Gate work-function (ϕ_m)	5.1 eV	5.1 eV
Well doping (N_A)	10^{16} cm^{-3}	10^{16} cm^{-3}
Drain Voltage (V_{DS})	0.05 V, 1 V	0.05 V, 1 V
Channel length (L_G)	20-nm	20-nm
Energy gap (eV)	0.6 −1.1 eV	1.1 eV

The simulation methodology utilizes drift-diffusion carrier transport mobility model having high field saturation carrier densities with transverse field dependencies [22]. As SiGe is a compound material with mole fraction dependence, the effective intrinsic density and band gap narrowing model are used. To solve this, a self-consistent drift-diffusion equation is used. Due to high N_D across lateral direction, OldSlotboom bandgap is narrowing, and Shockley–Read–Hall Recombination mechanism is taken into account [23].

The model calculates the intrinsic carriers for Si material hence it improves the carrier mobility under high field saturation. The simulations are carried out using Sentaurus TCAD 2D simulator [24, 25]. Figure 1c illustrates the I_D-V_{GS} characteristics of the SOI JLT device, and the models utilized for the simulations are calibrated with the model parameters of Colinge et al. [16]. It is observed that simulation results are in good agreement with the calibrated data. The current characteristics of the devices SOI JLCT and ETSG-OI JLCT explore using high-k spacers are plotted in Fig. 1c. The ETSG-OI JLCT at mole fraction (x) 0.25 and the I_{ON} shows 20% improvement over SOI JLCT. This implies that Si content is high in $Si_{1-x}Ge_x$ device layer and signifies Si material properties.

3 Results and Discussions

The section discusses in detail about the simulated results achieved through device simulator. Along with short channel effects, the energy and electric field across lateral direction is observed for ETSG-OI JLCT. The I_D-V_{GS} characteristics of SOI and ETSG-OI JLCT are shown in Fig. 2a, b at two different drain voltages $V_{D,Lin} = 0.05$ V and $V_{D,Sat} = 1$ V, respectively. The obtained threshold voltage (V_{TH}) values at linear and saturation voltages for both the devices are calculated and shown in Table 2. These values are further employed to evaluate DIBL and I_{ON}-I_{OFF} ratio. The schemes evolved to establish the device performances are fully depleted channel; high-k spacers, high doping concentration, mole fraction variation, and tuning ϕ_m are

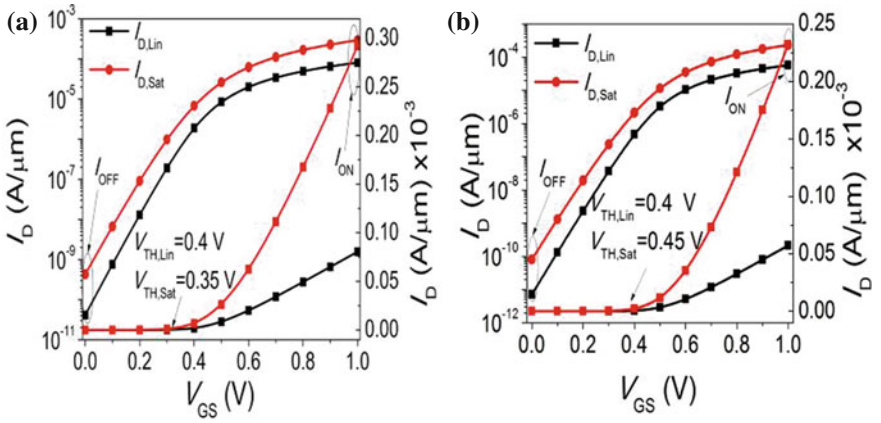

Fig. 2 **a** I_D with respect to V_{GS} for ETSG-OI JLCT (x = 0.2). L_G = 20-nm, ϕ_m = 5.1 eV, N_D = 1.5×10^{19} cm^{-3}. **b** I_D with respect to V_{GS} for ETSG-OI JLCT (x = 0.2). L_G = 20-nm, ϕ_m = 5.1 eV, N_D= 1.5×10^{19} cm^{-3}

Table 2 Computed parameters of JLCT devices at $V_{D,Lin}$ = 0.05 V and $V_{D,Sat}$ = 1 V

Device	ETSG-OI JLCT			SOI JLCT
	x = 0.25	x = 0.5	x = 0.75	
$V_{TH,Lin}$ (V)	0.4	0.42	0.5	0.45
$V_{TH,Sat}$ (V)	0.35	0.35	0.4	0.4
DIBL (mV/V)	52.63	73.68	105.26	52.63
$I_{ON,Lin}$ (A/μm)	8.05×10^{-5}	8.22×10^{-5}	8.04×10^{-5}	5.72×10^{-5}
$I_{ON,sat}$ (A/μm)	2.92×10^{-4}	2.62×10^{-4}	2.29×10^{-4}	2.32×10^{-4}
$I_{OFF,Lin}$ (A/μm)	4.15×10^{-11}	2.20×10^{-11}	4.13×10^{-11}	7.10×10^{-12}
$I_{OFF,sat}$ (A/μm)	4.32×10^{-10}	2.06×10^{-10}	2.03×10^{-10}	8.05×10^{-11}
$V_{TH,Lin}$ (V)	0.4	0.42	0.5	0.45
$V_{TH,Sat}$ (V)	0.35	0.35	0.4	0.4

attributed to enhance the device ability. These parameters are included in ETSG-OI JLCT and are well benefited in achieving high I_{ON} from Fig. 2a with that of SOI JLCT from Fig. 2b.

The principle of operation of JLCT devices conducts through bulk conduction mechanism. Due to this reason, the cut line is taken across the lateral direction of device layer, and the energy band diagram with position for both the devices is shown in Fig. 3a. The thickness of the device layer is extremely thin about (T_{Si} = 5-nm) and the importance of these devices reduces channel leakage currents and variation in chips, this also boasts a back-bias feature [6]. The thinner substrate devices are intrinsically low leakage and regain good control of SCEs. One consequence is the ability to aggressively shrink the gate length, making it easier to fit devices

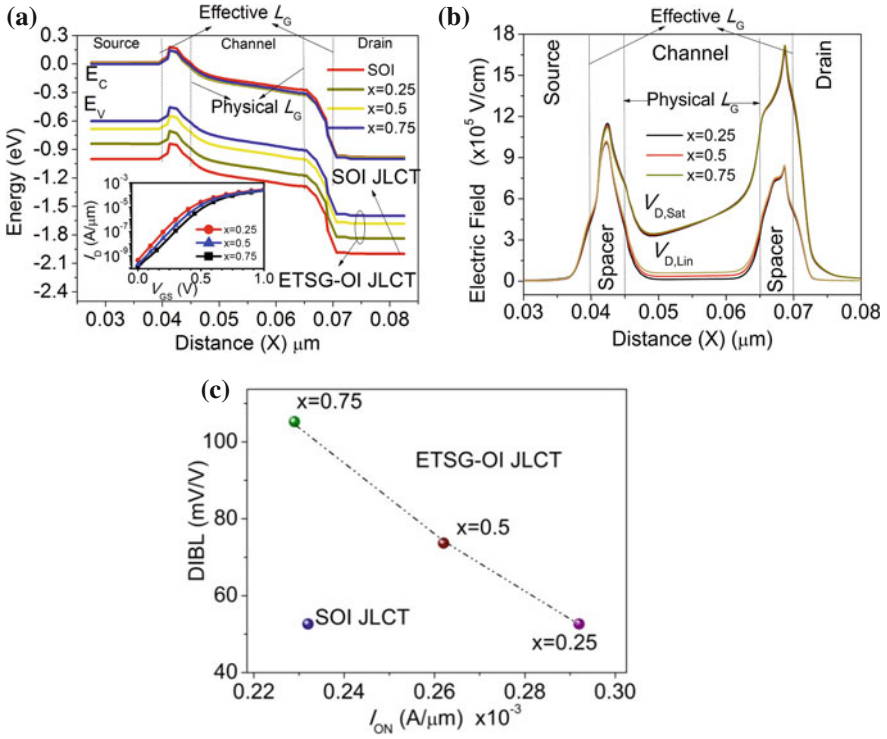

Fig. 3 **a** Energy with respect to distance. **b** Electric field with respect to distance. **c** DIBL-I_{ON} for ETSG-OI JLCT and SOI JLCT is shown. SiGe channel (x = 0.25, 0.5, 0.75), high-k spacers HfO_2, $V_{D,Sat}$ = 1 V and T_{Si} = 5-nm. Inset shows the effect of I_D-V_{GS} (x = 0.25, 0.5, 0.75) L_G = 20-nm

into smaller and smaller pitches and therefore increase logic density to continue Moore's law. In ETSG-OI JLCT, the device layer with SiGe for different value of "x" is considered (x = 0.25, 0.5, 0.75) from [26]. Figure 3a plots the energy band as function of position; the bandgap varies from 1.1 eV to 0.6 eV due to the existence of SiGe material. In SOI JLCT structure, the channel is Si and the E_G = 1.1 eV. Therefore, the difference between E_C and E_V is 1.1 eV. But in ETSG-OI JLCT as the value of "x" changes, an enormous variation between E_C and E_V is observed. At x = 0.25 the E_G = 0.8 eV, in this case, Si content (75%) is high in ETSG-OI JLCT. Gradually if the value of "x" increases, i.e., x = 0.75 E_G = 0.6 eV, this represents that the Ge content (75%) is high in SiGe device layer transistor.

Hence, the bandgap value of SiGe is evaluated with the change in mole fraction value. Due to the high doping concentration of device layer, the Fermi energy (E_{FN}, E_{FP}) for conduction and valence band E_{FP} is zero and E_{FN} is near to the E_C band which is the key merit of JL devices.

The inset figure from Fig. 3a represents the I_D-V_{GS} for different values of "x", the I_{ON} tends to decrease at higher value of "x". In JL devices bulk conduction

mechanism is detected, the high doping dependence generates high electric field at $V_G = 0$ V. Further, with an increase in the positive V_G low E-field at the midpoint of the channel is observed. In Insulator-to-Metal Transition (IMT) structures the direction of current flow, in JLT E-field is perpendicular to the current flow and conduction is at center of the device [27].

Figure 3b represents the electric field as a function of position for linear and saturation drain voltages. The JL device attains high electric field at fully depleted channel as the channel turns partially depletion the electric field is zero. As the value of "x" increases, the peak electric field tends to decrease with maximum gate and drain voltages depicted in Fig. 3b. Generally, the band bending occurs at biased condition, due to the formation of the depletion region and the movement of electronics from source to drain.

Figure 3c shows the DIBL as a function of I_{ON} is represented for both SG-OI JLCT and SOI JLCT. At x = 0.25, I_{ON} is improved in case of SG-OI JLCT but DIBL remain equal for both the devices and at x = 0.75 I_{ON} found to be less and DIBL is very high which is not considerable. In order to improve I_{ON} and DIBL for x = 0.75, a proper tuning of N_D and work-function are suggested [28].

References

1. Roy, K., Mukhopadhyay, S., Mahmoodi-Meimand, H.: Leakage current mechanisms and leakage reduction techniques in deep-submicrometer CMOS circuits. Proc. IEEE **91**, 305–327 (2003)
2. The international technology roadmap for semiconductors (2015)
3. Balestra, F., Cristoloveanu, S., Benachir, M., Brini, J., Elewa, T.: Double-gate silicon-on-insulator transistor with volume inversion: a new device with greatly enhanced performance. IEEE Electron Device Lett. **8**, 410–412 (1987)
4. Fashtami, T.N., Ziabari, S.A.S.: Performance investigation of gate-all-around nanowire FETs for logic applications. Indian J. Sci. Technol. **8**, 231 (2015)
5. Seidel, R.V., Graham, A.P., Kretz, J., Rajasekharan, B., Duesberg, G.S., Liebau, M., Unger, E., Kreupl, F., Hoenlein, W.: Sub-20 nm short channel carbon nanotube transistors. Nano Lett. **5**, 147–150 (2005)
6. Majumdar, A., Ouyang, C., Koester, S.J., Haensch, W.: Effects of substrate orientation and channel stress on short-channel thin SOI MOSFETs. IEEE Trans. Electron Devices **57**, 2067–2072 (2010)
7. Gundapaneni, S., Ganguly, S., Kottantharayil, A.: Bulk planar junctionless transistor (BPJLT): an attractive device alternative for scaling. IEEE Electron Device Lett. **32**, 261–263 (2011)
8. Lilienfeld, J.E.: Method and apparatus for controlling electric currents (1930)
9. Kranti, A., Yan, R., Lee, C.W., Ferain, I., Yu, R., Akhavan, N.D., Razavi, P., Colinge, J.P.: Junctionless nanowire transistor (JNT): properties and design guidelines. In: Proceedings of the ESSDERC, pp. 357–360 (2010)
10. Colinge, J.-P., Gao, M.H., Romano-Rodriguez, A., Maes, H., Claeys, C.: Silicon-on-insulator gate-all-around device. In: 1990 International Technical Digest on Electron Devices Meeting (IEDM'90), pp. 595–598 (1990)
11. Ho, B., Sun, X., Shin, C., Liu, T.-J.K.: Design optimization of multigate bulk MOSFETs. IEEE Trans. Electron Devices **60**, 28–33 (2013)
12. Gupta, M., Kranti, A.: Sidewall spacer optimization for steep switching junctionless transistors. Semicond. Sci. Technol. **31**, 65017 (2016)

13. en.wikipedia.org/wiki/Mole_fraction
14. Bindu, B., DasGupta, N., DasGupta, A.: Analytical model of drain current of Si/SiGe heterostructure p-channel MOSFETs for circuit simulation. IEEE Trans. Electron Devices **53**, 1411–1419 (2006)
15. Laval, S.: The use of strain in silicon germanium heterostructure MOSFET technology (2003)
16. Colinge, J.-P., Lee, C.-W., Afzalian, A., Akhavan, N.D., Yan, R., Ferain, I., Razavi, P., O'Neill, B., Blake, A., White, M., Kelleher, A.-M., McCarthy, B., Murphy, R.: Nanowire transistors without junctions. Nat. Nanotechnol. **5**, 225–229 (2010)
17. Zhu, W.J., Tamagawa, T., Gibson, M., Furukawa, T., Ma, T.P.: Effect of Al inclusion in HfO_2 on the physical and electrical properties of the dielectrics. IEEE Electron Device Lett. **23**, 649–651 (2002)
18. Wu, M., Alivov, Y.I., Morkoc, H.: High-K dielectrics and advanced channel concepts for Si MOSFET. J. Mater. Sci. Mater. Electron. **19**, 915–951 (2008)
19. Fischetti, M.V., Laux, S.E.: Band structure, deformation potentials, and carrier mobility in strained Si, Ge, and SiGe alloys. J. Appl. Phys. **80**, 2234–2252 (1996)
20. Sun, Y., Thompson, S.E., Nishida, T.: Physics of strain effects in semiconductors and metal-oxide-semiconductor field-effect transistors. J. Appl. Phys. **101**, 104503 (2007)
21. Tezuka, T., Sugiyama, N., Takagi, S.: Fabrication of strained Si on an ultrathin SiGe-on-insulator virtual substrate with a high-Ge fraction. Appl. Phys. Lett. **79**, 1798–1800 (2001)
22. Maiti, C.K., Armstrong, G.A.: Applications of silicon-germanium heterostructure devices. CRC Press (2001)
23. Shockley, W., Read Jr., W.T.: Statistics of the recombinations of holes and electrons. Phys. Rev. **87**, 835 (1952)
24. www.synopsys.com/: Sentaurus TCAD User's Manual. In: Synopsys Sentaurus Device. Synopsys (2012)
25. L-2016.03: Sentaurus ^{TM} device user. (2014)
26. Jones, M.H., Jones Stephen, H.: The general properties of Si, Ge, SiGe, SiO2 and Si3N4. Va. Semicond (2002)
27. Colinge, J.P., Lee, C.W., Akhavan, N.D., Yan, R., Ferain, I., Razavi, P., Kranti, A., Yu, R.: Junctionless transistors: physics and properties. In: Semiconductor-On-Insulator Materials for Nanoelectronics Applications, pp. 187–200. Springer (2011)
28. Vandana, B., Patro, B.S., Mohapatra, S.K., Das, J.K.: Exploration towards electrostatic integrity for SiGe on insulator (SG-OI) on junctionless channel transistor (JLCT). Facta Univ. Ser. Electron. Energ. **30**, 383–390 (2017)
29. Gundapaneni, S., Ganguly, S., Kottantharayil, A.: Enhanced electrostatic integrity of short-channel junctionless transistor with high-spacers. IEEE Electron Device Lett. **32**, 1325–1327 (2011)

Analysis of Graphene/SiO_2/p-Si Schottky Diode by Current–Voltage and Impedance Measurements

Pramila Mahala, Ankita Dixit and Navneet Gupta

Abstract We explore the electrical properties of graphene–silicon dioxide–p–silicon Schottky junction diode using current–voltage characteristics and impedance analysis. Ideality factor, rectification ratio, and series resistance are extracted from the experimental data. A linear response of series resistance of graphene/SiO_2/p-Si Schottky diode is observed with respect to change in forward bias voltage from 0 to 2 V.

Keywords Schottky diode · Graphene · Impedance analysis · Silicon

1 Introduction

Graphene, two-dimensional sheet of sp2- hybridized carbon, have extraordinary properties like high transparency (it absorbs only 2.3% of light that passes through it) good thermal and electrical conductivity [1, 2]. The huge scientific and technological interest in graphene has been driven as promising candidates for future semiconductor industries because of its extraordinary properties [2, 3]. Due to high electrical conductivity, it uses as an active layer in electronic device applications and graphene also uses as a metal electrode in electronic devices due to its high transparency and good conductivity which results in the formation of a Schottky contact with various semiconducting materials. The graphene–semiconductor Schottky contact structure has recently been employed in graphene-based devices such as solar cells [4], sensors, lithium-ion battery [5] and LEDs [2, 6]. Therefore, Schottky contact between

P. Mahala (✉) · A. Dixit · N. Gupta
Department of Electrical and Electronics Engineering, Birla Institute of Technology and Science (BITS), Pilani 333031, Rajasthan, India
e-mail: pramila.mahala98@gmail.com

A. Dixit
e-mail: ankitadixit.199@gmail.com

N. Gupta
e-mail: ngupta@pilani.bits-pilani.ac.in

B. S. Rawat et al. (eds.), *Advances in Signal Processing and Communication* ,
Lecture Notes in Electrical Engineering 526,
https://doi.org/10.1007/978-981-13-2553-3_57

graphene and semiconductor need to explore briefly. The Schottky device is the simplest and widely used structure, thus, the analysis of Schottky contact between graphene and semiconductor can be considered as an important topic in graphene device application research.

Schottky diodes have various advantages such as low saturation or leakage current and low forward voltage drop. As a result, Schottky diode is extensively used in a variety of RF and microwave applications. In conventional Schottky diode, semiconductor is sandwiched between two metals. One metal makes ohmic contact with semiconductor and other metal makes Schottky contact [7]. Usually, the Schottky diode is a metal–semiconductor device but by inserting insulating layer, between metal and semiconductor, its characteristics and electrical properties are enhanced. MIS Schottky diode offers higher rectification ratio and lower leakage or saturation current [8]. MIS device has nonideal electrical properties therefore frequency-dependent impedance analysis is very important to get accurate and consistent results about fabricated Schottky semiconductor devices.

In this work, we have investigated detailed electrical properties of graphene/SiO_2/p-Silicon/Ag Schottky diode with SiO_2 oxide layer between graphene and semiconductor using current–voltage characteristics and impedance analysis.

2 Experimental

The p-Si as a substrate or active layer is used in this study. Silicon wafer is oxidized by both dry oxidation (O_2) and wet oxidation (H_2O) process. The silicon wafers are placed in a furnace under dry oxidation conditions for 10 min. After that, the wafers are exposed to wet oxidation condition for 130 min. Then again dry environment is applied for 10 min. Graphene is synthesized by mechanical exfoliation of highly oriented pyrolytic graphite (HOPG). As HOPG consist of various graphene layers in the stack, they have Van der Waals attraction force between adjacent graphene layers. This attraction force is overcome by peeling the layer by the scotch tape, and then multi-layer graphene is achieved. Synthesized graphene is transferred to the SiO_2/p-Si/Ag structure. Silver paste with a thickness of around 1–2 μ painted on the whole backside of the substrate (p-Silicon). The total thickness of silicon dioxide is 700 nm.

The current–voltage characteristics are performed by a KEITHLEY source meter and GPIB data transfer card for current–voltage measurements are used and data are recorded by an interface. Impedance analysis is performed by using L-C-R meter. Impedance spectra are recorded in the frequency range from 10^1 to 10^5 Hz with a constant DC, i.e., room temperature voltage 25 mV. A response of virtual resistance and capacitance are observed with respect to change in forward bias voltage from 0 to 2 V.

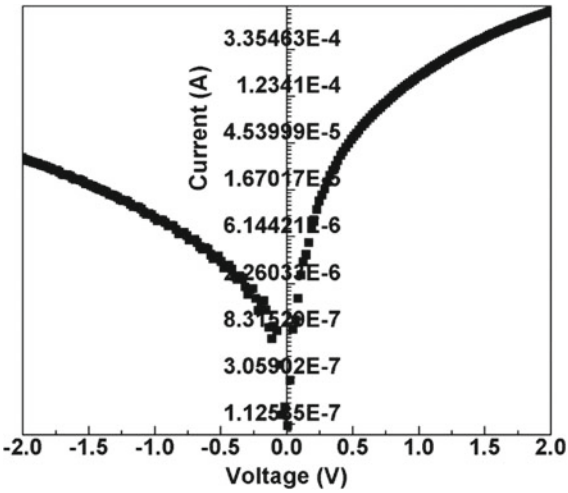

Fig. 1 Current–voltage characteristics of graphene/SiO_2/p-Si Schottky device in forward and reverse bias

3 Result and Discussion

3.1 Current–Voltage Characteristics

The dark current–voltage characteristics of the graphene/SiO_2/p-Si Schottky diode is shown in Fig. 1, It shows typical rectifying behavior. The I-V characteristics of an MIS Schottky diode can be analyzed by the relationship between the diode current and voltage drop across the junction and it can be described by thermionic emission theory as given by following Eq. (1) [7, 9].

$$I = I_0 e^{\frac{qv - IR_S}{nKT}} \left[1 - e^{-\frac{q(V - IR_S)}{KT}}\right] \tag{1}$$

where I_0 is the reverse saturation current, n is the ideality factor, K is the Boltzmann constant, q is the elementary charge, and T is the absolute temperature in Kelvin. The reverse saturation current can be expressed by Eq. (2).

$$I_0 = A\mathrm{A}^* T^2 e^{\left(-\frac{q\Phi_b}{kT}\right)} \tag{2}$$

where A is the contact area, A* is the Richardson constant i.e. 32 A/cm^2 K^2 for p-silicon, T is the temperature and Φ_b is the zero barrier height. Reverse saturation current is 11.2×10^{-8}. A which is calculated from Fig. 1 and now barrier height can be calculated by using Eq. (3), i.e., 0.536 eV.

$$\Phi_b = \frac{KT}{q} \log\left(\frac{I_o}{A\mathrm{A}^* T^2}\right) \tag{3}$$

The ideality factor of the graphene/SiO_2/p-Si Schottky diode can be calculated by the following Eq. (4) [8]

$$n = \frac{q}{KT}\frac{d(V)}{d(lnI)} \tag{4}$$

The ideality factor is calculated from the slope of Fig. 1 in the forward voltage range from 0.5 to 1.5 V and is found to be 9.3. The obtained ideality factor and reverse saturation current shows that graphene/SiO_2/p-Si Schottky diode follows a metal–insulator–semiconductor configuration rather than ideal Schottky barrier diode. At higher forward bias, the I-V characteristics show nonlinearity behavior that indicates a continuum of interface states, in which interface states are at equilibrium with the semiconductor. On the other hand, graphene/SiO_2/p-Si Schottky diode shows good rectifying behavior with a relatively low reverse saturation current density. There are several parameters, which root deviations from ideal behavior and those must be taken into account. These parameters can be ideality factor, interface states at Schottky junction, series resistance, etc., and these are main parameters of the diode. These parameters exhibit a downward curvature at higher forward bias in the I-V characteristics of the Schottky diode. In that case, Cheung's method can be used to obtain the series resistance and ideality factor for the Schottky diode.

Cheung's functions are expressed by [8]

$$\frac{dV}{d(lnI)} = IR_s + n\left(\frac{kT}{q}\right) \tag{5}$$

To obtain series resistance, the plots of dV/dlnI versus I is plotted as shown in Fig. 2 to determine n and R_s values. The slope of this plot gives a series resistance value, i.e., 407.3 Ω and intercept at y-axis is equal to $n\left(\frac{kT}{q}\right)$. The $\frac{kT}{q}$ is the thermal voltage, here, q is magnitude of electrical charge on the electron equal to 1.602×10^{-19} Coulomb, k is a Boltzmann constant. At room temperature, it is calculated approximately as 25.85 mV. Therefore, the calculated ideality factor from the y-axis intercept is 9.34.

4 Impedance Analysis

Figure 3 shows the Bode plots of the graphene/SiO2/p-Si Schottky diode with a different forward bias voltage. The total impedance is plotted versus the frequency. As shown in the Fig. 3, in the higher frequency range the modulus of the impedance is almost similar for the three forward bias voltage. This can be explained considering that the contribution to the total impedance is mainly due to the resistance of the material and it is not affected by the different conditions [4].

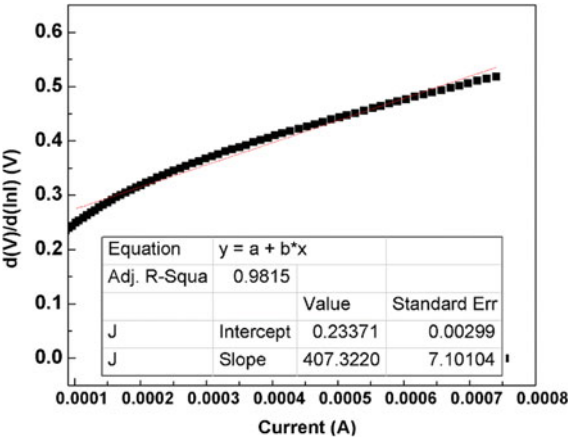

Fig. 2 Plot of d(V)/d(lnI) for graphene/SiO_2/p-Si Schottky device

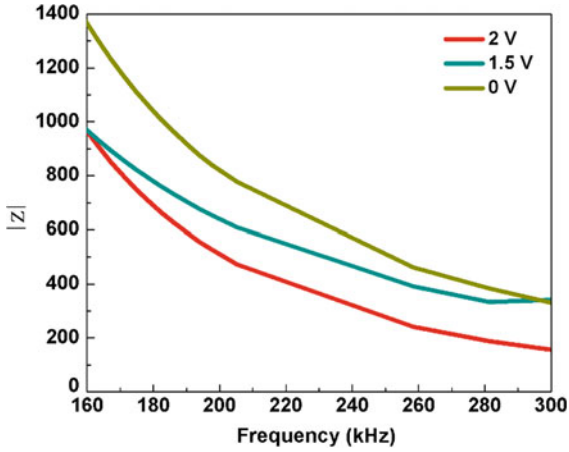

Fig. 3 Amplitude of total impedance with respect to frequency from 150 to 300 kHz for graphene/SiO_2/p-Si Schottky device

With the bias voltage modulus of total impedance is varying it signifying the bias dependence of capacitance and resistance values. As forward bias increasing the modulus of total impedance decreasing because the width of depletion or space charge region is decreasing which decreases the resistance offered by the Schottky junction device. Bulk resistance (series resistance not included) of the Schottky diode is plotted in Fig. 4 for three individual forward bias voltages. Figure 4 shows that decreasing resistance exhibits a downward curvature with respect to increasing forward bias voltage.

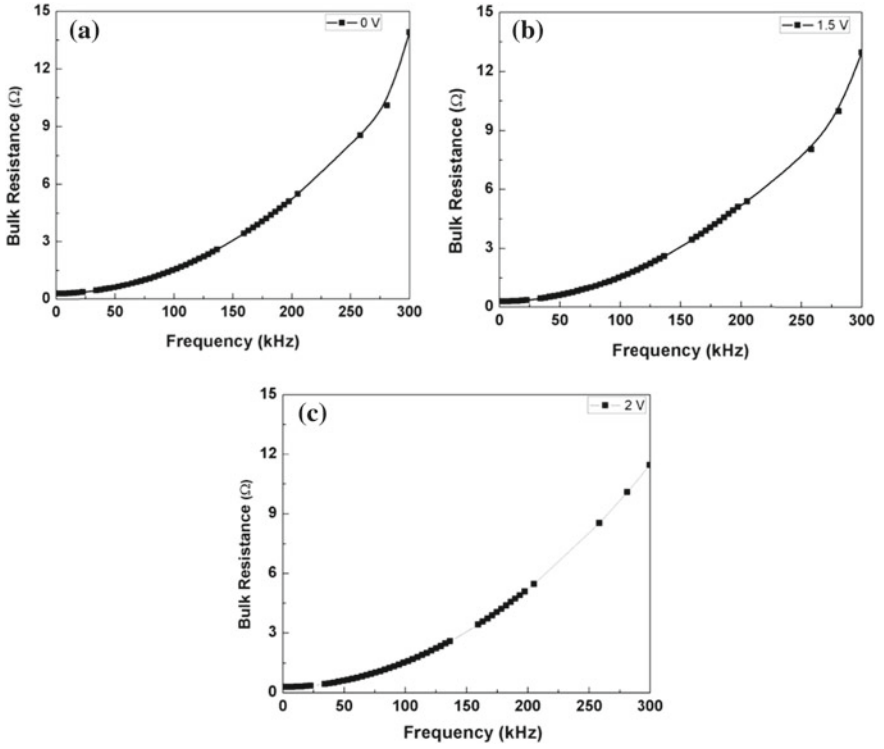

Fig. 4 Real part of total impedance with respect to frequency from 0 to 300 kHz for graphene/SiO_2/p-Si Schottky device

5 Conclusion

The current–voltage characteristics and impedance analysis of graphene/SiO_2/p-Si Schottky diode have been investigated. The obtained results recommend that graphene/SiO_2/p-Si structure follow a metal–insulator–semiconductor configuration rather than the ideal diode. The insulating oxide layer modifies the electrical parameters of graphene/SiO_2/p-Si Schottky diode. The series resistance and ideality factor are found to be 407.3 Ω and 9, respectively.

Acknowledgements This work has been supported by DST, SERB-NPDF, No. PDF/2017/002640. We thank Dr. Sumitra Singh from CSIR-CEERI, Pilani for providing HOPG to the synthesis of graphene.

References

1. Casero, E., Parra-Alfambra, A.M., Petit-Domínguez, M.D., Pariente, F., Lorenzo, E., Alonso, C.: Differentiation between graphene oxide and reduced graphene by electrochemical impedance spectroscopy (EIS). Electrochem. Commun. **20**(1), 63–66 (2012)
2. Mahala, P., Kumar, A., Nayak, S., Behura, S., Dhanavantri, C., Jani, O.: Graphene, conducting polymer and their composites as transparent and current spreading electrode in GaN solar cells. Superlattices Microstruct. **92** (2016)
3. Dixit, A., Dixit, D., Chandrodaya, V.V., Kajla, A.: Graphene: a new era of technology **3**(3), 4–7 (2013)
4. Bonanni, A., Pumera, M.: High-resolution impedance spectroscopy for graphene characterization. Electrochem. Commun. **26**(1), 52–54 (2013)
5. Zhang, Y.Q., et al.: Silicon/graphene-sheet hybrid film as anode for lithium ion batteries. Electrochem. Commun. **23**(1), 17–20 (2012)
6. Behura, S.K., Mahala, P., Nayak, S., Yang, Q., Mukhopadhyay, I., Jani, O.: Fabrication of bilayer graphene and theoretical simulation for its possible application in thin film solar cell. J. Nanosci. Nanotechnol. **14**(4) (2014)
7. Mahala, P., Behura, S.K., Kushwaha, A.S., Ray, A., Jani, O., Dhanavantri, C.: A study on the 2D simulation of Pt/InGaN/GaN/metal Schottky junction solar cell. Semicond. Sci. Technol. **28**(5) (2013)
8. Okutan, M., Yakuphanoglu, F.: Analysis of interface states and series resistance of Ag/SiO2/n-Si MIS Schottky diode using current-voltage and impedance spectroscopy methods. Microelectron. Eng. **85**(3), 646–653 (2008)
9. Yim, C., McEvoy, N., Duesberg, G.S.: Characterization of graphene-silicon Schottky barrier diodes using impedance spectroscopy. Appl. Phys. Lett. **103**(19), 1–6 (2013)

Simulation Study of Uncoupled Electrical Equivalent Model of Piezoelectric Energy Harvesting Device Interfaced with Different Electrical Circuits

Shradha Saxena, Rakesh Kumar Dwivedi and Vijay Khare

Abstract Piezoelectric energy harvester system has fascinated rigorous consideration in the area of self-powered wireless sensor networks. A piezoelectric energy harvesting system constitutes three components, namely, piezoelectric device, interfacing circuits, and storage element. In this paper, a simulation study of the coupled modeling of device equivalent uncoupled model has been carried out with four electrical circuits, namely, SBR, self-powered P-SSHI and S-SSHI, and modified PSSHI circuits. Here, modified PSSHI circuit is the recently developed interfacing circuit that has the advantage of less cost and reduced circuit complexity. From the simulated results, it has been observed that P-SSHI circuit provides maximum piezoelectric voltage (KV) and zero phase difference between piezoelectric voltage and input vibration current. Moreover, this technique provides maximum power (530 mW) and maximum output voltage (600 V) across optimal resistance (680 K).

Keywords Interface circuits · Piezoelectric energy harvesting · P-SSHI · S-SSHI SBR

1 Introduction

In recent years, the use of renewable power sources has changed the electronics world from bulky devices to the self-powered, wearable electronic devices. For energy

S. Saxena (✉) · V. Khare
Department of Electronics and Communications Engineering, Jaypee Institute of Information Technology, Noida 201309, India
e-mail: shradha.saxena@jiit.ac.in

V. Khare
e-mail: vijay.khare@jiit.ac.in

R. K. Dwivedi
Department of Physics and Materials Science & Engineering, Jaypee Institute of Information Technology, Noida 201309, India
e-mail: rk.dwivedi@jiit.ac.in

B. S. Rawat et al. (eds.), *Advances in Signal Processing and Communication* ,
Lecture Notes in Electrical Engineering 526,
https://doi.org/10.1007/978-981-13-2553-3_58

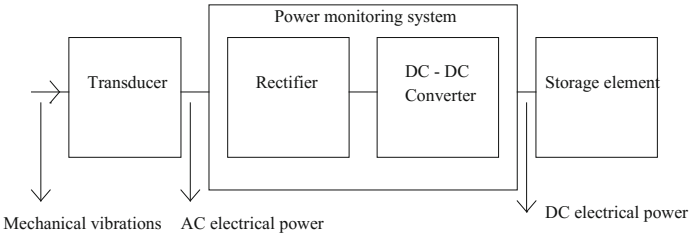

Fig. 1 The complete energy harvesting system [2]

harvesting purpose, mechanical vibration has been chosen as one of the efficient ambient energy sources among others such as radio frequency, and thermal and solar sources. This is due to its large range of power density [1]. The vibration to electrical energy conversion is mainly performed by piezoelectric, electromagnetic, and electrostatic transducing techniques. Further, piezoelectric transducing technique based on piezoelectric effect has been renowned as the best technique due to its high electromechanical coupling, high power density, and good compatibility properties [1]. In literature, mainly two types of piezoelectric effect have been defined: (i) Direct effect and (ii) indirect effect. According to the direct effect, piezoelectric materials are electrically polarized in response to an applied mechanical stress, while in indirect effect piezoelectric materials get strained when subjected to electrical field [2]. The complete piezoelectric energy harvesting system has been shown in Fig. 1. The transducer that constitutes the piezoelectric element converts the vibration energy into electrical energy. Since this generated electrical energy is alternating (AC) in nature and storage buffer usually required DC voltage, therefore a rectifier circuit is required [2]. Moreover, the internal impedance of piezoelectric element is capacitive in nature, and therefore in order to transfer maximum power to the load, a DC-to-DC converter is required for impedance matching purpose.

In this paper, a brief electromechanical modeling of piezoelectric energy harvester has been represented. Then, the response of different interfacing circuits has been analyzed when they are coupled with the device equivalent electrical model. This complete paper has been divided into six sections. The introduction has been mentioned in Sect. 1. Further, a brief study of electromechanical modeling of piezoelectric energy harvesting device has been summarized in Sect. 2. Moreover, a detailed simulation study of coupled modeling of device with different interfacing circuits has been carried out in Sect. 3. In Sect. 4, the simulation results have been discussed and analyzed. Finally, a conclusion has been made in Sect. 5.

2 Electromechanical Modeling of Piezoelectric Energy Harvester

In literature, many researchers have developed analytical models to predict and optimize the amount of electrical energy that could be harvested. The generic model of kinetic energy harvesters, which is clamped at one end and having a proof mass on the free hand as shown in Fig. 2a, was first developed by Williams and Yates [3]. Such generic model can be represented by mass-spring-damper with fixed base as shown in Fig. 2b, which relates the input vibration with the output relative displacement of the system [4]. According to the D'Almbert's law, the system can be expressed by Eq. (1):

$$m\frac{\mathrm{d}^2 z}{\mathrm{d}t^2} + d\frac{\mathrm{d}z}{\mathrm{d}t} + k_s z + F_e = m\frac{\mathrm{d}^2 y}{\mathrm{d}t^2} = ma \tag{1}$$

where $y(t)$ and $\frac{\mathrm{d}^2 y}{\mathrm{d}t^2}$ represent the input vibration and acceleration (a), $z(t)$ is the relative displacement of the mass with respect to the vibrating cantilever beam, k_s is the spring constant representing beam stiffness, d is the damping which is the sum of mechanical and electrical damping of the system, m is the effective mass of the beam itself and the proof mass, and F_e is the restoring force applied by transducer on the proof mass due to electromechanical force. Moreover, for piezoelectric transduction mechanism, if F is the force acting on the piezoelectric material which causes an elongation z in the horizontal direction, then electrical parameters can be correlated with the mechanical parameters according to the following relations [4] as represented by Eq. (2):

$$E = -\frac{V_p}{h}; q = Dbl; T = \frac{F}{bh}; S = \frac{z}{l}; I = \frac{\mathrm{d}q}{\mathrm{d}t} \tag{2}$$

where l, b, and h are length, width, and thickness of the beam; E is the electric field; V_p is the voltage develop across piezoelectric material; q is the charge; D is the electrical displacement; S is the strain; and I is the current. According to the set of equations defined by Eq. (2), the constitutive equations of piezoelectric material be written as in Eqs. (3) and (4):

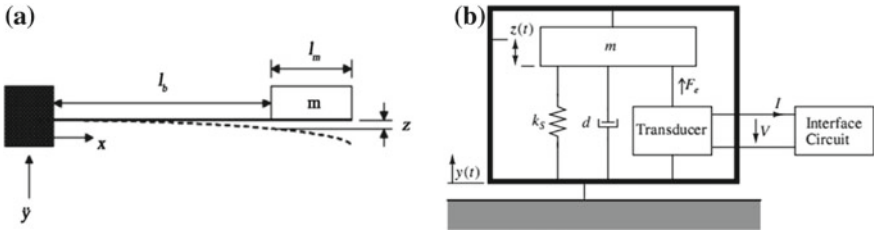

Fig. 2 Piezoelectric energy harvesting system **a** Cantilever beam-based device [3] and **b** Device equivalent mechanical model [4]

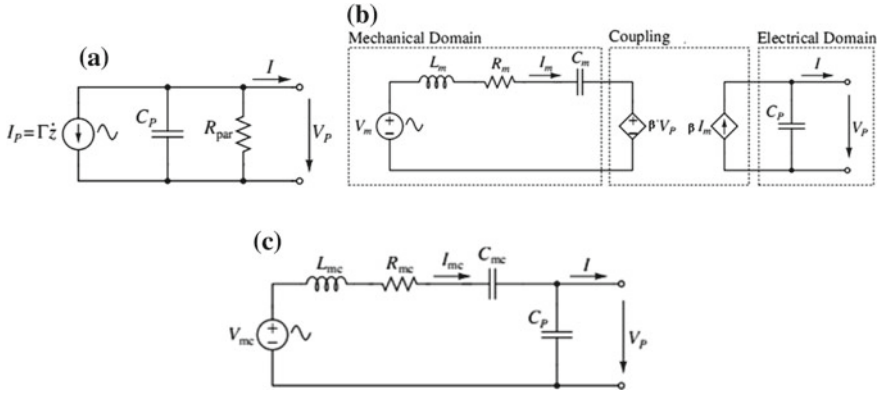

Fig. 3 Equivalent electromechanical model of piezoelectric energy harvester **a** Uncoupled [5], **b** Coupled [6], and **c** Simplified coupled [6]

$$F = k_p z + \beta V_p \tag{3}$$

$$I = \beta \frac{\mathrm{d}z}{\mathrm{d}t} - C_p \frac{\mathrm{d}V_p}{\mathrm{d}t} \tag{4}$$

where K_p and C_p, the stiffness and intrinsic capacitance of piezoelectric material, and β, the electromechanical coupling factor [4], have been expressed in Eq. (5):

$$K_p = \frac{bh}{ls_{11}^E}; C_p = \left(\varepsilon_{33}^T - \frac{\mathrm{d}_{31}^2}{s_{11}^E}\right)\frac{bl}{h}; \beta = \frac{\mathrm{d}_{31} b}{s_{11}^E} \tag{5}$$

All these parameters are dependent upon material properties. In addition, on considering force F as restoring force Fe applied on proof mass, and on substituting its value in Eq. (1), the spring-mass-damper system can be modeled by Eqs. (6) and (7).

$$ma = m\frac{\mathrm{d}^2 z}{\mathrm{d}t^2} + d\frac{\mathrm{d}z}{\mathrm{d}t} + kz + \beta V_p \tag{6}$$

$$I = \beta \frac{\mathrm{d}z}{\mathrm{d}t} - C_p \frac{\mathrm{d}V_p}{\mathrm{d}t} \tag{7}$$

where $k = k_s + k_p$ is the total stiffness of the piezoelectric cantilever beam. These two equations are enough to represent the device equivalent electrical model. From Eq. (7), an uncoupled electrical equivalent model [5] can be drawn as shown in Fig. 3a. Here, R_{par} defined the dielectric losses of piezoelectric material and its value is usually very high (> 10 MΩ). Further, input current source can be represented as

$$I_p = \beta \frac{\mathrm{d}z}{\mathrm{d}t} = a\frac{\beta m}{\mathrm{d}} \tag{8}$$

Moreover, by substituting electrical current (I_m) in place of mechanical velocity (dz/dt) in Eqs. (6) and (7), a coupled electrical equivalent model [6] can be obtained as shown in Fig. 3b. The modified equations can be expressed as

$$ma = m\frac{\mathrm{d}I_m}{\mathrm{d}t} + dI_m + k\int I_m dt + \beta V_p \tag{9}$$

$$I = \beta I_m - C_p\frac{\mathrm{d}V_p}{\mathrm{d}t} \tag{10}$$

Here, Eqs. (9) and (10) represent the mechanical and electrical equivalent parts of the cantilever beam, while dependent sources represent the coupling between them. Moreover, it can be observed in Fig. 3b that all mechanical parameters like mass, total stiffness, total damping, and alternating input force have been modeled as inductor (L_m = m), capacitor (C_m = 1/k), resistor (R_m = d), and voltage source (V_m = ma), respectively. Further, by transferring all the mechanical parameters on the electrical side, a more simplified coupled electrically equivalent model [6] can be obtained as shown in Fig. 3c, where circuit components can be expressed as

$$V_{mc} = \frac{ma}{\beta},\ L_{mc} = \frac{m}{\beta^2},\ R_{mc} = \frac{\mathrm{d}}{\beta^2},\ \text{and}\ C_{mc} = \frac{\beta^2}{k} \tag{11}$$

3 Simulations and Analysis of Different Interfacing Circuits

This section represents the coupled modeling of device uncoupled equivalent model with four interfacing circuits [7], namely, standard bridge rectifier (SBR), self-powered standard parallel and series synchronous switch harvesting on inductor (SSHI), and modified parallel SSHI (M-PSSHI) [8].

3.1 Electromechanical Model Parameters Extraction of Piezoelectric Energy Harvester

In this section, an industrial-level macroscale brass-reinforced bending actuator (Model no. T226-A4-503X) made by Piezo-systems Inc. [9] has been chosen as a harvesting device and its equivalent electromechanical model has been derived. This bending actuator constitutes two layers of piezoelectric material PZT-5A which are drawn on each side of inactive layer of brass material. Moreover, four electrode layers have been drawn on top and bottom surfaces of both piezo-layers for electrical connection purpose. Further, the one end of actuator is fixed and a proof mass has been attached on its free end. All the geometric dimensions, key parameters, and the extracted parameters of equivalent electrical model are listed in Table 1.

Table 1 Device parameters **a** Geometric dimensions and key parameters of device [9], **b** Extracted parameters

a

Parameters		Values
1. Piezoelectric layer	Length (mm)	31.6
	Width (mm)	31.7
	Thickness (mm)	0.275
2. Substrate layer	Length (mm)	53.2
	Width (mm)	31.7
	Thickness (mm)	0.126
3. Proof mass	Length (mm)	21.6
	Width (mm)	31.7
	Thickness (mm)	6.66
4. Mass of energy harvester (g)		10.5
5. Proof mass (g)		34.7
6. Base acceleration (m/s^2)		0.2
7. Effective mass (m), kg		0.414
8. Effective stiffness (k), N/m		19900
9. Coupling factor (), N/V		0.00961

b

S.no	Equivalent electrical parameters	Expression used	Values
1.	Resonant frequency (ω)	$\omega = \sqrt{\frac{k}{m}}$	219.2 rad
2.	Total Damping (d)	$d = 2m\omega\xi$	0.420
3.	Piezoelectric capacitance (C_p)	$C_p = (\varepsilon_{33}^T - \frac{d_{31}^2}{s_{11}^E})\frac{bl}{h}$	4.21×10^{-s} F
4.	Equivalent resistance	$R_e = \frac{d}{\beta^2}$	4.54 kΩ
5.	Equivalent inductance	$L_e = \frac{m}{\beta^2}$	4.48 kH
6.	Equivalent capacitance	$C_e = \frac{\beta^2}{k}$	4.64 nF
7.	Equivalent voltage source	$V_e = \frac{ma}{\beta}$	8.616 V
8.	Equivalent current source	$I_e = a\frac{\beta m}{d}$	1.89 mA
9.	Dielectric losses	$R_p = \frac{1}{\tan\xi(\omega C_p)}$	425.3 MΩ

Table 2 Performance parameters of different interfacing circuits

S. No.	Circuit techniques	Expression of optimal resistance	Optimal resistance	Output voltage	Output power
1.	SEH	$R_{opt} = \frac{\pi}{2C_p\omega}$	170.6 KΩ	100 V	60 mW
2.	P-SSHI	$R_{opt} = \frac{\pi}{(1-q_{LC})C_p\omega}$	680 KΩ	600 V	530 mW
3.	S-SSHI	$R_{opt} = \frac{\pi(1-q_{LC})}{2\omega C_p(1+q_{LC})}$	43.9 KΩ	103 V	247 mw
3.	M-PSSHI	$R_{opt} = \frac{\pi}{(1-q_{LC})C_p\omega}$	601.4 KΩ	300 V	120 mW

3.2 Coupled Modeling of Device Equivalent Electrical Model with Different Interfacing Circuits

The simulation of coupled modeling of device with SBR, P-SSHI, S-SSHI, and M-PSSHI circuits has been done in Cadence and arranged in Fig. 4a, b, c, and d, respectively.

4 Results and Discussions

The variation of voltage across piezoelectric capacitor with respect to input current for all above circuits has been shown in Fig. 5. It has been observed in Fig. 5a that in SBR technique the amplitude of piezoelectric voltage is very small and is out of phase with respect to input current, while Fig. 5b shows that P-SSHI technique increases the magnitude of piezoelectric voltage and provides zero phase difference between input current and piezoelectric voltage. Moreover, from the response of S-SSHI as shown in Fig. 5c, it has been concluded that although this technique provides zero phase difference, the amplitude of piezoelectric voltage is smaller than P-SSHI. Furthermore, it can be stated in Fig. 5d that M-PSSHI technique provides comparable response between P-SSHI and S-SSHI. Yet, it does not provide zero phase difference but it shows the advantage of increased piezoelectric voltage and reduced complexity of circuit. All these simulated results are in well correlation with the results as defined in [8]. Moreover, the performance parameters of all four circuits have been analyzed across optimal resistance [8]. The expressions and the observations have been listed in Table 2. It can be observed from Table 2 P-SSHI technique provides maximum output power and output voltage as compared to standard interface technique.

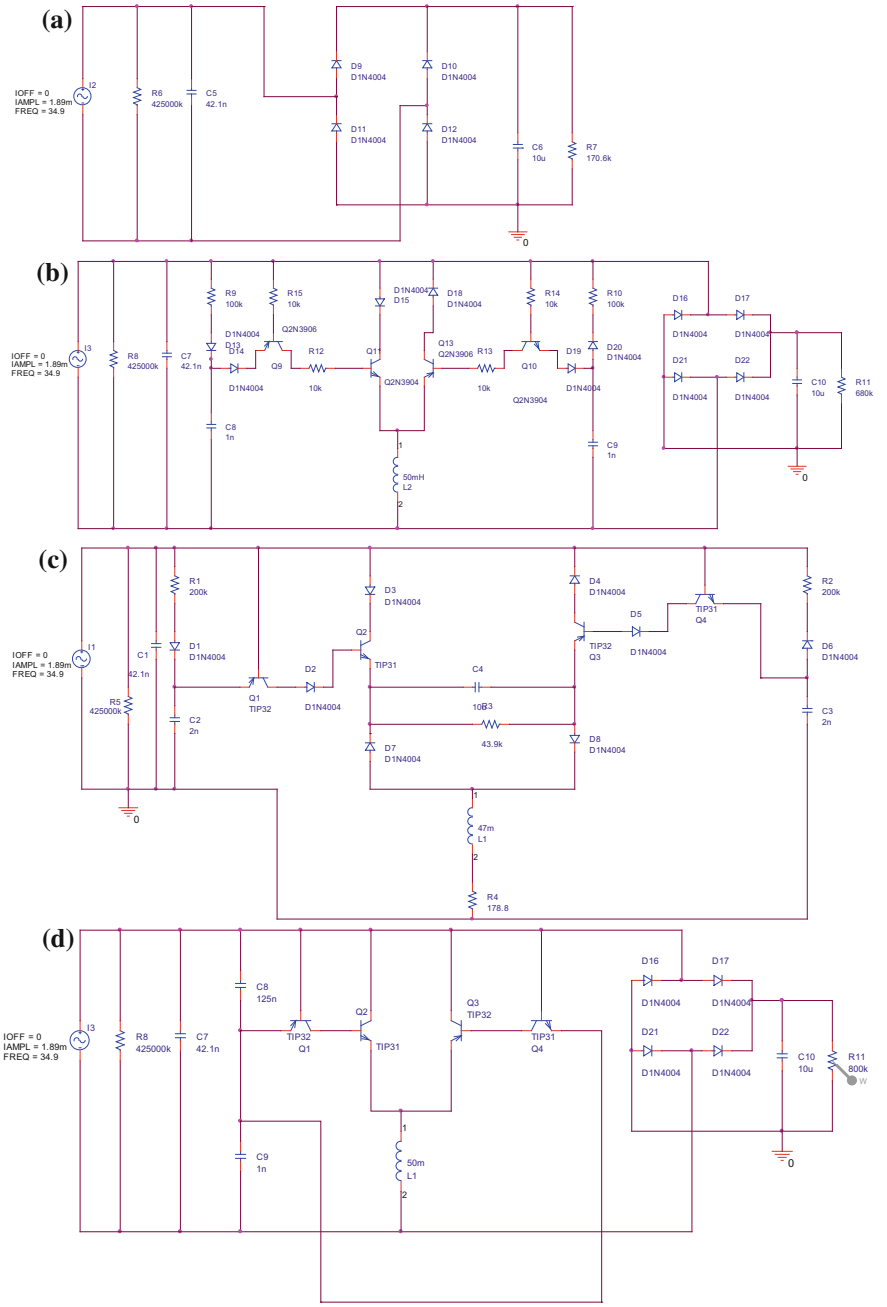

Fig. 4 Interfacing of device equivalent electrical model with different electrical circuits **a** SBR, **b** P-SSHI, **c** S-SSHI, and **d** M-PSSHI

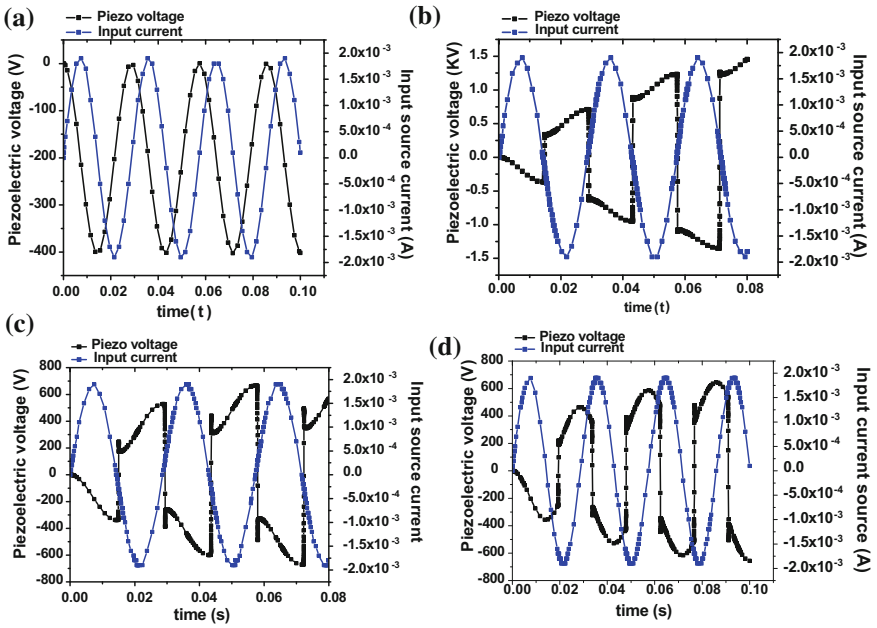

Fig. 5 The response of piezoelectric voltage with respect to input current source for different interfacing circuits **a** SBR, **b** P-SSHI, **c** S-SSHI, and **d** M-PSSHI

5 Conclusion

This paper presents a coupled modeling of piezoelectric energy harvesting device with different interfacing circuits. In this view, first a brief study of electromechanical modeling of piezoelectric energy harvesting device and of interfacing circuits has been presented. Further, an industrial-level macroscale brass-reinforced bending actuator (Model no. T226-A4-503X) has been considered as piezo-device, and its equivalent electrical model parameters have been calculated. Then, the equivalent uncoupled electrical model of this device has been interfaced with four circuits, namely, SBR, P-SSHI, S-SSHI, and M-PSSHI. Since SBR, P-SSHI, and SSHI are the standard interface circuits as defined in literature, this paper also introduced a recently developed modified parallel SSHI (M-PSSHI) circuit which uses less number of components as compared to others. Finally, the performance parameters of all four circuits have been analyzed. From the investigations, it has been observed that P-SSHI circuit provides maximum piezoelectric voltage (KV) and zero phase difference between piezoelectric voltage and input vibration current. Moreover, this technique provides maximum power (530 mW) and maximum voltage (600 V) across optimal resistance (680 K). Furthermore, from the results, it can be stated that the performance of M-PSSHI technique is in between P-SSHI and S-SSHI techniques. Although, in this technique, there exists phase difference, the values of

power (120 mW) and voltage (300 V) are considerable. Moreover, this technique has the advantage of simple circuitry and less cost as compared to others.

References

1. Yu, H., Zhou, J., Deng, L., Wen, Z.: A Vibration-Based MEMS Piezoelectric Energy Harvester and Power Conditioning Circuit: Sensors **14**(2), 3323–3341 (2014)
2. Daniels, A., Zhu, M., Tiwari, A.: Evaluation of piezoelectric material properties for a higher power output from energy harvesters with insight into material selection using a coupled piezoelectric-circuit–finite element method. IEEE Trans. Ultrason. Ferroelectr. Frequency Control **60**(12), 2626–2663 (2013)
3. Williams, C.B., Yates, R.B.: Analysis of a micro-electric generator for microsystems. Sens. Actuators A: Phys. **52**, 8–11 (1996)
4. D'hulst, R.: In Power Processing Circuits for Vibration-Based Energy Harvesters: Ph.D. thesis, KU Leuven (2009)
5. Ajitsaria, J., Choe, S.Y., Shen, D., Kim, D.J.: Modeling and analysis of a bimorph piezoelectric cantilever beam for voltage generation. Smart Mater. Struct. **16**, 447–454 (2007)
6. Kong, N., Ha, D.S., Erturk, A., Inman, D.J.: Resistive impedance matching circuit for piezoelectric energy harvesting. J. Intell. Mater. Syst. Struct. **21**(13), 1293–1302 (2010)
7. Eltamaly, A.M., Addoweesh, K.E.: A Novel Self Power SSHI Circuit for Piezoelectric Energy Harvester. IEEE Trans. Power Electron. **32**(10), 7663–7673 (2009)
8. Chen, Y.Y., et al.: Piezoelectric Power Transducers and Its Interfacing Circuitry on Energy Harvesting and Structural Damping Applications: Ph.D. thesis, NU Taiwan (2013)
9. Piezo Systems, Inc.: Piezo Systems, Inc. Catalog #8: (2011)

Variability Study Using α-Power-Based MOSFET Model for Ultradeep Submicron Digital Circuit Design

Shruti Kalra and A. B. Bhattacharyya

Abstract The device dimensions and characteristics that are assumed while designing circuits are not at all same after fabrication. These variations in itself may vary from one device to another. The varying device behavior from one copy of device to another in a particular fashion and due to a particular reason is known as variability. At an ultradeep submicron technology node where the device dimensions are approaching atomic scales, various second order variations such as dopant granularity & line edge roughness becomes significant source of variability. These types of variations are known as "atomistic" variations and are generally random in nature but the effect of these variations on adjacent devices may be correlated with each other. In this paper, statistical analysis which becomes very important for designing at ultradeep submicron technology node and lower supply voltages are performed to understand the source of variations and its impact on circuit performance.

1 Introduction

Variations in device characteristics as per their cause can be classified as:

1. Process variations
2. Environmental variations
3. Modeling variations

The above variations can vary inter-die, intra-die or as a combination of both. In an intra-die variation, two identical devices in a circuit have different characteristics whereas in an inter-die variation, two identical devices on different dies performs

S. Kalra (✉)
Jaypee Institute of Information Technology, Noida, Uttar Pradesh, India
e-mail: shruti.kalra@jiit.ac.in

A. B. Bhattacharyya
National Institute of Technology, Durgapur, Durgapur, India
e-mail: abbhattacharyya@yahoo.com

B. S. Rawat et al. (eds.), *Advances in Signal Processing and Communication*,
Lecture Notes in Electrical Engineering 526,
https://doi.org/10.1007/978-981-13-2553-3_59

differently. Thus, analyzing these variabilities and its impact on circuit performance and finally the "yield" are the major design challenges at ultradeep submicron technology nodes [1].

1.1 Variability Sources

1. Process variations: The variations due to change in process parameters such as doping and geometrical features are referred to as process variations. These occur due to the inability or the limitation of controlling fabrication process and effects the electrical behavior of the device [2].
2. Environmental variations: The changes in the nearby surroundings due to variation in temperature, power supply, switching activities etc., can effect the performance of the circuits. Variation in nearby temperature degrades the performance of devices and circuits both. Leakage currents too increase drastically with an increase in temperature leading to increase in power dissipation. This mechanism will lead to thermal runaway where the current and the temperature continuously rise till failure occurs. Lowering the supply voltage reduces the device fan out thereby reducing the risk of circuit failure [3].
3. Modeling variations: The use of inaccurate device models that do not reflect such variations perfectly is the main cause of variations due to modeling. Increasing model precision results in complex equations that are computationally inefficient. Therefore, a certain tradeoff is always required while analyzing and simulating circuits [4].

Other than abovementioned effects, other physical effects that contribute in variability analysis are: hot electron, electro-migration, Negative Bias Thermal Instability (NBTI) etc. NBTI and hot electron degrades the device performance which increases over time as it is varying the threshold voltage. Electro-migration varies the interconnect resistance to increase by decreasing the physical width. The propagation delay also increases due to increase in RC values [5].

1.2 Variability Classification

It has been discussed that while designing circuits, inter-die and intra-die variations are to be separately considered. Variations due to intra-die cause same parameter variation in two identical copy of circuits. In order to consider the atomistic variation, each device on a die requires different set of parameters. Thus, various random variables are needed. Although, the variables do depend on each other, but for simplifying simulation & analysis, we generally consider that the variables are not correlated with each other for an intra-die variations [6, 7]. It is to be noted that when the devices are kept close together in a chip, one set of parameters will be correlated

with another set. However, the degree to which the parameters are correlated and modeling this correlation are open research problems. Currently, many researchers are focusing their research on modeling since it is most importantly required for analysis and simulation. Models are already proposed in the literature defining the proximity effect [8].

Variations in the device characteristics from one die to another, from one wafer to another and from one lot to another are known as inter-die variations. Although both inter-die and intra-die variations occur on a chip, for simplifying the analysis, the intra-die variations are sometimes disregarded in order to just concentrate on inter-die variations. Intra-die variations require less number of random variables to represent the deviation from the nominal value. One of the examples of intra-die variations is the variation in the gate length produced due to varying exposure time in the fabrication process. The inter-die variations can be modeled as [9]:

$$P(i) = P_0 + \Delta P(i) \tag{1}$$

Here, P_0 is the device parameter nominal value, $P(i)$ modeled variation for the circuit i and $\Delta P(i)$ is the random variable with zero mean of the $i_t h$ sample. The random variable is assumed to have Gaussian distribution. In order to define both intra-die and inter-die variability, a parameter $P(i, x, y)$ for a coordinate (x, y) is defined as:

$$P(I, X, Y) = P_0 + \Delta P(i) + \Delta Q(i, x, y) \tag{2}$$

Here, $\Delta Q(i, x, y)$ provides (x, y) dependent random variation expressed as:

$$\Delta Q(i, x, y) = \Delta Q_s(i, x, y) + \Delta R(i, x, y) \tag{3}$$

Here, $\Delta R(i, x, y)$ is statistically independent component and $\Delta Q_s(i, x, y)$ is spatially correlated component. In this paper, an attempt has been made to study performance variability for basic CMOS inverter using updated α-power MOSFET model. α-power model is one of the most widely used short channel MOSFET model because of its simplest nature and high degree of precision. The paper is organized as follows: Sect. 2 describes the sources of variability in MOSFET. Section 3 introduces the α-power MOSFET model used for analysis. Section 4 summarizes the results obtained from Monte Carlo simulations and Sect. 5 concludes the entire paper.

2 MOSFET Variability

Atomistic variability effects become significant below 45 nm technology node and will always be present regardless of how best the circuit is made. The modeling of atomistic variability can only be done statistically. In MOSFET, there are following three forms in which atomistic variability occurs [10]:

1. Random dopant fluctuations: It refers to today's fabrication process in which very small number of dopant atoms are introduced into the silicon at very high energies. Collision and scattering of the dopant atoms will continue until the process of thermal annealing causes the dopant atoms to replace the position of silicon atoms and further diffuse their position. It is precisely impossible to control the position and the distribution of dopant atoms and therefore each device will have different distribution. With this, threshold voltages which are a function of dopant concentration will vary from one device to another. Earlier, since the dopant atoms were large, this variation was very small. In scaled devices, since the number of dopant atoms are less, incrementing or decrementing the atoms through an integer value is a discrete process instead of continuous one. Also, due to very small number of dopant atoms involved, smallest variation in this number can cause a very large variation in the performance of the device because the performance is determined by the number of carrier ratio in different channels.
2. Gate line edge roughness: It occurs at the channel junction when other materials used in lithography process cause deviation from the straight line boundaries. During the process of fabrication, photo-resist material is first spin-coated on the silicon wafer, then exposed to ultraviolet light using the photo mask and then is exposed to heat for curing the photo resist. Finally, the exposed or unexposed area of the photo resist is dissolved using a developer solution. Line edge roughness occurs at the boundary of the mask as larger grains of a material tends to dissolve more as compared to the smaller grains. Earlier, since the device dimensions were large, this effect was not at all significant but for scaled devices, the line edge roughness is the same while the other dimensions are reducing. Therefore, such variations becomes important and can vary boundaries up to 5 nm in the lithography process used today [11].
3. Oxide thickness variation: This refers to the deviation in the vertical dimension of the gate oxide thickness under the gate. The roughness at the interface of $Si - SiO_2$ and gate to SiO_2 will cause variability since only a few atoms are contributing to the thickness of SiO_2 layer.

Although much research has been done to analyze performance when the device parameters vary, some experts say that variation in the length of the gate is more critical while others say that fluctuations in the doping are critical. The performance of the device varies in an inter-die due to variation in the exposure time and intra-die due to the effect of lithography process. Variation in the gate length causes the inter-die variability whereas random doping causes the intra-die variability. Table 1 shows the measured variation in threshold voltage of 35 nm MOSFET done by [12]. It can be clearly seen from the table that the variability introduced due to random dopant fluctuations is the most significant one.

Thus, variation in the performance of a device will, in turn, affect the performance of an integrated circuit. This will reduce the overall yield and increase the manufacturing cost resulting in reduced advantage of scaling.

Table 1 Forms of atomistic variability

Fluctuation	V_{th} (mV)	σV_{th} (mV)
Line edge roughness	126	19
Random dopant fluctuation	133	33.2
Variation in oxide thickness	122	1.8
Combining dopant fluctuations and variation in gate length	126	38.7

3 CMOS Inverter Delay Based on α-Power MOSFET Model

The EKV based continuous drain current model [13] was updated to $\alpha-$power form in our earlier paper [14] where the value of α can be obtained through interpolating the currents of weak and strong inversion region for a particular technology node using BSIM simulations. Just to summarize the model, the updated α-power law-based MOSFET ON current (drain current at which gate to source voltage V_{gs} is equal to drain to source voltage V_{ds}) can be expressed as:

$$I_{ON} = I_S ln^{\alpha}\left[1 + exp\left(\frac{V_{dd} - V_{th}}{2n\phi_t}\right)\right] \tag{4}$$

Here, I_S is the specific current equal to $I_S = 2n\mu_{eff}C_{ox}\phi_t^2 W/L$, n is the subthreshold slope, C_{ox} is the oxide capacitance, μ_{eff} is the effective mobility, ϕ_t is the thermal voltage, W is the channel width and L is the effective channel length. The value of α can be obtained using interpolation of weak and strong inversion (Table 2).

The OFF current at which gate to source voltage $V_{gs} = 0$ can be expressed as [15]:

$$I_{OFF} = I_S exp\left(\frac{V_{dd} - V_{th}}{n\phi_t}\right) \tag{5}$$

By utilizing the drain current model described above, an expression for delay is determined for a CMOS inverter. To begin with, consider the instance of discharging the output capacitance with NMOS, the propagation delay t_p of a gate can be expressed as:

$$t_p = \frac{C_L V_{dd}}{I_{ON}} \tag{6}$$

Table 2 The value of α at various technology nodes at deep saturation

Technology (nm)	α (α)
32	1.088
45	1.178
65	1.261
90	1.337
130	1.395

Here, C_L is the load capacitance. I_{ON} is the ON current of NMOS. Putting the value of I_{ON} from (4)

$$t_p = \frac{C_L V_{dd}}{2n\mu_{eff} C_{ox} \frac{W}{L} \phi_t{}^2} \frac{1}{IC} \tag{7}$$

Here,

$$IC = ln^{\alpha} \left[1 + exp\left(\frac{V_{dd} - V_{th}}{2n\phi_t} \right) \right] \tag{8}$$

Load capacitance C_L corresponds to the sum of intrinsic capacitance from the driving stage and load capacitance of the fan out gates. Thus C_L is proportional to:

$$C_L \propto C_{ox} L(\xi_i W_i + W_{i+1}) \tag{9}$$

Here, ξ is the ratio of parasitic capacitance of the driver stage and input gate capacitance of the fan out. i and i + 1 are the annotations for driver and load stage respectively. Thus, W in Eq. (7) becomes W_i. Putting the value C_L in Eq. (7),

$$t_p = \frac{L^2}{2n\mu_{eff}\phi_t{}^2} \frac{V_{dd}}{IC} \frac{\xi_i W_i + W_{i+1}}{W_i} \tag{10}$$

For N number of stages along the path, the path delay can be approximated as:

$$t_{p,i} = \frac{L^2}{2n\mu eff\phi_t{}^2} \frac{V_{dd}}{IC} \sum_{i=1}^{N} \frac{\xi_i W_i + W_{i+1}}{W_i} \tag{11}$$

$$t_{p,i} = k_{pd} \frac{V_{dd}}{IC} t_{p,i}(W) \tag{12}$$

Here, k_{pd} is the technology dependent factor and $t_{p,i}(W)$ is depends on transistor size. In nutshell, delay for N stages can be often expressed in terms of average propagation delay t_p of single stage and the logic depth Ld.

$$t_{p,i} = t_p Ld$$

Generally, while designing integrated circuits, device models are verified on worstcase condition of a parameter that is varying. It is expected that if a circuit is designed under worstcase condition, it will provide higher yield. In worstcase analysis, we determine the parameter values under worstcase conditions and analyze the circuit performance. It is also to be noted that over estimating the device performance directly affects the design effort and overall cost. Designing circuits under worst case condition with statistical analysis is the most widely accepted approach nowadays because in ultradeep submicron technology node where the degree of variability is on a higher side, estimating the performance utilizing only the worstcase corner models

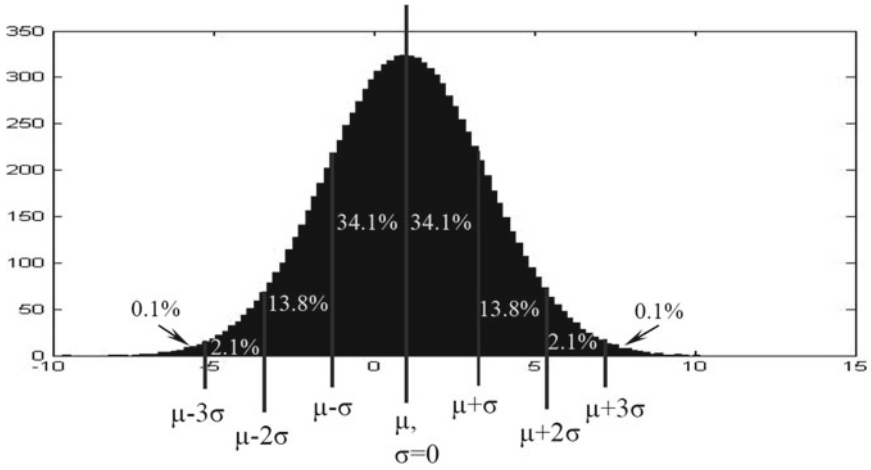

Fig. 1 Monte Carlo analysis

is unsuitable. Practically, we independently choose one variable at a time having ± 2 or ± 3 standard deviation from its mean value and having Gaussian distribution. Here, an assumption is made that the parameter variations are uncorrelated with each other. The worst case analysis is performed by introducing variations either the process parameters or in the parameters that characterize a device. Since there are numerous parameters that are used to characterize a device, more practical option is to identify the parameters whose variation causes serious consequences.

In order to illustrate the process of worstcase analysis, let us first identify one parameter whose value is varying from one die to another randomly. Its mean is μ and standard deviation is σ. Assuming no intra-die variations, the design of the circuit is done in a way ensuring variation of $\pm 3\sigma$ from the mean. That means 99% of the device copies has been taken care off while designing as shown in Fig. 1.

4 Delay Analysis Using Monte Carlo Simulations

Monte Carlo named after a famous casino represents the behavior of mathematical functions using random sampling. The behavior of Monte Carlo algorithm is pseudo-random. The term pseudo-random means that any person knowing the algorithm can predict the values of the variables generated. The process of Monte Carlo analysis is as follows [16]:

1. Determine the characteristics of the input vectors.
2. Generate random vectors by applying proper distribution.
3. Compute the behavior of the system for each of the random vectors generated.
4. Estimate the probability distribution function of the output measured.

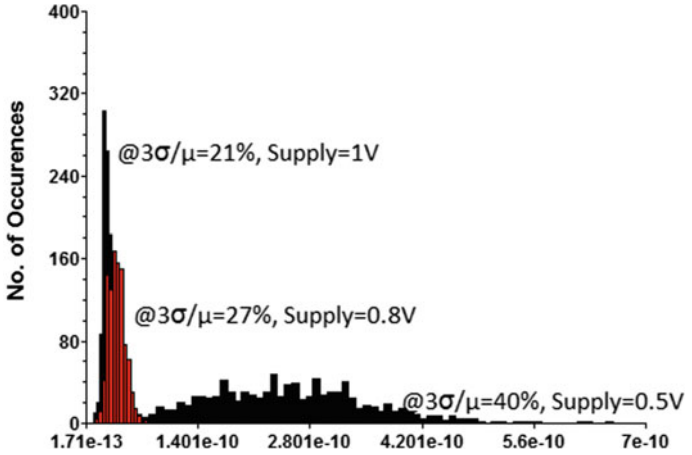

Fig. 2 Variation of single inverter delay driving the load of FO4 at 90 nm

In order to analyze the effect of variability, Monte Carlo simulations are performed using HSPICE at various technology nodes to see the effect of variation on α and in turn delay of CMOS inverter. The same analysis was repeated for the chain of 50 inverters. Figure 2 shows the variation of single inverter driving the load of FO4 at around 90 nm. It can be seen from the plot that as the supply voltage decreases, the amount of variation can go up to 40%. Figure 3 shows the variability for the chain of

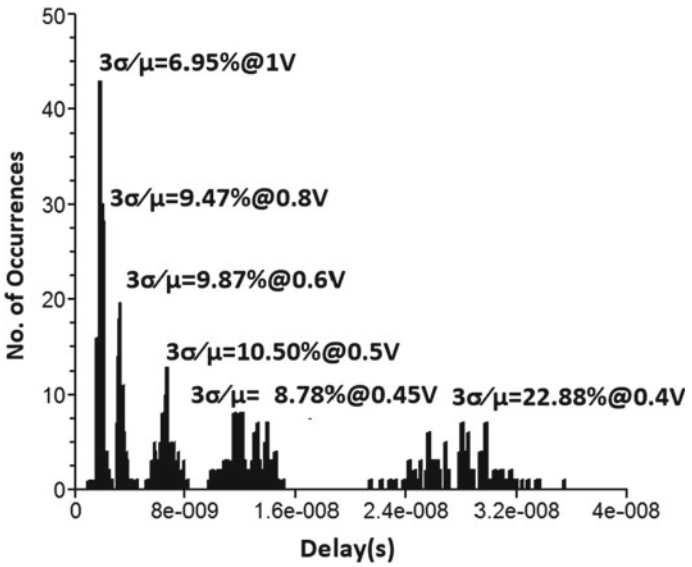

Fig. 3 Process variation for the chain of 50 inverters at 32 nm

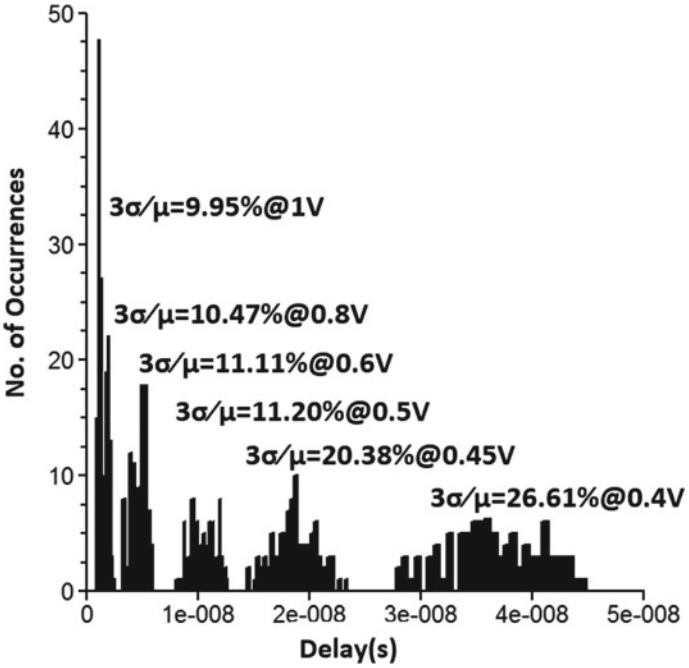

Fig. 4 Process variation for the chain of 50 inverters at 22 nm

50 inverters at 32 nm technology node and Fig. 4 shows he variability for the chain of 50 inverters at 22 nm technology node.

Following two major observations are made:

1. As the supply voltage decreases, the drain current becomes highly sensitive to change in threshold voltage since random dopant fluctuations will be a significant factor near threshold. Thus, as the supply voltage decreases, the delay variation with respect to change in process parameters increases almost exponentially.
2. As the technology scales, line edge roughness becomes significant. Thus, The amount of increase in delay variation with respect to process variation increases.

5 Conclusion

Designing circuits at lower technology nodes and lower supply voltages are efficient design techniques in terms of high throughput performance and energy consumed. Although, when the circuits are designed at lower supply voltages, they suffer from delay variations due to variability in the process parameters. Device models available in literature either can model drain current in strong inversion region or weak inversion region. But, due to the increase in demand for low power electronics, designing

near threshold moderate inversion is gaining interest to researchers. In this paper, an attempt has been made to capture the value of drain current in any of the inversion regions through mathematical interpolated value of α. The resultant drain current of different technology nodes and at different supply voltages is used to study the impact of process variations on the delay of CMOS inverter chain.

References

1. Bernstein, K., Frank, D., Gattiker, A., Haensch, W., Ji, B., Nassif, S., Nowak, E., Pearson, D., Rohrer, N.: High-performance CMOS variability in the 65-nm regime and beyond. IBM J. Res. Dev. **50**, 433–449 (2006)
2. Gerrer, L., Brown, A.R., Millar, C., Hussin, R., Amoroso, S.M., Cheng, B.: Accurate simulation of transistor-level variability for the purposes of TCAD-based device-technology cooptimization. IEEE Trans. Electron. Devices **62**, 1739–1745 (2015)
3. Li, Y., Hwang, C., Li, T.: Random-dopant-induced variability in nano-CMOS devices and digital circuits. IEEE Transactions on Electron Devices **56**, 1588–1597 (2009)
4. Jooypa, H., Dideban, D.: Impact analysis of statistical variability on the accuracy of a propagation delay time compact model in nano-CMOS technology. J. Comput. Electron. **17**(1), 192–204 (2017)
5. Mahapatra, S., Parihar, N.: A review of NBTI mechanisms and models. Microelectron. Reliab. **81**, 127–135 (2018)
6. Saha, S.: Modeling Process Variability in Scaled CMOS Technology. IEEE Des. Test Comput. (2011)
7. Asenov, A., Ding, J., Reid, D., Asenov, P., Amoroso, S., Adamu-Lema, F., et al.: Unified approach for simulation of statistical reliability in nanoscale CMOS transistors from devices to circuits. In: 2015 IEEE International Symposium on Circuits and Systems (ISCAS), pp. 2449–2452 (2015)
8. Bhushan, M., Ketchen, M.B., Polonsky, S., Gattiker, A.: Ring oscillator based technique for measuring variability statistics. In: Proceedings of the IEEE International Conference on Microelectronic Test Structures, ICMTS, pp. 87–92 (2006)
9. Agarwal, A., Blaauw, D., Zolotov V.: Statistical timing analysis for intra-die process variations with spatial correlations. In: Proceedings of the 2003 IEEE/ACM International Conference on Computer-Aided Design, pp. 900. IEEE Computer Society (2003)
10. Tudor, B., Wang, J., Chen, Z., Tan, R., Liu, W., Lee, F.: An accurate MOSFET aging model for 28 nm integrated circuit simulation. Microelectron. Reliab. **52**, 1565–1570 (2012)
11. Rathore, R., et al.: Line edge roughness induced threshold voltage variability in Nano-scale FinFETs. Superlattices and Microstruct. **103**, 304–313 (2017)
12. Roy, G., Brown, A., Adamu-Lema, F., Roy, S., Asenov, A.: Simulation study of individual and combined sources of intrinsic parameter fluctuations in conventional Nano-MOSFETs. IEEE Trans. Electron. Devices **53**, 3063–3070 (2006)
13. Enz, C., Vittoz, E.: Charge-Based MOS Transistor Modeling. Wiley, Chichester, England (2006)
14. Kalra, S., Bhattacharyya, A.: Ultra low power design for digital CMOS circuits operating near threshold. Int. J. Electron. Telecommun. **63** (2017)
15. Markovic, Dejan, C. Wang, L. Alarcon, T. Liu, and J. Rabaey: Ultralow-power design in near-threshold region. In: Proceedings of the IEEE, pp. 237–252 (2010)
16. Alexander, C.: Random-dopant-induced drain current variation in Nano-MOSFETs: a three-dimensional self-consistent monte carlo simulation study using ab initio ionized impurity scattering. IEEE Trans. Electron. Devices **55**(11), 3251–3258 (2008)

Field-Plated AlInN/AlN/GaN MOSHEMT with Improved RF Power Performance

Satya Narayan Mishra, Kanjalochan Jena, Rupam Goswami and Anand Agrawal

Abstract This paper proposes an AlInN/GaN Metal Oxide Semiconductor High Electron Mobility Transistor (MOSHEMT) employing a gate-field-plated technique with an objective to investigate the dependence of RF power performance. Detailed RF power analysis of the device is carried out using Silvaco Technology Computer-Aided Design (TCAD). Numerical simulations are carried out using nonlocal energy balance (EB) transport model. The results reveal that the gate-field-plated AlInN/GaN MOSHEMT possesses high prospects of delivering high currents and high power in microwave applications.

Keywords AlInN/GaN · Breakdown voltage · Gate field plate · MOSHEMT Cut-off frequency

1 Introduction

The physical limit and performance of silicon-based semiconductor devices in terms of power handling, breakdown voltage, high frequency, and maximum temperature of operation have reached an optimum value. Microwave power transistors are necessary component for all major aspect of human activities such as communica-

S. N. Mishra · K. Jena · R. Goswami
School of Electronics Engineering, Kalinga Institute of Industrial Technology, Bhubaneswar 751024, Odisha, India
e-mail: snmishrafet@kiit.ac.in

K. Jena
e-mail: kanjalochan.jenafet@kiit.ac.in

R. Goswami
e-mail: rupam.goswamifet@kiit.ac.in

A. Agrawal (✉)
Department of Electronics and Communication Engineering, Jaypee Institute of Information Technology, Noida 201309, Uttar Pradesh, India
e-mail: anand.agrawal@iitg.ernet.in

B. S. Rawat et al. (eds.), *Advances in Signal Processing and Communication* ,
Lecture Notes in Electrical Engineering 526,
https://doi.org/10.1007/978-981-13-2553-3_60

tion systems, entertainment, and military applications. Rapid developments in RF power electronics have exceptionally increased the need for high output power density, operating voltage, and temperature. In recent past, there have been remarkable emphases on the development of high-performance microwave transistors and amplifiers based on wide bandgap materials such as GaAs, SiC, and GaN [1, 2]. Recently, AlInN/AlN/GaN MOSHEMTs have emerged as promising devices for high-power RF/microwave applications owing to their superior properties such as large band offset between AlInN and GaN, strong spontaneous polarization effect resulting in high sheet charge density in the 2DEG, and strain-free heterojunction, minimizing the structural defects caused by the lattice mismatch [3]. Different field-plate structures including the gate field plate (FP), source FP, and double FPs were used in GaN-based heterostructures which modulate the electric field distribution along a channel, thus improving the forward off-state blocking characteristics, and hence the breakdown voltage [4–7]. This work proposes a gate-field-plated MOSHEMT device to achieve improved RF power performance which will enable the device to be extremely useful to operate with high supply voltage and harsh conditions.

Section 2 describes the structural details and modeling assumptions for TCAD numerical simulation of the proposed device. Various power-related calculations are done for the proposed device and the results are discussed in Sect. 3. Section 4 draws the conclusions of this work.

2 Proposed Device and Simulation Setup

The structure of a field-plated AlInN/AlN/GaN MOSHEMT whose RF power performance is compared with a conventional MOSHEMT is shown in Fig. 1. A MOSHEMT without any field-plate structure is also simulated as reference. The schematic diagram shown in Fig. 1 is a field-plated MOSHEMT with a gate length of 1 μm, separation of 13 μm between the source and the drain, and of 2 μm between the source and the gate.

The detailed numerical simulations are done on 2D TCAD Silvaco simulator [8] using the nonlocal energy balance (EB) transport model. The physics-based models used to simulate the operation of MOSHEMT consist of Poisson's equation, Maxwell's laws, continuity equations, and mathematical representation of the nonlocal energy balance (EB) transport model. Several significant physical effects are considered, which include narrowing of the band gap, electric field-based mobility, and spontaneous and piezoelectric polarizations. The doping concentrations of AlGaN and GaN layers are considered as 10^{15} and 10^{13} cm^{-3}, respectively. The mobility of electrons in the GaN buffer is taken to be 1600 cm^2/Vs. The net interface charge at AlN/GaN arising out of spontaneous and piezoelectric polarizations is taken into account by employing positive sheet charge $= 10^{13}$ cm^{-2}. Approximately, nine large signal input amplitudes have been defined using WAVEFORM statement. The Ni gate is supplied with each of these waveforms in order of its amplitudes using the LOOP statement. EXTRACT statement is used to calculate a number of

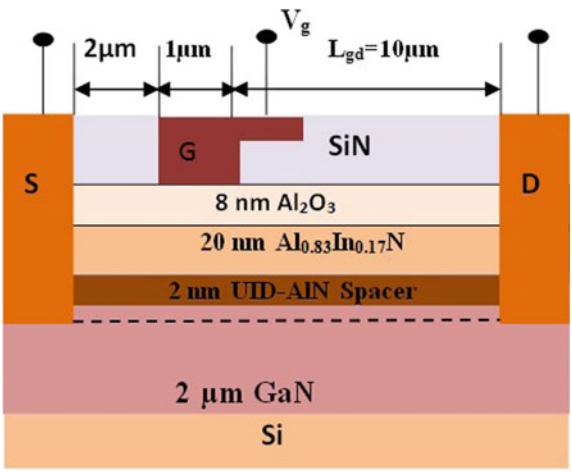

Fig. 1 Schematic diagram of a field-plated AlInN/AlN/GaN MOSHEMT

large signal parameters. After each waveform simulation is complete, a number of large signal parameters are calculated using a number of EXTRACT statements. Exact time at which the peak voltages occurred is determined by extracting the peak voltages (both input and output). To calculate the correct power, both currents and voltages are extracted at a time when peak voltage occurs so that the phase between current and voltage can be taken into account.

3 Results and Discussion

In this subsection, the effects of field plates on small output power, efficiency, and cut-off frequency are presented. The requirements for high power and high frequency are large breakdown voltage and high electron velocity. The wide bandgap of AlInN in addition to the field-plate architecture leads to higher breakdown voltages because the ultimate breakdown field is measured at the value which band-to-band impact ionization occurs. The high breakdown electric field reduces the need for voltage conversion and provides the potential to derive high efficiency, an important parameter for amplification [9, 10].

Figure 2 shows the power sweep of AlInN/AlN/GaN MOSHEMT without a field plate, which exhibits a maximum power gain of 12.9 dB. When the peak power-added efficiency (PAE) is 17.43%, the device provides an output power of 31.45 dBm and a power gain of 10.96 dB. The output power characteristics were measured at 10 GHz with a drain bias of 30 V and gate voltage of −2 V.

By including a gate field plate, a maximum power gain of 16.21 dB is obtained as shown in Fig. 3. When the peak power-added efficiency is 64.87%, the transistor has an output power of 36.69 dBm and a power gain of 15.69 dB. The DC current gain of a MOS transistor is not a realizable quantity and is not used in practice because the

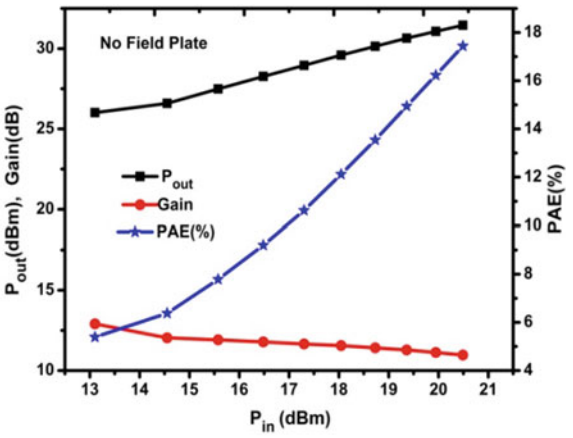

Fig. 2 Power output, gain power, and PAE of AlInN/AlN/GaN MOSHEMT

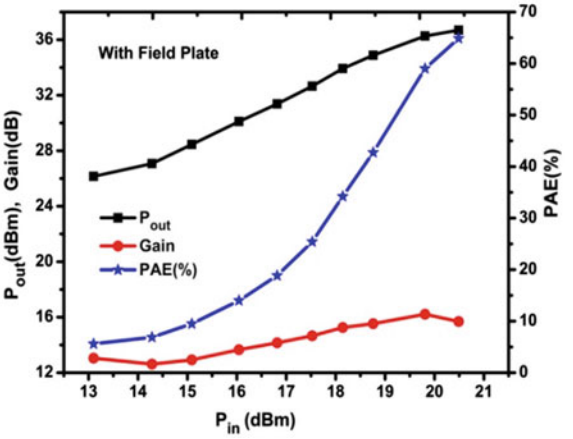

Fig. 3 Power output, gain power, and PAE of AlInN/AlN/GaN MOSHEMT with gate field plate

gate current is ideally zero. Even under practical scenario, the gate current is very less. When high frequency is applied to the MOS transistor, the incremental current is said to enter at the input of the device through the high-frequency capacitances, and this gives a value of current gain. A very important parameter that gives the information about the speed of the device is the unity gain frequency or the unity current gain cut-off frequency.

Figure 4 shows the comparative current gains for the two structures, i.e., one without field plate and other with the field plate. To extract the unity gain cut-off frequency, a horizontal line from the 0 dB point in the Y-axis is drawn, and thereafter, a vertical line is drawn from the intersection point. These two vertical lines intersect the frequency axis at unit-gain frequency. It is observed that for the non-field-plated device, the f_t is 6 GHz, and that for the field-plated device, it stands at about 50 GHz.

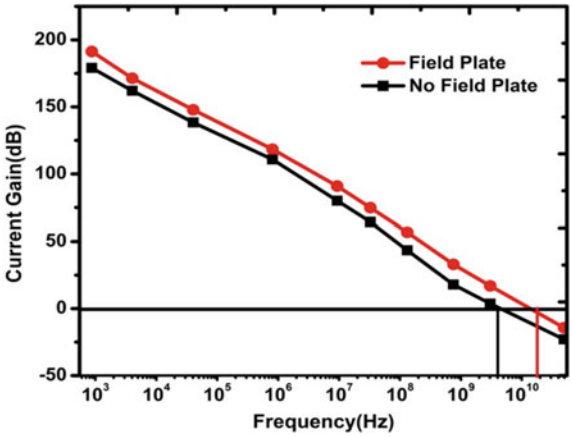

Fig. 4 Current gain as a function of frequency for AlInN/AlN/GaN MOSHEMT with and without field plate

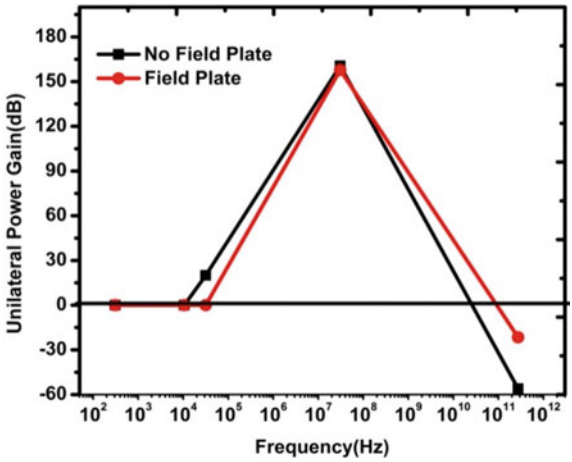

Fig. 5 Curve showing unilateral power gain for the device with and without field plate

Unilateral power gain is one of the figures of merits defining the maximum oscillating frequency of the transistor. In other words, it is defined as the frequency up to which the transistor has a gain or a fundamental frequency up to which the transistor acts like an amplifier. The maximum oscillating frequency (f_{max}) is found to be 65 GHz for non-field-plated device, and 200 GHz for field-plated device as shown in Fig. 5.

Stern stability factor is a figure of merit which is used to check the stability of a transistor. This stability factor is calculated for both the structures as shown in Fig. 6. For values greater than 1, the circuit is stable for those values of input and output impedances. For values lesser than 1, the circuit has instability and is likely to oscillate at some frequency. It is found that the field-plated device shows instability as compared to the device without field plate. So, the field-plated device is very useful for high-frequency operation but also introduces an instability as compared to

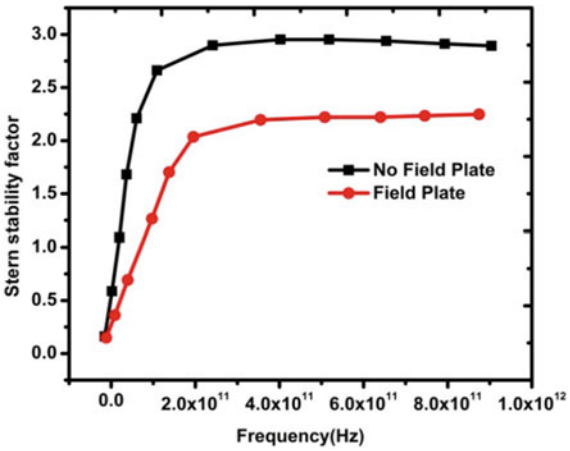

Fig. 6 Stern stability factor for MOSHEMT with and without field plate

non-field-plated device. The above results show a potential application of the gate-field-plated AlInN/GaN MOSHEMT to deliver maximum output power at microwave frequency range.

4 Conclusion

A systematic study has been performed to analyze the large signal output power analysis of the proposed field-plated AlInN/AlN/GaN device by simulating a typical 10 GHz large signal input and measured P_{out} (output power), gain, and PAE (power-added efficiency). TCAD simulation results reveal that the FP design can realize the possibility of achieving both high breakdown voltage and high cut-off frequency and oscillating frequency.

References

1. Colangeli, S., Bentini, A., Ciccognani, W., Limiti, E., Nanni, A.: GaN-based robust low-noise amplifiers. IEEE Trans. Electron Devices **60**(10), 3238–3248 (2013)
2. Jung, S.-C., Hammi, O., Ghannouchi, F.M.: Design optimization and DPD linearization of GaN-based unsymmetrical doherty power amplifiers for 3G multicarrier applications. IEEE Trans. Microw. Theory Tech. **57**(9), 2105–2112 (2009)
3. Jena, K., Swain, R., Lenka, T.R.: Physics-based mathematical model of 2DEG sheet charge density and DC characteristics of AlInN/AlN/GaN MOSHEMT. Int. J. Numer. Model. **30**(1) (2017)
4. Jena, K., Swain, R., Lenka, T.R.: Impact of a drain field plate on the breakdown characteristics of AlInN/GaN MOSHEMT. J. Korean Phys. Soc. **67**(9), 1592–1596 (2015)
5. Wei, M., Cui, Y., Yue, H., et al.: Development and characteristic analysis of a field-plated Al_2O_3/AlInN/GaN MOS HEMT. Chin. Phys. B **20**(1), 0172031–0172035 (2011)

6. Lei, Z.S., Yuan, W., Xiao-Lei, Y., Yu, L.Z., Chong, W., Cheng, Z.J., Hua, M.X., Yue, H.: Reverse blocking enhancement of drain field plate in Schottky-drain AlGaN/GaN high-electron mobility transistors. Chin. Phys. B **23**(9), 097305-1–097305-5 (2014)
7. Hwang, K., Tong, E.K.: Semiconductor devices having improved field plates. U.S. Patent 7498223, 1 Apr 2005
8. Silvaco Inc.:http://www.silvaco.com/examples/tcad/section21/example11/index.html. Accessed 16 Jan 2018
9. Cho, K.H., Kim, Y.S., Lim, J., Choi, Y.H., Han, M.K.: Design of AlGaN/GaN HEMTs employing mesa field plate for breakdown voltage enhancement. Solid-State Electron. **54**, 405–409 (2010)
10. Mishra, U.K., Shen, L., Kazior, T.E., Wu, Y.-F.: GaN-based RF power devices and amplifiers. Proc. IEEE **96**(2), 287–305 (2008)

Analysis of RSNM and WSNM of 6T SRAM Cell Using Ultra Thin Body FD-SOI MOSFET

Vimal Kumar Mishra, Narendra Yadava, Kaushal Nigam, Bajrang Bansal and R. K. Chauhan

Abstract The read and write stability of SRAM cell depends on the high-performance CMOS technologies (FD-SOI technology), due to low power dissipation, and high switching and inter-die variability. This paper first analyzed the electrical behavior of ultrathin body fully depleted silicon-on-insulator (UTB FD-SOI) MOSFET. It is demonstrated that the FD-SOI MOSFET has high I_{on} to I_{off} ratio (better switching) and low threshold voltage. By taking into account of high switching of UTB FD-SOI MOSFET, it is further used to form a 6T SRAM cell. The read and write behavior of 6T SRAM cell has been studied using the read static noise margin (RSNM) and write static noise margin (WSNM). It is observed that the results obtained from the behavior of SNM show that the design of SRAM cell is more robust and highly stable. Further, the results were compared and contrasted with the reported literature, i.e., FinFET- and SOI MOSFET-based SRAM cell. The structures were designed and simulated using Synopsys TCAD device simulator.

Keywords SRAM · SNM · Switching and UTB FD-SOI MOSFET

V. K. Mishra (✉) · K. Nigam · B. Bansal
Department of Electronics and Communication Engineering,
Jaypee Institute of Information Technology, Noida, India
e-mail: vimal.mishra34@gmail.com

K. Nigam
e-mail: kaushal.nigam@jiit.ac.in

B. Bansal
e-mail: bajrangbnsl@gmail.com

N. Yadava · R. K. Chauhan
Department of Electronics and Communication Engineering, Madan Mohan
Malaviya University of Technology, Gorakhpur, India
e-mail: narendrayadava5@gmail.com

R. K. Chauhan
e-mail: rkchauhan27@gmail.com

B. S. Rawat et al. (eds.), *Advances in Signal Processing and Communication* ,
Lecture Notes in Electrical Engineering 526,
https://doi.org/10.1007/978-981-13-2553-3_61

1 Introduction

In the last four decades, the semiconductor industry has shown an incredible pace of improvement in electronic products. The semiconductor industry has an impact on every aspect of life from military applications to consumer products, from electronic voting machines to personal communication devices, thousands of microwave antennas to the simple wireless TV remote. All these trends have been possible due to the industry's ability to reduce the minimum feature size used to produce integrated circuits. The decreasing cost per function with increased productivity and better quality of computing, communication, made possible the current pace of development [1].

Almost all of these applications need information stored in one form or another. The semiconductor memory array can store large quantities of data, and hence are necessary for all digital systems. The ever-increasing need for information storage is driving memory design to more compact design and higher density data storage. The storage capacity of memory arrays approximately doubles every year (Moore's law). The area efficiency, memory access time, and dynamic and static power consumption are some of the important performance criteria that dictate the design consideration of the memory array. The fundamental component of any memory array consists of MOS-based devices in particular, and these devices are part of any CMOS configuration; therefore, to study the impact on any electronic system, it is necessary to work on the fundamental component of memory, i.e., MOS transistors.

Over recent years, the scaling in CMOS technology has been very aggressive. With ultrathin dimensions, the technology is facing many critical challenges and reliability issues. Aggressive scaling has resulted in the augmentation of many challenges in MOS transistors [2].

The challenges associated with current MOS technology are its drain-induced barrier lowering, V_{th} roll-off, off-state leakage current, parasitic capacitances, and resistances that severely limit the performance of these devices.

To overcome these issues, the new device architecture has been proposed by several researchers of which some of the designs were based on multigate MOSFETs (FinFET) [3], FD and PD silicon-on-insulator (SOI) MOSFETs [4, 5], TBRS FD-SOI MOSFET [6], MS FD-SOI MOSFET [7], and junctionless MOS transistors [8]. Of these devices, the FD-SOI MOSFETs have been considered as an alternative to conventional bulk MOS transistors and FinFET in the design of the memory array, particularly SRAM cell. Further, the scaled-down FD-SOI MOSFET formed the ultrathin body (UTB) FD-SOI MOSFET [9].

In the UTB FD-SOI MOSFET, because of a thin film of the silicon layer, space charge is well controlled by the gate rather than the drain. The inverse subthreshold slope of UTB FD-SOI is lower, I_{on} to I_{off} ratio is higher, and threshold voltage is lower which result in high switching. Due to high switching in the UTB FD-SOI MOSFET, the SRAM cell constitutes with UTB FD-SOI MOSFET and forms the better read and write stability.

In this paper, first, study the electrical behavior of UTB FD-SOI MOSFET. Afterward, the UTB FD-SOI MOSFET-based 6T SRAM cell has been studied. For stabil-

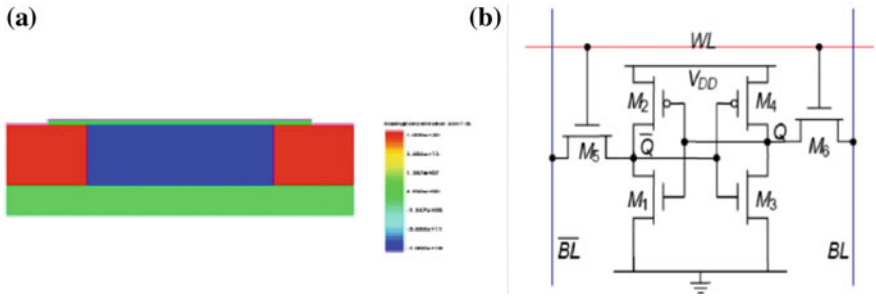

Fig. 1 **a** Device design of n- and p-UTB FD-SOI MOSFET **b** The 6T SRAM cell circuit configuration

ity, the static noise margin (SNM) of SRAM cell has been taken. The read and write SNM of 6T SRAM cell has also been obtained and then compared with the conventional MOS and FD-SOI MOS-based SRAM cell. The device design and 6T SRAM simulations were performed using mixed-mode simulation in TCAD simulator, i.e., Sentaurus and Cogenda device simulators.

2 Device Structure and Specifications

The architecture of static random access memory (SRAM) has been mostly used due to low power dissipation, robust design, and less chip area. The circuit configuration of most popular 6T SRAM cell is shown in Fig. 1b. The basic component transistor that has been used in SRAM cell is UTB FD-SOI MOSFET. Figure 1a shows the device design and meshing of n- and p-type UTB FD-SOI MOSFET at 50 nm gate length. The UTB FD-SOI MOSFET has been optimized using Sentaurus device simulator [10]. The physics models that have been included in the TCAD simulator are the Shockley–Hall–Read, band-to-band tunneling, quantum potential, mobility, drift-diffusion model, and Auger recombination. Further, the 6T SRAM cell circuit configuration is formed using the mixed-mode simulation.

3 Results and Discussions

The fundamental block of any 6T SRAM consists of a latch with two stable operating states as shown in Fig. 1b. This component is also termed as a 1-bit SRAM cell. The latch circuit can be designed using different types of inverter circuits such as n-MOS inverter, resistive load inverter, etc. These inverter circuits are associated with problems related to area consumption, power dissipation, and voltage swing. The use of such inverter circuits therefore increases the power dissipation in SRAM

cells. Noise margin also gets affected, specifically the static noise margin (SNM). To overcome these issues, CMOS inverter circuit has been used. It consists of one n-MOS (pull-down) and one p-MOS (pull-up) device. The CMOS inverter circuit also shows the low power dissipation and high noise margin (NM). Therefore, CMOS-based inverter circuits are preferred for the design of 1-bit SRAM cell. The 1-bit cell shown in Fig. 1b consists of two cross-coupled CMOS inverters. This 1-bit SRAM cell is driven by two n-MOS (access) transistors. Depending on the potted state of the latch, the data being held in the bit cell will be interpreted either as logic "0" or as logic "1".

The read and write operations on the data contained in the memory cell are done through the bitline (Bl and Blb). The memory cell is controlled by the corresponding wordline (Wl). The two access switches consisting of n-MOS pass transistors are used to connect the 1-bit SRAM cell to the bitlines.

The performance of 1-bit SRAM cell depends on the electrical performance of the CMOS inverter circuit. To have a better response, one has to design the circuit for desired threshold voltage (Vm), sharp voltage transfer characteristics (VTC) curve, and minimum transient delay. The access transistor also plays an important role to access the data from the latch circuit. So, for fast read and write operations in the SRAM cell, the access transistor should have high I_{on} to I_{off} ratio, minimum threshold voltage, low subthreshold slope, and minimum DIBL [3]. To achieve these issues with the device, several configurations have been proposed in the literature [3–7]. Effort has been made in this work also to have a better electrical performance of CMOS inverter circuits using various types of new n- and p-type MOS transistors. For this, the transistor that has been used to form 6T SRAM cell is UTB FD-SOI MOSFET. The input characteristic curve of UTB FD-SOI MOSFET is shown in Fig. 2. Owing to the insulator (SiO_2) region at the bottom of the silicon region, it causes the reduction in leakage current, and therefore the off-state current has reduced. The high-K (HfO_2) is being used as the gate oxide to reduce leakage tunnel current from UTB to gate. The lombarity mobility model is used for studying the behavior of high-K in TCAD. Hence, use of high-K as a front gate oxide and the use of SiO_2 as a bottom oxide reduce the overall leakage current which help to reduce the off-state current. The off-state current observed from the curve is 10e-11 A and on-state current observed is 1 mA; hence, the I_{on} to I_{off} ratio is 10^9 which shows that the device has high switching. This high switching behavior due to high I_{on} to I_{off} ratio offers to achieve improvement in both read and write stability of 6T SRAM cell.

6T SRAM cell, as shown in Fig. 1b, can be accessed using bitlines to read and write data operation. Data is stored as 1 or 0 as one of the two metastable states at Q and Qb.

In the current technology node beyond 100 nm, the data retention is the major functional challenge for the SRAM cell due to leakage current, increasing variability, and supply voltage scaling. Therefore, the stability of SRAM cell is determined by the static noise margin (SNM) [1]. It is defined that the SRAM cell tolerated the maximum DC noise voltage without affecting the stored data bit [9, 11]. However, it is observed by the graphical method, i.e., butterfly curve [1]. The SNM of both

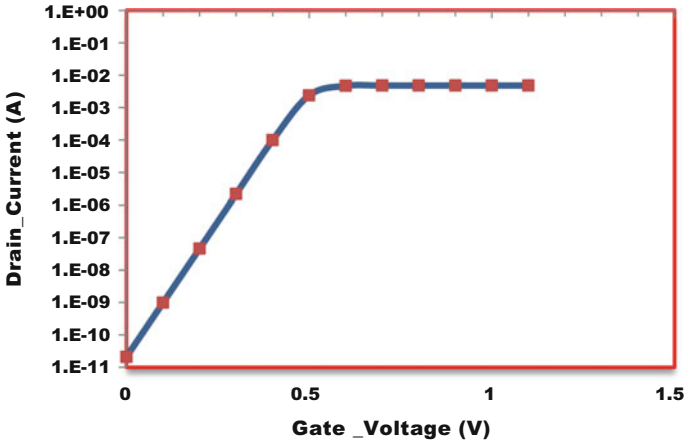

Fig. 2 Transfer characteristic of UTB FD-SOI MOSFET

transfer characteristic curves is obtained by the square fitting method, that is, the largest square is being fitted between the overlapped transfer characteristic curves obtained from the CMOS inverter circuit as shown in Fig. 3. The performance of stability is also determined by the properly matched aspect ratio between the pull-down and pull-up transistor of the SRAM cell. The ratio should also be maintained between the access transistor of n-MOS and p-MOS transistor of the CMOS latch circuit [1]. If the ratio is not properly matched, then the metastable point of the SRAM cell is vulnerable. As a result, the asymptotical limit for the SNM of SRAM cell is determined and the maximal square side is obtained due to the threshold voltage of CMOS inverter circuit at half of the supply voltage, i.e., ½ V_{dd}.

The SRAM cell has three working modes: (1) Read stability, (2) write ability, and (3) hold analysis [12]. The read and write stability of SRAM cell is major concern for the researchers; therefore, in this work, the focus is on the working of read stability and write ability.

In the read operation, both the bitlines are pre-charged and kept floating when wordline is asserted, node storing 0 pulls the related built-in (Bl/Blb) down through the access transistor and pull-down transistor and the other bitline will remain pre-charged; hence, the data stored is read by bitlines in the form of the voltage level of bitlines. As discussed above, it is important to avoid cell flipping (destruction of saved data) while reading operation so that the strength of the pull-down n-MOS transistor is more than that of the access n-MOS transistor for proper read operation.

For write operation, i.e., Data 0 or 1 being written in the memory cell, the data to be written is given on bitline and inverted data is given to bitline bar. So, to write 0, bitline is given 0 and bitline bar is given 1 (vice versa, to write 1, bitline is given 1 and bitline bar is given 0) and then wordline is applied at input of passgates. If write 0 is performed and memory cell already has 0 as stored data, then no discharging of bitline takes place (same for write 1 operation and data 1 already stored). But if write

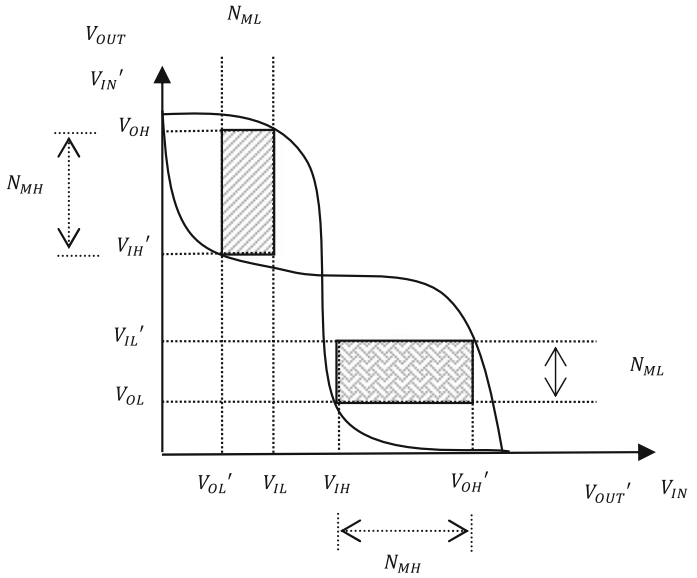

Fig. 3 Butterfly curve for measurement of SNM of SRAM using graphical method

0 operation is intended and cell contains 1 as stored data, then bitline will discharge node storing 1 through the connecting access transistor, and the pull-up transistor of opposite node will pull it up to 1 as inverters are cross-coupled. Here, it is important to have a correct write operation (i.e., data overwrite operation) that the strength of access n-MOS transistor is more than the pull-up p-MOS transistor. Hence, strong access transistors are required for desired write operation.

The UTB FD-SOI MOSFET exhibits higher I_{on} to I_{off} ratio that improves the performance metrics of 6T SRAM cell. As the UTB FD-SOI MOSFET has lower threshold voltage, it improves the noise margin (NM) of the inverter circuit which improves the stability in terms of SNM of the 6T SRAM cell formed by the device.

The supply voltage scaling is the effective way to reduce leakage current. Supply voltage scaling is challenging to the noise immunity. So, the effect of supply voltage scaling on the SNM of SRAM cell is of major concern for studying the electrical behavior. Figure 4a, b shows the effect of scaling of supply voltage on the RSNM and WSNM, respectively. Figure 4a shows that as the voltage scale-down the RSNM has decreased. The highest and lowest RSNM perceived from the figure are 315 mV and 60 mV at 1.1 V and 0.3 V supply, respectively. Similarly, Fig. 4b shows the effect of scaling of supply voltage on the WSNM. From the figure, it is observed that the highest and lowest WSNM are 380 mV and 90 mV at 1.1 V and 0.3 V, respectively.

Design of SRAM using the UTB FD-SOI MOS device improves the SNM consistently when compared with the conventional MOSFET and FD-SOI MOSFET as shown in Fig. 5a, b. Figure 5a shows the comparative bar chart of read static noise margin (RSNM) between the conventional MOS- and FD-SOI MOS-based

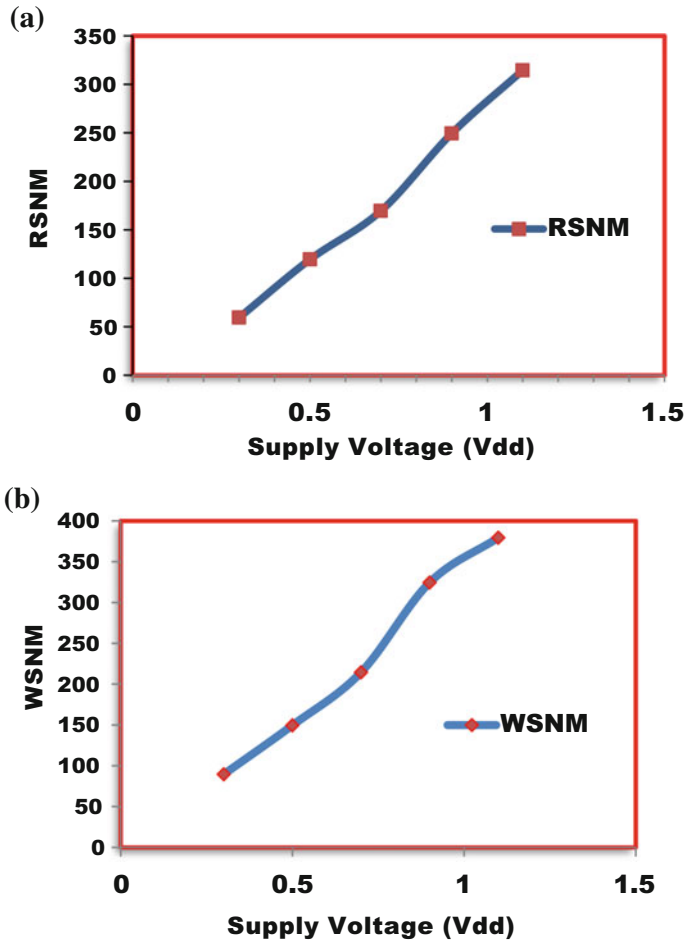

Fig. 4 SNM: **a** Read static noise margin (RSNM), **b** Write static noise margin (WSNM) of UTB FD-SOI MOSFET-based 6T SRAM cell for various supply voltages

SRAM cell with the UTB FD-SOI MOSFET-based SRAM cell. The UTB FD-SOI MOS-based 6T SRAM cell shows improvement in RSNM. Figure 5b shows the comparative bar chart of write static noise margin (WSNM) between the conventional MOS- and FD-SOI MOS-based SRAM cell with the UTB FD-SOI MOSFET-based SRAM cell. The UTB FD-SOI MOS-based 6T SRAM cell shows improvement in WSNM.

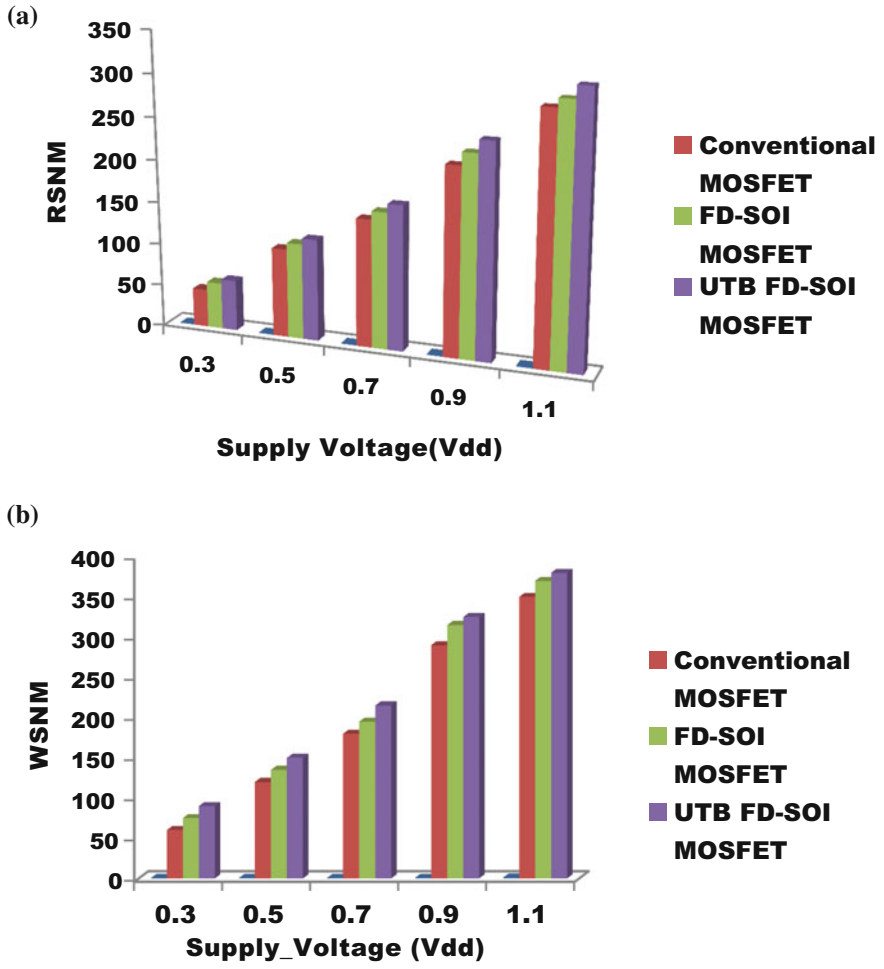

Fig. 5 Comparison between **a** Read static noise margin (RSNM), **b** Write static noise margin (WSNM) of UTB FD-SOI MOSFET-based 6T SRAM cell with the conventional MOSFET and FD-SOI MOSFET-based 6T SRAM cell

4 Conclusions

In this work, first we discussed the electrical behavior of UTB FD-SOI MOSFET. The device behavior perceived low off-state current (10^{-11} A) and high I_{on} to I_{off} ratio (10^9), and application of these devices in 6T SRAM cell has been analyzed using mixed-mode simulation in Sentaurus TCAD device simulator. Further, the read stability and write ability of 6T SRAM cell is analyzed. It was found that the RSNM and WSNM of the SRAM cell increase as the supply voltage increases. The highest RSNM and WSNM were 315 mV and 380 mV at 1.1 V, respectively. It

was also observed that the RSNM and WSNM of UTB FD-SOI MOSFET-based 6T SRAM cell were better when compared to conventional MOSFET and FD-SOI MOSFET.

References

1. Andrei, P., Sachdev, M.: CMOS SRAM Circuit Design and Parametric Test in Nano-Scaled Technologies. Springer (2008)
2. International Technology Roadmap for Semiconductors, Edition of ITRS. (2016)
3. Ebrahimi, B., Zeinolabedinzadeh, S., Kusha, A.A.: Low Standby power and robust FinFET based SRAM design. In: Symposium on VLSI, ISVLSI'08. IEEE Computer Society Annual, pp. 185–190. IEEE (2008)
4. Mishra, V.K., Chauhan, R.K.: Performance analysis of fully depleted ultra thin body (FD UTB SOI MOSFET) based CMOS inverter circuit for low power digital applications. In: Advances in Intelligent System and Computing, pp. 375–382 (2016)
5. Cheng, K.G., Khakifirooz, A.: Fully depleted SOI (FDSOI) technology. Sci. China Inf. Sci. **59**, 1–15 (2016)
6. Mishra, V.K., Chauhan, R.K.: Performance analysis of fully depleted SOI tapered body reduced source (FD-SOI TBRS) MOSFET for low power digital applications. Adv. Intell. Syst. Comput. 361–368 (2017)
7. Mishra, V.K., Chauhan, R.K.: Performance analysis of modified source and tunnel diode body contact based fully-depleted silicon-on-insulator MOSFET for low power digital applications. J. Nanoelectron. Optoelectron. 12, 59–66 (2017)
8. Singh, J., Sahu, C.: Device and Circuit Performance Analysis of Double Gate Junctionless Transistors at Lg = 18 nm, pp. 1–6 (2014)
9. Pi-Ho Hu, V.: Reliability-tolerant design for Ultra-Thin-Body GeOI 6T SRAM cell and sense amplifier. IEEE J. Electron. Devices Soc. **99** 107–111 (2017)
10. Guide, S.D.U.: Mountain View. Synopsys Inc, CA (2010)
11. Grosser, E., Stucchi, M., Maex, K., Dehane, W.: Read stability and write-ability analysis of SRAM cells for nanometer technologies. IEEE J. Solid-State Circuits **41**, 2577–2588 (2006)
12. Mazurier, J., Weber, O., Andrieu, F., Toffoli, A., Rozeau, O., Poiroux, T., Allain, F., Perreau, P., Beranger, C.F., Thomas, O., Belleville, M., Faynot, O.: On the Variability in Planar FDSOI Technology: From MOSFETs to SRAM Cells. vol. 58. IEEE Transactions on Electron Devices, (2011) 2326–2337